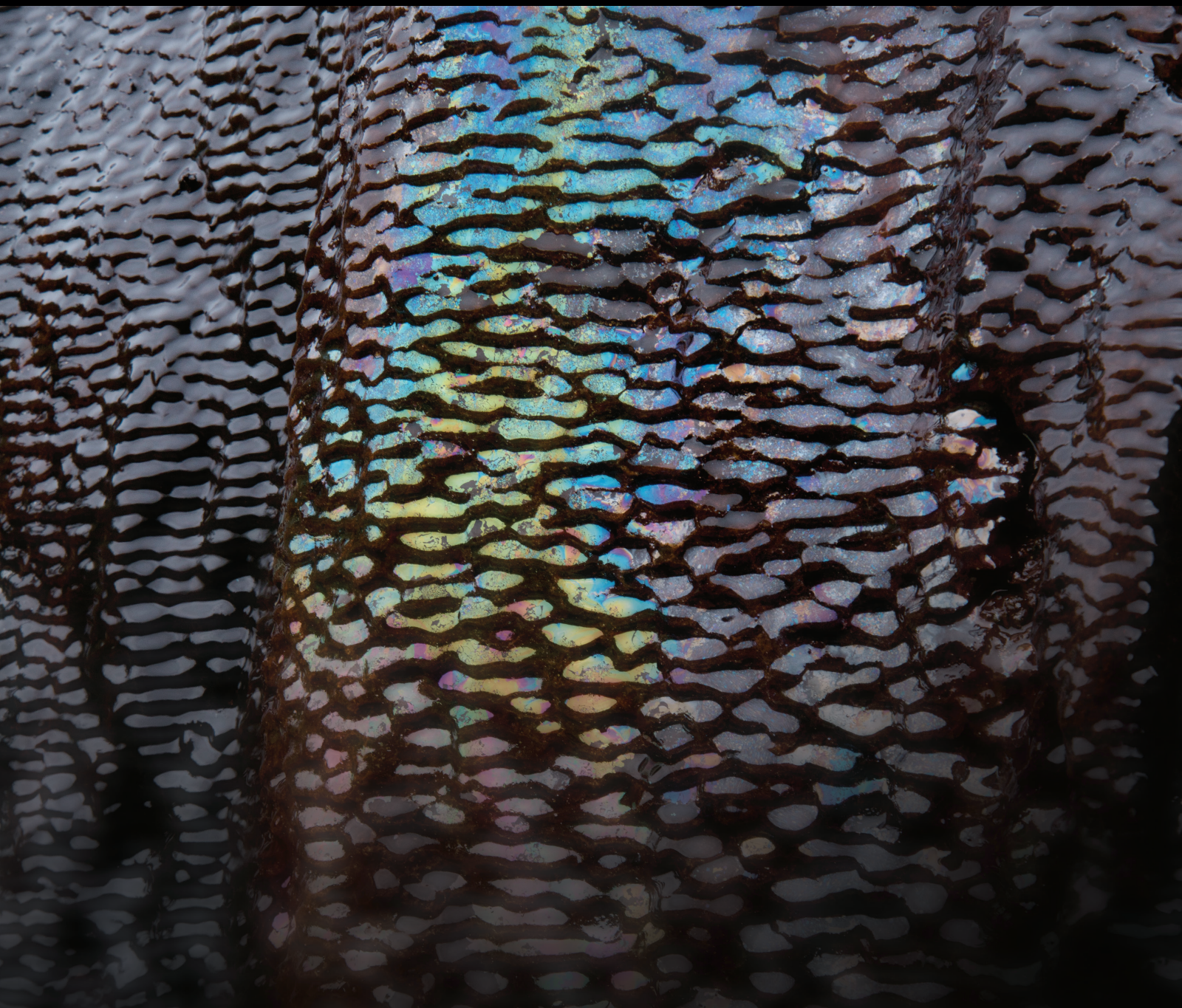


Flow and Transport in Porous Media: A Multiscale Focus

Lead Guest Editor: Amgad Salama

Guest Editors: Shuyu Sun, Mohamed El Amin, Yi Wang, and Kundan Kumar






Flow and Transport in Porous Media: A Multiscale Focus

Geofluids

Flow and Transport in Porous Media: A Multiscale Focus

Lead Guest Editor: Amgad Salama

Guest Editors: Shuyu Sun and Kundan Kumar



Copyright © 2017 Hindawi. All rights reserved.

This is a special issue published in "Geofluids." All articles are open access articles distributed under the Creative Commons Attribution License, which permits unrestricted use, distribution, and reproduction in any medium, provided the original work is properly cited.

Editorial Board

Mauro Cacace, Germany
Timothy S. Collett, USA
Cinzia Federico, Italy
Tobias P. Fischer, USA
Paolo Fulignati, Italy
Salvatore Inguaggiato, Italy
Francesco Italiano, Italy

Karsten Kroeger, New Zealand
Cornelius Langenbruch, USA
Stefano Lo Russo, Italy
John A. Mavrogenes, Australia
Ferenc Molnar, Finland
Julie K. Pearce, Australia
Daniele Pedretti, Finland

Marco Petitta, Italy
Christophe Renac, France
Andri Stefansson, Iceland
Richard E. Swarbrick, UK
Mark Tingay, Australia
Micol Todesco, Italy

Contents

Flow and Transport in Porous Media: A Multiscale Focus

Amgad Salama, Shuyu Sun, Mohamed F. El Amin, Yi Wang, and Kundan Kumar
Volume 2017, Article ID 7579015, 3 pages

Using BIB-SEM Imaging for Permeability Prediction in Heterogeneous Shales

C. J. A. Sinn, J. Klaver, R. Fink, M. Jiang, J. Schmatz, R. Littke, and J. L. Urai
Volume 2017, Article ID 4709064, 19 pages

Geofluid Systems of Koryaksky-Avachinsky Volcanoes (Kamchatka, Russia)

A. Kiryukhin, V. Lavrushin, P. Kiryukhin, and P. Voronin
Volume 2017, Article ID 4279652, 21 pages

Fluid Flow and Heat Transport Computation for Power-Law Scaling Poroperm Media

Peter Leary, Peter Malin, and Rami Niemi
Volume 2017, Article ID 9687325, 12 pages

Gas-Water Flow Behavior in Water-Bearing Tight Gas Reservoirs

Renyi Cao, Liyou Ye, Qihong Lei, Xinhua Chen, Y. Zee Ma, and Xiao Huang
Volume 2017, Article ID 9745795, 16 pages

Lattice Boltzmann Simulations of Fluid Flow in Continental Carbonate Reservoir Rocks and in Upscaled Rock Models Generated with Multiple-Point Geostatistics

J. Soete, S. Claes, H. Claes, N. Janssens, V. Cnudde, M. Huysmans, and R. Swennen
Volume 2017, Article ID 7240524, 24 pages

Flow and Transport in Tight and Shale Formations: A Review

Amgad Salama, Mohamed F. El Amin, Kundan Kumar, and Shuyu Sun
Volume 2017, Article ID 4251209, 21 pages

Experimental Study on the Effects of Stress Variations on the Permeability of Feldspar-Quartz Sandstone

Fugang Wang, Zhaoxu Mi, Zhaojun Sun, Xufeng Li, Tianshan Lan, Yilong Yuan, and Tianfu Xu
Volume 2017, Article ID 8354524, 15 pages

Modeling and Analysis of Magnetic Nanoparticles Injection in Water-Oil Two-Phase Flow in Porous Media under Magnetic Field Effect

Mohamed F. El-Amin, Ahmed M. Saad, Amgad Salama, and Shuyu Sun
Volume 2017, Article ID 3602593, 12 pages

Modelling of River-Groundwater Interactions under Rainfall Events Based on a Modified Tank Model

Wen Nie, Yongchang Liang, Lin Chen, and Wei Shao
Volume 2017, Article ID 5192473, 11 pages

Logging Characteristics and Identification Methods of Low Resistivity Oil Layer: Upper Cretaceous of the Third Member of Qingshankou Formation, Daqingzijing Area, Songliao Basin, China

Congjun Feng, Murray Gingras, Mengsi Sun, and Bing Wang
Volume 2017, Article ID 2915646, 13 pages



Determining the REV for Fracture Rock Mass Based on Seepage Theory

Lili Zhang, Lu Xia, and Qingchun Yu

Volume 2017, Article ID 4129240, 8 pages

A Pore-Scale Simulation on Thermal-Hydromechanical Coupling Mechanism of Rock

Rui Song, Mengmeng Cui, Jianjun Liu, P. G. Ranjith, and Yun Lei

Volume 2017, Article ID 7510527, 12 pages

Computing and Comparing Effective Properties for Flow and Transport in Computer-Generated Porous Media

Rebecca Allen and Shuyu Sun

Volume 2017, Article ID 4517259, 24 pages

Editorial

Flow and Transport in Porous Media: A Multiscale Focus

Amgad Salama,¹ Shuyu Sun,² Mohamed F. El Amin,³ Yi Wang,⁴ and Kundan Kumar⁵

¹University of Regina, Regina, SK, Canada

²King Abdullah University of Science and Technology, Thuwal, Jeddah, Saudi Arabia

³Effat University, Jeddah, Saudi Arabia

⁴National Engineering Laboratory for Pipeline Safety/MOE Key Laboratory of Petroleum Engineering, Beijing Key Laboratory of Urban Oil and Gas Distribution Technology, University of Petroleum, Beijing 102249, China

⁵University of Bergen, Bergen, Norway

Correspondence should be addressed to Amgad Salama; amgad.salama@uregina.ca

Received 10 September 2017; Accepted 14 September 2017; Published 26 October 2017

Copyright © 2017 Amgad Salama et al. This is an open access article distributed under the Creative Commons Attribution License, which permits unrestricted use, distribution, and reproduction in any medium, provided the original work is properly cited.

Porous media are ubiquitous in almost all of our daily life applications, from small scale biological cell membranes to field scale subsurface reservoirs (e.g., groundwater, petroleum, and geothermal) and beyond. It is indeed a challenge to account for such vast pool of length scales in a unified framework. In fact, the continuum hypothesis furnishes a suitable framework for the study of problems related to porous media applications. However, there exist situations of several interesting applications that occur at the boundaries between different scales (e.g., in fractured media). Phenomena that develop across the boundaries of different scales are, generally, difficult to handle. Variables at different scales have been recognized to have different meanings, interpretations, and measuring windows. Therefore, there is currently a large interest, among researchers, to develop theories and algorithms that are able to link these scales in a seamless manner. Meanwhile, the success to adapt the continuum hypothesis rely, to a large extent, on our understanding of the underlying physics at the small scale. As an example, the attempts to generalize the use of traditional Darcy's law on problems related to transport phenomena in tight formations (e.g., shales) necessitated the need to revisit the physics involved during the flow and transport in nanoscale passages such that correct upscaling to field applications is realized. Furthermore, new emerging applications including the transport of nanomaterials, new emerging contaminants, and new remediation technologies require, probably, newer insight into the way we model porous media problems. We, therefore, solicited high quality

original research or review articles focusing on all aspects of flow and transport in porous media to be submitted to this special issue. The aim has been to bring together state-of-the-art research contributions on the rich topics related to transport phenomena in porous media with emphasis on length scale span. Several applications have been thought including subsurface petroleum reservoirs, groundwater flows, shale gas transport, flows in tight formations, pore scale modeling, coupled flow and heat transfer problems, and numerical algorithms. The call for contributions has found particular interest among researchers and we needed to extend the time of the special issue per the many requests we received from interested scholars. We received a total of 22 submissions, and after two rounds of rigorous review, 13 papers were accepted one of which is a review article.

In the paper "Computing and Comparing Effective Properties for Flow and Transport in Computer-Generated Porous Media," R. Allen and S. Sun conducted pore scale simulation to examine, numerically, effective properties (i.e., permeability, hydraulic tortuosity, and diffusive tortuosity) of three different digital porous media samples, including in-line array of uniform shapes, staggered-array of squares, and randomly distributed squares. They highlighted that hydraulic and diffusive tortuosity can be quantitatively different by up to a factor of ten in the same pore geometry, which indicates these tortuosity terms cannot be used interchangeably. They also find when a pore geometry is characterized by an anisotropic permeability, the diffusive tortuosity (and correspondingly the effective diffusion coefficient) can also be anisotropic.

In the paper “A Pore-Scale Simulation on Thermal-Hydromechanical Coupling Mechanism of Rock,” R. Song et al. presented a pore scale thermal-hydromechanical coupling study of the flow of immiscible two-phase system in a perfect-plastic rock. A rock matrix and pore space system are reconstructed using micro-CT image. The rock deformation and fluid flow are simulated using ANSYS and CFX software, respectively. They highlight that the rising of effective pressure or temperature would lead to a decline of the porosity and permeability and that the drop ratio of permeability is larger than that of porosity. They also found that the relative permeability of oil and water decreases with the increasing of the effective pressure.

In the paper “Determining the REV for Fracture Rock Mass Based on Seepage Theory,” L. Zhang et al. indicated that the equivalent porous medium approximation may be the main method in the study of the seepage in fractured rock mass system. The key to the method is the ability to define a representative elementary volume (REV). They highlight that not all types of fractured rock mass have REV. The more intensive the fractures are, the better the penetration and the better the permeability of the rocks, which means the easier it is to become equivalent to porous media.

In the paper “Logging Characteristics and Identification Methods of Low Resistivity Oil Layer: Upper Cretaceous of the Third Member of Qingshankou Formation, Daqingzijing Area, Songliao Basin, China,” C. Feng et al. highlight the importance of the identification and evaluation of low resistivity oil layer in logging interpretation. This is mainly due to small resistivity contrast between oil and water layers. The study focuses on low resistivity thick layer sandstone in Qingshankou Formation at Daqingzijing oilfield, along with comprehensive data of logging, core, oil test, and production test.

In the paper “Modelling of River-Groundwater Interactions under Rainfall Events Based on a Modified Tank Model,” W. Nie et al. combined experiments and modelling to develop a novel tank model to simulate the ground water table and river levels due to rainfall events. The parameter training of the model used learning algorithms to predict the pore water pressure using laboratory conditions.

In the paper “Experimental Study on the Effects of Stress Variations on the Permeability of Feldspar-Quartz Sandstone,” F. Wang et al. studied the impact of injection processes of CO₂ sequestration on the hydraulic properties of reservoirs. The repeated loading and unloading involved in the multistage injection process implied that the hydraulic properties such as permeability evolved with time. An interesting observation from this study is the effect of multiple stress cycles on the micropore structure and the clay mineral content having a close relationship with the microscopic pore structure of the rock. This showed that the permeability of rocks of the same type with different clay mineral contents displayed different responses to stress.

In the paper “Fluid Flow and Heat Transport Computation for Power-law Scaling Poroperm Media,” P. Leary et al. implemented finite-element modelling methodology for a Dm-scale fracture sequence embedded in a Hm-scale crustal volume. Heat transport by fault-borne fluid flow of tight gas

sands in terms of Peclet number has been considered. They concluded that the crustal flow simulation using a single global numerical mesh may be the best.

In the paper “Modeling and Analysis of Magnetic Nanoparticles Injection in Water-Oil Two-Phase Flow in Porous Media Under Magnetic Field Effect,” M. F. El-Amin et al. investigated the transport of magnetic nanoparticles in a water-oil, two-phase system under the influence of permanent magnetic field. They show that the location of the permanent magnet with respect to the inlet in a countercurrent two-phase system has significant effect in the flow field.

In the paper “Geofluid Systems of Koryaksky-Avachinsky Volcanoes (Kamchatka, Russia),” A. Kiryukhin et al. used seismic data to identify dyke swarms and potential heat sources to understand the role of volcanic eruptions in the adjacent thermal mineral springs. The isotope dating techniques showed the magmatic origins of CO₂ and thermobiogenic origins of methane. A thermal hydrodynamic modelling was used to study the possible heat and mass sources to explain the observations of this interesting volcanic geofluid system.

In the paper “Gas-Water Flow Behavior in Water-Bearing Tight Gas Reservoirs,” R. Cao et al. investigated the impact of mobile water on the gas flowing in tight pores. They presented mathematical models to describe flow behaviors of gas and water in tight gas formations, which account for the threshold pressure gradient, stress sensitivity, and relative permeability.

In the paper “Lattice Boltzmann Simulations of Fluid Flow in Continental Carbonate Reservoir Rocks and in Upscaled Rock Models Generated with Multiple-Point Geostatistics,” J. Soete et al. used Palabos which is a software tool for particle-based modelling of classic computational fluid dynamics along with 3D pore network models to study fluid flow characteristics in continental carbonates. In addition, permeability simulations were performed on rock models generated with multiple-point geostatistics (MPS)

In the paper “Using BIB-SEM Imaging for Permeability Prediction in Heterogeneous Shales,” C. J. A. Sinn et al. uses organic-rich shale samples from a lacustrine sedimentary sequence of the Newark Basin (New Jersey, USA). The study uses Broad Ion Beam polishing with Scanning Electron Microscopy (BIB-SEM) to obtain high-resolution pore scale images. This is used to determine pore system properties. The permeability is computed using the widely used Carman-Kozeny models followed by validation through the experiments.

In the review paper “Flow and Transport in Tight and Shale Formations: A Review,” A. Salama et al. presented a comprehensive review on the modeling of transport phenomena in tight and shale formations. They covered a wide range of phenomena occurring in shale and tight formations.

Acknowledgments

The guest editorial team would like to thank authors for all their contributions to this special issue. Given the space limitations, a number of high quality contributions could not be accommodated. The editors also wish to thank the anonymous reviewers for their time and dedication in providing

their critical reviews that help focus the goal of this special issue. We hope that you will enjoy reading this special issue devoted to this exciting and fast-evolving field as much as we have done.

Amgad Salama
Shuyu Sun
Mohamed F. El Amin
Yi Wang
Kundan Kumar

Research Article

Using BIB-SEM Imaging for Permeability Prediction in Heterogeneous Shales

C. J. A. Sinn,^{1,2} J. Klaver,³ R. Fink,² M. Jiang,³ J. Schmatz,³ R. Littke,² and J. L. Urai¹

¹Structural Geology, Tectonics and Geomechanics (GED), Energy and Mineral Resources Group (EMR), RWTH Aachen University, Lochnerstrasse 4-20, 52056 Aachen, Germany

²Institute of Geology and Geochemistry of Petroleum and Coal (LEK), Energy and Mineral Resources Group (EMR), RWTH Aachen University, Lochnerstrasse 4-20, 52056 Aachen, Germany

³MaP-Microstructure and Pores GmbH, Lochnerstrasse 4-20, 52064 Aachen, Germany

Correspondence should be addressed to C. J. A. Sinn; caspar.sinn@rwth-aachen.de

Received 14 April 2017; Revised 11 August 2017; Accepted 24 August 2017; Published 23 October 2017

Academic Editor: Kundan Kumar

Copyright © 2017 C. J. A. Sinn et al. This is an open access article distributed under the Creative Commons Attribution License, which permits unrestricted use, distribution, and reproduction in any medium, provided the original work is properly cited.

Organic-rich shale samples from a lacustrine sedimentary sequence of the Newark Basin (New Jersey, USA) are investigated by combining Broad Ion Beam polishing with Scanning Electron Microscopy (BIB-SEM). We model permeability from this 2D data and compare our results with measured petrophysical properties. Three samples with total organic carbon (TOC) contents ranging from 0.7% to 2.9% and permeabilities ranging from 4 to 160 nD are selected. Pore space is imaged at high resolution (at 20,000x magnification) and segmented from representative BIB-SEM maps. Modeled permeabilities, derived using the capillary tube model (CTM) on segmented pores, range from 2.3 nD to 310 nD and are relatively close to measured intrinsic permeabilities. SEM-visible porosities range from 0.1% to 1.8% increasing with TOC, in agreement with our measurements. The CTM predicts permeability correctly within one order of magnitude. The results of this work demonstrate the potential of 2D BIB-SEM for calculating transport properties of heterogeneous shales.

1. Introduction

The pore network is the main control on transport processes in low-porous media, such as gas shales [1, 2]. Thus, it is of interest to develop improved methods for understanding controls and to upscale pore structural information from nanometer-scale to larger rock volumes [3]. Argon Broad Ion Beam (BIB) and Focused Ion Beam (FIB) milling are techniques that offer new insight in microstructures through high-resolution imaging. While BIB milling is commonly used to analyze mm-sized 2D sections, FIB is limited to μm -sized volumes [4, 5]. By using these imaging methods, it is possible to receive a solid idea of a shale's internal (micro) structure and pore geometry (e.g., [6–11]). BIB milling in combination with SEM imaging delivers direct information about pore sizes, their morphology and spatial distribution, rock microstructure, and potential anisotropy as well as core damage due to sample handling (e.g., [3, 12–25]). Additionally, in combination with energy dispersive X-ray

spectroscopy (EDX), BIB-SEM enables the identification of individual grains [26, 27]. However, subjective selection of representative study areas on the cross-section as well as the resolution—a major part of the pore space can exist below resolution—restrict these techniques. Due to the small-scale nature of pores in shales other imaging techniques, for example, MicroCT, are not suited for pore imaging. So far SEM is the most practical tool to image these pores properly [28]. Nevertheless, it remains challenging to upscale pore system characteristics from the nanometer-scale of SEM investigations to the centimeter scale of petrophysical experiments to the meter scale of reservoirs.

As the properties of a rock's pore system directly govern permeability, image-derived pore-scale models (also known under the term *digital rock physics*) are used to study porous media, especially for conventional rocks, such as sandstone or carbonate [29, 30]. However, building a pore network model for 3D flow simulations in heterogeneous fine-grained rocks is an unresolved issue. Some approaches extract 3D

TABLE 1: Drilling sites, geological origin, and current depth of the sample material.

Sample	Well #	Formation	Member	Depth [m]
NJ-001	Titusville 2	Passaic	Perkasie	21.98
NJ-019	Princeton 2	Lockatong	Ewing creek	54.86
NJ-023	Nursery 1	Lockatong	Wilburtha	928.06

pore data directly from FIB-SEM [31] or use the Markov chain Monte Carlo (MCMC) reconstruction method on 2D images [32, 33]. Whether these complex pore network models are representative for the sample is another uncertainty [17, 31, 34]. Kelly et al. 2015 pointed out that FIB-SEM investigation volumes of shales are not suited to resolve local heterogeneities, and thus, larger areas of investigation are necessary. Moreover, extracting a percolating pore network in shales with FIB-SEM remains a challenge since most pore throats are below the pixel resolution [15, 20, 35, 36].

In contrast, this work aims to determine pore system properties and permeabilities by BIB-SEM imaging in 2D from three different shale samples. Permeability predictions are based on a simple model [37, 38] that relates pore microstructure with permeability. The BIB-SEM derived permeability results are then validated by experiments on the exact same sample plugs.

2. Materials and Methods

2.1. Sample Material. Three samples (Table 1) with a decreasing porosity, permeability, and TOC trend according to their labeling (NJ-001, NJ-019 and NJ-023) were selected from cores drilled during the Newark Basin Coring Project (NBCP) from 1990 to 1993. These laminated, organic-rich lacustrine shales from the Triassic Passaic and Lockatong formation (~214 to 222 Ma) are of good quality featuring no macroscopically visible fractures or secondary mineralization (e.g., [39–42]). From each sample location, a cylindrical sample plug was drilled parallel to the bedding, which was used for porosity and gas permeability measurements as well as BIB-SEM imaging.

2.2. Bulk Measurements

2.2.1. XRD, TOC, and VR_r Analyses. Bulk mineralogical compositions were derived from X-ray diffraction (XRD) patterns of randomly oriented powder preparations. The measurement was done on a *Bruker AXS D8 Advance* diffractometer using a $CuK\alpha$ -radiation produced at 40 kV and 40 mA (analysis performed by Rietveld refinement). Details of the sample preparation and evaluation are described in [43].

Total organic carbon (TOC) and total inorganic carbon (TIC) were measured on powdered samples with a *liquiTOC II* analyzer. The instrument analyzes the released CO_2 during one temperature ramp without previous acidification.

Vitrinite reflectance (VR_r) measurements were performed on polished blocks under oil immersion ($n_e = 1.518$) using a *Zeiss Axio Imager* microscope. Details on sample

preparation, the analytical procedure, and instrumentation are described in [44, 45].

2.2.2. He-Porosity and Gas Permeability. He-porosities were calculated by combining skeletal densities from helium expansion (pycnometry) and bulk densities from cylindrical sample plug dimensions ($\phi_{He} = 1 - \rho_{sk}/\rho_b$). Details on the setup and measuring procedure were previously described in [46, 47].

Gas permeability coefficients were measured on the same cylindrical sample plugs drilled parallel to bedding with helium gas as permeate at 25°C (298 K) in dry condition. They were installed into triaxial flow cells and then loaded to a confining pressure level of 40 MPa. After installation, the system was flushed with helium and leak-tested. Permeability measurements were conducted at confining pressure levels of 40, 30, 20, and 10 MPa during unloading. At each confining pressure level, nonsteady state flow tests (pressure pulse decay) were then performed at various pore pressures from 0.5 to 5 MPa. From the pressure incline/decline versus time series, apparent permeability coefficients were calculated. Details on the experimental setup, pressure pulse decay tests, and gas permeability calculation procedure are described in [46, 48].

Due to gas slippage, measured apparent gas permeability coefficients are higher than “intrinsic” permeability coefficients. Gas slippage effects were corrected by applying the Klinkenberg-correction on the apparent permeability data of a given confining pressure level [46, 47, 49, 50]. The Klinkenberg-corrected permeability versus stress couples was then extrapolated by an exponential expression to “unstressed” conditions to be able to compare them to the results of “unstressed” BIB-SEM measurements [49–51].

2.3. Microstructural Investigation

2.3.1. Sample Preparation. The end of all plugs used for the permeability measurement were cut off and used for BIB-SEM investigation. Subsamples were cut dry into rectangular blocks of $3 \times 5 \times 5$ mm using a low-speed microdiamond saw. Subsampling was based on macroscopic investigations, that is, checking for milling locations perpendicular to the bedding plane featuring visibly different kinds of layers, for example, darker (more clayey) and brighter (siltier) layers. These locations were then BIB-polished by a *JEOL SM-09010 polisher* to produce planar, Gaussian-shaped cross-sections of approx. 2 mm^2 . The samples were subsequently coated to prevent charging of the sample during imaging. For details about the protocol see [21].

The end trim of the plugs used for the permeability measurement of samples NJ-001 and NJ-019 was additionally polished perpendicular to the bedding using sand paper (SiC) in preparation of cm^2 scale energy dispersive X-ray spectroscopy (EDX) analysis.

2.3.2. BIB-SEM Analysis. The Field Emission SEM used for image acquisition in this work is a *Zeiss SUPRA 55* equipped with a backscattered electron (BSE), secondary electron (SE2), and EDX detector.

Pores can be identified on BIB-polished surfaces using a SE2 detector at low acceleration voltages of 3 to 5 kV [21]. The BSE detector was used to record the density contrast at the same area on the cross-section applying acceleration voltages of 15 to 20 kV. Element maps, showing the intensity of an element, were produced simultaneously using the EDX detector. Subsequently, the recorded images were stitched together automatically forming large mosaics by using the software *Oxford Instruments*© *AZtecEnergy*. All BIB-SEM images were scanned perpendicular to the bedding.

Several image mosaics were scanned at different magnifications to gain microstructural information at multiple scales. For each sample, at least one BIB cross-section was prepared, and typical layers were selected based on their mineralogical composition and mapped at high resolution with the SE2 detector, and when relevant, also with the BSE and EDS detector: (1) plug analysis on complete plug surfaces at 125x magnification (BSE and EDX with a pixel resolution of $2.4 \mu\text{m}$); (2) subsample overviews of 250x magnification for identifying cross-section locations (BSE and EDX with pixel sizes of $1.2 \mu\text{m}$ and $2.4 \mu\text{m}$, resp.); (3) detailed recording of the BIB-SEM cross-sections at 2,500x magnification (BSE and EDX with pixel sizes of 120 nm and 240 nm, resp.); plus (4) high-resolution mosaic maps of 10,000x to 20,000x magnification for in-depth mineral phase and porosity identification (SE2, BSE, and EDX with pixel sizes of 15 nm, 30 nm, and 60 nm resp.). High-resolution mapping comprises three mosaic maps (SE2, BSE, and EDX) for sample NJ-001 and NJ-019, each, plus one map for sample NJ-023.

Assuming that the pore space is strongly linked to the mineral phases, the representative elementary area (REA) of mineralogy is an approximation for the representative area of porosity [19]. A box counting method (as described in detail in [21]) was employed to determine decreasing fluctuations in the mineralogical distribution ($\pm 5\%$) at which an area is considered to be representative.

2.3.3. Digital Image Analysis. The segmentation of mineral phases included thresholding and automatic image treatment based on BSE and EDX maps using different toolsets within *ESRI*© *ArcGIS*. The mineralogical composition was quantified by assessing the element intensities of the EDX maps, where high Si counts were interpreted as quartz, high K, and intermediate Si as K-feldspar, high Na as Na-feldspar (albite), and high Ca counts as carbonates (dolomite/ankerite). Pyrite and OM were segmented from BSE micrographs and the remaining area was considered as clay. Besides an identification of mineral phases, mineral grain sizes, shapes, and spatial distributions were qualitatively assessed.

Porosity was segmented from SE2 images utilizing a “seed and grow” algorithm [52]. Appropriate morphological indicators to quantify and distinguish distinctive characteristics between pores or cracks are elongation, derived through a pore’s axial ratio (see Appendix A, (A.1)), and roundness, obtained by the circularity of a single pore’s boundary (see Appendix A, (A.2)). For the flow model, segmented pores were converted into polygons and evaluated by using the capillary tube model (CTM).

2.3.4. Upscaling to Larger Rock Volumes (Plugs). Macroscale EDX analysis of the surface of the plug’s end trim with 125x magnification allowed distinguishing layers with typical mineralogy that can be used for upscaling to a respective plug’s mineral content. To compare permeability predictions of a single layer to the measured permeabilities of respective plugs (both parallel to the bedding), typical layers of sample NJ-001 and NJ-019 were assessed via EDX intensity measurements. The total plug area was then separated into typical layers to obtain the area proportions of each representative layer.

To identify the properties of distinct layers, each layer is characterized by a BSE/EDX mosaic map (Figure 8). The quantitative properties of these maps, in particular the dominant mineralogical composition, are then used to distinguish three main types of layers within the plug. This procedure allows extrapolating representatively to the plug scale (cm). Finally, CTM estimated permeabilities of each single mosaic map are normalized to the 2D areal fraction of the plug’s respective layer surfaces to receive realistic (upscaled) permeabilities (Table 5).

2.4. Capillary Tube Modeling. We used the CTM similar to [51]. It assumes idealized capillary bundles [37, 38] and represents the permeability by a combination of Darcy’s law with the Hagen–Poiseuille equation, describing laminar flow through a cylindrical pipe (see Appendix B, (B.1)–(B.10)). With the tortuosity τ (ratio of the true length of a pore path l compared to the straight-line distance between those points L) and the hydraulic pore radius r_{hyd} (to consider the complexity of the pore shape, pore area divided by its perimeter) of a capillary system, the individual flow through a single pore is described by the permeability k (m^2):

$$k = \frac{r_{\text{hyd}}^2 \phi}{8\tau^2}. \quad (1)$$

where ϕ stands for the porosity. However, since there is no uniform pore radius in these shales and BIB-SEM enables quantification of a range of pore sizes, the equation above is rewritten to derive permeability for a single pore k (m^2) by taking into account its effect on porosity (a pore’s area S_{pore} (m^2) divided by the total mosaic area S_{mosaic} (m^2)) and sum these up for the total permeability k_{total} (m^2):

$$k_{\text{total}} = \sum_{i=1}^n (k_i) = \sum_{i=1}^n \left(\frac{r_{\text{hyd},i}^2}{8\tau^2} \cdot \frac{S_{\text{pore},i}}{S_{\text{mosaic}}} \right), \quad \text{for } n \in N. \quad (2)$$

The tortuosity characterizes flow pathways in shales and describes the connectivity of the pore network. If tortuosity

TABLE 2: Petrophysical measurements of the investigated samples featuring elemental analysis, helium pycnometry (He), non-steady-state gas permeability measurements, and vitrinite reflectance data. *Klinkenberg-corrected helium permeability extrapolated to zero effective stress.

Sample	TOC [wt.%]	TOC [vol.%]	Bulk density [g/cm ³]	He grain density [g/cm ³]	He-porosity [%]	Permeability [nD]*	VR _r [%]
NJ-001	3.85	8.39	2.54	2.68	5.27	160.33	2.52
NJ-019	1.82	4.07	2.61	2.72	3.75	43.15	2.05
NJ-023	0.76	1.74	2.68	2.72	1.66	3.94	2.70

TABLE 3: XRD data of all investigated samples listing mineral groups (bold) and their corresponding minerals (italic).

Sample	Quartz	Feldspar	<i>Albite</i>	<i>K-feldspar</i>	Carbonate	<i>Calcite</i>	<i>Dolomite/ankerite</i>	Clay + mica	<i>Chlorite</i>	Pyrite + others	Total
NJ-001	13.6	36.9	36.9	0.0	30.8	1.0	29.8	17.1	1.9	1.6	100.0
NJ-019	0.7	46.8	14.0	32.7	20.1	0.0	20.1	31.6	0.0	0.8	100.0
NJ-023	1.2	36.4	25.7	10.7	37.9	0.0	37.9	23.6	7.1	0.9	100.0

equals 1, flow may be fully described by the Hagen–Poiseuille equation [53]. Values of 10 imply a traversed flow path of ten times the actual (theoretically shortest) path length. In accordance with the work of [51] a tortuosity of $\tau = 10$ is applied in this study.

Besides, modeling of the cumulative permeability coefficients can be optimized by correcting the visible porosities for isolated *IntraP*-pores and induced microcracks.

3. Results

3.1. Bulk Properties

3.1.1. Mineralogy and Maturity. The samples vary in TOC, with the highest organic content in sample NJ-001 and lowest organic content in sample NJ-023 (Table 2). The maturity of all samples ranges from ~ 2.1 to 2.7% VR_r. Their mineral composition is different from organic-rich marine shales with respect to (1) absent or low quartz content from <1 to 13%; (2) significant higher proportion of feldspar(s) with ~ 36 to 47%; and (3) a similarly high amount of carbonates with ~ 20 to 38% throughout all samples (Table 3).

3.1.2. He-Porosity and Gas Permeability. Bulk densities vary between 2.54 g/cm³ (NJ-001) and 2.68 g/cm³ (NJ-023) and grain densities between 2.68 and 2.72 g/cm³. As a result, calculated He-porosity values of sample NJ-001 are highest with approx. 5.1% followed by NJ-019 with 4.1% and NJ-023 with 1.4% (Table 2).

Similarly, Klinkenberg-corrected permeabilities (extrapolated to zero stress) decrease from sample NJ-001 to NJ-023. Sample NJ-001 shows highest permeability with $k_{\text{inf}} \cong 160$ nD (approx. $1.58 \cdot 10^{-19}$ m²) followed by NJ-019 with $k_{\text{inf}} \cong 43$ nD (ca. $4.26 \cdot 10^{-20}$ m²) and sample NJ-023 shows lowest permeability with $k_{\text{inf}} \cong 4$ nD (approx. $3.89 \cdot 10^{-21}$ m²) (Table 2).

3.2. Qualitative Description of Mineralogy, Microstructure, and Pore Morphology. All samples are characterized by a

very heterogeneous fabric with a variety of different clasts embedded in a fine-grained matrix framework. Grains occur in a wide range of sizes and mostly touch each other. Layering lies within submillimeter to centimeter scale (NJ-001 slightly more distinct than NJ-019 or NJ-023). In between clasts, dispersed OM, intercalated by clay minerals, is evident and qualitatively analyzed to be gradually less from sample NJ-001 to NJ-023 according to the chosen TOC sequence. The given samples feature three typical submillimeter layers with an abundance of large albite (Figure 1(a)) or carbonate (dolomite/ankerite) clasts (Figures 1(b) and 4). Additionally, distinct sulfur-rich layers featuring a variety of euhedral pyrites are visible in sample NJ-001 (Figure 1(c)). As clasts in all samples are mostly in contact to one another, the fabric is classified as a grain supported matrix. The matrix itself (gray) features dispersed OM (black) intercalated by other types of minerals (more or less elongated) possibly belonging to the phyllosilicates (e.g., mica).

The feldspar-rich laminae are responsible for the high porosities in the investigated samples (Figure 1 versus Figures 4 and 5), especially as NJ-001 features significantly more silty layers on the plug scale (Figure 8). Similar laminae, responsible for regulating flow, were also found by Lei et al. 2015 [54] in Chinese organic-rich lacustrine shales.

Mineralogy and Microstructure. Carbonate grains (blue, Figure 1) represent the biggest and most distinct clasts of typical rhombohedral habits, ranging in size from <1 μm up to approx. 50 μm in diameter in sample NJ-001. In sample NJ-019 and NJ-023 Ca-clasts (blue, Figures 4 and 5) are less common and typically not larger than 20 μm (commonly <5 μm) in size. Feldspars (pink, Figure 1) also feature some relatively large clasts of up to about 25 μm , but their size is mainly below 10 μm . In contrast to sample NJ-001, the samples NJ-019 and NJ-023 exhibit two different types of feldspar, sodium-containing feldspar, here albite (lower gray values on the BSE) as well as potassium-containing feldspar (higher gray values on the BSE). The morphology of albite clasts (pink, Figures 4 and 5) is relatively distinct and their size

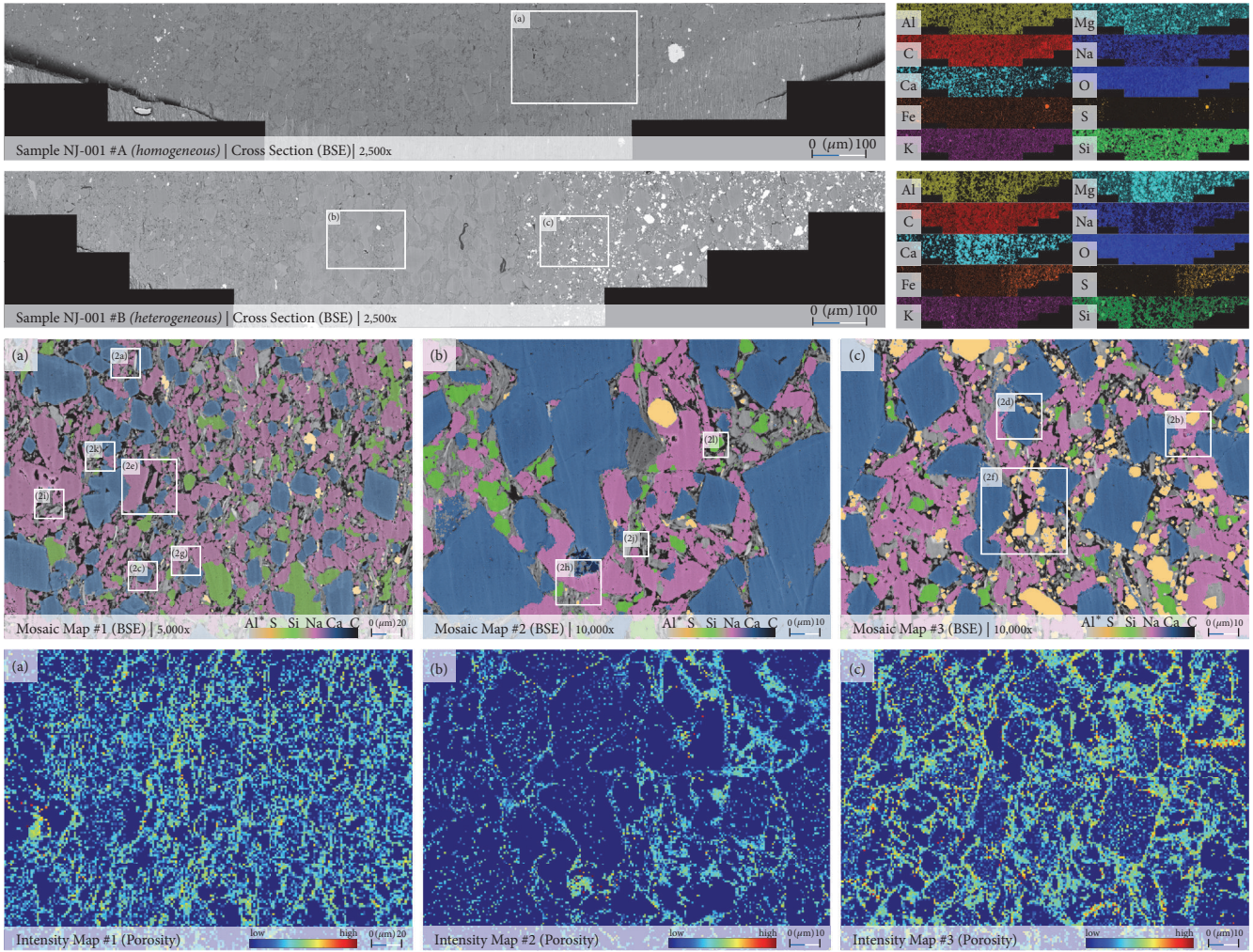


FIGURE 1: BIB-SEM investigation of sample NJ-001 including their local porosity maps and selected areas of interest depicted in Figure 2. All BIB-SEM images were investigated perpendicular to the bedding. The intensity of local porosities is the pore area proportion of each cell illustrated via a log color scale. Pyrites (corresponding to the element S) appear in a bright yellow; silicates (corresponding to Si) are colored green (in this sample: quartz); feldspars (corresponding to Na) are colored pink; carbonates (corresponding to Ca) are colored blue; OM (corresponding to C) is colored black. EDX element maps are illustrated for a rough assessment of possible mineralogical constituents.

represents the biggest clasts within these samples with less than $5\ \mu\text{m}$ up to approx. $100\ \mu\text{m}$ in diameter. The morphology of K-feldspar clasts (green) is similar, though their sizes are of only a few μm up to about $25\ \mu\text{m}$ in diameter. In sample NJ-001, quartz grains (green, Figure 1) are usually small ($<10\ \mu\text{m}$), though they exist also in sizes of more than $20\ \mu\text{m}$ while quartz is almost absent in sample NJ-019 and NJ-023. Pyritic grains (yellow, Figure 1) of sizes up to $10\ \mu\text{m}$ in sample NJ-001 are common while pyrite is very rare in sample NJ-019 and NJ-023.

Comparing the qualitative results to typical features of marine shales, lacustrine shales are often differentiated by (1) thin recurring (seasonal) laminae [55, 56]; (2) siltier layers, particularly rich in albite and carbonate (dolomite/ankerite); (3) no/little presence of calcareous fossils [18, 21, 57] or framboidal pyrite [25, 58]; (4) overall relatively low visible

porosity; and (5) relatively low visible OM porosity for these high maturities.

Pore Morphologies. Porosity in all samples is predominantly distributed between clasts and OM interfaces (see also [59]) and thus allocated to *InterP* porosity according to the pore space classification of Loucks et al. [60]. However, if certain types of grains contain pore space, its typical morphology and distribution can be assessed as well (Figure 2).

- (i) Few albite grains embody large pores (*IntraP*) of up to ca. $10\ \mu\text{m}$ (in direction of the longest axis), with angular morphologies, typically occurring at the clast's rims progressing into the center (see also [61, 62]). Completely isolated and centered pores are considered as fluid inclusions (see also [63]) and

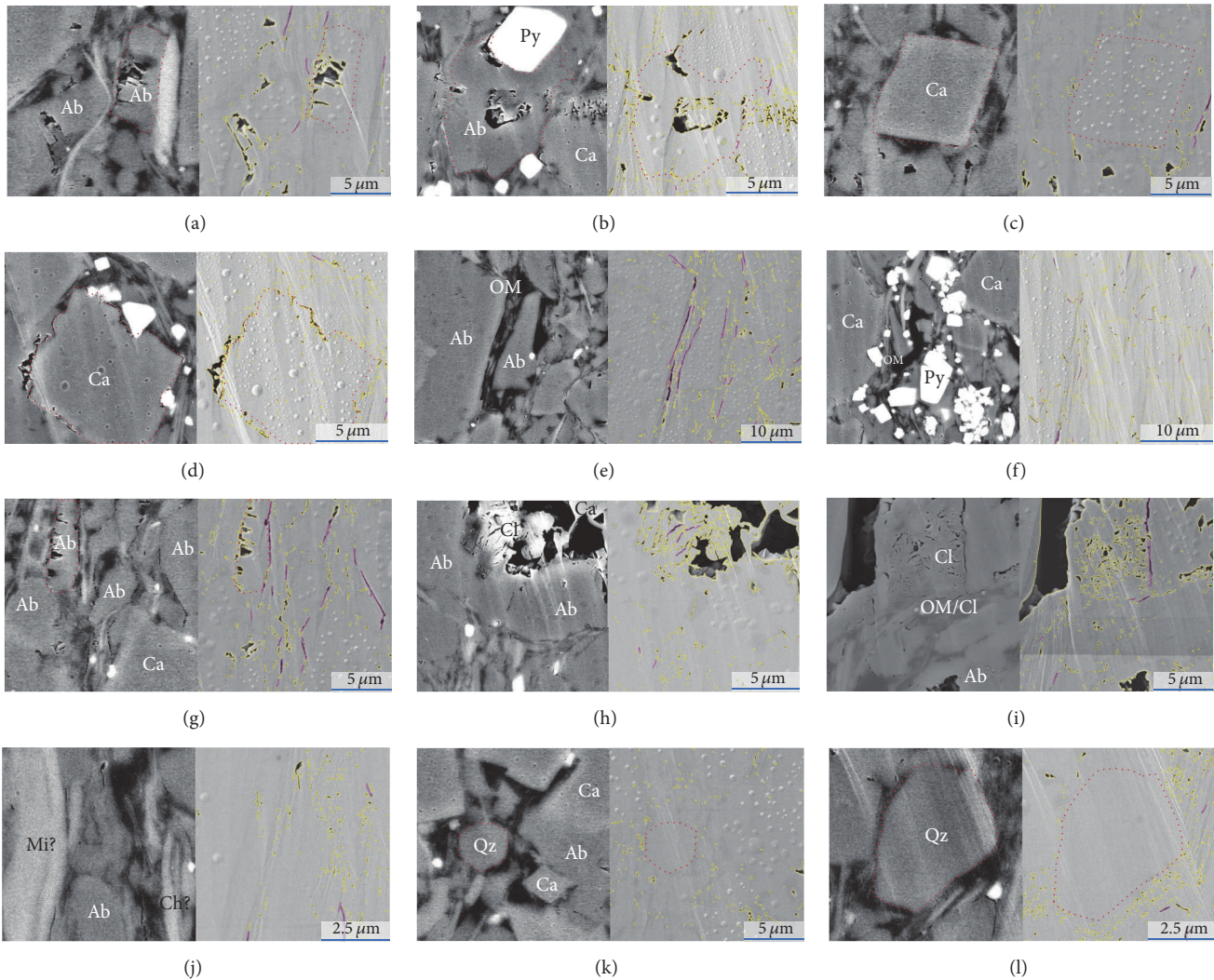


FIGURE 2: Mineralogical, microstructural, and morphological features of clasts (red), pore space (yellow/purple), and rock matrix showing BSE (a, c, e, g, i, k) and SE2 (b, d, f, h, j, l) recordings of sample NJ-001. Grains occur in a wide range of sizes but were chosen according to their characteristic properties for this illustration (e.g., due to partial idiomorphism). Porosity is predominantly distributed between clasts and OM interfaces (*InterP*), representing very narrow elongated slits along grain boundary interfaces within the polycrystalline matrix. Minerals phases are as follows: Ab, albite; Ca, carbonate; Ch, chlorite; Cl, clay; Fs, feldspar; Mi, mica; OM, organic matter; Py, pyrite; Qz, quartz.

- excluded in the CTM as described in chapter 0 (cf. Figures 2(a) and 2(b)).
- (ii) Some carbonates feature cluttered pores (*InterP*) along their edges (cf. Figure 2(d)), plus very few grains show large pores (*IntraP*) of up to ca. 5 μm (cf. Figure 2(h)).
 - (iii) Quartz and pyrite show almost no associated porosity (cf. Figures 2(b), 2(f), 2(k), and 2(l)).
 - (iv) Relatively small pores are located within the dispersed occurring OM (cf. Figures 2(j) and 2(l)).
 - (v) All other types of intergranular porosity (*InterP*) can be considered to be either very small pores or very narrow elongated slits along slightly dilatant grain boundaries interfaces (cf. Figures 2(e) and 2(f)).

The visible porosity of sample NJ-019 and NJ-023 is significantly less but occurs similar to the cavities described in sample NJ-001 (Figure 6). Similarly, pores are found predominantly in between the interfaces of OM and clasts (cf. Figures 6(b), 6(e), 6(f), 6(g), and 6(h)) and some large pores are situated within feldspar or carbonate grains (cf. Figures 6(a) and 6(d)). In contrast, clear clay platelets seem to feature elongated pores (cf. Figures 6(i) and 6(j)).

High magnified images revealed porosity (*IntraP*) that is omnipresent within the dispersed OM in sample NJ-001 (Figure 3(a)), but not within the dark, comparatively large individual particles of the OM (Figure 4(b)). Almost no pores are associated with the OM in sample NJ-019 and NJ-023 (Figure 6) which is affirmed by additional SE2 scans under very high magnifications (Figure 3(b)). Similar to the Triassic

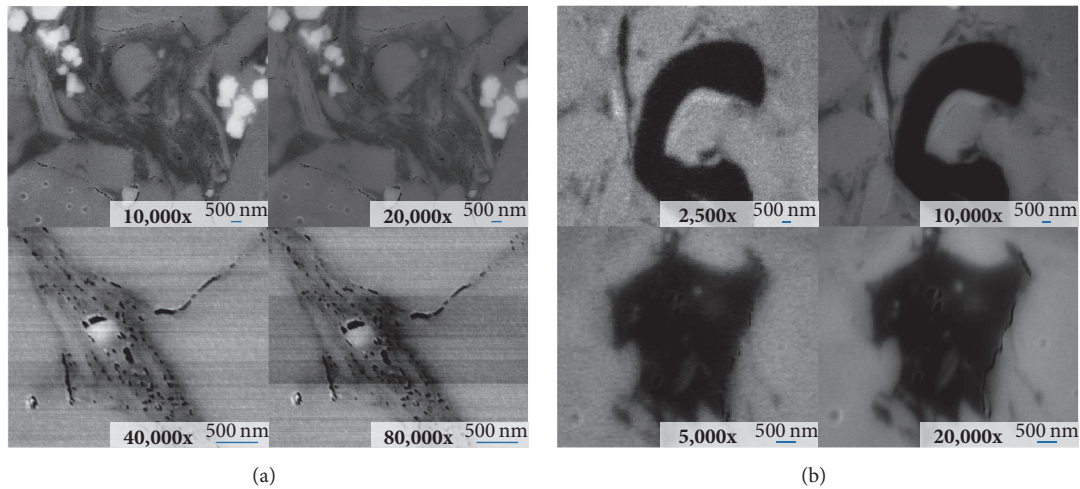


FIGURE 3: Dispersed OM pervaded by porosity in sample NJ-001 (a) and almost no OM porosity in sample NJ-019 or NJ-023 (b).

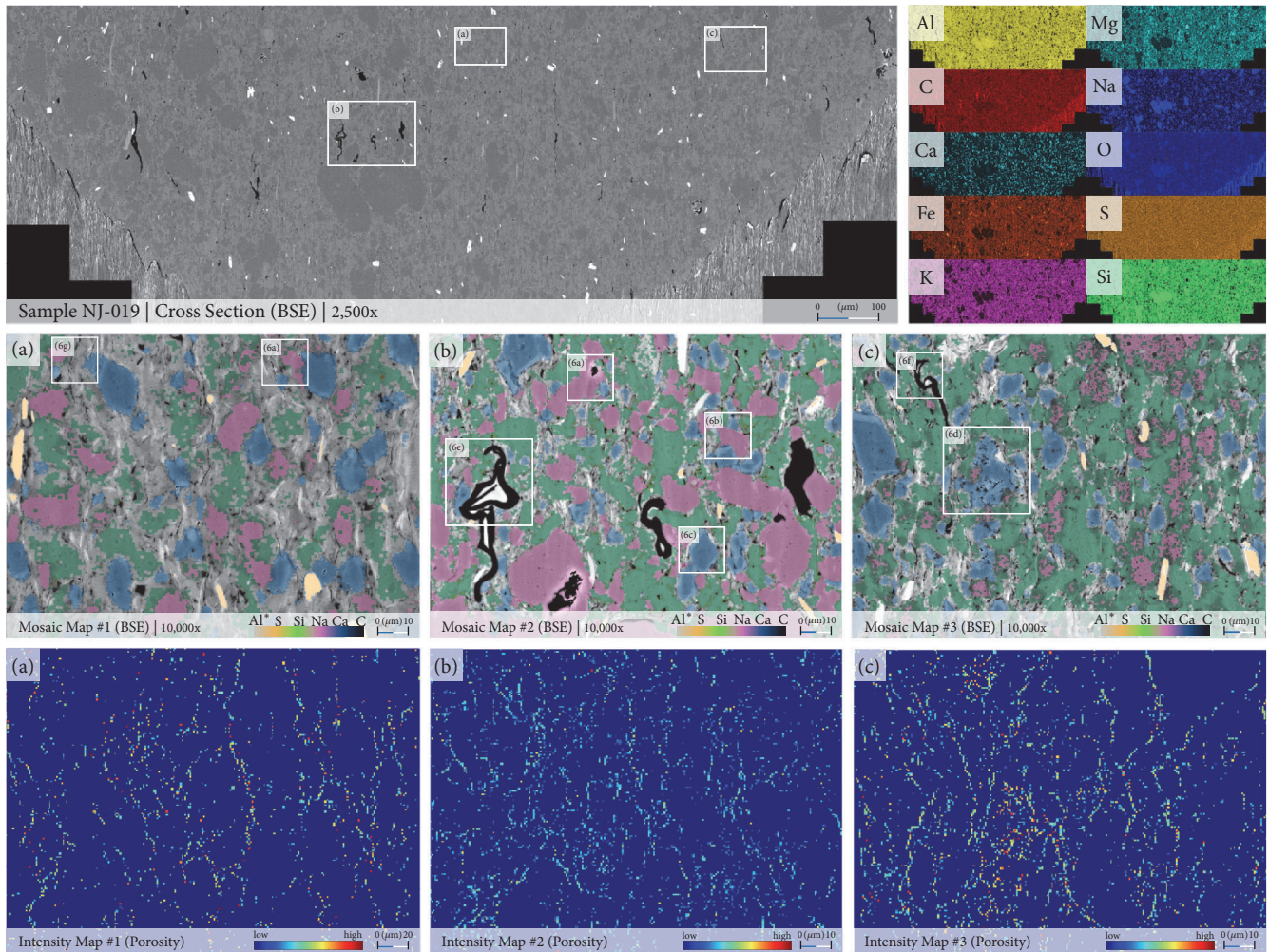


FIGURE 4: BIB-SEM investigation of sample NJ-019 including their local porosity maps and selected areas of interest depicted in Figure 6. Pyrites (corresponding to the element S) appear in a bright yellow; silicates (corresponding to Si) are colored green (in this sample assumed to represent K-containing feldspar grains); Na-feldspars (corresponding to Na) are colored pink; carbonates (corresponding to Ca) are colored blue; OM (corresponding to C) is colored black.

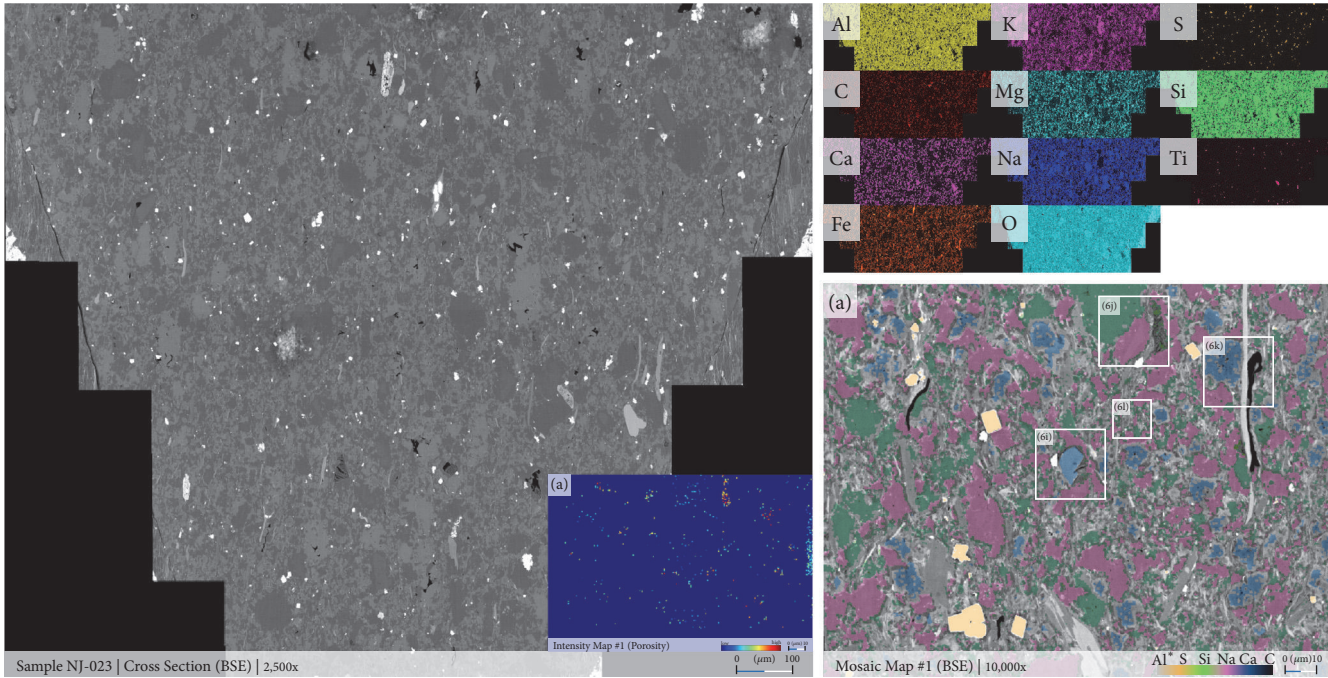


FIGURE 5: BIB-SEM investigation of sample NJ-023 including local porosity map and selected areas of interest depicted in Figure 6. Due to very narrow milling results, the exact location of NJ-023's high-resolution map cannot be indicated within the illustrated cross-section of this sample as it was imaged approx. 2 mm besides in another proximal cross-section.

black shales investigated by Loucks et al. 2017 [64], most of the OM pores are located in migrated solid bitumen.

This indicates the presence of at least two different OM types, interpreted as

- (i) dispersed bitumen that migrated into cavities between grains;
- (ii) primary terrestrial vitrinite and inertinite particles.

Furthermore, the investigated lacustrine shale samples on average exhibit less visible porosity ($\sim 0.8\%$) than their marine organic-rich counterparts at similar maturity. In contrast to other studies on overmature organic-rich marine shales (e.g., [15, 22, 24, 26]), pores within the given lacustrine samples are rarely associated with the OM, even though the dispersed OM and primary terrestrial vitrinite or inertinite particles could be identified as OM Types A and C found in marine shales [22]. The dispersed OM identified in all samples only exhibits pronounced OM porosity in the high-resolution images of NJ-001 (Figures 2(j), 2(l), and 3(a)). Besides, the number of OM pores does not increase with further maturity as stated in numerous studies of lacustrine shales [65, 66], mostly since samples NJ-019 and NJ-023 contain less OM and little to none OM porosity. Considering the high vitrinite reflectance values ($2.0\% < VR_r < 3.5\%$) and the lack of significant visible large OM pores, the hydrocarbon potential can be classified as poor. The relatively small amount of visible OM porosity could also be related to the fact that lacustrine shales are dominated by kerogen of terrestrial source generally hosting less OM porosity [20, 67, 68].

3.3. Quantitative Description of Mineralogy and Pore Space

3.3.1. Mineralogical Composition. The mineralogical proportions of the investigated samples vary when comparing the microstructure of sample NJ-001 to NJ-019 and NJ-023, respectively (Figure 7). Qualitative trends described before, such as distinct layering in sample NJ-001, are recognizable quantitatively as well.

EDX results show that the mineral content varies most with up to approx. 27%, 16%, and 8% for carbonate, feldspar (albite), and pyrite, respectively, in the maps of sample NJ-001. Variability of the mineralogical proportions between maps of sample NJ-019 is up to approx. 36%, 28%, and 21% for clays, quartz/silicates (correctly classified as K-feldspar by XRD analysis), and albite, respectively (Figure 9). Bulk XRD results only exhibit profound variations in comparison to the EDX results of the mineralogy of sample NJ-023 with variations of clays (ca. 30%) and carbonates (ca. 33%). All other distinguished mineral phases in every sample vary by less than 7% compared to the EDX findings.

3.3.2. Porosity and Pore Morphology. All pores below 18 pixels (equal to 72 and 144 nm in diameter at 20,000x or 10,000x magnification, resp.) in size must be considered with caution since pores of these sizes are below the practical pore resolution (PPR). Microcracks (narrow elongated pores) that may originate from drilling, core recovery operations, drying, or sample preparation are identified and removed.

Total visible porosities between all mosaic maps range from approx. 2.0% (NJ-001) to almost no visible porosity

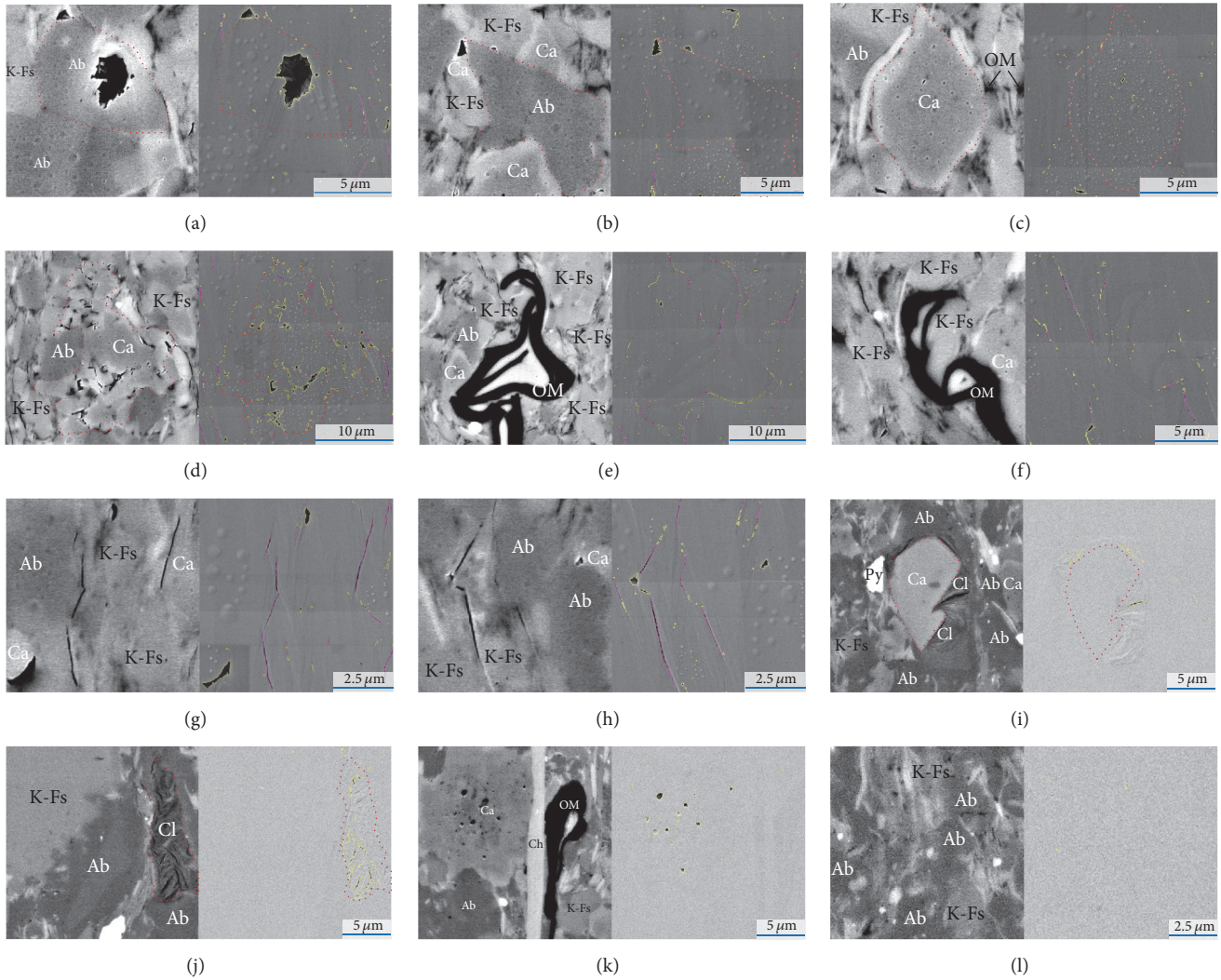


FIGURE 6: Mineralogical, microstructural, and morphological features of clasts (red), pore space (yellow/purple), and rock matrix of sample NJ-019 and NJ-023. Grains occur in a wide range of sizes but were chosen according to their characteristic properties for this illustration. Porosity is predominantly distributed between clasts and OM interfaces (*InterP*), representing very narrow elongated slits along grain boundary interfaces within the polycrystalline matrix. Mineral phases are as follows: Ab, albite; Ca, carbonate; Ch, chlorite; Cl, clay; K-Fs, potassium feldspar; OM, organic matter; Py, pyrite.

(NJ-023), while considering only pores above the PPR lowers these values slightly (up to ca. 1.7%) (Table 4). Visible porosities differ between 1.4% in the carbonate-dominating layer (Map #2), 1.8% in feldspar/carbonate mixed layer (Map #3), and 2.0% in the feldspar-rich layer (Map #1) for sample NJ-001 (only Map #1 of sample NJ-001 was imaged with a pixel size of 30 nm instead of 15 nm). The highest visible porosities in sample NJ-019 (0.9%) are also located in the feldspar-rich layers (Map #2), while the clay and silicate-rich layers (Map #1 and Map #3) feature both about 0.5% (Figure 9). In general, the pore orientation follows the bedding.

Initial classifications of pore types according to Desbois et al. 2009 [4] and Heath et al. 2011 [69] distinguished pores not only based on the location of their occurrence (as proposed by Loucks et al. [60]) but also in consideration of their actual shapes. Similarities are observed in the given samples as

well, featuring several different types of pores as previously described.

3.3.3. Proportion of Organic Matter Porosity. Very high magnification images (40,000 to 80,000x) revealed omnipresent porosity within the OM in sample NJ-001, while samples NJ-019 and NJ-023 show no OM porosity (Figure 3). Based on simple thresholding the porosity of the organic phase in sample NJ-001 was estimated to be ca. $6 \pm 2\%$. Given the high OM proportion of about 8.4% in this sample, the OM porosity may be a significant fraction of the total porosity.

3.3.4. Pore Size Distributions. Pore frequency histograms with power law based bin sizes are given in Figure 10. The normalized distributions suggest a power law distribution over about four orders of magnitude, except a few outliers, for

TABLE 4: Overview of parameters received through the pore shape analysis. All parameters excluding cracks (as well as the power law exponent) are also given above the practical pore resolution of 18 pixels (PPR).

Sample	Mosaic map	Magnification	Area [μm^2]	Number of pores		Visible porosity		Avg. circularity		Avg. AR		D
				total	>PPR	total [%]	>PPR [%]	total	>PPR	total	>PPR	
NJ-001	Map #1	10,000x	301×185	32,187	12,228	2.01	1.72	0.60	0.31	0.55	0.40	2.36
	Map #2	20,000x	120×90	21,507	5,313	1.43	1.21	0.60	0.32	0.60	0.48	2.12
	Map #3	20,000x	134×94	76,740	8,519	1.83	1.38	0.59	0.31	0.67	0.45	2.32
NJ-019	Map #1	20,000x	79×60	2,331	904	0.53	0.47	0.50	0.26	0.44	0.22	2.02
	Map #2	20,000x	120×81	4,562	1,559	0.85	0.79	0.52	0.23	0.47	0.29	1.87
	Map #3	20,000x	123×89	4,368	1,632	0.45	0.40	0.52	0.30	0.46	0.29	2.03
NJ-023	Map #1	20,000x	126×95	853	241	0.07	0.07	0.60	0.55	0.65	0.50	1.84

TABLE 5: Experimental permeabilities (intrinsic) as well as modeled permeabilities (cumulated and upscaled, resp.). Cumulated values show the modeled permeability of each mosaic map derived from the CTM. Upscaled values were normalized (weighted average) to characteristic layer proportions of a whole plug surface (Figure 8). *Total* includes every visible pore, while *corrected* only accounts for pores above the PPR and excludes microcracks as well as *IntraP*-pores in albite in some maps. Marked values (*) feature these maps where relatively large *IntraP*-pores in albite were subtracted from the calculated permeabilities (Figure 13).

Sample	Map	Major element	Intrinsic k [nD]	Cumulated k [nD]		Upscaled k [nD]	
				<i>Total</i>	<i>Corrected</i>	<i>Total</i>	<i>Corrected</i>
NJ-001	Map #1	Na	160.3	800.8	215.3*	665.8	310.1
	Map #2	Ca		537.6	520.8*		
	Map #3	S		38.4	37.6		
NJ-019	Map #1	Ca	43.1	7.9	3.0	323.1	43.1
	Map #2	Na		1,208.4	131.0*		
	Map #3	K		14.5	13.3		
NJ-023	Map #1	—	3.9	2.3	2.3	2.3	2.3

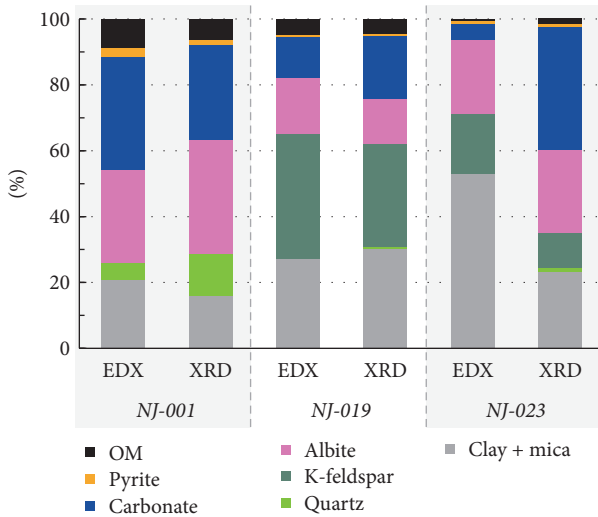


FIGURE 7: Comparison of EDX and XRD (plus TOC) data, where XRD can be seen as the intrinsic mineralogical composition.

instance, some single large pores, which do not line up with the log-log best fit (Figure 11). The power law exponent varies between approx. 1.9 and 2.4 with and 1.8 and 2.3 without

cracks. In sample NJ-001, small pores seem to contribute more to the total porosity due to their higher power law exponents ($D \approx 2.1$) compared to NJ-019 ($D \approx 2.0$).

3.4. *Permeability Predictions.* Cumulated permeability graphs of each individual mosaic are presented in Figure 12. Modeling of the cumulative permeability coefficients was done after correcting the visible porosities for

- (1) isolated, relatively large *IntraP*-pores within albite (Figure 13);
- (2) pores below the PPR;
- (3) visible microcracks (all pores with an AR threshold value of ≤ 0.2 and circularity of ≤ 0.3) which are assumed to be artefacts from sample handling.

Through the investigation of characteristic plug layering, three representative layers of each formation were identified (Maps #1 to #3 of samples NJ-001 and NJ-019, resp.). For upscaling, the predicted permeability values of each mosaic are normalized (by the weighted average) to the total area proportions of each plug. Hence, the weighted average permeability of the three samples changes from 665.8, 323.1, and 2.3 nD to 310.1, 43.1, and 2.3 nD, respectively, after taking the

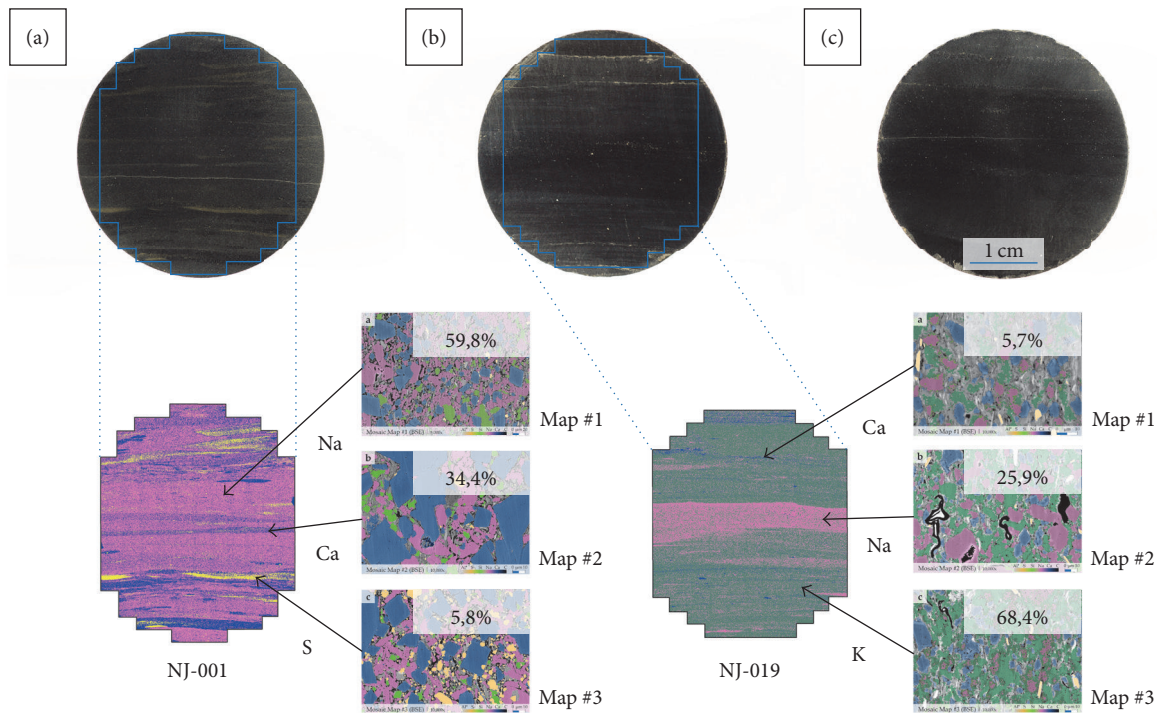


FIGURE 8: Photographs of all three samples (top) plus distinct layers based on EDX analysis (bottom) and their respective area fractions of the plug surface for sample NJ-001 and NJ-019.

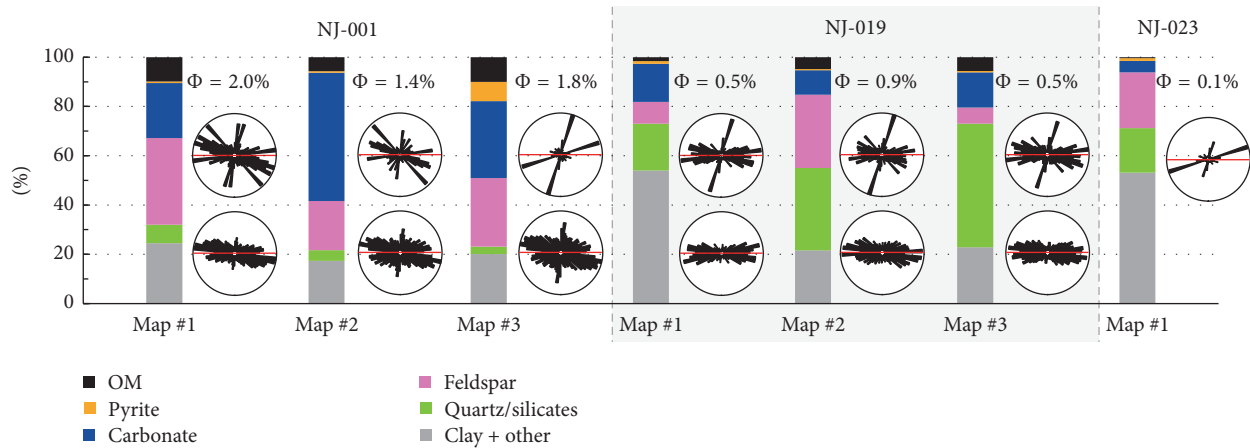


FIGURE 9: Summary of BIB-SEM investigation results showing EDX mineral compositions (bars) and visible porosities as well as pore orientations of all pores (top), respectively, excluding microcracks and pores below the PPR (bottom) of each mosaic map.

mineralogical composition of the plugs NJ-001, NJ-019, and NJ-023 into account (Table 5).

The sum of modeled permeability coefficients of microcracks ranges from $k < 1$ nD (NJ-001 Map #3) up to about 12 nD (NJ-001 Map #1) within all maps, depending on the frequency of these cracks. Pores below the PPR do not add up to relevant calculated values (predicted k values of ca. < 0.1 to 2 nD between all maps).

4. Discussion

4.1. Comparison of Bulk Properties and BIB-SEM Results. The mineralogical compositions of EDX and XRD are similar for samples NJ-001 and NJ-019 (Figure 7), even though XRD results are much more accurate than measuring the bulk composition of an area via EDX. Accordingly, significant differences in carbonate and clay content of EDX versus XRD

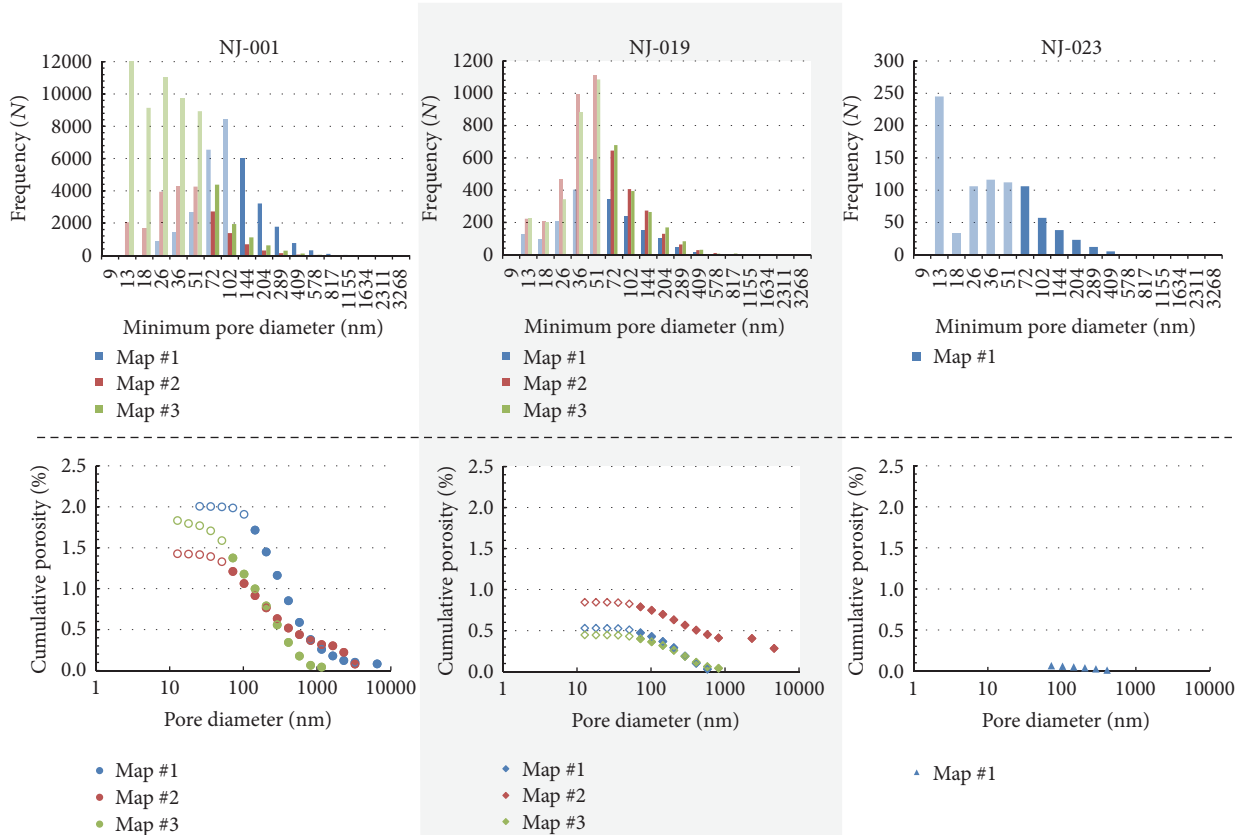


FIGURE 10: Pore size histograms and cumulative visible porosity for all samples.

findings occur in sample NJ-023. The difference is related to sampling heterogeneity between the plugs and the cut-offs used for XRD due to rapid changes in the mineralogical composition within a few centimeters.

Except for the fraction of OM, no other mineral phase shows a clear correlation between its fraction and the porosity trend (Figure 14), implying that the OM is the controlling factor of total and visible porosity in the investigated samples, particularly in NJ.001. Although the recognition of OM porosity in sample NJ-001 lies mostly below the PPR with the given pixel resolution, a proportion of the OM porosity is visible at 20,000x magnification (Figures 2(j) and 2(l)). Also, a considerably higher power law exponent in NJ-001 compared to the other samples corresponds to the porous nature of the OM (Figure 11 and Table 4), as exponents above 2 are an indicator of a dominating contribution of small pores to the total porosity [18, 67]. On the contrary, the lower total porosity and permeability of sample NJ-019 and NJ-023 feature lower D values. Additionally, differences in porosity along the investigated samples are most likely linked to the occurrence of silty layers. The biggest pores are located around feldspars and carbonate grains (as shown on the local porosity maps in Figures 1 and 4) implying that porosity and permeability are mostly bound to these two mineral phases.

Moreover, solid trends between mineralogy, microstructure, and pore properties throughout all investigated scales

imply representative sampling. The bulk measurements exhibit clear correlations between petrophysical properties such as the trend of decreasing He-porosities as well as permeability coefficients along with decreasing TOC content (Table 2). Visible porosities (Table 4) as well as experimentally measured porosities (BIB-SEM versus MIP versus He-pycnometry) follow this trend as well.

4.2. Validating BIB-SEM Derived Permeability Predictions. Unlike sandstones, shales do not feature clear poro-perm relationships [51, 70]. As indicated by Busch and Amann-Hildenbrand [71], caution is advised when using permeability prediction models for shales, especially when the predictions are of empirical origin. In this study, we applied the theoretical CTM based on real pore geometries to predict permeability with an assumption on the tortuosity of the pore network.

We used the pore system characteristics of typical layers that were resolved by BIB-SEM for upscaling to plug scale (Figure 8) to allow a precise and meaningful comparison with measured permeabilities. We assume that the microstructural investigations are representative for certain dominant layers. Since NJ-023 features no clear layering and a very low porosity, we investigated macroscale layering perpendicular to the bedding only for sample NJ-001 and NJ-019 by EDX mapping.

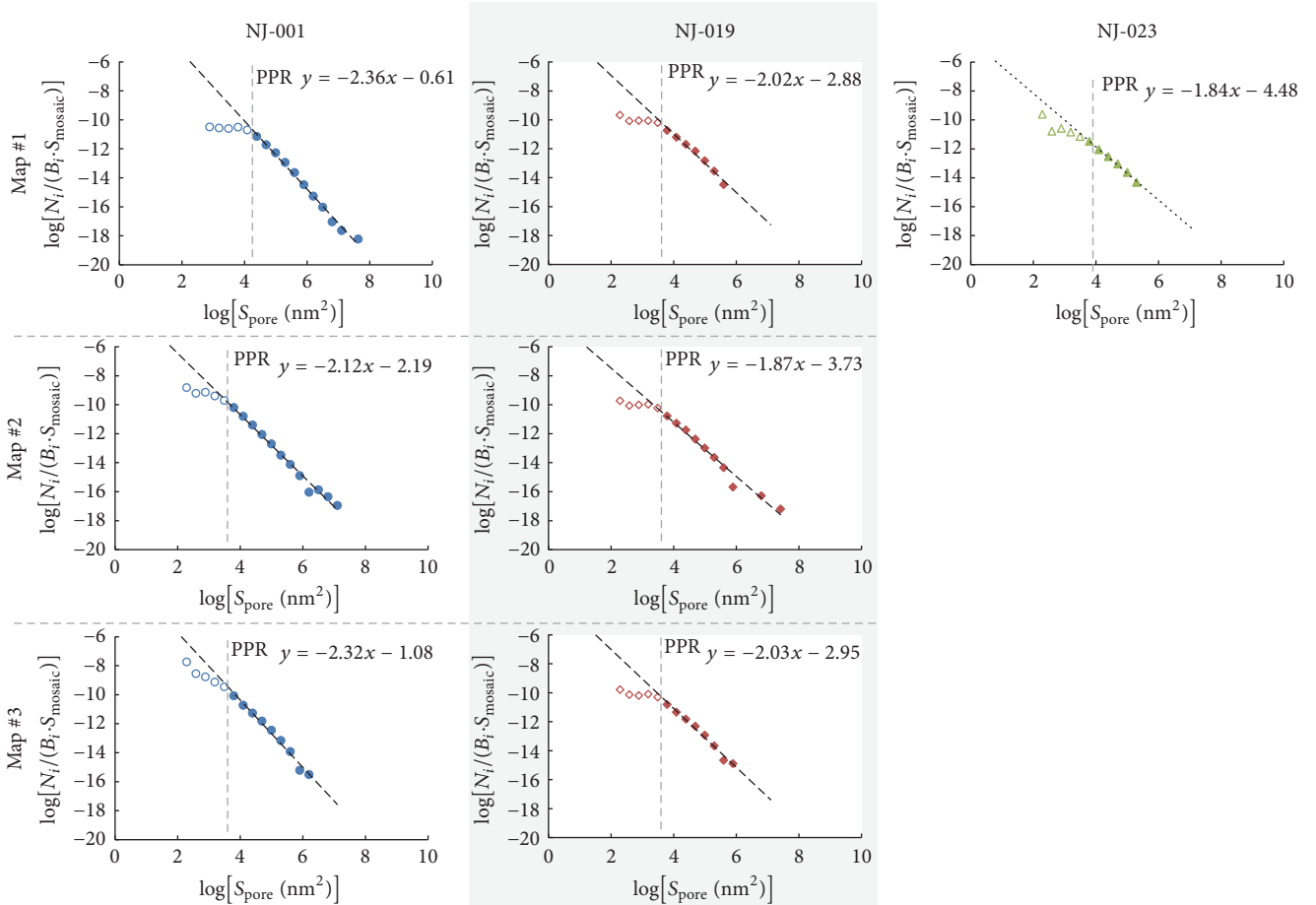


FIGURE 11: Log-log pore size distributions for all three samples.

For the permeability calculation, several adjustments on the pore data were conducted as they were expected to influence the modeled permeability coefficient. Very narrow, elongated pore shapes, identified as microcracks, do not influence the predicted permeabilities significantly (the predicted k values of all maps are < 12 nD) (Figure 12). For the prediction of permeability using the CTM, pores below the PPR were excluded, even though they do not add up to relevant calculated values (the predicted k values of all maps are < 2 nD). This is reasonable as their individual permeability coefficients are up to five orders of magnitude below the total permeabilities of the investigated micrographs, although pores below the PPR make up to $\sim 39\%$ of total pore frequency in some maps (Table 4). Considering the hydraulic radius rather than the geometric radius explains the minor difference between the permeability prediction of narrow elongated pores (i.e., microcracks) and tiny round pores (i.e., pores below the PPR). Additionally, in three of the total seven maps with considerable amounts of albite (NJ-001 Map #1, Map #2, and NJ-019 Map #2), large *IntraP*-pores within these albite clasts were excluded from the permeability calculations as they are assumed to be either completely isolated from

the pore network (fluid inclusions) or “dead-end” pores. However, most pores typically occur at the rims of albite progressing towards the clast’s center, that is why they were not excluded in the permeability calculations.

Albite and its distinct porosity seem to control permeability since the albite rich maps show the highest calculated permeability (Table 5), even though isolated pores were excluded from the calculations. In general, porosity alterations are common in feldspars (e.g., [72, 73]). Carbonate clasts exhibit similar but slightly less porosity compared to albite, featuring the most pore space around grain boundaries (Figure 2(d)). However, this accounts only for carbonates in sample NJ-001 as their fabric is denser compared to the other samples (NJ-019 and NJ-023). The quantitative permeability predictions correspond well to these qualitative observations with the highest predicted permeabilities within the Na-rich maps (ca. 801 and 1,208 nD) and generally high permeability coefficients of the Ca-rich map in sample NJ-001 (ca. 538 nD) (Table 5). This suggests that the coarse-grained material is most important in controlling fluid flow due to less compaction resulting in larger pores. Furthermore, the porous nature of OM in NJ-001 suggests that the pores in

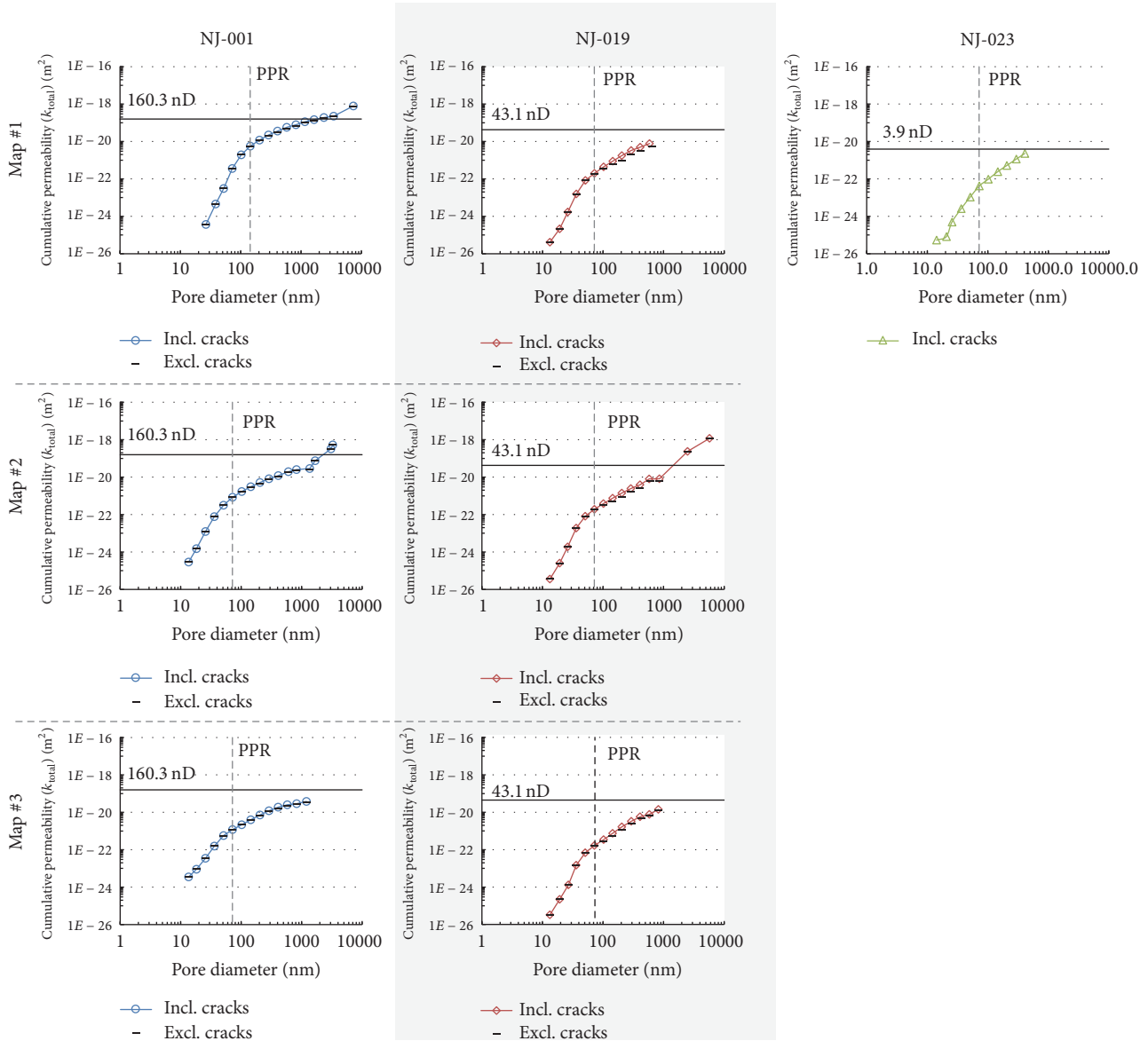


FIGURE 12: Results of the capillary tube model (predicted permeabilities), indicating the importance of pore sizes when adding up the single permeabilities within each pore bin size. Solid lines mark the experimentally derived permeabilities.

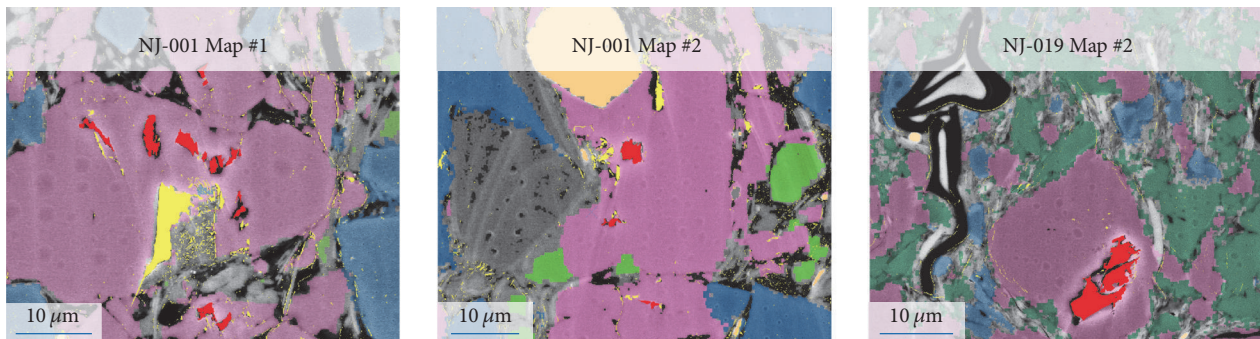


FIGURE 13: Examples of pore space corrections illustrated for Map #1 and Map #2 of sample NJ-001 and Map #2 of sample NJ-019. Large, isolated *IntraP*-pores (red) within albite clasts (pink) are excluded; remaining is the corrected pore space (yellow) used in the CTM calculations. The pore space (yellow/red) appears distorted to fit SE2 image data to the BSE images. CTM calculations were conducted on original pore geometries.

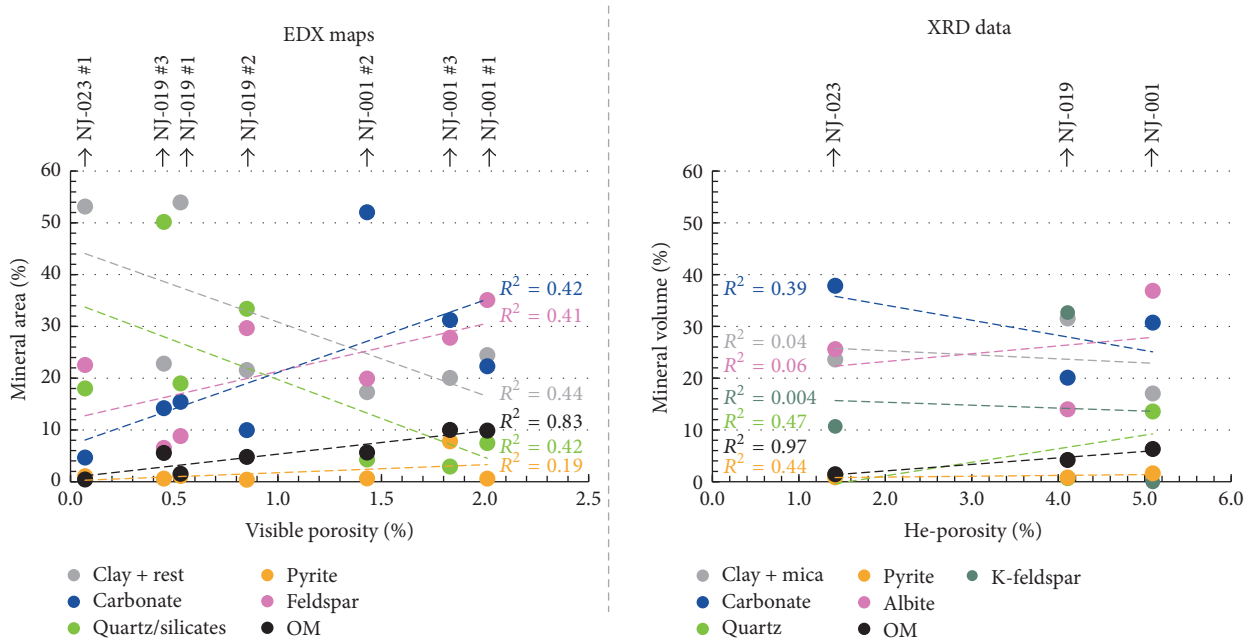


FIGURE 14: Comparison of EDX and XRD (plus TOC) data in regard to the correlation of mineral phases and porosity. Only OM reveals a clear trend with porosity, both, independently of applying direct (EDX) versus indirect (XRD plus TOC) types of investigation.

the OM also add to transport pathways and add up to the calculated permeabilities. However, their small pore sizes probably result in small absolute permeabilities.

Limitations of stereological modeling apply to the CTM calculations as well. Obtaining adequate tortuosity values, especially from 2D data, is problematic. A 3D investigation could deliver different tortuosity factors. By choosing a tortuosity of $\tau = 10$ a good fit between intrinsic and calculated permeability could be established. Values of around 5 to 10 are commonly used for permeability predictions in very tight rock samples that are strongly lithified and feature very low-porous rock fabrics (e.g., [71, 74–77]), though one should be careful as different notations of the CTM exist in the literature (regarding τ versus τ^2).

For validating the BIB-SEM based permeabilities, the results are compared to the experimentally derived permeabilities measured on the exact same sample plugs. Assessing the mineralogy and microstructure is key to allow upscaling to greater sample volumes for meaningful comparison. This was established by normalizing the results of the CTM to the plug scale in this study. The final results of the corrected and upscaled BIB-SEM permeabilities are 310 nD, 43 nD, and 2 nD for sample NJ-001, NJ-019, and NJ-023, respectively. These values are at maximum twice or half, respectively, when compared to the experimentally derived permeabilities (160.3, 43.1, and 3.9 nD). A good correlation of permeabilities modeled by the CTM compared to measured permeabilities by gas permeation was also found by Philipp et al. 2017 [51].

5. Conclusions

- (i) BIB-SEM is a powerful tool that can deliver meaningful permeability values parallel to bedding from

2D pore areas based on simple capillary tube models as shown in this study for the heterogeneous Newark Shale.

- (ii) Upscaling pore system characteristics and permeability predictions from μm -sized mosaic maps to cm-sized plugs is achieved by assessing the mineralogy and associated pore properties of laminae with distinct characteristics individually via BIB-SEM and EDX.
- (iii) BIB-SEM derived permeabilities of the heterogeneous Newark Shale on the plug scale (upscaled) are representative and close to experimentally measured permeabilities.
- (iv) Silty laminae and OM porosity control porosity and permeability of the lacustrine Newark Shale.

Appendix

A. Pore Parameters for the Statistical Evaluation

Pore elongation is based on a pore’s axial ratio (AR) after assessing the “minimum bounding geometry” with the parameters width (w) and length (l):

$$AR = \frac{w}{l}. \tag{A.1}$$

The circularity describes the pore area in relation to its circumference and is a geometrical indicator for the overall roundness. It is expressed as a function of pore area (S_{pore})

and pore perimeter (P_{pore}):

$$\text{Circularity} = \frac{4\pi S_{\text{pore}}}{P_{\text{pore}}^2}. \quad (\text{A.2})$$

B. Detailed Derivation of the CTM

Fluid flow through porous media is described by Darcy's law for incompressible media:

$$Q = -\frac{kA\Delta p}{\Delta L\eta}. \quad (\text{B.1})$$

Here, Q is the volume flow rate ($\text{m}^3 \text{s}^{-1}$), A the cross-sectional area (m^2) of the porous medium, k the permeability (m^2), η the dynamic viscosity (Pa s), and $\Delta p/\Delta L$ the pore pressure gradient (Pa m^{-1}) in the direction of fluid flow.

The Hagen–Poiseuille equation describes laminar flow through a long cylindrical pipe of constant cross-section (a capillary tube):

$$Q = -\frac{r_{\text{hyd}}^4 \pi \Delta p}{8\eta l}. \quad (\text{B.2})$$

Here, r is the hydraulic radius of the capillary, η the dynamic viscosity (Pa s) of the permeating fluid, and Δp the pressure difference (Pa) over the length l .

Combining Darcy's law (see (B.1)) with Poiseuille's law (see (B.2)) delivers

$$Q = -\frac{kA\Delta p}{\Delta L\eta} = -\frac{r_{\text{hyd}}^4 \pi \Delta p}{8\eta l}. \quad (\text{B.3})$$

With the assumption of a sample cube of the length L and the cross-sectional area A across which the pressure gradient is applied, the 3D-porosity of a single capillary tube with the length l is defined as

$$\phi = \frac{\pi r^2 l}{AL}. \quad (\text{B.4})$$

Solving (B.4) for the area A and combing it with (B.3) enable us to express the permeability k as

$$k = \frac{r_{\text{hyd}}^2 \phi L^2}{8l^2}. \quad (\text{B.5})$$

Including the tortuosity ($\tau = l/L$) in (B.5) as well yields a permeability coefficient of a single tortuose capillary pathway:

$$k = \frac{r_{\text{hyd}}^2 \phi}{8\tau^2}. \quad (\text{B.6})$$

Porosity of a sample cube with a single capillary can also be derived from the 2D BIB-SEM data by using areas instead of volumes and thereby neglecting the 3rd dimension:

$$\phi = \frac{S_{\text{pore}}}{S_{\text{mosaic}}}. \quad (\text{B.7})$$

Here, S_{pore} is the pore area (m^2) and S_{mosaic} the total area of the mosaic map (m^2). Inserting (B.7) into (B.6) yields

$$k = \frac{r_{\text{hyd}}^2}{8\tau^2} \cdot \frac{S_{\text{pore}}}{S_{\text{mosaic}}}. \quad (\text{B.8})$$

The hydraulic radius can also be calculated from the BIB-SEM data by

$$r_{\text{hyd}} = \frac{S_{\text{pore}}}{P_{\text{pore}}}. \quad (\text{B.9})$$

The total permeability k_{total} (m^2) of a specific area, for example, a complete SE2 mosaic map S_{mosaic} , is then calculated by adding up all single permeability values of each pore:

$$k_{\text{total}} = \sum_{i=1}^n (k_i) = \sum_{i=1}^n \left(\frac{r_{\text{hyd}_i}^2}{8\tau^2} \cdot \frac{S_{\text{pore}_i}}{S_{\text{mosaic}}} \right), \quad (\text{B.10})$$

for $n \in N$.

Conflicts of Interest

The authors declare that there are no conflicts of interest regarding the publication of this paper.

Acknowledgments

The authors thank P. Bertier of the Clay and Interface Mineralogy (CIM) research group at the RWTH Aachen University for providing them with the thorough XRD analysis. P. E. Olsen is acknowledged for his allowance to sample the Newark Basin Coring Project cores and his help in the IODP core store at Rutgers University.

References

- [1] F. Javadpour, D. Fisher, and M. Unsworth, "Nanoscale gas flow in shale gas sediments," *Journal of Canadian Petroleum Technology*, vol. 46, no. 10, pp. 55–61, 2007.
- [2] F. P. Wang and R. M. Reed, "Pore Networks and Fluid Flow in Gas Shales," in *Proceedings of the SPE Annual Technical Conference and Exhibition*, 8 pages, 2009.
- [3] R. G. Loucks, R. M. Reed, S. C. Ruppel, and D. M. Jarvie, "Morphology, genesis, and distribution of nanometer-scale pores in siliceous mudstones of the mississippian barnett shale," *Journal of Sedimentary Research*, vol. 79, no. 12, pp. 848–861, 2009.
- [4] G. Desbois, J. L. Urai, and P. A. Kukla, "Morphology of the pore space in claystones - Evidence from BIB/FIB ion beam sectioning and cryo-SEM observations," *eEarth Discussions*, vol. 4, no. 1, pp. 15–22, 2009.
- [5] G. Desbois, J. L. Urai, M. E. Houben, and Y. Sholokhova, "Typology, morphology and connectivity of pore space in claystones from reference site for research using BIB, FIB and cryo-SEM methods," *EPJ Web of Conferences*, vol. 22005, pp. 1–6, 2010.
- [6] S. Bernard and B. Horsfield, "Thermal maturation of gas shale systems," *Annual Review of Earth and Planetary Sciences*, vol. 42, pp. 635–651, 2014.

- [7] G. R. Chalmers, R. M. Bustin, and I. M. Power, "Characterization of gas shale pore systems by porosimetry, pycnometry, surfacearea, andfield emission scanning electron microscopy/transmission electron microscopy image analyses: examples from the Barnett, Woodford, Haynesville, Marcellus, and Doig units," *AAPG Bulletin*, vol. 96, no. 6, pp. 1099–1119, 2012.
- [8] K. L. Milliken and M. E. Curtis, "Imaging pores in sedimentary rocks: foundation of porosity prediction," *Marine and Petroleum Geology*, vol. 73, pp. 590–608, 2016.
- [9] Q. R. Passey, K. M. Bohacs, W. L. Esch, R. Klimentidis, and S. Sinha, "From oil-prone source rock to gas-producing shale reservoir - Geologic and petrophysical characterization of unconventional shale-gas reservoirs," in *CPS/SPE International Oil & Gas Conference and Exhibition in China*, pp. 1707–1735, 2010.
- [10] J. M. Rine, E. Smart, W. Dorsey, K. Hooghan, and M. Dixon, "Comparison of porosity distribution within selected north american shale units by SEM examination of argon-ion-milled samplesargon-ion-milled samples," in *AAPG Memoir 102: Electron Microscopy of Shale Hydrocarbon Reservoirs*, W. K. Camp, E. Diaz, and B. Wawak, Eds., pp. 137–152, American Association of Petroleum Geologists, Tulsa, Oklahoma, USA, 2013.
- [11] C. H. Sondergeld, R. J. Ambrose, C. S. Rai, and J. Moncrieff, "Micro-structural studies of gas shales," in *SPE Unconventional Gas Conference*, pp. 1–17, Society of Petroleum Engineers, Pittsburgh, Pennsylvania, USA, 2011.
- [12] S. Bernard, B. Horsfield, H.-M. Schulz, R. Wirth, A. Schreiber, and N. Sherwood, "Geochemical evolution of organic-rich shales with increasing maturity: A STXM and TEM study of the Posidonia Shale (Lower Toarcian, northern Germany)," *Marine and Petroleum Geology*, vol. 31, no. 1, pp. 70–89, 2012.
- [13] M. E. Curtis, R. J. Ambrose, and C. H. Sondergeld, "Structural characterization of gas shales on the micro- and nanoscales," in *Canadian Unconventional Resources and International Petroleum Conference*, Society of Petroleum Engineers (SPE) & Canadian Society for Unconventional Resources, Calgary, Alberta, Canada, 2010.
- [14] M. E. Curtis, R. J. Ambrose, C. H. Sondergeld, and C. S. Rai, "Transmission and scanning electron microscopy investigation of pore connectivity of gas shales on the nanoscale," in *North American Unconventional Gas Conference and Exhibition*, Society of Petroleum Engineers, The Woodlands, Tex, USA, 2011.
- [15] M. E. Curtis, C. H. Sondergeld, R. J. Ambrose, and C. S. Rai, "Microstructural investigation of gas shales in two and three dimensions using nanometer-scale resolution imaging," *AAPG Bulletin*, vol. 96, no. 4, pp. 665–677, 2012.
- [16] S. Hemes, G. Desbois, J. L. Urai, M. De Craen, and M. Honty, "Variations in the morphology of porosity in the boom clay formation: insights from 2D high resolution BIB-SEM imaging and Mercury injection Porosimetry," *Geologie en Mijnbouw/Netherlands Journal of Geosciences*, vol. 92, no. 4, pp. 275–300, 2013.
- [17] S. Hemes, G. Desbois, J. L. Urai, B. Schröppel, and J.-O. Schwarz, "Multi-scale characterization of pore microstructures in Boom Clay (HADES, Mol, Belgium) using a combination of μ -CT, BIB-SEM and serial FIB-SEM techniques," in *Microporous and Mesoporous Materials*, vol. 208, pp. 1–20, 2014.
- [18] M. E. Houben, G. Desbois, and J. L. Urai, "Pore morphology and distribution in the Shaly facies of Opalinus Clay (Mont Terri, Switzerland): Insights from representative 2D BIB-SEM investigations on mm to nm scale," *Applied Clay Science*, vol. 71, pp. 82–97, 2013.
- [19] M. E. Houben, G. Desbois, and J. L. Urai, "A comparative study of representative 2D microstructures in Shaly and Sandy facies of Opalinus Clay (Mont Terri, Switzerland) inferred from BIB-SEM and MIP methods," *Marine and Petroleum Geology*, vol. 49, pp. 143–161, 2014.
- [20] J. Klaver, S. Hemes, M. Houben, G. Desbois, Z. Radi, and J. L. Urai, "The connectivity of pore space in mudstones: insights from high-pressure Wood's metal injection, BIB-SEM imaging, and mercury intrusion porosimetry," *Geofluids*, vol. 15, no. 4, pp. 577–591, 2015.
- [21] J. Klaver, G. Desbois, J. L. Urai, and R. Littke, "BIB-SEM study of the pore space morphology in early mature Posidonia Shale from the Hils area, Germany," *International Journal of Coal Geology*, vol. 103, pp. 12–25, 2012.
- [22] J. Klaver, G. Desbois, R. Littke, and J. L. Urai, "BIB-SEM characterization of pore space morphology and distribution in postmature to overmature samples from the Haynesville and Bossier Shales," *Marine and Petroleum Geology*, vol. 59, pp. 451–466, 2015.
- [23] K. L. Milliken, W. L. Esch, R. M. Reed, and T. Zhang, "Grain assemblages and strong diagenetic overprinting in siliceous mudrocks, Barnett Shale (Mississippian), Fort Worth Basin, Texas," *AAPG Bulletin*, vol. 96, no. 8, pp. 1553–1578, 2012.
- [24] K. L. Milliken, M. Rudnicki, D. N. Awwiller, and T. Zhang, "Organic matter-hosted pore system, Marcellus Formation (Devonian), Pennsylvania," *AAPG Bulletin*, vol. 97, no. 2, pp. 177–200, 2013.
- [25] R. M. Slatt and N. R. O'Brien, "Pore types in the Barnett and Woodford gas shales: contribution to understanding gas storage and migration pathways in fine-grained rocks," *AAPG Bulletin*, vol. 95, no. 12, pp. 2017–2030, 2011.
- [26] S. Bernard, L. Brown, R. Wirth et al., "FIB-SEM and TEM investigations of an organic-rich shale maturation series from the lower toarcian posidonia shale, Germany: nanoscale pore system and fluid-rock interactions," in *AAPG Memoir 102: Electron Microscopy of Shale Hydrocarbon Reservoirs*, W. K. Camp, E. Diaz, and B. Wawak, Eds., pp. 53–66, American Association of Petroleum Geologists, Tulsa, Oklahoma, USA, 2013.
- [27] J. Schmatz, J. L. Urai, S. Berg, and H. Ott, "Nanoscale imaging of pore-scale fluid-fluid-solid contacts in sandstone," *Geophysical Research Letters*, vol. 42, no. 7, pp. 2189–2195, 2015.
- [28] P. H. Nelson, "Pore-throat sizes in sandstones, tight sandstones, and shales," *AAPG Bulletin*, vol. 93, no. 3, pp. 329–340, 2009.
- [29] H. Andrä, N. Combaret, J. Dvorkin et al., "Digital rock physics benchmarks-Part II: computing effective properties," *Computers & Geosciences*, vol. 50, pp. 33–43, 2013.
- [30] N. Saxena, G. Mavko, R. Hofmann, and N. Srisutthiyakorn, "Estimating elastic moduli of rocks from thin sections," *Computers and Geosciences*, vol. 102, pp. 79–99, 2017.
- [31] S. Kelly, H. El-Sobky, C. Torres-Verdín, M. T. Balhoff, and C. Torres-Verdín, "Assessing the utility of FIB-SEM images for shale digital rock physics," in *Advances in Water Resources*, pp. 1–15, 2015.
- [32] L. Chen, L. Zhang, Q. Kang, H. S. Viswanathan, J. Yao, and W. Tao, "Nanoscale simulation of shale transport properties using the lattice Boltzmann method: Permeability and diffusivity," *Scientific Reports*, vol. 5, Article no: 8089, 2015.
- [33] J. Ma, J. P. Sanchez, K. Wu, G. D. Couples, and Z. Jiang, "A pore network model for simulating non-ideal gas flow in micro- and nano-porous materials," *Fuel*, vol. 116, pp. 498–508, 2014.

- [34] M. J. Blunt, B. Bijeljic, H. Dong et al., "Pore-scale imaging and modelling," *Advances in Water Resources*, vol. 51, pp. 197–216, 2013.
- [35] G. H. Grathoff, M. Peltz, F. Enzmann, and S. Kaufhold, "Porosity and permeability determination of organic-rich Posidonia shales based on 3-D analyses by FIB-SEM microscopy," *Solid Earth*, vol. 7, no. 4, pp. 1145–1156, 2016.
- [36] M. E. Houben, N. J. Hardebol, A. Barnhoorn et al., "Fluid flow from matrix to fractures in early jurassic shales," *International Journal of Coal Geology*, vol. 175, pp. 26–39, 2017.
- [37] P. C. Carman, *Flow of Gases through Porous Media*, Butterworths Scientific Publications, London, UK, 1956.
- [38] J. Kozeny, "Über die kapillare Leitung des Wassers im Boden (Concerning capillary conduction of water in the ground)," in *Akademie der Wissenschaften in Wien*, vol. 136, pp. 271–306, 1927.
- [39] P. E. Olsen, "On the use of the term newark for triassic and early jurassic rocks of eastern North America," *Newsletters on Stratigraphy*, vol. 7, no. 2, pp. 90–95, 1978.
- [40] P. E. Olsen, D. V. Kent, B. Cornet, W. K. Witte, and R. W. Schlische, "High-resolution stratigraphy of the Newark rift basin (early Mesozoic, eastern North America)," *Bulletin of the Geological Society of America*, vol. 108, no. 1, pp. 40–77, 1996.
- [41] P. E. Olsen and D. V. Kent, "Milankovitch climate forcing in the tropics of pangea during the late triassic," *Palaeogeography, Palaeoclimatology, Palaeoecology*, vol. 122, no. 1–4, pp. 1–26, 1996.
- [42] M. O. Withjack and R. W. Schlische, "A review of tectonic events on the passive margin of eastern North America," in *Proceedings of the 25th Annual Bob F. Perkins Research Conference: Petroleum Systems of Divergent Continental Margin Basins*, pp. 203–235, Houston, Texas, USA, 2005.
- [43] M. Gasparik, A. Ghanizadeh, P. Bertier, Y. Gensterblum, S. Bouw, and B. M. Krooss, "High-pressure methane sorption isotherms of black shales from the Netherlands," *Energy and Fuels*, vol. 26, no. 8, pp. 4995–5004, 2012.
- [44] R. Littke, J. L. Urai, A. K. Uffmann, and F. Risvanis, "Reflectance of dispersed vitrinite in Palaeozoic rocks with and without cleavage: Implications for burial and thermal history modeling in the Devonian of Rursee area, northern Rhenish Massif, Germany," *International Journal of Coal Geology*, vol. 89, no. 1, pp. 41–50, 2012.
- [45] V. F. Sachse, R. Littke, H. Jabour, T. Schümann, and O. Kluth, "Late Cretaceous (Late Turonian, Coniacian and Santonian) petroleum source rocks as part of an OAE, Tarfaya Basin, Morocco," *Marine and Petroleum Geology*, vol. 29, no. 1, pp. 35–49, 2012.
- [46] A. Ghanizadeh, A. Amann-Hildenbrand, M. Gasparik, Y. Gensterblum, B. M. Krooss, and R. Littke, "Experimental study of fluid transport processes in the matrix system of the European organic-rich shales: II. Posidonia Shale (Lower Toarcian, northern Germany)," *International Journal of Coal Geology*, vol. 123, pp. 20–33, 2014.
- [47] A. Ghanizadeh, M. Gasparik, A. Amann-Hildenbrand, Y. Gensterblum, and B. M. Krooss, "Experimental study of fluid transport processes in the matrix system of the European organic-rich shales: I. Scandinavian alum shale," *Marine and Petroleum Geology*, vol. 51, pp. 79–99, 2014.
- [48] A. Hildenbrand, S. Schlömer, and B. M. Krooss, "Gas breakthrough experiments on fine-grained sedimentary rocks," *Geofluids*, vol. 2, no. 1, pp. 3–23, 2002.
- [49] R. Fink, B. M. Krooss, and A. Amann-Hildenbrand, "Stress-dependence of porosity and permeability of the Upper Jurassic Bossier shale: an experimental study," in *Geomechanical and Petrophysical Properties of Mudrocks*, E. H. Rutter, J. Mecklenburgh, and G. K. Taylor, Eds., Geological Society of London, London, UK, 2017.
- [50] R. Fink, B. M. Krooss, Y. Gensterblum, and A. Amann-Hildenbrand, "Apparent permeability of gas shales – Superposition of fluid-dynamic and poro-elastic effects," *Fuel*, vol. 199, pp. 532–550, 2017.
- [51] T. Philipp, B. Laurich, G. Desbois et al., "The effect of microstructural heterogeneity on pore size distribution and permeability in Opalinus Clay (Mont Terri, Switzerland): insights from an integrated study of laboratory fluid flow and pore morphology from BIB-SEM images," in *Geomechanical and Petrophysical Properties of Mudrocks, Special Publications*, E. H. Rutter, J. Mecklenburgh, and K. G. Taylor, Eds., vol. 454, Geological Society, London, UK, 2017.
- [52] M. Jiang, J. Klaver, J. Schmatz, and L. U. Janos, "Nanoscale porosity analysis in geological materials," in *14th International Congress for Stereology and Image Analysis*, University of Liège, Liège, Belgium, 2015.
- [53] C. F. Berg, "Permeability description by characteristic length, tortuosity, constriction and porosity," *Transport in Porous Media*, vol. 103, no. 3, pp. 381–400, 2014.
- [54] Y. Lei, X. Luo, X. Wang et al., "Characteristics of silty laminae in Zhangjiatan shale of southeastern Ordos Basin, China: implications for shale gas formation," *AAPG Bulletin*, vol. 99, no. 4, pp. 661–687, 2015.
- [55] P. E. Olsen, "Tectonic, climatic, and biotic modulation of lacustrine ecosystems - examples from neward supergroup of Eastern North America," in *Lacustrine Basin Exploration: Case Studies and Modern Analogs*, B. Katz, Ed., pp. 209–224, American Association of Petroleum Geologists, Palisades, New York, USA, 1990.
- [56] B. Zolitschka, P. Francus, A. E. K. Ojala, and A. Schimmelmann, "Varves in lake sediments – a review," in *Quaternary Science Reviews*, vol. 117, pp. 1–14, 2015.
- [57] J. Klaver, G. Desbois, R. Littke, and J. L. Urai, "BIB-SEM pore characterization of mature and post mature Posidonia Shale samples from the Hils area, Germany," *International Journal of Coal Geology*, vol. 158, pp. 78–89, 2016.
- [58] D. S. Jennings and J. Antia, "Petrographic characterization of the eagle ford shale, South Texas: mineralogy, common constituents, and distribution of nanometer-scale pore types," in *AAPG Memoir 102: Electron Microscopy of Shale Hydrocarbon Reservoirs*, W. K. Camp, E. Diaz, and B. Wawak, Eds., pp. 101–114, American Association of Petroleum Geologists, 2013.
- [59] X. Tang, J. Zhang, X. Wang et al., "Shale characteristics in the southeastern Ordos basin, China: implications for hydrocarbon accumulation conditions and the potential of continental shales yishan slop jinxi folding," *International Journal of Coal Geology*, vol. 128–129, pp. 32–46, 2014.
- [60] R. G. Loucks, R. M. Reed, S. C. Ruppel, and U. Hammes, "Spectrum of pore types and networks in mudrocks and a descriptive classification for matrix-related mudrock pores," *AAPG Bulletin*, vol. 96, no. 6, pp. 1071–1098, 2012.
- [61] Y. Hou, S. He, J. Wang, N. B. Harris, C. Cheng, and Y. Li, "Preliminary study on the pore characterization of lacustrine shale reservoirs using low pressure nitrogen adsorption and field emission scanning electron microscopy methods?: a case study of the upper jurassic emuerhe formation, Mohe basin, northeastern," *Canadian Journal of Earth Sciences*, vol. 306, pp. 294–306, 2015.

- [62] M. Wang, R. W. T. Wilkins, G. Song et al., "Geochemical and geological characteristics of the Es3L lacustrine shale in the Bonan sag, Bohai Bay Basin, China," *International Journal of Coal Geology*, vol. 138, pp. 16–29, 2015.
- [63] J. Schmatz and J. L. Urai, "The interaction of migrating grain boundaries and fluid inclusions in naturally deformed quartz: A case study of a folded and partly recrystallized quartz vein from the Hunsrück Slate, Germany," *Journal of Structural Geology*, vol. 33, no. 4, pp. 468–480, 2011.
- [64] R. G. Loucks, S. C. Ruppel, X. Wang et al., "Pore types, pore-network analysis, and pore quantification of the lacustrine shale-hydrocarbon system in the late triassic Yanchang formation in the Southeastern Ordos basin, China," *Interpretation*, vol. 5, no. 2, pp. 63–79, 2017.
- [65] F. Jiang, J. Chen, Z. Xu et al., "Organic matter pore characterization in lacustrine shales with variable maturity using nanometer-scale resolution X-ray computed tomography," *Energy & Fuels*, 2017.
- [66] X. Tang, J. Zhang, Z. Jin et al., "Experimental investigation of thermal maturation on shale reservoir properties from hydrous pyrolysis of Chang 7 shale, Ordos Basin," *Marine and Petroleum Geology*, vol. 64, pp. 165–172, 2015.
- [67] S. Giffin, R. Littke, J. Klaver, and J. L. Urai, "Application of BIB-SEM technology to characterize macropore morphology in coal," *International Journal of Coal Geology*, vol. 114, pp. 85–95, 2013.
- [68] R. G. Loucks and R. M. Reed, "Scanning-electron-microscope petrographic evidence for distinguishing organic-matter pores associated with deposition organic matter versus migrated organic matter in mudrocks," *GCAGS Journal*, vol. 3, pp. 51–60, 2014.
- [69] J. E. Heath, T. A. Dewers, B. J. O. L. McPherson et al., "Pore networks in continental and marine mudstones: Characteristics and controls on sealing behavior," *Geosphere*, vol. 7, no. 2, pp. 429–454, 2011.
- [70] C. E. Neuzil, "How permeable are clays and shales?" *Water Resources Research*, vol. 30, no. 2, pp. 145–150, 1994.
- [71] A. Busch and A. Amann-Hildenbrand, "Predicting capillarity of mudrocks," *Marine and Petroleum Geology*, vol. 45, pp. 208–223, 2013.
- [72] M. El-Tabakh, R. Riccioni, and B. C. Schreiber, "Evolution of late triassic rift basin evaporites (passaic formation): newark basin, eastern North America," *Sedimentology*, vol. 44, no. 4, pp. 767–790, 1997.
- [73] A. M. Wolela and E. H. Gierlowski-Kordesch, "Diagenetic history of fluvial and lacustrine sandstones of the Hartford Basin (Triassic-Jurassic), Newark Supergroup, USA," *Sedimentary Geology*, vol. 197, no. 1-2, pp. 99–126, 2007.
- [74] H. Darabi, A. Ettehad, F. Javadpour, and K. Sepehrnoori, "Gas flow in ultra-tight shale strata," *Journal of Fluid Mechanics*, vol. 710, pp. 1–18, 2012.
- [75] L. M. Keller, L. Holzer, R. Wepf, and P. Gasser, "3D geometry and topology of pore pathways in opalinus clay: implications for mass transport," *Applied Clay Science*, vol. 52, no. 1-2, pp. 85–95, 2011.
- [76] L. M. Keller, P. Schuetz, R. Erni et al., "Characterization of multi-scale microstructural features in opalinus clay," *Microporous and Mesoporous Materials*, vol. 170, pp. 83–94, 2013.
- [77] H. Pape, C. Clauser, and J. Iffland, "Variation of permeability with porosity in sandstone diagenesis interpreted with a fractal pore space model," *Pure and Applied Geophysics*, vol. 157, no. 4, pp. 603–619, 2000.

Research Article

Geofluid Systems of Koryaksky-Avachinsky Volcanoes (Kamchatka, Russia)

A. Kiryukhin,¹ V. Lavrushin,² P. Kiryukhin,³ and P. Voronin¹

¹*Institute of Volcanology and Seismology, FEB RAS, Piip 9, Petropavlovsk-Kamchatsky 683006, Russia*

²*Geological Institute RAS, Pyzhevsky 7, Moscow 119017, Russia*

³*EPAM, Zastavskaya 22-2, Mega Park, Saint Petersburg 196084, Russia*

Correspondence should be addressed to A. Kiryukhin; avkiryukhin2@mail.ru

Received 23 February 2017; Revised 4 July 2017; Accepted 20 July 2017

Academic Editor: Kundan Kumar

Copyright © 2017 A. Kiryukhin et al. This is an open access article distributed under the Creative Commons Attribution License, which permits unrestricted use, distribution, and reproduction in any medium, provided the original work is properly cited.

The Koryaksky-Avachinsky volcanogenic basin, which has an area of 2530 km², is located 25 km from Petropavlovsk-Kamchatsky City and includes five Quaternary volcanoes (two of which, Avachinsky (2750 masl) and Koryaksky (3456 masl), are active), and is located within a depression that has formed atop Cretaceous basement rocks. Magma injection zones (dikes and chamber-like shapes) are defined by plane-oriented clusters of local earthquakes that occur during volcanic activity (mostly in 2008–2011) below Koryaksky and Avachinsky volcanoes at depths ranging from –4.0 to –2.0 km and +1.0 to +2.0 km, respectively. Water isotopic (δD , $\delta^{18}O$) data indicate that these volcanoes act as recharge areas for their adjacent thermal mineral springs (Koryaksky Narzans, Isotovskiy, and Pinachevskiy) and the wells of the Bystrinsky and Elizovo aquifers. Carbon $\delta^{13}C$ data in CO₂ from CO₂ springs in the northern foothills of Koryaksky Volcano reflect the magmatic origin of CO₂. Carbon $\delta^{13}C$ data in methane CH₄ reservoirs penetrated by wells in the Neogene-Quaternary layer around Koryaksky and Avachinsky volcanoes indicate the thermobiogenic origin of methane. Thermal-hydrodynamic TOUGH2 conceptual modeling is used to determine what types of hydrogeologic boundaries and heat and mass sources are required to create the temperature, pressure, phase, and CO₂ distributions observed within the given geological conditions of the Koryaksky-Avachinsky volcanic geofluid system.

1. Introduction

Avachinsky and Koryaksky volcanoes are located 25–30 km from the city of Petropavlovsk-Kamchatsky, which has a population of approximately 250 thousand people, contains in its interior significant resources of underground heat and groundwater, and represents a potential danger (see Appendix A with Figures). The cone of Avachinsky Volcano was formed 3500 years ago and has produced 15 historical eruptions since 1737. Koryaksky Volcano experienced a significant increase in fumarolic activity in 2008–2009 [1]. The Koryaksky-Avachinsky Basin contains two fresh groundwater reservoirs (Elizovo and Bystrinsky), which are used as the water supply of Petropavlovsk-Kamchatsky and its neighboring cities. The Ketkino low-temperature geothermal field is used for balneological purposes; it also features projects of the EGS utilization of the magma chamber of Avachinsky Volcano. Nevertheless, the geofluid system of

the Koryaksky-Avachinsky volcanoes is not fully understood in terms of its heat source distributions and the types of hydrologic boundaries on the surfaces of the volcanoes, which prevents more extensive use of its potential resources.

Magma injections below active volcanoes have been a significant focus of recent studies [2–4], which revealed their hydrofracturing nature and the plane-oriented swarms of earthquakes with which they are associated. Thus, in this paper, we used plane-oriented earthquake clusters (retrieved from the Kamchatka Branch of the Geophysical Survey Russia Academy of Sciences (KB GS RAS) catalogs 2001–2016) to track dikes injected below the above-mentioned volcanoes [5, 6]. The magma injection zones (i.e., dikes and chamber-like shapes) defined using this method were defined as heat sources for their adjacent hydrogeological reservoirs and surface features (hot springs and fumaroles) in terms of thermal-hydrodynamic models.

Thus, this paper focuses on the Koryaksky-Avachinsky volcanic cluster and aims to achieve the following objectives: (1) using seismic data to identify dike swarms and magma chambers (i.e., potential heat sources); (2) using deep wells, thermal features, and the geochemistry of cold springs (i.e., water and carbon isotopes and water and gas chemistry) and temperature data to estimate the pressure/temperature/phase parameters of reservoirs and their mass/heat recharge conditions; (3) using TOUGH2-modeling, based on the above-mentioned data, to verify and estimate the role of Koryaksky Volcano as an injector of magma and cold water into adjacent structures and the creation of hydrothermal circulation and geothermal and gas reservoirs. It is also noteworthy that the rate and extent of water injection into the plumbing systems of active volcanoes are crucial to prevent or trigger catastrophic eruptions (i.e., hundreds of km³ in size) due to heat overbalance between magma and water injection rates, as was shown earlier by Fournier and Pitt [8] using Yellowstone caldera as an example.

2. Brief Review of Studies of Magma Plumbing Systems of Volcanoes

Volcanoes and crustal magma chambers result from the ascent of magma from primary magma chambers at depths of 150–200 km [11]. Crustal magma chambers are fed by magma from primary magma reservoirs (zones of magma accumulation) and supply magma needed for the formation of inclined dikes, sills, and dikes, including magma-feeding dikes that produce the eruption of magma onto the ground surface for the generation of volcanic edifices themselves. The formation of sills and dikes during initial emplacement through the viscous shells of magma chambers expands the chambers. Many dikes are “frozen” in their host rocks and do not reach the ground, whereas others change their orientations during propagation and become sills. A review of paleovolcanological evidence and the existing thermohydrodynamic models of magma chambers shows the following characteristics (Gudmundsson, 2012): (1) many crustal magma chambers are produced from sills; (2) active crustal magma chambers inject magma into associated volcanoes, with most chambers existing in a partially molten (pore-like) state; (3) ellipsoids are thermally stable shapes of magma chambers; (4) any discussion of hydraulic fracturing and the injection of dikes should consider the excess pressure of magma (and the strength of the host rocks needed to resist hydrofracturing, which is 1–6 MPa); (5) the excess pressure during eruptions decreases in an exponential manner, until the dike loses its hydraulic connection to the chamber; (6) the pressure of magma in the chamber during a period of repose must equal the overall lithostatic pressure; (7) the conditions that lead to hydraulic fracture at the top of a magma chamber are reached in two ways, either by increasing the absolute pressure of the magma in the chamber due to injection from the magma reservoir or by decreasing the horizontal stress due to regional extension; and (8) the local stress field around the magma chamber depends on the shape and depth of the

chamber, as well as the geomechanical properties and layering of the host rocks.

Hydraulic fracturing is more difficult when the fluid is subject to “freezing” because in this case one needs greater discharge rates to maintain thermal balance above the solidus. For this reason, magma injections in the form of dikes should have larger apertures (up to 1–10 m), which can be deduced from both theoretical calculations and geological observations.

The formation of new fissures by hydraulic fracturing and the renewal of activity on preexisting faults are accompanied by seismicity due to the generation of shear fissures in the zone immediately adjacent to the main aseismic zone of a hydraulic fracture fissure (i.e., a seismicity trigger). For this reason, it may be hypothesized that the planes that host microearthquake clusters have the same orientation as the hydraulic fracture fissures produced during magma injection (emplacement). The magnitudes of strike-slip earthquakes with slip amplitudes of 0.1 mm to 1 cm and fissure lengths of a few hundred meters are estimated to range from 1 to 2. This is consistent with the sensitivity of the local seismograph networks that are operated in the area of the Koryaksky-Avachinsky volcanic cluster.

The results of hydrogeomechanical CFRAC modeling [12, 13] show that it is feasible that plane-oriented clusters of earthquakes beneath active volcanoes may indicate processes of magma fracking or dike formation [6, 14].

The approach to this problem is also motivated by the observations reported by Sigmundsson et al. [3], who described the injection of magma from the magma chamber beneath the Bardarbunga central-type volcano, Iceland, which occurred in August 2014 and was accompanied by a dike that was propagated at a distance of 50 km. Bardarbunga volcano (which has a caldera that is 8 × 11 km in size and produced 23 eruptions during the last 1100 years) is located in the central part of the Icelandic rift zone (with an extension rate of 19 mm/year). The magma chamber of Bardarbunga volcano is assumed to be located at a depth of 10–15 km. The volume of lava erupted in 2014 is estimated to be 1.4 km³ (thus representing the largest lava eruption in Iceland since 1783). Seismic event data were used to identify the shape of the 50 km long segmented dike, which included 11 plane-oriented earthquake clusters (with the number of earthquakes, which had magnitudes of up to 5, ranging from 57 to 1181). The injection of the dike lasted for 22 days. It is noteworthy that the first dike segment was normal to the caldera boundary (along the axes of least stress), while the next dike that was generated coincided with the strike of the rift zone. The eruption started at the last dike segment and lasted for 6 months. GPS and InSAR data yielded an estimate of the volume of the dike system of 0.6 km³ and that of a dike wall opening of 320 cm; the decrease in the volume of the magma chamber was estimated to be 0.3 km³.

Ground deformation that occurred during the 2012–2013 eruption of Tolbachik Volcano (Kamchatka) (9 months, 0.54 km³) was estimated based on multiple satellite-based radar observations (InSAR) [15]. Climatic conditions (snow cover) made comparisons of interferograms only feasible for

the surveys conducted in August-September 2012 and 2013. The results of 3D geomechanical modeling indicated that the deformation observed during the time span of interest (1 year) was the result of the emplacement of a radial dike into Tolbachik Volcano (with a dip angle of 80° to the west-northwest). Later, a more detailed analysis of seismic data preceding the November 27, 2012, Tolbachik lava eruption [5] revealed that the injection of magma resulted in a series of dikes trending west-northwestward at absolute depths ranging from -4 to +3 km in a zone situated to the southeast of the Ploskii Tolbachik Volcano edifice. The dikes penetrated into a nearly horizontal permeable zone at an absolute depth of approximately zero, producing sills and emplacing a magma-conducting dike along the top of the zone of cinder cones (with a dip angle of 50° toward the azimuth at 300°), which was located 5.5 km from the epicenter of the initial magma injection.

Another example was presented by Dumont et al. [4], who identified numerous dike injections (in a 60 km × 5 km area) in the Afar rift system produced during 2005–2010 using InSAR and seismic data. A mid-segment magma chamber at a depth of ~4 km and a crustal chamber at a depth of more than 15 km are considered to be sources of the dike injections, which occurred in different directions above the source magma chambers along rift-zone axes.

The above discussion shows that the injection of magma beneath volcanoes during the generation of dikes and sills due to magma-driven fracturing is largely analogous to the injection of fluids into wells, which is associated with the subsequent hydraulic fracturing and fissure generation in their host formations. The data from observations of fluids injected into wells in oil, gas, and geothermal fields have been widely used to evaluate the geometry of fracture systems and the state of stress in the reservoirs using seismic data [16]. This approach may also be applied in order to understand magmatic fracturing occurring beneath active volcanoes.

Finally, after magmatic activity ends or shifts to another volcanic funnel, water comes there. An example of the high-rate cold springs (0.7–6.8 m³/s) located in the eastern foothills of the Cascades (Oregon) was given by James et al. [17]. Their water isotopic (δD , $\delta^{18}O$) data indicated that the summits of the Cascade volcanoes serve as a recharge area for these springs, which are located 30–60 km apart. Thus, the magmatic plumbing systems of dormant volcanoes switch to inject cold water into adjacent hydrological reservoirs.

3. Geological Setting

3.1. Hydrogeological Stratification. The Koryaksky-Avachinsky volcanogenic basin, which has an area of 2530 km², contains five Quaternary volcanoes (two of which, Avachinsky (2750 masl) and Koryaksky (3456 masl), are active) and subbasins of volcanogenic and sedimentary Neogene-Quaternary deposits that are up to 1.4 km thick (Figure 1). The basin is located in a depression that has formed atop Cretaceous basement rocks and is generally characterized by a low-temperature gradient of 24°C/km.

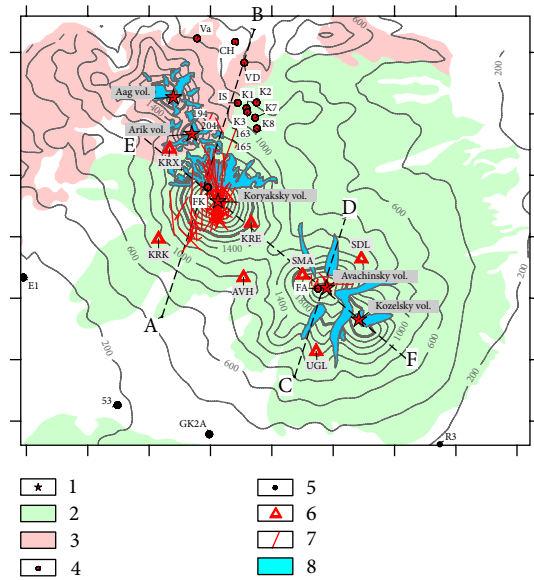


FIGURE 1: Geological map of the Koryaksky-Avachinsky volcanogenic basin. (1) The summits of the Avachinsky, Koryaksky, Kozelsky, Arik, and Aag volcanoes; (2) Avachinsky, Koryaksky, Kozelsky volcanoes, and their eruptive products; (3) Pinachevsky extrusions Q₂₋₃; (4) thermal features (for details, see Table 1): FA, fumaroles on Avacha Volcano; FK, fumaroles on Koryaksky Volcano; K1, K2, K3, K7, and K8, thermal mineral springs of Koryaksky Narzan; IS, Izotovskiy; VD, Vodopadny; CH, Chistinsky; Va, Vakinsky; (5) deep hydrogeological wells; (6) KB GS RAS seismograph stations; (7) dikes traced at -3000 masl below Koryaksky Volcano and 1500 masl below Avachinsky Volcano; (8) glaciers. Notes: (1) the isolines show the topographic surface, and the ticks along the axes represent intervals of 5 km. (2) For the extended map, including positions of all deep wells, see Figure 1 in Kiryukhin et al. [7].

The basin basement comprises Upper Cretaceous K₂, which is represented by metamorphic rocks of metasandstone, metasilstone, and phyllites with interbedded shales and microquartzites. The porosity values of these rocks are a few tenths of a percent. The matrix of these rocks has a low permeability of 0.001–0.01 mD. However, there are fracture zones that can be used to test the flows of reservoir water, which have flow rates ranging from 0.05 to 6.1 kg/s at a depth interval of 1438–1490 m (well E1, Figure 1). The average thermal conductivity of the Cretaceous deposits is 2.8 W/m C°.

The Miocene (N₁)-Quaternary aquifer complex is composed of pyroclastic and volcanogenic-sedimentary formations. Their porosity values are quite high and range from 0.36 to 0.48; their well productivity indexes range from 0.004 kg/s/bar (well P2) to 0.1 kg/s/bar (well GK1 Pinachevskaya). The average thermal conductivity of the Paleogene-Quaternary deposits is 1.5 W/m C°. The aquifer system of the Pinachevsky Q₁₋₂ extrusions is composed of andesite and rhyolite extrusions and includes vent andesite, dacite, and rhyolite formations (with thicknesses of more than 200–500 m). According to laboratory studies, their porosity is 0.12 and their permeability is 24 mD.

TABLE 1: Hot and cold springs of the Koryaksky-Avachinsky volcanogenic basin.

Name	##	E	N	Z masl
Cold Spring C5	CS	158.8070	53.3243	910
Cold spring C7	C7	158.7975	53.3434	899
Chistinsky Narzan	CH	158.7287	53.4367	602
Avacha Fumarole Left	FA	158.8309	53.2559	2720
Avacha Fumarole NZ frac	FA	158.8301	53.2563	2672
Avacha Fumarole Central	FA2	158.8339	53.2546	2720
Koryaksky Fumarole	FK	158.6960	53.3300	2900
Isotovskiy S	IS	158.7322	53.3920	786
Koryaksky Narzan 1	KI	158.7429	53.3882	920
Koryaksky Narzan 2	K2	138.7552	33.3924	800
Koryaksky Narzan 3	K3	158.7439	53.3852	922
Koryaksky Narzan 7	K7	158.7535	53.3812	899
Koryaksky Narzan 8	K8	158.7557	53.3733	967
Vodopadny	VD	158.7400	53.4215	569

The artesian volcanogenic basin (AVB) includes the aquifers of water-glacial formations, which comprise Holocene alluvial deposits, Upper Pleistocene-Holocene marine and alluvial-marine horizons, Upper Pleistocene glacial and fluvioglacial complexes, Holocene aquifers, and a proluvial and diluvial-proluvial complex. Its permeability ranges from 10 to 3000 mD, according to the results of the well-testing of the Bystrinsky freshwater reservoir.

3.2. Magmatic Activity beneath Koryaksky-Avachinsky Volcanoes from 2000–2016

3.2.1. Seismic Data and Method of Plane-Oriented Clusters Identification. In this study, we assume that the emplacement of magma in a fractured medium beneath active volcanoes is analogous to the injection of fluids into wells with subsequent hydraulic fracturing occurring in their host formations. Six stations can record seismicity in the Koryaksky-Avachinsky volcanic cluster (Figure 1). The absolute uncertainty in the locations of the hypocenters and epicenters of microearthquakes in this area is estimated to be 1 km [18, 19]. A total of 5160 earthquakes have been recorded by the Kamchatka Branch Geophysical Survey Russia Academy of Sciences (KB GS RAS) as having occurred in the edifices and basement of the Koryaksky-Avachinsky volcanoes during the period between January 2000 and July 2016. Our treatment of this dataset using the method outlined below yielded 1540 earthquakes comprising 204 plane-oriented clusters for the period between January 2008 and February 2016.

Cluster identification was carried out using our Frac-Digger program (RU #Reg. 2016616880). The following is a brief explanation of the algorithm used in this program. The first element of the cluster is removed from the initial list during each iteration. The following criteria are used to include a new event in a cluster: (1) a time difference ($\delta t = 1$ day); (2) a distance difference in the horizontal plane ($\delta R < 6$ km); and (3) a requirement of a nearly planar orientation (i.e., a distance from the event to the plane (δZ) that is less

than 200 m). When the resulting cluster contains more than five elements ($N > 5$), that cluster is treated as completed and is added to the list of plane-oriented clusters. All elements of a resulting cluster are removed from the initial list of elements (in cases when the cluster size > 5). This procedure is then reiterated until the initial list of elements is exhausted.

The calculation of the parameters of a plane-oriented cluster is based on a list of cluster elements. Each element i contains the coordinates (x_i, y_i, z_i) . For N (the number of elements in the cluster) points with coordinates (x_i, y_i, z_i) , we can find the equation of the fitting plane $z = ax + by + c$ using the least-squares method. The solution thus reduces to solving a set of linear equations as follows:

$$\begin{bmatrix} \sum x_i^2 & \sum x_i y_i & \sum x_i \\ \sum x_i y_i & \sum y_i^2 & \sum y_i \\ \sum x_i & \sum y_i & n \end{bmatrix} \begin{bmatrix} a \\ b \\ c \end{bmatrix} = \begin{bmatrix} \sum x_i z_i \\ \sum y_i z_i \\ \sum z_i \end{bmatrix}. \quad (1)$$

These equations are then solved using Cramer's rule. In this way, we obtain the coefficients a, b, c for the equation of a plane, which is defined as $z = ax + by + c$. The next step is to find the unit vector that is normal to the fitting plane $\mathbf{n} = (a/\Delta, b/\Delta, -1/\Delta)$, where Δ is the determinant of the equations that result in the following geological parameters: dip angle $\beta = \arccos(1/\Delta) * 180/\pi$ and the azimuth of dip $\alpha = \arctan(a/b) * 180/\pi$. The analysis of the sensitivity of this algorithm, where plane-oriented clusters are selected according to the criteria of temporal and spatial proximity, indicates that the above criteria produce selection results that are both physically and geologically reasonable (Appendix B). The results of the hydrogeomechanical CFRAC modeling [12, 13] performed indicate that it is feasible that plane-oriented clusters of earthquakes beneath active volcanoes may indicate magma fracking or dike formation processes [6, 14].

3.2.2. Distributions of Dikes, Sills, and Magma Chambers. The analysis of the seismic activity at Koryaksky Volcano

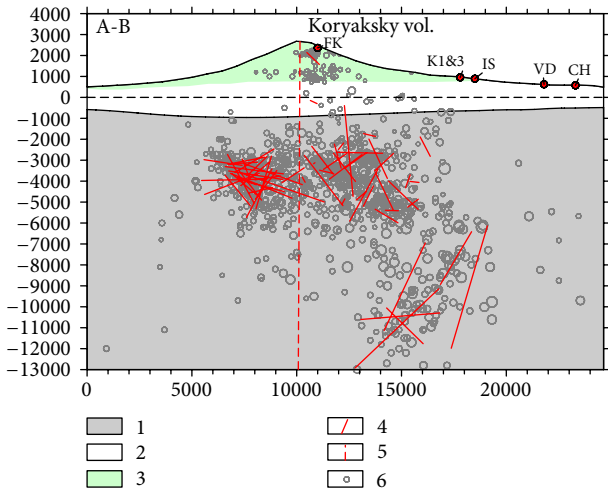


FIGURE 2: Geological cross-sectional AB (see Figure 1). (1) Basement with metamorphic Upper Cretaceous K_2 rocks in its upper part; (2) Miocene (N_1)-Quaternary aquifer complex; (3) Koryaksky Volcano (or/and Avachinsky Volcano in Figures 3 and 4); (4) traces of dikes and sills, defined from plane-oriented MEQ clusters; (5) assumed main feeding magma channels of Koryaksky Volcano (or/and Avachinsky Volcano in Figures 3 and 4); (6) earthquake hypocenters, in which their sizes are proportional to their magnitudes (KB GS RAS data 2001–2016). The ticks along the axes represent intervals of 1 km, and axes are labeled in meters.

(Figure 1) revealed the following geomechanical features (Figures 1–4): (1) the 2008–2009 summit steam-gas eruption of Koryaksky Volcano was accompanied by 153 plane-oriented earthquake clusters that are interpreted here to represent zones where dikes and sills were emplaced during magma injection; (2) the precursory period of this eruption began with magma filling the crustal chamber (the top is at an absolute depth of -3 km and the chamber is 2.5 km wide) near the southwestern base of Koryaksky Volcano (from July 2008 to January 2009); (3) magma was injected into a nearly meridional zone (7.5 by 2.5 km, with absolute depths ranging from -2 to -5 km) in the northern sector of Koryaksky Volcano simultaneously during the most intense period of the summit steam-gas eruption (from February 2009 to March 2010); (4) following the saturation of the plumbing system beneath Koryaksky Volcano, magma was injected into the cone of Avachinsky Volcano (2010–2016, at absolute depths ranging from 1 to 2 km).

4. Koryaksky-Avachinsky Basin Discharge/Recharge Conditions Based on Gas, Chemical, and Isotopic Data

Intervals of deep sampling wells (Table 2(a)) that encountered the basement of the Koryaksky-Avachinsky Basin are characterized by their chemical composition, which corresponds to the dilution of oceanic sediment water due to the infiltration of meteoric waters. Therefore, these mostly represent dominantly Cl-Na waters with minor concentrations of HCO_3 , Ca, Mg, and SO_4 . There is no indication of significant water

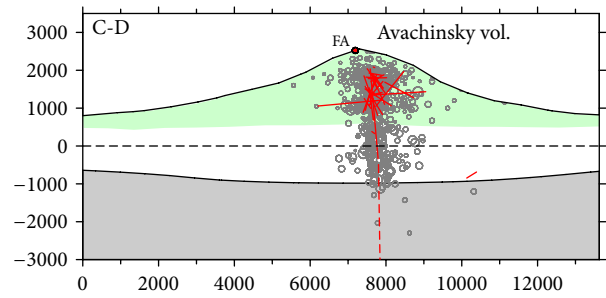


FIGURE 3: Geological cross-sectional CD (see Figure 1). Legend is the same as in Figure 2, and axes are labeled in meters.

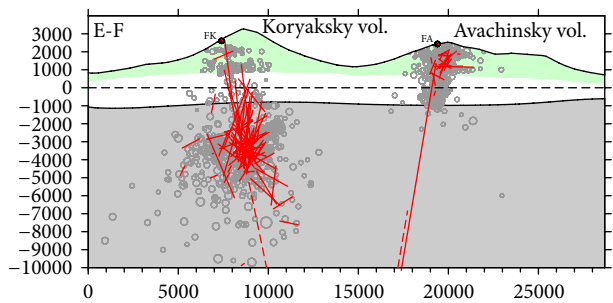


FIGURE 4: Geological cross-sectional EF (see Figure 1). Legend is the same as in Figure 2, and axes are labeled in meters.

metamorphism, and their Cl/Na ratios are close to seawater values. Increases in the concentrations of Ca and Mg may be related to CO_2 -leaching processes from the host rocks.

Fluids of volcanic basement rocks (outside the magma injection zones) are characterized by gas compositions containing a broad distribution of methane (~ 70 vol.%, wells R3, K1, GK1, Table 3(a)). The most striking example is well R3, which reveals a gas reservoir at the depth interval of 366–455 m, which has a pressure of 24.2 bar. Testing this well showed the production of 3.15 kg/s of water and 4.02 l/s of gas at a discharge temperature of $18^\circ C$ and depths ranging within 366–1503 m.

Thermal mineral waters discharged by springs on the foothills of volcanoes differ significantly from waters circulated in basement rocks. Spring waters are characterized by the presence of CO_2 in the gas phase (Table 3(b)), lower pH values (Table 2(b)) and lower salinity values (1– ~ 4 g/l); these are related to the significant mixing of these waters with meteoric waters at near-surface conditions. This represents HCO_3 -Na water with low Cl concentrations that are comparable to the Cl concentrations of adjacent rivers and creeks. Increases in their SO_4 concentrations are also observed, especially in the Isotovskiy spring (IS). All of the above-mentioned features may be explained as a result of the interaction of meteoric waters enriched by volcanic CO_2 gas upflows with volcanogenic rocks. CO_2 leaching may produce enrichments in Na and sometimes Ca. Sources of SO_4 may include either volcanic gases (with CO_2) or leaching by meteoric waters from hydrothermally altered rocks in the subcrater zones of volcanoes. The formation of such waters in kinetically

TABLE 2

(a) Water chemical compositions of deep wells of the Koryaksky-Avachinsky volcanogenic basin, according to sampling data collected from 1970–2014. Wells: GK1, GI, K6, R3, R2, 53, EI, KO1, K5, and K6 (well positions shown in Figure 1). GK1, GI: data from G. Ryabinin (pers. com., 2011); R2, R3 (A. Evtukhov et al., 1995), and EI: Kopylova G. (pers. com., 2011). The remaining samples were collected by A. Kiryukhin and T. Rychkova, and analyses were performed in the Central Chemistry Lab of the Institute of Volcanology FEB RAS. T_{SiO_2} and $T_{\text{Na-K}}$: hydrogeochemical geothermometers ($T_{\text{SiO}_2} = 1309/(5.19 - \log 10(I3)) - 273$, Fournier, 1977; and $T_{\text{Na-K}} = 855.6/(\log 10(\text{Na}/\text{K}) + 0.8573) - 273$, White, 1970).

#	Data	pH	HCO ₃ ⁻	Cl ⁻	SO ₄ ⁻	Na ⁺	K ⁺	Ca ²⁺	Mg ²⁺	SiO ₂	Na/K	T _{Na-K}	T _{SiO₂}
GK1	04.10.1970	7.5	207	2199		1050	70	241			15	148	
GI	14.04.1988	8.8	502	4929	100	3450	48	24	24		72	42	
K6	17.11.1990	8.5		2124		1175	25	119	24	46	47	65	98
K8	17.11.1990	8.3	14	6358	13	3125	91	598	234	44	34	85	96
R3	05.06.1992	7.6	144	12869	16	6667	167	679	271	61	40	75	111
R2	15.03.1993	8.2	518	6901		4308	0	110	122	11			43
EI	30.08.2011	12.1	68	344	10	285	47	36	2	2	6		
53	05.07.2011	8.2	51	24	154	28	3	28	22	35	9	195	86
GK1	28.07.2014	6.9	60	6594	173	3387	132	778	0	59	26	105	110
KO1	09.06.2014	8.2	26	5460	53	2759	75	689	0	26	37	80	74
K5	30.06.2014	8.9	16	2411	5	1336	37	180	0	39	36	81	91
K6	09.06.2014	7.2	139	2375	2	1337	53	208	0	52	25	105	104

(b) Water chemical compositions (ppm) of hot and cold springs of the Koryaksky-Avachinsky volcanogenic basin, according to sampling data collected from 2011 to 2016, #: denoted names, see Table 1 for explanation; gas, l/s; water, kg/s. The samples were collected by A. V. Kiryukhin, and analyses were performed in the Central Chemistry Lab of the Institute of Volcanology FEB RAS. T_{SiO_2} and $T_{\text{Na-K}}$: hydrogeochemical geothermometers ($T_{\text{SiO}_2} = 1309/(5.19 - \log 10(I3)) - 273$, Fournier, 1977; and $T_{\text{Na-K}} = 855.6/(\log 10(\text{Na}/\text{K}) + 0.8573) - 273$, White, 1970).

#	Data	T °C	gas	ω	pH	HCO ₃ ⁻	Cl ⁻	SO ₄ ⁻	Na ⁺	K ⁺	Ca ²⁺	Mg ²⁺	SiO ₂	Na/K	T _{Na-K}	T _{SiO₂}
K8	09.07.2010	12		2	6.3	1072	21	40	56	11	86	137	104	4.9	281	139
K1	09.07.2010	10		10	6.4	687	40	78	50	9	60	101	84	5.7	257	128
K2	09.07.2010	11		15	6.2	877	45	91	62	12	67	131	94	5.0	278	134
K3	09.07.2010	11			6.5	667	36	77	47	9	62	97	82	5.4	265	126
IS	25.09.2010	48		0.10	7.4	787	33	1167	150	29	415	136	99	5.1	273	137
K7	25.09.2010	9			7	788	31	128	55	13	70	117	90	4.4	296	132
K2	25.09.2010				7.4	872	43	102	61	13	51	142	81	4.9	281	126
IS	28.07.2011	39		0.07	6.9	800	28	1114	323	103	401	2	66	3.1	359	115

TABLE 2: Continued.

#	Data	T°C	gas	ω	pH	HCO ₃ ⁻	Cl ⁻	SO ₄ ⁻	Na ⁺	K ⁺	Ca ²⁺	Mg ²⁺	SiO ₂	Na/K	T _{Na-K}	T _{SiO₂}
K1	29.07.2011				6.6	678	32	115	64	14	76	92	40	4.6	291	92
K2	29.07.2011	14			6.3	866	41	134	80	21	84	120	51	3.8	322	103
VD	29.07.2011	42			6.5	429	<0.3	67	47	22	38	47	111	2.1	448	143
C5	30.07.2011			~1000	6.5	9	1	1	1	1	1	1	3	1.0		
K1	14.08.2012	11			6.4	661	28	81	55	8	68	83	169	6.5	240	169
K8	14.08.2012	12			6.4	774	25	202	85	16	98	103	80	5.4	266	125
K2	14.08.2012	13			6.3	960	21	9	74	9	212	36	98	8.0	213	136
IS	14.08.2012	46			6.6	813	50	1536	162	91	501	137	54	1.8	499	106
K1	06.08.2013	12		15-20	6.5	696	33	98	67	10	63	90	94	6.9	231	134
K2	06.08.2013	13		10	6.2	857	43	53	73	13	69	109	103	5.5	263	139
IS	06.08.2013	46		0.20	6.5	852	35	1003	153	37	386	106	115	4.1	309	145
K3	07.08.2013	13			6.5	657	34	58	66	10	66	90	95	6.9	232	134
K1	08.08.2014	13			6.5	664	34	154	50	8	80	101	87	6.3	243	130
K2	08.08.2014	14			6.2	798	44	138	63	12	62	120	91	5.4	264	132
IS	08.08.2014				6.6	805	30	769	157	29	419	24	101	5.3	267	138
C7	09.08.2014	2		~1000	6.8	52	2	3	4	1	12	2	60	3.3		
C5	09.08.2014	4		~1000	6.7	5	1	2	1	0	2	0	13	7.3		
AV2166	10.08.2014				5.6	6	2	3	1	0	3	0	12	7.1	228	45
K2	05.08.2015	14	6.4	6.40	6.3	812	46	93	56	12	82	109	156	4.5	293	164
IS	05.08.2015				6.7	868	138	1287	129	39	481	173	156	3.3	350	164
K1	05.08.2015				6.2	562	37	106	58	9	74	81	155	6.5	238	163
K1	03.08.2016				6.2	555	36	86	50	10	70	79	72	5.3	269	120
K2	03.08.2016				5.9	748	46	99	61	14	88	105	77	4.4	295	123
IS	03.08.2016				6.3	658	28	1316	162	32	445	102	93	5.1	275	133
K7	04.08.2016				5.9	682	32	73	42	14	86	90	67	3.1	360	116
K8	04.08.2016				6	1053	14	48	60	12	104	119	86	5.0	277	129
VD	03.08.2016				6	236	1	15	23	9	43	1	125	2.7	393	150
CHD	03.08.2016				4.6	26	0	7	5	2	5	0	54	3.4	343	106
CHF	04.08.2016				4.7	1	1	12	3	0	4	0	24	6.3	245	71
SH	04.08.2016				8.5	18	1	1	1	1	15	4	86	1.3		
C5	05.08.2016				6.7	7	1	3	1	0	3	0	7	6.0		
AV2200	06.08.2016				5.3	0	1	4	1	0	2	0	2			

TABLE 3

(a) Gas chemistry (vol%) and carbon isotopic data of deep wells of the Koryaksky-Avachinsky volcanogenic basin, according to sampling data collected from 1988 to 2013. Wells: GK1, K1, and R3 (well positions are shown in Figure 1). GK1, G1, data from G. Ryabinin (pers. com., 2011); the remaining samples were collected by A. Kiryukhin and T. Rychkova. Chemical analyses were performed in the Central Chemistry Lab (Guseva V. I.). Isotopic analyses ($\delta^{13}\text{C}$) were performed by B. G. Pokrovsky

##	Data	$T^{\circ}\text{C}$	H_2	Ar	O_2	N_2	CO_2	CH_4	Sum	$\delta^{13}\text{C}(\text{CH}_4)$	$\delta^{13}\text{C}(\text{CO}_2)$
GK1	25.05.1988		0	0.1	0.0	20.9	0.2	78.7	99.9		
K1	07.08.2013		0.005	0.1	0.1	22.6	0.7	71.3	94.8	-34	-27.7
R3	23.10.2013		0.017		0.1	37.5	0.1	60.7	98.4	-61	-49.7

(b) Gas chemistry (vol%) and carbon isotopic data of hot and cold springs of the Koryaksky-Avachinsky volcanogenic basin, according to sampling data collected from 2011–2016; ##, denoted names, see Table 1 for explanation. Sampling was performed by A. Kiryukhin, T. Rychkova, and V. Lavrushin. Chemical analyses were performed in the Central Chemistry Lab (Guseva V. I.). Isotopic analyses ($\delta^{13}\text{C}$) were performed by B. G. Pokrovsky

##	Data	$T^{\circ}\text{C}$	H_2	Ar	O_2	N_2	CO_2	CH_4	Sum	$\delta^{13}\text{C}(\text{CH}_4)$	$\delta^{13}\text{C}(\text{CO}_2)$
K2	09.07.2010		0	0.1	0.2	11.0	88.6	0.04	99.9		
K2	25.09.2010		0.001	0.3	2.9	28.8	68.1	0.03	100.1		
K2	06.08.2013		0.105	0.2	0.1	23.7	75.6	0.04	99.7		
K2	06.08.2013				0.1	27.1	72.4	0.05	99.7	-40.3	-8.8
K3	06.08.2013				0.0	62.2	37.7	0.05	100.0	-23.1	-9
CH	29.07.2011		0	0.0	0.0	2.5	96.7	0.08	99.3		
IS	06.08.2013	46	<0.005	0.0	0.3	2.9	95.2	0.00	98.4	-36.8	-6.9
FA	10.08.2014	166	0.686	2.4	0.3	3.4	92.0	0.45	99.2		-6.8
IS	08.08.2014		0.001	0.1	0.3	4.7	94.7	0.01	99.8		
K2	08.08.2014	14	0.005	0.2	0.2	32.9	65.0	0.05	98.5		
K2	05.08.2015	14	0.008	0.3	0.7	28.2	70.7	0.03	99.9		
FA	07.08.2015	94	0.370	0.4	7.1	30.3	60.8	0.05	99.0		
FA	07.08.2015	94	0.400	0.4	6.4	27.4	64.5	0.06	99.0		
FA	06.08.2016	94	0.31	0.5	4.54	17.62	76.1	0.03	99.1		-10.1
K1	03.08.2016		<0.005	0.93	2.09	76.38	19.7	0.05	99.1		-11.6
K2	03.08.2016		<0.005	0.42	1.54	70.67	27.0	0.03	99.6		-21
K8	04.08.2016		<0.005	0.55	1.02	20.44	76.8	0.01	98.8	-50.7	-18.7
VD	03.08.2016		<0.005	0.24	2.36	12.52	84.5	0.04	99.7		-22.1
CHD	03.08.2016		<0.005	0.27	1.87	26.57	70.5	0.35	99.5	-22.3	-8.1
CHF	04.08.2016		<0.005	0.68	9.5	35.56	48.0	0.35	94.0	-34	-6

active zones is reflected by a wide range of geothermometry values (200–300°C) (Table 2(b)), while basement waters show a narrower range of geothermometry values.

The conditions of water recharge in the Koryaksky-Avachinsky volcanogenic basin and thermal mineral springs can be easily identified using the isotopic compositions (δD , $\delta^{18}\text{O}$) of water (Figure 5). The light isotopic compositions of the Koryaksky Narzan, Izotovskiy, and Pinachevsky-2 springs, as well as the wells of the Bystrinsky groundwater reservoir, correspond to recharge areas at elevations of 2000–2500 masl (which can only represent the slopes of Koryaksky and Avachinsky volcanoes, especially their glacier sites). The water recharge areas of the Chistinsky Narzany group are located at elevations of 800–1500 masl, which correspond to the position of the central part of the Pinachevsky extrusions, with the Arik and Aag volcanoes. The chemical and gas compositions of the fluids of thermal mineral springs in the zone of magmatic injections differ sharply from those of the basement groundwater, as their gas compositions predominantly

comprise CO_2 (78–97.5%) and record high-temperature Na-K geothermometry values (more than 290–320°C) (Table 2(b)).

The $\delta^{13}\text{C}$ carbon isotopic compositions of the CO_2 in the free gas samples of the carbonated springs on the north slope of Koryaksky Volcano (K2, K3 and IS) (Table 3(b)) range from -9.0 to -6.9‰, which is within the range recorded by the Koryaksky and Avachinsky fumaroles (see below); they also record a significant magmatic fraction in the CO_2 component of the above-mentioned springs [20]. The carbon $\delta^{13}\text{C}$ isotopic compositions of the CH_4 in the free gas samples from the methane wells of K1 (Ketkinsky geothermal field, $\delta^{13}\text{C} = -34\text{‰}$) and R3 (Radyginskaya area $\delta^{13}\text{C} = -61\text{‰}$) differ significantly: gases discharged from well K1 formed at higher temperature conditions than the gases penetrated by well R3, where a significant fraction of methane is “marsh methane” of a microbial origin. Interestingly, the wells in the gas condensate fields in western Kamchatka fall within this range from -36.9 to -38‰ (Nizhne-Kvakchikskoye) and -43.1‰ (Kshukskoye) as a result of the magma-hydrothermal gas

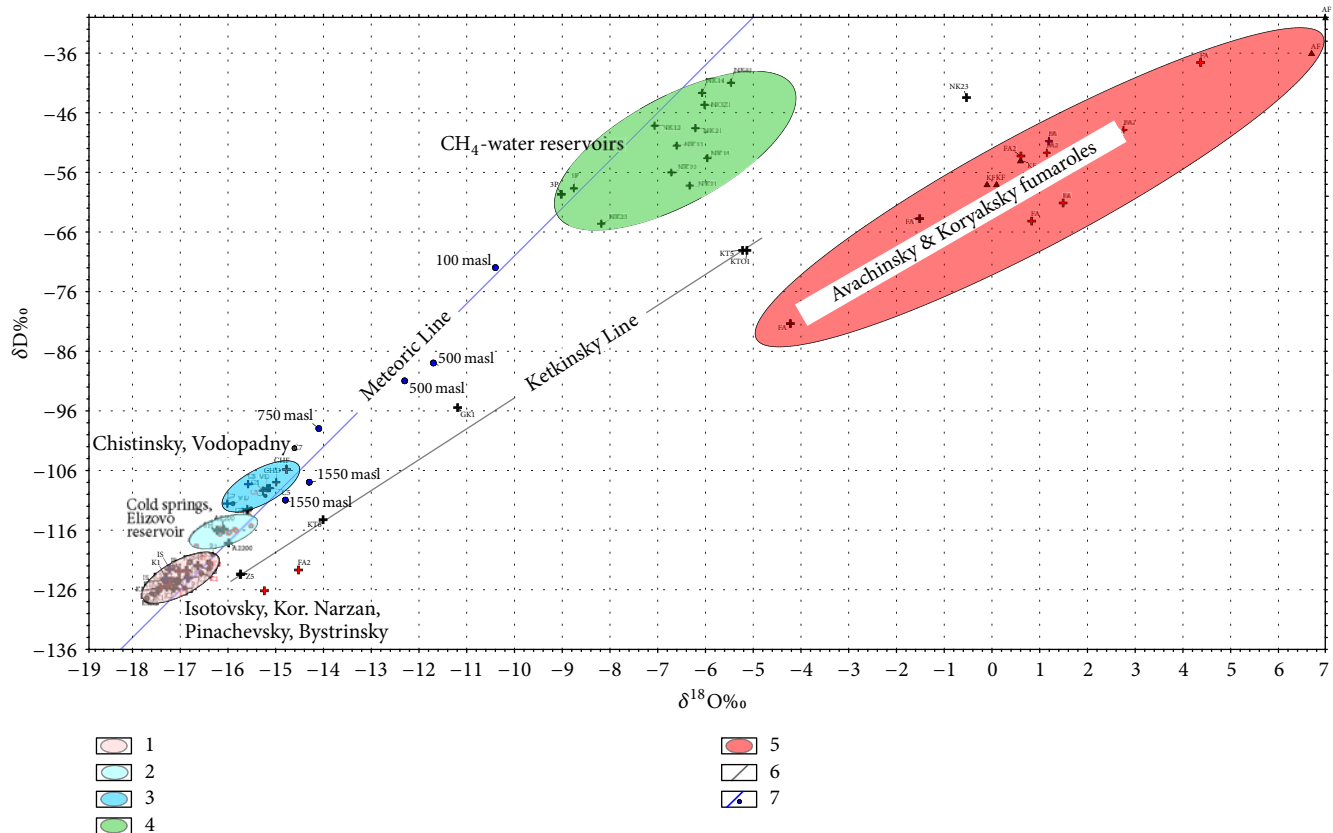


FIGURE 5: Isotopic compositions of water (δD and $\delta^{18}O$). (1) Cluster of hot mineral springs (Isotovskiy, Koryakskiy Narzan, Pinachevskiy, total of 36 samples, 2010–2016) and Bystrinskiy cold groundwater reservoir (7 samples from 2010–2016); (2) one cold spring at a foothill of Avachinskiy Volcano (2200 masl) and Elizovo cold groundwater reservoir (7 samples, 2014–2016); (3) cluster of hot mineral springs (Chistinskiy, Vodopadnyy, total of 4 samples, 2014–2016) and cold springs at a north foothill of Koryakskiy Volcano (total of 7 samples, 2010–2016); (4) water phase from Western Kamchatka CH_4 -water reservoirs (Kshuuskoy, Nizhne-Kvakchichskiy, total of 12 samples, 2010–2016); (5) water condensate from Avachinskiy and Koryakskiy Volcano fumaroles (14 samples, 1997, 2010–2016); (6) Ketkinskyy geothermal field line (5 samples, 2014); (7) Kamchatka representative sites of meteoric water samples (with elevations, masl) and meteoric line. Sampling was performed by A. Kiryukhin (1–7), T. Rychkova (6), Y. Taran (5), N. Malik (5), and P. Voronin (3). Analyses of samples were performed by P. O. Voronin and A. Y. Polyakov using an LGR IWA 45EP isotopic analyzer.

generation induced in its host volcanogenic-sedimentary rocks. Nevertheless, the low values of $\delta^{13}C$ (CO_2) (from -49.7 to -16.8 ‰) observed in methane wells indicate that some CO_2 here has a nonmagmatic origin (Table 3(a)) and is paragenetically related to methane sources.

According to Taran, gases from the fumaroles of Avachinskyy and Koryakskyy volcanoes (FA, FK, Figure 5) are characterized by a range of isotopic composition reflecting the mixture of meteoric and magmatic (-58 ‰ $< \delta D < -30$ ‰, -0.1 ‰ $< \delta^{18}O < +7$ ‰, $-11.8 < \delta^{13}C < -5.2$) end members. The presence of high methane concentrations (up to 0.3–0.6 mmole/mole) suggests that a considerable amount of regional methane reaches thermal water from the basements of volcanoes. The analyses of our samples of the Avachinskyy fumaroles that were collected during 2014–2016 and those of the Ketkinskyy geothermal field that were collected in 2014 generally support the above-mentioned mixing model (Figure 5).

5. Conceptual Thermal-Hydrodynamic Modeling of the Formation of the Hydrothermal System beneath Koryakskyy Volcano

5.1. TOUGH2 Model Setup. Thermal-hydrodynamic modeling was used here as a tool to verify a conceptual model of the formation of a hydrothermal reservoir beneath the active Koryakskyy Volcano. For this purpose, we applied the TOUGH2 family of codes, which was designed for the modeling of multiphase nonisothermal flows in porous/fractured reservoirs [21]. Here, we used TOUGH2 with different fluid equations of state (EOS) modules, corresponding to the conditions of the geofluids of Koryakskyy Volcano: EOS1, water in two phases; EOS1 + tracer, water in two phases plus tracer, which here is considered to be a chloride; and EOS2, water plus CO_2 in two phases.

The model geometry includes the upper part of the volume of the dike injection beneath Koryakskyy Volcano and the

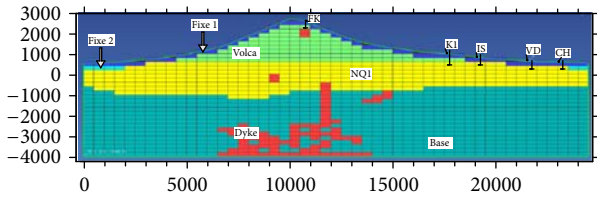


FIGURE 6: Model grid, zonation, and boundary conditions (Base, NQ1, Volca, Dike, Fixe 1, Fixe 2, see Table 4), and thermal features assigned as “wells on deliverability” (FK, KI, IS, VD, CH, see Table 1). This model position corresponds to the vertical cross-sectional AB shown in Figure 2. Horizontal and vertical axes are labeled in meters.

surface thermal features on its northern slope (i.e., Koryaksky Narzan and Isotovskiy thermal mineral springs). This model corresponds to the vertical cross-sectional AB shown in Figure 2. The bottom of the model was restricted to an absolute depth of -4 km, while the top of the model coincides with the top surface of Koryaksky Volcano. A 2D rectangular grid was generated using regular subdivisions in its horizontal and vertical directions, of $\Delta X = 500$ m ($NX = 49$) and $\Delta Z = 200$ m ($NZ = 35$), respectively; thus, the total number of model elements was 1276 (excluding elements above the topographic surface). A model width of $\Delta Y = 1$ km ($NY = 1$) was also assigned.

The following geological units were represented in the model as domains with different petrophysical properties: (1) basement metamorphic rocks (domain “Base”), (2) Neogene-Pleistocene volcanogenic-sedimentary rocks (domain “NQ1”), (3) Koryaksky volcanic rocks (domain “Volca”), and (4) magma injection units (domain “Dike”) (Figure 6 and Table 4(a)). We also defined model domains to assign different types of near-surface boundary conditions: (5) fixed-state boundary conditions (two-phase P, Sg, and P_{CO_2}) on the top surface of Koryaksky Volcano (domain “Fixe1”); and (6) fixed-state boundary conditions (single-phase P, T, P_{CO_2} , and Cl) on the foothills of Koryaksky Volcano at an elevation of 300 masl (domain “Fixe2”) (Table 4(b)). Fixed-state boundary conditions reflect unsaturated conditions in Koryaksky Volcano (“Fixe1”) and conditions of adjacent local groundwater aquifer systems (with water level elevations of up to 300 masl) (“Fixe2”). Other initial conditions assigned to the model are shown in Table 4(b).

The sources and sinks in the model were assigned using the following method (Table 4(c)). Conductive heat flux was defined in the bottom of the model, and constant heat rates were assigned to the model elements corresponding to dike injection zones with a possible grid resolution (Figure 6, Table 4(c)). Constant mass rates of CO_2 were assigned to the same model elements (if using module EOS2). These sources were considered to be unknown parameters during the calibration of the model (to match geothermometers for hot mineral springs and CO_2 content data). The discharge thermal features were modeled in terms of “wells” using the “well on deliverability” option (Table 4(c)); each “well” (FK, KI, IS, VD, CH) represented in the model corresponds to a thermal feature according to Table 1.

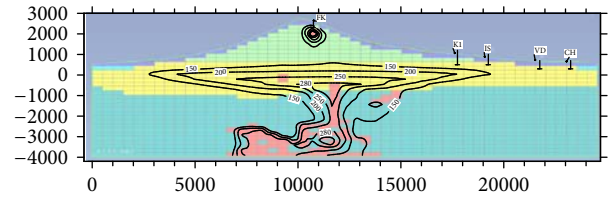


FIGURE 7: Distributions of modeled temperatures ($^{\circ}C$) (TOUGH2-EOS1) (6A). Horizontal and vertical axes are labeled in meters.

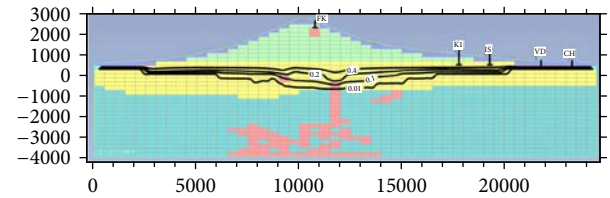


FIGURE 8: Distributions of modeled gas saturation values (S_g) (TOUGH2-EOS1) (6A). Horizontal and vertical axes are labeled in meters.

The time of the modeling was defined as 7000 years. We believe that the shape of Koryaksky Volcano and the conditions of magma injection did not change significantly during this period. This time also corresponds to the duration of the postglacial period in Kamchatka, when relatively stable meteoric water recharge conditions of Koryaksky Volcano were maintained.

5.2. Conceptual TOUGH2 Modeling Results. We performed a number of direct TOUGH2 runs to estimate the rates of the heat sources assigned in the zones of dike injections (“Dike” domain in the model). In the range of 0.1 to 10 MW per model element (the volume of each element is $1 \cdot 10^8$ m³, and a total of 85 elements of the “Dike” domain occur in the model), the value of 1 MW was found to be reasonable to explain the temperature evolution of the hydrothermal system below Koryaksky Volcano to match the estimated geothermometry temperatures (253–333 $^{\circ}C$) in the thermal mineral springs discharged on the northern foothills of Koryaksky Volcano (i.e., Koryaksky Narzan, Isotovskiy, see Table 2(b)).

Figure 7 shows that, after 7000 years of the evolution of the hydrothermal system, the volume of the geothermal reservoir at temperatures above 250 $^{\circ}C$ reached 12.0 km³, with a maximum temperature of 323 $^{\circ}C$. This reservoir is located at an absolute depth below -0.3 km. The volume of the two-phase subreservoir at the same time is estimated to be 5.2 km³, with its saturation ranging from 0.05 to 0.19 (Figure 8).

The distributions of fluid pressures after 7000 years show a significant relative pressure minimum of -78 bar at an elevation of -3.9 km at the base of a high-temperature upflow zone (Figure 9); that pressure difference pumps down water from the shallow meteoric groundwater systems on the foothills of Koryaksky Volcano (where the fixed-state pressure/temperature boundary is assigned in the “Fixe2”

TABLE 4

(a) Rock material properties used in the model. Notes: Corey relative permeability values of $S_{lr} = 0.3$ and $S_{gr} = 0.05$ and a specific heat of $1000 \text{ J/kg}^\circ\text{C}$ were assigned to all model domains. Rock density, porosity, and heat conductivity data are from Chernyak et al. [9], whereas permeability data are from Kiryukhin et al. [10], using analogous reservoirs

Domain parameters	Model domains					
	Base	NQ1	Volca	Dike	Fixe 1 (Fixed State)	Fixe 2 (Fixed State)
Permeability, 10^{-15} m^2	1	10–100	1000	1000	1000	10–100
Porosity	0.02	0.20	0.2	0.02	0.2	0.20
Density, kg/m^3	2700	2200	2200	2700	2200	2200
Heat conductivity, $\text{W/m}^\circ\text{C}$	2.0	1.4	1.4	2.0	1.4	1.4

(b) Initial and boundary conditions assigned in the model

Primary variables	EOS module	Model domains					
		Base	NQ1	Volca	Dike	Fixe 1 (fixed state)	Fixe 2 (fixed state)
Pressure Pa	EOS1/EOS2	Hydrostatic $\Delta P/\Delta Z = 10 \text{ MPa/km}$					$1e5$
Temperature $^\circ\text{C}$	EOS1/EOS2	$\frac{\Delta T}{\Delta Z} = 24^\circ\text{C/km}$					
Saturation	EOS1/EOS2						0.9
Chloride mass fraction	EOS1 + tracer	$19e-3$					$1e-6$
CO_2 partial pressure, Pa	EOS2						40

(c) Sources/sinks assigned in the model

Sources/Sinks	Model domains		
	Base	NQ1	Dike
Heat flux/rate	0.05 W/m^2 (lower boundary)		$1.0\text{--}2.5 \text{ MW}$
Mass rate (CO_2)			$1e-3 \text{ kg/s}$
Wells on deliverability $\text{PI} = 1e-11 \text{ m}^3$, $\text{Pb} = 1 \text{ bar}$	Thermal features: FK, KI, IS, VD, CH		

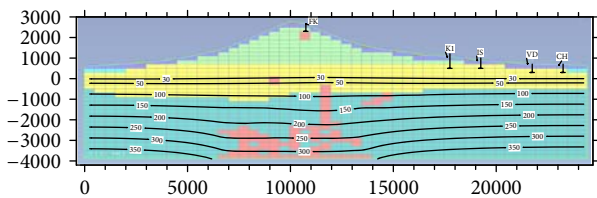


FIGURE 9: Distributions of modeled pressures (bar) (TOUGH2-EOS1) (6A). Horizontal and vertical axes are labeled in meters.

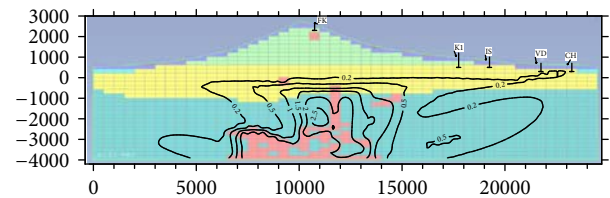


FIGURE 10: Distributions of modeled partial CO_2 pressures (bar) (TOUGH2-EOS2) (CO2-8). Horizontal and vertical axes are labeled in meters.

domain of the model, see Figure 6) into the deep geothermal reservoir.

The issue of CO_2 distribution in the hydrothermal system was analyzed using the TOUGH2 model with a CO_2 (EOS2) fluid module [21]. In this model, sources of CO_2 were assigned to a magma injection region (Table 4(c)), assuming the magmatic origin of CO_2 in the hydrothermal system below Koryaksky Volcano (see Section 3 and Table 3(b)).

The TOUGH2-EOS2 output modeling results of the evolution of the hydrothermal system are similar to those obtained above (without CO_2) in terms of their temperature, pressure, and saturation distributions, while the CO_2 partial pressures (which reach up to 2.4 bar) cause some maximum temperatures to decrease (-7°C) and saturations to increase (+0.08) in the geothermal reservoir. Figure 10 shows the distributions of partial CO_2 pressures in this model, which reach values of above 1 bar in regions of dike intrusions (with

a maximum value of 2.5 bar), follow high-temperature circulation patterns, and diffuse into cold water inflow regions based on the nonlinear solubility properties of CO_2 .

The distribution of chloride brines in a hydrothermal system was analyzed using the TOUGH2-EOS1+tracer option, where a tracer is assigned as a chloride mass fraction in a fluid. Chloride brines (of up to 13 g/kg) were found in the deep wells of the basement and the Neogene rock units of the Koryaksky-Avachinsky volcanogenic basin. Therefore, in this model, we consider the scenario of an initially seawater-saturated basin (with chloride concentrations of 19 g/kg, or a mass fraction of 0.019) as the initial conditions before magma injection started (Table 4(b)). Figure 11 shows the distribution of the mass fraction of chloride in the model; it also clearly shows a diluted meteoric water circulation pattern (along the 0.0135 isoline) that traces a streamline

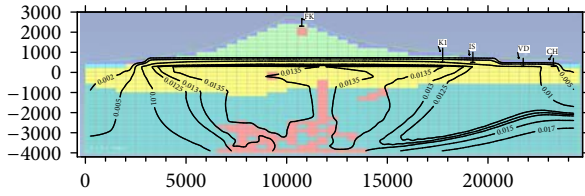


FIGURE 11: Distributions of modeled chloride Cl^- mass fractions (TOUGH2-EOS1 + tracer) (6B + CL). Horizontal and vertical axes are labeled in meters.

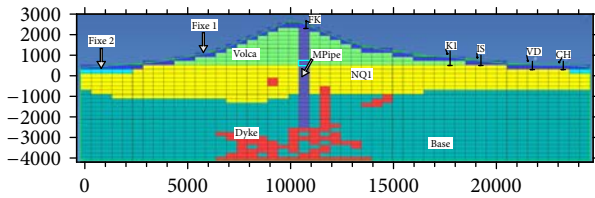


FIGURE 12: Revised model grid, zonation, and boundary conditions (compare to Figure 6) (6A + I). Domain MPipe (Koryaksky Volcano funnel) has been added, and the blue rectangle inside this domain corresponds to the water level in the volcano funnel. Horizontal and vertical axes are labeled in meters.

from a shallow meteoric groundwater system (representing the recharge area for the hydrothermal system) into a region of deep dike intrusions (where heat sources also act as pumps) and then passes to a discharge area zone, where the Koryaksky Narzan and Isotovskiy hot springs, KI and IS, are defined in this model.

6. Discussion

In this section, the results of the model are matched to observations in order to improve the model; we also discuss the ability of the model to reproduce the temperature response of hot springs to recent dike injections. Finally, the powers of the modeled heat sources are compared to that of Koryaksky Volcano in terms of the heat content of its erupted lava.

6.1. Asymmetric Discharge of Hot Springs and Distribution of Centripetal Pressures. The distribution of the temperatures output by the TOUGH2 modeling (Figure 7) is rather symmetrical in shape, but all of the hot springs adjacent to Koryaksky Volcano are located in an area that is 7 to 12 km to the north (Figure 1). Another observed misfit between the modeling results and observations is a centripetal trend of deep well levels rising toward the centers of the Koryaksky-Avachinsky volcanic cluster [7, Figure 7], while the distribution of TOUGH2 modeled pressures (Figure 9) shows a decrease in pressure toward the center of the volcano at an elevation of -1000 masl (Figure 8).

A reasonable way to adjust the model to the above-mentioned observations is to assume that cold water injection occurs beneath Koryaksky Volcano, which shifts the thermal anomaly in the northern direction and builds up pressure in the bottom of the volcanic structure. To do this, a domain defined as MPipe was added to the model (Figure 12). MPipe

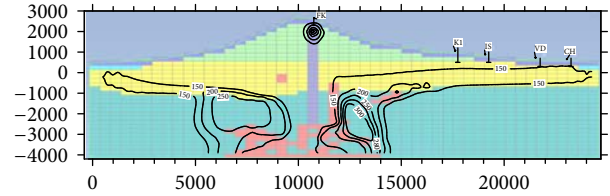


FIGURE 13: Distributions of modeled temperatures ($^{\circ}\text{C}$) (TOUGH2-EOS1) (6A + I). Horizontal and vertical axes are labeled in meters.

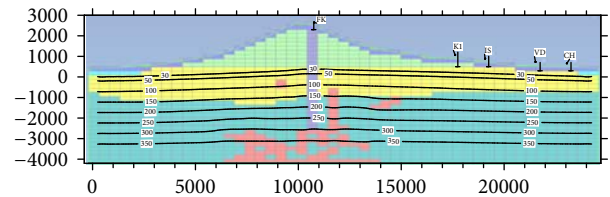


FIGURE 14: Distributions of modeled pressures (bar) (TOUGH2-EOS1) (6A + I). Horizontal and vertical axes are labeled in meters.

represents the funnel of Koryaksky Volcano in the model, where cold water may recharge the underlying volcanic structure. One element of the MPipe domain was assigned in fixed-state conditions (at a pressure of 1 bar and a temperature of 10°C) to define the water level position in the volcano funnel at 700 masl. We also increased the heat rates of the sources up to 2.5 MW (Table 4(c)).

The temperature distribution in this case was reshaped from a symmetrical (Figure 7) to an asymmetrical (Figure 13) form, with explicit thermal outflow occurring in the northern direction (KI, IS, VD, CH thermal features) and a hidden geothermal reservoir beneath the southern foothills of Koryaksky Volcano. The volume of the geothermal reservoir at a temperature above 250°C reached 8.5 km^3 , with a maximum temperature of 339°C . This reservoir is located at an absolute depth below -1.0 km. Figure 14 shows that pressures now have a centripetal distribution, with a relative pressure maximum of $+12.1$ bar at an elevation of -3.9 km at the base of the high-temperature upflow zone. Fluid circulation also switched from a free convection mode (Figure 9) to a forced convection mode (Figure 14). This modeling scenario also shows a significant increase of 93 bar in the fluid pressure at the base of the high-temperature upflow zone (Figure 14 compared to Figure 9), while single-phase conditions prevailed beneath the structure of Koryaksky Volcano.

Assigning to the TOUGH2-EOS2 model recharge rates of CO_2 sources in an injection area (Table 4(c)) generates two separate CO_2 -enriched reservoirs with partial CO_2 pressures of up to 1.5–2.0 bar (with CO_2 concentrations of 30–40 g/kg) (Figure 15). The larger reservoir is shallower and is aligned beneath the known CO_2 hot springs (i.e., KI, IS, VD, CH).

The analysis of the redistribution of chloride brines due to hydrothermal circulation was performed using the TOUGH2-EOS1 + tracer option, where the tracer is assigned as a chloride mass fraction in the fluid. In the case of volcanic funnel-type water recharge conditions, nearly the entire basin is purged and diluted of chloride within a few thousand years.

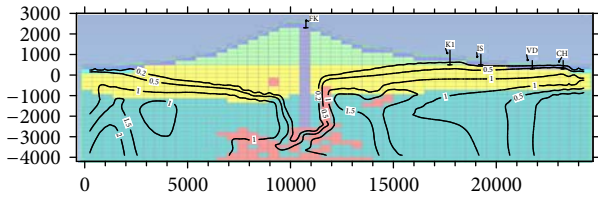


FIGURE 15: Distributions of modeled CO₂ partial pressures (bar) (TOUGH2-EOS2) (CO₂-8 + 2I). Horizontal and vertical axes are labeled in meters.

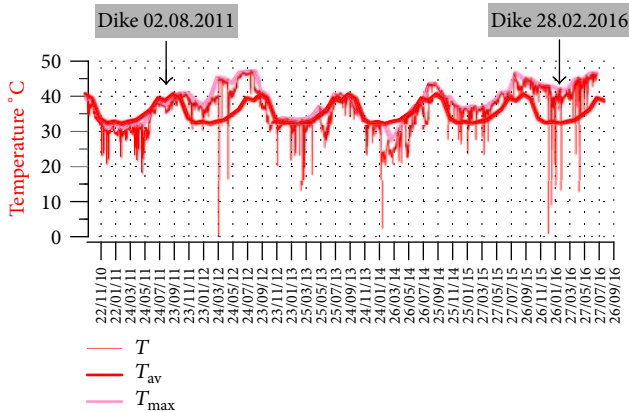


FIGURE 16: Temperatures recorded in Isotovskiy hot spring and suggested times of dike injections in adjacent areas (#194, 2.08.2011 and #204, 28.02.2016). T , observational data; T_{av} , annual maximum monthly temperature; T_{max} , maximum monthly temperature.

Thus, it is most feasible that the chloride component observed in the thermal features on the northern slope of Koryaksky Volcano has a magmatic origin.

6.2. Temperature Response of the Isotovskiy Hot Spring to Dike Injections. Observational temperature data in hot mineral springs located on the northern slope of Koryaksky Volcano represent an additional possible data source for the verification of thermal-hydrodynamic models. The Isotovskiy hot spring is located 7 km from the summit of Koryaksky Volcano (Figure 1) and is characterized by flowing temperatures of up to 50°C. The temperature monitoring of this spring was performed during the time period of 2010–2016 using the HOBO U12 temperature logger (with a 15 min⁻¹ frequency of records) (Figure 16). During the observational period, four plane-oriented earthquake clusters (produced by dike injections) were identified in this local area (##163, 165, 194, and 204; these numbers are shown in Figure 1).

Figure 16 shows that a postmagmatic temperature increase of 6–12°C occurred during winter, from October 2011 to June 2012, after event #194 (which is interpreted to represent a dike injection that occurred on 02.08.2011). At this time, the maximum monthly temperature T_{max} increase of 6–12°C is compared to the annual maximum monthly temperature T_{av} . In other words, the temperature perturbation caused by the suggested dike injection was recorded 2 months after the dike injection occurred; then,

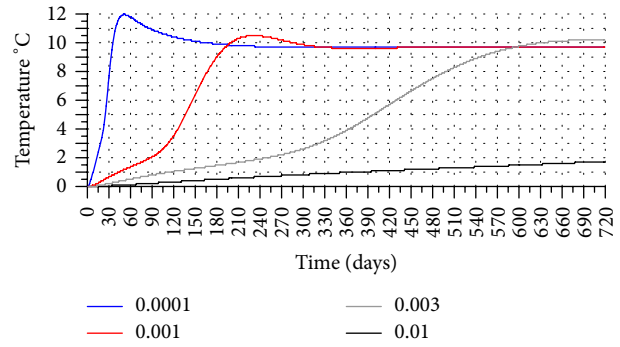


FIGURE 17: Thermal response (temperature rise, °C) in a model element corresponding to Isotovskiy hot spring after additional heat sources (4×8 MW) were assigned in the model 2 km apart. Note: active circulation volume (volume fraction) used as a model sensitivity parameter here. (TOUGH2-EOS1) (6A + I+).

this temperature increase was maintained over a 10-month time period. Another anomalous temperature increase in Isotovskiy of up to 10°C was associated with a dike injection that occurred on 28.02.2016.

Modeling (using the model parameters defined in Section 4) shows that a distance of ≈ 1 km (between the heat source and the observational point) represents the upper distance limit of such thermal responses. This is close to the value of 2 km observed in the field (Figure 1). Nevertheless, it is difficult to establish definite conclusions about this, as a coarse grid is used in the model and the seismic event coordinate data may not be accurate. The fracture porosity (or fluid active circulation volume) may also significantly increase the distance of the propagation of a temperature anomaly from a heat source (dike) to the point of heat discharge (hot spring). Additional modeling shows that the thermal response of an increase of 11°C in a few months may be achieved at a distance of 2 km, if the fluid active circulation volume is defined as 0.001 (volume fraction) in the model and the heat sources in the dike injection region are assigned as 8 MW (Figure 17).

6.3. Geothermal Budget of Koryaksky Volcano. The relationship between volcanic, hydrothermal, and seismic activity is another issue that the analysis of the Koryaksky-Avachinsky volcanic cluster can be used to assess. Using the identified geothermal resource data from the world's eight largest geothermal-producing countries and the allocation of active volcanoes around the world, Stefansson [22] suggested that there is a linear relationship between the number of active volcanoes and the geothermal potential that can be used for the production of electricity, which statistically means that one active volcano has an average potential close to that of a hydrothermal system, which is capable of producing 158 MWe of geothermal power. Nevertheless, it is still not clear why, how, and where active volcanoes store their energy when they are not erupting magma onto the Earth's surface.

The TOUGH2-modeling of Koryaksky Volcano yields an example of this mechanism. A total of 85 model elements were assigned heat sources with a rate of 2 MW; thus, the

total heat power used to run a model hydrothermal system was 170 MW, and this value should be doubled to 340 MW (since we need to at least double the width of the 2D model from 1 km to 2 km to cover the area of dike injections and surface thermal features, Figure 1). Koryaksky Volcano was characterized by an average magma rate of 150 kg/s during its lifetime of 45 kY [23]. This corresponds to an average heat power of Koryaksky Volcano of 150 MW (as 1 kg/s of magma is approximately converted to a heat rate of 1 MW). That means that double this heat power (and magma rate) is needed to run the hydrothermal system beneath Koryaksky Volcano.

In the model was specified cold water recharge through the volcanic funnel by using a constant fluid pressure in model element #1149 at an elevation of 700 masl, which yields a water recharge of 289 kg/s; thus, the total cold water recharge required to run a real hydrothermal system should be doubled to 578 kg/s (since we need to at least double the width of the 2D model from 1 km to 2 km to cover the area of dike injections and surface thermal features, Figure 1). The area of the structure of Koryaksky Volcano at an elevation above +2000 masl is estimated to be 18.5 km², most of which is covered by glaciers and permanent snow fields. Assuming that the annual atmospheric water precipitation rate at these elevations is more than 5000 mm [24], this may produce a water recharge rate of more than 3 m³/c. If only 20% of this flow is converted into the underground drain, it would be sufficient to provide water recharge to its underlying hydrothermal systems.

7. Conclusions

(1) The fluid recharge/discharge conditions of the Koryaksky-Avachinsky volcanogenic basin were studied using water (δD and $\delta^{18}O$) and $\delta^{13}C$ (gas) isotopic data. The isotopic compositions (δD , $\delta^{18}O$) of the thermal mineral springs (Koryaksky Narzans, Isotovskiy, and Pinachevskiy) and wells of the Bystrinsky and Elizovo aquifers indicated that water recharge occurred from +2000 to +2500 masl at glaciers on the summits of Koryaksky and Avachinsky volcanoes. Chistinsky Narzans was fed from the central part of the Pinachevskiy extrusions (Aric and Aag volcanoes) at elevations of 800–1500 masl. The $\delta^{13}C$ isotopic compositions of CO₂ sampled from Koryaksky Narzan and Isotovky revealed its magmatic origin. Thus, CO₂ springs in the northwestern foothills of Koryaksky Volcano formed as a result of the mixing of magmatic gases and melting glacial waters. The hydrothermal reservoir beneath the northern slope of Koryaksky Volcano records geothermometric temperatures ranging from 253 to 333°C and CO₂ contents of up to 3 g/kg (Koryaksky Narzan).

(2) Plane-oriented clusters of seismic events (KB GS RAS data of 2000–2016) below Koryaksky and Avachinsky volcanoes were used to identify magma injection zones: (1) the shallow crustal magma chamber (i.e., a combination of sills and dikes) below the southwestern base of Koryaksky Volcano at absolute depths ranging from –2 to –5 km, with a width of 2.5 km; (2) dike accumulation in a nearly north-south zone (7.5 by 2.5 km, with absolute depths ranging from –2 to –5 km) in the northern sector of Koryaksky Volcano;

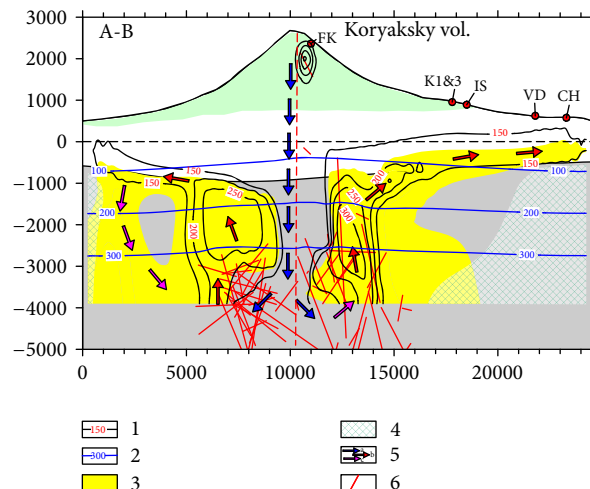


FIGURE 18: Conceptual TOUGH2-based model of hydrothermal circulation beneath Koryaksky Volcano. 1: temperatures, °C; 2: pressures, bar; 3: regions with CO₂ partial pressures above 1 bar (i.e., CO₂ mass fractions more than 0.02); 4: regions with chloride concentrations of more than 5 ppm; 5: fluid flows: a, cold, b, hot, and c, intermediate; 6: dike injection regions. For additional explanation of this figure, see legend in Figure 2.

and (3) the shallow magma chamber (i.e., a combination of sills and dikes) in a cone of Avachinsky Volcano at absolute depths ranging from 1 to 2 km, with a width of 1 km.

(3) Conceptual TOUGH2 modeling was used to understand and explain the mechanism of the formation of the hydrothermal system beneath Koryaksky Volcano (Figure 18). For this purpose, the following terms were found to be crucial in this model: (1) heat sources of 20 MW/km³ and gas (CO₂) sources of 10 g/s/km³ acting during 7000 years in the above-defined zones of magma injections; and (2) cold water recharge of 580 kg/s through the volcanic funnel to the deep dike injection area. The modeling results reasonably match the Na-K geotemperature estimates of geothermal reservoirs (300°C), the isotopic values (δD , $\delta^{18}O$) of high-level meteoric water recharge, the concentrations of magmatic CO₂ (up to 4 g/kg) in the hot springs on the northern slope of Koryaksky Volcano, the thermal reaction to the 02.08.2011 dike injection recorded in Isotovskiy hot spring, and the fluid dilution of the original seawater basin beneath the volcano due to cold water recharge circulation. This modeling also indicates that a hidden high-temperature geothermal reservoir is present beneath the southern slope of Koryaksky Volcano (at an elevation of –1 km), which may become a subject of future drilling explorations.

Appendix

A. Photos of the Thermal Features of the Koryaksky-Avachinsky Volcanic Cluster (Kamchatka)

See Figures 19–30.



FIGURE 19: Koryaksky Volcano burst of activity in 2009. Photo by A. V. Kiryukhin.



FIGURE 20: Koryaksky fumarole (FK), 01 Oct. 2010. Photo by A. V. Kiryukhin.



FIGURE 21: Koryaksky-Avachinsky volcanoes cluster, August 2016. Photo by D. Afanasiyev.



FIGURE 22: Avachinsky fumarole (FA2) sampling on August 2014. Photo by A. V. Kiryukhin.



FIGURE 23: Koryaksky Narzan-1 mineral hot spring (K1), August 2016, Koryaksky Volcano is on a 7 km apart background. Photo by A. V. Kiryukhin.



FIGURE 24: Koryaksky Narzan-2 mineral hot spring (K2), August 2014. Photo by A. V. Kiryukhin.

B. Analysis of the Sensitivity of the Frac-Digger Algorithm to the Criteria of Temporal and Spatial Proximity

This section demonstrates the feasibility of using the Frac-Digger program to extract plane-oriented clusters of seismic events (dikes, fracs) from seismic data catalogs within a reasonable range of a base set of temporal and spatial proximity parameters. The input data used for this test include 5160 seismic events collected by KB GS RAS during the time period from Jan. 2000 to July 2016 using the seismic station



FIGURE 25: Koryaksky Narzan-8 mineral hot spring (K8). A 4 m drop of the spring discharge elevation in 6 years is clearly seen. Photo by A. V. Kiryukhin.



FIGURE 26: Isotovskiy mineral hot spring (IS), August 2015. Photo by A. V. Kiryukhin.



FIGURE 27: Bystrinsky groundwater reservoir wells, July 2013. Photo by A. V. Kiryukhin.



FIGURE 28: Cold spring (C5) on a Northern slope of Koryaksky Volcano, August 2013. Photo by V. Lavrushin.



FIGURE 29: Cold spring (C7) on a Northern slope of Koryaksky Volcano, August 2012. Photo by A. V. Kiryukhin.



FIGURE 30: Hot mineral springs on a Northern slope of Koryaksky Volcano. K1, K2, and K8: Koryaksky Narzan 1, 2, and 8, correspondingly; IS, Isotovskiy. July 2011. Photo by A. V. Kiryukhin.

network around the Koryaksky-Avachinsky volcanic group. We ran Frac-Digger by varying a base set of parameters, which are responsible for the selection of the plane-oriented clusters: (1) N , cluster size, $N = 6, 8, 10$; (2) the distance (δZ) from the event to the plane, $\delta Z = 150, 200, 300$ m; and (3) the time interval (δt) allocated to the cluster, $\delta t = 1, 7, 30$ days.

Figures 31, 32, and 33 show that if the cluster size N varies from 6 to 10, we obtain (1) estimated average depths of dike injections remain at elevations ranging from -4000 to -2500 masl (Koryaksky) and from 1000 to 2000 masl (Avachinsky) (Figure 31); (2) estimated average dip angles of dikes remain in the range of 59.18 to 59.44° (Figure 32); and

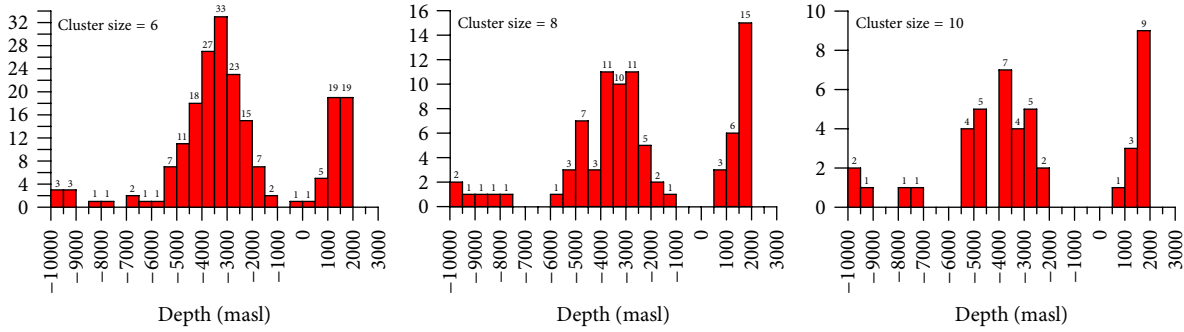


FIGURE 31: Histograms of the Frac-Digger sensitivity of the estimated depths of dikes to the cluster size (or the number of events in cluster N).

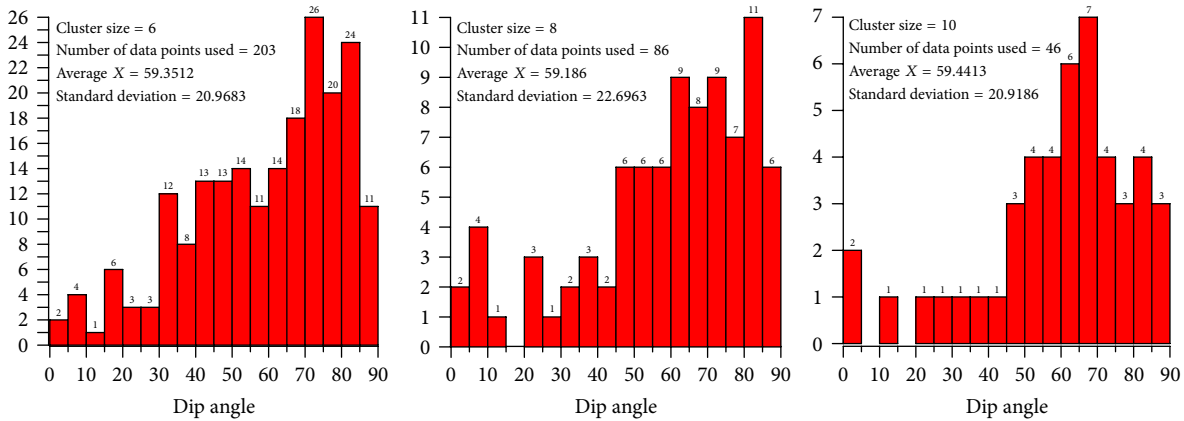


FIGURE 32: Histograms of the Frac-Digger sensitivity of the estimated dip angles of dikes to the cluster size (or the number of events in cluster N).

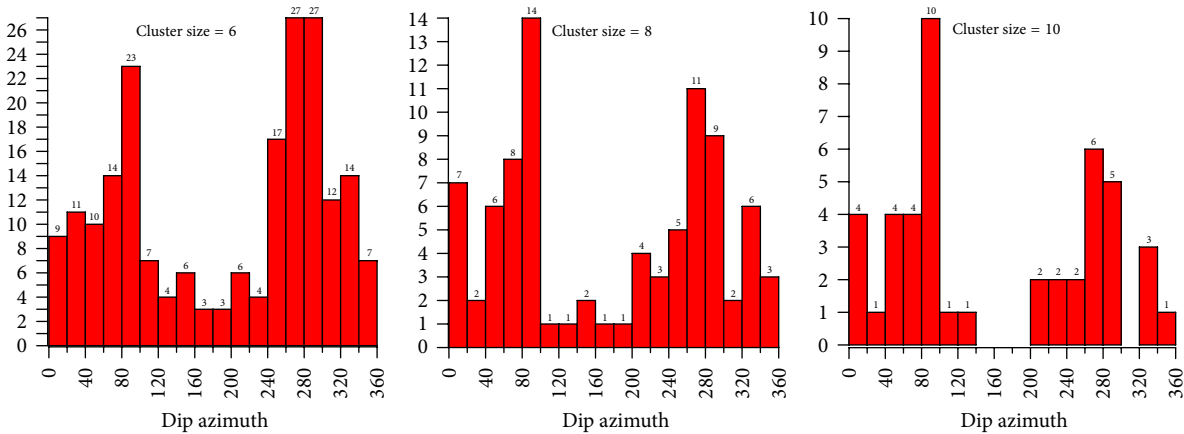


FIGURE 33: Histograms of the Frac-Digger sensitivity of the estimated dip azimuths of dikes to the cluster size (or the number of events in cluster N).

(3) the estimated dip azimuths of dikes show two dominant directions at 90° (east) and 270° (west) (Figure 33).

Figures 34, 35, and 36 show that if the distance (δZ) from the event to the plane varies from 150 to 300 m, we obtain the following: (1) estimated average depths of dike injections remain at elevations ranging from -4000 to -3000 masl (Koryaksky) and from 1000 to 2000 masl (Avachinsky) (Figure 34); (2) estimated average dip angles of dikes remain in the range of 58.12 to 59.35° (Figure 35); and

(3) the estimated dip azimuths of dikes show two dominant directions at 90° (east) and 270–290° (west) (Figure 36).

Figures 37, 38, and 39 show that if the time interval (δt) allocated to the cluster varies from 1 to 30 days, we obtain the following: (1) estimated average depths of dike injections remain at elevations from -4000 to -3000 masl (Koryaksky) and from 500 to 2000 masl (Avachinsky) (Figure 37); (2) estimated average dip angles of dikes remain in the range of 59.35 to 63.64° (Figure 38); and (3) the estimated dip azimuths

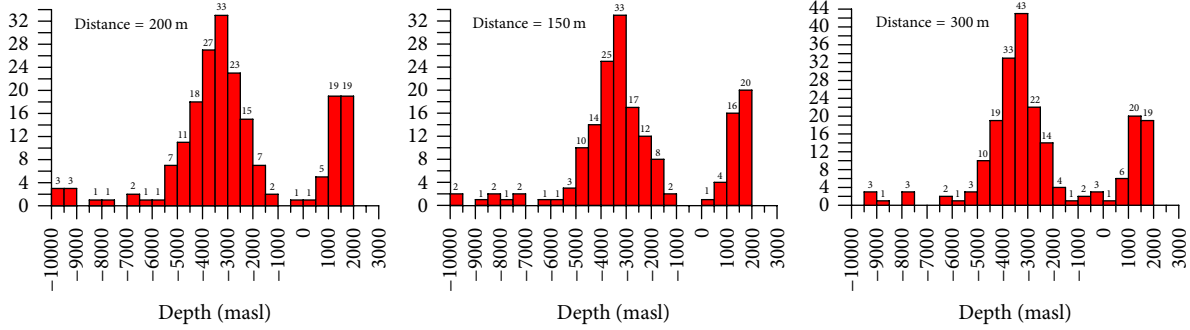


FIGURE 34: Histograms of the Frac-Digger sensitivity of the estimated depths of dikes to the distance from the event to the plane (δZ).

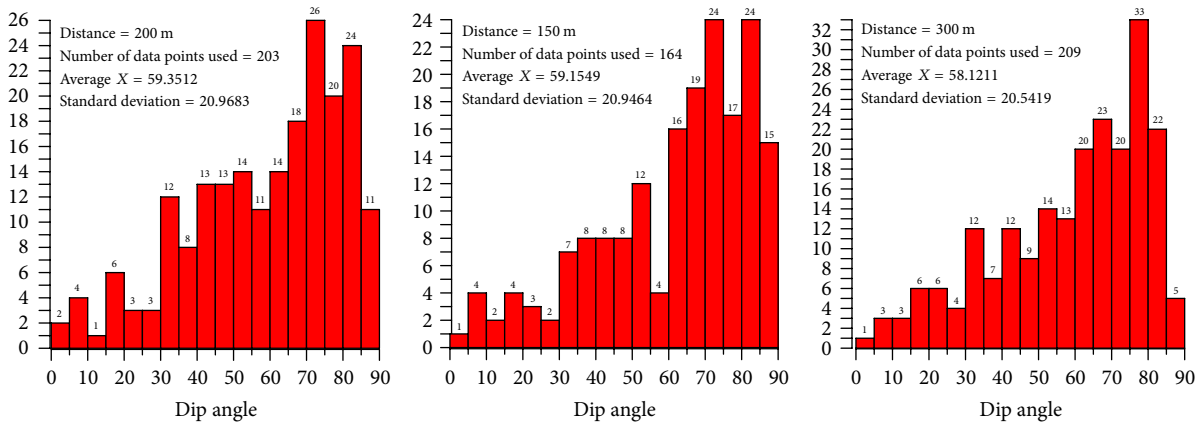


FIGURE 35: Histograms of the Frac-Digger sensitivity of the estimated dip angles of dikes to the distance from the event to the plane (δZ).

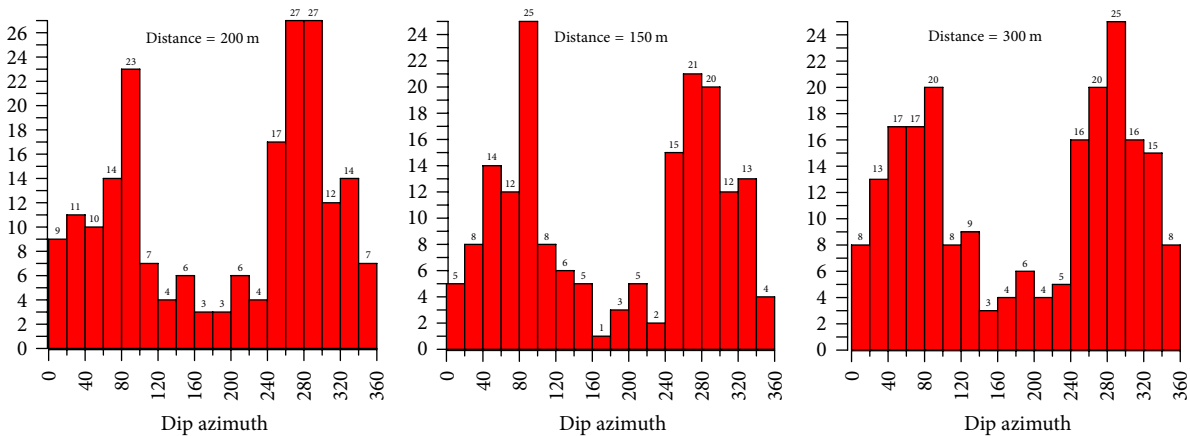


FIGURE 36: Histograms of the Frac-Digger sensitivity of the estimated dip azimuths of dikes to the distance from the event to the plane (δZ).

of dikes show two dominant directions at 70–90° (east) and 270–290° (west) (Figure 39).

Finally, Figure 40 shows the Frac-Digger sensitivity of estimated dike traces at a depth of -3000 masl below Koryaksky Volcano determined using a range of the above-mentioned base sets of temporal and spatial proximity

parameters. It can be visually seen that the main trends of dike orientation are maintained, despite the fact that the parameters of cluster selection have been significantly changed. This indicates the reasonably low sensitivity of the Frac-Digger algorithm to spatial criteria (δZ , proximity or distance from the event to the plane; N , the number of events

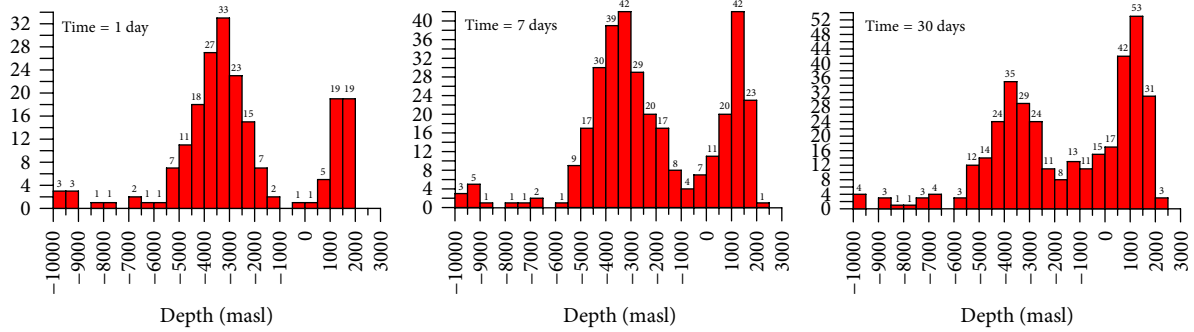


FIGURE 37: Histograms of the Frac-Digger sensitivity of the estimated depths of dikes to the time difference (δt) allocated to the plane-oriented cluster.

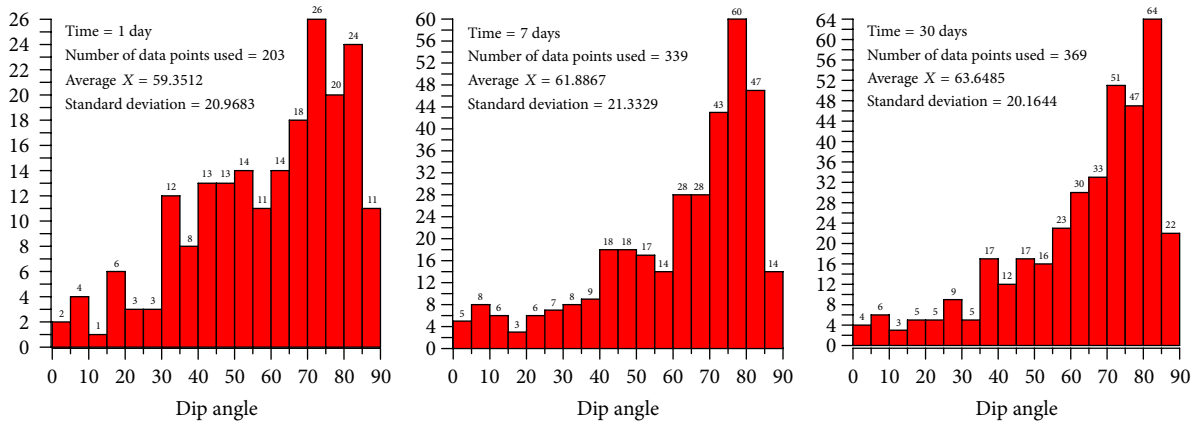


FIGURE 38: Histograms of the Frac-Digger sensitivity of the estimated dip angles of dikes to the time difference (δt) allocated to the plane-oriented cluster.

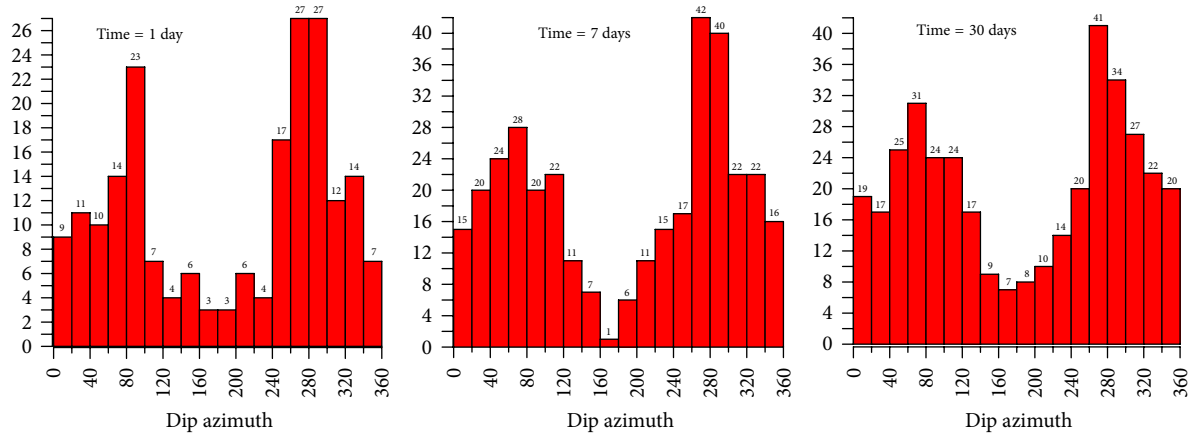


FIGURE 39: Histograms of the Frac-Digger sensitivity of the estimated dip azimuths of dikes to the time difference (δt) allocated to the plane-oriented cluster.

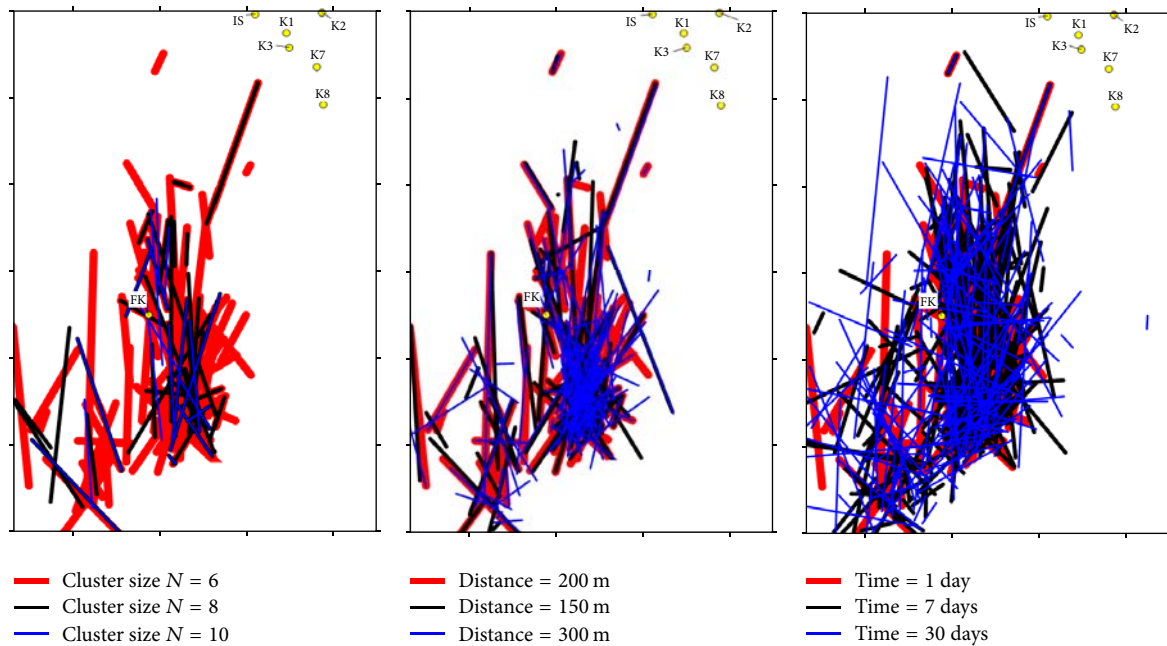


FIGURE 40: Frac-Digger sensitivity of the estimated dike traces. Dike traces at depths of -3000 masl below Koryaksky Volcano were estimated using Frac-Digger with different input parameters: cluster size (or the number of events in cluster N), distance from the event to the plane (δZ), and time differences (δt). The thermal features FK, K1, K2, K7, K8, and IS are given for reference, and the ticks along the axes represent intervals of 2 km.

included in a cluster) and temporal proximity criteria (δt , the time interval allocated for earthquake events included in a cluster), as is demonstrated above.

Conflicts of Interest

The authors declare that they have no conflicts of interest.

Acknowledgments

This work was funded by the Russia Science Foundation Project no. 16-17-10008.

References

- [1] V. V. Ivanov, "Activation of Koryaksky Volcano (Kamchatka) in late 2008 - early 2009: evaluation of heat and aqueous fluid removal, conceptual model of magma ascent and Eruption development forecast," in *Proceedings of the conference dedicated to the Day of Volcanology*, pp. 24–39, Far East Branch of Russian Academy of Science, Vladivostok, Russia, 2010.
- [2] A. Gudmundsson, "Magma chambers: formation, local stresses, excess pressures, and compartments," *Journal of Volcanology and Geothermal Research*, vol. 237–238, pp. 19–41, 2015.
- [3] F. Sigmundsson, A. Hooper, S. Hreinsdóttir et al., "Segmented lateral dyke growth in a rifting event at Barrparbunga volcanic system," *Iceland//Nature*, vol. 517, pp. 191–194, 2015.
- [4] S. Dumont, Y. Klinger, A. Socquet, C. Doubre, and E. Jacques, "Magma influence on propagation of normal faults: Evidence from cumulative slip profiles along Dabbahu-Manda-Hararo rift segment (Afar, Ethiopia)," *Journal of Structural Geology*, vol. 95, pp. 48–59, 2017.
- [5] A. V. Kiryukhin, S. A. Fedotov, and P. A. Kiryukhin, "A geomechanical interpretation of the local seismicity related to eruptions and renewed activity on Tolbachik, Koryakskii, and Avacha Volcanoes, Kamchatka, in 2008–2012," *Journal of Volcanology and Seismology*, vol. 10, no. 5, pp. 275–291, 2016.
- [6] A. Kiryukhin and J. Norbeck, "Analysis of magma injection beneath an active volcano using a hydromechanical numerical model," in *Proceedings of the 42nd Workshop on Geothermal Reservoir*, pp. 740–747, Engineering Stanford University, Stanford, California, Calif, USA, 2017.
- [7] A. Kiryukhin, Y. Manukhin, S. Fedotov et al., "Geofluids of Avachinsky-Koryaksky Volcanogenic Basin, Kamchatka, Russia," in *Proceedings of the of the World Geothermal Congress*, pp. 1–12, Melbourne, Australia, April 2015.
- [8] R. O. Fournier and A. M. Pitt, "Yellowstone magmatic-hydrothermal system, U. S. A.," in *Proceedings of the International Symposium on Geothermal Energy, International Volume*, pp. 319–327, Geothermal Resources Council, Davis, CA, USA, 1985.
- [9] V. P. Chernyak, I. A. Ryzhenko et al., *Laboratory Estimation of Filtrational And Heat Properties of Rocks at Temperatures up to 120°C and Pressures 50 Mpa Aiming at Exploration of The Yuzhno-Berezhny and Nizhne-Ozernovsky Sites of Kamchatka*, Report ITTF AN USSR, Kiev, Ukraine, 1987.
- [10] A. Kiryukhin, L. Vorozheikina, P. Voronin, and P. Kiryukhin, "Thermal and permeability structure and recharge conditions of the low temperature Paratunsky geothermal reservoirs in Kamchatka, Russia," *Geothermics*, vol. 70, pp. 47–61, 2017.
- [11] S. A. Fedotov, *Magmatic Feeding Systems and Mechanism of Volcanic Eruptions*, Nauka, 2006.
- [12] M. W. McClure, *Modeling and characterization of hydraulic stimulation and induced seismicity in geothermal and shale gas*

- reservoirs [Ph.D. thesis], Stanford University, Stanford, California, Calif, USA, 2012.
- [13] M. W. McClure, "CFRAC (version 1.2)," *Complex Fracturing Research Code User's Guide (Version 20)*, 2014.
- [14] A. Kiryukhin, "Analysis of Magma Injection Beneath an Active Volcano Using a Hydromechanical Numerical Model (CFRAC)," in *Proceedings of the EAGE conference, Horizontal wells*, vol. 4, Kazan, Russia, 2017.
- [15] P. Lundgren, A. Kiryukhin, P. Milillo, and S. Samsonov, "Dike model for the 2012-2013 Tolbachik eruption constrained by satellite radar interferometry observations," *Journal of Volcanology and Geothermal Research*, vol. 307, pp. 79–88, 2015.
- [16] M. D. Zoback, *Reservoir Geomechanics*, Cambridge University Press, Cambridge, UK, 2010.
- [17] E. R. James, M. Manga, T. P. Rose, and G. B. Hudson, "The use of temperature and the isotopes of O, H, C, and noble gases to determine the pattern and spatial extent of groundwater flow," *Journal of Hydrology*, vol. 237, no. 1-2, pp. 100–112, 2000.
- [18] *Earthquakes in Russia in the year 2013*, GS RAN, Obninsk, 2015.
- [19] *Earthquakes in Russia in the year 2014*, GS RAN, Obninsk, 2016.
- [20] W. C. Evans, R. H. Mariner, D. Bergfeld, K. M. Revesz, and J. P. McGeehin, "Carbon isotope composition of CO₂ at Cascade Arc volcanoes," in *WRI*, pp. 195–198, Mexico, 2010.
- [21] K. Pruess, C. Oldenburg, and G. Moridis, "TOUGH2 user's guide version 2," Tech. Rep. LBNL-43134, Lawrence Berkeley National Laboratory Report LBNL_43134, Berkeley, California, Calif, USA, 1999.
- [22] V. Stefansson, "World geothermal assessment," in *Proceedings of the World Geothermal Congress '05*, pp. 1–6, Antalya, Turkey, 2005.
- [23] B. G. Polyak and I. V. Melekestsev, "Volcanoes productivity," *Journal of Volcanology and Seismology*, vol. 5, pp. 22–37, 1981.
- [24] E. A. Vakin, *Hydrogeology of Recent Volcanic Structures and Hydrotherms of South-East of Kamchatka. Dissertation, Degree of Candidate Geological-Mineralogical Sciences*, 1968.

Research Article

Fluid Flow and Heat Transport Computation for Power-Law Scaling Poroperm Media

Peter Leary,¹ Peter Malin,¹ and Rami Niemi²

¹Advanced Seismic Instrumentation and Research, 1311 Waterside, Dallas, TX 75218-4475, USA

²St1 Deep Heat Ltd, Purotie 1, 00381 Helsinki, Finland

Correspondence should be addressed to Peter Leary; pcl@asirseismic.com

Received 22 February 2017; Accepted 20 August 2017; Published 19 October 2017

Academic Editor: Mohamed Fathy El-Amin

Copyright © 2017 Peter Leary et al. This is an open access article distributed under the Creative Commons Attribution License, which permits unrestricted use, distribution, and reproduction in any medium, provided the original work is properly cited.

In applying Darcy's law to fluid flow in geologic formations, it is generally assumed that flow variations average to an effectively constant formation flow property. This assumption is, however, fundamentally inaccurate for the ambient crust. Well-log, well-core, and well-flow empirics show that crustal flow spatial variations are systematically correlated from mm to km. Translating crustal flow spatial correlation empirics into numerical form for fluid flow/transport simulation requires computations to be performed on a single global mesh that supports long-range spatial correlation flow structures. Global meshes populated by spatially correlated stochastic poroperm distributions can be processed by 3D finite-element solvers. We model wellbore-logged Dm-scale temperature data due to heat advective flow into a well transecting small faults in a Hm-scale sandstone volume. Wellbore-centric thermal transport is described by Peclet number $P_e \equiv a_0 \varphi v_0 / D$ (a_0 = wellbore radius, v_0 = fluid velocity at a_0 , φ = mean crustal porosity, and D = rock-water thermal diffusivity). The modelling schema is (i) 3D global mesh for spatially correlated stochastic poropermeability; (ii) ambient percolation flow calibrated by well-core porosity-controlled permeability; (iii) advection via fault-like structures calibrated by well-log neutron porosity; (iv) flow $P_e \sim 0.5$ in ambient crust and $P_e \sim 5$ for fault-borne advection.

1. Introduction

Numerical models of fluid flow in crustal rock describe a process which cannot be readily observed on any but the smallest scales. The statistical nature of subsurface rock physical property fluctuations is thus a key aspect of crustal flow modelling. Flow and heat transport simulations computed using faulty rock property statistical distributions can lead to faulty conclusions about the unseen fluid flow processes. It is almost certainly the case that the statistical character of rock properties currently attributed to subsurface crustal flow is improperly influenced by the statistics of rock property distributions observed at the surface. In consequence, simulations of subsurface flow and heat transport are often, even typically, poor representations of crustal flow reality.

The root observational snag began with the work of Darcy and Dupuit [1, 2]. Darcy and Dupuit jointly concluded that important fluid flow structures in the Paris Basin limestone formations occurred via the infrequent and narrow but laterally persistent clastic formations with flow properties that

resembled those of unconsolidated sands used by municipal hydraulic engineers to filter groundwater [3]. In an era in which fluid mechanics was coming of age, fluid flow through unconsolidated sands was recognised through the work of Darcy and Dupuit to be markedly different from fluid flow through pipe-like channels regarded as characteristic of the Paris Basin limestones and chalks. Darcy's law, for which loss of hydraulic head was directly proportional to flow velocity in unconsolidated filtration column sands and in clastic groundwater formations, was the formal outcome of the Darcy-Dupuit groundwater observations.

It was not understood at the time and remained overlooked a century later (e.g., [4–8]) that unconsolidated sands with little or no internal structure are a faulty model for poroperm properties of subsurface clastic rock. An array of present-day well-log, well-core, and well-production evidence indicates that the process of sediment consolidation imprints on sedimentary crustal formations a set of scale-independent random spatial correlations that control

formation permeability at all scales [9–16]. Of particular significance is the existence of through-going fluid flow paths at the largest spatial correlation scales. The highly attested spatially correlated nature of crustal rock flow properties violates the central limit theorem, the master tenet of geological thinking, and thus invalidates the standard statistical sampling approach to managing fluid flow at depth in the crust. The fundamental error concerning the statistical nature of crustal fluid flow property distributions remains generally unrecognized (e.g., [17, 18]).

The following discussion undertakes to present a straightforward physically motivated computational framework in which proper stochastic procedures represent the spatially correlated distributions of unknown crustal flow properties in a manner which allows finite-element solvers to provide more realistic flow and heat transport simulations. We first review the mathematical and physical origins of the normal distribution used to represent stochastic processes in which significant degrees of spatial or temporal correlation are absent. We then introduce the vast array of well-specific empirical evidence that spatial correlations exist throughout the stochastic processes controlling fluid flow in crustal rock and indicate how the observed spatially correlated flow properties can be represented in numerical meshes amenable to finite-element simulation of fluid flow and heat transport of the crust. Last, we implement our finite-element modelling methodology for a Dm-scale fracture sequence embedded in a Hm-scale crustal volume of tight gas sands. Within this crustal volume a temperature survey in a newly drilled wellbore gave evidence of heat transport by fault-borne fluid flow. Our simulations duplicate the observed wellbore temperature distribution and assign Peclet numbers to the ambient and fault-borne advection flows that are consistent formal analytic solutions for wellbore-centric advective heat flow. We conclude that crustal flow simulation is best performed using a single global numerical mesh in which to embed a suitable scale range of spatially correlated crustal flow structures.

2. Spatial Correlation in Crustal Flow Property Distributions

2.1. Normal Distributions versus the Statistical Character of Spatially Correlated Crustal Porosity. Crustal reservoir flow modellers can be said to face a problem similar to that which Gauss formally solved in his 1809 treatise on celestial motion [19]. A collection of celestial observations $\{x_i\}$, $i = 1 \dots n$, was taken to represent a “true” celestial mechanics value x_0 , measurements which were disturbed by a range of unknown physical processes that generated the observational spread $\{x_i\}$. The problem was to determine what estimated value amidst the scattered data $\{x_i\}$ best approximates the actual physical value x_0 . In devising what has come to be called the “least squares” solution to the problem of inexact data, Gauss saw that the population distribution of “unbiased” random processes centered on an assumed value \underline{x} formalised by de Moivre in 1738 for “fair” games of chance [20],

$$p(x_i | \underline{x}) = \exp(-\eta(x_i - \underline{x})^2), \quad (1)$$

could formally give a clear probability maximum if the unknown parameter \underline{x} is the arithmetic mean of $\{x_i\}$, $\underline{x} = (1/n) \sum x_i$. Maximizing the probability worked, however, if, but only if, the value of each event x_i is independent of all other events. That is, if (1) is assumed to represent the probability $p(x_i | \underline{x})$ of event x_i given the unknown parameter value \underline{x} , then for independent event values x_i , the probability P of observation set $\{x_i\}$ is the product of all event probabilities,

$$P = \prod p(x_i | \underline{x}) = \exp(-\eta \sum (x_i - \underline{x})^2). \quad (2)$$

Evaluating (2) for the condition $\partial P / \partial \underline{x} = 0$ maximizes P if $\underline{x} = (1/n) \sum x_i$. Normalizing the total probability to unity, the factor η in (1)-(2) is related to the width σ of the normal distribution centered on mean value \underline{x} , $\eta = 1/(2\sigma^2)$.

The statistical distribution of independent random events (1) is conveniently summarized by the familiar Gaussian normal distribution controlled by two parameters, the sample mean \underline{x} and the sample standard deviation σ . It follows immediately that the sample values of the mean and standard deviation converge on the actual mean and standard deviation in direct proportion to the square root of the number of samples, \sqrt{n} . Gauss’s least squares solution procedure thus appears to be both compact and complete and as such pervades scientific and practical applications [21].

In 1860 Maxwell gave forceful physical testament to the role of event independence by effectively using (1) to establish the statistical physics of ideal gases using molecular velocities as events x_i . Application of (1) to the collective microscopic actions leading to macroscopic gas pressure and temperature assumes that each molecule velocity before and after collisions is independent of the velocities of all other molecules. In the words of Maxwell [22], “If experiments on gases are inconsistent with the hypothesis of these propositions, then our theory, though consistent with itself, is proved to be incapable of explaining the phenomena of gases.” In making the reasonable assumption that molecular motion is suitably independent before and after collisions, Maxwell accurately established the micromechanical nature of gas pressure and temperature uniformity throughout a volume of an ideal gas.

Traditional crustal reservoir modelling proceeds in a like manner. As with Gauss and Maxwell, the mean and standard deviation of porosity sample $\{\varphi_i\}$ are assumed to reliably reflect the mean and standard deviation for the reservoir at large [18]. Following Maxwell’s analysis of an ideal gas, we can put the microscale independence assumption to the test. For a well-log sequence $\{\varphi_i\}$ of porosity values measured at equal intervals $\ell \sim$ meter along a crustal wellbore, we ask if the physical events producing porosity sample $\{\varphi_i\}$ are independent. To answer this test question, we note that a condition for physical property estimates $\{\varphi_i\}$ to be independent is that the autocorrelation function of the data sequence $\{\varphi_i\}$

$$A_j \propto \sum \varphi_i \varphi_{i+j} \quad (3)$$

is zero for all nonzero lags, $j \neq 0$. Assuming this property for (3), cosine transformation of an autocorrelation function [23]

yields for A_j a constant power-spectrum for crustal sample sequence $\{\varphi_i\}$ as a function of spatial frequency k ,

$$S(k) \propto \sum_j A_j \cos(2\pi jk) = A_0 \cos(2\pi \cdot 0 \cdot k) = \quad (4)$$

$$A_0 \sim \text{constant.}$$

We thus find that event independence applied to any well-log sequence $\{\varphi_i\}$ of n values taken at uniform sample length ℓ over length $L = n\ell$ implies that the power-spectrum of the sequence is constant across the spatial frequency range $1/L < k < 1/2\ell$.

It is straightforward to determine that well-log power-spectra for crustal porosity, and for crustal rock properties in general, consistently violate spectral condition (4) at all relevant scale lengths [9, 10]. Well-log spectra are observed worldwide to scale inversely with spatial frequency k over five decades of scale length,

$$S(k) \sim \frac{1}{k^\beta}, \quad \beta \sim 1, \quad 1/\text{km} < k < 1/\text{cm}. \quad (5)$$

Heeding Maxwell, we see from empirical observation (5) that crustal porosity sample sets $\{\varphi_i\}$ are spatially correlated rather than spatially uncorrelated. It follows that, at least formally, sample well-log porosity sequences $\{\varphi_i\}$ cannot be meaningfully interpreted as unbiased representations of the porosity distribution in the formation at large.

2.2. Spatial Correlations in Crustal Permeability. The impact on fluid flow of spatially correlated porosity distributions in crustal volumes emerges from considering well-core poro-perm systematics. Well-core poro-perm sequences worldwide [11, 15] show that changes in the logarithm of core permeability κ_i closely track spatial changes in core porosity φ_i ,

$$\delta\varphi_i \propto \delta \log(\kappa_i), \quad i = 1 \cdots n. \quad (6)$$

Empirical relation (6) is heuristically plausible. If porosity is spatially correlated at all scales (i.e., porosity spatial fluctuations obey spectral scaling relation (5)), then connectivity between pores is plausibly spatially correlated as well. In mathematical terms, if porosity is expressed as a numerical density, $\varphi_i \propto N_i$, the ability of pores to link together to produce larger scale permeability is plausibly proportional to the combinatorial factor $N_i! \sim N_i(N_i-1)(N_i-2)(N_i-3) \cdots 1$. Spatial fluctuations in pore density δN_i then create changes in pore connectivity $\delta \log(N_i!)$, giving a simple physical interpretation to empirical relation (6) through Stirling's formula [24], $\log(N!) \sim N(\log N - 1)$.

The large-scale effect of spatial correlations in porosity and permeability is seen by integrating well-core-scale spatial fluctuation correlation relation (6) from the scale of sample interval $\ell \sim$ meter between individual cores samples to the Hm-scale of reservoir formations spanned by well-core sequences. Hm-scale crustal permeability spatial fluctuations can thus be expressed as

$$\kappa_i \approx \underline{\kappa} \exp(\alpha(\varphi_i - \underline{\varphi})), \quad (7)$$

where α is a dimensionless integration constant to be determined empirically.

Observed values of the integration constant α are typically 20–40 for crustal reservoir formations with porosity $\varphi \sim 0.1$ –0.3 [14, 15]. For basement rock with lower porosity $\varphi \sim 0.01$, $\alpha \sim 300$ [16]. As crustal porosity is often quasi-normally distributed over typically small ranges, for example, $\varphi \sim 0.1$ –0.3, the observed values of $\alpha \sim 20$ –40 mean that (7) is effectively a lognormal distribution for permeability at the scales of crustal well-production. Lognormal well-production distributions consistent with (7) are observed worldwide for conventional oil/gas fields [25], unconventional oil/gas fields [26], geothermal fields [27], basement rock groundwater aquifers [28, 29], and fossil flow aqueous mineral deposits [30–32].

The trio of essentially universal crustal property empirics—well-log spatial fluctuation spectral scaling (5), well-core spatial correlation (6) between porosity and the logarithm of permeability, and lognormal distributions of well-production (7)—implies that spatially correlated randomness at all scale lengths conditions fluid flow throughout the crust. Contrary to the commonly accepted prescription that a given geological formation is effectively uniform in flow properties [4–8], the statistical tactic of spatial averaging over poro-perm properties cannot properly represent the significant degree of flow heterogeneity inherent in crustal rock. Because of power-law scaling (5), the deviation from a mean or medial permeability background grows with the scale of the flow system. To be relevant to crustal flow heterogeneity, numerical realisations of crustal flow properties must simulate the crust's inherent spatial correlation and in particular allow for the largest stochastic spatial fluctuations to occur at the largest scales.

2.3. Numerical Representation of the Grain-Scale Physical Character of Crustal Permeability. Numerical realisation of the combined crustal poro-perm empirics (5)–(7) has a simple grain-scale pictorial basis.

While power-law spectral scaling (5) loosely resembles a fractal distribution [33], it is in fact a considerably more powerful physical statement than is implied by fractals. Fractal scaling in a physical system is a statement about population numbers within a system without implications for spatial organization within the system. In contrast, spectral scaling (5) is a physical statement about spatial organization of the crustal poro-perm volume elements: in crustal rock everywhere, there is a tendency for crustal volume elements at any given scale to have poro-perm properties similar to the poro-perm properties of neighbouring crustal volume elements of the same scale [9].

Spatial organization such as implied by (5) for crustal rock is observed in a wide range of physical systems [34]. Such systems can be described as undergoing a “critical state order-disorder” phase change. In the crust, (5) implies that an order-disorder phase change occurs throughout the brittle-fracture crustal section lying between the “ordered” ductile lower crust and the “disordered” disaggregated uppermost crust [9, 10]. In the ordered lower crust, porosity is largely absent as fluids tend to be absorbed in hydrated mineral

complexes, with deformation occurring by plastic dislocation within an elastic continuum. In the disordered uppermost crust, porosity reaches a form of “critical value” associated with spatial dissociation of grains, with fluids moving freely through the medium [18]. The fluid flow properties of the order-disorder transition state in the brittle-fracture crust are radically distinct from those of lower crustal ductile state and uppermost-crustal disaggregation state.

A prominent feature of critical state order-disorder phase transitions is that power-law scaling exponents are independent of the physical nature of microscale elements [34]. With this independence from microscopic physical properties, we can conceptualize rock in terms of a binary physical state that is easily represented numerically. These states are (i) intact grain-grain cement bond contacts forbidding passage of pore fluids and (ii) disrupted grain-grain cement bond contacts permitting passage of pore fluids.

In this binary-state perspective, crustal rock critical state order-disorder phase transition properties are equivalent to a percolation lattice for which through-going fluid flow pathways are highly improbable for defect densities below a threshold value and highly probable for defect densities above the threshold value [35]. The effective physical parameter describing rock as a critical state binary population is the fraction N of defective grain-grain contacts relative to the population of intact grain-grain contacts. It is well known for percolation lattices that the transition between nonflowing and flowing lattice states occurs over a narrow range of defect densities centered on a “critical state” threshold defect density N_{crit} [35].

Regarding crustal rock as a critical state percolation lattice, rock in the ductile lower crustal represents the rock state with defect density below the percolation threshold, and rock in the cohesionless uppermost-crust represents the rock state with defect density above the percolation threshold. The intervening crustal domain of cohesive brittle-fracture rock is perpetually maintained at the critical state percolation density N_{crit} by the opposing actions of two ongoing crustal processes: (i) damage injection by tectonic finite strain at grain-grain contact that tends to drive the crust to the disordered state of uppermost-crustal disaggregation and (ii) healing/sealing by aqueous chemical disposition at grain-grain contacts that tends to drive the crust to the ordered state of lower crustal ductility.

A steady-state percolation system balanced between gaining and losing grain-scale defects is consistent with studies of the fracture state of the crust. Laboratory experiments and numerical modelling identify strain levels of order $\epsilon \sim 0.003$ and above as creating an elastic damage within the crustal fabric [36]. At the same time, field data assess ambient crustal strain levels in the seismically inactive Fennoscandian crust of order $\epsilon \sim 0.003$ and above [37]. A binary population picture of crustal rock focused on cement-contacts is consistent with studies of the role cements play in crustal rock mechanics. Macroscopic elastic moduli are often directly proportional to the moduli of the bonding material [38]. Compression tests on a solid skeleton of glass beads demonstrate that small amounts of epoxy resin cement act to localize strain in the cements, thus preventing crushing of the glass beads [39].

Numerical simulation of composite materials shows that the effective elastic moduli are strongly affected by the presence of cement material in the range of 1% to 10% of the composite medium [40].

In sum, a broad range of crustal studies is consistent with on-going finite strain damage in rock naturally concentrating in the grain-grain cement bond contact sites that can be associated with crustal poroperm empirics (5)–(7). Numerical representation of the fundamental spatial correlation properties of crustal rock is achieved though (i) allowing numbers between zero and one to represent the range of defect densities within elementary crustal volumes at the nodes of a computational mesh, (ii) generating power-law scaling spatial correlations between those nodal values across the mesh, and (iii) specifying permeability within the mesh by taking the exponent of the nodal effective porosity values scaled by the empirical parameter α appearing in (7). This representation of crustal properties is most effectively achieved for a single global mesh that allows the maximum representation of the crust’s long-range spatial correlation physics at all scales from mm to km. For the purpose of modelling crustal flow and heat transport, crustal poroperm structures controlling fluid flow can be embedded in a single global mesh.

3. Numerical Modelling of Fracture-Borne Heat Transport in Crustal Rock

Crustal rock poroperm empirics (5)–(7) interpreted in terms of a generic percolation lattice of flow/no-flow sites are readily represented on a node-based numerical mesh. Finite-element solvers operating on such meshes can then compute Darcy pressure-gradient flow and the fluid transport of heat or solutes. As empirics (5)–(7) focus on long-range spatial correlations supporting critical state percolation backbone flow through a model crustal volume, numerical realisation of the crustal state is most efficiently achieved by making the support mesh encompass the entire model volume. Such global meshes effectively encode the scale-independent spatial correlation connectivity of grain-scale cement bond contact defects over the largest range of scales possible for a given mesh node count. Given that numerical mesh computation cannot match the 20-octave or greater physical process bandwidth of natural rock, feasible computational meshes represent degrees of coarse-graining over the sub-mm to mm scales of rock poropermeability. However, because of the observed five decades of well-log spectral power-law scaling (5) from cm to km, the necessary numerical coarse-graining from sub-mm to cm to dm and above does not significantly compromise numerical representations of large-scale crustal fluid flow processes, provided the spatial correlation structures are allowed to span the entire computational volume in a global mesh.

3.1. Illustration of Global Mesh Representation of Crustal Poroperm Structures. Wellbore-based experiments conducted in western Colorado Cretaceous sedimentary tight gas sands provide an opportunity to apply empirics (5)–(7)

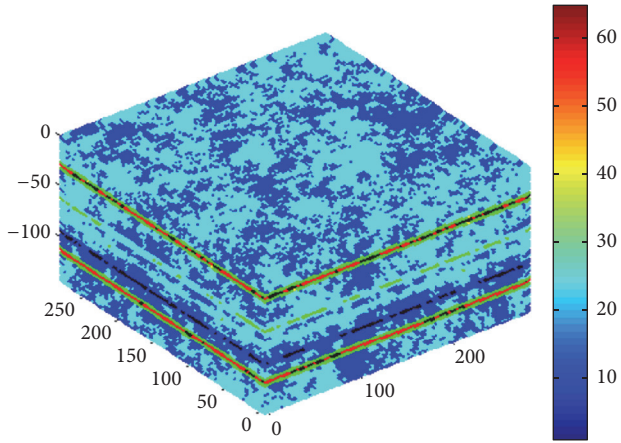


FIGURE 1: Effective porosity distribution in 2 Hm-scale simulation of the MWX crustal volume transected by a vertical wellbore. The colour-bar codes the degree of porosity in the section. Cool colours denote the 3D ambient distribution of spatially correlated porosity in accord with spatial fluctuation power-law spectral scaling (5) for well-log porosity range $0.1 < \varphi < 0.3$. Warm colours denote elevated effective porosity with elevated poroconnectivity parameter α controlling permeability via (7). These layers represent crustal faults that intersect the transecting wellbore at depths recording spikes in neutron porosity well-log.

to modelling to Hm-scale crustal flow and heat transport. The 1995 MWX Multiwell Experiment project [41] drilled a quartet of wellbores to investigate hydrofracture stimulation of tight gas-bearing sands. The potential for active heat transport in the crustal study volume was observed in one of the wellbores as a sequence of thermal gradient spikes in a 200 m section of wellbore at 2.1–2.3 km depth. The thermal gradient spikes coincide with neutron porosity well-log fluctuation spikes in the same well. Interpreting the porosity spikes as evidence for fluid-conductive faults, it is logical that the spatially coincident thermal gradient spikes are due to advective heat entering the wellbore via fracture-borne fluids. The MWX field situation is pictured in Figure 1 as an ambient effective porosity crustal volume with a sequence of embedded fluid-conductive fracture horizons.

Regional erosion relief of order ~ 850 meters due to the nearby Colorado River makes it plausible that a regional hydraulic head can drive fracture-borne fluids into a newly drilled wellbore on a sufficiently large scale to generate an observable thermal signature. MWX project data for the specific 2 Hm-scale crustal volume intersected by the observation wellbore are shown in Figures 2–6. The MWX support data include a well-log porosity sequence $\{\varphi_i\}$ to fix spatial fluctuation spectral scaling (5), detailed well-log spatial thermal data to fix the system advected heat flow structure, and sizeable amounts of core-scale poroform data to fix the poroform-spatial correlation (6) and the poroconnectivity parameter α (7).

In Figure 1, a global mesh supports a stochastic numerical realisation of the MWX poroform parameters and structures needed to simulate flow and/or heat transport of a crustal flow regime:

- (i) Systematic spatial correlation of porosity at all scales controlled by power-law scaling exponent $\beta \sim 1$ in (5)
- (ii) Control of node-scale permeability (6) by node-scale porosity fluctuations in the range $0.1 < \varphi < 0.3$
- (iii) Control of multi-node-scale permeability by poroconnectivity parameter $20 < \alpha < 60$ in (7)
- (iv) Control of sedimentary flow structures as needed by formation-based changes in porosity and poroconnectivity parameter.

The temperature field recorded by a vertical wellbore through the Figure 1 crustal volume can be computed by assuming that (i) regional topographic head drives fluids from the crustal volume periphery into the wellbore in proportion to the permeability of the crustal section at each depth along the wellbore and (ii) system heat withdrawal at the wellbore varies along the wellbore with the degree at which fluid flows into the wellbore from the fixed temperature at the volume periphery.

With reference to Figure 1, this model flow scenario is imposed by setting no-flow boundary conditions on the top and bottom of the crustal volume, setting constant pressure and temperature boundary conditions at the volume periphery, and fixing a constant withdrawal of advected heat from the central wellbore. By assuming a stratified flow approximation consistent with the well-log porosity spike sequence, it is possible to set a wellbore-centric flow Peclet number $P_e \equiv a_0 \varphi v_0 / D$ for radial flow through each section of the model [16], where v_0 is the characteristic fluid flow velocity at the wellbore radius a_0 , φ is flow medium porosity, and D is the characteristic thermal diffusivity for the rock-water system. For low-permeability sections of the crustal volume, fluid flow will be limited to low Peclet numbers implying little advected heat, while for high permeability sections of the crustal volume, that is, the faults, heat flow will achieve higher Peclet numbers.

3.2. MWX Crustal Poroperm Parameter Values. Figures 2-3 display MWX well-log and well-core data used to control the Figure 1 MWX crustal volume poroperm distributions consistent with empirical poroperm properties (5)–(7). Figure 2 shows the wellbore neutron porosity log $\{\varphi_i\}$ over wellbore depth interval 1200–2500 m (a) and the log-log plot of porosity fluctuation spectral power as a function of scale length in the spatial frequency range $1 \text{ cycle/km} < k < 900 \text{ cycles/km}$ (b). The observed power-law spectral scaling exponent of (5) is $\beta \sim 1$. Figure 3 validates the strong spatial correlation empirics (6) for well-core porosity φ and the logarithm of well-core permeability κ (a) and evaluates the poroconnectivity integration constant of (7), $\alpha \sim 24$ (b).

The observed MWX wellbore porosity and temperature gradient phenomenology is displayed in Figures 4-5 for an 800 m crustal interval.

Figure 6 expands the view of the 200 m thermally active interval between 2.1 and 2.3 km and identifies the close spatial relationship between detrended wellbore temperature (blue) and well-log porosity (red). The coincidence of wellbore

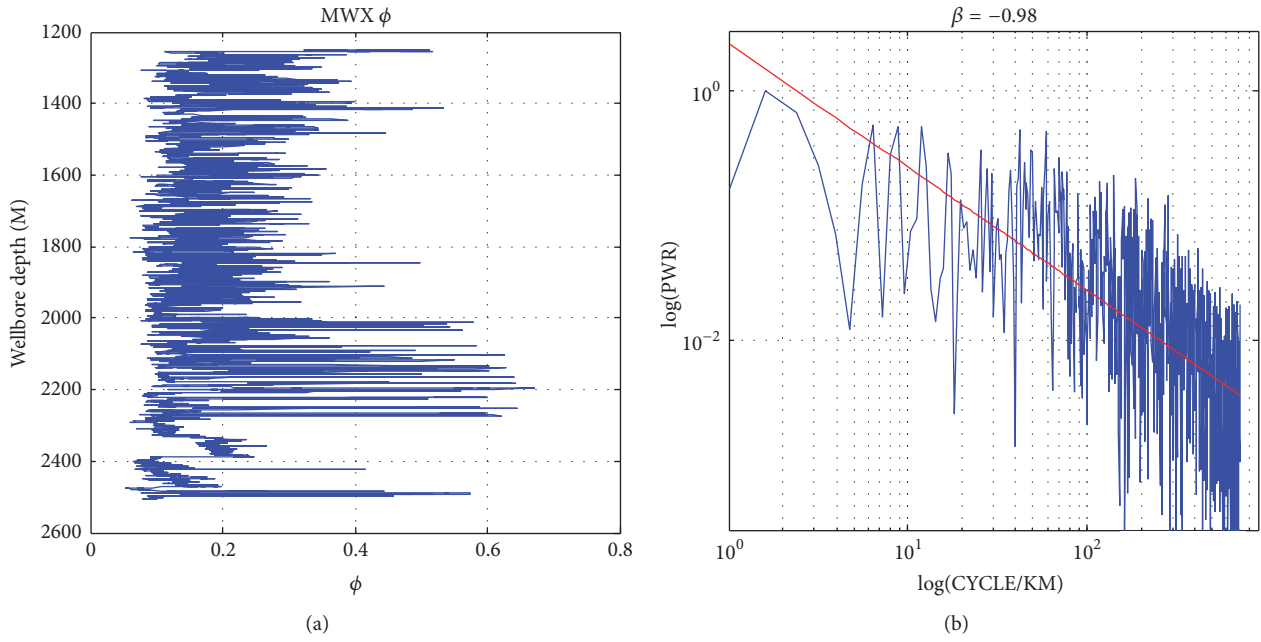


FIGURE 2: MWX crustal empirical property (5): wellbore neutron porosity log (a) and porosity log power-spectrum with power-law scaling exponent $\beta \sim 0.98$ (b).

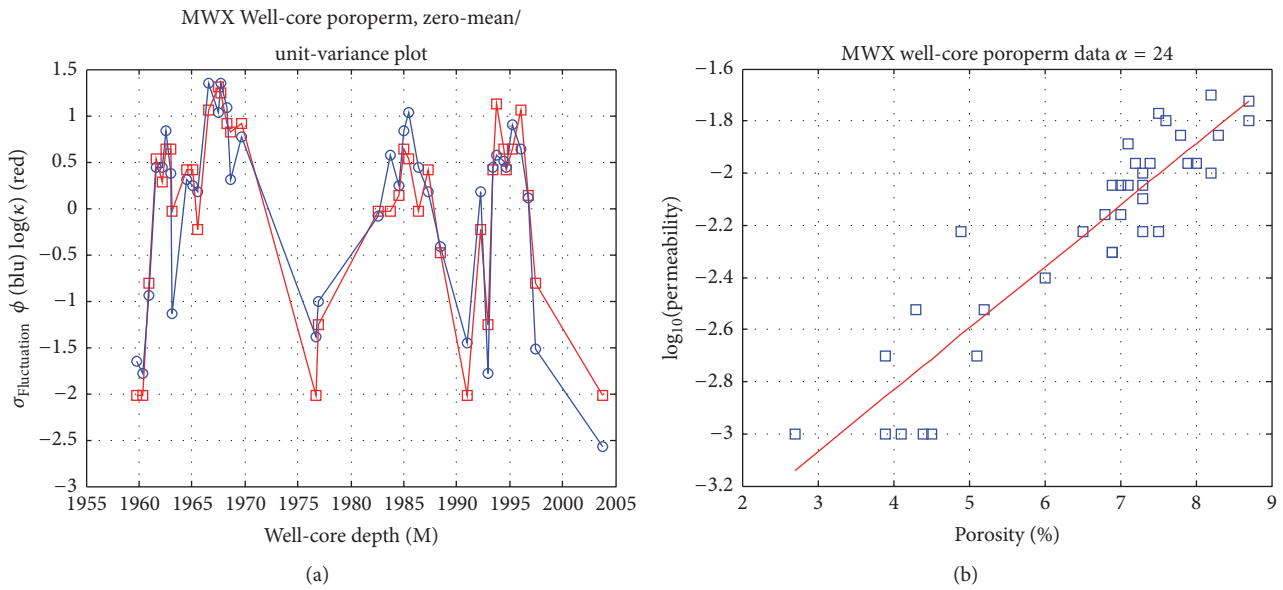


FIGURE 3: (a) MWX empirical property (6): spatially correlated well-core porosity (blue) and logarithm of well-core permeability (red); poroperm data normalized to zero-mean/unit-variance. (b) MWX empirical property (7): well-core porosity against log(permeability) (blue) with best-fit slope for $\alpha \sim 24$ (red).

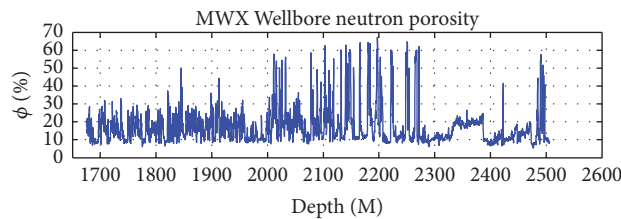


FIGURE 4: Neutron porosity wellbore log of MXW well between 1675 and 2520 meters.

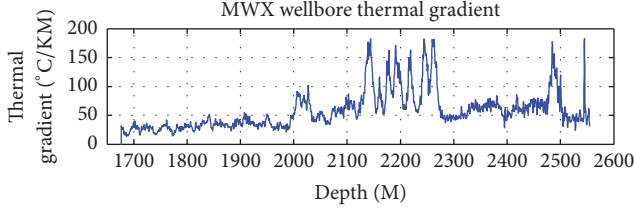


FIGURE 5: Thermal gradient wellbore log of MXW well between 1675 and 2520 meters.

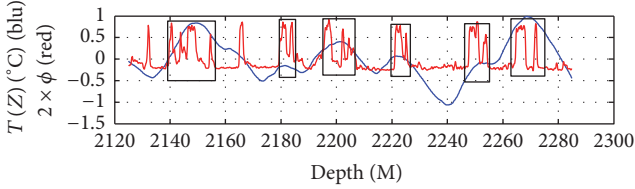


FIGURE 6: MWX wellbore temperature profile (blue) overlying wellbore porosity profile (red); the porosity data are exaggerated by a factor 2. Temperature maxima occur at the porosity maxima.

temperature maxima and wellbore porosity spikes is flagged by rectangles.

The Figure 6 spatial correspondence of temperature and porosity maxima implies a simple fluid flow model in which the ambient crustal volume of empirical poroperm properties fixed by Figures 2-3 data hosts a series of fluid flow horizons with poroperm properties consistent with observed weight and location of well-log porosity spikes. It is assumed that drilling the wellbore generated fluid flow paths within an undisturbed steady-state crustal volume and that the wellbore-disturbed fluid flow and heat advection paths correspond to the observed porosity spikes. For simplicity, we assume that the thermal mass of the rock is great enough and the fluid flow disturbance is mild enough that the wellbore fluid is in local thermal equilibrium with the flow/heat advection structure. The observed Figure 6 spatial distribution of wellbore temperature disturbance is then computed on the modelling assumption that heat is extracted from the crustal section at the wellbore and that the resulting temperature profile along the wellbore is due to varying degrees of fluid flow into the central wellbore in response to the steady withdrawal of crustal heat via the wellbore.

3.3. Finite-Element Modelling of Fracture-Borne Heat Transport in an Empirically Constrained Stochastic Poroperm Crust. The equation of thermal energy transport arises from combining Darcy's law of fluid flow velocity proportional to the fluid pressure gradient,

$$\mathbf{v} = \frac{\kappa}{\mu} \nabla P, \quad (8)$$

with conservation of matter,

$$\frac{1}{B} \times \frac{\partial P}{\partial t} = \nabla \cdot \mathbf{v}, \quad (9)$$

and conservation of thermal energy,

$$C_r \rho_r \partial_t T = \nabla \cdot (K \nabla T - C_w \rho_w T \mathbf{v}). \quad (10)$$

In (8), κ is spatially variable permeability [m^2] and μ is constant fluid viscosity [Pa/s]; in (9) B is the essentially constant elastic bulk modulus of the poroperm medium [Pa]; in (10) K is the essentially constant thermal conductivity of rock [$\text{W/m} \cdot \text{C}$] and $C_r \rho_r$ and $C_w \rho_w$ [$\text{J/m}^3 \cdot \text{C}$] are, respectively, the essentially constant volumetric heat capacity of rock and water.

Computation of temperature fields (10) subject to thermal boundary conditions and fluid flow within the system requires specifying the system permeability structure $\kappa(x, y, z)$ as illustrated by the Figure 1 stochastic porosity distribution on a single global mesh. For steady-state fluid flow, that is, setting $\nabla \cdot \mathbf{v} = 0$, the pressure field is determined by solving the pressure field for given fluid flow boundary conditions,

$$\begin{aligned} \nabla \cdot (\kappa(x, y, z) \nabla P(x, y, z)) \\ = \kappa(x, y, z) \nabla \cdot \nabla P(x, y, z) + \nabla \kappa(x, y, z) \\ \cdot \nabla P(x, y, z) = 0. \end{aligned} \quad (11)$$

The pressure boundary conditions are uniform pressure at the sides of the crustal section, zero-flow across the upper and lower crustal layers, and advected heat loss at the central wellbore. The evolving temperature is then determined by solving for given thermal boundary and initial conditions,

$$\begin{aligned} \partial_t T(x, y, z, t) \\ = \nabla \cdot [D \nabla T(x, y, z, t) - \eta T(x, y, z, t) \mathbf{v}(x, y, z)]. \end{aligned} \quad (12)$$

In parallel with the pressure boundary conditions, the thermal boundary conditions are uniform temperature at the sides, zero-flow at the upper and lower layers, and a fixed heat flow from the crustal section into the central wellbore. The essentially constant thermal properties for water and rock, rock thermal conductivity K , and volumetric heat capacities $C_w \rho_w$ and $C_r \rho_r$ give for (12) constant rock thermal diffusivity $D \equiv K/C_r \rho_r \sim 3 \text{ W/m} \cdot \text{C}/840 \text{ J/kg} \cdot \text{C}/2400 \text{ km/m}^3 \sim 1.5 \cdot 10^{-6} \text{ m}^2/\text{s}$ and constant heat capacity ratio $\eta \equiv C_w \rho_w/C_r \rho_r \sim 4280 \text{ J/kg} \cdot \text{C}/1000 \text{ km/m}^3/(840 \text{ J/kg} \cdot \text{C}/2400 \text{ km/m}^3) \sim 2$.

Figure 7 shows the computed model thermal curve (red) in relation to the MWX (detrended) wellbore temperature profile from Figure 6 (blue). The model temperature distribution is fixed by siting the four principal porosity spikes at the locations given by the Figure 4 wellbore porosity log, with the porosity-controlled permeability parameter weight associated with each porosity spike consistent with Figure 4 data. The overall magnitude of the model temperature field is matched to the data by adjusting the (unknown) average heat extraction rate at the model wellbore.

Figure 8 shows the fluid velocity field for a uniform pressure external boundary condition draining fluid into the central wellbore via the Figure 1 poroperm distribution. Blue

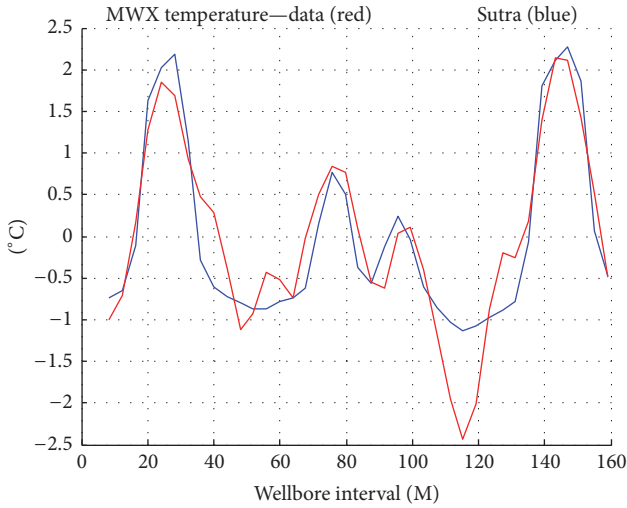


FIGURE 7: MWX wellbore temperature profile (red) overlying model temperature profile (blue) computed by finite-elements solution of (11)-(12) on global mesh of Figure 1 stochastic poroperm property distribution.

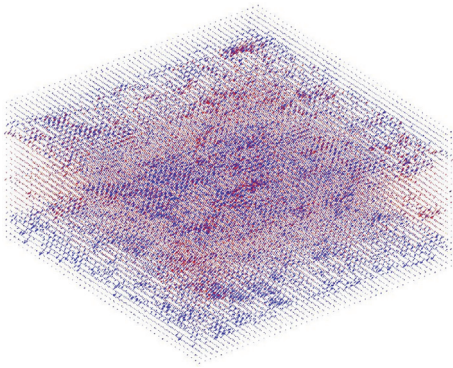


FIGURE 8: MWX crustal section fluid flow velocity vector distribution from Figure 1 poroperm structure. Blue arrows denote fluid flow in the major fault horizons of Figure 1. Red arrows denote fluid flow in the remaining crustal volume. It can be noted that Figure 1 spatial poroperm heterogeneity leads to azimuthally erratic flow paths within the faults and within the embedding ambient crustal volume. In the present horizontally stratified flow structure, heat transport modelled by spatially averaged flow will probably provide a reasonable wellbore temperature distribution. In the presence of more complex faulting, however, a spatially averaged poroperm medium would provide a poor approximation to the resultant erratic wellbore temperature distribution.

arrows indicate the spatially variable flow in the two “strong” poroperm fault channels, while red arrows indicate spatially variable flow of the ambient crustal flow including flow in the two lesser poroperm fault channels. The time-evolving thermal field (12) is computed for the Figure 8 velocity field, yielding the central wellbore temperature distribution of Figure 7.

Using the Figure 8 fluid flow velocity field within the Figure 1 crustal section, the model extracted heat can be compared with the fluid flow velocity field for a mean model

flow v_0 at a given wellbore-centric radius a_0 . These model data combine with rock system thermal diffusivity D to estimate the wellbore-centric heat advection Peclet number $P_e \equiv a_0 \phi v_0 / D$. Identifying the model Peclet number allows in turn comparison of the wellbore-centric model heat transport system with analytic solutions to wellbore-centric advective flow [16].

It can be noted in Figure 8 that fluid flow in the poroperm medium is not azimuthally homogenous within the nodal planes of the computational mesh. There is no reason to suppose that such flow homogeneity exists in actual crustal rock, whether in the ambient rock mass itself, or in any faults embedded in the ambient rock mass. The standard modelling tactic is to ignore all such azimuthal flow heterogeneity by assuming spatial averaging over the heterogeneity eliminates any problems flow heterogeneity might cause. In many crustal flow cases, spatial averaging returns adequate modelling results. This is particular likely in low-velocity flow transport of heat because the thermal properties of crustal rock vary a little in space and with rock composition. In the stratified flow structure of Figure 1, spatially averaged flow bringing heat to a central wellbore provides an adequate transport picture. A different situation can, however, be easily imagined if the sequence of faults is taken to be horizontal planar features if Figure 1 were in fact a more spatially complex volume of flow paths. The central wellbore temperature field could in that instance be far more erratic along the wellbore axis and would effectively defeat attempts at modelling through spatially averaged model poroperm distributions.

3.4. Wellbore-Centric Flow Heat Advection Peclet Number P_e .

Setting up and executing the modelling task posed by applying (11)-(12) to the Figure 1 flow system geometry is simplified by working in a wellbore-centric radial flow approximation in which fluid flow is assumed to be effectively radial within and between the “fault” flow channels designated by the Figure 4 wellbore porosity data. Equation (11) flow in Figure 1 radial sections can be approximated, $v(r) \sim r_0 v_0 / r$. For radial component divergence operator $\nabla \cdot \mathbf{A}(r) = (1/r) \partial_r (r A_r)$, (12) becomes

$$\partial_t T(r, t) = D \left[\partial_r^2 T(r, t) + \frac{(1 - \eta P_e)}{r} \partial_r T(r, t) \right], \quad (13)$$

where $P_e \equiv r_0 \phi v_0 / D$ is a wellbore-centric radial flow Peclet number fixing the ratio of advected heat flow $r_0 \phi v_0$ to thermal conduction heat flow parameter D . Steady-state advective flow $T(r)$ for advective radial flow between inner radius r_0 at temperature T_0 and outer radius r_1 at temperature T_1 has the analytic expression [16]

$$T(r) = T_0 + \frac{(T_1 - T_0) \left((r/r_0)^{P_e} - 1 \right)}{\left((r_1/r_0)^{P_e} - 1 \right)} \quad (14)$$

(steady-state).

The analytic expression for (13) time-evolving temperature field $T(r, t)$ is given by Carslaw & Jaeger [42]. For a line-source heat pulse of energy Q joules per unit length,

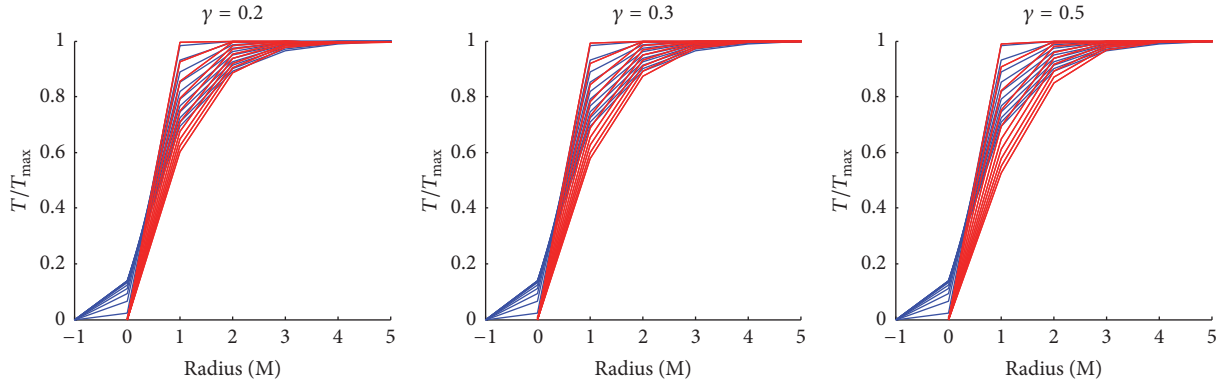


FIGURE 9: MWX ambient crustal section fluid flow heat advection spatiotemporal profiles for three values of Peclet number $P_e = 2\gamma = a_0\phi v_0/D$. Blue curves are numerical model temperature fields; red curves are analytic temperature fields (16). Panels are titled by effective Peclet number $P_e = 2\gamma$ determined by analytic wellbore-centric advective flow temperature field for a sequence of model evolution times. Away from the high porosity sections of the wellbore where fluid flows into the wellbore, the effective Peclet number $P_e \sim 0.5$ implies advective heat flow on the order of thermal conduction heat flow. The analytic curves are reasonable fits to the numerical curves because the model fluid inflow is more or less uniform along the wellbore axis as assumed for the analytic expression.

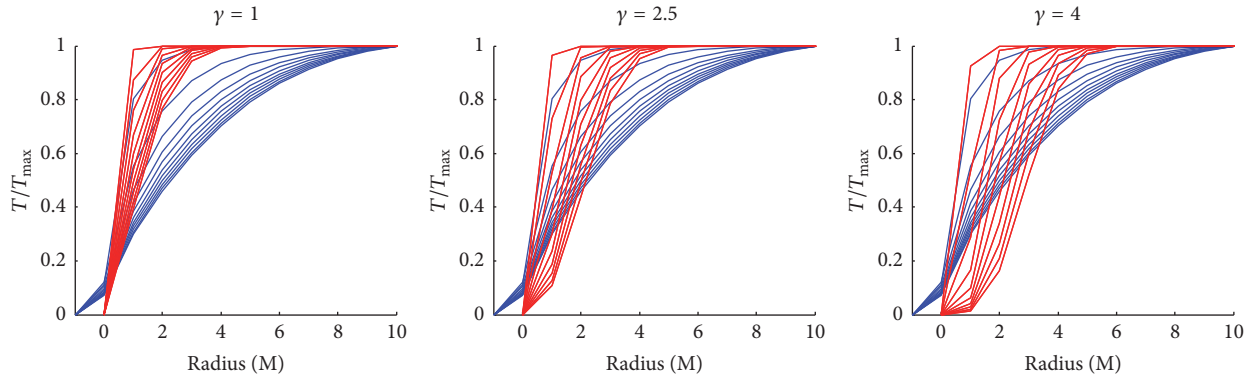


FIGURE 10: MWX fault-controlled crustal section fluid flow heat advection spatiotemporal temperature profiles $T(r, t)$ for three values of Peclet number $P_e = 2\gamma = a_0\phi v_0/D$. Blue curves are numerical model temperature fields; red curves are analytic temperature fields (16). At the high poroperm sections of the wellbore where fluid flows into the wellbore, the effective Peclet number $P_e = 2\gamma \sim 5$ implies that the effective fault-borne advective heat flow is of order 10 times the ambient crustal sections above and below the fault intersections. The numerical temperature field deviates from the analytic temperature field at larger radii because the fault-borne fluid radial inflow from the localized fault intersections along the wellbore expands axially along the wellbore where the analytic expression assumes no axial flow along the wellbore.

the time-evolving temperature field is controlled by Peclet number as $\gamma \equiv P_e/2$,

$$T(r, t) = \frac{Q}{4\pi K t \Gamma(\gamma + 1)} \left(\frac{r^2}{4Dt} \right)^\gamma \exp\left(-\frac{r^2}{4Dt} \right), \quad (15)$$

with $\Gamma(\gamma + 1)$ the gamma function of argument $\gamma + 1$ [24]. The solution for Figure 1 advective flow approximated by a line source of radius a at temperature T_0 into an infinite medium initially at temperature zero is [42]

$$T(r, t) = T_0 + \frac{2}{\pi} \cdot T_0 \cdot \left(\frac{r}{a} \right)^\gamma \cdot \int \frac{dk}{k} \exp(-k^2 Dt) \cdot \frac{[J_\gamma(kr) Y_\gamma(ka) - Y_\gamma(kr) J_\gamma(ka)]}{[J_\gamma^2(ka) + Y_\gamma^2(ka)]}. \quad (16)$$

Approximations to radial flow temperature distribution (16) computed for the fluid flow velocity field illustrated in Figure 8 give the model and simulation $T(r, t)$ field approximations compared in Figures 9-10 for, respectively, low and high poroperm flow sections of the Figure 1 crustal section.

In Figure 9, the low poroperm flow section numerical model $T(r, t)$ approximation (blue traces) can be fit to analytic expressions (red traces) for low values of wellbore-centric Peclet number $P_e = 2\gamma = a_0\phi v_0/D \sim 0.5$. In Figure 10, the high poroperm flow section numerical approximation (blue) is less well matched to the analytic expressions (red) because the numerical model flow is for a narrow axial range of fluid inflow at each fault intersection with the wellbore, while the analytic expression assumes axial symmetry. This disparity aside, the order of magnitude increase in Peclet number $P_e = 2\gamma = a_0\phi v_0/D \sim 5$ for the high poroperm sections of model flow in blue is in general agreement with the analytic expression in red.

4. Discussion/Summary

We have interpreted a series of coincident wellbore porosity and temperature spikes in a Hm-scale block of tight gas sandstone as instances of thermal advection in localized fracture-based fluid flow systems intersected by the wellbore. Our modelling of the observed wellbore temperature events demonstrates how finite-element solvers using a single global mesh can use local well-log details to simulate 3D Darcy flow and heat transport in the complex heterogeneous poroperm flow structures that pervade crustal rock.

A global mesh can represent both large- and small-scale stochastic spatial fluctuations in ambient crustal flow structure given by empirics (5)–(7). MWX tight gas sand well-log and well-core data validate these stochastic representations via three physical parameters:

- (i) Well-log fluctuation power-law spectral scaling exponent, $\beta \sim 1$, observed across the cm-km range of scale lengths
- (ii) Well-core and well-log porosity $0.1 < \varphi < 0.3$ typical of clastic sedimentary rock, and $0.3 < \varphi < 0.5$, observed for wellbore fracture-site intervals
- (iii) Well-core poroconnectivity parameter $\alpha \sim 24$ typical of ambient sedimentary rock, and $\alpha \sim 60$ elevated for model localized fault structures in clastic formations.

Our approach to flow and transport simulation in spatially correlated crustal poroperm media contrasts with conventional spatial averaging approaches such as effective-media (e.g., [4–8]) and/or fluid flow primarily conducted by (assumed) laminar flow planar fractures (e.g., [43–48]). Conceptually and numerically, the emphasis lies with flow heterogeneity due to long-range spatial correlations rather than flow involving numerical meshes representing flow between more or less uniform poroperm blocks. As illustrated in Figure 1, a single global 3D mesh allows a complete range of flow-physical properties by assigning numerical values to mesh nodes representing flow structures embedded long-range spatially correlated poroperm distributions. Embedded poroperm structures with higher porosities and higher poroconnectivity represent fluid flow and heat transport via macroscopic crustal fault structures. The global mesh numerical mesh solver used here is Sutra [49]. Comparable results for steady-state 3D flow and transport are obtained with the Matlab Partial Differential Equation Toolbox [50].

Wellbore-specific crustal flow complexity naturally extends from the MWX crustal fluid flow to flow in low-porosity, low-permeability basement rock. Well-log, well-core, and well-production data validate crustal flow empirics (5)–(7) for basement rock porosities $\varphi \sim .01$ and associated poroconnectivity parameters $\alpha \sim 300$ –700 [16]. Application of data-driven modelling control can thus give a perspective on Enhanced/Engineered Geothermal System (EGS) flow stimulation in terms of wellbore-centric Peclet number $P_e \equiv a_0 \varphi v_0 / D$.

In MWX crustal rock of ambient mean porosity φ , fluid flow of Peclet number $P_e \sim 5$ into a wellbore for an observed fault interval $\ell \sim 5$ m produces wellbore fluid outtake

$V = 2\pi r_0 \varphi v_0 \ell = 2\pi P_e \ell D \sim 10^{-4} \text{ m}^3/\text{s} \sim 0.1 \text{ L/s}$ across each 5 m fracture interval. Each of the observed fracture intervals may be inferred to produce $\sim 10 \text{ m}^3$ of fluid per day. For an MWX 2 km wellbore of volume $\sim 60 \text{ m}^3$, the rate of fluid flow from one of the major observed MWX fractures displaces the wellbore fluid column in one week. At such low wellbore flow rates, the observable thermal effects of the wellbore disturbance of the ambient steady-state flow/thermal regimes are local to the wellbore-centric fault fluid flow.

Using wellbore temperatures to estimate the Peclet number of a natural heat advection system helps to calibrate EGS wellbore flow stimulation. Extrapolating the natural fracture-borne fluid flow associated with $P_e \sim 5$ from a 5 m interval to 1 km wellbore intervals, the total fluid production by the wellbore is 2 liters per second. An EGS stimulation producing 2 liters/second is roughly equivalent to achieving crustal stimulations of 200 MWX crustal fractures of 5 m thickness and 20-meter radius for each km of EGS production wellbore.

For EGS stimulation of basement rock, the physical properties to be varied are porosity φ and poroconnectivity parameter α . Porosity is shifted from $\varphi \sim 10\%$ for clastic reservoir rock to $\varphi \sim 1\%$ for basement rock, and poroconnectivity parameter $\alpha \sim 24$ for clastic reservoir rock is shifted to $\alpha \sim 300$ for basement rock [16]. Fundamental crustal flow empirics (5)–(7) suggest that crustal flow stimulation naturally proceeds via increased poroconnectivity parameter α rather than increased porosity φ . Noting that increased flow via increased α requires far less work against confining stresses than does increased flow via increased φ , as characteristic of past EGS efforts [43–48], presents a clear implication for future EGS stimulation efforts.

Conflicts of Interest

The authors declare that there are no conflicts of interest regarding the publication of this paper.

Acknowledgments

The research presented in this paper wholly was funded by Stl Deep Heat Ltd, Purotie 1, 00381 Helsinki, Finland.

References

- [1] H. Darcy, *Les Fontaines publiques de la ville de Dijon*, Victor Dalmont, Paris, France, 1856.
- [2] J. Dupuit, *Etudes Theoriques et Pratiques sur le Mouvement des Eaux dans les Canaux Decouverts et a Travers les Terrains Permeables*, Dunod, Paris, France, 2nd edition, 1863.
- [3] G. O. Brown, “Henry Darcy and the making of a law,” *Water Resources Research*, vol. 38, no. 7, pp. 1–12, 2002.
- [4] M. Muskat, *The Flow of Homogeneous Fluids through Porous Media*, McGraw-Hill, 1937.
- [5] M. A. Biot, “General theory of three-dimensional consolidation,” *Journal of Applied Physics*, vol. 12, no. 2, pp. 155–164, 1941.
- [6] D. R. Horner, “Pressure build-up in wells,” in *Third World Petroleum Congress*, pp. 503–523, The Hague, 1951.

- [7] M. K. Hubbert, "Darcy's law and the field equations of the flow of underground fluids," *International Association of Scientific Hydrology. Bulletin*, vol. 2, no. 1, pp. 23–59, 1957.
- [8] J. Bear, *Dynamics of Fluids in Porous Media*, American Elsevier, New York, NY, USA, 1972.
- [9] P. C. Leary, "Special section-assessment of schemes for earthquake prediction: Rock as a critical-point system and the inherent implausibility of reliable earthquake prediction," *Geophysical Journal International*, vol. 131, no. 3, pp. 451–466, 1997.
- [10] P. C. Leary, "Fractures and physical heterogeneity in crustal rock," in *Heterogeneity in the Crust and Upper Mantle: Nature, Scaling, and Seismic Properties*, J. A. Goff and K. Holliger, Eds., pp. 155–186, Kluwer Academic/Plenum Publishers, New York, NY, USA, 2002.
- [11] P. C. Leary and F. Al-Kindy, "Power-law scaling of spatially correlated porosity and log(permeability) sequences from North-Central North Sea Brae oilfield well core," *Geophysical Journal International*, vol. 148, no. 3, pp. 426–442, 2002.
- [12] P. C. Leary and L. A. Walter, "Crosswell seismic applications to highly heterogeneous tight gas reservoirs," *First Break*, vol. 26, no. 3, pp. 49–55, 2008.
- [13] Leary P. C., P. E. Malin, and J. A. Pogacnik, "Computational EGS – heat transport in 1/F-noise fractured media," in *Proceedings of the 37th Workshop on Geothermal Reservoir Engineering*, Stanford University, 30 January–1 February, 2012.
- [14] P. Malin, P. Leary, E. Shalev et al., "Flow Lognormality and Spatial Correlation in Crustal Reservoirs: II – Where-to-Drill Guidance via Acoustic/Seismic Imaging," in *Proceedings of the World Geothermal Congress 2015 (WGC '15)*, Melbourne, Victoria, Australia, 19–24 April 2015.
- [15] J. Pogacnik, P. Leary, P. Malin, P. Geiser, R. Rugis, and B. Valles, "Flow Lognormality and Spatial Correlation in Crustal Reservoirs: III – Natural Permeability Enhancement via Biot Fluid-Rock Coupling at All Scales," in *Proceedings of the World Geothermal Congress 2015 (WGC '15)*, Melbourne, Victoria, Australia, 19–24 April 2015.
- [16] P. Leary, P. Malin, and R. Niemi, "Finite Element Modelling of Wellbore-Observed Fracture-Borne Heat Advection – Application to EGS Stimulation in Basement Rock," in *Proceedings of the 42nd Workshop on Geothermal Reservoir Engineering*, Stanford University, 13–15 February 2017.
- [17] S. Ingebritsen, W. Sanford, and C. Neuzil, *Groundwater in Geological Processes*, Cambridge University Press, 2006.
- [18] G. Mavko, T. Mukerji, and J. Dvorkin, *The Rock Physics Handbook*, Cambridge University Press, 2009.
- [19] D. A. Sprott, "Gauss's contributions to statistics," *Historia Mathematica*, vol. 5, no. 2, pp. 183–203, 1978.
- [20] H. M. Walker, "De Moivre on the law of normal probability," in *A Source Book in Mathematics*, D. E. Smith, Ed., p. 78, Dover, 1985.
- [21] S. M. Stigler, "Gauss and the invention of least squares," *The Annals of Statistics*, vol. 9, no. 3, pp. 465–474, 1981.
- [22] J. C. Maxwell, "Illustrations of the dynamical theory of gases," in *Kinetic Theory: Selected Readings in Physics*, S. G. Brush, Ed., vol. 2, pp. 148–171, Pergamon Press, 1965.
- [23] R. Bracewell, *The Fourier Transform and Its Applications*, McGraw Hill, 2000.
- [24] M. Abramowitz and I. Stegun, *Handbook of Mathematical Functions*, vol. 55 of *National Bureau of Standards Applied Mathematics Series*, 1972.
- [25] US Energy Information Administration, "Distribution and production of oil and gas wells by state," 2011, <https://www.eia.gov/naturalgas/archive/petrosystem/petrosysog.html>.
- [26] IEA, "Special Report: Golden Rules for Golden Age of Gas, International Energy Agency," 2012, http://www.iea.org/publications/freepublications/publication/WEO2012_Golden-RulesReport.pdf.
- [27] IFC, *Success of Geothermal Wells: A Global Study*, International Finance Corporation, Wash, USA, 2013.
- [28] G. Gustafson, "Strategies for groundwater prospecting in hard rocks: a probabilistic approach," *Norges geologiske undersøkelse Bulletin*, vol. 439, pp. 21–25, 2002.
- [29] D. Banks, P. Gundersen, G. Gustafson, J. Mäkelä, and G. Morland, "Regional similarities in the distributions of well yield from crystalline rocks in Fennoscandia," *Norges geologiske undersøkelse Bulletin*, vol. 450, pp. 33–47, 2010.
- [30] H. J. de Wijs, "Statistics of ore distribution. Part I: frequency distribution of assay values," *Journal of the Royal Netherlands Geological and Mining Society*, vol. 13, pp. 365–375, 1951.
- [31] H. J. de Wijs, "Statistics of ore distribution Part II: theory of binomial distribution applied to sampling and engineering problems," *Journal of the Royal Netherlands Geological and Mining Society*, vol. 15, pp. 124–125, 1953.
- [32] D. G. Krige, *Lognormal-de Wijsian Geostatistics for Ore Evaluation*, South African Institute of Mining and Metallurgy, Johannesburg, South African, 1981.
- [33] B. B. Mandelbrot, *The Fractal Geometry of Nature*, WH Freeman and Co., 1983.
- [34] J. J. Binney, N. J. Dowrick, A. J. Fisher, and M. E. J. Newman, *The Theory of Critical Phenomena: An Introduction to the Renormalization Group*, Oxford University Press, 1995.
- [35] D. Stauffer and A. Aharony, *Introduction to Percolation Theory*, CRC Press, Taylor & Francis, 1994.
- [36] Y. Hamiel, O. Katz, V. Lyakhovsky, Z. Reches, and Y. Fialko, "Stable and unstable damage evolution in rocks with implications to fracturing of granite," *Geophysical Journal International*, vol. 167, no. 2, pp. 1005–1016, 2006.
- [37] T. J. Craig, E. Calais, L. Fleitout, L. Bollinger, and O. Scotti, "Evidence for the release of long-term tectonic strain stored in continental interiors through intraplate earthquakes," *Geophysical Research Letters*, vol. 43, no. 13, pp. 6826–6836, 2016.
- [38] B. C. Trent and L. G. Margolin, "A numerical laboratory for granular solids," *Engineering Computations*, vol. 9, no. 2, pp. 191–197, 1992.
- [39] H. Yin and J. Dvorkin, "Strength of cemented grains," *Geophysical Research Letters*, vol. 21, no. 10, pp. 903–906, 1994.
- [40] J. Dvorkin, A. Nur, and H. Yin, "Effective properties of cemented granular materials," *Mechanics of Materials*, vol. 18, no. 4, pp. 351–366, 1994.
- [41] J. C. Lorenz, "MWX - The Multiwell Experiment in the Piceance Basin, Colorado: Reprise from 30 Years Ago," *AAPG Search and Discovery*, Article ID 70129, 2012.
- [42] H. S. Carslaw and J. C. Jaeger, *Conduction of Heat in Solids*, Clarendon Press, Oxford, UK, 1959.
- [43] J. E. Warren and P. J. Root, "The Behavior of Naturally Fractured Reservoirs," *Society of Petroleum Engineers Journal*, pp. 245–255, 1963.
- [44] A. C. Gringarten, P. A. Witherspoon, and Y. Ohnishi, "Theory of heat extraction from fractured hot dry rock," *Journal Geophysical Research*, vol. 80, pp. 1120–1124, 1975.

- [45] M. C. Cacas, E. Ledoux, G. de Marsily et al., "Modeling fracture flow with a stochastic discrete fracture network: Calibration and validation: 2. The transport model," *Water Resources Research*, vol. 26, no. 3, pp. 491–500, 1990.
- [46] J. W. Tester, B. J. Anderson, A. S. Batchelor et al., *The Future of Geothermal Energy: Impact of Enhanced Geothermal Systems (EGS) on the United States in the 21st Century*, Massachusetts Institute of Technology, 2006.
- [47] K. Pruess, C. Oldenburg, and G. Moridis, "TOUGH2 User's Guide, Version 2.1," Tech. Rep. LBNL-43134, Lawrence Berkeley National Laboratory, 2012.
- [48] D. Sutter, D. B. Fox, B. J. Anderson, D. L. Koch, P. R. von Rohr, and J. W. Tester, "Sustainable heat farming of geothermal systems: a case study of heat extraction and thermal recovery in a model EGS fractured reservoir," in *Proceedings of the 36th Workshop on Geothermal Reservoir Engineering*, Stanford University, 31 January–2 February 2011.
- [49] C. I. Voss and A. M. Provost, "Sutra - A model for saturated-unsaturated, variable-density ground-water flow with solute or energy transport," Tech. Rep. 02-4231, USGS Water-Resources Investigations, 2010.
- [50] Matlab, *Partial Differential Equation Toolbox User's Guide*, The MathWorks Inc., Natick, Mass, USA, 2015.

Research Article

Gas-Water Flow Behavior in Water-Bearing Tight Gas Reservoirs

Renyi Cao,¹ Liyou Ye,² Qihong Lei,³ Xinhua Chen,¹ Y. Zee Ma,⁴ and Xiao Huang¹

¹School of Petroleum Engineering, China University of Petroleum, Beijing 102249, China

²Department of Porous Flow & Fluid Mechanics, PetroChina RIPED, Langfang 065007, China

³Research Institute of Exploration and Development, Changqing Oil Field, PetroChina, Shaanxi 710021, China

⁴Schlumberger, Denver, CO 80202, USA

Correspondence should be addressed to Renyi Cao; caorenyi@126.com

Received 6 March 2017; Accepted 31 July 2017; Published 27 September 2017

Academic Editor: Shuyu Sun

Copyright © 2017 Renyi Cao et al. This is an open access article distributed under the Creative Commons Attribution License, which permits unrestricted use, distribution, and reproduction in any medium, provided the original work is properly cited.

Some tight sandstone gas reservoirs contain mobile water, and the mobile water generally has a significant impact on the gas flowing in tight pores. The flow behavior of gas and water in tight pores is different than in conventional formations, yet there is a lack of adequate models to predict the gas production and describe the gas-water flow behaviors in water-bearing tight gas reservoirs. Based on the experimental results, this paper presents mathematical models to describe flow behaviors of gas and water in tight gas formations; the threshold pressure gradient, stress sensitivity, and relative permeability are all considered in our models. A numerical simulator using these models has been developed to improve the flow simulation accuracy for water-bearing tight gas reservoirs. The results show that the effect of stress sensitivity becomes larger as water saturation increases, leading to a fast decline of gas production; in addition, the nonlinear flow of gas phase is aggravated with the increase of water saturation and the decrease of permeability. The gas recovery decreases when the threshold pressure gradient (TPG) and stress sensitivity are taken into account. Therefore, a reasonable drawdown pressure should be set to minimize the damage of nonlinear factors to gas recovery.

1. Introduction

Water-bearing tight gas reservoirs, as part of unconventional reservoirs, attract more and more attention. In comparison with non-water-bearing tight gas reservoirs, the gas recovery of water-bearing tight gas reservoirs is generally lower, and three factors strongly influence the development of water-bearing gas reservoirs and flow behavior. The first influencing factor is the threshold pressure gradient (TPG) due to mobile water and small pore-throat, which needs to be overcome for initiating flow. The second influencing factor is the stress sensitivity of the permeability, which is common for tight gas reservoirs but intensified by water existence. The third influencing factor is the gas-water relative permeability, which is impacted by the variation of drawdown pressure. These three factors may act together and affect the gas flow and production of tight gas reservoirs. Accurate description and reasonable characterization of nonlinear features of gas flow are the foundation for predicting gas production.

The theories and models regarding the effect of TPG on water-oil two-phase flow have been proposed [1–6], and experiments were conducted to study the pseudo-TPG and analyze the reason for which the pseudo-TPG has to be overcome for flow in ultra-low permeability tight reservoirs [3, 7, 8]. However, less attention has been paid to the effect of water saturation on TPG of gas phase, especially for water-bearing tight gas reservoirs. Water saturation influences the gas flow by changing the gas slip factor. The gas slip factor will decrease with the increase of water saturation [9]. Ding et al. [10] conducted experimental studies about the dynamic threshold pressure in a water-bearing tight gas reservoir and found that TPG varied with the change of pore pressure and water saturation. Cores with a higher water saturation had a higher TPG than cores with a lower water saturation, and the TPG showed higher-amplitude change as well (TPG sensitivity coefficient is bigger). The question is, how will permeability and water saturation simultaneously affect the TPG of water-bearing tight gas reservoirs?

Stress sensitivity of formation has been quite extensively studied. In one of the earliest studies of permeability sensitivity to the stress, Fatt and Davis [11] found that the magnitude of the formation permeability reduction ranged from 11% to 41%. Confining pressure acting on the rock core has a very important impact on the magnitude of permeability. Thomas and Ward [12] found that gas permeability of tight sandstone formations would be markedly reduced with increasing overburden pressure. Permeability reduction of cores due to stress in other formations was also studied by other authors [13–15]. A comprehensive study on micro-pore-throat structure and pore-throat distribution of tight reservoir rock using SEM and constant-rate mercury injection technology was also reported (Yu et al. [16]). Quantitatively, Jones and Owens [17] proposed a coefficient to describe permeability stress sensitivity as follows:

$$s_J = \frac{\left\{1 - \left[K_g(\sigma_{\text{eff}})/K_g(\sigma_{\text{eff}} = 6.89)\right]^{1/3}\right\}}{\lg(\sigma_{\text{eff}}/6.89)}. \quad (1)$$

Luo et al. [18] conducted experiments using gas to analyze stress sensitivity. The Klinkenberg permeability of cores used in the experiments ranges from 0.1 mD to 3 mD. Based on the experiments, they derived the following equation (or coefficient) to characterize the stress sensitivity:

$$s_L = \frac{-\lg(K_{g\text{min}}/K_{g\text{0}})}{\lg(\sigma_{\text{eff max}}/\sigma_{\text{eff 0}})}. \quad (2)$$

These studies all imply that rock permeability reduction due to the increase of effective stress could significantly affect oil well productivity, especially for tight formations. However, there is still little research on the stress sensitivity of water-bearing tight gas reservoir. Water is the wetting phase for most formations. There is a water film attached on the inner surface of pores. Though the water film is thin, it has a significant impact on the flow (normally in micro- or nanometer scale) of tight gas reservoirs. The thickness of the water film is a function of pore pressure, and thus it is stress sensitivity. Once the stress changes, the flow channel will vary due to the changing boundary layer. Correspondingly, the flow capacity of formation will make a difference. Yet, whether the magnitude of water saturation will affect the stress sensitivity remains unknown.

Relative permeability plays an essential role for reservoir simulation and production prediction. A number of studies have been published on the relative permeability of different types of formations. Burdine [19] investigated the relative permeability using pore size distribution data. Corey [20] presented a method of calculating relative permeability with exponential coefficients based on the empirical understanding. Fatt [21] simulated the overburden pressure and investigated gas-oil relative permeability under different overburden pressures. Al-Quraishi and Khairy [22] investigated the effect of pore pressure variation on the oil-water relative permeability curves at fixed overburden pressures and the effect of confining pressure on the relative permeability curves at constant pore pressure. However, reports on the effect

of the drawdown pressure on the relative permeability are less common. According to Gao et al. [23], the drawdown pressure gradient significantly affects the gas-water relative permeability, and the relative permeability curve moves to the right as the drawdown pressure gradient increases; however, the mechanism of the relationship between the drawdown pressure gradient and the gas-water relative permeability was not discussed in that article. Mo et al. [24] investigated the effect of the drawdown pressure on the relative permeability of tight gas reservoirs and showed that the displacement pressure had a significant effect on the relative permeability.

Three factors strongly influence the development of the water-bearing gas reservoir and flow behavior. The first factor is the TPG due to mobile water and small pore-throats, which needs to be overcome for initiating flow. The second factor is the stress sensitivity of the gas permeability, which is common for a tight gas reservoir but intensified by presence of water. The third factor is the gas-water relative permeability, which changes with variation of drawdown pressure. These three factors work simultaneously and affect the gas flow and production of tight gas reservoirs. Accurate description and characterization of nonlinearity of gas flow are fundamental for predicting gas production.

This article analyzes these three influencing factors of gas recovery and flow behavior of water-bearing gas reservoirs and then presents a gas-water two-phase flow model for tight gas reservoirs while quantifying and analyzing the effect of each nonlinear factor on gas well productivity and recovery. Finally, measurements for enhanced gas recovery of water-bearing tight gas reservoirs are made. This model provides theoretical basis for the development of tight gas reservoir.

2. Flow Behavior and Formation Properties of Water-Bearing Tight Gas Reservoirs

Experimentations of flow behavior and formation properties in tight gas reservoir bearing water [25–27] have shown that water influences stress sensitivity of tight reservoirs and increases threshold pressure gradient. In addition, the capacity of gas-water two-phase percolation is significantly different under different displacement pressure gradient.

2.1. Method of Experiment. We carried out the core displacement experiments by a series of the radius of 2.5-centimeter and the length of 5-centimeter natural cores. And experimental apparatus and experimental process are the same as the conventional core displacement experiments, and the main experiment equipment is core holding unit, circulating pump, pressure sensor, and so forth. Experimental steps include core evacuation, saturated water, saturated gas, and displacement.

We studied the threshold pressure gradient under different water saturation by taking the core saturation to different initial water saturation and then carrying out the displacement experiments and measured the stress sensitivity coefficient under different water saturation to study the relationship between stress sensitivity coefficient and water saturation and permeability; and a series of relative permeability

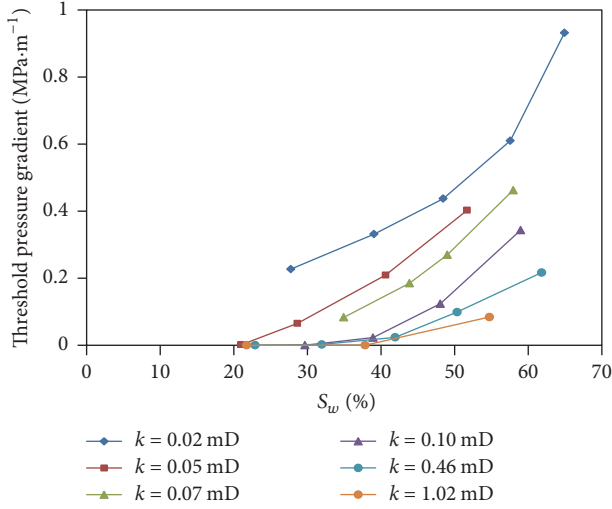


FIGURE 1: The relationship between water saturation (S_w) and threshold pressure gradient for different permeabilities.

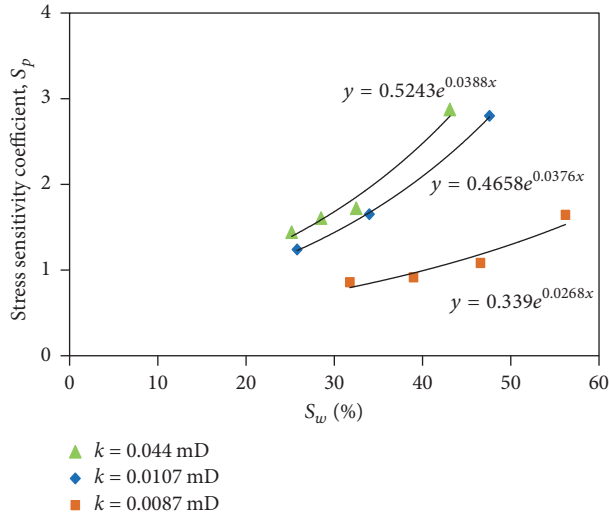


FIGURE 2: Relationship between water saturation (S_w) and stress sensitivity coefficient.

curves were conducted under different displacement pressure gradient to study the relationship between displacement pressure and relative permeability. For the details and results of experiments, one could refer to the papers by Ye [25, 27], and parts of results were redrawn in Figures 1–3.

2.2. Effect of Threshold Pressure Gradient. For a gas reservoir without mobile water, the gas is continuous phase and gas viscosity is very low, and there is no TPG for single gas phase flowing in tight formations. When the water saturation is higher than irreducible water saturation, the mobile water could impact the gas flow. This is because the water exists in the surface of rock at small throat due to water wettability in tight formation and the gas distributes in pores, and this phenomenon results in mutual interaction between water phase and gas phase. For the water-gas two phases in tight

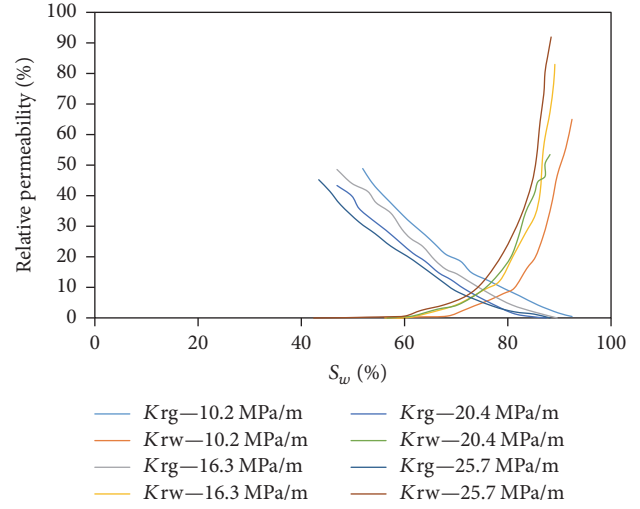


FIGURE 3: Gas-water relative permeability under different draw-down pressure gradient.

formations, if the gas phase starts flowing, the gas should break the block of water phase in throat and drive the water phase starting to flow, and this process should overcome some extra pressure gradient. As such, the block of water to gas results in TPG, and the motion equation with TPG could be described as follows:

$$v = -\frac{K}{\mu} [\nabla p - \lambda]. \quad (3)$$

The experiments show that the TPG of gas-water two-phase flow is correlated to water saturation and permeability (Figure 1 and [27]), and the TPG is the function of water saturation and permeability. The fitting equation to the experiment results indicate that when the irreducible water saturation is constant, the TPG and permeability have a power relationship:

$$\lambda = aK^{b(1-S_w)}e^{S_w}, \quad (4)$$

where a and b are fitting coefficients.

2.3. Effect of Stress Sensitivity. When gas flows as a single phase in a tight gas reservoir, stress significantly affects gas well productivity.

$$\frac{K}{K_i} = \left(\frac{\sigma}{\sigma_i}\right)^{-S_p} = \left(\frac{p_c - p}{p_c - p_i}\right)^{-S_p}, \quad (5)$$

where S_p is the factor of stress sensitivity, such as $S_p = cK^{-n}$. This formula is widely used to study effect of stress sensitivity and can be applied to water-bearing gas reservoirs. However, the coefficients in this formula must be refitted when it is applied to various reservoirs.

However, when water is also present in a tight gas reservoir, water not only affects the gas flow, but also has an effect on the stress of the reservoir [28, 29]. Experimental results show that stress is intensified as water saturation

increases (Figure 2 and [27]). It is mainly because the presence of water reduces the flow path of gas. For tight gas reservoirs with larger original water saturation, the stress variation during production will result in a redistribution of water film and thus affects gas permeability, intensifies stress sensitivity, and thus aggravates stress damage. In addition, the physicochemical reactions between water and minerals in tight sandstones reduce the compressive strength of rock and further intensify stress sensitivity. Therefore, water presence will strengthen the stress of tight sandstones.

Stress sensitivity coefficient of water-bearing tight gas reservoirs is

$$S_p = cK^{-n} e^{d \cdot S_w}. \quad (6)$$

2.4. Relative Permeability of Gas-Water Flow. Understanding the relative permeability is important for the prediction of production performance of water-bearing tight gas reservoirs. Compared to the conventional gas reservoirs of low permeability, the relative permeability of gas-water flow in tight formations is more complex because of the extremely small pores and throats. The comparison of gas-water two-phase flow experiments under different pressures shows that displacement pressure gradient impacts the gas-water relative permeability. The experimental results (Figure 3) show that as displacement pressure increases [27], the relative permeability of water increases sharply, while the relative permeability of gas reduces, and the residual gas saturation reduces. Therefore, gas-water relative permeability and the endpoint of saturation are a function of both water saturation and pressure gradient, such as

$$\begin{aligned} K_g &= KK_{rg}(S_w, \nabla p) \\ K_w &= KK_{rw}(S_w, \nabla p) \\ S_{gr} &= S_{gr}(\nabla p). \end{aligned} \quad (7)$$

3. Model of Gas-Water Flow in Tight Formation

To simplify the gas-water two-phase flow modeling while honoring nonlinear flow behavior, the following assumptions are made in the model construction and percolation simulation:

- (1) The simulation process is gas-water two-phase flow with capillary force taken into account.
- (2) Gas and water are mutually immiscible and water phase is incompressible.
- (3) Stress effect to the formation porosity is neglected.
- (4) Fluid flow happens under constant temperature.
- (5) Gravity force is ignored.

3.1. Motion Equation. For gas-water two-phase flow in tight gas reservoirs, we take the separate single phase flow conforming to Darcy's law. As for the expression of pressure

gradient, TPG has to be deducted from the displacement pressure gradient.

$$\begin{aligned} \vec{v}_g &= -\frac{K(p)K_{rg}}{\mu_g} [\text{grad}(p_g) - \lambda] \\ \vec{v}_w &= -\frac{K(p)K_{rw}}{\mu_w} [\text{grad}(p_w) - \lambda], \end{aligned} \quad (8)$$

where TPG is expressed in (4).

3.2. Continuity Equation. In gas-water two-phase percolation, the continuity equations are as follows:

Gas phase:

$$\begin{aligned} -\left(\frac{\partial(\rho_g v_{gx})}{\partial x} + \frac{\partial(\rho_g v_{gy})}{\partial y} + \frac{\partial(\rho_g v_{gz})}{\partial z}\right) + q_g \\ = \frac{\partial(\phi \rho_g S_g)}{\partial t}. \end{aligned} \quad (9)$$

Water phase:

$$\begin{aligned} -\left(\frac{\partial(\rho_w v_{wx})}{\partial x} + \frac{\partial(\rho_w v_{wy})}{\partial y} + \frac{\partial(\rho_w v_{wz})}{\partial z}\right) + q_w \\ = \frac{\partial(\phi \rho_w S_w)}{\partial t}. \end{aligned} \quad (10)$$

3.3. Permeability and Stress Relationship

$$K(p) = K_i \left(\frac{p_c - p}{p_c - p_i} \right)^{-S_p}, \quad (11)$$

where stress sensitivity coefficient is $S_p = cK^{-n} e^{d \cdot S_w}$.

3.4. Model of Relative Permeability of Gas and Water. The relative permeability model could be obtained by interpolating the relative permeability under low (Figure 4(a)) and high (Figure 4(b)) pressure. The relative permeability model is shown in the following equations:

$$\begin{aligned} S_{wD} &= \frac{S_w - S_{wc}}{1 - S_{wc} - (1 - S_{gr})} \\ K_{rw} &= f \times S_{wD}^n \\ K_{rg} &= g \times (1 - S_{wD})^m \\ S_{gr} &= S_{grh} + \frac{S_{grl} - S_{grh}}{\Delta p_h - \Delta p_l} (\Delta p_h - \Delta p_l), \end{aligned} \quad (12)$$

where S_{wD} is the dimensionless water saturation; f, g, m, n are the fitting coefficients; Δp_h is the high displacement pressure gradient; Δp_l is the low displacement pressure gradient; S_{grl} is the residual gas saturation corresponding to Δp_l ; S_{grh} is the residual gas saturation corresponding to Δp_h .

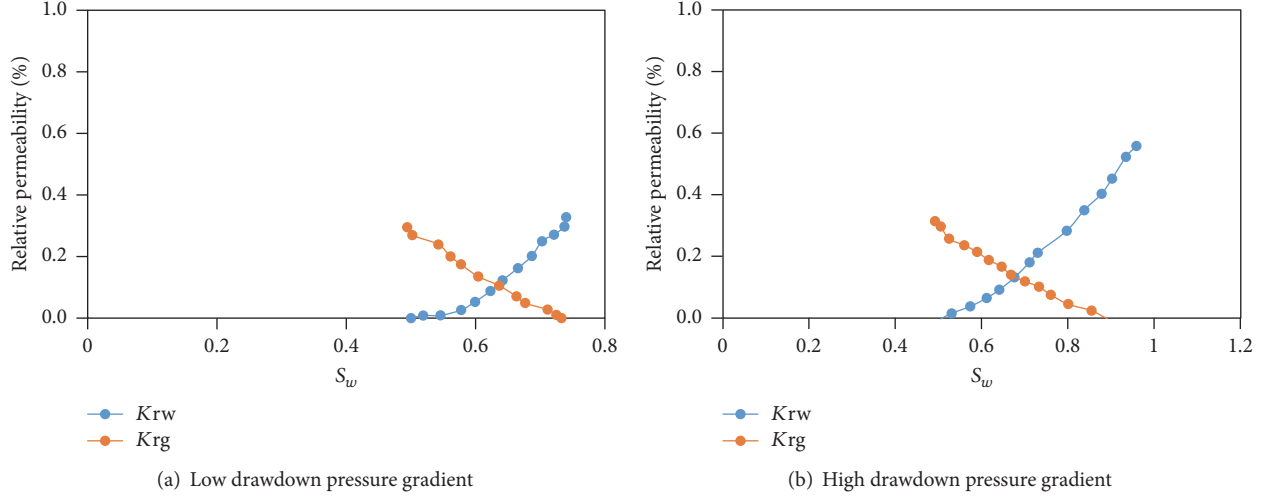


FIGURE 4: Gas-water relative permeability under different drawdown pressure gradient.

3.5. *Fundamental Differential Equation.* From all the aforementioned equations together, we can get the fundamental differential equation as follows:

For water phase,

$$\begin{aligned} \nabla \cdot \left[\frac{K(p)K_{rw}}{B_w \mu_w} (\nabla p_g - \nabla p_{cgw} - \lambda_w) \right] + \frac{q_w}{\rho_{wsc}} \\ = \frac{\partial}{\partial t} \left(\frac{\phi S_w}{B_w} \right). \end{aligned} \quad (13)$$

For gas phase,

$$\nabla \cdot \left[\frac{K(p)K_{rg}}{B_g \mu_g} (\nabla p_g - \lambda_g) \right] + \frac{q_g}{\rho_{gsc}} = \frac{\partial}{\partial t} \left(\frac{\phi S_g}{B_g} \right). \quad (14)$$

Multiply the right term of (13) and (14), $(\partial/\partial t)(\phi S_w/B_w)$ and $(\partial/\partial t)(\phi S_g/B_g)$, with B_w and B_g , respectively, and then combine them together as follows:

$$\begin{aligned} B_g \frac{\partial}{\partial t} \left(\frac{\phi S_g}{B_g} \right) + B_w \frac{\partial}{\partial t} \left(\frac{\phi S_w}{B_w} \right) \\ = \phi \frac{\partial S_g}{\partial t} + S_g \frac{\partial \phi}{\partial p_g} \frac{\partial p_g}{\partial t} - \frac{\phi S_g}{B_g} \frac{\partial B_g}{\partial p_g} \frac{\partial p_g}{\partial t} - \phi \frac{\partial S_w}{\partial t} \\ + S_w \frac{\partial \phi}{\partial p_g} \frac{\partial p_g}{\partial t} - \frac{\phi S_w}{B_w} \frac{\partial B_w}{\partial p_g} \frac{\partial p_g}{\partial t} \\ = (S_w + S_g) \frac{\partial \phi}{\partial p_g} \frac{\partial p_g}{\partial t} - \phi S_w \frac{1}{B_w} \frac{\partial B_w}{\partial p_g} \frac{\partial p_g}{\partial t} \\ - \phi S_g \frac{1}{B_g} \frac{\partial B_g}{\partial p_g} \frac{\partial p_g}{\partial t} \end{aligned}$$

$$\begin{aligned} &= \frac{\partial \phi}{\partial p_g} \frac{\partial p_g}{\partial t} + \phi S_w \left(-\frac{1}{B_w} \frac{\partial B_w}{\partial p_g} \frac{\partial p_g}{\partial t} \right) \\ &- \phi S_g \frac{1}{B_g} \frac{\partial B_g}{\partial p_g} \frac{\partial p_g}{\partial t}. \end{aligned} \quad (15)$$

According to the definition of compressibility, the compressibility of water, gas, and rock can be written as follows:

$$\begin{aligned} C_w &= -\frac{1}{B_w} \frac{\partial B_w}{\partial p_g} \\ C_g &= -\frac{1}{B_g} \frac{\partial B_g}{\partial p_g} \\ C_r &= \frac{1}{\phi} \frac{\partial \phi}{\partial p} = \frac{1}{\phi} \frac{\partial \phi}{\partial p_g} \\ C_t &= C_r + C_g S_g + C_w S_w \end{aligned} \quad (16)$$

$$\frac{\partial \phi}{\partial p_g} \frac{\partial p_g}{\partial t} = \frac{\partial \phi}{\partial p} \frac{\partial p}{\partial t}.$$

Therefore, (15) can be rewritten as

$$\begin{aligned} \frac{\partial \phi}{\partial p_g} \frac{\partial p_g}{\partial t} + \phi S_w \left(-\frac{1}{B_w} \frac{\partial B_w}{\partial p_g} \frac{\partial p_g}{\partial t} \right) - \phi S_g \frac{1}{B_g} \frac{\partial B_g}{\partial p_g} \frac{\partial p_g}{\partial t} \\ = \phi \left[\frac{1}{\phi} \frac{\partial \phi}{\partial p_g} \frac{\partial p_g}{\partial t} + S_w \left(-\frac{1}{B_w} \frac{\partial B_w}{\partial p_g} \frac{\partial p_g}{\partial t} \right) \right. \\ \left. - \frac{S_g}{B_g} \frac{\partial B_g}{\partial p_g} \frac{\partial p_g}{\partial t} \right] = \phi \left[\frac{1}{\phi} \frac{\partial \phi}{\partial p_g} + S_w \left(-\frac{1}{B_w} \frac{\partial B_w}{\partial p_g} \right) \right. \end{aligned}$$

$$\begin{aligned}
& + S_g \left(-\frac{1}{B_g} \frac{\partial B_g}{\partial p_g} \right) \frac{\partial p_g}{\partial t} = \phi (C_r + C_w S_w \\
& + C_g S_g) \frac{\partial p_g}{\partial t} = \phi C_t \frac{\partial p_g}{\partial t}.
\end{aligned} \tag{17}$$

By combining the above equations, it yields the basic differential equation in the following form:

$$\begin{aligned}
& B_g \nabla \cdot \left(\frac{K(p) K_{rg}}{B_g \mu_g} \nabla p_g \right) - B_g \nabla \cdot \left(\frac{K(p) K_{rg}}{B_g \mu_g} \lambda_g \right) \\
& + B_g \frac{q_g}{\rho_{gsc}} + B_w \nabla \cdot \left(\frac{K(p) K_{rw}}{B_w \mu_w} \nabla p_g \right) - B_w \nabla \\
& \cdot \left(\frac{K(p) K_{rw}}{B_w \mu_w} \nabla p_{cgw} \right) - B_w \nabla \cdot \left(\frac{K(p) K_{rw}}{B_w \mu_w} \lambda_w \right) \\
& + B_w \frac{q_w}{\rho_{wsc}} = \phi C_t \frac{\partial p_g}{\partial t}.
\end{aligned} \tag{18}$$

4. Model Discretization and Solution

For the simplicity of model solution, pressure, p , is used to substitute the gas phase pressure p_g and M_i is introduced into the calculation:

$$M_i = \frac{K_{ri}}{\mu_i B_i}, \quad \text{where } i = g, w. \tag{19}$$

4.1. Pressure Term

$$\begin{aligned}
& V_{i,j,k} \nabla \cdot (K(p) M_g \nabla p) = \frac{\partial}{\partial x} \left[K(p) M_g \frac{\partial p}{\partial x} \right] \\
& + \frac{\partial}{\partial y} \left[K(p) M_g \frac{\partial p}{\partial y} \right] + \frac{\partial}{\partial z} \left[K(p) M_g \frac{\partial p}{\partial z} \right] \\
& = \Delta y_j \Delta z_k \left\{ [K(p) M_g]_{i+1/2} \frac{p_{i+1}^{n+1} - p_i^{n+1}}{\Delta x_{i+1/2}} \right. \\
& - [K(p) M_g]_{i-1/2} \frac{p_i^{n+1} - p_{i-1}^{n+1}}{\Delta x_{i-1/2}} \left. \right\} \\
& + \Delta x_i \Delta z_k \left\{ [K(p) M_g]_{j+1/2} \frac{p_{j+1}^{n+1} - p_j^{n+1}}{\Delta y_{j+1/2}} \right. \\
& - [K(p) M_g]_{j-1/2} \frac{p_j^{n+1} - p_{j-1}^{n+1}}{\Delta y_{j-1/2}} \left. \right\} \\
& + \Delta x_i \Delta y_j \left\{ [K(p) M_g]_{k+1/2} \frac{p_{k+1}^{n+1} - p_k^{n+1}}{\Delta z_{k+1/2}} \right. \\
& - [K(p) M_g]_{k-1/2} \frac{p_k^{n+1} - p_{k-1}^{n+1}}{\Delta z_{k-1/2}} \left. \right\}.
\end{aligned} \tag{20}$$

The complete subscript of (20) is expressed as follows:

$$\begin{aligned}
\Delta x_i &= \Delta x_{i,j,k} \\
[K(p) M_g]_{i+1/2} &= [K(p) M_g]_{i+1/2,j,k} \\
\frac{p_{i+1}^{n+1} - p_i^{n+1}}{\Delta x_{i+1/2}} &= \frac{p_{i+1,j,k}^{n+1} - p_{i,j,k}^{n+1}}{\Delta x_{i+1/2,j,k}} \\
V_{i,j,k} &= \Delta x_i \Delta y_j \Delta z_k.
\end{aligned} \tag{21}$$

The pressure term for water phase can also be discretized likewise.

$$\begin{aligned}
& V_{i,j,k} \nabla \cdot (K(p) M_w \nabla p) \\
& = \Delta y_j \Delta z_k \left\{ [K(p) M_w]_{i+1/2} \frac{p_{i+1}^{n+1} - p_i^{n+1}}{\Delta x_{i+1/2}} \right. \\
& - [K(p) M_w]_{i-1/2} \frac{p_i^{n+1} - p_{i-1}^{n+1}}{\Delta x_{i-1/2}} \left. \right\} \\
& + \Delta x_i \Delta z_k \left\{ [K(p) M_w]_{j+1/2} \frac{p_{j+1}^{n+1} - p_j^{n+1}}{\Delta y_{j+1/2}} \right. \\
& - [K(p) M_w]_{j-1/2} \frac{p_j^{n+1} - p_{j-1}^{n+1}}{\Delta y_{j-1/2}} \left. \right\} \\
& + \Delta x_i \Delta y_j \left\{ [K(p) M_w]_{k+1/2} \frac{p_{k+1}^{n+1} - p_k^{n+1}}{\Delta z_{k+1/2}} \right. \\
& - [K(p) M_w]_{k-1/2} \frac{p_k^{n+1} - p_{k-1}^{n+1}}{\Delta z_{k-1/2}} \left. \right\}.
\end{aligned} \tag{22}$$

The pressure term in percolation formulation can be written as

$$\begin{aligned}
& h_{i,j,k} p_{i,j,k-1}^{n+1} + a_{i,j,k} p_{i,j-1,k}^{n+1} + b_{i,j,k} p_{i-1,j,k}^{n+1} + c_{i,j,k} p_{i,j,k}^{n+1} \\
& + f_{i,j,k} p_{i+1,j,k}^{n+1} + e_{i,j,k} p_{i,j+1,k}^{n+1} + l_{i,j,k} p_{i,j,k+1}^{n+1},
\end{aligned} \tag{23}$$

where

$$\begin{aligned}
h_{i,j,k} &= \frac{\Delta x_i \Delta y_j}{\Delta z_{k-1/2}} \left\{ B_g [K(p) M_g]_{k-1/2} \right. \\
& \left. + B_w [K(p) M_w]_{k-1/2} \right\} \\
a_{i,j,k} &= \frac{\Delta x_i \Delta z_k}{\Delta y_{j-1/2}} \left\{ B_g [K(p) M_g]_{j-1/2} \right. \\
& \left. + B_w [K(p) M_w]_{j-1/2} \right\} \\
b_{i,j,k} &= \frac{\Delta y_j \Delta z_k}{\Delta x_{i-1/2}} \left\{ B_g [K(p) M_g]_{i-1/2} \right. \\
& \left. + B_w [K(p) M_w]_{i-1/2} \right\}
\end{aligned}$$

$$\begin{aligned}
f_{i,j,k} &= \frac{\Delta y_j \Delta z_k}{\Delta x_{i+1/2}} \left\{ B_g [K(p) M_g]_{i+1/2} \right. \\
&\quad \left. + B_w [K(p) M_w]_{i+1/2} \right\} \\
e_{i,j,k} &= \frac{\Delta x_i \Delta z_k}{\Delta y_{j+1/2}} \left\{ B_g [K(p) M_g]_{j+1/2} \right. \\
&\quad \left. + B_w [K(p) M_w]_{j+1/2} \right\} \\
l_{i,j,k} &= \frac{\Delta x_i \Delta y_j}{\Delta z_{k+1/2}} \left\{ B_g [K(p) M_g]_{k+1/2} \right. \\
&\quad \left. + B_w [K(p) M_w]_{k+1/2} \right\} \\
c_{i,j,k} &= -\left(b_{i,j,k} + f_{i,j,k} + a_{i,j,k} + e_{i,j,k} + h_{i,j,k} + l_{i,j,k} \right).
\end{aligned} \tag{24}$$

4.2. TPG Term. The TPG term for gas phase can be written as

$$\begin{aligned}
&-B_g \nabla \cdot \left(\frac{K(p) K_{rg} \lambda_g}{B_g \mu_g} \right) \cdot V_{i,j,k} \\
&= \bar{H}_{i,j,k} \frac{1}{2} (\lambda_{gz_{k-1}} \Delta z_{k-1} + \lambda_{gz_k} \Delta z_k) \\
&\quad + \bar{A}_{i,j,k} \frac{1}{2} (\lambda_{gy_{j-1}} \Delta z_{j-1} + \lambda_{gy_j} \Delta z_j) \\
&\quad + \bar{B}_{i,j,k} \frac{1}{2} (\lambda_{gxi-1} \Delta z_{i-1} + \lambda_{gxi} \Delta z_i) \\
&\quad + \bar{F}_{i,j,k} \frac{1}{2} (\lambda_{gxi+1} \Delta z_{i+1} + \lambda_{gxi} \Delta z_i) \\
&\quad + \bar{E}_{i,j,k} \frac{1}{2} (\lambda_{gy_{j+1}} \Delta z_{j+1} + \lambda_{gy_j} \Delta z_j) \\
&\quad + \bar{L}_{i,j,k} \frac{1}{2} (\lambda_{gz_{k+1}} \Delta z_{k+1} + \lambda_{gz_k} \Delta z_k),
\end{aligned} \tag{25}$$

where

$$\begin{aligned}
\bar{H}_{i,j,k} &= \frac{\Delta x_i \Delta y_j}{\Delta z_{k-1/2}} \left\{ B_g [K(p) M_g]_{k-1/2} \right\} \\
\bar{A}_{i,j,k} &= \frac{\Delta x_i \Delta z_k}{\Delta y_{j-1/2}} \left\{ B_g [K(p) M_g]_{j-1/2} \right\} \\
\bar{B}_{i,j,k} &= \frac{\Delta y_j \Delta z_k}{\Delta x_{i-1/2}} \left\{ B_g [K(p) M_g]_{i-1/2} \right\} \\
\bar{F}_{i,j,k} &= -\frac{\Delta y_j \Delta z_k}{\Delta x_{i+1/2}} \left\{ B_g [K(p) M_g]_{i+1/2} \right\} \\
\bar{E}_{i,j,k} &= -\frac{\Delta x_i \Delta z_k}{\Delta y_{j+1/2}} \left\{ B_g [K(p) M_g]_{j+1/2} \right\} \\
\bar{L}_{i,j,k} &= -\frac{\Delta x_i \Delta y_j}{\Delta z_{k+1/2}} \left\{ B_g [K(p) M_g]_{k+1/2} \right\}.
\end{aligned} \tag{26}$$

The TPG term for water phase can be discretized likewise.

4.3. Capillary Pressure Term. The capillary pressure term could be written as

$$\begin{aligned}
&-B_w \nabla \cdot \left(\frac{K(p) K_{rw}}{B_w \mu_w} \nabla p_{cgw} \right) \cdot V_{i,j,k} \\
&= \bar{h}_{i,j,k} P_{cgwi,j,k-1}^{n+1} + \bar{a}_{i,j,k} P_{cgwi,j-1,k}^{n+1} + \bar{b}_{i,j,k} P_{cgwi-1,j,k}^{n+1} \\
&\quad + \bar{c}_{i,j,k} P_{cgwi,j,k}^{n+1} + \bar{f}_{i,j,k} P_{cgwi+1,j,k}^{n+1} + \bar{e}_{i,j,k} P_{cgwi,j+1,k}^{n+1} \\
&\quad + \bar{l}_{i,j,k} P_{cgwi,j,k+1}^{n+1},
\end{aligned} \tag{27}$$

where

$$\begin{aligned}
\bar{h}_{i,j,k} &= -\frac{\Delta x_i \Delta y_j}{\Delta z_{k-1/2}} \left\{ B_w [K(p) M_w]_{k-1/2} \right\} \\
\bar{a}_{i,j,k} &= -\frac{\Delta x_i \Delta z_k}{\Delta y_{j-1/2}} \left\{ B_w [K(p) M_w]_{j-1/2} \right\} \\
\bar{b}_{i,j,k} &= -\frac{\Delta y_j \Delta z_k}{\Delta x_{i-1/2}} \left\{ B_w [K(p) M_w]_{i-1/2} \right\} \\
\bar{f}_{i,j,k} &= -\frac{\Delta y_j \Delta z_k}{\Delta x_{i+1/2}} \left\{ B_w [K(p) M_w]_{i+1/2} \right\} \\
\bar{e}_{i,j,k} &= -\frac{\Delta x_i \Delta z_k}{\Delta y_{j+1/2}} \left\{ B_w [K(p) M_w]_{j+1/2} \right\} \\
\bar{l}_{i,j,k} &= -\frac{\Delta x_i \Delta y_j}{\Delta z_{k+1/2}} \left\{ B_w [K(p) M_w]_{k+1/2} \right\} \\
\bar{c}_{i,j,k} &= -\left(\bar{b}_{i,j,k} + \bar{f}_{i,j,k} + \bar{a}_{i,j,k} + \bar{e}_{i,j,k} + \bar{h}_{i,j,k} + \bar{l}_{i,j,k} \right).
\end{aligned} \tag{28}$$

4.4. Cumulative Term. The forward-differentiation method is used to deal with the cumulative term.

$$\phi C_t \frac{\partial p}{\partial t} = \phi C_t \frac{P_{i,j,k}^{n+1} - P_{i,j,k}^n}{\Delta t}. \tag{29}$$

4.5. Differential Equation

$$\begin{aligned}
&h_{i,j,k} P_{i,j,k-1}^{n+1} + a_{i,j,k} P_{i,j-1,k}^{n+1} + b_{i,j,k} P_{i-1,j,k}^{n+1} \\
&\quad + \left(c_{i,j,k} - V_{i,j,k} \frac{\phi C_t}{\Delta t} \right) P_{i,j,k}^{n+1} + f_{i,j,k} P_{i+1,j,k}^{n+1} \\
&\quad + e_{i,j,k} P_{i,j+1,k}^{n+1} + l_{i,j,k} P_{i,j,k+1}^{n+1} \\
&= -\bar{h}_{i,j,k} P_{cgwi,j,k-1}^{n+1} - \bar{a}_{i,j,k} P_{cgwi,j-1,k}^{n+1} \\
&\quad - \bar{b}_{i,j,k} P_{cgwi-1,j,k}^{n+1} - \bar{c}_{i,j,k} P_{cgwi,j,k}^{n+1} - \bar{f}_{i,j,k} P_{cgwi+1,j,k}^{n+1} \\
&\quad - \bar{e}_{i,j,k} P_{cgwi,j+1,k}^{n+1} - \bar{l}_{i,j,k} P_{cgwi,j,k+1}^{n+1} \\
&\quad - \bar{H}_{i,j,k} \frac{1}{2} (\lambda_{gz_{k-1}} \Delta z_{k-1} + \lambda_{gz_k} \Delta z_k) \\
&\quad - \bar{A}_{i,j,k} \frac{1}{2} (\lambda_{gy_{j-1}} \Delta z_{j-1} + \lambda_{gy_j} \Delta z_j)
\end{aligned}$$

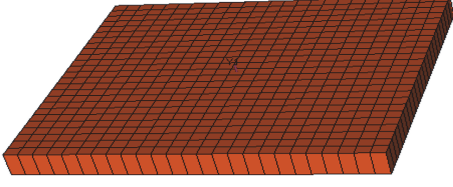


FIGURE 5: The schematic for the simulation model.

$$\begin{aligned}
& -\bar{B}_{i,j,k} \frac{1}{2} (\lambda_{gxi-1} \Delta z_{i-1} + \lambda_{gxi} \Delta z_i) \\
& -\bar{F}_{i,j,k} \frac{1}{2} (\lambda_{gxi+1} \Delta z_{i+1} + \lambda_{gxi} \Delta z_i) \\
& -\bar{E}_{i,j,k} \frac{1}{2} (\lambda_{gyj+1} \Delta z_{j+1} + \lambda_{gyj} \Delta z_j) \\
& -\bar{L}_{i,j,k} \frac{1}{2} (\lambda_{gzk+1} \Delta z_{k+1} + \lambda_{gzk} \Delta z_k) \\
& -\bar{H}'_{i,j,k} \frac{1}{2} (\lambda_{wzk-1} \Delta z_{k-1} + \lambda_{wzk} \Delta z_k) \\
& -\bar{A}'_{i,j,k} \frac{1}{2} (\lambda_{wyj-1} \Delta z_{j-1} + \lambda_{wyj} \Delta z_j) \\
& -\bar{B}'_{i,j,k} \frac{1}{2} (\lambda_{wxi-1} \Delta z_{i-1} + \lambda_{wxi} \Delta z_i) \\
& -\bar{F}'_{i,j,k} \frac{1}{2} (\lambda_{wxi+1} \Delta z_{i+1} + \lambda_{wxi} \Delta z_i) \\
& -\bar{E}'_{i,j,k} \frac{1}{2} (\lambda_{wyj+1} \Delta z_{j+1} + \lambda_{wyj} \Delta z_j) \\
& -\bar{L}'_{i,j,k} \frac{1}{2} (\lambda_{wzk+1} \Delta z_{k+1} + \lambda_{wzk} \Delta z_k) - V_{i,j,k} \\
& \cdot \left(B_g \frac{q_g}{\rho_{gsc}} + B_w \frac{q_w}{\rho_{wsc}} \right) - V_{i,j,k} \phi C_t \frac{P_{i,j,k}^n}{\Delta t}.
\end{aligned} \tag{30}$$

Equation (30) is the basic differential equation after discretization. The coefficient matrix of (30) is a seven-diagonal matrix with diagonal dominance. After the pressure of the gas phase is obtained through an implicit method, the pressure of the water phase can be obtained through capillary pressure explicitly. The relative permeability, threshold pressure gradient, and permeability under stress could be obtained through an explicit method.

5. Results and Discussion

5.1. Model Validation. A numerical model was built to simulate a homogeneous water-bearing tight gas reservoir of the Ordos Basin, located in Northwest China. The simulated vertical well is located at the center of the model, as shown in Figure 5. At the start of the simulation, we let the gas well produce at constant rate; when the bottom-hole pressure reaches a certain value, the production regime switches to constant bottom-hole pressure. Basic parameters

TABLE 1: Basic model parameters.

Reservoir area, m ²	202500
Reservoir depth, m	3300
Initial formation pressure, MPa	30.5
Porosity, %	8.5
Permeability, mD	0.1
Initial water saturation	0.40
Number of grid blocks	15 × 15 × 1
Step size of a block (DX, DY, DZ), m	30, 30, 10
Half-length of hydraulic fracture, m	100
Permeability of the hydraulic fracture, mD	50
Bottom hole pressure, MPa	5

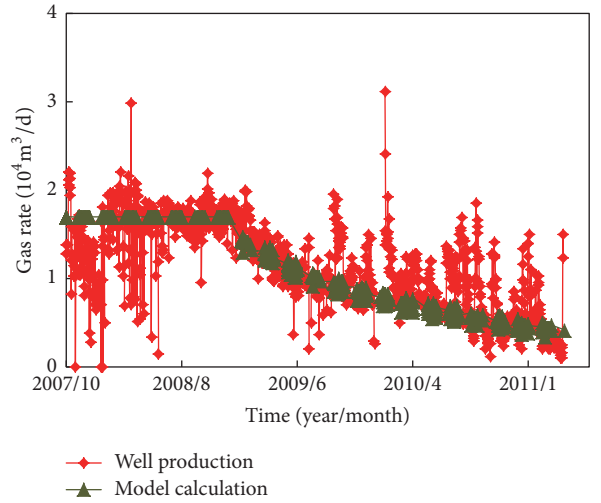


FIGURE 6: The comparison between well production and results of model calculation.

for the model calculation are listed in Table 1. The nonlinear percolation parameters in the Appendix are chosen according to the experiment results in Section 1.

The new numerical model is validated by comparing with the actual well performance. The results of comparison are shown in Figure 6. We can see from Figure 6 that the numerical model runs according to the setting regimes strictly. The model has a high accuracy at the period of constant bottom-hole pressure, although the initial production presents discrepancy with the actual gas rate, which can be explained by the actual varied production regimes. In general, there is a relatively high accuracy for the new numerical model.

5.2. The Effect of TPG. In order to analyze the influence of TPG to well productivity, the daily production rate and cumulative gas production are separately compared for the cases with and without considering TPG. The results of the simulation are shown in Figures 7 and 8. When neglecting the TPG, the gas production plateau can last 1201 days and the gas recovery during this stage is 54.39%. The ultimate gas recovery without TPG reaches 81.85%. While the TPG is taken into account, the period of stable production reduces to

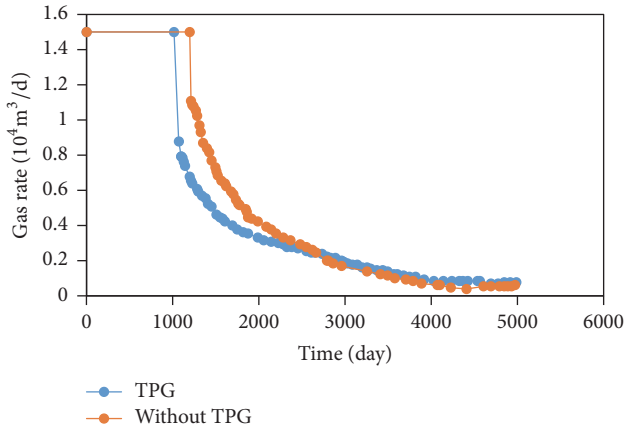


FIGURE 7: Effect of TPG on gas production.

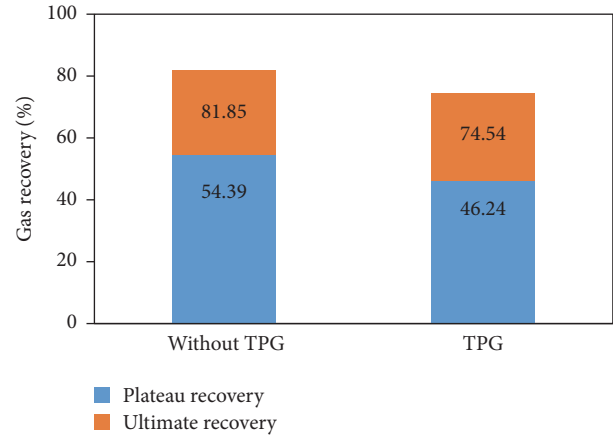


FIGURE 9: Gas recovery of different periods with or without TPG.

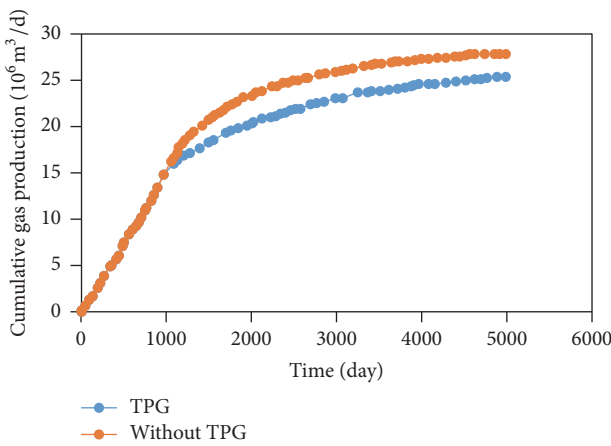


FIGURE 8: Effect of TPG on cumulative gas production.

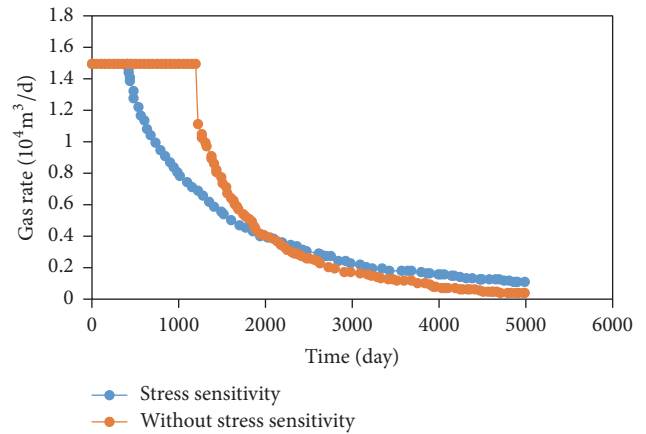


FIGURE 10: Effect of stress sensitivity on gas production.

1021 days and the gas recovery during this period decreases to 46.24%. The ultimate recovery with TPG is 74.54%, as shown in Figure 9. To sum up, when the TPG is included in the model, the production plateau will shrink and the gas recovery for both the stabilized production stage and the final recovery will decrease.

5.3. The Effect of Stress Sensitivity. The impact of stress sensitivity on gas productivity is simulated and the results are shown in Figures 10 and 11. When the stress sensitivity is considered, the production plateau reduces to 421 days and the gas recovery during this period is just 19.06%. The ultimate gas recovery of the simulation is 73.58%, as shown in Figure 12. Overall, the stabilized production stage reduces and the gas recovery decreases when the stress effect is considered.

5.4. The Joint Effect of TPG and Stress Sensitivity. When a gas well is put into production, both the TPG and stress sensitivity will have an effect on the gas productivity. The influence of the two factors to gas production is simulated and results are shown in Figures 13 and 14. It is seen that the production plateau reduces sharply from 1201 days to

61 days and the gas recovery during this period shrinks to 2.76%. The ultimate gas recovery is also severely affected and decreases to 55.49%, as shown in Figure 15. However, compared with gas recovery of the stabilized stage, the gas recovery of declining period is influenced by TPG and stress sensitivity relatively moderately. Therefore, TPG and stress sensitivity mainly infringe the duration and gas recovery of the stabilized period.

5.5. The Effect of Primary Water Saturation. Well performance under different primary water saturations varies tremendously. We analyze the impact of water presence to gas well by setting the water saturation from 40% to 55%. The initial daily gas rate is set to be $1.5 \times 10^4 \text{ m}^3/\text{d}$. The results are shown in Figures 16, 17, 18, and 19. It can be seen that, with the increase of the primary water saturation, the stabilized production period will be shortened, gas decline rate will slow down, and the gas recovery will decrease. In addition, the water rate will increase with the water saturation. In the case of the highest water saturation, the water rate accelerates fastest and reaches peak earliest. As for the gas-water ratio, when the water saturation is larger than 50%, the ratio will

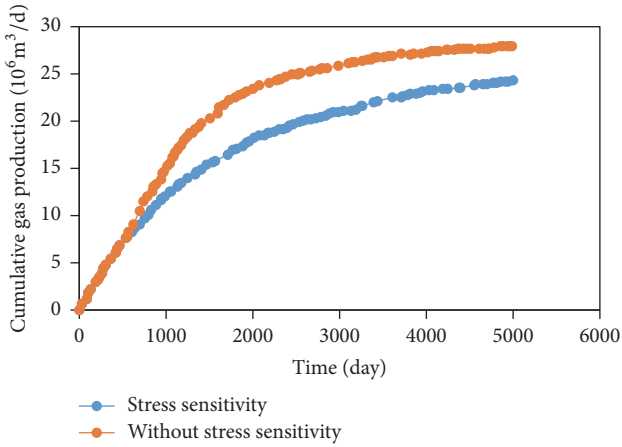


FIGURE 11: Effect of stress sensitivity on cumulative gas production.

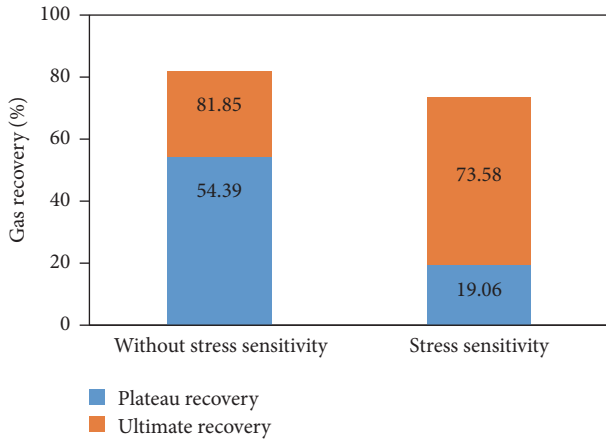


FIGURE 12: Gas recovery of different periods with or without stress sensitivity.

increase sharply as the production continues. Therefore, during the production process, reasonable drawdown pressure should be set to control the water transportation within formation so that the water accumulation could be avoided.

5.6. The Effect of Displacement Pressure Gradient. According to the pervious experiments, the pressure gradient will affect gas-water relative permeability. The pressure distribution of different production regimes has been simulated, as shown in Figure 20. As seen, the pressure gradient needed for gas flow is small and most of the simulated region contains pressure gradient less than 10.2 MPa/m. Only when the pressure gradient is greater than 10.2 MPa/m, the gas-water permeability will change. Therefore, the pressure gradient will have little effect on gas recovery through its influence on gas-water relative permeability.

6. Measurements for Enhanced Gas Recovery

From the above influential factor analysis, the gas productivity and recovery are greatly impacted by water saturation,

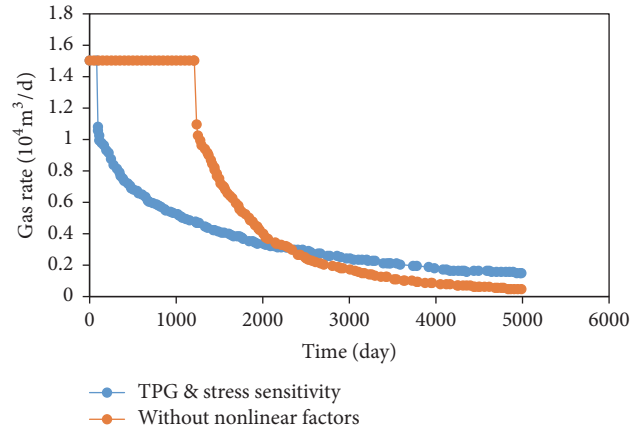


FIGURE 13: Effect of nonlinear factors on gas production.

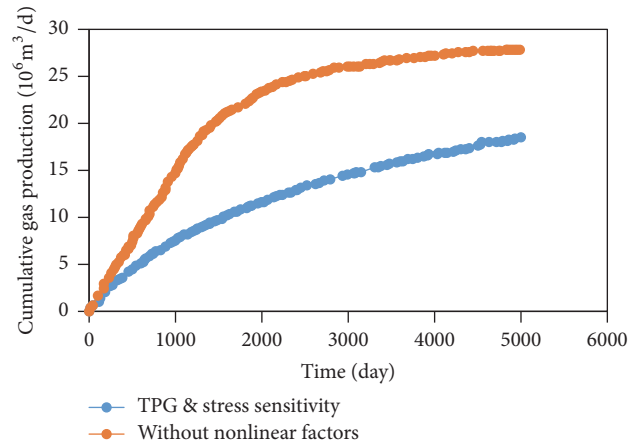


FIGURE 14: Effect of nonlinear factors on cumulative gas production.

TPG, and stress sensitivity. In order to obtain the optimal gas productivity, the development of water-bearing tight gas reservoirs should be optimized in several fronts, such as the well pattern, well location, and production regimes.

(1) Water should be avoided during the production process. Recognition of water saturation distribution is essential so that the high water saturation region should be detected and kept away.

(2) Due to the high stress sensitivity of tight gas reservoirs, the pressure drawdown near wellbore should be kept reasonable. In comparison with vertical wells, a fractured horizontal well could decrease the pressure drawdown efficiently and reduce the formation damage from stress.

(3) If the bottom-hole pressure is too low, the stress sensitivity near wellbore will be severe and the formation will be damaged. If the bottom-hole pressure is too high, the gas rate will be too small though the damage of stress could be prevented. Therefore, the drawdown pressure and gas rate need to be optimized so that the damage of stress could be minimized and gas recovery could be maximized.

Based on the parameters in Table 1, several cases with various gas rates have been simulated, and the results are shown in Table 2 and Figures 21–25. By increasing the gas rate,

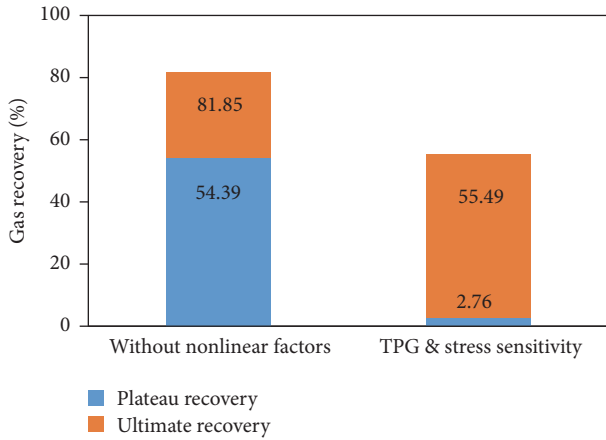


FIGURE 15: Gas recovery of different periods with or without TPG and stress sensitivity.

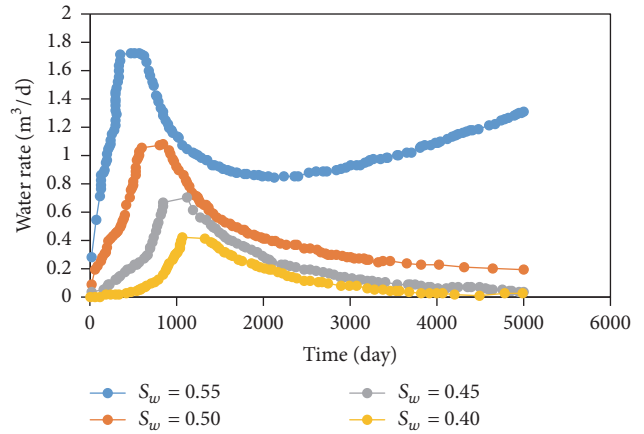


FIGURE 17: Effect of water saturation on water production.

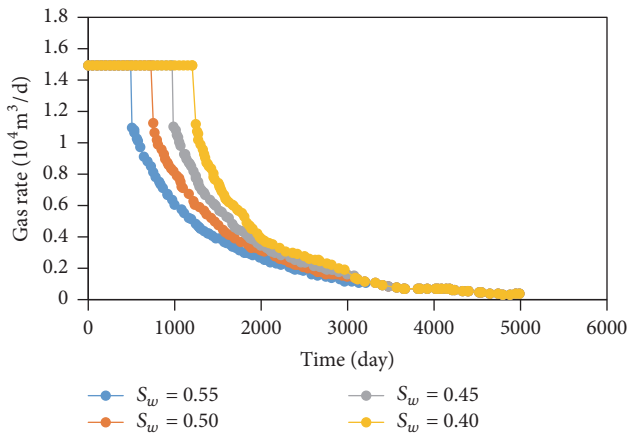


FIGURE 16: Effect of water saturation on gas production.

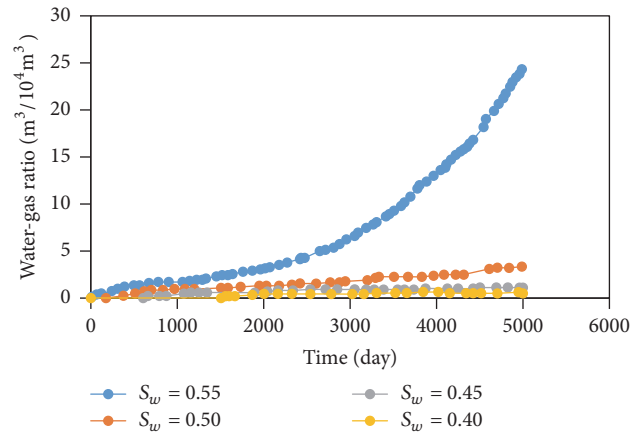


FIGURE 18: Effect of water saturation on gas-water ratio.

TABLE 2: Stabilized production period and gas recovery under different gas rates.

Gas rate ($10^4 \text{ m}^3/\text{d}$)	Stabilized production period (year)	Cumulative gas production (10^6 m^3)	Ultimate gas recovery (%)
1	5.7	27.18	82.06
1.5	3.3	27.11	81.85
2	2.2	27.06	81.71
3	1.2	26.95	81.37
4	0.7	26.55	80.15

the production plateau will be shortened sharply and the gas recovery will decrease as a result. If a stabilized production period of 2 or 3 years is aimed, the gas rate should be no more than $2 \times 10^4 \text{ m}^3/\text{d}$.

When the bottom-hole pressure reaches the initial critical value, the gas rate will decline quickly as shown in Figure 22. When the gas rate is $1.0 \times 10^4 \text{ m}^3/\text{d}$, though a relatively longer plateau and higher gas recovery could be obtained, the cumulative production stays lower during most of the

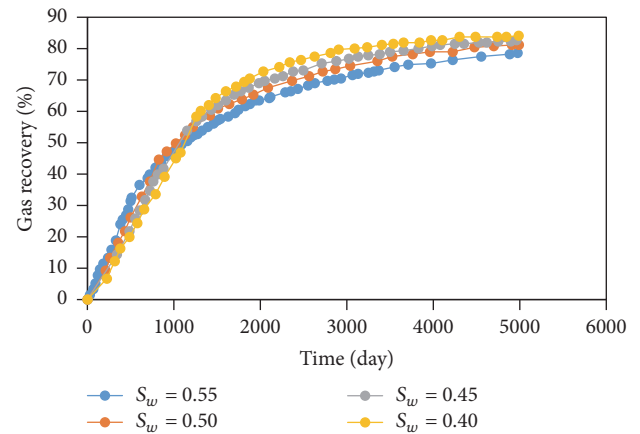


FIGURE 19: Effect of water saturation on gas recovery.

simulation process. When the gas rate is larger than $2 \times 10^4 \text{ m}^3/\text{d}$, the increase of cumulative gas recovery is limited (Figure 23).

From Figures 26 and 27, when gas rate increases, the water rate increases greatly and the time of peak water rate

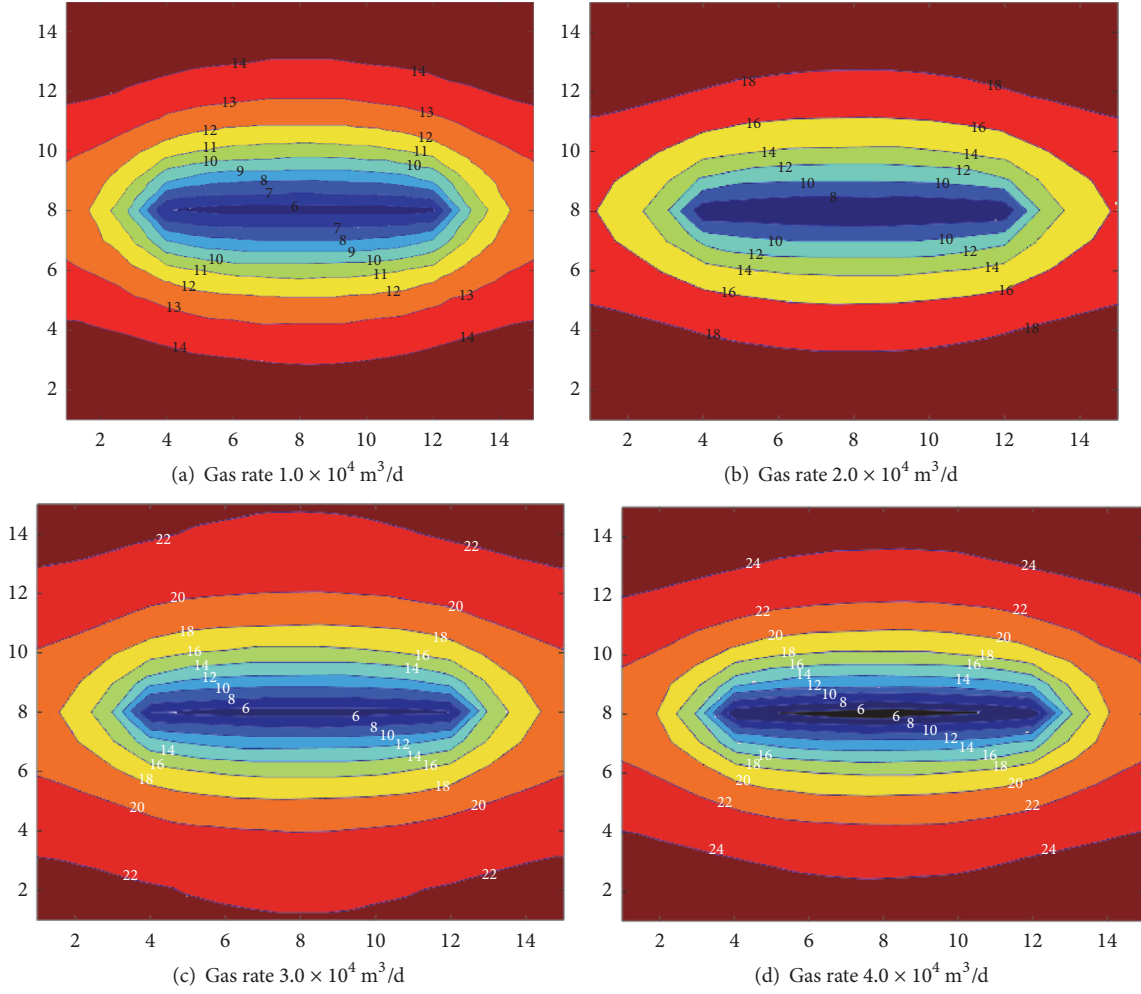


FIGURE 20: The pressure distribution after stabilized production stage under different gas rates.

is advanced; in addition, the trend of gas-water ratio will rise sharply and the value of gas-water ratio will increase.

7. Conclusions

A gas-water two-phase flow model is proposed, and it is applicable to tight gas reservoirs based on the percolation characteristics of tight gas reservoirs and with consideration of the effect of nonlinear factors on gas well production. When considering threshold pressure and media deformation, the duration of the plateau production period and gas recovery decreases. Notice also that the media deformation has a more significant effect on well production than the threshold pressure. In summary, the following points are drawn from this study.

(1) Water is basically immobile when the primary water saturation is small. The plateau reduces with the increase of drawdown pressure. The productivity of gas well decreases sharply when the bottom-hole pressure reaches the initial critical pressure and the gas well produces at constant pressure.

(2) Presence of water changes the gas percolation. When there is high water saturation within the formation

and gas-water two-phase flow takes place, gas-water ratio increases with the drawdown pressure. Therefore, reasonable drawdown pressure should be set in a gas reservoir with high water saturation.

(3) When the stress sensitivity and TPG are considered, the plateau will be shortened and gas recovery during the period will decrease. In comparison with TPG, stress sensitivity has a larger effect on gas productivity.

(4) Pressure gradient has an effect on gas-water permeability. However, for a gas reservoir, if the drawdown pressure gradient is limited, the effect of gas-water permeability on gas productivity could be negligible (or small).

(5) Water should be prevented and reasonable drawdown pressure should be kept as possible during the gas production in order to optimize gas recovery.

Appendix

Simulation Parameters

TPG and permeability have a power relationship:

$$\lambda = aK^{b(1-S_w)}e^{S_w}, \quad (\text{A.1})$$

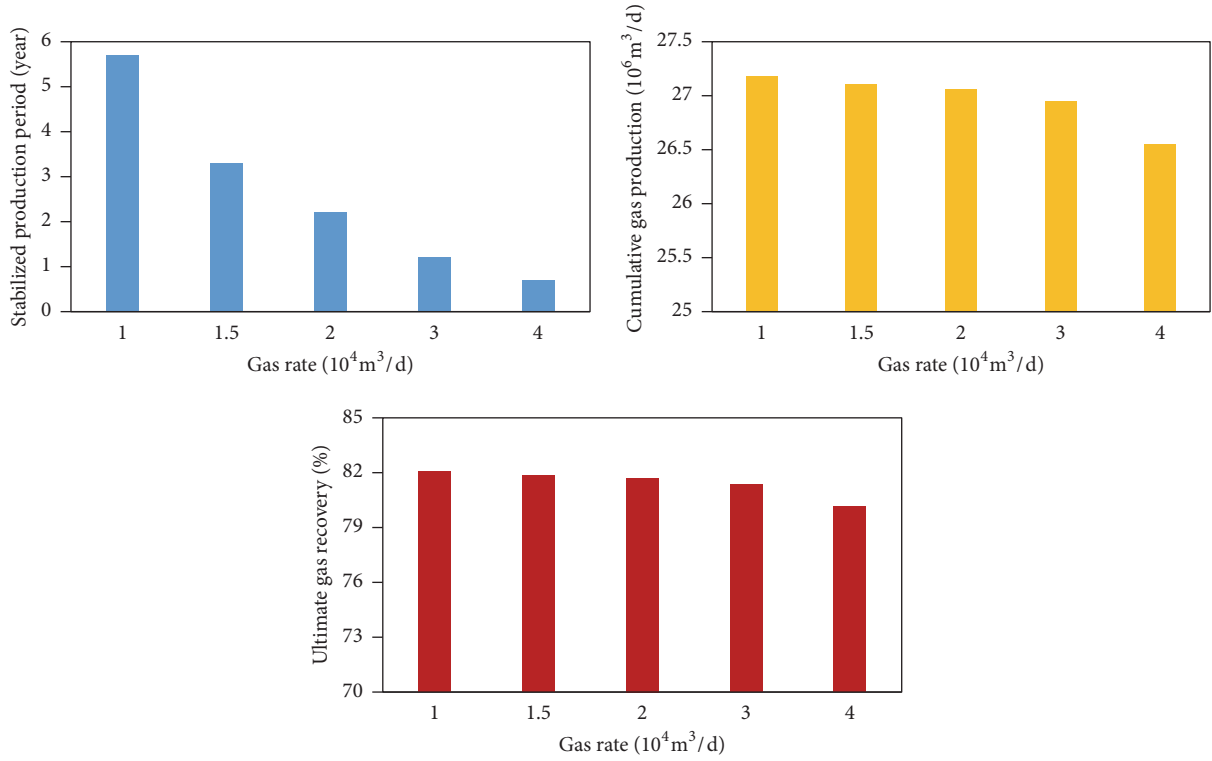


FIGURE 21: The stabilized production period, cumulative gas production, and gas recovery under different gas rates.

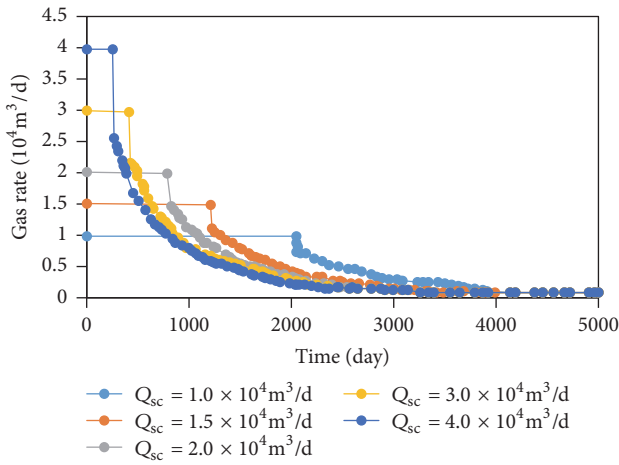


FIGURE 22: Gas rate under different initial gas rates.

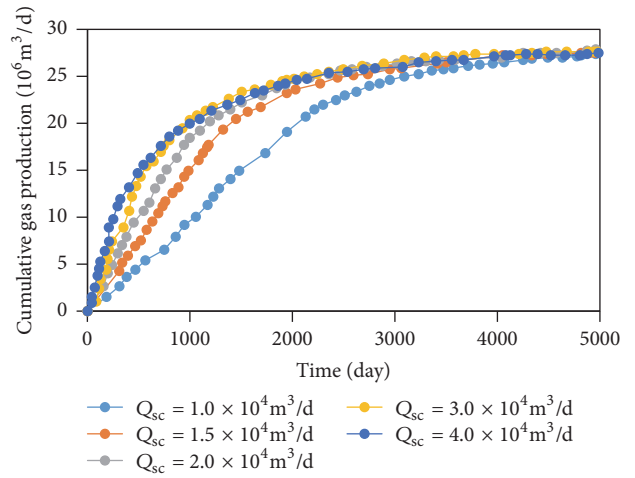


FIGURE 23: Cumulative gas production under different initial gas rates.

where a and S_w also have a power relation:

$$a = 2 \times 10^{-9} \times e^{(28.268 \cdot S_w)}. \quad (\text{A.2})$$

And b and S_w have a linear relation:

$$b = 3.576 \cdot S_w + 3.2692. \quad (\text{A.3})$$

Therefore, the relationship between permeability and water saturation is

$$\lambda_g = 2 \times 10^{-9} \times e^{(28.268 \cdot S_w)} K^{(3.576 \cdot S_w - 3.2692)}. \quad (\text{A.4})$$

The stress sensitivity coefficient is

$$S_p = a e^{b S_w} = \frac{1}{2} c (K_i)^{-n} e^{(-31.96 K_i + 4.12) S_w}, \quad (\text{A.5})$$

where $c = 0.2373$, $n = 0.3015$.

The threshold pressure gradient is

$$\lambda_g = 2 \times 10^{-9} \times e^{(28.268 \cdot S_w)} K^{(3.576 \cdot S_w - 3.2692)}. \quad (\text{A.6})$$

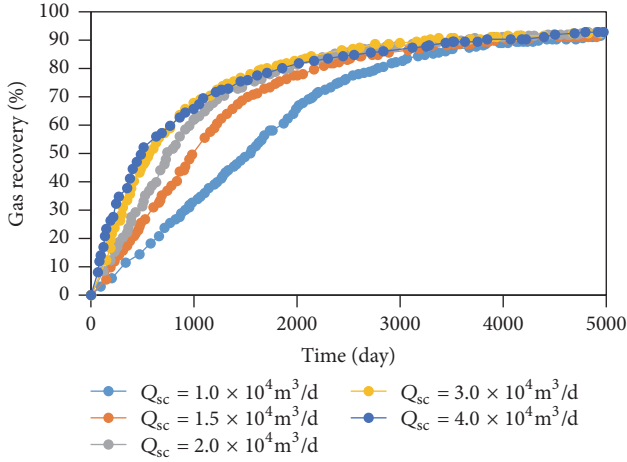


FIGURE 24: Gas recovery under different initial gas rates.

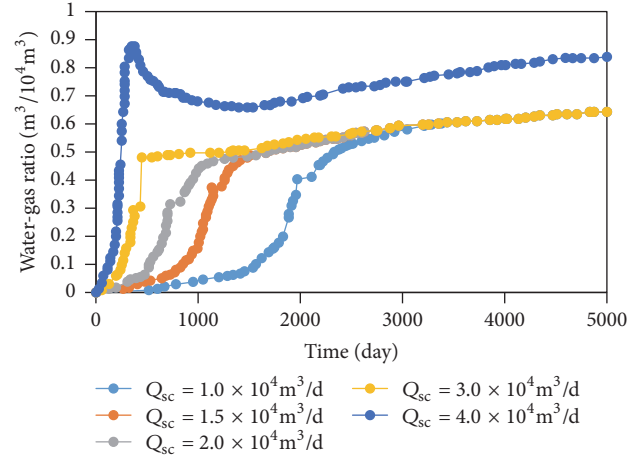


FIGURE 27: Gas-water ratio under different initial gas rates.

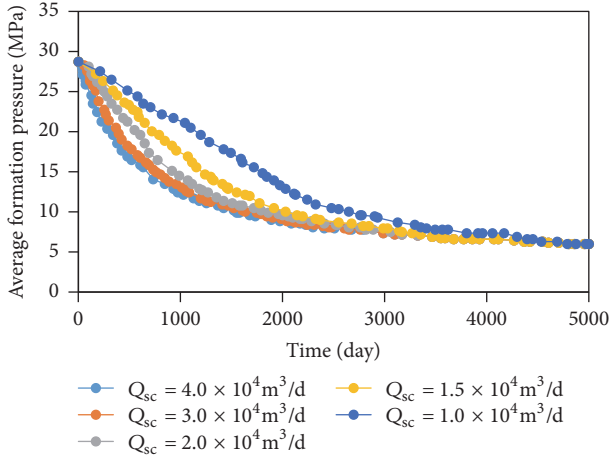


FIGURE 25: Average formation pressure under different initial gas rates.

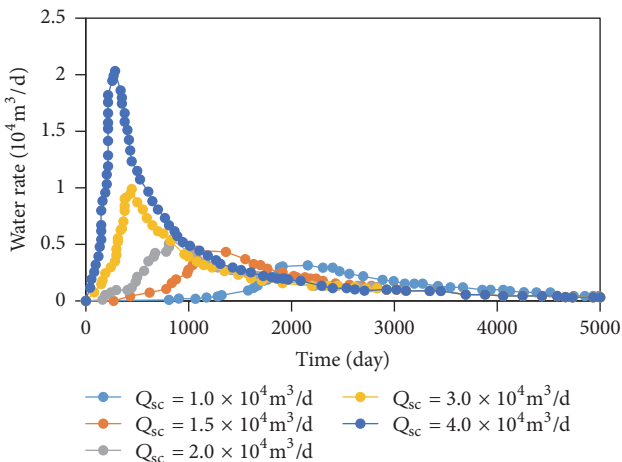


FIGURE 26: Water rate under different initial gas rates.

The relative permeability is

$$S_{wD} = \frac{S_w - S_{wc}}{1 - S_{wc} - (1 - S_{gr})}$$

$$K_{rw} = 0.325 \times S_{wD}^{2.087}$$

$$K_{rg} = 0.293 \times (1 - S_{wD})^{1.072} \quad (A.7)$$

$$K_{rw} = 0.55 \times S_{wD}^{1.442}$$

$$K_{rg} = 0.385 \times (1 - S_{wD})^{1.564}$$

Nomenclature

- B_g, B_w : Volume factor, decimal
 $K(p)$: Absolute permeability of the reservoir, μm^2
 K_{ij} : Relative permeability
 p_j : Pressure, MPa
 p_{cgw} : Gas-water capillary pressure, MPa
 S_j : Saturation
 S_{wc} : Initial water saturation
 S_{gr} : Residual gas saturation
 C_t : Total compressibility
 t : Time, s
 V_j, V_{js} : Underground volume and surface volume, cm^3
 \vec{v}_j : Percolation velocity, cm/s
 $p_{i+1/2}^n$: At the n th time step, the pressure of position $(i + 1/2, j, k)$.

Greek Symbols

- φ : Porosity
 μ_j : Viscosity, $\text{mPa}\cdot\text{s}$
 λ_j : Threshold pressure gradient
 ρ_j : Fluid density, g/cm^3

ρ_{gsc}, ρ_{wsc} : Density of gas and water under standard surface conditions, g/cm^3 .

Subscript

g : Gas phase
 w : Water phase.

Conflicts of Interest

The authors declare that there are no conflicts of interest regarding the publication of this article.

Acknowledgments

The authors are grateful to financial support of National Natural Science Foundation of China (no. 51674273), National Basic Research Program of China ("973 Program") (no. 2015CB250900), and Science Foundation of China University of Petroleum, Beijing (no. 2462015YQ0206).

References

- [1] L. K. Thomas, D. L. Katz, and M. R. Tek, "Threshold pressure phenomena in porous media," *Society of Petroleum Engineers Journal*, vol. 8, no. 2, pp. 174–184, 1968.
- [2] F. Boukadi, A. Bemani, M. Rumhy, and M. Kalbani, "Threshold pressure as a measure of degree of rock wettability and diagenesis in consolidated Omani limestone cores," *Marine and Petroleum Geology*, vol. 15, no. 1, pp. 33–39, 1998.
- [3] X. Wei, L. Qun, G. Shusheng, H. Zhiming, and X. Hui, "Pseudo threshold pressure gradient to flow for low permeability reservoirs," *Petroleum Exploration and Development*, vol. 36, no. 2, pp. 232–236, 2009.
- [4] W. Liu, J. Yao, and Y. Wang, "Exact analytical solutions of moving boundary problems of one-dimensional flow in semi-infinite long porous media with threshold pressure gradient," *International Journal of Heat and Mass Transfer*, vol. 55, no. 21–22, pp. 6017–6022, 2012.
- [5] J. Lu, "Pressure behavior of a hydraulic fractured well in tight gas formation with threshold pressure gradient," in *Proceedings of the SPE Middle East Unconventional Gas Conference and Exhibition*, Society of Petroleum Engineers, January 2012.
- [6] F. Civan, "Modeling gas flow through hydraulically-fractured shale-gas reservoirs involving molecular-to-inertial transport regimes and threshold-pressure gradient," in *Proceedings of the SPE Annual Technical Conference and Exhibition*, Society of Petroleum Engineers, October 2013.
- [7] S. Q. Li, L. S. Cheng, X. S. Li et al., "Nonlinear seepage flow of ultralow permeability reservoirs," *Petroleum Exploration and Development*, vol. 35, no. 5, pp. 606–612, 2008.
- [8] B. Q. Zeng, L. S. Cheng, and C. L. Li, "Low velocity non-linear flow in ultra-low permeability reservoir," *Journal of Petroleum Science and Engineering*, vol. 80, no. 1, pp. 1–6, 2011.
- [9] Q. J. Liu, B. H. Liu, X. B. Li et al., "The effect of water saturation on gas slip factor by pore scale network modeling," in *Proceedings of the SCA 2002 Symposium*, pp. 22–25, Monterey, Calif, USA, 2002.
- [10] J. Ding, S. Yang, X. Nie, and Z. Wang, "Dynamic threshold pressure gradient in tight gas reservoir," *Journal of Natural Gas Science and Engineering*, vol. 20, pp. 155–160, 2014.
- [11] I. Fatt and D. H. Davis, "Reduction in permeability with overburden pressure," *Journal of Petroleum Technology*, vol. 4, no. 12, p. 16, 1952.
- [12] R. D. Thomas and D. C. Ward, "Effect of overburden pressure and water saturation on gas permeability of tight sandstone cores," *Journal of Petroleum Technology*, vol. 24, no. 2, pp. 120–124, 1972.
- [13] J. Vairogs and V. W. Rhoades, "Pressure transient tests in formations having stress-sensitive permeability," *Journal of Petroleum Technology*, vol. 25, no. 8, pp. 965–970, 1973.
- [14] N. H. Kilmer, N. R. Morrow, and J. K. Pitman, "Pressure sensitivity of low permeability sandstones," *Journal of Petroleum Science and Engineering*, vol. 1, no. 1, pp. 65–81, 1987.
- [15] S. C. Jones, "Two-point determinations of permeability and PV vs. net confining stress," *SPE Formation Evaluation*, vol. 3, no. 1, pp. 235–241, 1988.
- [16] Z. L. Yu, S. S. Gao, and J. P. Liu, "Stress sensitivity of tight reservoir and its influence on oilfield development," *Acta Petroli Sinica*, vol. 28, no. 4, article 018, 2007.
- [17] F. O. Jones and W. W. Owens, "A laboratory study of low-permeability gas sands," *Journal of Petroleum Technology*, vol. 32, no. 9, pp. 1–631, 1980.
- [18] R. L. Luo, L. S. Cheng, and J. C. Peng, "A new method of determining relationship between permeability and effective overburden pressure for low-permeability reservoirs," *Journal of China University of Petroleum (Edition of Natural Science)*, vol. 2, article 020, 2007.
- [19] N. Burdine, "Relative permeability calculations from pore size distribution data," *Journal of Petroleum Technology*, vol. 5, no. 3, pp. 71–78, 1953.
- [20] A. T. Corey, "The interrelation between gas and oil relative permeabilities," *Producers Monthly*, vol. 19, no. 1, pp. 38–41, 1954.
- [21] I. Fatt, "The effect of overburden pressure on relative permeability," *Journal of Petroleum Technology*, vol. 5, no. 10, pp. 15–16, 1953.
- [22] A. Al-Quraishi and M. Khairy, "Pore pressure versus confining pressure and their effect on oil-water relative permeability curves," *Journal of Petroleum Science and Engineering*, vol. 48, no. 1–2, pp. 120–126, 2005.
- [23] S. S. Gao, L. Y. Ye, W. Xiong et al., "Seepage mechanism and strategy for development of large and low permeability and tight sandstone gas reservoirs with water content," *Journal of Oil and Gas Technology*, vol. 7, article 020, 2013.
- [24] S. Y. Mo, S. L. He, G. Lei, S. H. Gai, and Z. K. Liu, "Effect of the drawdown pressure on the relative permeability in tight gas: A theoretical and experimental study," *Journal of Natural Gas Science and Engineering*, vol. 24, pp. 264–271, 2015.
- [25] L. Ye, *Study on Percolation Mechanism and Reservoir Evaluation of Xujiache Low Permeability Sandstone Gas Reservoirs in Central Sichuan Basin*, Chinese Academy of Science, 2011.
- [26] R. Zhang, *Detailed Study on Gas-Water Relative Flow of Tight Gas Sandstone*, Northwest University, 2014.
- [27] L. Y. Ye, S. S. Gao, H. Z. Yang et al., "Water Production mechanism and development strategy of tight sandstone gas reservoirs," *Natural Gas Industry*, vol. 35, no. 2, pp. 41–46, 2015.
- [28] Y. Liu, Y. Pan, X. Zhen et al., "Influence of rock stress sensitivity in tight gas reservoir on characteristics of gas/water two phase

flows," *Complex Hydrocarbon Reservoirs*, vol. 6, no. 3, pp. 36–39, 2013.

- [29] X. Zheng, C. Zhigang, and L. Weichuan, "Gas/water flowing ability influence experimental study of permeability stress sensibility in tight gas reservoir," *Well Logging Technology*, vol. 4, pp. 360–363, 2013.

Research Article

Lattice Boltzmann Simulations of Fluid Flow in Continental Carbonate Reservoir Rocks and in Upscaled Rock Models Generated with Multiple-Point Geostatistics

J. Soete,¹ S. Claes,² H. Claes,¹ N. Janssens,¹ V. Cnudde,³ M. Huysmans,^{1,4} and R. Swennen¹

¹Earth and Environmental Sciences, KU Leuven, Celestijnenlaan 200E, 3001 Heverlee, Belgium

²Civil Engineering, KU Leuven, Kasteelpark Arenberg 40, 3001 Heverlee, Belgium

³ProGRes, Geology and Soil Science, Ghent University, Krijgslaan 281, S8, 9000 Ghent, Belgium

⁴Hydrology and Hydraulic Engineering, Vrije Universiteit Brussel, Pleinlaan 2, 1050 Brussel, Belgium

Correspondence should be addressed to J. Soete; jeroen.soete@kuleuven.be and S. Claes; steven.claes@kuleuven.be

Received 12 April 2017; Accepted 5 July 2017; Published 24 September 2017

Academic Editor: Yi Wang

Copyright © 2017 J. Soete et al. This is an open access article distributed under the Creative Commons Attribution License, which permits unrestricted use, distribution, and reproduction in any medium, provided the original work is properly cited.

Microcomputed tomography (μ CT) and Lattice Boltzmann Method (LBM) simulations were applied to continental carbonates to quantify fluid flow. Fluid flow characteristics in these complex carbonates with multiscale pore networks are unique and the applied method allows studying their heterogeneity and anisotropy. 3D pore network models were introduced to single-phase flow simulations in Palabos, a software tool for particle-based modelling of classic computational fluid dynamics. In addition, permeability simulations were also performed on rock models generated with multiple-point geostatistics (MPS). This allowed assessing the applicability of MPS in upscaling high-resolution porosity patterns into large rock models that exceed the volume limitations of the μ CT. Porosity and tortuosity control fluid flow in these porous media. Micro- and mesopores influence flow properties at larger scales in continental carbonates. Upscaling with MPS is therefore necessary to overcome volume-resolution problems of CT scanning equipment. The presented LBM-MPS workflow is applicable to other lithologies, comprising different pore types, shapes, and pore networks altogether. The lack of straightforward porosity-permeability relationships in complex carbonates highlights the necessity for a 3D approach. 3D fluid flow studies provide the best understanding of flow through porous media, which is of crucial importance in reservoir modelling.

1. Introduction

Porosity and permeability control the storage and fluid flow in reservoir rocks. An example of potential reservoir rocks is continental carbonates, such as travertines (a term here used *sensu lato* [1]), which are highly heterogeneous as a result of their geological evolution, influenced by sedimentary origin, diagenetic processes, and burial history. The latter processes influence the size and shape of pores, producing some of the most complex pore networks recorded in sedimentary rocks. Recent hydrocarbon discoveries highlighted the continental carbonate reservoir potential in the presalt exploration, offshore Brazil [2, 3] and in the Namibe basin, Angola [4–6]. Quantitative data about lithofacies' occurrence, distributions, and their related porosity and permeability are key to

understanding the reservoir behavior. The sedimentology of continental carbonates has been widely studied [7–13], but recently the focus of continental carbonate studies shifted towards the rocks' petrophysical properties like porosity, permeability, and acoustic velocities [14–22]. Noteworthy is the fact that the permeability inside rocks is strongly dependent on the geometric and topological properties of the porous medium at microscopic scales [23].

Many efforts have been made to reconstruct digital pore networks based on computer tomography (CT) to study the fluid flow in rock samples [24–29]. In this study, the 3D pore networks were acquired with different CT systems, which allowed scanning a range of sample volumes at different resolutions. After segmentation, the obtained pore networks

were loaded into Palabos, a software tool for classic computational fluid dynamics (CFD). The source code and scripts are available at the Palabos website [30].

In order to evaluate the reservoir potential of continental carbonates, a critical assessment has to be made regarding the scale at which petrophysical measurements should be performed. This requires covering several spatial scales. Multiscale flow modelling is defined as any method used to explicitly represent the flow properties at more than one scale within a reservoir [31]. Reservoir models typically cover at least twelve orders of magnitude, ranging from pore to core to interwell to full field simulations. Four general scale orders can be recognized, which are pore to lithofacies, lithofacies to geomodel, and geomodel to reservoir model. Multiple-point geostatistics (MPS) gained importance in the recent years for modelling geological structures at different spatial scales, from μm to m [32, 33]. For example, in the field of hydrology, MPS allows building models on decameter scale [34], while Okabe and Blunt [35] used the technique to model pore space on a micrometer scale. MPS enables simulating complex interconnected pore structures by directly inferring the patterns from training images and furthermore allows modelling heterogeneity. This allows simulation of complex interconnected structures [36, 37] and the upscaling of complex pore systems to scales relevant to flow property considerations.

In this study, the CFD were for the first time applied to representative continental carbonate samples, taken from different reservoir analogues, in order to study micro- to mesoscale fluid flow in lithofacies-specific pore networks. A major benefit to these models is that the samples are differentiated based on sedimentological interpretation. Furthermore, it was verified that scan resolution and also porosity and tortuosity influence the simulated permeability. In heterogeneous carbonates, pores sizes range over several orders of magnitude and pores at different scale influence the interconnectivity. It is thus necessary to study the pore network at different scales. Not only voxel and pore network based stochastic reconstruction methods [38, 39] but also simulated annealing and Markov Chain Monte Carlo methods [40] have been proposed to merge data obtained from multiscale imaging. Here, a MPS scale-independent workflow was proposed which integrates small- and large-scale pore patterns, thus generating large volume porosity models at high resolution. MPS contributes to the comprehension of reservoir behavior in rocks by solving the common reservoir upscaling problem. To verify whether generated pore patterns were accurate, a comparison between simulated and measured permeabilities on matching artificial and original samples was made. The latter assured that MPS can in future studies be used to optimize digital pore networks and the accuracy of simulated permeabilities.

2. Research Material

Continental carbonate samples from outcrops in the Ballık area (Turkey) and Süttő and Budakalász (Hungary) were selected for analysis. The continental carbonates are of Quaternary age. The dataset covered the four dominant facies

types present in the quarries, that is, the subhorizontal, reed, cascade, and waterfall facies (Figure 1), as defined by Claes et al. [1]. All of these facies types have pores at least varying from nanometer to centimeter scale and could have relevant contributions to fluid flow in this material. For a sedimentological background of the samples (out of the scope of this study), the reader is referred to earlier published literature [1, 14, 41, 42].

The facies types were usually characterized by different meso- and macropore networks, here defined as pores that have sizes of $1\text{--}100\ \mu\text{m}$ and $>100\ \mu\text{m}$, respectively. Pseudofenestral and interpeloidal pores, aligned along the layering, dominate the subhorizontal (Figure 1(a)) and cascade (Figure 1(b)) facies. In the latter, interlayer and shelter pores were also present between shrub crusts [1]. The reed facies (Figure 1(c)) was named after its characteristic phyto-moldic porosity. In the waterfall facies (Figure 1(d)), hanging plants on steep slopes became encrusted and generated highly porous zones in which well-connected phyto-moldic pores and high interstitial pore spaces formed framework porosity. It has to be noted that pore sizes of vugs, caverns, and shelters in these continental carbonates can exceed the sample size of classical plugs or cores.

3. Methodology

3.1. Core Analysis. Petrophysical measurements in this study were conducted on plugs with 2.5 cm and 3.4 cm diameter. These cylindrical plugs were taken in the core laboratory with a Hilti water-cooled diamond coring drill. After plugging, the samples were cut and polished to make the ends flat and parallel. In the first step of the research, samples were sent to Panterra Geoconsultants (Leiderdorp, Netherlands) for porosity-permeability analyses. The effective porosity in the plugs is measured by means of helium expansion porosimetry. Gas permeability, in this case with nitrogen gas (N_2), is measured in a steady-state permeameter.

3.2. Computer Tomography (CT). CT imagery is frequently applied in recent geomaterials research and industrial applications [43–46]. In this study, CT was used to simulate petrophysical properties in porous continental carbonate media. An inherent characteristic of CT is the relationship between resolution and sample size. The resolution of the scan (R) is a combination of the pixel size (d) of the detector, the magnification of the object (M), and the size of the X-ray focal spot (s). Equation (1) gives the relationship between these parameters:

$$R = \frac{d}{M} + s \left(1 - \frac{1}{M} \right), \quad (1)$$

$$M = \frac{\text{SDD}}{\text{SOD}},$$

where SSD is the source-detector distance and SOD is the source-object distance.

Different and new CT scanners generate scans at different and ever improving scan resolutions, which can influence the estimated porosity. For example, the HECTOR scanner

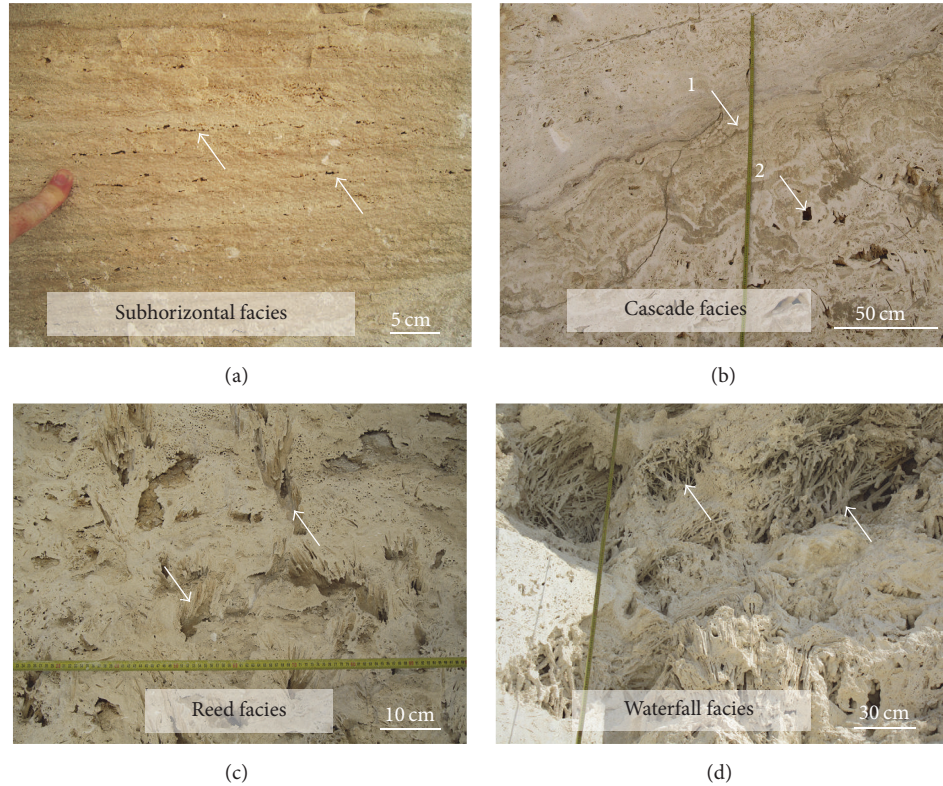


FIGURE 1: Dominant lithofacies types in the studied continental carbonate quarries. (a) Subhorizontal facies with pseudofenestral porosity (arrows). (b) Cascade facies with dendrite crusts (arrow 1) and shelter pores (arrow 2). (c) Reed facies with reed moldic porosity (arrows). (d) Waterfall facies with plant framework porosity (arrows).

developed at UGCT [47] has a 240 kV setup which allows the scanning of large core samples with a diameter of 10 cm at a $28 \mu\text{m}$ resolution. This resolution is normally only reachable on smaller plug samples using standard micro-CT scanners. HECTOR CT scans were processed in Octopus [48]. In addition to the HECTOR CT, samples in this study were also scanned with a Phoenix Nanotom S instrument (GE Measurement and Control Solutions, Wunstorf, Germany), equipped with a 180 kV/15 W high-performance nanofocus X-ray tube and a 2304×2304 pixel Hamamatsu detector [21]. Radiographs were reconstructed with the volume processing software Phoenix datos|x (GE Measurement and Control Solutions, Wunstorf, Germany) and images with an isotropic voxel size of 2, 4, 12, or $16 \mu\text{m}$ were exported. Slices were segmented in Matlab. Volume of Interest (VOI) selections and further analysis were done in Avizo Fire.

3.3. Representative Elementary Volume. The Representative Elementary Volume (REV) is a crucial concept when evaluating petrophysical properties of reservoir rocks. The REV or unit cell is the smallest volume over which a porosity measurement can be made which yields a value representative of the whole. In this study, porosity and the pore network are used as starting point to perform permeability simulations. Such simulations could only be correct if the REV for porosity was reached. When the REV for the porosity and pore types present is not reached, the pore network will yield variable

porosity and thus unrepresentative simulated permeabilities. The REV of 10 samples, with a scan resolution of $16 \mu\text{m}$, was determined according to the statistical REV calculation method described in Claes [49], which follows the approach of Bear [23]. The latter author used the chi-square criterion (χ^2) as a measure of porosity fluctuation inside a selected sample volume. The smaller this χ^2 value was, the closer the correspondence with the volume of the REV was. For each sample, the size of the REV was calculated 100 times, according to the procedure of Claes [49]. QQ plots of these 100 REV simulations and p value calculations of the chi-square goodness of fit test are used to verify whether the REV simulations are log-normally distributed. 95% confidence intervals for the REV were subsequently calculated. This method allowed determining objectively whether the characteristic meso- and macropores in the selected samples were representative.

3.4. Multiple-Point Geostatistics (MPS)

The Single Normal Equation Simulation (SNESim) Algorithm. Traditional geostatistical simulation algorithms can be subdivided into two groups based on their principal method: pixel based group and object based group. The former simulates one pixel at a time, while the latter fits an object or pattern onto the simulation grid in one step. One of the important differences between both methods is the ease with which they

can handle conditioning data. Pixel based methods are easily adapted to incorporate hard conditioning data. In contrast, object based methods faithfully fit the large-scale patterns but are difficult to condition to local data if that data is abundant. The multiple-point concept proposed by Journel [50] and Guardiano and Srivastava [51] combines the strengths of both methods. The main difference between MPS and traditional geostatistical methods is the use of a training image (TI). This TI is a representation of the expected geometry and spatial distribution of the objects present in the actual field and does not need to be a real image of the field. The simulation is performed pixelwise with the conditional probabilities respecting the conditional proportion of the TI. The TI must at least be the size of the REV to capture pore geometries and connections.

Figure 2 provides a schematic overview of the different elements used in a MPS approach, as well as its strengths for simulating complex geological structures. Figure 2(a) represents the original image, in which three facies types can be recognized. In Figure 2(b), the principal components of the original image are retained and a training image is created. Details concerning facies 2 (grey), with the lowest occurrence probability in Figure 2(a), are not retained in the training image and hence are not present in the simulated images (Figures 2(d) and 2(e)). Figure 2(c) shows the conditioning data (e.g., well data) used in the simulations. Figures 2(d) and 2(e) show the result of MPS simulations using the SNESim algorithm and the classical Sequential Indicator Simulation (SISim) algorithm, respectively. In Figure 2(d), the connectivity of facies 3 (black) is better preserved compared to the results in Figure 2(e). This observation indicates the advantage of a multiple-point approach in contrast to two-point correlations used in SISim.

In this study, the SNESim algorithm implemented by Strebelle [52] was used. Using this algorithm, the TI was scanned once and all conditional proportions were stored in a search tree data structure. In the next step, these proportions were used to create the simulated values. At each simulation node u , the search template τ_j was used to retrieve the conditional data event $\text{Dev}(u)$, which is defined as

$$\text{Dev}_j(u) = \{Z^s(u + h_1), \dots, Z^s(u + h_j)\}, \quad (2)$$

where $Z^s(u + h_j)$ is a filled-in nodal value.

SNESIM Algorithm

- (1) Define search template τ_j and construct search tree T_j specific to template τ_j .
- (2) Relocate hard data to the nearest simulation grid node and freeze them during simulation.
- (3) Define a random path visiting all locations to be simulated and for each location do the following:
 - (a) Find conditioning data event $\text{Dev}_j(u)$ defined by template τ_j .
 - (b) Retrieve conditional probability distribution function (CPDF) $P\{Z(u) = k \mid \text{Dev}_j(U)\}$ from T_j .

- (c) Draw a simulated value $Z(u)$ from the conditional distribution and add it to the dataset.

Several parameters play an important role in the obtained simulation results. They were varied in order to improve the results of the simulations. Liu [53] and Meerschman et al. [54] provide an extensive analysis of the influence of the different parameters on the simulations. The most important parameters for upscaling using MPS are described below.

In order to capture the large-scale structural information in MPS simulations, the original algorithm was adapted to allow the use of multigrids. Tran [55] introduced this technique to create a large-scale template with a reasonably small number of nodes. It was important to keep the number of nodes limited because otherwise the search tree would become too large, resulting in an exponential increase of calculation time. In a first step, nodes on the coarsest grid were simulated using the rescaled template. Subsequently, the nodes on the second coarsest grid were simulated and so on. The relationship between “ n ” different grids was expressed in (3). Figure 3 shows an example in which three multiple grids are used ($n = 3$):

$$\tau_j^n = \{2^{n-1}h_1, \dots, 2^{n-1}h_j\}. \quad (3)$$

In MPS, the TI is used to provide detailed information on which the simulation is based. This information is derived from the patterns present in the TI. However, often the marginal distributions of the different categories in the TI are not equal to those of the real sample, which needs to be simulated; that is, the percentages of occurrence of the different categories diverge between the TI and the desired simulation. Strebelle and Journel [32] implemented a method to adapt this discrepancy of the marginal category distribution. However, if the marginal probability of the TI and the desired marginal probability are not close enough to each other, the algorithm would not reproduce the desired proportions of each category present in the simulated images. The servo corrector, introduced by Strebelle [52], bends the running simulated marginal probability further towards the target proportions by introducing a parameter λ . The larger λ is, the stronger the impact of the applied correction is (see the following equation):

$$P^{\text{new}}(A \mid B) = P(A \mid B) + \mu(P(A) - P^c(A)), \quad (4)$$

$$\mu = \frac{\lambda}{1 - \lambda} \quad \lambda \in [0, 1],$$

where $P^c(A)$ is the proportion which was calculated based on the original sample and all previously simulated nodes. It is, however, important to note that $P(A)$ and the MPS cannot completely be decoupled; hence, the target proportions should not be too different from the TI [53].

MPS in Upscaling. Figure 4 provides a schematic outline of the workflow. Figure 4(a) is a detailed image (TI) obtained using μ CT. Hence, this dataset, with an isotropic voxel resolution of $4 \mu\text{m}$, holds detailed information about micrometer scale porosity, present in a specific facies type. Figure 4(b) originated from a medical CT dataset (200 by 200 by $500 \mu\text{m}^3$)

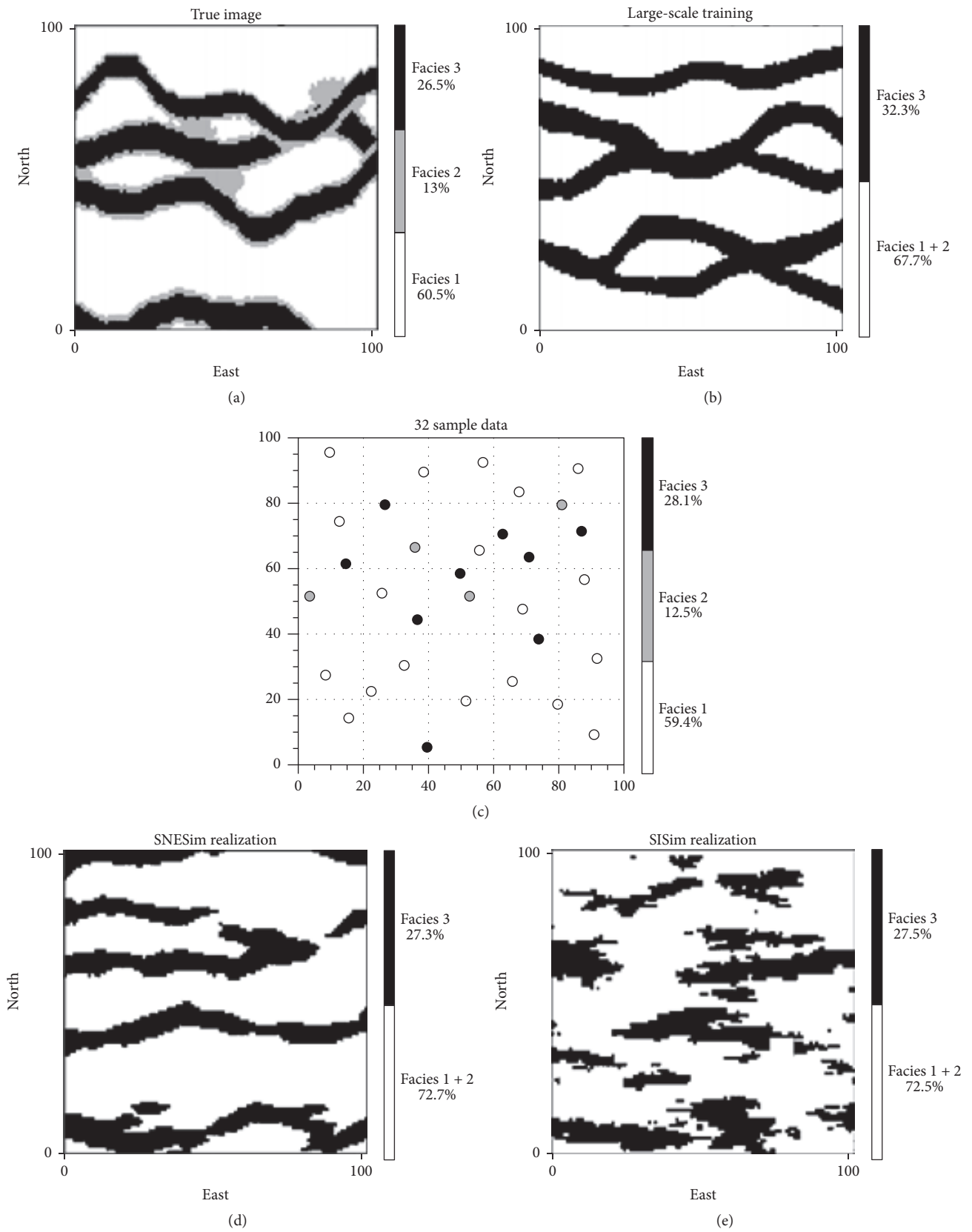


FIGURE 2: Example of MPS simulation of a meandering river system (after Strebelle [52]).

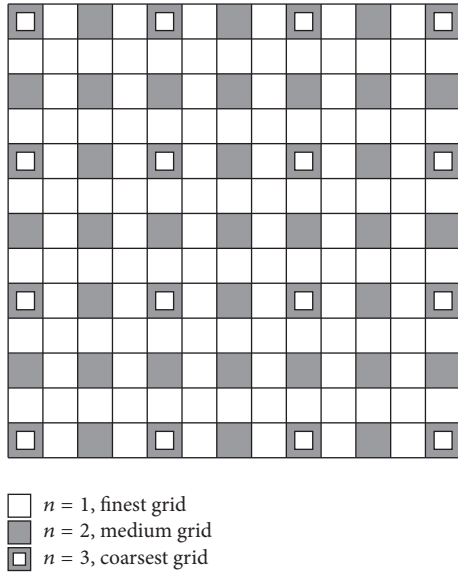


FIGURE 3: Example of the template using three multiple grids (after Remy et al. [64]).

of the same sample. Medical CT usually incorporates a much larger sample volume, as inferable from the difference in scale in Figures 4(a) and 4(b). The medical CT datasets provided information about the pore network on a larger spatial scale than the μ CT and was used as conditioning data in the simulations. Thus, the TI (2D slice in Figure 4(c)), derived from the μ CT scans, is representative of the nonresolved matrix of the medical CT (2D slice in Figure 4(d)). The TI porosity patterns were used to simulate micrometer scale matrix porosity, which is below the resolution of the medical CT. This approach allowed retaining the connectivity of the pore network over a larger spatial scale, resulting in more reliable pore network reconstructions (Figure 4(e)) as well as more accurate permeability simulations, at least if samples obeyed the REV criterion. In order to determine the conditioning data, the assumption that the centers of the larger pores stayed the same and were recognizable in all used datasets was made, that is, in TI, condition data, and simulated results, regardless of the resolution. Centers of the largest pores were obtained by applying the workflow described below.

The dataset with the largest voxel size was segmented (Figures 4(b) and 5(a)) and the distance map of the pore facies was calculated (Figure 5(b)). This resulted in a dataset in which the center of the pore had the highest value. Subsequently, the position of the pore center was calculated by using a regional maximum algorithm. The approach not only resulted in the position of the pore centers but also preserved information about the pore sizes. In order to retain more information about the larger pores in the dataset, a threshold distance was introduced, which was calculated as σ times the maximum distance.

Only distance map values higher than σ times the maximum distance were replaced by an index representative for the property under investigation. The effect of the newly

introduced parameter σ in the simulation workflow can be interpreted as follows: a small σ value will assign the property index to a larger amount of pore pixels around the pore center (Figure 5(c)), while a large σ value preserves more details about the center of the pores itself (Figure 5(d)).

By combining the patterns of the TI and the conditioning data, computer-generated rock samples were retrieved. Hence, this allowed investigating several other petrophysical parameters such as total and effective porosity, tortuosity, and permeability. Training images used in this upscaling workflow do not meet the ideal REV criterion that was previously mentioned. This option was willingly chosen because of computational cost, which is linearly related to the cube of the TI edge length. In the SNESim algorithm, all patterns are stored in the RAM of the computer and additional different patterns increase the CPU requirements. Therefore, an arbitrary size of 250^3 voxels has been chosen for training images. This corresponds to a size of 1 mm^3 at a resolution of $4 \mu\text{m}$. These TI volumes have been subjectively chosen in zones that are relevant for the simulated properties. The difference with the concept of an REV is that the volume of the REV should theoretically be able to select a random zone in the sample which should always be representative. This has now been changed to an operator controlled step, which should not influence the ultimate results.

3.5. Lattice Boltzmann Method (LBM) Simulations. Stationary, pressure-driven fluid flow through porous media was simulated in Palabos by imposing a constant pressure gradient between the inlet and outlet of the pore network. Instead of solving Navier-Stokes equations, LBM solves the discrete Boltzmann equation by simulating flow for Newtonian fluids with collision models. In the applied single-phase fluid simulations under laminar flow conditions, the permeability was described by Darcy's law (see the following equation):

$$K = \frac{\mu v}{(\Delta P/L)}, \quad (5)$$

where K is the permeability; μ is the fluid viscosity; v is the flow velocity; and $\Delta P/L$ is the pressure difference over the length of the pore network.

The network geometry was stored in an input or geometry file and was based on a stack of binary images (Figure 6(a)). In the input file, value zero (blue) was assigned to every fluid voxel. Value two (red) described internal rock voxels, neighboring only other rock voxels, and value one (green) was assigned to boundary voxels that touched both fluid and rock voxels (Figure 6(b)). In the geometry file, fluid pathways had to be sufficiently resolved to avoid nonhydrodynamic effects [25, 29]. This was ensured by stepwise refining of the binary image stacks. First, pore objects with an equivalent diameter shorter than two times the length of a voxel side were deleted. In a second step, only the effective porosity, that is, all the interconnected pore space at the scanned resolution, was selected.

In this study, the standard Bhatnagar-Gross-Krook (BGK) collision operator was applied, together with the D3Q19 lattice. Flow direction during the simulations was

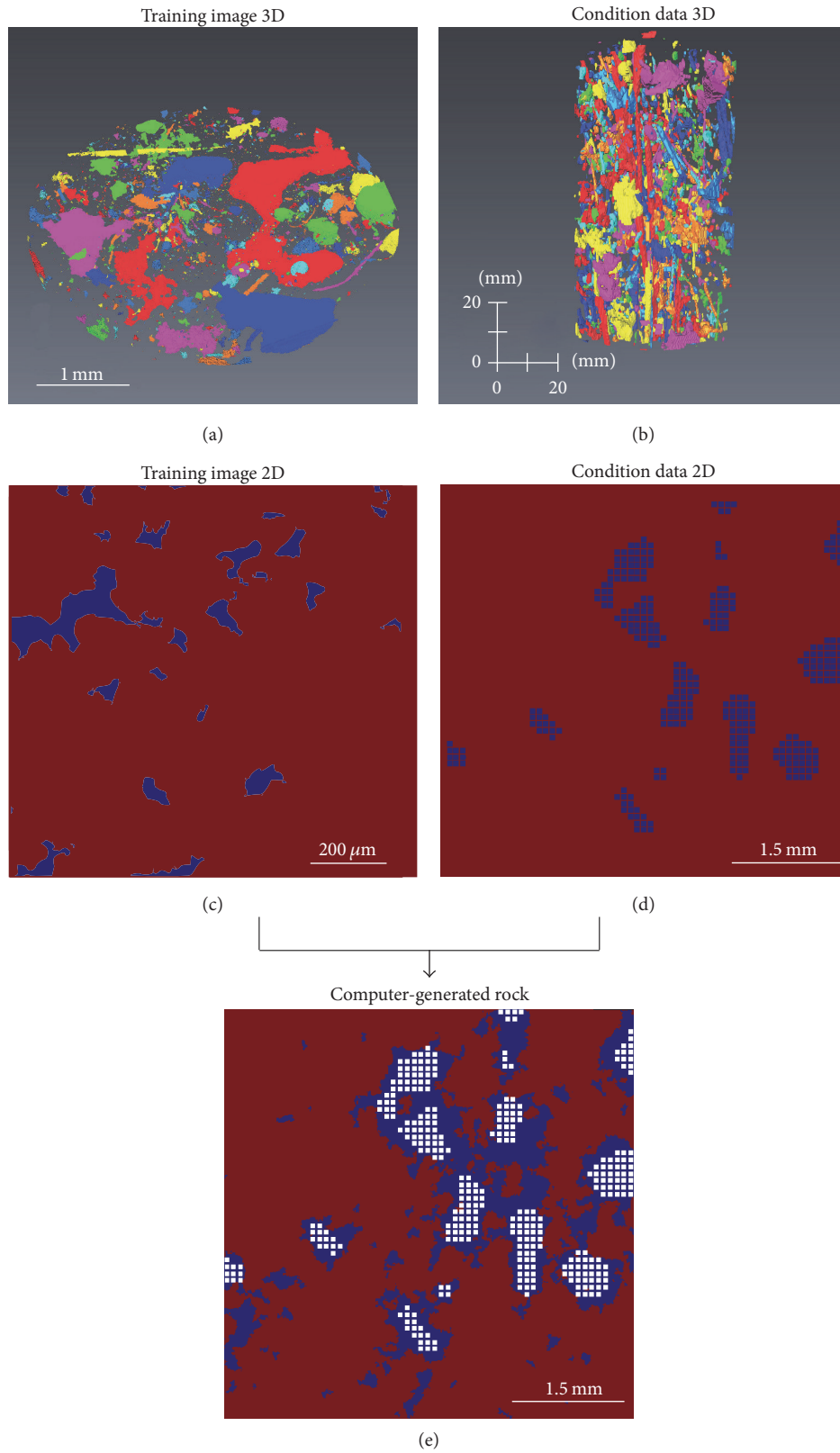


FIGURE 4: Schematic outline of the MPS upscaling workflow. (a) 3D training image at high resolution and (b) 3D conditioning data at low resolution. Colors indicate pore connectivity. (c) 2D slice through the TI shown in (a) and (d) through the conditioning data shown in (b). Pores are given in blue. (e) Computer-generated rock slice, with the conditioning data (white) plotted on top of the generated porosity (blue).

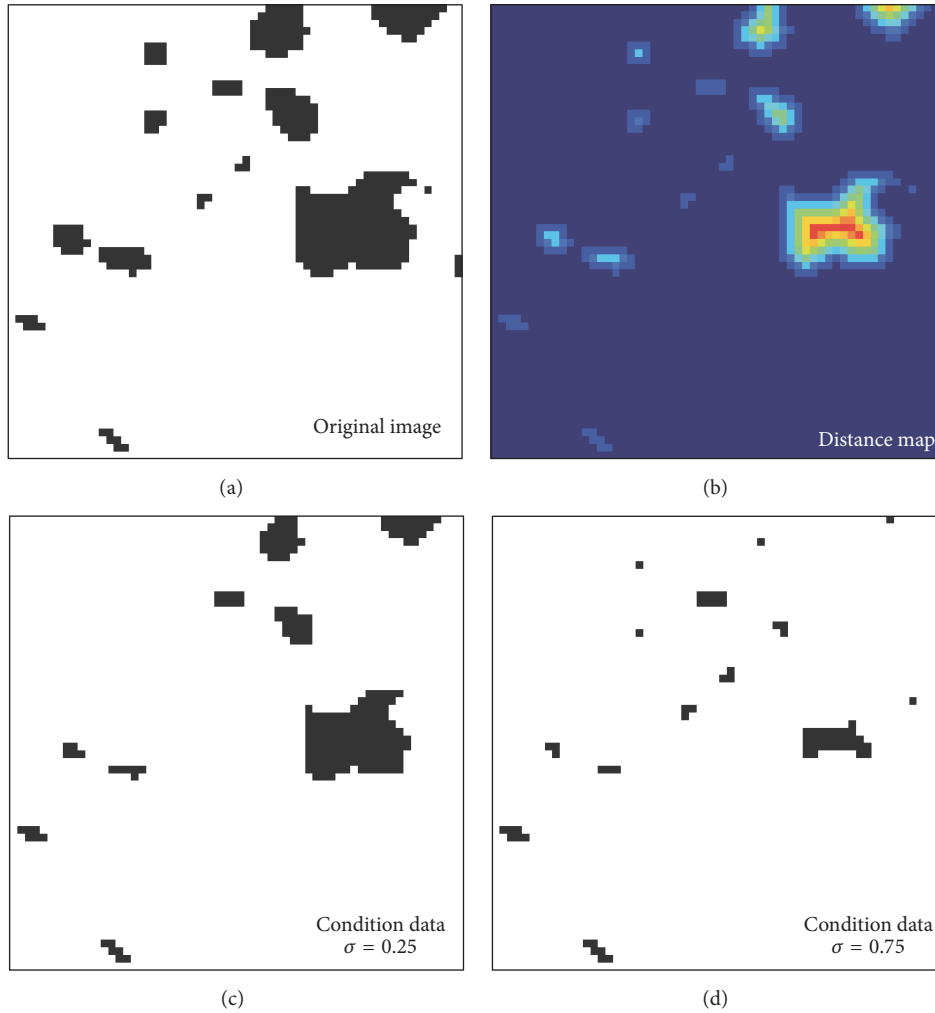


FIGURE 5: Workflow of generating the conditioning data used in the MPS approach. (a) The original image. (b) The calculated distance map based on the original image shown in (a). (c) The generated conditioning data for σ value of 0.25 and (d) for σ value of 0.75.

limited to a finite vector set, representing the particle travel directions. In case of the D3Q19 lattice, there are 18 discrete lattice velocities for a fluid particle at rest (Figure 7). Palabos comes with several lattice models, including the D3Q15, D3Q19, and D3Q27 lattices. The D3Q15 lattice was not used here because of the less accurate results and numerical instabilities at high Reynold's numbers [56, 57]. The D3Q27 lattice is more complex, when compared to the D3Q19 lattice. It provides eight additional particle transport directions, namely, to the corners of the cubic lattice nodes. Because of this, the accuracy of the model will increase, but so will the computational needs per iteration step. Both models were tested on the continental carbonates and yielded similar results, in agreement with earlier publications [56, 57]. Hence, continuing working with the D3Q19 lattice to limit the computational cost of the permeability simulations was decided.

The initial fluid velocity in the simulation was set to zero. The simulated flow accelerated during the iteration steps under influence of the fixed pressure gradient between the

inlet and outlet of the pore network. Fluid velocity vectors with terminal points that coincided with the fluid/rock interface underwent a bounce back with no slip boundary conditions. This means that particle displacement from a fluid node to a solid surface (Figure 8(a)) resulted in a bounce back vector with the same initial point and direction but the opposite sense (Figure 8(b)). The initial vectors (A, B, and C) and bounce back vectors (D, E, and F) neutralized each other and resulted in a zero velocity for the displacement towards the solid surface. The standard deviation of the average energy was calculated while running simulations in Palabos. As also mentioned by Degruyter et al. [25], steady state was reached when the standard deviation of the average energy fell below a given threshold value. In this study, the threshold value was set to 10^{-3} , with a maximum of 20000 iteration steps. Similar to Degruyter et al. [25], it was checked whether the permeability stayed constant when the applied pressure gradient was varied over several orders of magnitude. This ensured that laminar flow was established during the simulations [58, 59].

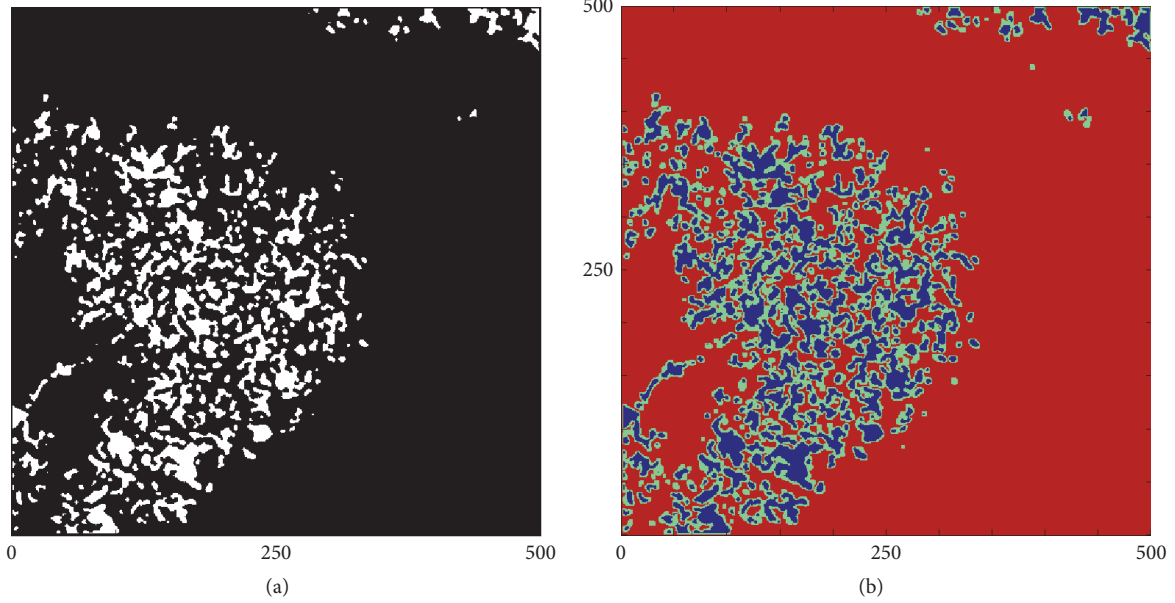


FIGURE 6: Input files, with (a) binary CT image and (b) conversion to geometry file in which fluid voxels are blue (value 0), internal rock voxels are red (value 2), and boundary voxels are green (value 1).

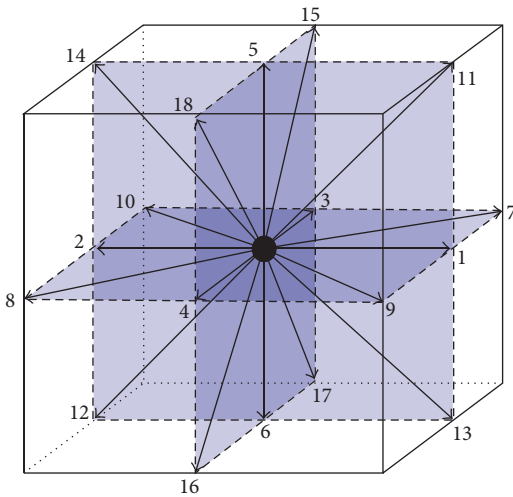


FIGURE 7: D3Q19 lattice with 18 discrete velocity directions for a particle at rest.

During the LBM simulations in Palabos, dimensionless lattice units are used to describe fluid flow properties, which are easily converted to any kind of physical system [57, 60]. In this study, the dimensionless lattice units were converted to Darcy units by multiplying with the square of the effective length of a voxel side. Knowing that the permeability in Darcy’s law is proportional to the ratio between fluid flow rate and the applied pressure gradient (ΔP) between the inlet and outlet (L) of the pore network, the permeability (K) was described as follows:

$$K = \frac{\Delta x^2 \mu_l \nu}{(\Delta P/L)}, \quad (6)$$

where Δx is the effective length of a voxel side; μ_l is the lattice viscosity; and ν is the fluid flow rate.

Permeability was simulated along the length axis (z -axis) of the plugs and spatial transformation of the binary images of nine samples allowed simulating permeability in the horizontal x and y directions, orthogonal to z -axis. Permeability measurements were carried out on CT-derived pore networks and rock models generated in the MPS approach with cubic (500 px^3) or cuboid volumes of 500 by 500 by 1000 pixels or 800 by 800 by 450 pixels, respectively.

3.6. Tortuosity. The porosity in rocks is defined by the amount of void spaces present in a sample. These pores could be connected in permeable pathways. Then, complexity (sinuosity) of the pathways for fluids through these pores is described by a property known as the tortuosity. This property provides information on the interconnectedness of the pore objects as part of a pore network and is used in transport models for porous media [61–63]. The tortuosity (τ) is defined by the length of the flow path (L_f) and the shortest trajectory (L_s) between a defined inlet and outlet plane in the direction of the applied pressure gradient (see the following equation, [63]):

$$\tau = \lim_{L_f \rightarrow \infty} \frac{L_f}{L_s}. \quad (7)$$

The tortuosity equals 1 for a straight path through the sample ($L_f = L_s$), and will be infinite for a cyclic path ($L_f \gg L_s$).

4. Results

The results below are presented in order of the subsequent steps in the simulation approach. First, the LBM method

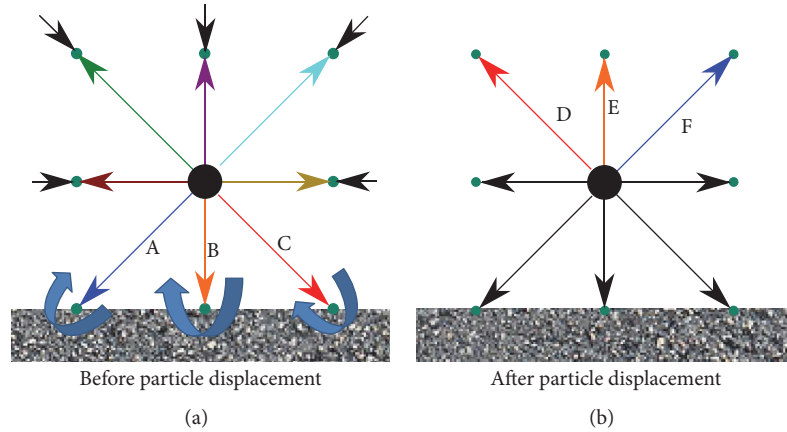


FIGURE 8: Bounce back conditions of fluid particles for a node at the fluid/rock interface. (a) Colored vectors are streamed to neighboring nodes and black vectors towards the node at the fluid/rock interface. Particles travelling into the solid surface are represented by vectors “A,” “B,” and “C.” (b) Black vectors of the neighboring nodes have been streamed to the node at the fluid/rock interface and, correspondingly, colored vectors have been streamed to neighboring nodes. Vectors “A,” “B,” and “C” cannot be streamed towards a neighboring node, since particle displacement is interrupted by the solid surface. The latter vectors were therefore bounced back according to vectors “D,” “E,” and “F” with, respectively, the same directions but in the opposite sense.

simulations were conducted on pore networks derived from natural samples and the effect of the scan resolution on CT based porosity and simulated permeability was checked. Subsequently, MPS was used to integrate high-resolution porosity patterns into lower-resolution, large-volume CT scans. LBM simulations were used to calibrate several MPS parameters and to verify whether the generated pore networks are a good representation of the real pore system.

4.1. Spatial Resolution Effect on the Recorded Pore Network. A comparison was made between datasets obtained by medical CT with $230\ \mu\text{m}$ resolution (Figures 9(a) and 9(e)) and the HECTOR scans with $28\ \mu\text{m}$ resolution (Figures 9(b) and 9(f)) of two different continental carbonate facies types: a reed facies and a subhorizontal sample. It is clear that much more detail is visible in the HECTOR scans. Figures 9(c) and 9(d) show the comparison of the visible porosity in both scans of both facies types. The mean porosity difference between both scans of the reed facies type was 1.5% (Figure 9(c)). The subhorizontal facies type was characterized by a larger mean porosity difference of 2.4% (Figure 9(d)). This was explained by pore volumes below the resolution of medical CT, which were more abundant in the latter facies type.

In order to assess the influence of resolution on smaller samples, a plug with 7 mm diameter was scanned at 3 different resolutions: $4\ \mu\text{m}$ (Figure 10(a)), $12\ \mu\text{m}$ (Figure 10(b)), and $16\ \mu\text{m}$ (Figure 10(c)). Figure 10(d) shows a comparison of the calculated porosity in function of plug height. The porosity difference between the $4\ \mu\text{m}$ and $16\ \mu\text{m}$ scan varied between 1.4 and 2.35% along the height of the sample. These observations illustrated the importance of resolution in correctly characterizing the pore networks. Below, a workflow is proposed to combine information of different datasets which have a different resolution in order to improve the accuracy of larger samples.

4.2. Representative Elementary Volume. Pore REV of ten μCT -scanned plugs (3.4 cm diameter) at $16\ \mu\text{m}$ resolution were calculated (Table 1). For all the samples, the REV was reached. The QQ plots of 100 REV simulations per sample (not shown) had determination coefficients of at least 0.94. The p value of the chi-square goodness of fit test was always well above the 0.05 hypothesis threshold. The latter tests implied that the null hypothesis was never rejected, that the calculated REV were lognormally distributed, and that upper and lower bounds of the 95% confidence intervals for the mean size of the REV could be calculated.

The confidence intervals for the side length and volume of the cubic REV are listed in Table 1. The scanned sample volumes were all representative for the pore types and sizes that they contained. The largest REV were found in samples originating from the reed lithofacies, which is in agreement with their heterogeneous pore networks that were observed by Claes [49]. The smallest REV were observed in the subhorizontal and cascade facies. The pore network had a more homogeneous distribution throughout these lithofacies. The volumes over which the permeability was simulated were chosen with the size of the REV kept in mind. Simulation cell volumes for samples from the reed facies, for example, which was the facies with the largest REV size, were always $1180\ \text{mm}^3$, while for the subhorizontal facies, which in general had a smaller REV size, simulation cells of $512\ \text{mm}^3$ could be used. The simulation cells were always at least over two times the REV volume.

4.3. Permeability Simulations. In total, 18 VOIs were prepared from continental carbonate plugs. The simulated permeabilities along the vertical and orthogonal horizontal axes are given together with other sample characteristics, such as lithofacies types and μCT calculated porosities (Table 2). The permeabilities obtained from LBM simulations are in

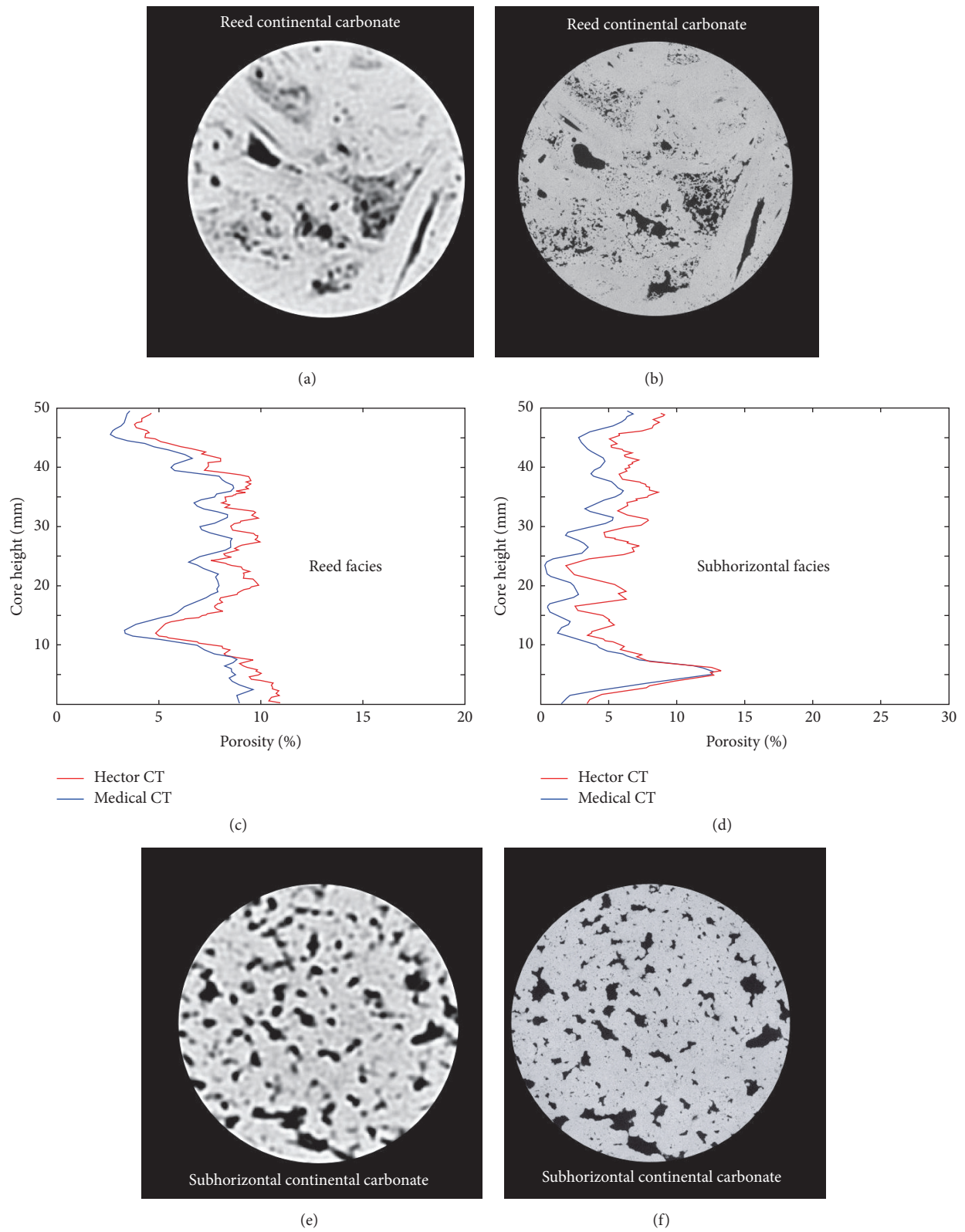


FIGURE 9: Influence of the resolution on the measured porosity network in whole cores with a diameter of 9.7 cm. ((a) and (b)) Medical CT and HECTOR slice of a reed continental carbonate with 230 μm and 28 μm resolution, respectively. (c) Comparison of the calculated porosity in function of the core height for a reed continental carbonate. (d) Comparison of the calculated porosity in function of the core height for a subhorizontal continental carbonate. ((e) and (f)) Medical CT and HECTOR slice of a subhorizontal continental carbonate, with 230 μm and 28 μm resolution, respectively.

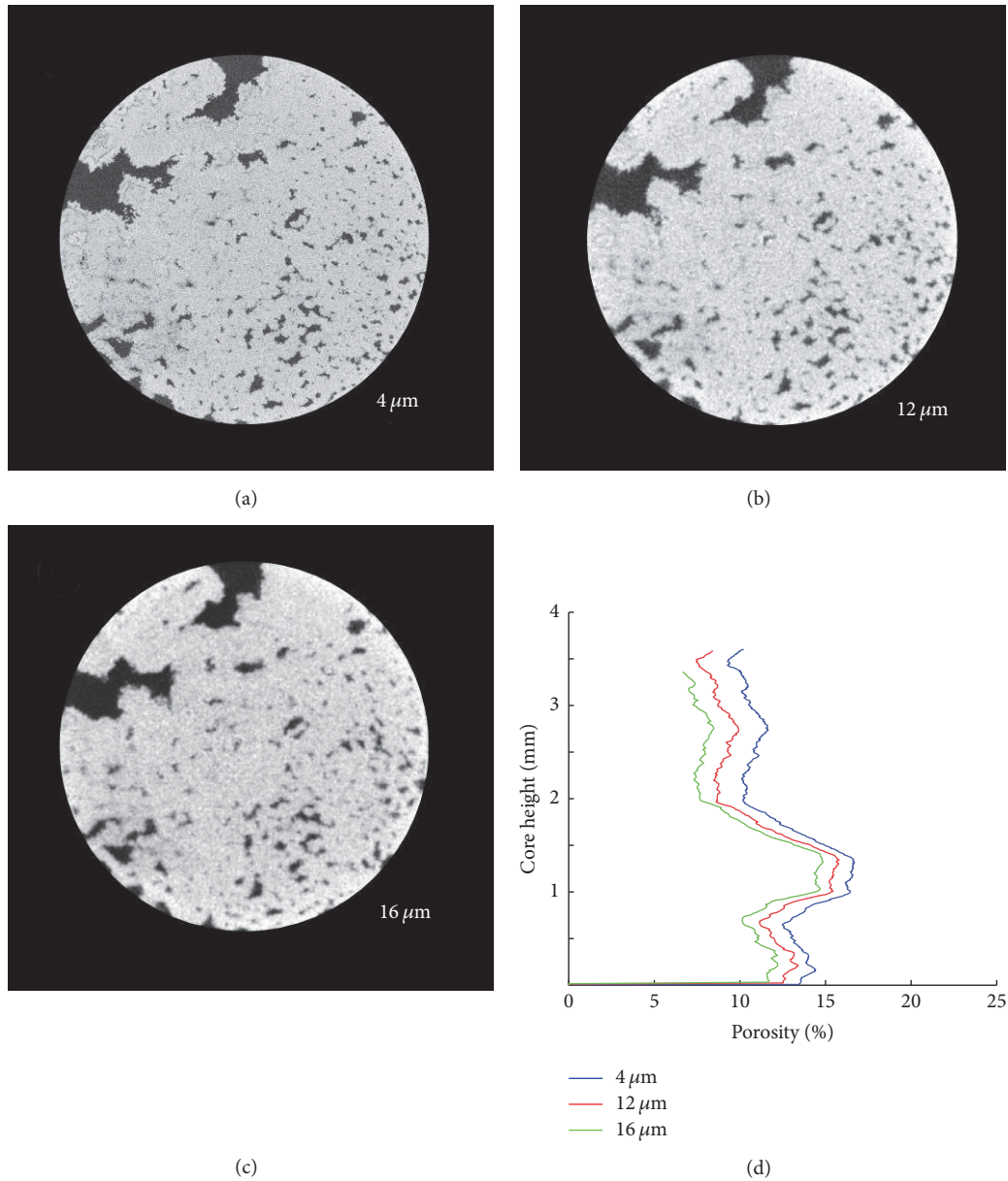


FIGURE 10: Influence of the resolution on the measured porosity network in a miniplug with a diameter of 7 mm. Comparison of the same slice scanned at (a) 4 μm , (b) 12 μm , and (c) 16 μm resolution. (d) Comparison of the calculated porosity in function of the plug height.

TABLE 1: REV size calculations.

Sample	Facies	QQ correlation	p value	REV side in mm		REV volume in mm^3	
				Lower 95% CI	Upper 95% CI	Lower 95% CI	Upper 95% CI
1	Subhor.	0.99	0.45	1.58	2.62	3.96	18.01
2	Subhor.	0.97	0.81	2.42	4.94	14.26	120.53
3	Subhor.	0.95	0.75	1.10	5.63	1.31	178.57
4	Subhor.	0.97	0.67	1.14	3.94	1.47	61.26
5	Reed	0.96	0.44	1.72	4.56	5.13	95.09
6	Reed	0.97	0.59	2.78	8.26	21.55	562.70
7	Reed	0.94	0.36	3.83	5.95	56.24	210.17
8	Cascade	0.97	0.18	1.96	4.71	7.56	104.73
9	Cascade	0.98	0.85	2.26	3.74	11.54	52.12
10	Waterfall	0.99	0.67	1.45	3.19	3.02	32.58

Note. With subhorizontal facies (Subhor.), quantiles (QQ), the statistical p value, and the confidence interval (CI).

TABLE 2: Permeability simulations.

Simulation	Facies	$K_{sim,z}$ (mD)	$K_{sim,x}$ (mD)	$K_{sim,y}$ (mD)	\emptyset (%)	$\emptyset_{c,z}$ (%)	τ_z
1	Subhor.	0	1456	28.6	9.2	0	/
2	Subhor.	0.1	14.8	99.5	6.2	5.0	4.9
3	Subhor.	0	/	/	0.8	0	/
4	Subhor.	0.4	22.0	9.6	3.4	1.7	3.3
5	Subhor.	1.8	/	/	7.2	4.8	2.9
6	Subhor.	100	/	/	12.3	11.7	2.4
7	Cascade	0.3	/	/	7.1	5.2	2.2
8	Cascade	0.7	11.7	0.5	7.9	7.1	3.3
9	Cascade	0	/	/	5.3	0	/
10	Reed	3.6	/	/	6.9	4.5	3.1
11	Reed	449	30780	17641	25.9	23.5	2.3
12	Reed	422	/	/	25.8	23.5	2.3
13	Reed	1.9	0	0	6.5	3.7	1.9
14	Reed	2325	0	179	12.2	1.7	1.6
15	Reed	62261	/	/	14.4	12.4	1.4
16	Waterfall	10.9	/	/	14.1	11.2	2.9
17	Waterfall	1931	84.3	178	32.7	32.0	1.5
18	Waterfall	1.0	0	0	11.1	4.6	2.1

Note. With vertical permeability simulations ($K_{sim,z}$) and orthogonal horizontal permeability simulations ($K_{sim,x}$ and $K_{sim,y}$), the μ CT calculated porosity (\emptyset), the connected porosity in the z direction ($\emptyset_{c,z}$), the tortuosity in the z direction (τ_z), and not-measured values or values that could not be determined (/).

good agreement with physical laboratory measurements conducted on continental carbonate samples (Figure 11). The laboratory core analyses were conducted on 5 cm³ or 10 cm³ cylindrical plugs, while volumes analyzed with LBM varied between 0.5 cm³ and 1.2 cm³.

Despite the volume difference in order of magnitude, a similar spread for porosity and permeability was observed for the core measurements and LBM simulations, with the latter plotting along the best fit curve to the core measurement data. The laboratory plug measurements include the data published in Soete [22], which indicated that the subhorizontal facies data plot mainly below 15% porosity and 100 mD. This is in agreement with the findings for both vertical and horizontal permeability in this study, where only one simulation for the subhorizontal facies yielded permeability > 100 mD and a median of 12 mD was found, while never exceeding 12.3% porosity.

For the cascade facies, phyto-rich samples were avoided and the simulations focused on samples containing shrub crust lithotypes. Dominant cascade pore types were therefore similar to those observed in the subhorizontal facies and yielded simulation results that were in the same range. The reed and waterfall facies were both characterized by a strong increase in calculated μ CT porosity. In the reed facies, this increase was due to the presence of reed moldic porosity [1, 21], which formed elongated tubes that locally ran through the simulation volumes. These tubes provided high permeability pathways. The simulated permeability in the reed facies exceeded core lab results from continental carbonates from the Ballik area (Turkey), published in Soete [22], but that was expected, since highly permeable reed samples from Süttő and Budakalász in Hungary [42] were

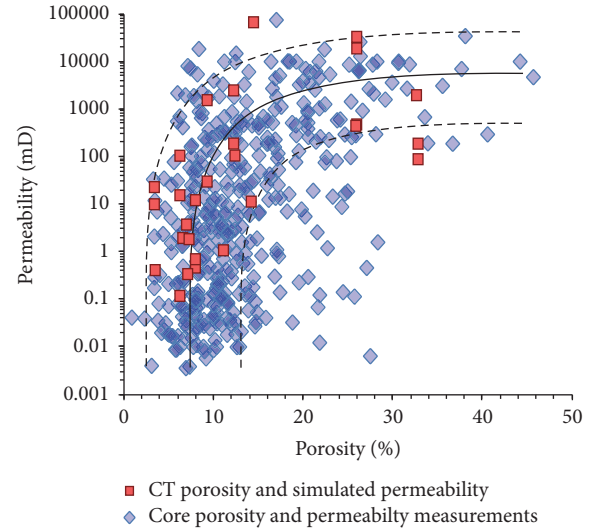


FIGURE 11: Porosity-permeability cross-plot for laboratory core measurements and LBM simulations. The black line is the best fit curve to the data and the dashed lines delineate the zone defined by 90% of the data points closest to the best fit curve.

added to the dataset of this study. Waterfall pore types captured in the VOIs possessed grass and bryophyte moldic pores that together formed plug scale framework porosity.

Framework porosity, formed by plants larger than grass and bryophytes, was not included in this study. This explained the somewhat lowered permeability results for the LBM approach when compared to laboratory-measured permeability for the waterfall facies [22]. The similarities between

TABLE 3

(a) Effect of resolution and volume on permeability (16 μm to 4 μm)

Sample	$K_{16\mu\text{m}}$	$K_{4\mu\text{m}}$	$\text{VOI}_{16\mu\text{m}}$	$\text{VOI}_{4\mu\text{m}}$
1	1581.7	2215.4	1180 mm ³	18.4 mm ³
2	22	112.8	1180 mm ³	18.4 mm ³
3	34.8	2.8	1180 mm ³	18.4 mm ³
4	100.5	10.7	1180 mm ³	18.4 mm ³

(b) Effect of changing resolution on permeability (4 μm to 2 μm)

Sample	$K_{4\mu\text{m}}$	$K_{2\mu\text{m}}$	$\text{VOI}_{4\mu\text{m}}$	$\text{VOI}_{2\mu\text{m}}$
5	63.8	60.4	2.3 mm ³	2.3 mm ³
6	15.4	15.7	2.3 mm ³	2.3 mm ³

Note. $K_{16\mu\text{m}}$, $K_{4\mu\text{m}}$, and $K_{2\mu\text{m}}$ represent simulations at resolution of 16, 4, and 2 μm . Table 3(a) shows effect of resolution and volume on permeability and Table 3(b) shows difference for simulations at 2 and 4 μm resolution over identical volumes.

measured and simulated permeabilities lead to the verification that the analyzed tomographic volumes qualify as permeability REV's. The μCT scans were thus at high enough spatial resolution to capture the primary permeability contributors of the pore network.

Miniplugs (7 mm diameter) were taken from some of the samples to further investigate the effect of sample size and spatial resolution on simulation results. Miniplugs were μCT -scanned at 4 μm resolution and permeability was simulated over a volume of 18.4 mm³, which was in most cases below the calculated pore REV of the samples. It was shown in Figure 10 that porosity increased for a resolution step from 16 to 4 μm . Based on the increasing porosity, higher permeabilities were expected for scans at 4 μm resolution. Despite the higher porosity and sharper μCT images, the volumes of 4 μm scans were too limited to capture the variability of the pore network. The 4 μm miniplug simulations (no REV reached), although within the order of magnitude, yielded permeabilities that overestimated and underestimated the 16 μm plug simulations, in which the REV was reached (Table 3(a)).

In addition, two miniplug VOI scans were conducted at 2 μm resolution, the highest achievable resolution for the Phoenix Nanotom S instrument in these rocks. The 2 μm VOI scans were projected back in their respective 4 μm miniplug scans. Permeability simulations for the latter VOIs were not expected to be representative, since both 2 μm and 4 μm scans were based on volumes below the REV size for porosity. The latter simulations were purely conducted to demonstrate the effect of spatial resolution. The simulations that were conducted over the exact same volumes but at different spatial scales yielded similar results (Table 3(b)). The latter demonstrated that an increase in resolution from 4 to 2 μm did not significantly improve the accuracy of the digital pore network. Based on the above observations, it was concluded that the best digital representations of the pore network were in this case achieved in 4 μm resolution CT scans but with VOIs that equal at least $\text{VOI}_{16\mu\text{m}}$. Achieving 4 μm resolution while scanning large VOIs is at this point impossible and would need significant improvement of CT

scanning equipment. An MPS workflow (see Section 3.6) that integrates high-resolution pore network details into large volume datasets and that captures the variability of the pore network can provide a solution and is thus proposed in this paper.

The total porosity (\emptyset) and connected porosity in z direction ($\emptyset_{c,z}$) were calculated from μCT -scanned samples. For some samples, $\emptyset_{c,z}$ was slightly smaller, which meant that the majority of recorded pore objects in the μCT scans contributed to the connectivity. Other samples displayed large differences between total and connected porosity, for example, in simulation 14 (12.4 versus 1.4%). This indicated pore network heterogeneity and isolated porosity in the simulated flow direction at the resolution of the acquired CT images. The simulated permeability along z -axis ($K_{\text{sim},z}$) of the samples was plotted against \emptyset and $\emptyset_{c,z}$ (Figure 12). Porosity was in this case plotted on the vertical axis of the graph to clearly show the lowering from \emptyset to $\emptyset_{c,z}$. A power-law relationship was observed between $K_{\text{sim},z}$ and $\emptyset_{c,z}$, with a determination coefficient of 0.75. This implied that good permeability estimates could be obtained from μCT porosity calculations at 16 μm resolution. However, it has to be kept in mind that pores below the 16 μm resolution could influence flow properties in continental carbonates but were not considered in these permeability estimations. Two high-permeability outliers with relatively low porosities can be observed and will be further discussed in the next section (Section 4.4).

4.4. Tortuosity. The tortuosity (τ) was calculated and plotted against permeability (Figure 13). Tortuosity controlled permeability in the studied complex pore networks. The observed power-law relationship between τ_z and $K_{\text{sim},z}$ was consistent with findings of studies treating volcanic rocks, where increasing tortuosity results in lower permeabilities [25, 26, 65]. Highest tortuosities were reported for the subhorizontal and cascade facies, while the waterfall and reed facies had the lowest tortuosities (Table 2). Tortuosity of the pore network helped to understand discrepancies between porosity and permeability. Two outliers from the porosity-simulated permeability regression line (sample 14 and 15 in Figure 12) were highlighted in the tortuosity-simulated permeability cross-plot (Figure 13). Both samples are part of the reed facies and $\emptyset_{c,z}$ consists of only a few reed molds. The limited, patchy reed mold presence did not result in high overall porosities for the samples. Despite the limited porosity, both samples are characterized by low tortuosities, indicative for the straight, high velocity flow paths that the reed molds provide through the sample.

4.5. Simulating Permeability in Orthogonal x and y Directions. For nine samples, including four from the subhorizontal and cascade facies and five from the reed and waterfall facies, the permeability was also simulated in the horizontal x and y directions, orthogonal to the vertical simulations along z -axis, totaling 18 horizontal simulations. These operations were limited to nine samples because of the high computational cost of the rotation and simulation procedures. The simulations $K_{\text{sim},x}$, $K_{\text{sim},y}$, and $K_{\text{sim},z}$ for the nine

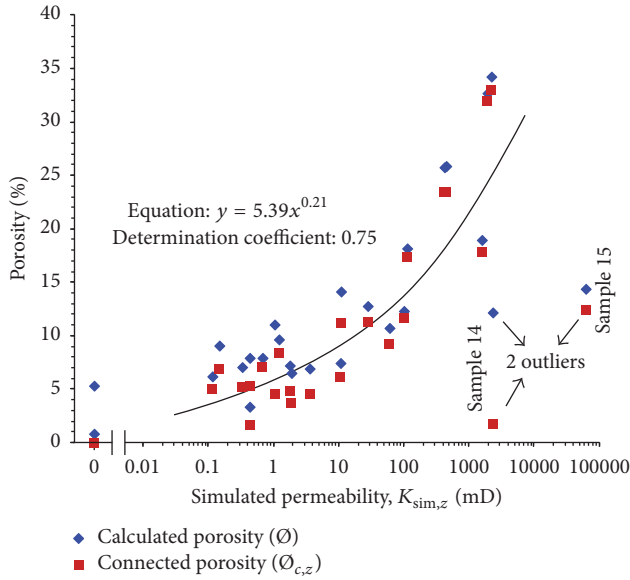


FIGURE 12: Cross-plot of the calculated total and connected μ CT porosity (resp., blue and red symbols) versus the permeability.

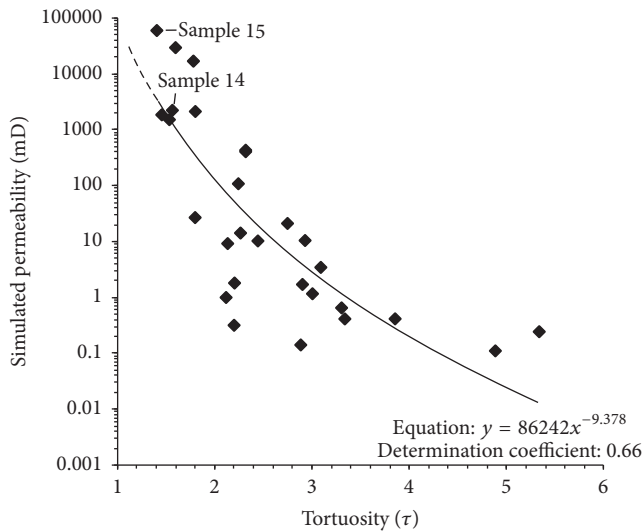


FIGURE 13: Tortuosity-simulated permeability cross-plot. A moderate power-law relationship is observed between these parameters.

samples were plotted and the influence of different facies types and related pore types on the results was checked (Figure 14). For the subhorizontal and cascade facies, the highest permeabilities were observed in the horizontal direction, often being over an order of magnitude higher than the vertical permeability of the same sample. Even in sample A118, where an open network in the vertical direction was absent, high horizontal permeabilities were encountered. Pseudofenestral, interpeloidal, interlayer, and shelter porosities in the subhorizontal and cascade facies were described as pore types that appear aligned with the horizontal or inclined laminations. In the vertical direction, these pore types were usually discontinuous and overgrown by younger

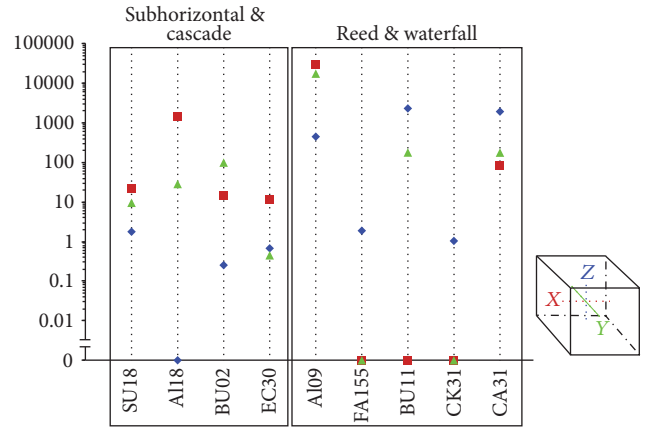


FIGURE 14: Simulated permeability $K_{sim,x}$ (red), $K_{sim,y}$ (green), and $K_{sim,z}$ (blue) for four subhorizontal and cascade samples and five reed and waterfall samples.

rock fabrics, which formed barriers and resulted in low vertical permeabilities (<2 mD). A pore network volume rendering of a subhorizontal facies sample, which included gastropod moldic pores (Figure 15(a)), demonstrated this low connectivity in z direction. The alignment of the pores along the laminations provided better horizontal connectivity.

For the reed facies, permeability was strongly dependent on reed moldic pores. The 3D visualization of flow paths inside a reed sample (Figure 15(b)) demonstrated the heterogeneous nature of fluid flow through these porous media. High velocities were achieved within only a couple of reed tubes, which dominated the fluid flow. Depending on the orientation of the reed molds, that is, eroded (horizontal) or in-growth position (vertical), the direction of the highest permeability differed; for example, in sample A109, which contained eroded reed, the highest permeability was achieved in the horizontal direction (Figure 14).

Grass and bryophyte framework pores in the waterfall facies formed vertically oriented pore networks. The small framework pipes yielded high permeabilities in the vertical direction, while the horizontal connectivity was dependent on the connections between individual pipes. The horizontal permeability was therefore lowered in samples from the waterfall facies, for example, samples CK31 and CA31 (Figure 14). The streamline rendering (Figure 15(c)) shows the low tortuous path in z direction, with relatively straight connections between the bottom and top plane of the sample.

4.6. Permeability Simulations on the MPS Generated Rock Models. In Section 3.3, the spatial resolution effect on simulated permeability on the scanned sample set was shown. The results demonstrated that (1) high resolution scans were needed to capture micrometer scale pores which impacted flow properties and that (2) lower-resolution CT scans should be performed on sufficiently large volumes to fully capture the heterogeneity of the pore network. In order to overcome the volume versus resolution problem of CT scanners, MPS-generated rock models are used as input for permeability simulations. The latter allowed assessing the applicability of

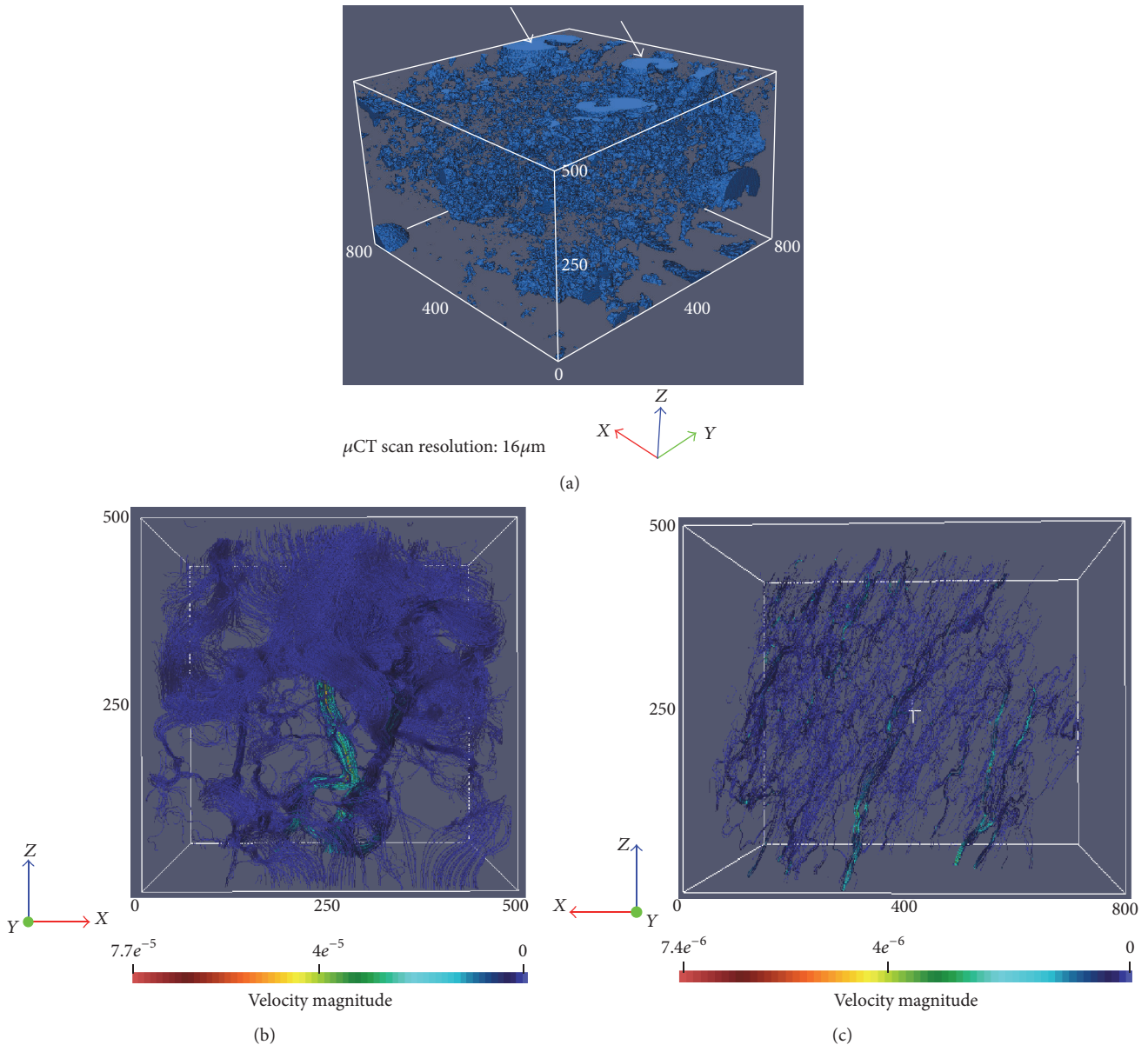


FIGURE 15: (a) Pore network volume rendering of a sample from the subhorizontal facies (800 by 800 by 500 pixels). The majority of the pores are aligned horizontally. Notice that some gastropod molds are present (see arrows). (b) 3D streamline velocity distribution within a sample from the reed facies, with preferential flow in z direction, along vertical tubes, from $z = 0$ to $z = 500$ pixels. (c) 3D streamline velocity distribution within a sample from the waterfall facies, with preferential flow in z direction from $z = 0$ to $z = 500$ pixels. The velocity magnitude is given in nondimensional lattice units.

the MPS workflow in generating larger-volume rock models at higher resolutions.

In order to assess the influence of the above-introduced conditioning data MPS parameter σ on the rock models, a series of simulations were performed using different σ values (Figures 16(a)–16(d)), while keeping all other parameters equal. The simulations were performed on continental carbonate samples from the reed facies. This facies type was chosen because of its typical abundant open porosity network and the characteristic elongated shape of the pore bodies. The latter resulted in permeability values of 50 mD and higher [41]. The TI had a resolution of $4\mu\text{m}$ and the

conditioning dataset had a resolution of $16\mu\text{m}$. Hence, the resulting simulated dataset contained the volume of the larger $16\mu\text{m}$ CT scans, with a higher $4\mu\text{m}$ resolution. The TI had a size of 250^3 pixels or $1000^3\mu\text{m}$. The search template distance is 25 pixels. The servo corrector was kept zero and six multigrids were used. The TI volume was chosen with extra care in order to represent the typical patterns or in this case pore structures. The resulting simulated samples are shown in Figure 16. The shape of the pores corresponded well with pore shapes that were present in the TI. Rod- and blade-shaped pores made up 50% of the pores. Because permeability was measured in the direction of the aligned pore shapes, a

permeability value of around 1000 mD was expected based on petrophysical measurements indicated in Figure 11.

Analyzing the shape of the pores, according to the classification of Claes et al. [66], provided an excellent tool for the quality control of the simulation. Similar pore shape occurrence percentages between the physical sample to be simulated and the MPS simulated sample were indicative of good quality simulations. The results also indicated high dependency on conditioning data in order to retain the desired larger-scale connectivity in the simulated sample. The connectivity of the pore network had a direct influence on the simulated permeability values of the simulated rock samples. The permeability values increased when more conditioning data, that is, lower σ values, were used in the simulation. Simulated permeability values were in the expected range for reed continental carbonate samples, but the most representative permeabilities were found for $\sigma = 0.25$, that is, the largest amount of conditioning data. Large amounts of conditioning data were needed to simulate complex carbonate rocks.

In order to further test the applicability of the workflow, three adjacent volumes of a sample from the subhorizontal facies were simulated using a TI (250^3 pixels) with a resolution of $4 \mu\text{m}$. Figure 17(a) depicts the conditioning data ($1600 \times 1600 \times 800$ pixels) used in a simulation of this facies type, which had a resolution of $16 \mu\text{m}$ and σ value of 0.25. Three different zones were generated using the same TI and the results (800^3 pixels) were depicted in Figures 17(b), 17(c), and 17(d), respectively.

The TI was selected inside a porous layer characteristic for this facies type. The resulting subvolumes had a side length of 3.2 mm and hence depicted only one sedimentary lamina. This explained why the typical horizontal layering of these samples, with porous and less porous layers, was not clearly visible in the simulated volumes. They would only have become visible when the spatial scale of both the TI and simulation grid was increased. The resulting simulated permeability values ranged from 0 mD, in case no connected network was present, to 203 mD. Hence, the permeability values were highly dependent on the provided conditioning data, as was already demonstrated in the reed facies samples in Figure 16. Consistent with the laboratory permeability measurements, the overall values were lower compared to the reed facies (1367 mD for $\sigma = 0.25$, Figure 16(d)). The lower permeabilities in the vertical direction for the subhorizontal facies were in line with the findings in Section 3.5, where permeability was simulated in horizontal and vertical directions. The simulated rock models preserved the characteristic laminated pore structure of the subhorizontal facies, with limited connectivity in the vertical direction.

The unique datasets generated by the HECTOR scans provided an excellent case study to evaluate the potential of the proposed workflow. Because of their detailed resolution ($28 \mu\text{m}$), HECTOR scans delivered excellent TI. The medical CT scan data provided the larger-scale conditioning data and had a resolution of $230 \mu\text{m}$ in x and y directions and $500 \mu\text{m}$ in z direction. This allowed performing petrophysical simulations on core samples. In this case, the difference in TI resolution and conditioning data was more than

doubled compared to the first set of simulations. This allowed simulating artificial samples at a larger spatial scale with a resolution of $28 \mu\text{m}$. Because of the porosity difference between the TI and the generated rock sample, a servo factor of 0.75 was used. If a lower value was used, the porosity value of the simulated rock samples became too high, resulting in visually unrealistic models and unrealistic simulated permeability values. For example, when the reed sample (Figure 18(c)) was simulated using a servo factor of 0, the calculated permeability became 22 D. This observation illustrated the importance of the servo factor, which should be taken higher when the resolution difference increases. A clear difference between the simulated porosity networks of both the reed and subhorizontal facies types was observed. The moldic reed pores were retained in the simulation. In contrast, typical sequences of porous and less porous layers in subhorizontal samples were observed in simulated samples.

The simulation-obtained permeabilities were in the expected order of magnitude compared to measured values. Moreover, the anticipated difference between the subhorizontal and reed facies type pore networks was clearly apparent. In the subhorizontal sample, no open network was present in z direction (K_h shown in Figure 18(a)). Figures 18(b) and 18(d) show the simulation results in which the same TI was used as in Figures 18(a) and 18(c), respectively, but the conditioning data were derived from a different sample of a similar facies type. Simulations with the same TI but different CD demonstrated that the quality of the HECTOR based TI was sufficient to be used on multiple samples.

5. Discussion

CT scanning and computational fluid dynamics (CFD) proved to be excellent tools for the investigation of flow properties in complex continental carbonate pore networks. Different flow properties and paths were observed for different facies types and their characteristic pore types. Consistent with De Boever et al. [16] and Claes et al. [66], the permeability was higher for samples from the reed and waterfall facies. The subhorizontal and cascade facies were characterized by lower permeabilities and often yielded higher permeabilities horizontally in contrast to the vertical direction.

The main factors influencing the permeability in continental carbonates were connected porosity ($\Phi_{c,z}$) and tortuosity (τ). For both variables, a power-law relationship with the permeability was established. However, the determination coefficients (0.75 and 0.66, resp.) revealed data scatter; hence, permeability predictions based on either of these variables alone were not very accurate. τ and $\Phi_{c,z}$ counteracted each other at several occasions, like when porosity would overestimate simulated permeability of a sample and when tortuosity would underestimate it and vice versa. Therefore, more accurate permeability predictions for a given sample were obtained by using (8), which includes both $\Phi_{c,z}$ and τ :

$$K = 43121\tau^{-9.4} + (1.38e^{-4}) * \sqrt[0.2056]{\Phi_{c,z}}. \quad (8)$$

A cross-plot of predicted versus LBM-simulated permeability (determination coefficient of 0.85) illustrates how τ and

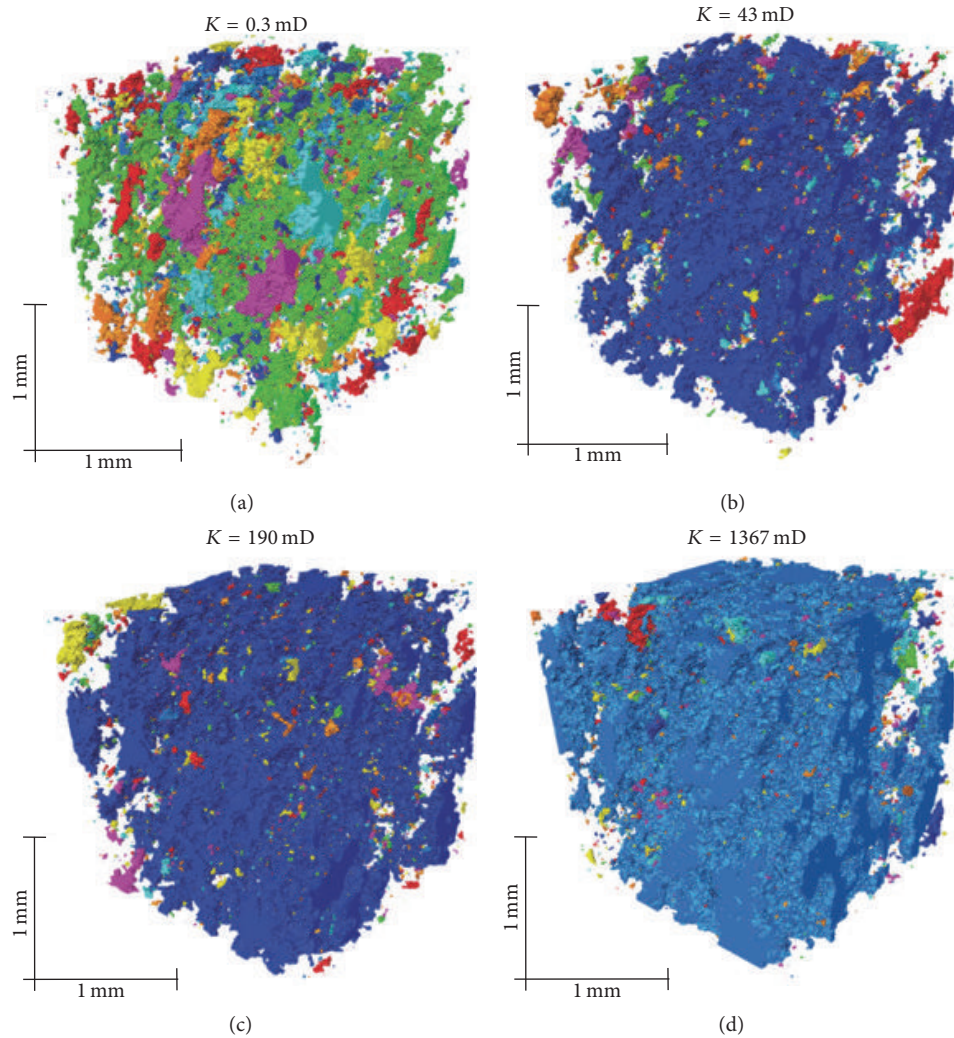


FIGURE 16: Computer-generated models of a reed facies sample with different σ values, which controls the level of conditioning data used. (a) No conditioning data; (b) $\sigma = 0.75$; (c) $\sigma = 0.50$; and (d) the largest amount of conditioning data with $\sigma = 0.25$ (colors indicate connectivity). The more the conditioning data approaches the “truth,” the more the simulated permeability approaches the laboratory measured permeability.

$\phi_{c,z}$ interact in the determination of the permeability of the samples under investigation (Figure 19). LBM-simulated permeability was slightly overestimated by the predicted permeability at low values. The predicted values tend to eliminate the most extreme values, limiting the 0.1–10000 mD simulated permeability range to 0.35–4500 mD in the estimations.

The REV measurements and CFD simulations demonstrated the effect of sample scale and spatial resolution on the permeabilities. Claes (2015) confirmed that different REV sizes can be found at different scales, corresponding to different geological length scales. Here, only pores below plug size were considered in REV analyses. For this pore scale, the porosity REV was reached in all $16 \mu\text{m}$ VOIs, over which permeability simulations were performed. Large-scale framework pores, caverns, and decimeter-sized vugs were, however, also encountered in the field but do not form a part of this research. Increasing the sample scale to include decimeter-sized vugs would drastically increase the REV

size. In general, with increasing sample size, new porosity REV would be encountered whenever new large-scale pore types would be introduced. Macroscopic observations also showed that large-scale framework, cavern, and vug porosity were mainly interconnected through the pores encountered within the studied plugs. The main pore scales governing connectivity and fluid flow at the scale of the carbonate body were therefore expected to be included in this study.

In general, the following can be concluded: the larger the CT analyzed volume and the finer the scan resolution, the more realistic the representation of the pore network. The MPS workflow proposed in this manuscript allows generating artificial rock samples which can be used to investigate the influence of rock heterogeneity on fluid flow dynamics. Moreover, this technique permits bridging the gap between different datasets with different resolutions. The workflow was used on datasets where the resolution of the conditioning data was four and eight times the resolution of the TI. In both cases, the simulations yielded realistic results.

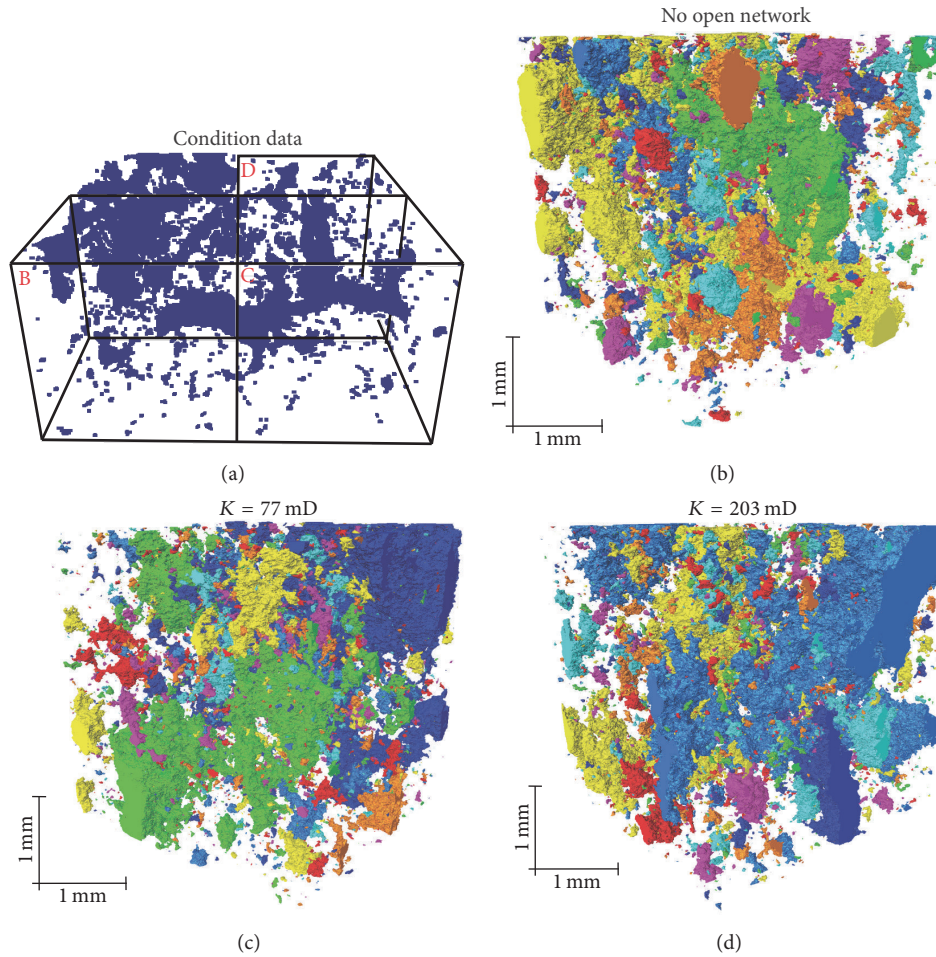


FIGURE 17: Computer-generated models of a subhorizontal facies sample with $\sigma = 0.25$. (a) Conditioning data, with three different subvolumes “B,” “C,” and “D” indicated. (b) Simulated rock model based on the conditioning data in subvolume “B”; (c) simulated rock model based on the conditioning data in subvolume “C”; and (d) simulated rock model based on the conditioning data in subvolume “D.” The same TI is used in each simulation. Similar colors indicate pores that are connected.

The amount of conditioning data, determined by the σ value, and the use of the servo factor proved to be important parameters to obtain realistic simulations. Comparing measured and simulated permeabilities showed that $\sigma = 0.25$ yielded the most realistic pore networks models for the investigated continental carbonate samples. Large amounts of conditioning data were necessary to model pore networks of continental carbonate samples in a representative way. The MPS workflow was applied to upscale from miniplug (diameter 7 mm) to plug (diameter of 3.81 cm) and to large core volumes (diameter of 9.7 cm), but Zhang [67] also proved the applicability of MPS datasets on larger spatial scales such as borehole imaging and facies distribution models in reservoir modelling.

The LBM simulations for generated rock models are plotted on top of the measured relationship between porosity and permeability for continental carbonate plug samples (Figure 20). The simulated volumes were indicated in red. The simulated values follow the general trend and are therefore considered to be realistic.

6. Drawbacks and Future Perspectives

As with all modelling techniques, there are some drawbacks to this research even though efforts are made to reduce them. In this paper, the choice for fluid flow modelling techniques and upscaling approaches is based on the need for correctly representing the porous network. This is achieved by avoiding simplifications as much as possible. In first instance, this is evidenced by the chosen CFD method. The LBM approach is chosen as it offers a good trade-off between computational power and representativeness. In LBM, the fluids are represented as small packages in individual voxels rather than as individual molecules. The actual pore network is used in the simulations rather than simplifications that pore topology models typically use. In order to obtain realistic permeability simulations, representative pore networks are preferred, even though simplifications would decrease the computational cost drastically.

Secondly, the choice was made to improve resolution of spatially larger models rather than simplifying the problem

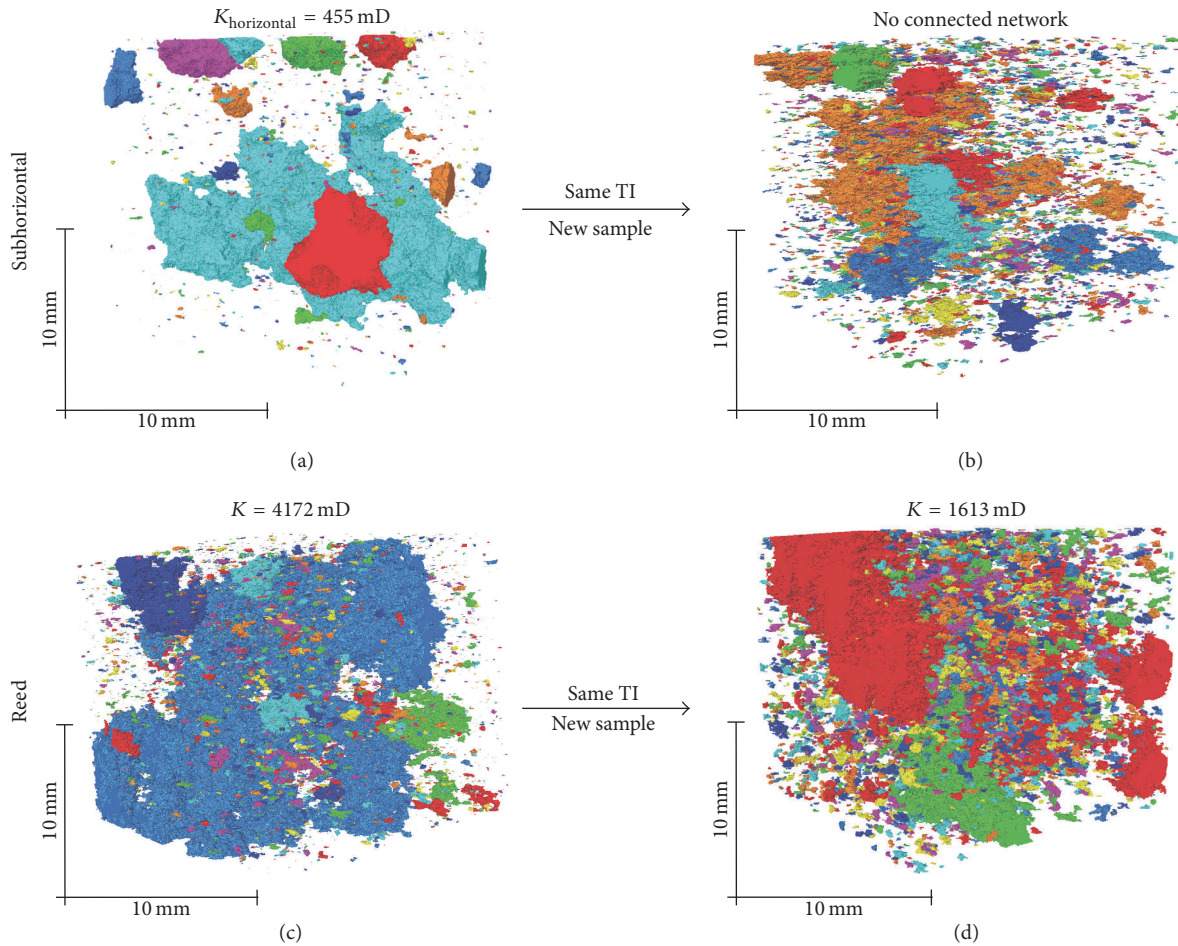


FIGURE 18: Computer-generated models based on a TI of a HECTOR scan (resolution of $28 \mu\text{m}$) and conditioning data based on medical CT data. (a) Subhorizontal sample with TI and conditioning data based on the same sample. (b) Subhorizontal sample with TI and conditioning data based on a different sample. (c) Reed sample with TI and conditioning data based on the same sample. (d) Reed sample with TI and conditioning data based on a different sample. The colors indicate pore connectivity.

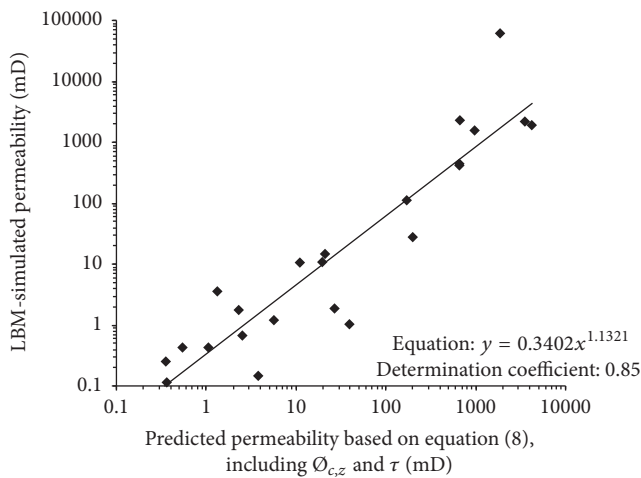


FIGURE 19: Predicted versus simulated permeabilities. The predicted permeabilities are based on an average between the permeability calculated from tortuosity and connected porosity for each sample.

through classical upscaling techniques that smoothen out small-scale variations. This choice is made based on the rationale that small-scale features, variations, and heterogeneities hold the information that can determine large-scale reservoir properties. This rationale is not only relevant in, for example, unconventional reservoirs, but also in carbon capture and storage (CCS), in which the smallest pores are used for capillary capture of fluids.

The use of multiple-point statistics in upscaling is still a relatively new approach and as such a methodology which is not yet perfected. Known issues include the determination of input parameters in the SNESim algorithm and its computational requirements. A lot of parameters, like the number of multigrids, search template size, and λ parameter, have to be adjusted in the SNESim algorithm, which introduces subjectivity into the models. To avoid subjectivity as much as possible, the workflow is here calibrated with physical laboratory experiments. Visual inspection is always applied on the results to ensure that (1) a good fit between simulated

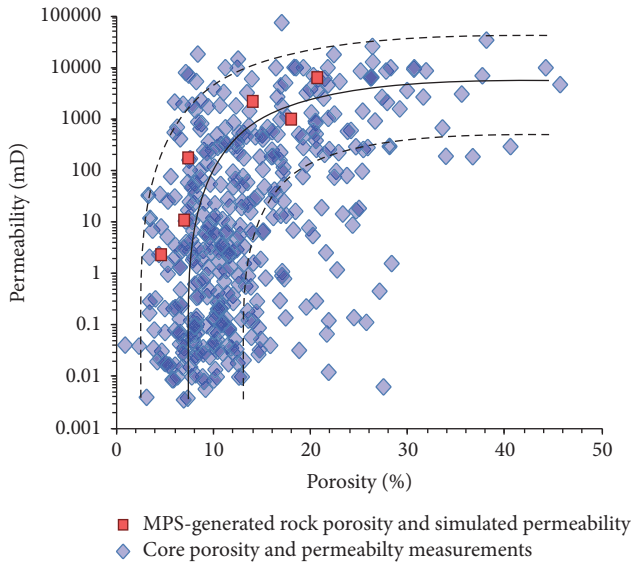


FIGURE 20: Porosity-permeability plot of continental carbonate samples: Palabos permeability simulation results on computer-generated rock volumes are indicated in red.

properties and physical measurements is obtained and that (2) models are geologically relevant.

Apart from visual inspection, it is observed that the σ -parameter for conditioning data is best kept constant for specific upscaling problems. A σ -parameter of 0.25 is an ideal value when the resolution for the TI and conditioning data differs with a factor of 4. A σ -parameter of 0.75 proved to be more appropriate for a factor of 8 resolution difference. This difference in the σ -parameter is logical given the difference in the amount of overlap in the samples. Another drawback is that even when applying the σ -factor, it sometimes occurs that new larger pores are unnecessarily generated. The larger pores are, however, expected to be sufficiently represented in the lower-resolution scans. The training images are chosen at 250^3 voxels, which is smaller than the REV, to limit the computational cost. The selection of these smaller training images was user-controlled in order to select highly representative zones. The quality of the TI therefore will not be compromised by the smaller size.

The final drawback of any upscaling technique that aims to increase resolution, while also increasing scale, is computational cost. For example, increasing the resolution by a factor of 4 increases the required storage space by a factor of 4^3 . Such volumes might easily exceed the abilities of standard workstations to model fluid flow. Because of the computer power limitation, this research focused on μ CT and HECTOR scans, which yield sample volumes smaller than the outcrop scale macropores that are regularly present in carbonates. Such oversized pores potentially influence large-scale fluid flow and can thus be important components in reservoir models. Even though these pores have not been treated here, they could be incorporated into models with the proposed reservoir scale upscaling purpose, as it is intrinsically scale-invariant. There is, ad hoc, no method that allows imaging of oversized pores three-dimensionally. MPS

input data such as training images or conditioning data could nevertheless be created through photogrammetry or LiDAR [68, 69] or through methods that use 2D input data like field pictures to generate 3D volumes, similar to Okabe and Blunt [35]. Generating models that include macropores observed at outcrop scale, that is, vugs, framework porosity, caverns, and fractures, can significantly increase the sensitivity towards reservoir scale fluid flow. Outcrop scale and plug to core scale models, however, have to be considered separately, since incorporating all elements of a multiscale pore system would make the models extremely large and computationally expensive.

The future of MPS-driven upscaling techniques should aim to reduce subjective parameters as much as possible. Both this research and the research by Zhang [67] indicate that MPS is a potent method in upscaling of reservoir properties, but neither of these approaches provides the most solid solution. For fluid flow experiments on increasingly larger models, it might be required to use intensive parallel computing, apply modified versions of the LBM, or use pore network models with microlinks [24] in order not to nullify the increased resolution.

7. Conclusion

Transport properties are fundamental in the characterization of reservoir bodies. In this study, computed tomography of continental carbonate samples and Lattice Boltzmann Method (LBM) permeability simulations were applied to obtain 3D quantifications of the pore network and flow paths. Working with 3D datasets was an absolute necessity to understand flow in complex continental carbonates, because accurate estimates of properties which govern fluid flow in a rock, that is, connectivity, tortuosity, and so forth, could not be obtained from 2D observations. The simulated permeabilities were in good agreement with physical plug and core permeabilities. Power-law relationships were observed between permeability and connected porosity on one hand and permeability and tortuosity on the other hand. Estimates of rock permeability for a sample were strongly improved by including both tortuosity and connected porosity. Both parameters balance one another, and so their integration allows better prediction of the fluid flow through the complex porous network of continental carbonate samples.

The subhorizontal and cascade facies were associated with pseudofenestral and interpeloidal pores and yielded the lowest porosities and permeabilities. The reed and waterfall facies, with, respectively, reed moldic and framework porosity, were characterized by much better reservoir properties. The resulting porosities easily surpassed 30% and exceeded 50 D, in both measured and simulated permeabilities. Facies and pore type-dependent heterogeneity was observed. Better horizontal connectivity and permeability for the subhorizontal and cascade facies were in contrast to the generally higher vertical permeabilities that were observed for samples from the reed and waterfall facies.

The proposed multiple-point geostatistics (MPS) workflow is an additional tool to solve common problems in the upscaling of reservoir properties. An additional advantage

of this scale-independent approach is its applicability on 2D as well as 3D datasets. MPS does not introduce general averaging that is commonly used in upscaling.

The workflow allowed upscaling to realistic models at different scales by starting from detailed, high-resolution information and incorporating it into larger-scale models. Moreover, using recent advances in fluid flow models, this workflow has the potential to replace expensive permeability measurements on large core samples and can serve as input for simulations of multiphase fluid flow. The results have also indicated that the TI image can be used for different samples of the same facies type. This would allow scanning samples more quickly using conventional medical CT scanners. When a more detailed description of a part of the pore network is desired, a pore model can be generated using this workflow.

The here-presented innovative and integrated LBM-MPS workflow was applied in continental carbonate rocks with complex pore networks. The methodology is directly applicable to other lithologies, comprising different pore types, pore shapes, and pore networks altogether. The lack of straightforward porosity-permeability relationships in complex carbonates highlights the necessity for a 3D approach. Studying fluid pathways in 3D provides the best possible understanding of flow through porous media and will be of crucial importance in reservoir modelling.

Conflicts of Interest

The authors declare that there are no conflicts of interest regarding the publication of this paper.

Acknowledgments

The authors thank the owners and managers of the respective quarries for allowing them to work in actively excavated environments, which provided insight into the 3D pore networks of the continental carbonate rocks. They would like to thank Herman Nijs for aiding in practical matters during the sample preparation processes. The authors would like to acknowledge the Hercules Foundation (Flanders) for founding the micro- and nano-CT project for the hierarchical analysis of materials. J. Soete was funded by a Ph.D. grant from “Agentschap voor Innovatie door Wetenschap en Technologie” (IWT), Flanders, Belgium. Last but not least, they would like to thank Professor Mehmet Özkul and Sándor Kele for their help and the interesting discussions during the field trips in Turkey and Hungary.

References

- [1] H. Claes, J. Soete, K. Van Noten et al., “Sedimentology, three-dimensional geobody reconstruction and carbon dioxide origin of Pleistocene travertine deposits in the Ballik area (south-west Turkey),” *Sedimentology*, vol. 62, no. 5, pp. 1408–1445, 2015.
- [2] J. G. S. Terra, A. R. Spadini, A. B. França et al., “Classificações clássicas de rochas carbonáticas,” *Boletim Geociências Petrobras*, vol. 18, no. 1, pp. 9–29, 2010.
- [3] V. P. Wright, “Lacustrine carbonates in rift settings: The interaction of volcanic and microbial processes on carbonate deposition,” *Geological Society Special Publication*, vol. 370, no. 1, pp. 39–47, 2012.
- [4] A. Saller, S. Rushton, L. Buambua, K. Inman, R. McNeil, and J. A. D. Dickson, “Presalt stratigraphy and depositional systems in the Kwanza Basin, offshore Angola,” *AAPG Bulletin*, vol. 100, no. 7, pp. 1135–1164, 2016.
- [5] S. Schröder, A. Ibekwe, M. Saunders, R. Dixon, and A. Fisher, “Algal–microbial carbonates of the Namibe Basin (Albian, Angola): Implications for microbial carbonate mound development in the South Atlantic,” *Petroleum Geoscience*, vol. 22, no. 1, pp. 71–90, 2016.
- [6] I. Sharp, K. Verwer, H. Ferreira et al., “Pre- and Post-Salt Non-Marine Carbonates of the Namibe Basin, Angola,” in *Microbial Carbonates in Space and Time: Implications for Global Exploration and Production*, pp. 52–53, The Geological Society, London, UK, 19–20 June 2013.
- [7] T. D. Ford and H. M. Pedley, “A review of tufa and travertine deposits of the world,” *Earth-Science Reviews*, vol. 41, no. 3–4, pp. 117–175, 1996.
- [8] B. W. Fouke, J. D. Farmer, D. J. Des Marais et al., “Depositional facies and aqueous-solid geochemistry of travertine-depositing hot springs (Angel Terrace, Mammoth Hot Springs, Yellowstone National Park, U.S.A.),” *Journal of Sedimentary Research*, vol. 70, no. 3, pp. 565–585, 2000.
- [9] L. Guo and R. Riding, “Hot-spring travertine facies and sequences, Late Pleistocene, Rapolano Terme, Italy,” *Sedimentology*, vol. 45, no. 1, pp. 163–180, 1998.
- [10] S. Kele, M. Özkul, I. Fórizs et al., “Stable isotope geochemical study of Pamukkale travertines: New evidences of low-temperature non-equilibrium calcite-water fractionation,” *Sedimentary Geology*, vol. 238, no. 1–2, pp. 191–212, 2011.
- [11] H. M. Pedley and M. Rogerson, *Tufas and Speleothems Unraveling the Microbial and Physical Controls*, 362, Geological Society, London, UK, 2010.
- [12] A. Pentecost, *Travertine*, Springer, 2005.
- [13] M. Özkul, S. Kele, A. Gökgöz et al., “Comparison of the Quaternary travertine sites in the Denizli extensional basin based on their depositional and geochemical data,” *Sedimentary Geology*, vol. 294, pp. 179–204, 2013.
- [14] H. Claes, M. Degros, J. Soete et al., “Geobody architecture, genesis and petrophysical characteristics of the Budakalász travertines, Buda Hills (Hungary),” *Quaternary International*, pp. 1–22, 2016.
- [15] H. Claes, M. Marques Erthal, J. Soete, M. Özkul, and R. Swennen, “Shrub and pore type classification: Petrography of travertine shrubs from the Ballik-Belevi area (Denizli, SW Turkey),” *Quaternary International*, vol. 437, pp. 147–163, 2017.
- [16] E. De Boever, A. Foubert, D. Oligschlaeger et al., “Multi-scale approach to (micro)porosity quantification in continental spring carbonate facies: Case study from the Cakmak quarry (Denizli, Turkey),” *Geochemistry, Geophysics, Geosystems*, vol. 17, no. 7, pp. 2922–2939, 2016.
- [17] M. M. Erthal, E. Capezzuoli, A. Mancini, H. Claes, J. Soete, and R. Swennen, “Shrub morpho-types as indicator for the water flow energy - Tivoli travertine case (Central Italy),” *Sedimentary Geology*, vol. 347, pp. 79–99, 2017.
- [18] S. Khatib, P. Rochette, M. C. Alçiçek, A.-E. Lebatard, F. Demory, and T. Saos, “Études stratigraphique, sédimentologique et paléomagnétique des travertins de Kocabaş, Bassin de Denizli, Anatolie, Turquie, contenant des restes fossiles quaternaires,” *L’Anthropologie*, vol. 118, no. 1, pp. 16–33, 2014.

- [19] A.-E. Lebatard, M. C. Alçiçek, P. Rochette et al., “Dating the Homo erectus bearing travertine from Kocabaş (Denizli, Turkey) at at least 1.1 Ma,” *Earth and Planetary Science Letters*, vol. 390, pp. 8–18, 2014.
- [20] P. Ronchi and F. Cruciani, “Continental carbonates as a hydrocarbon reservoir, an analog case study from the travertine of Saturnia, Italy,” *AAPG Bulletin*, vol. 99, no. 4, pp. 711–734, 2015.
- [21] J. Soete, L. M. Kleipool, H. Claes et al., “Acoustic properties in travertines and their relation to porosity and pore types,” *Marine and Petroleum Geology*, vol. 59, pp. 320–335, 2015.
- [22] J. Soete, *Pore network characterization in complex carbonate systems, a multidisciplinary approach [Ph.D. Thesis]*, Department Geography-Geology, Faculty of Sciences, KU Leuven, Belgium, 2016.
- [23] J. Bear, *Dynamics of Fluids in Porous Media*, Dover Publications, Mineola, New York, USA, 1972.
- [24] T. Bultreys, L. Van Hoorebeke, and V. Cnudde, “Multi-scale, micro-computed tomography-based pore network models to simulate drainage in heterogeneous rocks,” *Advances in Water Resources*, vol. 78, pp. 36–49, 2015.
- [25] W. Degruyter, O. Bachmann, and A. Burgisser, “Controls on magma permeability in the volcanic conduit during the climactic phase of the Kos Plateau Tuff eruption (Aegean Arc),” *Bulletin of Volcanology*, vol. 72, no. 1, pp. 63–74, 2010.
- [26] W. Degruyter, A. Burgisser, O. Bachmann, and O. Malaspina, “Synchrotron X-ray microtomography and lattice Boltzmann simulations of gas flow through volcanic pumices,” *Geosphere*, vol. 6, no. 5, pp. 470–481, 2010.
- [27] J. Domitner, C. Hölzl, A. Kharicha et al., “3D simulation of interdendritic flow through a Al-18wt.%Cu structure captured with X-ray microtomography,” in *Proceedings of IOP Conference Series: Materials Science and Engineering*, vol. 27, June 2011.
- [28] H. Dong, S. Fjeldstad, L. Alberts, S. Roth, S. Bakke, and P. Øren, “Pore network modelling on carbonate: A comparative study of different micro-CT network extraction methods,” in *Proceedings of the International Symposium of the Society of Core Analysts*, pp. 1–12, 2008.
- [29] B. Ferréol and D. H. Rothman, “Lattice-Boltzmann simulations of flow through Fontainebleau sandstone,” *Transport in Porous Media*, vol. 20, no. 1-2, pp. 3–20, 1995.
- [30] FlowKit Ltd, “Palabos, Parallel Lattice Boltzmann Solver,” 2011–2012, <http://www.lbmethod.org/palabos>.
- [31] P. Ringrose and M. Bentley, *Reservoir Model Design: A Practitioner's Guide*, Springer, Dordrecht, The Netherlands, 2015.
- [32] S. B. Strebelle and A. G. Journel, “Reservoir Modeling Using Multiple-Point Statistics,” in *Proceedings of the SPE Annual Technical Conference and Exhibition*, Society of Petroleum Engineers, New Orleans, Louisiana, USA, 2001.
- [33] G. Mariethoz, J. Straubhaar, P. Renard, T. Chugunova, and P. Biver, “Constraining distance-based multipoint simulations to proportions and trends,” *Environmental Modelling and Software*, vol. 72, pp. 184–197, 2015.
- [34] M. Huysmans and A. Dassargues, “Modeling the effect of clay drapes on pumping test response in a cross-bedded aquifer using multiple-point geostatistics,” *Journal of Hydrology*, vol. 450–451, pp. 159–167, 2012.
- [35] H. Okabe and M. J. Blunt, “Prediction of permeability for porous media reconstructed using multiple-point statistics,” *Physical Review E*, vol. 70, no. 6, Article ID 066135, p. 066135/10, 2004.
- [36] J. Caers and T. Zhang, “Multiple-point geostatistics: a quantitative vehicle for integrating geologic analogs into multiple reservoir models,” in *Integration of Outcrop and Modern Analogs in Reservoir Modeling*, G. M. Grammer, P. M. Harris, and G. P. Eberli, Eds., vol. 80, pp. 383–394, AAPG Memoir, 2004.
- [37] A. Journel and T. Zhang, “The necessity of a multiple-point prior model,” *Mathematical Geology*, vol. 38, no. 5, pp. 591–610, 2006.
- [38] Z. Jiang, M. I. J. Van Dijke, K. S. Sorbie, and G. D. Couples, “Representation of multiscale heterogeneity via multiscale pore networks,” *Water Resources Research*, vol. 49, no. 9, pp. 5437–5449, 2013.
- [39] K. M. Gerke, M. V. Karsanina, and D. Mallants, “Universal stochastic multiscale image fusion: An example application for shale rock,” *Scientific Reports*, vol. 5, Article ID 15880, pp. 1–13, 2015.
- [40] J. Yao, C. Wang, Y. Yang, R. Hu, and X. Wang, “The construction of carbonate digital rock with hybrid superposition method,” *Journal of Petroleum Science and Engineering*, vol. 110, pp. 263–267, 2013.
- [41] E. De Boever, A. Foubert, B. Lopez et al., “Comparative study of the Pleistocene Cakmak quarry (Denizli Basin, Turkey) and modern Mammoth Hot Springs deposits (Yellowstone National Park, USA),” *Quaternary International*, 2016.
- [42] Á. Török, A. Mindszenty, H. Claes, S. Kele, L. Fodor, and R. Swennen, “Geobody architecture of continental carbonates: “Gazda” travertine quarry (Sütto, Gerecse Hills, Hungary),” *Quaternary International*, pp. 1–22, 2016.
- [43] V. Cnudde and M. N. Boone, “High-resolution X-ray computed tomography in geosciences: a review of the current technology and applications,” *Earth-Science Reviews*, vol. 123, pp. 1–17, 2013.
- [44] K. A. Alshibli and A. H. Reed, *Advances in Computed Tomography for Geomaterials: GeoX 2010*, Wiley-ISTE, 2010.
- [45] D. Wildenschild and A. P. Sheppard, “X-ray imaging and analysis techniques for quantifying pore-scale structure and processes in subsurface porous medium systems,” *Advances in Water Resources*, vol. 51, pp. 217–246, 2013.
- [46] K. Remeysen and R. Swennen, “Application of microfocus computed tomography in carbonate reservoir characterization: Possibilities and limitations,” *Marine and Petroleum Geology*, vol. 25, no. 6, pp. 486–499, 2008.
- [47] B. Masschaele, M. Dierick, D. V. Loo et al., “HECTOR: A 240kV micro-CT setup optimized for research,” *Journal of Physics: Conference Series*, vol. 463, no. 1, Article ID 012012, 2013.
- [48] J. Vlassenbroeck, M. Dierick, B. Masschaele, V. Cnudde, L. Van Hoorebeke, and P. Jacobs, “Software tools for quantification of X-ray microtomography at the UGCT,” in *Proceedings of the 10th International Symposium on Radiation Physics (ISRP'10)*, vol. 580, pp. 442–445, Nuclear Instruments and Methods in Physics Research, Section A: Accelerators, Spectrometers, Detectors and Associated Equipment, 2007.
- [49] S. Claes, *Pore classification system and upscaling strategy in travertine reservoir rocks [Ph.D. Thesis]*, Department Geography-Geology, Faculty of Sciences, KU Leuven, Belgium, 2015.
- [50] A. G. Journel, “Geostatistics: roadblocks and challenges,” in *Geostatistics Tróia '92*, A. Soares, Ed., vol. 5 of *Quantitative Geology and Geostatistics*, pp. 213–224, Kluwer Academic Publications, Dordrecht, The Netherlands, 1993.
- [51] F. B. Guardiano and R. M. Srivastava, “Multivariate Geostatistics: Beyond Bivariate Moments,” in *Geostatistics Tróia '92*, A.

- Soares, Ed., vol. 5 of *Quantitative Geology and Geostatistics*, pp. 133–144, Kluwer Academic Publications, Dordrecht, The Netherlands, 1993.
- [52] S. B. Strebelle, *Sequential Simulation Drawing Structures from Training Images [Ph.D. Thesis]*, Stanford University, 2000.
- [53] Y. Liu, “Using the Snesim program for multiple-point statistical simulation,” *Computers and Geosciences*, vol. 32, no. 10, pp. 1544–1563, 2006.
- [54] E. Meerschman, G. Pirot, G. Mariethoz, J. Straubhaar, M. Van Meirvenne, and P. Renard, “A practical guide to performing multiple-point statistical simulations with the Direct Sampling algorithm,” *Computers and Geosciences*, vol. 52, pp. 307–324, 2013.
- [55] T. T. Tran, “Improving variogram reproduction on dense simulation grids,” *Computers and Geosciences*, vol. 20, no. 7-8, pp. 1161–1168, 1994.
- [56] R. Mei, W. Shyy, D. Yu, and L.-S. Luo, “Lattice Boltzmann method for 3-D flows with curved boundary,” *Journal of Computational Physics*, vol. 161, no. 2, pp. 680–699, 2000.
- [57] J. Latt and M. J. Krause, “OpenLB User Guide,” 2006–2015, <http://optilb.com/openlb>.
- [58] T. J. Pedley, “Introduction to fluid dynamics,” *Scientia Marina*, vol. 61, no. 1, pp. 7–24, 1997.
- [59] R. W. Fox, A. T. McDonald, and P. J. Pritchard, *Introduction to Fluid Mechanics*, John Wiley and Sons, 7th edition, 2006.
- [60] J. Latt, “Choice of units in lattice Boltzmann simulations,” 2008, <http://www.palabos.org>.
- [61] Y. Watanabe and Y. Nakashima, “RW3D.m: Three-dimensional random walk program for the calculation of the diffusivities in porous media,” *Computers and Geosciences*, vol. 28, no. 4, pp. 583–586, 2002.
- [62] Y. Nakashima and T. Yamaguchi, “DMAP.m: A Mathematica® program for three-dimensional mapping of tortuosity and porosity of porous media,” *Bulletin of the Geological Survey of Japan*, vol. 55, no. 3-4, pp. 93–103, 2004.
- [63] C. J. Gommers, A.-J. Bons, S. Blacher, J. H. Dunsmuir, and A. H. Tsou, “Practical methods for measuring the tortuosity of porous materials from binary or gray-tone tomographic reconstructions,” *AIChE Journal*, vol. 55, no. 8, pp. 2000–2012, 2009.
- [64] N. Remy, A. Boucher, and J. Wu, *Applied Geostatistics with SGeMS: A User’s Guide*, Cambridge University Press, 2009.
- [65] C. Bouvet de Maisonneuve, O. Bachmann, and A. Burgisser, “Characterization of juvenile pyroclasts from the Kos Plateau Tuff (Aegean Arc): Insights into the eruptive dynamics of a large rhyolitic eruption,” *Bulletin of Volcanology*, vol. 71, no. 6, pp. 643–658, 2009.
- [66] S. Claes, J. Soete, V. Cnudde, and R. Swennen, “A three-dimensional classification for mathematical pore shape description in complex carbonate reservoir rocks,” *Mathematical Geosciences*, vol. 48, no. 6, pp. 619–639, 2016.
- [67] T. Zhang, “MPS-Driven Digital Rock Modeling and Upscaling,” *Mathematical Geosciences*, vol. 47, no. 8, pp. 937–954, 2015.
- [68] D. Hodgetts, “Laser scanning and digital outcrop geology in the petroleum industry: A review,” *Marine and Petroleum Geology*, vol. 46, pp. 335–354, 2013.
- [69] A. Pickel, J. D. Frechette, A. Comunian, and G. S. Weissmann, “Building a training image with Digital Outcrop Models,” *Journal of Hydrology*, vol. 531, pp. 53–61, 2015.

Review Article

Flow and Transport in Tight and Shale Formations: A Review

Amgad Salama,¹ Mohamed F. El Amin,² Kundan Kumar,³ and Shuyu Sun⁴

¹University of Regina, Regina, SK, Canada

²Effat University, Jeddah, Saudi Arabia

³University of Bergen, Bergen, Norway

⁴King Abdullah University of Science and Technology, Thuwal, Saudi Arabia

Correspondence should be addressed to Amgad Salama; amgad.salama@uregina.ca

Received 23 April 2017; Accepted 24 July 2017; Published 18 September 2017

Academic Editor: Andri Stefansson

Copyright © 2017 Amgad Salama et al. This is an open access article distributed under the Creative Commons Attribution License, which permits unrestricted use, distribution, and reproduction in any medium, provided the original work is properly cited.

A review on the recent advances of the flow and transport phenomena in tight and shale formations is presented in this work. Exploration of oil and gas in resources that were once considered inaccessible opened the door to highlight interesting phenomena that require attention and understanding. The length scales associated with transport phenomena in tight and shale formations are rich. From nanoscale phenomena to field-scale applications, a unified frame that is able to encounter the varieties of phenomena associated with each scale may not be possible. Each scale has its own tools and limitations that may not, probably, be suitable at other scales. Multiscale algorithms that effectively couple simulations among various scales of porous media are therefore important. In this article, a review of the different length scales and the tools associated with each scale is introduced. Highlights on the different phenomena pertinent to each scale are summarized. Furthermore, the governing equations describing flow and transport phenomena at different scales are investigated. In addition, methods to solve these equations using numerical techniques are introduced. Cross-scale analysis and derivation of linear and nonlinear Darcy's scale laws from pore-scale governing equations are described. Phenomena occurring at molecular scales and their thermodynamics are discussed. Flow slippage at the nanosize pores and its upscaling to Darcy's scale are highlighted. Pore network models are discussed as a viable tool to estimate macroscopic parameters that are otherwise difficult to measure. Then, the environmental aspects associated with the different technologies used in stimulating the gas stored in tight and shale formations are briefly discussed.

1. Introduction

The problems associated with the scarcity of energy resources are intensified by the increased level of demands. Human beings are nowadays consuming more energy resources than ever before. Three fossil fuels, namely, petroleum, natural gas, and coal, have provided more than 80% of total US energy consumption for more than a century, EIA [1]. The depletion of energy resources from fossil fuels has reached alarming levels that necessitate decision-makers, research institutes, and industry to search for alternative energy resources. It seems, however, that mankind is not yet in the position to abandon totally his dependence on energy from fossil resources. In 2015, the renewable share of energy consumption in the United States was at its largest at nearly 10%, EIA [1]. The vast majority of our energy demands are satisfied by energy from fossil resources. Other energy resources (e.g.,

from renewable sources) may not be sufficient to supply our energy needs. Furthermore, most of our machinery, transportation, and devices are adapted to utilize energy from fossil resources. Therefore, there is still a trend to continue draining resources of fossil fuels to the last drop. Oil and gas resources can be divided in terms of their accessibility into conventional and unconventional resources. In the last decade, when the price of the oil exceeded considerably \$100, it became economic to search for oil/gas resources in hardly accessible reservoirs using unconventional technologies. Although many of these projects have, nowadays, stopped due to the current decline in oil price, they are expected to resume once the price of the oil climbs up again. Based on projections in the US production of oil and gas from unconventional resources, tight oil production is expected to reach 7 million barrels per day and shale-gas production is expected to reach 79 billion cubic feet per day in 2040.

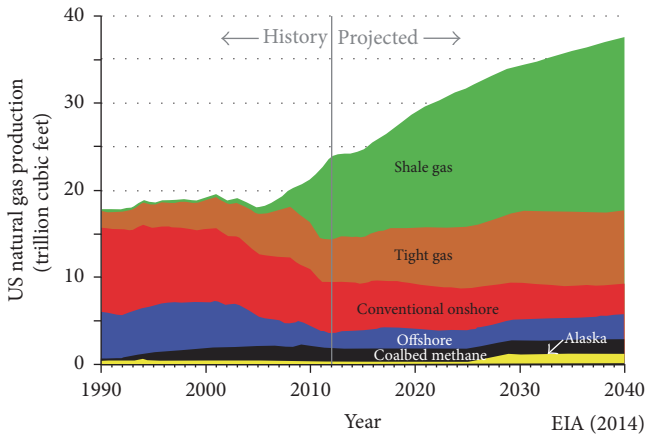


FIGURE 1: Projected growth of US shale-gas production [2].

Such increase in the production of tight oil and shale gas is driven by technological improvements that have reduced drilling costs and improved drilling efficiency. Figure 1 shows projected growth of the US shale-gas production until 2040, EIA [2]. New technologies have indeed increased our capacity to acquire resources that have once been thought inaccessible. In other words, energy resources that are easily accessible no longer exist and, nowadays, the search has been for resources that require larger investment and new technologies that are able to mine and to transport these resources at reasonable costs.

In the oil and gas industry, the types of oil and gas deposits are classified into what are called plays (Figure 2). Such plays are categorized based on many factors including the geology and the technology required to produce the oil. As seen in Figure 2, the fringe regions surrounding the area of historical production (halo zone) are likely to contain oil. The reason they have not been included with the early production region may be that the geologic properties are not as favorable as those within previously producing areas. Different technologies are used for different plays. To displace the oil contained in the halo zones, new technologies including horizontal wells have been used. The geologic formations in the halo zone are generally characterized by lower permeability. Therefore, oil reservoirs, in which geologic formations are of lower permeability (i.e., tight), require newer technologies to get access to oil reserves and also to be able to displace the oil. The distinction between conventional and unconventional reservoirs has been, in most cases, based on formation permeability. Unconventional reservoirs are acquired using horizontal wells as compared with vertical wells that have been traditionally used in conventional reservoirs. The purpose of drilling a horizontal well as compared with vertical wells is to increase the contact area between the reservoir and the wellbore. The horizontal leg of the well can extend up to 5 km. To stimulate tight oil reservoirs once the well has been drilled, hydraulic fracturing is used. In this process, fluids are pumped into the wellbore at very high pressure to open existing fractures or to create new ones. Through these fractures, oil can flow to the wellbore (Figure 3). The types of fracture fluids vary depending on the reservoir formations

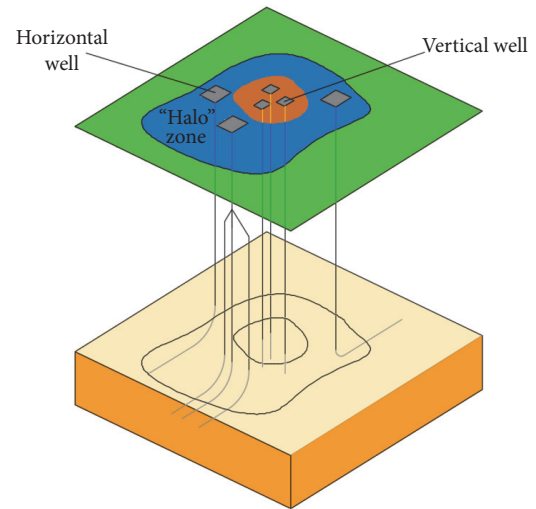


FIGURE 2: Oil reservoirs are divided into plays, each of which bears particular characteristics. The region in which oil/gas reserves are easily accessible with conventional technology is called conventional play, whereas those inaccessible regions surrounding conventional play are called unconventional play. They require unconventional technologies to access the oil/gas reserves. At the early stage of production of oil and/or gas from a reservoir, easily accessible oil and gas flow relatively easy to the production wells. When such oil and/or gas are depleted, oil and gas in the halo region are considered. Modified from the Canadian Society for Unconventional Resources.

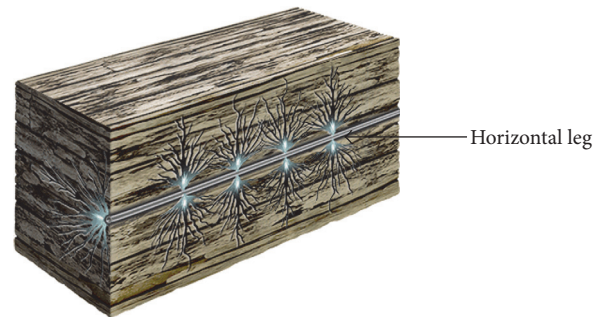


FIGURE 3: Horizontal wells are used in unconventional reservoirs because they provide larger area of contact with the formations. The horizontal leg of the well is perforated and a fluid under considerably higher pressure is injected to stimulate the formation of fractures (adapted from <http://fracfocus.ca/>).

with the water representing the base fluid. Additives (0.5% to 2% of the total fracturing fluid volume) are added to the water to reduce friction, control microorganism growth, and prevent corrosion. To maintain the fractures open during the production, sand particles (proppants) are pumped with the fracturing fluids. The volume of fracturing fluids and the amount of proppant used of hydraulic fracturing vary depending on the required rate of production.

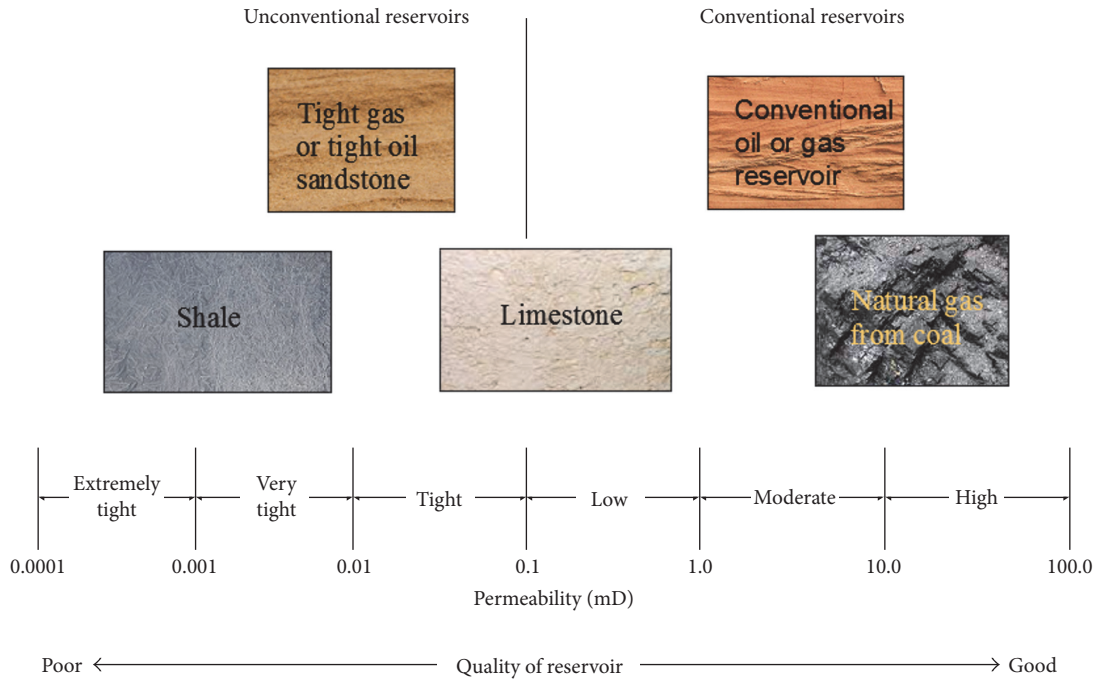


FIGURE 4: The classifications of oil and gas reservoirs as conventional and unconventional may be dependent on the permeability contrast. In formations where the permeability of host rock is quite small, unconventional technologies are required to increase productivity, which are otherwise uneconomical using conventional technologies.

2. Characteristics of Tight and Shale Formations

Tight and shale formations are rocks with pores so small or poorly connected that the oil and natural gas cannot flow through them easily. In these formations, hydrocarbons in the form of crude oil, natural gas, and natural gas liquids may exist in considerable quantities. Like all hydrocarbons, they formed over millions of years, when organic material (e.g., plants and microorganisms) was buried and subjected to increasing heat and pressure and slowly transformed to oil and natural gas. Some of these hydrocarbons escaped into adjacent rock layers that are relatively easy to extract because of their relatively higher porosity and permeability. However, the majority remained locked in tighter, lower permeability layers where they could not be extracted through conventional means. The classification of petroleum reservoirs into conventional and unconventional is in part related to the technology used to extract entrapped oil and gas. Conventional oil reservoirs are those where the geologic formations are characterized by relatively higher permeability that allows easy transport of oil/gas reserves. On the contrary, unconventional reservoirs are characterized by permeability which is much lower such that conventional techniques to displace the oil/gas may not work. Figure 4 shows a schematic diagram of the classification of geologic formations according to their permeability.

Shale formations are one of the tightest rock formations in terms of their permeability. Most of the oil and gas reserves exist in an organic portion of rock mass called kerogen. Figure 5 shows an aerial view of shale sample where

a kerogen area exists. The kerogen region is highly porous where shale gas exists in the pore space and adsorbed at the surface. Organic matter consists of kerogen (~90%) and bitumen (~10%). Figure 6 shows a schematic diagram for the composition of typical shale formation. As indicated by Bohacs et al. [3], Prasad et al. [4], Passey et al. [5], Wang and Cao [6], and others, when kerogen matures, it produces oil and gas. Kerogen does not have a specific structure as it is a mixture of organic materials in which the chemical compounds can vary from one sample to another. Kerogen maturation occurs when it is subjected to higher temperature for longer periods of time. Thermal decomposition breaks small molecules leaving behind a more resistant kerogen residue. The smaller molecules become eventually natural gas.

3. Characteristic Length Scales

Porous media exist almost everywhere around us from naturally occurring media to manmade systems. They encounter a larger spectrum of length scales ranging between global and regional scales all the way towards micro- and even nanoscales. Groundwater, petroleum, and geothermal reservoirs are examples of such larger size domains whereas cells, membranes, and living organisms are examples of micro- and nanosize domains. Porous media applications even extend beyond our planet towards nearby terrestrial planets to explore, for example, the existence of water underneath the surface in geologic formations. Porous media applications also span quite a large spectrum of time scales, from phenomena that take very long time scales to be of noticeable

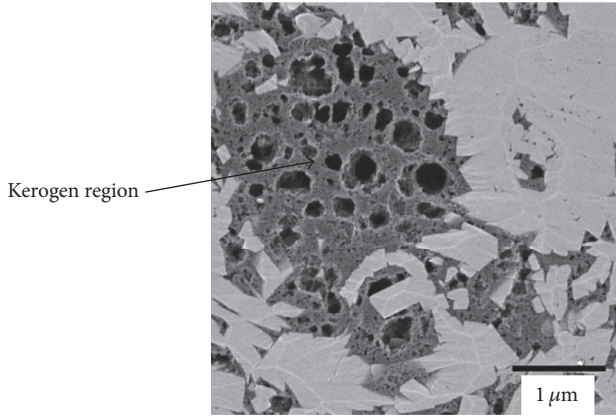


FIGURE 5: Kerogens in the shale formations are the regions in which most of the gas resources exist (adapted from <https://fei.com/>).

influence (e.g., groundwater flows) to others that take quite shorter period of time (e.g., flows in fluidized bed reactors). Therefore, no wonder there is extensive interest devoted to characterizing, understanding, and modeling several phenomena in porous media. Having such a wide spectrum of length and time scales, there exist several frameworks to handle such rich systems. One may be able to highlight three such frameworks. These are molecular scale simulations, pore-scale simulations, and continuum scale simulations. In all these simulation methodologies, upscaling techniques are required to produce integral variables that can easily be determined and measured. Two length scales are important in determining which framework may be used. These are the length scale characteristic to the domain and the length scale characteristic to the heterogeneity. Therefore, if the length scale characterizing the domain, L , is much larger than that associated with the scale of heterogeneity, d , (i.e., if $L \gg d$), the continuum hypothesis may apply (Whitaker [7–9]; Gray [10]; Hassanizadeh and Gray [11]; Cushman [12]; Carbonell and Whitaker [13]; Bachmat and Bear [14]; Quintard and Whitaker [15]). If, on the other hand, the length scale associated with the domain is on the order of the scale of heterogeneity (i.e., if $L \sim d$), the continuum approach may not be appropriate and a more detailed description at the pore scale may be required. In some situations, it so happens that the characteristic length scale is on the order of the average distance between molecules of the fluids such that even pore-scale simulation may not be correct. In this case, molecular simulations may be the appropriate framework. Figure 7 shows a schematic representation of the various length scales associated with porous media. The first graph to the left is an example of a domain that can be treated as a continuum, the middle graph may be treated using pore-scale modeling approaches including pore network models, and the last graph may be studied using molecular simulation techniques. To establish the continuum hypothesis, an averaging volume (called representative elementary volume, REV) over which upscaled quantities are determined needs to be defined. Such averaging volume is chosen such that upscaled quantities are free from scaling variations. To establish such requirements,

the length scale characterizing the REV, ℓ , should be large enough compared with pore-scale heterogeneity, d , and small enough compared with the size of the domain, L (Salama and Van Geel [16, 17]). Therefore,

$$d \ll \ell \ll L. \quad (1)$$

Several approaches have been used to derive the equations governing flow and transport in porous media. These include the method of volume averaging, theory of homogenization, and theory of mixtures. Within the method of volume averaging, the pioneering works of Whitaker and his group, Bear and his group, Gray and Hassanizadeh, and others have paved the road for the advancement in the study of flow and transport in porous media. Salama and Van Geel highlighted the notion that the averaging process can be understood by requiring that the amount of any conservative quantity within any control volume (larger than or equal to the REV) must be the same whether calculated using pore-scale equations or upscaled one. To facilitate the analysis, Hassanizadeh and Gray [11] introduced the phase function γ_β which is defined such that $\gamma_\beta = 1$ in the β -phase and $\gamma_\beta = 0$ elsewhere. Salama and Van Geel [16, 17] postulated that if V is an arbitrary volume such that $V \geq \text{REV}$, then the following relationships apply:

$$\begin{aligned} \int_V \gamma_\beta(\mathbf{r}, t) dV &= \int_V \varepsilon_\beta(\mathbf{r}, t) dV, \\ \int_V \rho_\beta \gamma_\beta(\mathbf{r}, t) dV &= \int_V \langle \rho_\beta \rangle^\beta \varepsilon_\beta(\mathbf{r}, t) dV, \\ \int_V \rho_\beta \psi_\beta \gamma_\beta(\mathbf{r}, t) dV &= \int_V \langle \rho_\beta \rangle^\beta \langle \psi_\beta \rangle^\beta \varepsilon_\beta(\mathbf{r}, t) dV, \end{aligned} \quad (2)$$

where ρ_β is the density of the β -phase, ψ_β is any intensive property per unit mass (e.g., energy and momentum per unit mass), ε_β is the volume fraction of the β -phase, and the quantities in $\langle \rangle$ are averaged over the volume of the β -phase. When the volume is the REV, such integrations produce formulas for upscaling. When the characteristic length of the domain of interest is on the order of the average distances between molecules (sometimes the mean free path is used instead), then the collision of molecules with the boundaries becomes significant. In other words, in such cases, the molecules spend more time in the vicinity of the walls rather than in the bulk. Under these circumstances, the assumption of thermodynamic equilibrium becomes questionable. That is, momentum and energy transport and the convergence to equilibrium are based on the collisions between molecules in the bulk fluid, which no longer exist at higher Knudsen number. In such small size domains, even the definitions of macroscopic variables (e.g., density, pressure, and temperature) as a manifestation of the average of the behavior of fluid particles within a representative volume may not be unique and will essentially be size-dependent. Under these conditions, the tools of molecular simulation become more appropriate to handle the state of equilibrium rather than classical bulk-phase thermodynamics. The Knudsen number is used to characterize when the continuum approach fails to apply in fluids. Knudsen number is the ratio of the mean free

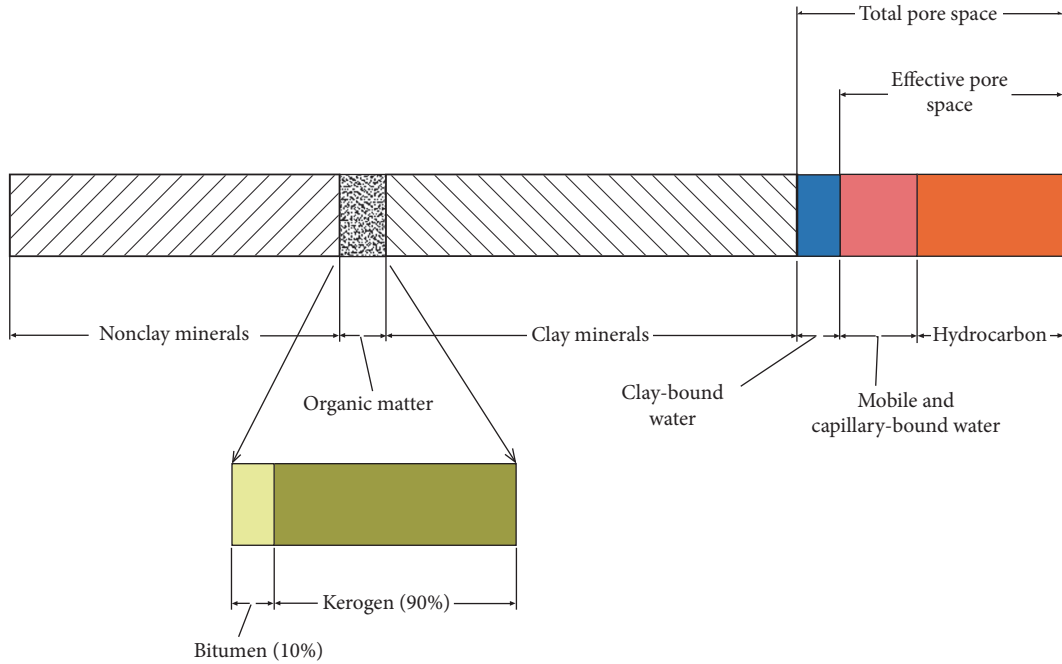


FIGURE 6: Schematic representation of the composition of typical shale formation, adapted from Prasad et al. [4].

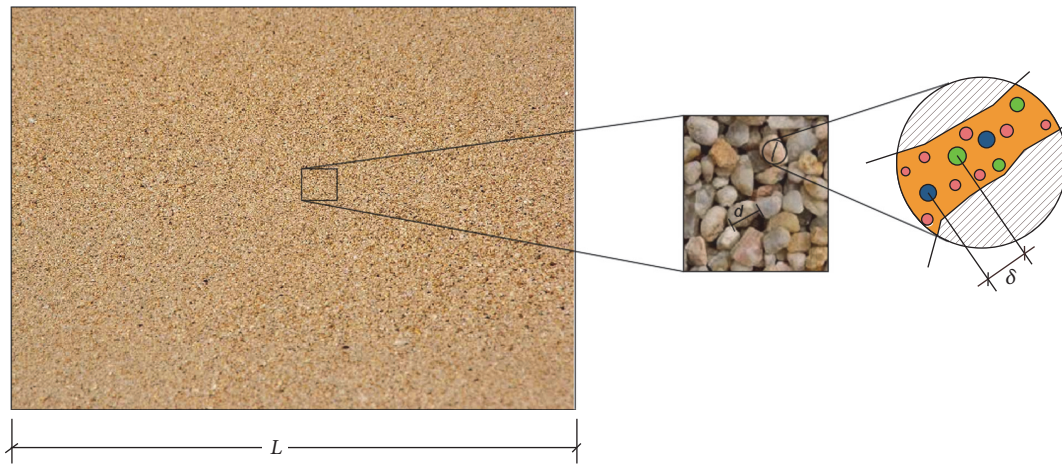


FIGURE 7: Porous media are rich in length scales. From scales that span several tens of kilometers to several tens of nanometers, a unified framework may be difficult to encounter phenomena occurring at such large spectrum of length scales. Every scale has its relevant variables that are, generally, different than respective variables at different scales. Upscaling is necessary to communicate relevant data between different scales.

path and the characteristic length scale of the study domain (i.e., $Kn = \lambda/L$). Figure 8 shows a map of the different flow categories when the length scale of the domain decreases (i.e., increasing Knudsen number).

4. Thermodynamics Associated with Transport Phenomena in Tight Formations

Classical thermodynamics is based on a set of postulates that determines the state of the system under different conditions. If a system is disturbed, its constituents interact in an attempt

to return to its initial state or to establish a new equilibrium state. The constituents of the system interact with each other and across the boundary with the surroundings in a definite manner that is determined by the laws of thermodynamics. The collisions of the molecules of the system in the bulk help homogenize local disturbances quickly. When the characteristic length scale of the system is on the order of the average distance between the particles, the collision with the walls of the system becomes dominant. Under these circumstances, a number of interesting phenomena have been observed: (1) momentum transfer is increasingly controlled by the wall

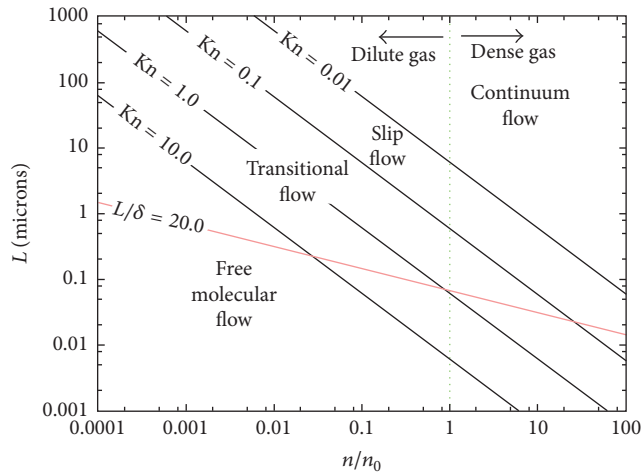


FIGURE 8: Flow categories with the increase in Knudsen number (<https://wikiversity.org/>). In this Figure, L is the characteristic wetted length of the domain under investigation, δ is the mean molecular spacing, n is the number density of the gas, and n_0 is the number density of the gas at 0°C and 1 atm.

collisions, (2) the fluid and flow properties start to fluctuate in a selected differential volume due to the lack of a sufficient number of molecules needed for statistical accuracy, (3) gas attains finite velocities in the close proximity of the wall (i.e., gas slips over the wall), and (4) thermodynamic variables like pressure drop, shear stress, heat flux, and corresponding mass flow rate cannot be predicted from flow and heat transfer models based on the continuum hypothesis. The appropriate flow and heat transfer models depend on the range of the Knudsen number as depicted in Figure 8. These and others necessitate that all the assumptions of classical thermodynamics need to be revisited.

5. Pore-Scale Phenomena

Natural porous materials abound in the earth, such as expansive bentonite clays and porous limestone, and in living organisms, such as the mastoid bone with its porous air cavities. Extraction of natural gas from pores in shale by hydraulic fracturing has transformed the energy agenda of the US and the whole world (Kobek et al., 2015). Understanding the properties of these pores in terms of their structure and transport properties is now emerging as a grand challenge in terms of the scaling from the microscopic or nanoscale regime to the macroscopic world. This transition from the nanoscale to a macroscopic world is known as mesoscale science, in which the field of pore-scale phenomena is now emerging as one of the frontiers of science and many engineering disciplines and dominating the extraction of these resources. Permeability is one of the most fundamental properties of any reservoir rock required for modeling hydrocarbon production. However, shale permeability has not yet been understood fully because of the complexities involved in modeling flow through pore throats (Sakhaee-Pour et al., 2012). New pore-scale models with a reservoir simulation algorithm to predict gas production in gas-bearing shales

have been proposed in recent years, especially concentrating on the permeability determination with the development of shale-gas engineering, which simultaneously consider the effects of slip flow (Klinkenberg effects) and Knudsen diffusion [18, 19].

6. Klinkenberg Effect in Shale

Slippage of fluid continuum upon encountering a solid surface has been investigated by Navier since the middle of the nineteenth century when he proposed an extended length where the velocity profile extrapolates to zero. Such extended length is, generally, so small in regular bulk flows in which the characteristic length scale is considerably larger than the average distance between particles. In micro- and nanochannels, however, such condition may not be satisfied and flow slippage may become pronounced. In shale formations, flow slippage in nanosize pores and fractures needs to be accounted for. Due to the gas-slippage effect, the permeability of a sample to a gas varies with the molecular weight of the gas and the applied pressure, which was first proposed by Klinkenberg [20] and so called Klinkenberg effect thereafter. He determined that the slippage of gases along the pore walls gives rise to an apparent dependence of permeability on pressure, which could be concluded as that liquid permeability (k_L) is related to gas permeability (k_g) by

$$k_L = \frac{k_g}{1 + b/p}, \quad (3)$$

where p is the mean flowing pressure and b is a constant for a particular gas in a given rock type. This non-Darcy effect occurs when the mean free path length of the gas molecules is close to the average size of pores in a porous medium. This condition results in the acceleration of individual gas molecules along the flow path [21]. The Klinkenberg effect is especially important in low-permeable rocks, so it attracted more and more attention with the development of shale gas in recent years (Civan [22], Tanikawa and Shimamoto [23]). Wu et al. [24] proposed a set of new analytical solutions developed for analyzing steady-state and transient gas flow through porous media including Klinkenberg effects, which have been used to design new laboratory and field testing techniques to determine the Klinkenberg parameters. Other popular approaches for determination of shale-gas permeability are presented by Pazos et al. [25] and Sakhaee-Pour et al. (2012).

Experiments have been designed and performed to measure the shale permeability, to verify the effect theory, and to obtain the Klinkenberg parameter, which can be found in Jones [26], Faulkner and Rutter [27], Tanikawa and Shimamoto [28], Cui et al. [29], and Davarzani et al. [30]. Generally, the pore network is constructed based on scanning electron microscope (SEM) images and a drainage experiment in shale. Currently, there are three methods in common use for determining permeability of very low permeability rocks in the laboratory. These include (i) studying the permeation of inert gas (e.g., helium) through a core sample under either falling pressure or steady-state pressure techniques, (ii) building a digital realization of the core

sample and performing a CFD analysis to determine the overall resistance, and (iii) using mercury (Hg) intrusion curves (from Hg porosimetry). Permeability measurements on rock core under confined conditions have been routinely used for conventional oil and gas reservoirs for over 50 years. However, traditional steady-flow permeability measurement (American Petroleum Institute (API) 1998) on core samples of very tight rocks such as most gas shales and coal is not practical because of the time scales involved and the instrumentation requirements for measuring extremely small pressure drops or flow rates. Another method for approximating permeability is by using Hg injection curves from Hg porosimetry. The relationship between Hg injection curves and permeability has been investigated by a number of authors (Thomeer, 1960, 1983; Swanson, 1981; Kamath, 1992, Carles et al., 2007). In Swanson's (1981) method, for example, permeability is calculated by considering the Hg saturation and capillary pressure at the apex of a hyperbolic log-log Hg injection plot. Swanson (1981) developed and calibrated the relationship between permeability and Hg intrusion data from a suite of sandstone and carbonate samples. Hg intrusion as a permeability tool is not further considered in this paper, except to note that permeability or diffusion measurements on unconfined samples are at best instructive because permeability is known to vary with effective stress by several orders of magnitude (i.e., Bustin, 1997, [31]). Another traditional technique of measuring shale permeability using crushed samples was designed by Luffel and others (1992 and 1993) to measure matrix permeability only by eliminating natural and drilling induced microfractures. Although drilling induced fractures are common (Boyer and others, 2006), they can be minimized by selecting core plugs at locations without drilling induced fractures. Because pore networks in organic matter are most likely connected through microfractures, the connectivity of organic pore network can be significantly reduced in crushed samples. Although pore networks in organic matter and natural microfractures are important properties of shale and critical to shale-gas production, they are too small to be properly quantified in the laboratory or reservoir simulation. The compromissory but easy way is to include them in core permeability measurements as part of a lumped permeability value. By including important organic and microfracture pore networks, this lumped permeability can characterize gas shales better than the true matrix permeability. Theoretically enhanced models incorporating the Klinkenberg effect and using effective method to calculate the permeability of gas transport in gas-bearing shale formations have been presented to govern gas flow in shale reservoir, as shown by Civan [32, 33], Civan et al. [34], and Al-Bulushi et al. [35].

7. Knudsen Diffusion in Shale

When the mean free path of gas molecules is on the same order as the tube dimensions (as in shale), Knudsen diffusion, which is a typical kind of free-molecule diffusion, becomes important. Due to the influence of walls, Knudsen diffusion includes the effect of the porous medium. Gas mass flux

by diffusion with negligible viscous effects in a nanopore is described as [36]

$$J_D = -\frac{MD_k}{10^3 RT} \nabla p, \quad (4)$$

where M is molar mass, D_k is the Knudsen diffusion constant, R ($=8.314$ J/mol/K) is the gas constant, and T is absolute temperature in Kelvin. The Knudsen diffusion constant is defined as [37]

$$D_k = \frac{2r}{3} \left(\frac{8RT}{\pi M} \right)^{0.5}, \quad (5)$$

where M represents the molecular weights of gas and r is the mean pore size of the porous media. Many experiments have been performed to measure the Knudsen diffusion constant, which can be found in (exclusive for those listed in the above session) Reinecke and Sleep [38], Jarvie [39], and Freeman et al. [40]. Different algorithms to simulate gas diffusion have also been developed in [41, 42]. Malek and Coppens [43] studied the effects of surface roughness on Knudsen regime diffusion in porous media. Knudsen diffusion is a result of collisions of gas molecules with the pore walls, rather than intramolecular collisions, so we always consider that Knudsen diffusion and molecular diffusion compete with one another by a "resistances in series" approach [44]. Welty et al. [45] presented the different types of diffusion as shown in Figure 9. Combining Darcy's law in unconventional systems with the total mass flux formula in the shale, we obtain the formula for the apparent permeability, which replaces the intrinsic permeability in conventional media. A commonly used formula for computing the apparent permeability of shale based on Klinkenberg effects and Knudsen diffusion is [46]

$$k_{\text{app}} = k_{\infty} \left(1 + \frac{b}{p_m} \right), \quad (6)$$

where $k_{\infty} = d^2 \phi / 32 \tau$ and $b = (\mu/R)(2/\alpha - 1) \sqrt{8\pi RT/M}$. Here, k_{∞} is the intrinsic permeability (i.e., the permeability for sufficiently large pressure, sometimes called liquid permeability), k_{app} is the apparent permeability, d is the average pore size diameter, τ is the effective tortuosity of the pores (if the pore spaces are assumed to be straight and cylindrical capillaries, the effective tortuosity is equal to 1), R is the universal gas constant, with the unit of J/mol/K, M is molecular weight of the fluid, with the unit of kg/kmol, α is the tangential momentum accommodation coefficient, dimensionless, μ is the dynamic viscosity of the fluid, and T is the temperature in K.

We would like to comment that the above Knudsen diffusion description fails to capture systems having very small pores on the order of 1 nm such as in mature kerogen. In this situation, a gas molecule has a size similar to the pore dimension. This situation is very different from the Knudsen regime. In fact, in this situation, conventional fluid viscosity no longer makes sense because gas molecules interact essentially with the pore walls instead of interacting with gas molecules themselves. When the size of the gas

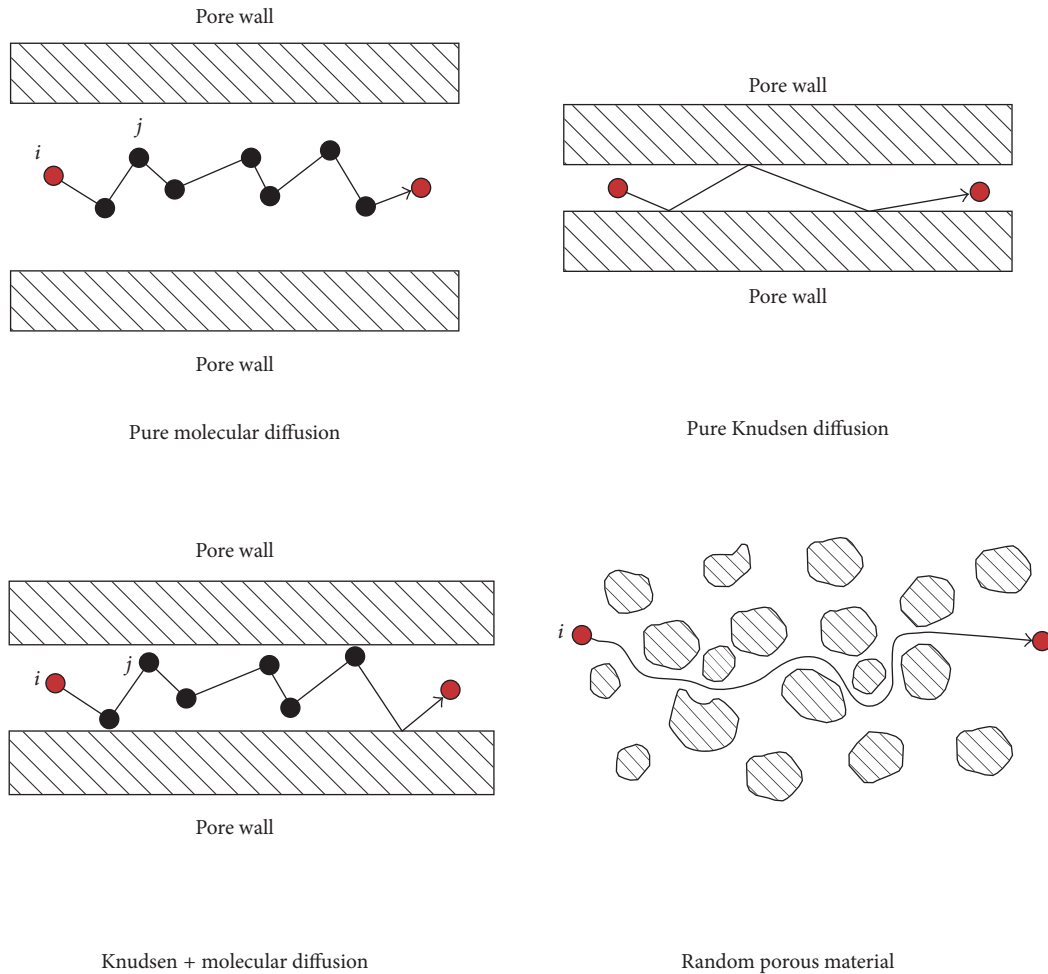


FIGURE 9: Types of porous diffusion. Shaded areas represent nonporous solids (adapted from [45]).

molecules is only slightly smaller than the pore dimension, the diffusion rate that occurred is usually much larger than predicted by Knudsen diffusion because of the superlubricity effect. When the size of the gas molecules becomes larger than the pore dimension, the diffusion rate is rapidly reduced to zero because of the molecular sieving effect.

8. Pore Network Models

As indicated earlier, in tight and shale formations, the permeability is quite small such that reliable measurements may not be readily possible. Although the flow in a bulk sample of the shale rock is difficult to measure, it can be calculated if the internal structure of a rock sample is known. With the advancement in imaging technologies, nowadays, it became possible to construct a realization of the internal structure of rock samples using series of images. X-ray computed microtomography (micro-CT) is used to produce slice pictures of the rock sample that are then used to construct a pore network model mimicking the real pore structure (Figure 10). The flow in these systems can easily be studied using, for example, the Hagen-Poiseuille approximation (for single-phase flows), which can then be used to estimate the

absolute permeability of the rock sample. Furthermore, the study of the problem of drainage and imbibition can also be considered using the pore network to estimate the relative permeability characteristics of the rock sample.

Several experimental techniques have been explored to provide three-dimensional details of the microstructures of rock samples. Computed tomography is a nondestructive imaging technique used to characterize the internal structure of several things including rock samples. Three types of CT systems are in common use, namely, medical CT, industrial X-ray generation tube, and synchrotron microtomography (Hazlett [47], Wildenschild et al. [48], Withers [49], and Schlüter et al. [50]). The typical spatial resolution range that medical CT systems can achieve may be between 200 and 500 microns, industrial X-ray tube systems range from 50 to 100 microns, and synchrotron based systems are from 1 to 50 microns. A recent review on these imaging techniques can be found in Blunt et al. [51]. On the other hand, other techniques including focused ion beams (FIB) and scanning electron microscopy (SEM) are essentially destructive (Tomutsa et al. [52], Curtis et al. [53], and Lemmens et al. [54]). SEM can be used to extract two-dimensional planar images of the microstructures. However, they do not provide the third

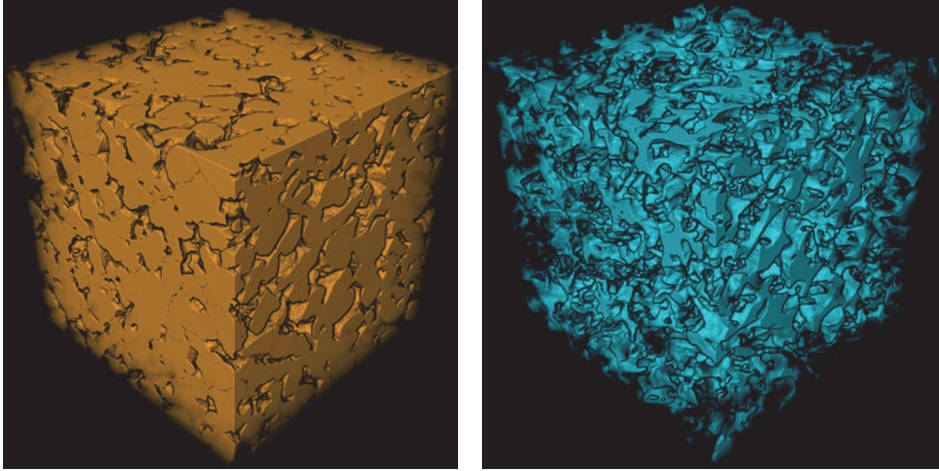


FIGURE 10: A 3D realization of the pore structure that can be used to construct a pore network (from <http://corelab.com>). Such pore network provides a reasonable approximation of the real rock sample. It can be used to determine many of the important parameters relevant to the macroscopic core sample (e.g., porosity, absolute permeability, and relative permeability).

spatial extent of the sample which is essential to determine connectivity regions. While FIB is very effective in generating higher resolution three-dimensional images, it is very much time-consuming due to the refocusing and repositioning requirements. A combination of FIB and SEM is usually used to compute structural details of porous media (Michael et al. [55], Keller et al. [56]). Nuclear magnetic resonance imaging (NMR), on the other hand, allows the imaging of the interior of the rocks to obtain the spatial distribution across a much larger scale (Callaghan [57], Blümich et al. [58]). NMR has the advantage that it requires shorter measurement time compared with other methods, which allows the analysis of larger quantities of samples to characterize field-scale hydraulic properties. For porosity measurements, mercury intrusion technique is probably the most popular for characterizing porous materials with pore sizes ranging from 3 nm to 500 μm (Giesche [59], León and León [60], and Rouquerol et al. [61]). Gas adsorption, on the other hand, is based on the adsorption behavior of the porous material, which, in turn, is a function of microstructural characteristics of the porous material. Traditionally, nitrogen (N_2), argon (Ar), and carbon dioxide (CO_2) are frequently used as adsorbates depending on the nature of the porous materials (Ravikovitch et al. [62], Groen et al. [63], and Settano et al. (2009)). A recent review on the methods discussed earlier can be found in Xiong et al. [64]. The next step after preparing the stack of images that describe the spatial distribution of the real rock sample is to build a three-dimensional realization of the pore space in the network. As reported by Xiong et al. [64], there exist a number of techniques to construct a pore network model (PNM) representing a given porous medium. They may be categorized into three methods, namely, statistical reconstruction (Adler and Thovert [65], Levitz [66], Roberts and Torquato [67], Ioannidis and Chatzis [68], and Manwart et al. [69]), grain-based model (Bryant et al. [70], Bakke and Oren [71], Lerdahl et al. [72], and Oren and Bakke [73]), and direct mapping model (Al-Raoush and

Wilson [74], Jiang et al. [75], Shin et al. [76], and Raouf and Hassanizadeh [77]). Once the pore network structure has been established, different interesting phenomena can be investigated. These include the estimation of absolute permeability, relative permeability, adsorption, dissolution, and precipitation, biomass growth, and others. In shale and tight formations, the absolute permeability is estimated using the Hagen-Poiseuille's law which takes the form

$$q_{ij} = \frac{A_{ij}^2 G_{ij}}{\mu \ell_{ij}} (p_i - p_j), \quad (7)$$

where q_{ij} is the volumetric flow rate through the pore throat connecting pore bodies i and j , ℓ_{ij} is the length of the pore throat, A_{ij} is the cross-sectional area, μ is the viscosity, and p_i and p_j are the pressures in the corresponding pore bodies. The above relationship is used for every pore throat to obtain the flow rates and therefore the absolute permeability may be obtained. For two-phase flows, things become more complicated by the existence of the interfaces and the capillary effects (El-Amin et al. [78], Naraghi and Javadpour [79], Zhang et al. [80, 81], Lia et al. [82], Landry et al. [83], Gerami et al. [84], and Dong et al. [85]). A good review can be found in the work of Joekar-Niasar and Hassanizadeh [86].

9. Macroscopic Governing Equations

The permeability of shale reservoirs is very low compared to the permeability of conventional reservoirs. The gas production from a shale reservoir depends on the existence of natural or artificial fracture networks. So, the mathematical models describing flow and transport in fractured porous media are considered as the main framework to model fluid transfer between shale matrix and fractures. Traditionally, dual-continua models have been used to describe the transport in fractured porous media which consist of

matrix blocks and fractures. In these models, Darcy's law is assumed to be the main flow driver. The transport in matrix blocks has been described by several mechanisms such as Knudsen diffusion in nanopores, desorption from kerogen, and diffusion in solid. For example, Hadjiconstantinou [87] and Javadpour [46] discussed different mechanisms to investigate the shale-gas production rates. They employed Klinkenberg effect which considers the slippage coefficient to describe the diffusion mechanism. On the other hand, during depressurization of shale-gas reservoirs, induced stresses on the rock system can further reduce the pore space, which affects permeability. To account for such stress-dependent permeability upon depressurizing the reservoir, Raghavan and Chin [88] proposed a formula that considers permeability as a function of the pressure. Other researchers such as Raghavan and Chin [88] and Chipperfield et al. [89] proposed other relationships defining how permeability is related to the stress state. Other modeling approaches including fractional derivative formulation have also been implemented (e.g., [90]). The modeling of shale-gas reservoir is divided into two different main models. The first one is the dual-continua model (e.g., [80, 81, 91]) and the second one is the discrete fracture model (e.g., [92, 93]).

10. Dual-Continuum Model

Warren and Root [94] were the first to develop an idealized model to study the behavior of flow in fractured porous media based on dual-continua models. Bustin et al. [31] used a standard dual-continuum model to study the permeability effect. Ozkan et al. [95] used the dual-porosity model, in which the matrix was considered as uniform radius spherical blocks. They considered both the matrix diffusive Darcy flow and the fractures stress-dependent permeability for naturally fractured reservoirs ignoring sorption and desorption processes. Also, Moridis et al. [96] used the standard dual-continuum model to describe several mechanisms in kerogen. Wu and Fakcharoenphol [97] used a generalized dual-continuum methodology and proposed general reservoir simulators ignoring the adsorption and desorption processes. They implemented a general theoretical fracture model for simulating fluid and heat flow processes in fractured unconventional reservoirs. Guo et al. [98] developed a mathematical model including the above-mentioned mechanisms to describe the flow behavior in tight shale-gas formation. Recently, El Amin [99] presented an analytic solution using the power-series method for the apparent permeability Klinkenberg model. Arbogast and his coworkers made significant contributions in deriving the dual-porosity models (e.g., [100–103]). Furthermore, Showalter and his coworker highlighted some of the mathematical properties of the dual-porosity models (e.g., [104–106]).

In the matrix blocks of shale strata, free gas and adsorbed gas coexist with each other. Mass accumulation term for free gas per unit volume is $\varphi\rho$, for a single-phase gas reservoir. The adsorbed gas is estimated as 20%~85% of shale gas. Mass accumulation term which describes adsorbed gas on the matrix surface is $\sum(1 - \varphi)q_a$ [107], where q_a is the adsorbed gas volume per unit area of shale surface. The most common

way to describe this process is the Langmuir isotherm model [18, 29, 34, 40], which is expressed as

$$q_a = \frac{\rho_s M_w}{V_{\text{std}}} \left(\frac{V_L p_m}{P_L + p_m} \right), \quad (8)$$

where V_{std} is the mole volume under standard condition (0°C , 1 atm); V_L is the Langmuir volume; P_L is the Langmuir pressure; ρ_s is the density of shale core; p_m is the matrix pressure; M_w is the molecular weight. The two mass accumulation terms of both free and adsorbed gas are combined, $\sum(\varphi\rho + (1 - \varphi)q_a)$. The real gas law is considered, $pV = ZRT(m/M_w)$, where p is the pressure, R is the gas constant, T is the temperature, m is the mass, V is the gas volume, and Z is the gas deviation factor. The mass density of the gas becomes $\rho = (\gamma/Z)p$, $\gamma = M_w/RT$. In order to calculate Z , one may use the cubic Peng-Robinson equation of state [108]:

$$Z^3 - (1 - B)Z^2 + (A - 3B^2 - 2B)Z - (AB - B^2 - B^3) = 0, \quad (9)$$

where $A = a_T P/R^2 T^2$, $B = b_T P/RT$, $a_T = 0.45724(R^2 T_c^2/P_c)$, and $b_T = 0.0778(RT_c/P_c)$. T_c and P_c are the critical temperature and critical pressure, respectively. The Klinkenberg method [20] was used to correct the effective gas permeability to a liquid-equivalent permeability using a “gas-slippage” factor. The Klinkenberg effect becomes significant in modeling gas flow in reservoirs in systems with low pressure or low permeability. The matrix apparent permeability can be written as [46]

$$k_m = k_{m0} \left(1 + \frac{b_m}{P_m} \right), \quad (10)$$

where $b_m = \sqrt{8\pi RT/M_g}(\mu_g/r)(2/\alpha - 2984/3000)$, where α is the tangential momentum accommodation coefficient, which takes values within the range [0, 1]. For the gas flow in fractures, we consider Knudsen diffusion and viscous flow. The mass flux may be represented as

$$J_f = -\frac{\rho_f k_{f0}}{\mu_g} \left(1 + \frac{b_f}{P_f} \right) \nabla P_f, \quad (11)$$

where $b_f = D_{kf} \mu_g / k_{f0}$. The apparent permeability of fractures is expressed as

$$k_f = k_{f0} \left(1 + \frac{b_f}{P_f} \right). \quad (12)$$

Knudsen diffusion coefficient, D_{kf} , for the fracture system is defined as [46]

$$D_{kf} = \sqrt{\frac{\pi RT k_{f0} \varphi_{0,f}}{M_w}}, \quad (13)$$

where $\varphi_{0,f}$ is the initial fracture porosity. The dual-porosity dual permeability (DPDP) model has two mass conservation equations, one for the matrix blocks continuum and the other

for the fractures continuum, coupled with a transfer term. The mass exchange between matrix blocks and fractures is represented by a shape factor [109]. Warren and Root [94] defined the shape factor for cubic matrix blocks as $\sigma = 2n(n + 2)/l^2$, where n is the set of normal fractures, $l = 3L_xL_yL_z/(L_xL_y + L_yL_z + L_zL_x)$ is a characteristic length, and L_x, L_y , and L_z are lengths of the sides of a cubic matrix block. Some other methods have been considered to handle the matrix–fracture connection such as the boundary conditions method [110]. The transfer of gas between the matrix and fracture systems is represented by

$$S = \frac{k_{m0}\gamma\sigma(P_m + b_m)(P_m - P_f)}{\mu_g}, \quad (14)$$

where σ is the crossflow coefficient between the fracture and matrix systems. The fluid flows into the fracture from the matrix represented by a sink term. In order to define this sink term, we present the model developed by Aronofsky and Jenkins [111] for gas production from a vertical well; namely,

$$q_p = \frac{k_{f0}\theta\gamma}{Z\mu_g[\ln(r_e/r_w) + S + D_q]}P_f(P_{fe} - P_w), \quad (15)$$

where $\theta = 2\pi$ when the production well is placed in the center, while $\theta = \pi/2$ when the production well is located in the corner; P_w is the bottom hole pressure; P_{fe} is the average fractures pressure around the well; r_w is well radius; r_e is the drainage radius, which can be calculated by

$$r_e = \begin{cases} 0.14\sqrt{2[(\Delta x)^2 + (\Delta y)^2]}, & \text{if } k_x = k_y, \\ 0.28\frac{\sqrt{(k_y/k_x)^{1/2}\Delta x^2 + (k_x/k_y)^{1/2}\Delta y^2}}{(k_y/k_x)^{1/4} + (k_x/k_y)^{1/4}}, & \text{if } k_x \neq k_y, \end{cases} \quad (16)$$

where Δx and Δy are the grid lengths in x and y directions. Terzhagi (1936) reported that rock deformation based on effective stresses has also some effects on the transport of fluids in fractured systems. Biot and Willis [112] developed a generalization for the effective stress model such that the permeability and the porosity are both dependent on the stress. The porosities φ_m, φ_f are related to the mean effective stress according to the following set of equations [97]:

$$\varphi_\beta = \varphi_{r,\beta} + (\varphi_{0,\beta} - \varphi_{r,\beta})\exp(-a\sigma'_\beta), \quad \beta = m, f, \quad (17)$$

where σ'_β is the effective stress which is defined by $\sigma'_\beta = \sigma_\beta - \alpha_\beta P_\beta$; σ_m is the mean total stress in matrix blocks; σ_f is the mean total stress in fractures; α_m, α_f are Biot's effective parameters. The derivative of the porosity is given as

$$\varphi'_\beta = \frac{\partial\varphi_\beta}{\partial P_\beta} = a\alpha_\beta(\varphi_{0,\beta} - \varphi_{r,\beta})e^{-a\sigma'_\beta}, \quad \beta = m, f, \quad (18)$$

where $\varphi_{0,m}$ is the initial porosity of the matrix system; $\varphi_{0,f}$ is the initial porosity of the fractures system. The stress evaluation is added to each term of the mass accumulation equation.

Therefore, the DPDP model consists of two equations that can be finally written as

$$\begin{aligned} F_1(P_m) \frac{\partial P_m}{\partial t} - \nabla \cdot \left(\frac{\gamma k_{m0}}{\mu_g} \left(1 + \frac{b_m}{P_m} \right) P_m \nabla P_m \right) &= -S, \\ F_2(P_f) \frac{\partial P_f}{\partial t} - \nabla \cdot \left(\frac{\gamma k_{f0}}{\mu_g} \left(1 + \frac{b_f}{P_f} \right) P_f \nabla P_f \right) & \\ &= S - q_p, \end{aligned} \quad (19)$$

where $F_1(P_m) = \{(\gamma/Z)[\varphi_m + \varphi'_m P_m] + (1 - \varphi_m)\rho_s M_w V_L P_L / V_{\text{std}}(P_L + P_m)^2 - \rho_s M_w V_L \varphi'_m / V_{\text{std}}(P_L + P_m)\}$ and $F_2(P_f) = (\gamma/Z)(\varphi_f + \varphi'_f P_f)$.

11. Discrete Fracture Model

The discrete fracture model (DFM), a well-known reduced modeling technique for the simulation of flow and transport in the fractured porous media [113–115], is reviewed in this section. In the single discrete fracture modeling, each fracture is represented explicitly using high resolution mesh (El Amin et al. [116]). So, as fractures have high permeability and big variations in physics, a denser mesh is required in fractures than in the matrix. For example, Baca et al. [117] presented a two-dimensional model for single-phase flow with heat and solute transfer in fractured porous media. Juanes et al. [118] proposed a finite-element formulation for a single-phase flow in fractured formations. Matthai et al. [119] introduced numerical investigations for two-phase flow in fractured porous media using control-volume finite-element method. Cipolla et al. [120] introduced numerical modeling using automated unstructured gridding method to simulate the well performance from the complex fractures. Sheng et al. [121] employed the extended finite-element method to study the gas transport of shale in a complex fracture network. The discrete fracture model for a single-phase flow with fluid exchange between the fracture and the surrounding rock matrix where fractures are treated as interfaces of dimension $(n - 1)$ was considered by Martin et al. [122]. Jaffré et al. [123] extended this model for the case of two-phase flow. The interaction between the matrix and the fracture is effected by Robin boundary condition along the two sides of the fracture, and the flux discontinuity through the fracture is represented by a source term. Also, nonlinear transmission conditions may be of relevance when considering reactive flow in fractured media. Pop et al. [124] employed nonlinear transmission conditions for reactive flow in fractured media. Recently, the phase field modeling of flow in fractured media has been considered by Lee et al. [125] and Mikelić et al. [126, 127]. The embedded discrete fracture models have been employed by Li and Lee [128] and Moinfar et al. [129] discretized the complex fractures into a number of segments while the matrix is treated as structured grids. Jiang and Younis [130] used the two hybrid methods, namely, embedded discrete fracture models with multiple interacting continua and the coupling of unstructured DFM with continuum type. The fracture networks' complexity has important effects on the well performance. The fractures may

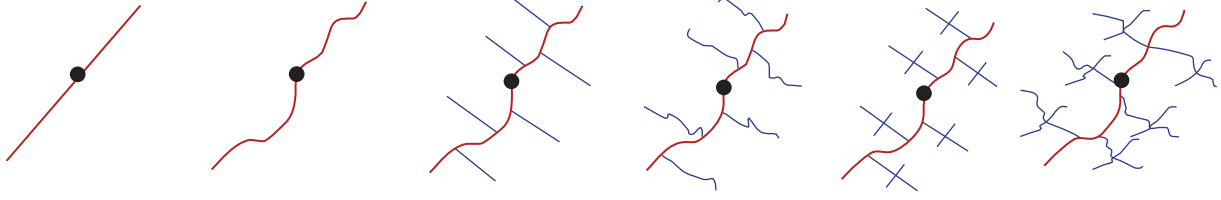


FIGURE 11: Some examples of different complex planar/nonplanar hydraulic fracture networks [92].

be planar or nonplanar, natural or hydraulic. Some examples of different complex planar/nonplanar hydraulic/natural fracture networks are shown in Figure 11 [92]. The hydraulic fractures are connected with natural fractures and wellbores are connected in different schemes.

As the fracture network consists of nodes connected with segments, the pressure drop from the node $j + 1$ node to the node j node may be given as [131]

$$P_{j+1} - P_j = \int_{y_{j+1}}^{y_j} \left\{ D_j q_j(y) + ND_j (q_j(y))^2 \right\} dy, \quad (20)$$

$$j = 1, 2, \dots, N_f,$$

where $q_j(y) = q_{j+1} + q_{fj}(y - y_{j+1})$ is the gas flow rate at node j of the fracture segment, $D_j = (\mu_g/\rho_g k_f w_f h_f)_j$ is the coefficient of Darcy flow for gas at the fracture segment j , and $ND_j = \rho_g \beta / (\rho_g w_f h_f)_j^2$ is the coefficient of non-Darcy flow. q_{fj} is the gas flux at the fracture segment j , k_f is the fracture permeability, w_f is the fracture width, h_f is the fracture height, and β is the non-Darcy Forchheimer coefficient. Considering time variation from the time step k to $k + 1$, the mass balance in the pore j is given as the summation of all the mass flux connected with the pore j [80, 81]:

$$P_j^{k+1} = P_j^k - \sum_{i=s}^e \left(F \frac{\pi r^4}{8\mu} \frac{P_j^k + P_i^k}{2} + \frac{2r}{3} \sqrt{\frac{8RT}{\pi M}} \right) \cdot \frac{P_j^k - P_i^k}{l_{ji}} \frac{\Delta t}{(4/3)\pi r_j^3}, \quad (21)$$

where F is the slippage coefficient and l_{ji} is the pore center distance between the pore j and the pore i .

12. Numerical Methods for Solving the Governing Laws

On the other hand, simulation of transport phenomena is computationally challenging because it demands high accuracy and local mass conservation. Transport in geological media involves long durations; even tiny errors in each step can accumulate to a huge error. Porous media manifest dramatically different spatial and temporal scales. Heterogeneity, anisotropy, and discontinuity of medium properties require special treatment for computationally efficient approximation of advection, diffusion, dispersion, and chemical reactions. Some numerical approximation schemes

fail to preserve important physical and/or mathematical principles and lead to erroneous simulation results. These challenges are addressed, for example, by Moortgat et al. [132], Sun and Wheeler [133, 134], Kou and Sun [135], Dawson et al. [136], Kou and Sun [137], Radu et al. [138], Radu and Pop [139], Vohralík and Wheeler [140], Vohralík [141], Marchand et al. [142], and many others. In general, using mixed finite-element method (MFEM) and finite volume methods in reservoir simulation and transport in porous media is required as they are locally mass conservative. On the other hand, new algorithms have been developed to speed up the computations that could, otherwise, be considerably slow. In particular, in programming languages that require repeating interpretations (like Matlab and Python), loops and logical statements can consume a considerable amount of time just for translation. Sun et al. [143] developed a technique that vectorizes all the difference operations replacing totally the loops. This makes the algorithm's speed compare very well with those developed using languages that do not require repeated interpretation (like FORTRAN, C, and C++). Later, Salama et al. [144] generalized this algorithm to the problem of two-phase flows in porous media. Salama et al. [145, 146] also developed what they called the experimenting field algorithm in which the matrix of coefficients of a linear system is constructed automatically, rather than being inputted manually. This technique has been tested in various cases and shows to be very effective (Salama et al. [147–149], Wu et al. [150], Negara et al. [151, 152], and El-Amin et al. [153]). Furthermore, Salama et al. [154] and Salama [155] developed a technique that numerically solves the problem of flow towards a well in an efficient manner. This technique is very accurate even when the mesh closer to the well is coarse.

The next paragraphs provide only a fleeting study of an otherwise rich and active area of research for numerical methods for flow and transport in porous media. For more discussions on this subject, the readers are advised to refer to excellent textbooks on this subject (e.g., Helmig [156], Chen et al. [157], and Nordbotten and Celia [158]). The conservation laws that describe various transport phenomena in porous media (e.g., those presented in this paper) are in the form of partial differential equations (PDEs). The analytical solutions of these equations are very limited to simple problems, geometries, and boundary conditions. Therefore, it is likely that researchers will look for numerical methods to solve various transport problems in porous media. In these methods, the solutions are obtained at discrete points inside the domain rather than at every point as is the case in analytical methods. Several classes of numerical

methods have been adapted to solving different problems in porous media including finite differences, finite elements, finite volume, boundary elements, and spectral methods. The methodologies and requirements for each method can be classified into two general categories, namely, methods that directly approximate the derivatives (e.g., finite differences, classes of finite volume) and methods that approximate the solution functions themselves. In the former methods, the derivatives must exist to at least as much as the governing differential equations require. These methods, therefore, do not allow possible approximate solutions that do not satisfy the governing PDEs strongly. The later class of numerical methods have the advantage that they can generate approximate solutions that can satisfy the governing equations weakly, or in other words in an integral sense. The first methods are straightforward and therefore in this review we highlight some of the features of the second class of numerical methods.

The mixed method is based on the conservation law together with the constitutive law for the flux in terms of pressure (Darcy's law) and solving the flux variable and the pressure together. Since this preserves the structure of the equations, this approach is in consistence with the required properties of the numerical methods. Though, in the previous section, equations are derived to model the flow using non-Darcy models, we limit the discussion here to the Darcy model. The mixed method being discussed here can be directly adapted to those developed in the previous section for nonzero P .

$$\begin{aligned}\mathbf{u} &= -\frac{k}{\mu}\nabla p, \\ \nabla \cdot \mathbf{u} &= f.\end{aligned}\quad (22)$$

The weak formulation for the above equations is obtained by using w , \mathbf{v} as test functions, multiplying the governing equations of mass conservation and Darcy's law, respectively, and integrating over the domain Ω . This yields

$$\begin{aligned}(\nabla \cdot \mathbf{u}, w) &= (f, w), \\ (\mu \mathbf{k}^{-1} \mathbf{u}, \mathbf{v}) &= (p, \nabla \cdot \mathbf{v}),\end{aligned}\quad (23)$$

for all w , \mathbf{v} . In the above equations, the notation (f, w) implies the inner product which is defined as

$$(f, w) = \int_{\Omega} f w \, d\Omega. \quad (24)$$

Note that, in the above, partial integration has been used for putting the derivative from pressure to test function \mathbf{v} . Further, it has been assumed that the boundary conditions are such that the boundary terms cancel out. The inner product above is a standard L^2 inner product and the integration has been performed over the domain Ω . The test functions w and \mathbf{v} belong to different spaces justifying the nomenclature of the mixed method.

The finite-element spaces for the solutions \mathbf{u} and p and for the test functions \mathbf{v} and w are chosen to be the same.

However, the choice for vector spaces for \mathbf{u} and p cannot be made independently and has to satisfy a compatibility condition known as the inf-sup condition. In general, the heterogeneities and the nonlinearities including advancing fronts in the porous media imply that the regularity of the solution is quite low. This motivates the use of low order finite-element space. Raviart and Thomas [159], later extended by Nédélec [160], introduced the first family of mixed finite-element spaces for the pressure equation under consideration. For the lowest order, approximation satisfying an inf-sup condition is given in terms of Raviart-Thomas elements, denoted as RT0. For this approximation, the scalar spaces (e.g., for pressure, p_h) are chosen as constants in each element of the mesh of the domain, whereas the vector spaces, say for the flux, \mathbf{u}_h , are chosen to be piecewise linear. The degrees of freedom for the flux unknowns are at the mesh edges. The flux unknowns are taken to be constant at each edge and the linear extrapolation in the interior of each element is taken to ensure that $\nabla \cdot \mathbf{u}_h = p_h$. This ensures the inf-sup compatibility condition.

In the coupled flow and transport problems being considered here, the mixed method provides several advantages over the conformal finite-element method. It is noted that the heterogeneities in the permeability imply that the gradient of the pressure will have discontinuities and will be rough. However, the flux is smoother. Thus, the mixed method computes the flux explicitly and accurately and the flux has a physical meaning. In fact, the discrete equation for the flux represents the conservation equation and hence reflects the physics of the problem. In the transport model, the flux is used for the convection of the reactant species and the accuracy of the flux is an important consideration for the accuracy of concentration profiles. The immediate disadvantages are the increase in the number of unknowns and the linear system losing its positive definiteness. To overcome these deficiencies, a quadrature is used to approximate the flux unknowns in terms of pressure unknowns that can be locally inverted. The flux unknowns are then eliminated giving rise to a system with only pressure unknowns. Such a system is positive definite and it can be shown theoretically that the approximation in using the quadrature does not lead to any loss in convergence order [161].

13. Characteristic Method for Transport Equation

The multiphase flow or the transport of chemical species is characterized by the presence of front of the chemical species being transported or of saturation. This is due to the hyperbolic character of the governing equations and is manifested because of stronger advection compared to diffusion. In the multiphase flow, the behavior is described by the degeneracy of the governing models where the nature of equation changes from parabolic to hyperbolic, and in the transport of the chemical species case, the stronger advection including limited diffusion means that the numerical schemes have to include both features of parabolic and hyperbolic. However, the schemes used for parabolic equations do not work well when the governing equations

are advection dominated, especially capturing the sharp fronts while ensuring the conservation of local mass. The design of numerical schemes therefore has to incorporate the hyperbolic nature of the transport equation for discretization. Several numerical methods have been developed that provide the adaptation from parabolic to hyperbolic: explicit method of characteristics, upstream-weighted finite differences [162], interior penalty Galerkin schemes [163], higher order Godunov schemes [164], streamline diffusion method [165], and modified method of characteristics-Galerkin finite-element procedure [166, 167]. The reader is referred to the textbook of Chen [168] for further discussions on the use of some of these techniques in porous media context.

14. Deformable Porous Media

The theoretical basis for the study of flow in deformable porous media based on the method of volume averaging can be found in the early work of Whitaker [169]. An important feature in tight and shale formations is that the property of the porous medium may evolve as a result of chemical reactions. Along with porosity, these properties include transport properties of the medium such as permeability and diffusivity. A nonnegligible change in the porosity may happen due to chemical reactions such as precipitation and dissolution [170]. The transport properties are typically considered as a function of porosity ([171–175] and many others) but in an evolving pore skeleton, these properties may change considerably as they depend on the details of the pore-scale geometry. To consider the effects due to the evolving microstructure is of crucial importance for obtaining reliable upscaled models, because otherwise features like pore clogging or damaging of the structure will not be captured at all. The existing models for reactive flow either do not include these features or are restricted to very simple geometries (e.g., 1D) as in the work of Alshawabkeh and Rahbar [176], or they use ad hoc proposed laws based on the porosity-permeability relationship. Nevertheless, to include the evolution of the microscale is complicated due to the complexity of the domain at the pore scale and the occurrence of free and moving boundaries (pores have a variable, solution dependent structure, which is not known a priori). Recently, problems with an evolving microstructure were considered for simplified geometries and saturated flow (see [177] and van Noorden et al., 2010 [178, 179]). Extensions to multiphase models having an evolving microstructure coupled to saturated/unsaturated flow (i.e., the pore space may be filled with water and air) are quite open. A consistent theory for the derivation of deformable porous media taking into account the detailed pore-scale geometry evolution and the corresponding changes in the transport properties is by far incomplete. The macroscale models consist of fully coupled, nonlinear, degenerate parabolic partial differential equations for flow, reactive transport and heat, and additional ordinary differential equations for the microstructural evolution. Two degeneracy types appear here: parabolic/elliptic due to saturated/unsaturated flow and parabolic/hyperbolic due to pore clogging. The design and implementation of

efficient and reliable numerical schemes for the macroscale system is therefore a very demanding task. The evolving geometry is reflected in the upscaled models through additional equations describing the topological changes describing the porosity and permeability. How to properly account for these topological changes is at present open despite early attempts made in the references cited above. For such models, it remains open to develop, implement, and analyze efficient multiscale, mass-conservative solution schemes. An immediate difficulty is in the increase of dimensions of the problem due to the fine scale evolving geometry description coupled to Darcy scale models.

Upscaling methods have thus far been mainly applied to rigid porous media. Any approach for upscaling should include the variation of the geometry at the pore scale. Recently, an extension of homogenization techniques was introduced by van Noorden [177] including a level set approach to capture the moving interfaces at pore scale. Assuming the fixed geometry for the precipitation-dissolution models allows performing rigorous analysis of the mathematical models. The related effective models describing convective-diffusive transport for the periodic case have been derived by Kumar et al. (2016). Effective equations for the convection dominated case leading to the Taylor dispersion including the moving boundary were developed by Kumar et al. [178, 180–184].

15. Environmental Aspects Related to Hydraulic Fracking

There is no doubt that there are potential environmental risks associated with acquiring energy resources from unconventional reservoirs using fracking technologies. The societal dilemma, however, lies in how to devise methodologies for obtaining the natural gas while limiting environmental damage. Global warming, whose adverse effects are, nowadays, signified and felt throughout the world, represents a pressing issue. Escaping methane, probably, represents the most serious and noticeable impact because of its direct and acute effect on the local environment. There have been several instances where groundwater and even surface water get contaminated with the release of gases from shale formations in relatively larger quantities. Groundwater distributed to houses in the nearby areas of drilling sites has been shown, in some cases, to catch fire due to the release of gases [185–187]. Such release of gases (mainly methane) not only contaminates water bodies but also contributes to air pollution. Global warming potential (GWP), a number that allows comparing the potential impact of different greenhouse gases (GHG) on global warming, indicates that methane warms the planet 86 times as much as CO_2 , according to the Intergovernmental Panel on Climate Change. Methane is 25 times more potent in trapping heat in the atmosphere than carbon dioxide. The major source of gas release from unconventional reservoirs may, probably, be attributed to the fracking technology used. That is, there is no guarantee that the stimulated fractures will be confined to where the wellbore exists. In other words, there are no measures to ensure that the stimulated fractures do not extend to the top edge of the formations. If this happens,

the gases can probably find a pathway to the top layer of the formation, thereby to the local groundwater reservoirs, and finally to the atmosphere. The risks and concerns of hydraulic fracking are generally associated with the contamination of groundwater, methane pollution and its impact on climate change, air pollution impacts, exposure to toxic chemicals, blowouts due to gas explosion, waste disposal, large volume water use in water-deficient regions, fracking-induced earthquakes, workplace safety, and others. In addition, chemical additives that are used in the drilling mud, slurries, and fluids, which are essentially required for the fracking processes, can generally leak into the local environments through fissures, sealing, cracks, faulty design, or construction of the cement well casings, among others. Each well utilizes millions of gallons of toxic fluid containing not only the added chemicals, but also other naturally occurring radioactive materials, liquid hydrocarbons, brine water, and heavy metals (Osborn et al. [188], Bamberger and Oswald [189], and Colborn et al. [190]). Fissures created by the fracking process can also create underground pathways for gases, chemicals, and radioactive materials.

16. Discussion and Conclusion

This paper reviewed aspects related to the flow and transport phenomena in tight and shale formations. These formations are believed to contain a considerable amount of hydrocarbon resources. The major characteristics of such formations compared with conventional reservoirs are that their permeability is so small that traditional techniques for producing oil and gas may not work. Unconventional methods are, therefore, required to be developed to facilitate the transport of oil and/or gas stored in these formations. Horizontal wells have been shown to be very effective in increasing the area of contact between the wellbore and the formation. To facilitate the transport of hydrocarbons, fractures are formed using fracking technology. Such fractures expose a larger area of the rock mass to thermodynamic conditions which results in the mobilization of entrapped and adsorbed gas. There are several aspects related to the process of fracturing the rock mass. These are related to the fact that there is no guarantee that these induced fractures are confined to the vicinity of the well leg. In other words, fractures may extend to the top layer of the formation, providing the released gas with a pathway to the local environment. There are several aspects related to the mechanisms involved in the release and transport of stored gas towards the production wells. Micro-CT analysis of rock samples indicates that the gas exists mostly in an organic region of the formation called kerogen. The gas is found in these regions adsorbed to the surface. When the pressure is decreased, the adsorbed molecules are derived to the pore space and then to the fractures network. The sizes of pore space in such formation give rise to whether the continuum hypothesis may be applicable in such small size conduits. Indeed, the characteristic length scale of pore space is approximately in the same order of magnitude as that of the average distance between gas particles. The Knudsen number, which compares the mean free path of the molecules and the characteristic length scale of the flow conduits, was shown

to be relatively large, violating therefore the constraints set by the continuum hypothesis. This necessitates the need to consider multiscale approaches including molecular scale, pore scale, and continuum scale phenomena. The fact that the Knudsen number may be larger than one highlighted the need to consider interesting physical phenomena, including flow slippage and Knudsen diffusion. Under these scenarios, the permeability has been shown to be a function of the pressure. Furthermore, the depressurization of shale-gas reservoirs induces several stress-induced deformations that, likewise, affect the permeability. To model these complex processes at the macroscopic level, two general frameworks have been proposed: the dual-continua approaches and the discrete fractures model. Several numerical techniques have been used in solving the governing equations including mixed finite-element methods, finite volume methods, and the method of characteristics. A comprehensive list of recent references have been included to help researchers interested in pursuing research in this field to find the appropriate material.

Conflicts of Interest

The authors declare that they have no conflicts of interest.

Acknowledgments

Shuyu Sun acknowledges that this work is supported by the KAUST research fund awarded to the Computational Transport Phenomena Laboratory at KAUST through Grant BAS/1/1351-01-01. In addition, Shuyu Sun thanks his Ph.D. student Tao Zhang for his help in collecting and compiling results on Klinkenberg effect and Knudsen diffusion in shale.

References

- [1] EIA report, 2016, <http://www.eia.gov>.
- [2] EIA report, 2014, <http://www.eia.gov>.
- [3] K. M. Bohacs, G. Grabowski, A. R. Carroll et al., *Production, destruction, and dilution: the many paths to source-rock development*, vol. 82, SEPM publications, 2005.
- [4] M. Prasad, A. Pal-Bathija, M. Johnston, M. Rydzy, and M. Batzle, "Rock physics of the unconventional," *Leading Edge (Tulsa, OK)*, vol. 28, no. 1, pp. 34–38, 2009.
- [5] Q. R. Passey, K. M. Bohacs, W. L. Esch, R. Klimentidis, and S. Sinha, "From oil-prone source rock to gas-producing shale reservoir - Geologic and petrophysical characterization of unconventional shale-gas reservoirs," in *Proceedings of the SPE Americas Unconventional Gas Conference 2011, UGC 2011*, pp. 1–29, 2010.
- [6] L. Wang and H. Cao, "Probable mechanism of organic pores evolution in shale: Case study in Dalong Formation, Lower Yangtze area, China," *Journal of Natural Gas Geoscience*, vol. 1, no. 4, pp. 295–298, 2016.
- [7] S. Whitaker, "Diffusion and dispersion in porous media," *AICHE Journal*, vol. 13, no. 3, pp. 420–427, 1967.
- [8] S. Whitaker, "Fluid motion in porous media," *Industrial & Engineering Chemistry*, vol. 61, no. 12, pp. 14–28, 1969.
- [9] S. Whitaker, *Method of Volume Averaging*, Kluwer, Boston, Mass, USA, 1st edition, 1999.

- [10] W. G. Gray, "A derivation of the equations for multi-phase transport," *Chemical Engineering Science*, vol. 30, no. 2, pp. 229–233, 1975.
- [11] M. Hassanizadeh and W. G. Gray, "General conservation equations for multi-phase systems: 1. Averaging procedure," *Advances in Water Resources*, vol. 2, pp. 131–144, 1979.
- [12] J. H. Cushman, "Multiphase transport equations. I. General equation for macroscopic statistical, local, space-time homogeneity," *Transport Theory and Statistical Physics*, vol. 12, no. 1, pp. 35–71, 1983.
- [13] R. G. Carbonell and S. Whitaker, "Heat and Mass Transfer in Porous Media," in *Fundamentals of Transport Phenomena in Porous Media*, J. Bear and M. Y. Corapcioglu, Eds., pp. 123–198, Dordrecht, Netherlands, 1984.
- [14] Y. Bachmat and J. Bear, "Macroscopic modelling of transport phenomena in porous media. I: The continuum approach," *Transport in Porous Media*, vol. 1, no. 3, pp. 213–240, 1986.
- [15] M. Quintard and S. Whitaker, "Transport in ordered and disordered porous media I: The cellular average and the use of weighting functions," *Transport in Porous Media*, vol. 14, no. 2, pp. 163–177, 1994.
- [16] A. Salama and P. J. Van Geel, "Flow and solute transport in saturated porous media: 2. Violating the continuum hypothesis," *Journal of Porous Media*, vol. 11, no. 5, pp. 421–441, 2008.
- [17] A. Salama and P. J. Van Geel, "Flow and solute transport in saturated porous media: 1. The continuum hypothesis," *Journal of Porous Media*, vol. 11, no. 4, pp. 403–413, 2008.
- [18] V. Shabro, C. Torres-Verdin, and F. Javadpour, "Numerical Simulation of Shale-Gas Production: From Pore-Scale Modeling of Slip-Flow, Knudsen Diffusion, and Langmuir Desorption to Reservoir Modeling of Compressible Fluid," in *Proceedings of the North American Unconventional Gas Conference and Exhibition*, The Woodlands, Tex, USA, 2011.
- [19] B. Yan, Y. Wang, and J. E. Killough, "Beyond dual-porosity modeling for the simulation of complex flow mechanisms in shale reservoirs," *Computational Geosciences*, vol. 20, no. 1, pp. 69–91, 2016.
- [20] L. J. Klinkenberg, "The permeability of porous media to liquids and gases," in *Drilling and production practice*, American Petroleum Institute, 1941.
- [21] C. A. McPhee and K. G. Arthur, "Klinkenberg permeability measurements: problems and practical solutions," *Advances in Core Evaluation II: reservoir Appraisal: Reviewed proceedings*, pp. 371–392, 1991.
- [22] F. Civan, "Reservoir formation damage fundamentals, modeling, assessment, and mitigation," in *Reservoir formation damage—fundamentals*, p. 1114, Gulf Professional Publisher, Elsevier, Burlington, MA, USA, 2nd edition, 2007.
- [23] W. Tanikawa and T. Shimamoto, "Comparison of Klinkenberg-corrected gas permeability and water permeability in sedimentary rocks," *International Journal of Rock Mechanics and Mining Sciences*, vol. 46, no. 2, pp. 229–238, 2009.
- [24] Y.-S. Wu, K. Pruess, and P. Persoff, "Gas Flow in Porous Media with Klinkenberg Effects," *Transport in Porous Media*, vol. 32, no. 1, pp. 117–137, 1998.
- [25] F. A. Pazos, A. Bhaya, and A. L. M. Compan, "Calculation of Klinkenberg permeability, slip factor and turbulence factor of core plugs via nonlinear regression," *Journal of Petroleum Science and Engineering*, vol. 67, no. 3–4, pp. 159–167, 2009.
- [26] S. C. Jones, "A rapid accurate unsteady-state Klinkenberg parameter," *SPE Journal*, pp. 383–397, 1972.
- [27] D. R. Faulkner and E. H. Rutter, "Comparisons of water and argon permeability in natural clay-bearing fault gouge under high pressure at 20°C," *Journal of Geophysical Research: Solid Earth*, vol. 105, no. 7, Article ID 2000JB900134, pp. 16415–16426, 2000.
- [28] W. Tanikawa and T. Shimamoto, "Klinkenberg effect for gas permeability and its comparison to water permeability for porous sedimentary rocks," *Hydrology and Earth System Sciences Discussions*, vol. 3, no. 4, pp. 1315–1338, 2006.
- [29] X. Cui, A. M. M. Bustin, and R. M. Bustin, "Measurements of gas permeability and diffusivity of tight reservoir rocks: Different approaches and their applications," *Geofluids*, vol. 9, no. 3, pp. 208–223, 2009.
- [30] H. Davarzani, M. Marcoux, P. Costeseque, and M. Quintard, "Experimental measurement of the effective diffusion and thermodiffusion coefficients for binary gas mixture in porous media," *Chemical Engineering Science*, vol. 65, no. 18, pp. 5092–5104, 2010.
- [31] A. M. Bustin, R. M. Bustin, and X. Cui, "Importance of Fabric on the Production of Gas Shales," in *Proceedings of the SPE Unconventional Reservoirs Conference*, Keystone, Colo, USA, 2008.
- [32] F. Civan, "Generalized Darcys law by control volume analysis including capillary and orifice effects," *J. Can. Petrol. Technol.*, vol. 47, no. 10, pp. 1–7, 2008.
- [33] F. Civan, "Effective correlation of apparent gas permeability in tight porous media," *Transport in Porous Media*, vol. 82, no. 2, pp. 375–384, 2010.
- [34] F. Civan, C. S. Rai, and C. H. Sondergeld, "Shale-gas permeability and diffusivity inferred by improved formulation of relevant retention and transport mechanisms," *Transport in Porous Media*, vol. 86, no. 3, pp. 925–944, 2011.
- [35] I. R. Al-Bulushi, R. S. Al-Maamari, and O. B. Wilson, "Brine versus Klinkenberg corrected gas permeability correlation for Shuaiba carbonate formation," *Journal of Petroleum Science and Engineering*, vol. 92–93, pp. 24–29, 2012.
- [36] E. A. Mason and A. P. Malinauskas, *Gas Transport in Porous Media*, Elsevier, Amsterdam, Netherlands, 1983.
- [37] R. E. Cunningham and R. J. Williams, *Diffusion in Gases and Porous Media*, Plenum press, New York, NY, USA, 1980.
- [38] S. A. Reinecke and B. E. Sleep, *Water Resources Research*, vol. 38, 2002.
- [39] D. Jarvie, "Evaluation of hydrocarbon generation and storage in Barnett Shale," in *Proceedings of the Petroleum Technology Transfer Council*, The University of Texas at Austin, Bureau of Economic Geology, 2004.
- [40] C. Freeman, G. J. Moridis, G. E. Michael, and T. A. Blasingame, "Measurement, Modeling, and Diagnostics of Flowing Gas Composition Changes in Shale Gas Wells," in *Proceedings of the SPE Latin America and Caribbean Petroleum Engineering Conference*, Mexico City, Mexico, 2012.
- [41] H. Hoteit and A. Firoozabadi, "Numerical Modeling of Diffusion in Fractured Media for Gas Injection and Recycling Schemes," in *Proceedings of the SPE Annual Technical Conference and Exhibition*, San Antonio, Tex, USA, 2006.
- [42] J. D. Hudson, F. Civan, G. Michel, D. Devegowda, and R. F. Sigal, "Modeling Multiple-Porosity Transport in Gas-Bearing Shale Formations," in *Proceedings of the SPE Latin America and Caribbean Petroleum Engineering Conference*, Mexico City, Mexico, 2012.

- [43] K. Malek and M.-O. Coppens, "Effects of surface roughness on self- and transport diffusion in porous media in the Knudsen regime," *Physical Review Letters*, vol. 87, no. 12, Article ID 125505, p. 125505/4, 2001.
- [44] F. Zhao, T. J. Armstrong, and A. V. Virkar, "Measurement of O₂-N₂ effective diffusivity in porous media at high temperatures using an electrochemical cell," *Journal of the Electrochemical Society*, vol. 150, no. 3, pp. A249–A256, 2003.
- [45] J. Welty, C. E. Wicks, G. L. Rorrer, and R. E. Wilson, *Fundamentals of Momentum, Heat and Mass Transfer*, Wiley-VCH, 2007.
- [46] F. Javadpour, "Nanopores and apparent permeability of gas flow in mudrocks (shales and siltstone)," *Journal of Canadian Petroleum Technology*, vol. 48, no. 8, pp. 16–21, 2009.
- [47] R. D. Hazlett, "Simulation of capillary-dominated displacements in microtomographic images of reservoir rocks," *Transport in Porous Media*, vol. 20, no. 1-2, pp. 21–35, 1995.
- [48] D. Wildenschild, C. M. P. Vaz, M. L. Rivers, D. Rikard, and B. S. B. Christensen, "Using X-ray computed tomography in hydrology: Systems, resolutions, and limitations," *Journal of Hydrology*, vol. 267, no. 3-4, pp. 285–297, 2002.
- [49] P. J. Withers, "X-ray nanotomography," *Materials Today*, vol. 10, no. 12, pp. 26–34, 2007.
- [50] S. Schlüter, A. Sheppard, K. Brown, and D. Wildenschild, "Image processing of multiphase images obtained via X-ray microtomography: a review," *Water Resources Research*, vol. 50, no. 4, pp. 3615–3639, 2014.
- [51] M. J. Blunt, B. Bijeljic, H. Dong et al., "Pore-scale imaging and modelling," *Advances in Water Resources*, vol. 51, pp. 197–216, 2013.
- [52] L. Tomutsa, D. B. Silin, and V. Radmilovic, "Analysis of chalk petrophysical properties by means of submicron-scale pore imaging and modeling," *SPE Reservoir Evaluation and Engineering*, vol. 10, no. 3, pp. 285–293, 2007.
- [53] M. E. Curtis, R. J. Ambrose, C. H. Sondergeld, and C. S. Rai, "Structural characterization of gas shales on the micro- and nano-scales," in *Proceedings of the Canadian Unconventional Resources and International Petroleum Conference*, SPE Paper 137693, Calgary, Canada, October 2010.
- [54] H. Lemmens, A. Butcher, and P. Botha, "FIB/SEM and automated mineralogy for core and cuttings analysis," in *Proceedings of the SPE Russian Oil and Gas Conference and Exhibition. Society of Petroleum Engineers.*, pp. 881–884, October 2010.
- [55] D. Michael, L. H. Uchic, B. J. Inkson, E. L. Principe, and P. Munroe, "Three-dimensional microstructural characterization using focused ion beam tomography," *MRS Bull.*, vol. 32, no. 8, 2007.
- [56] L. M. Keller, L. Holzer, R. Wepf, P. Gasser, B. Münch, and P. Marschall, "On the application of focused ion beam nanotomography in characterizing the 3D pore space geometry of Opalinus clay," *Physics and Chemistry of the Earth*, vol. 36, no. 17-18, pp. 1539–1544, 2011.
- [57] P. T. Callaghan, *Principles of Nuclear Magnetic Resonance Microscopy*, Oxford University Press on Demand, 1993.
- [58] B. Blümich, F. Casanova, and S. Appelt, "NMR at low magnetic fields," *Chemical Physics Letters*, vol. 477, no. 4-6, pp. 231–240, 2009.
- [59] H. Giesche, "Mercury porosimetry: a general (practical) overview," *Particle and Particle Systems Characterization*, vol. 23, no. 1, pp. 9–19, 2006.
- [60] C. A. León y León, "New perspectives in mercury porosimetry," *Advances in Colloid and Interface Science*, vol. 76-77, pp. 341–372, 1998.
- [61] J. Rouquerol, G. V. Baron, R. Denoyel et al., "The characterization of macroporous solids: An overview of the methodology," *Microporous and Mesoporous Materials*, vol. 154, pp. 2–6, 2012.
- [62] P. I. Ravikovitch, A. Vishnyakov, R. Russo, and A. V. Neimark, "Unified approach to pore size characterization of microporous carbonaceous materials from N₂, Ar, and CO₂ adsorption isotherms," *Langmuir*, vol. 16, no. 5, pp. 2311–2320, 2000.
- [63] J. C. Groen, L. A. A. Peffer, and J. Pérez-Ramírez, "Pore size determination in modified micro- and mesoporous materials. Pitfalls and limitations in gas adsorption data analysis," *Microporous and Mesoporous Materials*, vol. 60, no. 1-3, pp. 1–17, 2003.
- [64] Q. Xiong, T. G. Baychev, and A. P. Jivkov, "Review of pore network modelling of porous media: Experimental characterisations, network constructions and applications to reactive transport," *Journal of Contaminant Hydrology*, vol. 192, pp. 101–117, 2016.
- [65] P. M. Adler and J.-F. Thovert, "Real porous media: Local geometry and macroscopic properties," *Applied Mechanics Reviews*, vol. 51, no. 9, pp. 537–585, 1998.
- [66] P. Levitz, "Off-lattice reconstruction of porous media: Critical evaluation, geometrical confinement and molecular transport," *Advances in Colloid and Interface Science*, vol. 76-77, pp. 71–106, 1998.
- [67] A. P. Roberts and S. Torquato, "Chord-distribution functions of three-dimensional random media: approximate first-passage times of Gaussian processes," *Physical Review E. Statistical, Nonlinear, and Soft Matter Physics*, vol. 59, no. 5, part A, pp. 4953–4963, 1999.
- [68] M. A. Ioannidis and I. Chatzis, "A Mixed-Percolation Model of Capillary Hysteresis and Entrapment in Mercury Porosimetry," *Journal of Colloid And Interface Science*, vol. 161, no. 2, pp. 278–291, 1993.
- [69] C. Manwart, S. Torquato, and R. Hilfer, "Stochastic reconstruction of sandstones," *Physical Review E - Statistical Physics, Plasmas, Fluids, and Related Interdisciplinary Topics*, vol. 62, no. 1, pp. 893–899, 2000.
- [70] S. L. Bryant, P. R. King, and D. W. Mellor, "Network model evaluation of permeability and spatial correlation in a real random sphere packing," *Transport in Porous Media*, vol. 11, no. 1, pp. 53–70, 1993.
- [71] S. Bakke and P.-E. Oren, "3-D pore-scale modelling of sandstones and flow simulations in the pore networks," *SPE Journal*, vol. 2, no. 2, pp. 136–149, 1997.
- [72] T. R. Lerdahl, P. Oren, and S. Bakke, "A Predictive Network Model for Three-Phase Flow in Porous Media," in *Proceedings of the SPE/DOE Improved Oil Recovery Symposium*, Tulsa, Okla, USA, 2000.
- [73] P.-E. Oren and S. Bakke, "Process based reconstruction of sandstones and prediction of transport properties," *Transport in Porous Media*, vol. 46, no. 2-3, pp. 311–343, 2002.
- [74] R. I. Al-Raoush and C. S. Willson, "Extraction of physically realistic pore network properties from three-dimensional synchrotron X-ray microtomography images of unconsolidated porous media systems," *Journal of Hydrology*, vol. 300, no. 1–4, pp. 44–64, 2005.
- [75] Z. Jiang, K. Wu, G. Couples, M. I. J. Van Dijke, K. S. Sorbie, and J. Ma, "Efficient extraction of networks from three-dimensional porous media," *Water Resources Research*, vol. 43, no. 12, Article ID W12S03, 2007.
- [76] H. Shin, W. B. Lindquist, D. L. Sahagian, and S.-R. Song, "Analysis of the vesicular structure of basalts," *Computers and Geosciences*, vol. 31, no. 4, pp. 473–487, 2005.

- [77] A. Raouf and S. M. Hassanizadeh, "A new method for generating pore-network models of porous media," *Transport in Porous Media*, vol. 81, no. 3, pp. 391–407, 2010.
- [78] M. F. El-Amin, A. Salama, and S. Sun, "Numerical and dimensional investigation of two-phase countercurrent imbibition in porous media," *Journal of Computational and Applied Mathematics*, vol. 242, pp. 285–296, 2013.
- [79] M. E. Naraghi and F. Javadpour, "A stochastic permeability model for the shale-gas systems," *International Journal of Coal Geology*, vol. 140, pp. 111–124, 2015.
- [80] T. Zhang, A. Salama, S. Sun, and M. F. El-Amin, "Pore network modeling of drainage process in patterned porous media: a quasi-static study," *Journal of Computational Science*, vol. 9, pp. 64–69, 2015.
- [81] L. Zhang, D. Li, L. Wang, and D. Lu, "Simulation of Gas Transport in Tight/Shale Gas Reservoirs by a Multicomponent Model Based on PEBI Grid," *Journal of Chemistry*, vol. 2015, Article ID 572434, 2015.
- [82] T. Lia, H. Song, J. Wang, Y. Wang, and J. Killough, "An analytical method for modeling and analysis gas-water relative permeability in nanoscale pores with interfacial effects," *International Journal of Coal Geology*, vol. 159, pp. 71–81, 2016.
- [83] C. J. Landry, M. Prodanović, and P. Eichhubl, "Direct simulation of supercritical gas flow in complex nanoporous media and prediction of apparent permeability," *International Journal of Coal Geology*, vol. 159, pp. 120–134, 2016.
- [84] A. Gerami, P. Mostaghimi, R. T. Armstrong, A. Zamani, and M. E. Warkiani, "A microfluidic framework for studying relative permeability in coal," *International Journal of Coal Geology*, vol. 159, pp. 183–193, 2016.
- [85] T. Dong, N. B. Harris, K. Ayranci, C. E. Twemlow, and B. R. Nassichuk, "The impact of composition on pore throat size and permeability in high maturity shales: Middle and Upper Devonian Horn River Group, northeastern British Columbia, Canada," *Marine and Petroleum Geology*, vol. 81, pp. 220–236, 2017.
- [86] V. Joekar-Niasar and S. M. Hassanizadeh, "Analysis of fundamentals of two-phase flow in porous media using dynamic pore-network models: a review," *Critical Reviews in Environmental Science and Technology*, vol. 42, no. 18, pp. 1895–1976, 2012.
- [87] N. G. Hadjiconstantinou, "The limits of Navier-Stokes theory and kinetic extensions for describing small-scale gaseous hydrodynamics," *Physics of Fluids*, vol. 18, no. 11, Article ID 111301, 2006.
- [88] R. Raghavan and L. Chin, "Productivity Changes in Reservoirs With Stress-Dependent Permeability," in *Proceedings of the SPE Annual Technical Conference and Exhibition*, San Antonio, Tex, USA, 2002.
- [89] S. T. Chipperfield, J. R. Wong, D. S. Warner et al., "Shear dilation diagnostics: a new approach for evaluating tight gas stimulation treatments," in *Proceedings of the SPE Hydraulic Fracturing Technology Conference*, College Station, Tex, USA, 2007.
- [90] M. F. El Amin, A. G. Radwan, and S. Sun, "Analytical Solution for Fractional Derivative Gas-Flow Equation in Porous Media," *Results in Physics*, 2017.
- [91] T. D. Le, M. A. Murad, and P. A. Pereira, "A new matrix/fracture multiscale coupled model for flow in shale-gas reservoirs," *SPE Journal*, vol. 22, no. 1, pp. 265–288, 2017.
- [92] R. Yang, Z. Huang, W. Yu et al., "A comprehensive model for real gas transport in shale formations with complex non-planar fracture networks," *Scientific Reports*, vol. 6, Article ID 36673, 2016.
- [93] C. L. Cipolla, E. P. Lolon, J. C. Erdle, and V. Tathed, "Modeling well performance in shale-gas reservoirs," in *Proceedings of the SPE-125532-MS, SPE/EAGE Reservoir Characterization & Simulation Conference*, 2009.
- [94] J. Warren and P. Root, "The behavior of naturally fractured reservoirs," *Society of Petroleum Engineers Journal*, vol. 3, no. 3, pp. 245–255, 1963.
- [95] E. Ozkan, R. S. Raghavan, and O. G. Apaydin, "Modeling of fluid transfer from shale matrix to fracture network," in *Proceedings of the SPE Annual Technical Conference and Exhibition*, SPE-134830-MS, Society of Petroleum Engineers, Florence, Italy, September 2010.
- [96] G. J. Moridis, T. A. Blasingame, and C. M. Freeman, "Analysis of Mechanisms of Flow in Fractured Tight-Gas and Shale-Gas Reservoirs," in *Proceedings of the SPE Latin American and Caribbean Petroleum Engineering Conference*, Lima, Peru, 2010.
- [97] Y. Wu and P. Fakcharoenphol, "A Unified Mathematical Model for Unconventional Reservoir Simulation," in *Proceedings of the SPE EUROPEC/EAGE Annual Conference and Exhibition*, Vienna, Austria, 2011.
- [98] C. Guo, M. Wei, H. Chen, X. He, and B. Bai, "Improved numerical simulation for shale gas reservoirs," in *Proceedings of the Offshore Technology Conference Asia: Meeting the Challenges for Asia's Growth, OTC ASIA 2014*, pp. 2083–2099, March 2014.
- [99] M. F. El Amin, "Analytical solution of the apparent-permeability gas-transport equation in porous media," *European Physical Journal Plus*, vol. 132, no. 3, article no. 129, 2017.
- [100] T. Arbogast, J. Douglas, and U. Hornung, "Derivation of the double porosity model of single phase flow via homogenization theory," *SIAM Journal on Mathematical Analysis*, vol. 21, no. 4, pp. 823–836, 1990.
- [101] J. Douglas Jr. and T. Arbogast, "Dual-porosity models for flow in naturally fractured reservoirs," in *Dynamics of Fluids in Hierarchical Porous Media*, H. J. Cushman, Ed., pp. 177–221, Academic Press, London, UK, 1990.
- [102] T. Arbogast, "Gravitational forces in dual-porosity systems: I. Model derivation by homogenization," *Transport in Porous Media*, vol. 13, no. 2, pp. 179–203, 1993.
- [103] T. Arbogast, "Gravitational forces in dual-porosity systems: II. Computational validation of the homogenized model," *Transport in Porous Media*, vol. 13, no. 2, pp. 205–220, 1993.
- [104] U. Hornung and R. E. Showalter, "Diffusion models for fractured media," *Journal of Mathematical Analysis and Applications*, vol. 147, no. 1, pp. 69–80, 1990.
- [105] R. E. Showalter and N. J. Walkington, "Diffusion of fluid in a fissured medium with microstructure," *SIAM Journal on Mathematical Analysis*, vol. 22, no. 6, pp. 1702–1722, 1991.
- [106] M. Böhm and R. E. Showalter, "Diffusion in fissured media," *SIAM Journal on Mathematical Analysis*, vol. 16, no. 3, pp. 500–509, 1985.
- [107] R. B. Bird, W. E. Stewart, and E. N. Lightfoot, *Transport phenomena*, Wiley, 2007.
- [108] A. Firoozabadi, *Thermodynamics and applications in hydrocarbon reservoirs and production*, McGraw-Hill Education, 2015.
- [109] P. Sarma, "New transfer function for simulation of naturally fractured reservoirs with dual porosity models," *SPE Journal*, vol. 11, no. 3, 2006.
- [110] A. K. Dahaghi, "Numerical Simulation and Modeling of Enhanced Gas Recovery and CO₂ Sequestration in Shale Gas

- Reservoirs: A Feasibility Study,” in *Proceedings of the SPE International Conference on CO2 Capture, Storage, and Utilization*, New Orleans, La, USA, 2010.
- [111] J. Aronofsky and R. Jenkins, “A Simplified Analysis of Unsteady Radial Gas Flow,” *Journal of Petroleum Technology*, vol. 6, no. 7, pp. 23–28, 1954.
- [112] M. A. Biot and D. G. Willis, “The elastic coefficients of the theory of consolidation,” *Journal of Applied Mechanics*, vol. 24, pp. 594–601, 1957.
- [113] J. Noorishad and M. Mehran, “An upstream finite element method for solution of transient transport equation in fractured porous media,” *Water Resources Research*, vol. 18, no. 3, pp. 588–596, 1982.
- [114] M. Hui and B. Mallison, “System and Method for Predicting Fluid Flow Characteristics within Fractured Subsurface Reservoirs,” *US Patent Appl.*, 2009.
- [115] F. Marcondes, A. Varavei, and K. Sepehrnoori, “An Element-Based Finite-Volume Method Approach for Naturally Fractured Compositional Reservoir Simulation,” in *Proceedings of the 13th Brazilian Thermal Sciences Meeting*, Brazilian Society of Mechanical Sciences, Uberlandia, Brazil, 2010.
- [116] M. F. El Amin, S. Amir, A. Salama, D. Urozayev, and S. Sun, “Comparative study of shale-gas production using single- and dual-continuum approaches,” *Journal of Petroleum Science and Engineering*, vol. 157, pp. 894–905, 2017.
- [117] R. G. Baca, R. C. Arnett, and D. W. Langford, “Modelling fluid flow in fractured-porous rock masses by finite-element techniques,” *International Journal for Numerical Methods in Fluids*, vol. 4, no. 4, pp. 337–348, 1984.
- [118] R. Juanes, J. Samper, and J. Molinero, “A general and efficient formulation of fractures and boundary conditions in the finite element method,” *International Journal for Numerical Methods in Engineering*, vol. 54, no. 12, pp. 1751–1774, 2002.
- [119] S. Matthai, A. Mezentsev, and M. Belayneh, “Control-Volume Finite-Element Two-Phase Flow Experiments with Fractured Rock Represented by Unstructured 3D Hybrid Meshes,” in *Proceedings of the SPE Reservoir Simulation Symposium*, Houston, Tex, USA, 2005.
- [120] C. L. Cipolla, T. Fitzpatrick, M. J. Williams, and U. K. Ganguly, “Seismic-to-Simulation for Unconventional Reservoir Development,” in *Proceedings of the SPE Reservoir Characterisation and Simulation Conference and Exhibition*, Abu Dhabi, UAE, 2011.
- [121] M. Sheng, G. Li, S. N. Shah, and X. Jin, “Extended Finite Element Modeling of Multi-scale Flow in Fractured Shale Gas Reservoirs,” in *Proceedings of the SPE Annual Technical Conference and Exhibition*, San Antonio, Tex, USA, 2012.
- [122] V. Martin, J. Jaffre, and J. E. Roberts, “Modeling fractures and barriers as interfaces for flow in porous media,” *SIAM Journal on Scientific Computing*, vol. 26, no. 5, pp. 1667–1691, 2005.
- [123] J. Jaffré, M. Mnejja, and J. E. Roberts, “A discrete fracture model for two-phase flow with matrix-fracture interaction,” in *Proceedings of the 11th International Conference on Computational Science, ICCS 2011*, pp. 967–973, June 2011.
- [124] I. S. Pop, J. Bogers, and K. Kumar, “Analysis and upscaling of a reactive transport model in fractured porous media with nonlinear transmission condition,” *Vietnam Journal of Mathematics*, vol. 45, no. 1-2, pp. 77–102, 2017.
- [125] S. Lee, A. Mikelić, M. F. Wheeler, and T. Wick, “Phase-field modeling of proppant-filled fractures in a poroelastic medium,” *Computer Methods in Applied Mechanics and Engineering*, vol. 312, pp. 509–541, 2016.
- [126] A. Mikelić, M. F. Wheeler, and T. Wick, “Phase-field modeling of a fluid-driven fracture in a poroelastic medium,” *Computational Geosciences*, vol. 19, no. 6, pp. 1171–1195, 2015.
- [127] A. Mikelić, M. F. Wheeler, and T. Wick, “A phase-field method for propagating fluid-filled fractures coupled to a surrounding porous medium,” *Multiscale Modeling & Simulation. A SIAM Interdisciplinary Journal*, vol. 13, no. 1, pp. 367–398, 2015.
- [128] L. Li and S. H. Lee, “Efficient field-scale simulation of black oil in a naturally fractured reservoir through discrete fracture networks and homogenized media,” *SPE Reservoir Evaluation and Engineering*, vol. 11, no. 4, pp. 750–758, 2008.
- [129] A. Moinfar, A. Varavei, K. Sepehrnoori, and R. T. Johns, “Development of an efficient embedded discrete fracture model for 3D compositional reservoir simulation in fractured reservoirs,” *SPE Journal*, vol. 19, no. 2, pp. 289–303, 2014.
- [130] J. Jiang and R. M. Younis, “Hybrid coupled discrete-fracture/matrix and multicontinuum models for unconventional-reservoir simulation,” *SPE Journal*, vol. 21, no. 3, pp. 1009–1027, 2016.
- [131] W. Zhou, R. Banerjee, B. Poe, J. Spath, and M. Thambynayagam, “Semianalytical production simulation of complex hydraulic-fracture networks,” *SPE Journal*, vol. 19, no. 1, pp. 6–18, 2014.
- [132] J. Moortgat, S. Sun, and A. Firoozabadi, “Compositional modeling of three-phase flow with gravity using higher-order finite element methods,” *Water Resources Research*, vol. 47, no. 5, Article ID W05511, 2011.
- [133] S. Sun and M. F. Wheeler, “Symmetric and nonsymmetric discontinuous Galerkin methods for reactive transport in porous media,” *SIAM Journal on Numerical Analysis*, vol. 43, no. 1, pp. 195–219, 2005.
- [134] S. Sun and M. F. Wheeler, “Analysis of discontinuous Galerkin methods for multicomponent reactive transport problems,” *Computers & Mathematics with Applications. An International Journal*, vol. 52, no. 5, pp. 637–650, 2006.
- [135] J. Kou and S. Sun, “Convergence of discontinuous Galerkin methods for incompressible two-phase flow in heterogeneous media,” *SIAM Journal on Numerical Analysis*, vol. 51, no. 6, pp. 3280–3306, 2014.
- [136] C. Dawson, S. Sun, and M. F. Wheeler, “Compatible algorithms for coupled flow and transport,” *Computer Methods in Applied Mechanics and Engineering*, vol. 193, no. 23-26, pp. 2565–2580, 2004.
- [137] J. Kou and S. Sun, “An adaptive finite element method for simulating surface tension with the gradient theory of fluid interfaces,” *Journal of Computational and Applied Mathematics*, vol. 255, pp. 593–604, 2014.
- [138] F. A. Radu, I. S. Pop, and S. Attinger, “Analysis of an Euler implicit-mixed finite element scheme for reactive solute transport in porous media,” *Numerical Methods for Partial Differential Equations. An International Journal*, vol. 26, no. 2, pp. 320–344, 2010.
- [139] F. A. Radu and I. S. Pop, “Newton method for reactive solute transport with equilibrium sorption in porous media,” *Journal of Computational and Applied Mathematics*, vol. 234, no. 7, pp. 2118–2127, 2010.
- [140] M. Vohralík and M.-F. A. Wheeler, “Posteriori error estimates, stopping criteria, and adaptivity for two-phase flows,” *Comput. Geosci.*, vol. 17, pp. 789–812, 2013.
- [141] M. Vohralík, “Polynomial-degree-robust a posteriori estimates in a unified setting for conforming, nonconforming, discontinuous Galerkin, and mixed discretizations,” *SIAM J. Numer. Anal.*, vol. 53, pp. 1058–1081, 2015.

- [142] E. Marchand, T. Müller, and P. Knabner, "Fully coupled generalized hybrid-mixed finite element approximation of two-phase two-component flow in porous media," *Part I: formulation and properties of the mathematical model*, *Computational Geosciences*, vol. 17, no. 2, pp. 431–442, 2013.
- [143] S. Sun, A. Salama, and M. F. El Amin, "Matrix-oriented implementation for the numerical solution of the partial differential equations governing flows and transport in porous media," *Computers and Fluids*, vol. 68, pp. 38–46, 2012.
- [144] A. Salama, S. Sun, and M. F. El-Amin, "An efficient implicit-pressure/explicit-saturation-method-based shifting-matrix algorithm to simulate two-phase, immiscible flow in porous media with application to CO₂ sequestration in the subsurface," *SPE Journal*, vol. 18, no. 6, pp. 1092–1101, 2013.
- [145] A. Salama, S. Sun, and M. F. El Amin, "A multipoint flux approximation of the steady-state heat conduction equation in anisotropic media," *Journal of Heat Transfer*, vol. 135, no. 4, Article ID 041302, 2013.
- [146] A. Salama, S. Sun, and M. F. Wheeler, "Solving global problem by considering multitude of local problems: application to fluid flow in anisotropic porous media using the multipoint flux approximation," *Journal of Computational and Applied Mathematics*, vol. 267, pp. 117–130, 2014.
- [147] A. Salama, A. Negara, M. El Amin, and S. Sun, "Numerical investigation of nanoparticles transport in anisotropic porous media," *Journal of contaminant hydrology*, vol. 181, pp. 114–130, 2015.
- [148] A. Salama, S. Sun, and M. F. El Amin, "Investigation of thermal energy transport from an anisotropic central heating element to the adjacent channels: A multipoint flux approximation," *Annals of Nuclear Energy*, vol. 76, pp. 100–112, 2015.
- [149] A. Salama, S. Sun, and M. F. El Amin, "An algorithm for the numerical solution of the pseudo compressible Navier-Stokes equations based on the experimenting fields approach," in *Proceedings of the International Conference on Computational Science, ICCS 2002*, pp. 1229–1238, April 2002.
- [150] Y. Wu, A. Salama, and S. Sun, "Parallel simulation of wormhole propagation with the Darcy-Brinkman-Forchheimer framework," *Computers and Geotechnics*, vol. 69, pp. 564–577, 2015.
- [151] A. Negara, A. Salama, and S. Sun, "Multiphase flow simulation with gravity effect in anisotropic porous media using multipoint flux approximation," *Computers & Fluids. An International Journal*, vol. 114, pp. 66–74, 2015.
- [152] A. Negara, A. Salama, S. Sun, M. Elgassier, and Y. Wu, "Numerical Simulation of Natural Gas Flow in Anisotropic Shale Reservoirs," in *Proceedings of the Abu Dhabi International Petroleum Exhibition and Conference*, Abu Dhabi, UAE, 2015.
- [153] M. F. El-Amin, A. Salama, and S. Sun, "Numerical and dimensional analysis of nanoparticles transport with two-phase flow in porous media," *Journal of Petroleum Science and Engineering*, vol. 128, pp. 53–64, 2015.
- [154] A. Salama, W. Li, and S. Sun, "Finite volume approximation of the three-dimensional flow equation in axisymmetric, heterogeneous porous media based on local analytical solution," *Journal of Hydrology*, vol. 501, pp. 45–55, 2013.
- [155] A. Salama, "A finite volume approach to the problem of heat transfer in axisymmetric annulus geometry with internal heating element using local analytical solution techniques," *Kerntechnik*, vol. 79, no. 5, pp. 436–445, 2014.
- [156] R. Helmig, *Multiphase flow and transport processes in the subsurface: a contribution to the modeling of hydrosystems*, Springer, 1997.
- [157] Z. Chen, G. Huan, and Y. Ma, "Computational methods for multiphase flows in porous media," *Society for Industrial and Applied Mathematics*, 2006.
- [158] J. M. Nordbotten and M. A. Celia, *Geological Storage of CO₂: Modeling Approaches for Large-Scale Simulation*, vol. 256, John Wiley & Sons, 2011.
- [159] P. Raviart and J. Thomas, "A mixed finite element method for 2-nd order elliptic problems," *Mathematical aspects of finite element methods*, pp. 292–315, 1977.
- [160] J.-C. Nédélec, "Mixed finite elements in \mathbb{R}^3 ," *Numerische Mathematik*, vol. 35, no. 3, pp. 315–341, 1980.
- [161] T. Arbogast, M. F. Wheeler, and I. Yotov, "Mixed finite elements for elliptic problems with tensor coefficients as cell-centered finite differences," *SIAM Journal on Numerical Analysis*, vol. 34, no. 2, pp. 828–852, 1997.
- [162] M. R. Todd, P. M. O'Dell, and G. J. Hirasaki, "Methods for increased accuracy in numerical reservoir simulators," *Soc. Petrol. Engrg. J.*, vol. 12, pp. 515–530, 1972.
- [163] J. Douglas and J. E. Roberts, "Global estimates for mixed methods for second order elliptic equations," *Mathematics of Computation*, vol. 44, no. 169, pp. 39–52, 1985.
- [164] G. Chavent and J. Jaffré, *Mathematical models and finite elements for reservoir simulation*, Elsevier Science Publishers, New York, NY, USA, 1986.
- [165] C. Johnson, *Streamline diffusion methods for problems in fluid mechanics*, *Finite Elements in Fluids VI*, Wiley, New York, NY, USA, 1986.
- [166] C. N. Dawson, T. F. Russell, and M. F. Wheeler, "Some improved error estimates for the modified method of characteristics," *SIAM Journal on Numerical Analysis*, vol. 26, no. 6, pp. 1487–1512, 1989.
- [167] T. F. Russell and M. F. Wheeler, "Finite element and finite difference methods for continuous flows in porous media," *The Mathematics of Reservoir Simulation*, pp. 35–106, 1983.
- [168] Z. Chen, *Finite Element Methods and Their Applications*, Springer, Berlin, Germany, 2005.
- [169] S. Whitaker, "Flow in porous media III: Deformable media," *Transport in Porous Media*, vol. 1, no. 2, pp. 127–154, 1986.
- [170] P. F. Dobson, T. J. Kneafsey, E. L. Sonnenthal, N. Spycher, and J. A. Apps, "Experimental and numerical simulation of dissolution and precipitation: Implications for fracture sealing at Yucca Mountain, Nevada," *Journal of Contaminant Hydrology*, vol. 62–63, pp. 459–476, 2003.
- [171] S. Valliappan and N. Khalili-Naghadeh, "Flow through fissured porous media with deformable matrix," *International Journal for Numerical Methods in Engineering*, vol. 29, no. 5, pp. 1079–1094, 1990.
- [172] C. Zhao, B. E. Hobbs, H. B. Mühlhaus, A. Ord, and G. Lin, "Numerical modelling of double diffusion driven reactive flow transport in deformable fluid-saturated porous media with particular consideration of temperature-dependent chemical reaction rates," *Engineering Computations (Swansea, Wales)*, vol. 17, no. 4, pp. 367–385, 2000.
- [173] J. Taron, D. Elsworth, and K.-B. Min, "Numerical simulation of thermal-hydrologic-mechanical-chemical processes in deformable, fractured porous media," *International Journal of Rock Mechanics and Mining Sciences*, vol. 46, no. 5, pp. 842–854, 2009.
- [174] A. Madeo, F. dell'Isola, and F. Darve, "A continuum model for deformable, second gradient porous media partially saturated with compressible fluids," *Journal of the Mechanics and Physics of Solids*, vol. 61, no. 11, pp. 2196–2211, 2013.

- [175] J. Bear, *Dynamics of fluids in porous media*, Courier Corporation, 2013.
- [176] A. N. Alshawabkeh and N. Rahbar, "Parametric study of one-dimensional solute transport in deformable porous media," *Journal of Geotechnical and Geoenvironmental Engineering*, vol. 132, no. 8, pp. 1001–1010, 2006.
- [177] T. L. van Noorden, "Crystal precipitation and dissolution in a porous medium: effective equations and numerical experiments," *Multiscale Modeling & Simulation. A SIAM Interdisciplinary Journal*, vol. 7, no. 3, pp. 1220–1236, 2009.
- [178] K. Kumar, T. L. van Noorden, and I. S. Pop, "Effective dispersion equations for reactive flows involving free boundaries at the microscale," *Multiscale Modeling & Simulation. A SIAM Interdisciplinary Journal*, vol. 9, no. 1, pp. 29–58, 2011.
- [179] C. Bringedal, I. Berre, I. S. Pop, and F. A. Radu, "Upscaling of non-isothermal reactive porous media flow with changing porosity," *Transport in Porous Media*, vol. 114, no. 2, pp. 371–393, 2016.
- [180] K. Kumar, I. S. Pop, and F. A. Radu, "Convergence analysis of mixed numerical schemes for reactive flow in a porous medium," *SIAM Journal on Numerical Analysis*, vol. 51, no. 4, pp. 2283–2308, 2013.
- [181] K. Kumar, M. F. Wheeler, and T. Wick, "Reactive flow and reaction-induced boundary movement in a thin channel," *SIAM Journal on Scientific Computing*, vol. 35, no. 6, pp. B1235–B1266, 2013.
- [182] K. Kumar, M. van Helvoort, and I. S. Pop, "Rigorous upscaling of rough boundaries for reactive flows," *Z. angew. Math. Mech.*, vol. 94, no. 7–8, pp. 623–644, 2014.
- [183] K. Kumar, I. S. Pop, and F. A. Radu, "Convergence analysis for a conformal discretization of a model for precipitation and dissolution in porous media," *Numerische Mathematik*, vol. 127, no. 4, pp. 715–749, 2014.
- [184] K. Kumar, T. van Noorden, and I. S. Pop, "Upscaling of reactive flows in domains with moving oscillating boundaries," *Discrete and Continuous Dynamical Systems. Series S*, vol. 7, no. 1, pp. 95–111, 2014.
- [185] Media 1: <https://www.youtube.com/watch?v=4LBJsXWQRV8>.
- [186] Media 2: <https://www.youtube.com/watch?v=4findBGNOHs>.
- [187] Media 3: https://www.youtube.com/watch?v=Yd8pr6uFA_Y.
- [188] S. G. Osborn, A. Vengosh, N. R. Warner, and R. B. Jackson, "Methane contamination of drinking water accompanying gas-well drilling and hydraulic fracturing," *Proceedings of the National Academy of Sciences of the United States of America*, vol. 108, no. 20, pp. 8172–8176, 2011.
- [189] M. Bamberger and R. E. Oswald, "Impacts of gas drilling on human and animal health," *New solutions : a journal of environmental and occupational health policy : NS*, vol. 22, no. 1, pp. 51–77, 2012.
- [190] T. Colborn, C. Kwiatkowski, K. Schultz, and M. Bachran, "Hazard assessment articles natural gas operations from a public health perspective," *Human and Ecological Risk Assessment*, vol. 17, no. 5, pp. 1039–1056, 2012.

Research Article

Experimental Study on the Effects of Stress Variations on the Permeability of Feldspar-Quartz Sandstone

Fugang Wang,¹ Zhaoxu Mi,¹ Zhaojun Sun,¹ Xufeng Li,^{2,3} Tianshan Lan,¹ Yilong Yuan,¹ and Tianfu Xu¹

¹Key Laboratory of Groundwater Resources and Environment, Ministry of Education, Jilin University, Changchun 130012, China

²Center for Hydrogeology and Environmental Geology Survey, China Geological Survey, Baoding 071000, China

³Key Laboratory of Carbon Dioxide Geological Storage, Center for Hydrogeology and Environmental Geology Survey, China Geological Survey, Baoding 071000, China

Correspondence should be addressed to Fugang Wang; wangfugang@jlu.edu.cn

Received 20 February 2017; Revised 24 June 2017; Accepted 9 August 2017; Published 10 September 2017

Academic Editor: Kundan Kumar

Copyright © 2017 Fugang Wang et al. This is an open access article distributed under the Creative Commons Attribution License, which permits unrestricted use, distribution, and reproduction in any medium, provided the original work is properly cited.

The multistage and discontinuous nature of the injection process used in the geological storage of CO₂ causes reservoirs to experience repeated loading and unloading. The reservoir permeability changes caused by this phenomenon directly impact the CO₂ injection process and the process of CO₂ migration in the reservoirs. Through laboratory experiments, variations in the permeability of sandstone in the Liujiagou formation of the Ordos CO₂ capture and storage (CCS) demonstration project were analyzed using cyclic variations in injection pressure and confining pressure and multistage loading and unloading. The variation in the micropore structure and its influence on the permeability were analyzed based on micropore structure tests. In addition, the effects of multiple stress changes on the permeability of the same type of rock with different clay minerals content were also analyzed. More attention should be devoted to the influence of pressure variations on permeability in evaluations of storage potential and studies of CO₂ migration in reservoirs in CCS engineering.

1. Introduction

Global warming presents a serious threat to the living environment of humans. Reducing the emissions of carbon dioxide (CO₂) is a common challenge for countries worldwide. The technology of geological storage of CO₂ has attracted the attention of governments and scientists around the world as a direct and effective emission reduction technology recognized by the international community [1]. The China Geological Survey and the China Shenhua Group jointly launched a demonstration project of carbon dioxide geological storage in the Ordos Basin in 2010, and the Liujiagou formation is one of the target reservoirs. During the injection process, the reservoir will experience radial stress accumulations surrounding the injection well. In addition, the horizontal stress accumulation during this process will be greater near the injection well. The horizontal radial stress accumulation and injection pressure have obvious effects on the migration and injection of CO₂ in the reservoir.

The multistage and discontinuous nature of CO₂ injection causes the stress and injection pressure in the reservoirs to repeatedly increase and decrease. The micropore structure of the reservoir may change when reservoir stress field is disrupted. The permeability and other important physical properties of the reservoir may change in response [2, 3]. The variations in permeability during repeated reservoir stress changes, combined with changes in the pore structure characteristics, have great significance for the evaluation of the geological storage of CO₂, particularly the capacity, storage potential, and safety of the reservoirs used.

Numerous experimental and theoretical studies have focused on the relationship between stress variations and the permeability of low-permeability rocks in geotechnical engineering, hydraulic engineering, oil and gas reservoir development engineering, and other disciplines [4, 5]. Fatt et al. [6, 7] studied the effects of overburden pressure and confining pressure on sandstone permeability. The permeability and overburden pressure are negatively correlated,

TABLE 1: Mineralogical compositions of the samples (%).

Sample	Quartz	Plagioclase	K-feldspar	Calcite	Biotite	Kaolinite	Illite/smectite
S1	16	46	29	1	3	2	3
S2	10	12	42	7	4	5	20

as is the relationship between permeability and confining pressure. In addition, the change in the low-pressure zone is more obvious. Wu et al. [8] conducted an experimental study on the impact of pore pressure on permeability using three halite rocks with different compositions. The results show that permeability increases with increasing pore pressure and is influenced by the Klinkenberg effect. Wang et al. [9] used triaxial permeability tests while controlling the axial strain and found that the permeability of marble decreases as the difference between axial pressure and confining pressure increases. Vairogs et al. [10] and Xue et al. [11] suggested that changes in the effective stress affect the pore structure and skeletal structure of rocks, which affect the permeability of the rock. Peng et al. [12] argued that the permeability changes that occur during the elastic stage, the elastic-plastic stage, and the residual flow stage are different because of the differing degrees of rock deformation during the stress-strain process. Additionally, Jennings et al. [13], Peng et al. [12], and Wang et al. [14] constructed different mathematical models of permeability and confining pressure, including a cubic polynomial function, a logarithmic function, a power function, and other single-function mathematical models. Lan et al. [15] proposed a stress sensitivity coefficient model based on the analysis of stress sensitivity data obtained from samples of low-permeability sandstone from oil and gas reservoirs in the Sichuan Basin and Songliao Basin. In addition, they found that the greater the stress sensitivity coefficient, the stronger the reservoir stress sensitivity.

In the literature, there are lots of experiments and theoretical studies whose primary goal was to investigate the permeability stress sensitivity of low-permeability rocks. Additionally, the relationship between stress and permeability has been analyzed under the corresponding conditions. A variety of models that describe the relationship between stress and permeability have been constructed [16]. However, the constructed mathematical models do not have universal applicability, because the study objects differ in terms of rock type, mineral composition, and geochemical properties [17]. The correlation between rock permeability and pore structure is significant for a specific rock formation [2]. The influence of multiphase stress changes on the micropore structure of rock will lead to changes in rock permeability. However, studies of the relationship between the permeability and stress variation based on changes in the micropore structure of rocks are still rarely reported. In addition, the influence of the intermittent pressure dissipation that occurs during the CO₂ injection process on permeability has not received much attention from researchers. In a CCS project, the CO₂ injection process has a multistage and discontinuous nature due to equipment maintenance and other unforeseen events. Therefore, it is necessary to determine the influence of injection intervals on the recovery of permeability.

In this paper, a CO₂ reservoir formation, the Liujiagou formation, part of the Ordos CCS demonstration project in China, was selected as the focus of this study. Based on the specific operation conditions of the CCS project and the environmental characteristics of CO₂ reservoirs, the permeability changes in the target reservoir were analyzed under two types of conditions. One condition involved a fixed injection pressure and a variable confining pressure, and the other involved a fixed confining pressure and a variable injection pressure. Quantitative mathematical models of the effects of the confining pressure and injection pressure on the permeability of the rocks in the Liujiagou formation were constructed. The permeability changes have been analyzed, combining the changes in rock micropore structure before and after multiple stages of stress changes. The research results are helpful for numerical simulations and engineering practice in the geological storage of CO₂ at the Ordos CCS demonstration project.

2. Materials and Methods

2.1. Materials. The Ordos Basin is in the eastern part of Northwest China, and it has a total area of 28.2×10^4 km². The basin is rich in coal, oil, natural gas, and mineral resources, such as gypsum. It represents the new energy chemical industry base of China. The Ordos CCS demonstration project, the first CCS project in China, is located in the northeastern portion of the basin. The strata involved range in age from the Paleozoic to the Cenozoic, and their total thickness exceeds 5000 m. According to the engineering design, the Mesozoic (Triassic) Liujiagou formation and the underlying Paleozoic (Permian) strata are the target CO₂ storage formations, and these units consist mainly of interbedded sandstone and mudstone [18].

The Liujiagou formation is one of the important CO₂ reservoirs of the Ordos CCS demonstration project. The reservoir formation consists of low-permeability sandstone. It is present at a depth of 1576–1699 m and has a thickness of 123 m [19]. The porosity is 6.3%–13%, the permeability is 0.040~0.408 mD [3], the formation pressure range is 15.76~16.99 MPa [20], and the formation temperature is 52.74~56.03°C [21].

The sandstone rock samples from the Liujiagou formation used in this study are labeled S1 and S2, respectively (Figure 1). Sample S1 has a diameter of 3.792 cm, a length of 7.709 cm, and a porosity of 11.86%. Sample S2 has a diameter of 3.793 cm, a length of 7.482 cm, and a porosity of 11.87%. Both samples are feldspar-quartz sandstones and have similar porosity. However, the clay mineral content is approximately five times higher in S2 than in S1 (Table 1).

2.2. Equipment and Instruments. The experimental instrument used for the permeability tests is an HXKS-A high



FIGURE 1: Rock samples.

temperature and high-pressure pore fluid displacement test system. The system can be used to measure the permeability of rocks under different pressure conditions, and it can work stably for a long time (30 days) under set temperature and pressure conditions. The system consists of a pressure control system, a temperature control system, and a parameter measurement and control system. The outlet pressure and the confining pressure loading systems are controlled by two constant-speed, constant-pressure, single-cylinder pumps (ISCO-65D). The injection pressure loading system is controlled by a two-cylinder, constant-speed, constant-pressure pump (ISCO-100DX). These pumps work within a range of flow rates of 0.0001–45 mL/min, they have a maximum output pressure of 70 MPa, and the pressure is within 0.5% of the set pressure within 48 hours after a new pressure is selected.

The microscopic pore structure of the rock samples was tested using a 3H-2000PS1 specific surface area and pore size analyzer that was manufactured by Beijing Beishide Instrument Technology Corporation, Limited. The principle of this instrument uses the static volumetric method of isothermal physical adsorption. The adsorption isotherm is measured at 77 K (the temperature of liquid nitrogen), high-purity nitrogen acts as the adsorption medium, and the relative pressure used is 0.01–1.00. The range of pore diameters tested is 0.35–100.00 nm. The lowest measurable specific surface area is 0.005 m²/g. The minimum detection volume is 0.0001 cm³/g. The gas adsorption method can effectively reflect the distribution of nanopores in materials, and it has been widely used in assessing the porous structure of porous materials [22]. Changes in the permeability can be determined by testing the microscopic pore structure of rock samples before and after stress changes.

2.3. Experimental Method. The experimental procedure is shown below.

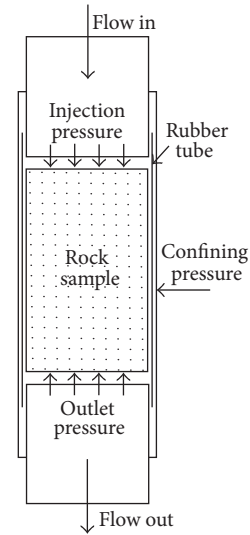


FIGURE 2: Schematic diagram of permeability tests.

(1) The rock samples were processed into cylindrical cores. The lithology and mineral compositions of the rock samples were assessed using X-ray diffractometry.

(2) Some rock samples were taken for use in nitrogen adsorption experiments to ascertain the micropore structure. To eliminate the irreducible water and the capillary water in the samples, the samples were pretreated at 300°C for 3 h under high vacuum before the experiment. The nitrogen adsorption and desorption isotherms of different partial pressures were then measured at 77 K using high-purity nitrogen as the adsorbent to determine the microscopic pore structure of the rock samples.

(3) The rock samples used to study stress-induced permeability changes were measured in terms of their lengths, diameters, and weights. After the samples were dried in a drying oven for 24 hours, the samples were put into a vacuum saturation bin and saturated with distilled water. The fully saturated cores were then placed in a core holder at a set temperature of 25°C to begin the permeability testing under different stress conditions (Figure 2).

(4) As the injection pressure changed, the confining pressure was held constant at 20 MPa. The distilled water was injected into the rock samples. The saturated permeability against water of the rock was measured under different injection pressures, starting from the initial pressure of 4 MPa and increasing to the maximum injection pressure of 18 MPa with a pressure increment of 2 MPa (the maximum pressure was less than the rock cracking pressure of 24.84 MPa). When the permeability experiment reached a steady state at a given injection pressure, the injection pressure was increased to the next injection pressure, according to the pressure increment, until the maximum injection pressure (18 MPa) was reached. In addition, the injection pressure was then unloaded at a pressure increment of 2 MPa until the initial pressure of 4 MPa was reached. The rock permeability was also measured at each pressure during the unloading process. The injection pressure loading and unloading process was repeated 3 times,

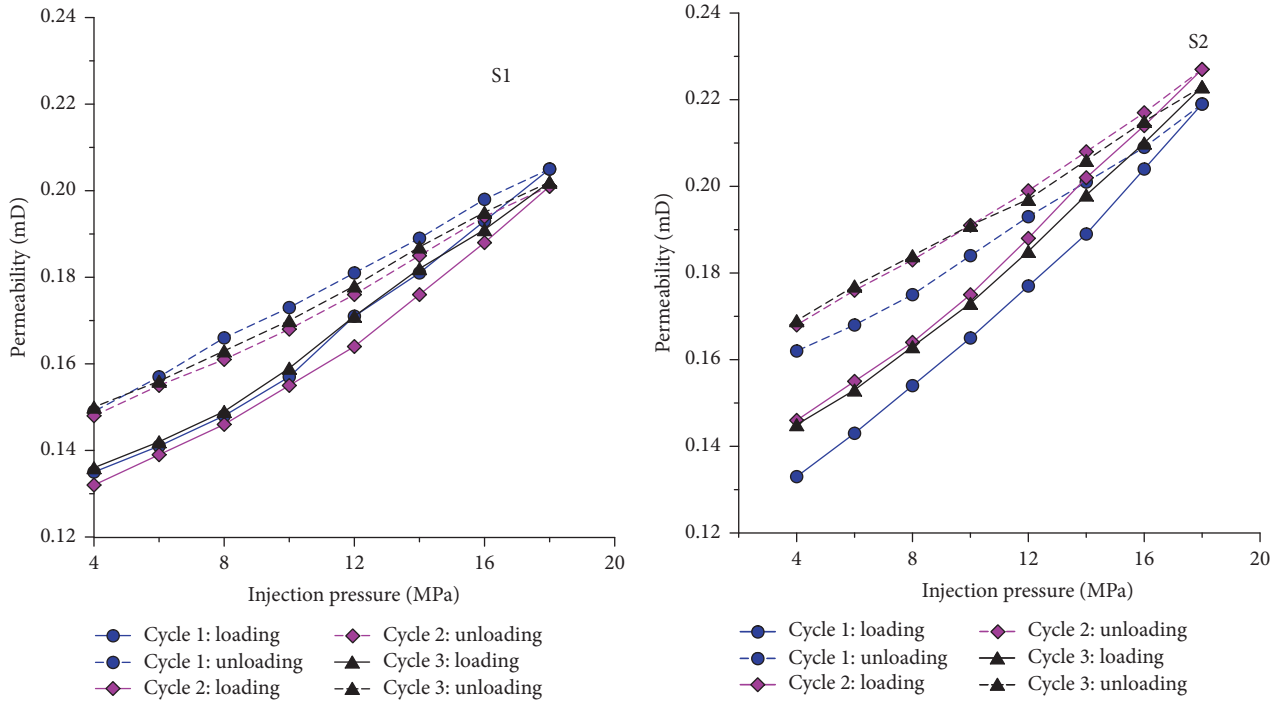


FIGURE 3: Relationship between permeability and injection pressure under constant confining pressure.

and the cycles were labeled Cycle 1, Cycle 2, and Cycle 3, respectively. The time interval between pairs of adjacent cycles was 24 hours. In addition, during these intervals, the pressure was released, and the experimental sample was removed from the core holder and stored immersed in distilled water.

(5) Under the variable confining pressure, the injection pressure was held constant at 4 MPa. The saturated permeability against water of the samples was measured under different confining pressures, starting at an initial pressure of 6 MPa and increasing to the maximum confining pressure of 20 MPa with a pressure increment of 2 MPa. The confining pressure loading and unloading process was repeated 3 times. The time interval between pairs of adjacent cycles was 24 hours. During these intervals, the pressure was released and the experimental sample was removed from the core holder and stored immersed in distilled water.

(6) Finally, the microscopic pore structure of the rock samples was tested again after all the permeability experiments under different stress conditions had been completed.

3. Results and Analysis

3.1. Influence of Changing Injection Pressure on Permeability

3.1.1. *Variation in Permeability under Changing Injection Pressure.* Figure 3 shows the changes in rock permeability with changing injection pressure in the three cycles of increasing and decreasing injection pressure under constant confining pressure.

The following observations can be made.

(1) Figure 3 shows that the rock permeability increases as the injection pressure increases and that a positive correlation exists between them. With decreasing injection pressure, the permeability of the rock gradually recovers, but the sample does not achieve the same permeability as it had at the same injection pressure during the load increasing stage. For example, for sample S1 in the first cycle of the experiment, when the injection pressure is 8 MPa, the permeability is 0.148 mD during the increasing injection pressure stage, whereas the permeability is 0.166 mD during the decreasing injection pressure stage.

(2) Figure 3 also shows that, for adjacent cycle experiments, the permeability curves overlap but do not completely coincide with each other. At each point with the same injection pressure, the permeability during the injection pressure loading stage is smaller than that during the unloading stage. For adjacent cycle experiments, the differences in the permeability values are very small for the last two cycles of the experiment, Cycle 2 and Cycle 3. Especially for sample S2, these phenomena are quite obvious when the permeability curves of Cycle 2 and Cycle 3 are compared.

The interval between adjacent cycle experiments has an obvious impact on the rock permeability, and this effect can be seen in the permeability values at 4 MPa at the beginning of each experiment. For example, for sample S2, the permeability at the start of Cycle 1 is 0.125 mD at 4 MPa. However, after the interval between Cycle 1 and Cycle 2, the permeability value changes to 0.145 mD when Cycle 2 begins at 4 MPa.

(3) We use k_u to denote the relative permeability increase between two adjacent points with different pressures during

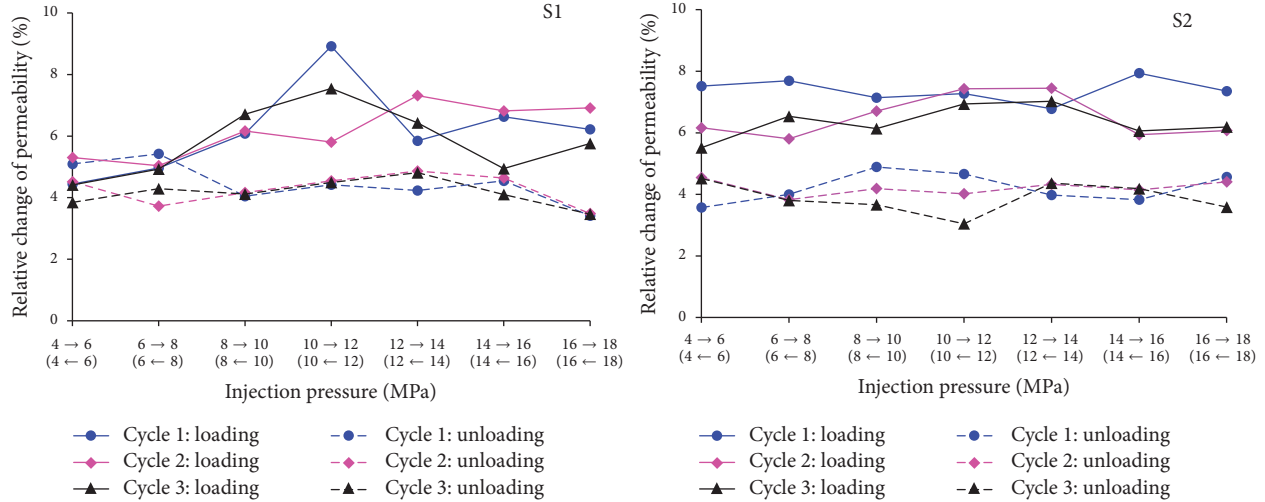


FIGURE 4: Relative changes in permeability under changing injection pressure conditions.

the injection pressure increasing stage for each cycle and k_d to denote the relative permeability decrease of the rock samples during the unloading stage.

$$k_u = \frac{k_{i+1} - k_i}{k_i} \times 100\%, \quad (1)$$

$$k_d = \frac{k_j - k_{j+1}}{k_j} \times 100\%,$$

where k_i and k_{i+1} represent the rock permeability values at two adjacent points i and $i+1$ with different pressures during the injection pressure loading stage in each cycle and k_j and k_{j+1} represent the permeability values at two adjacent points j and $j+1$ with different pressures during the injection pressure unloading stage.

The relative changes in rock permeability are shown in Figure 4.

Figure 4 shows that the increases in relative permeability range from 5% to 8% during the injection pressure loading stage and that the decrease in relative permeability ranges from 3% to 5% during the unloading stage. The variations are stable in both directions. For example, for sample S2, during Cycle 1, the maximum and minimum permeability changes are 7.94% and 6.78%, respectively, during the injection pressure loading stage. In contrast, the maximum and minimum permeability changes are 4.89% and 3.83%, respectively, during the unloading stage.

(4) For each cycle, we use Δk to denote the change in permeability at the same injection pressure during the injection pressure loading stage and the unloading stage.

$$\Delta k = \frac{k_j - k_s}{k_s} \times 100\%, \quad (2)$$

where k_s and k_j denote the rock permeability under the same injection pressure conditions during the injection pressure loading and unloading stages, respectively, for each cycle.

Figure 5 shows the change in permeability of the two samples as a function of the injection pressure for each cycle.

In Figure 5, the permeability changes in sample S2 for Cycle 1, Cycle 2, and Cycle 3 are 21.80%, 15.07%, and 16.55%, respectively, at 4 MPa and 2.45%, 1.40%, and 2.38% at 16 MPa, respectively. The change in permeability obviously decreases with increasing injection pressure. Therefore, the changes in permeability in higher-pressure zones are smaller than those in lower-pressure zones.

3.1.2. Construction of a Mathematical Model Describing the Relationship between Permeability and Injection Pressure. Based on the experimental results, the changes in permeability with the injection pressure have been analyzed in the preceding part of the text. Various mathematical models are tried to fit the experimental results, such as linear model, exponential model, power function model, and other forms. The variance is used to determine the fitting degree of experimental data and mathematical models. At last, we found that the exponential model that has the highest fitting degree between the injection pressure and the permeability was obtained:

$$k = k_0 e^{aP}, \quad (3)$$

where k is the rock permeability, mD; k_0 is the initial permeability, mD; P is the injection pressure, MPa; and a is a parameter obtained by fitting curves to the data.

In the first cycle experiment, the relationship and fitting curves between the permeability and the injection pressure during the pressure loading and unloading stages are shown in Figure 6.

All the mathematical models of the rock permeability and injection pressure for the two samples derived from the three cycle experiments are shown in Table 2. The quality of the fit to the data is high, and the average of the correlation coefficient R^2 values is 99.81%.

During the process of increasing and decreasing the injection pressure, the mathematical models obtained from different cycles are different. Thus, we should not expect a mathematical model obtained from one experiment to

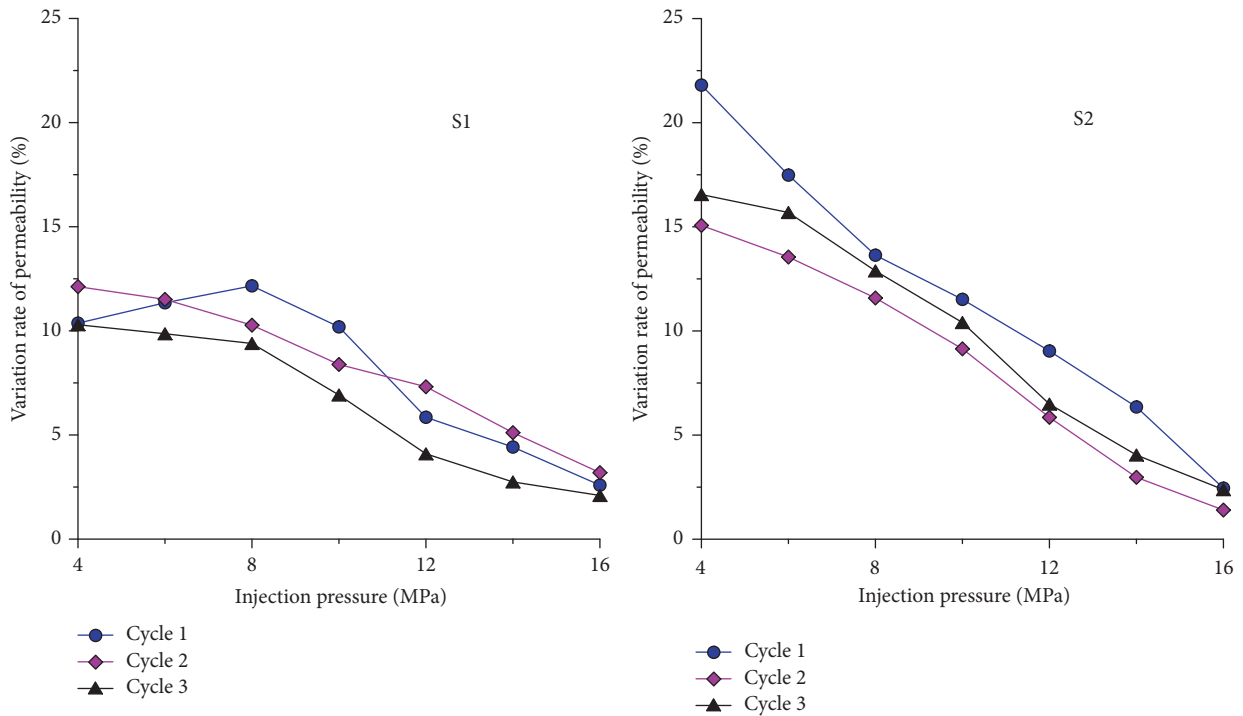


FIGURE 5: The relationship between the change in permeability and the injection pressure for each cycle experiment.

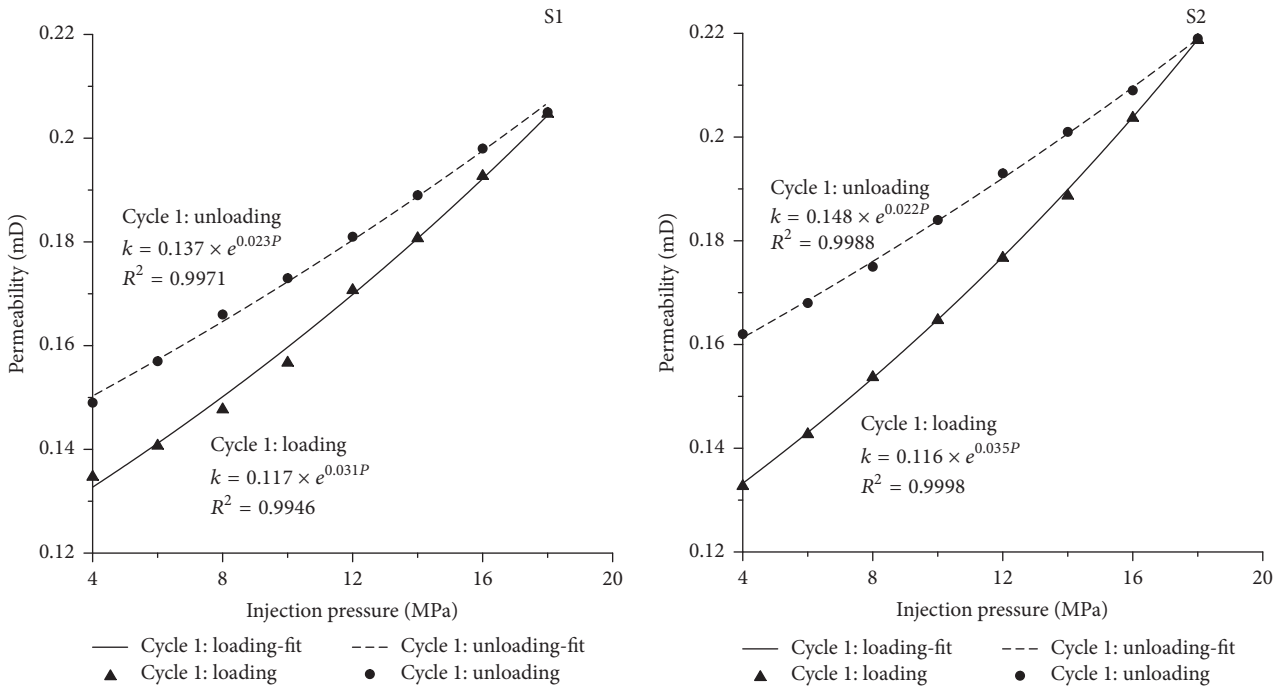


FIGURE 6: Fitting curves and mathematical models describing the relationship between the permeability and the injection pressure for the first cycle experiments.

accurately predict the permeability change at another time or under another set of operating conditions. But Figure 3 shows that, under the condition of changing injection pressure, the permeability can recover during the 24-hour interval, and the permeability curves of different cycles nearly overlap. The

rock deformation caused by the injection pressure change is elastic deformation. Thus, to a real engineer, each of the three permeability curves can be used to represent the relationship between the permeability and injection pressure for reservoir simulation.

TABLE 2: The fitting parameters in the mathematical models describing the relationship between permeability and injection pressure.

Sample	Cycle	Process	k_0	a	R^2
S1	1	Loading	0.117	0.031	0.9946
		Unloading	0.137	0.023	0.9971
	2	Loading	0.116	0.030	0.9964
		Unloading	0.135	0.022	0.9987
	3	Loading	0.120	0.029	0.9961
		Unloading	0.137	0.022	0.9990
S2	1	Loading	0.116	0.035	0.9998
		Unloading	0.148	0.022	0.9988
	2	Loading	0.128	0.032	0.9988
		Unloading	0.154	0.021	0.9998
	3	Loading	0.127	0.031	0.9994
		Unloading	0.157	0.020	0.9986

3.2. Influence of Changes in Confining Pressure on Permeability

3.2.1. *Variation of Permeability under Changes in Confining Pressure.* Figure 7 shows the variation in rock permeability with changing confining pressure in three cycles of increasing and decreasing confining pressure under a constant injection pressure.

The following observations can be made.

(1) Figure 7 shows that rock permeability decreases with increasing confining pressure in each cycle experiment and that the permeability and confining pressure are negatively correlated. With decreasing confining pressure, the permeability of the rock gradually recovers. However, the sample does not achieve the same permeability it had at the same confining pressure during the loading stage. In other words, the rock permeability does not recover fully during the confining pressure unloading stage. For example, for sample S1 with a confining pressure of 10 MPa, the permeability is 0.0833 mD during the confining pressure loading stage but 0.0763 mD during the unloading stage.

(2) Figure 7 also shows that the permeability curves do not overlap with each other during the three cycle experiments. The permeability curves of later cycles are always lower than the previous one. Thus, the permeability shows a significant decline in response to the cyclic changes. Hence, deformation of the rock specimen occurs under confining pressure, and the deformation decreased as the confining pressure is progressively removed. However, the recovery process takes a long time, and the samples do not fully recover during the confining pressure unloading process. Moreover, the initial permeability of subsequent cycles differs from the initial permeability. Thus, the permeability of the rock samples does not recover completely within the 24-hour interval between adjacent cycles.

(3) We use k_u to denote the relative permeability decrease between two adjacent points with different pressures in the confining pressure loading stage for each cycle and k_d to denote the rock relative permeability increase in unloading stage.

$$k_u = \frac{k_i - k_{i+1}}{k_i} \times 100\%,$$

$$k_d = \frac{k_{j+1} - k_j}{k_j} \times 100\%,$$
(4)

where k_i and k_{i+1} represent the rock permeability at two adjacent points with different pressures of i and $i + 1$, respectively, during the confining pressure loading stage for each cycle and k_j and k_{j+1} represent the permeability at two adjacent points j and $j + 1$, respectively, with different pressures during the unloading stage.

The relative changes in rock permeability are shown in Figure 8.

Figure 8 shows that the range of permeability values obtained under lower-pressure conditions is larger than that under higher-pressure conditions. For example, for sample S2, the relative changes in permeability in the three cycle experiments are 5.50%, 2.31%, and 2.17% when the confining pressure increases from 8 MPa to 10 MPa but 1.16%, 1.00%, and 0.81% when the confining pressure increases from 16 MPa to 18 MPa. The relative changes in permeability decrease with increasing confining pressure, and the change in permeability in the first confining pressure loading stage is clearly larger than in the other two stages. Therefore, during the first confining pressure loading phase, the size of the microcracks and pore throats, which represent the main channels for fluid flow in low-permeability rocks [23], changed substantially. This change resulted in a significant decrease in permeability (Figure 7).

(4) For each cycle experiment, we use Δk to denote the change in permeability at the same confining pressure during the confining pressure loading and unloading stages.

$$\Delta k = \frac{k_s - k_j}{k_s} \times 100\%,$$
(5)

where k_s and k_j denote the rock permeability under the same injection pressure conditions during the confining pressure

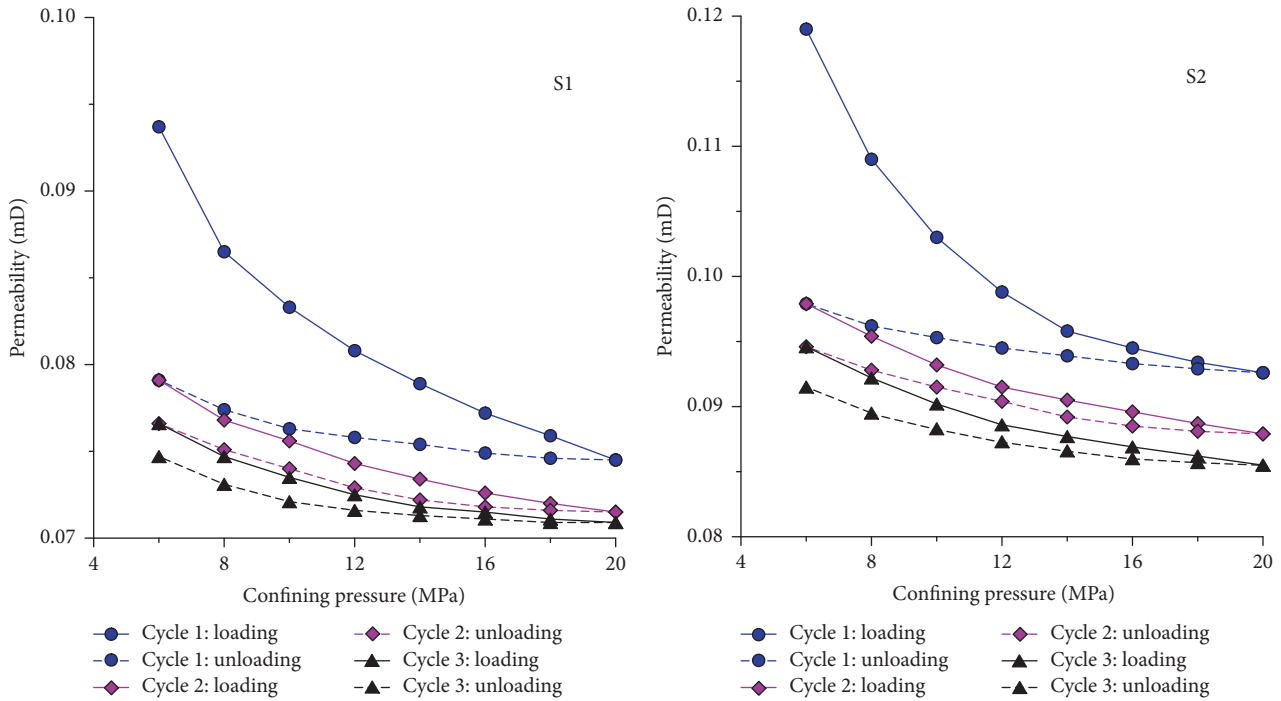


FIGURE 7: Relationship between permeability and confining pressure under constant injection pressure.

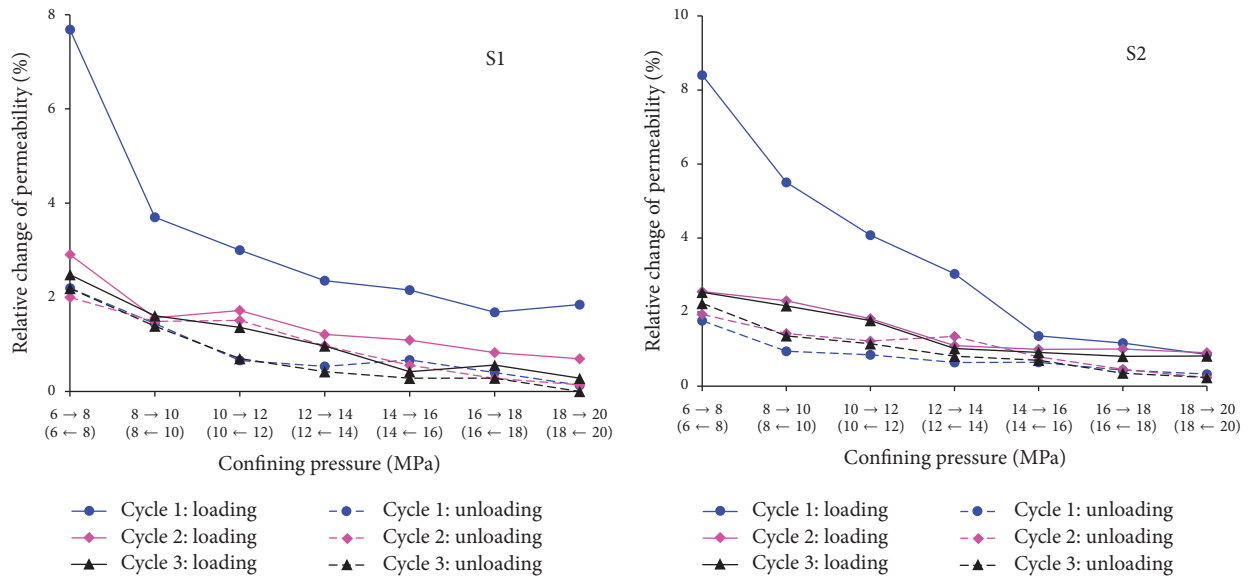


FIGURE 8: The relationships between relative changes in permeability and confining pressure.

loading and unloading stages, respectively, for each cycle experiment.

Figure 9 shows the change in permeability of the two samples as a function of the confining pressure in each cycle.

Figure 9 shows that, for each confining pressure cycling process, the changes in permeability are smaller in the high-pressure zone than in the low-pressure zone. The changes in the first cycle are quite significant compared to the other two cycles. The differences in the changes in permeability during Cycle 2 and Cycle 3 are small, and for sample 2, the two curves

tend to overlap each other in Figure 9. This result occurs primarily because the changes in confining pressure cause the rock sample to deform, leading to substantial changes in permeability (Figure 7) in the first confining pressure cycle. In addition, the deformation does not reverse, even though there is a 24-hour interval between adjacent cycles. For example, for sample S2, when the confining pressure is 6 MPa, the changes in permeability in Cycles 1, 2, and 3 are 17.73%, 2.73%, and 2.93%, respectively. The changes in permeability in Cycle 2 and Cycle 3 are far less than that in Cycle 1.

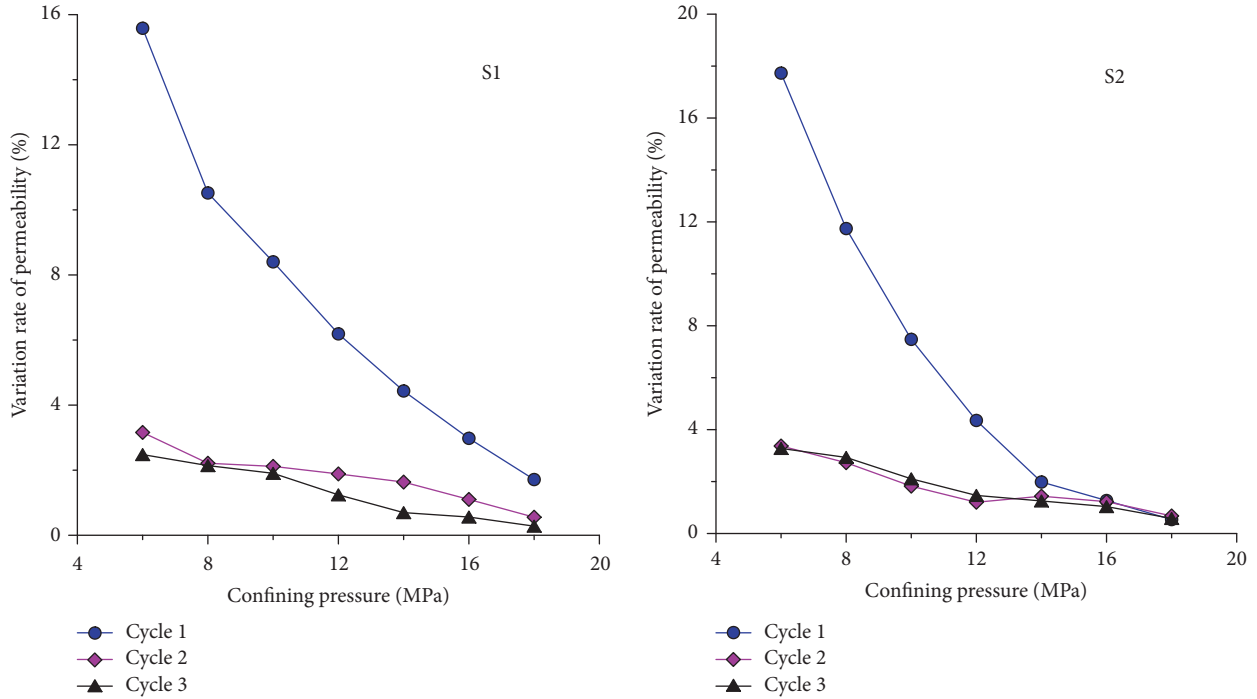


FIGURE 9: The relationship between changes in permeability and confining pressure in each cycle.

3.2.2. *Construction of a Mathematical Model Describing the Relationship between Permeability and Confining Pressure.* Based on the experimental results, the changes in permeability with confining pressure have been analyzed in the preceding part of the text. Different mathematical models are tried to fit the experimental results, such as linear model, exponential model, power function model, and other forms. The variance is used to determine the fitting degree of experimental data and mathematical models. The following fitting relationship between the confining pressure and the permeability was obtained:

$$k = k_0 P_c^a, \tag{6}$$

where k is the rock permeability, mD; k_0 is the initial permeability, mD; P is the confining pressure, MPa; and a is the parameter obtained by fitting curves to the data.

The relationships and fitting curves between the permeability and the confining pressure during the pressure loading and unloading stages in the first cycle experiment are shown in Figure 10.

All the mathematical models describing the relationship between the rock permeability and confining pressure for the two samples in the three cycle experiments are shown in Table 3. The quality of the fit to the data is high, and the average R^2 value is 97.86%.

Table 3 shows that, even for the same sample, the mathematical models obtained from different cycles of increasing and decreasing the confining pressure are different. Thus, we should not expect a mathematical model obtained from one experiment to accurately predict the permeability change at another time or under another set of operating conditions. Under the condition of changing confining pressure, the

permeability curves are significantly different for different cycles. The deformation of the rock caused by the confining pressure change is not elastic deformation. Even so, through the permeability curves, the change ranges of the permeability under different conditions can be obtained. The change ranges of permeability can be used as reference values to evaluate the reservoir performance.

3.3. *Comparative Analysis of the Influence of Confining Pressure and Injection Pressure on Permeability.* Similarities and significant differences exist between the influences of variable injection pressure and variable confining pressure on rock permeability. The following conclusions have been reached.

(1) Both the injection pressure and the confining pressure have significant effects on the rock permeability of the Liujiagou formation. For example, when the injection pressure is varied, the minimum and maximum permeabilities of S1 are 0.132 mD and 0.205 mD, respectively. Hence, the maximum permeability is 1.6 times the minimum permeability. In addition, when the confining pressure is varied, the initial permeability of S1 is 0.0937 mD. After three cycles of confining pressure variation, its permeability is 0.0709 mD, which is 24% less than the initial permeability.

(2) A negative correlation exists between the permeability and the confining pressure, but a positive correlation exists between the permeability and the injection pressure. When the injection pressure is varied, the permeability in the loading stage is smaller than that in the unloading stage under the same injection pressure conditions (Figure 3). In contrast, when the confining pressure is varied, the permeability in the loading stage is greater than that in the unloading stage for the same confining pressure conditions (Figure 7).

TABLE 3: Fitting parameters in the mathematical models of permeability and confining pressure.

Sample	Cycle	Process	k_0	a	R^2
S1	1	Loading	0.128	-0.182	0.9860
		Unloading	0.086	-0.049	0.9671
	2	Loading	0.092	-0.083	0.9968
		Unloading	0.085	-0.060	0.9749
	3	Loading	0.085	-0.064	0.9765
		Unloading	0.080	-0.042	0.9219
S2	1	Loading	0.169	-0.208	0.9621
		Unloading	0.106	-0.046	0.9935
	2	Loading	0.115	-0.089	0.9969
		Unloading	0.106	-0.064	0.9913
	3	Loading	0.110	-0.084	0.9943
		Unloading	0.101	-0.057	0.9817

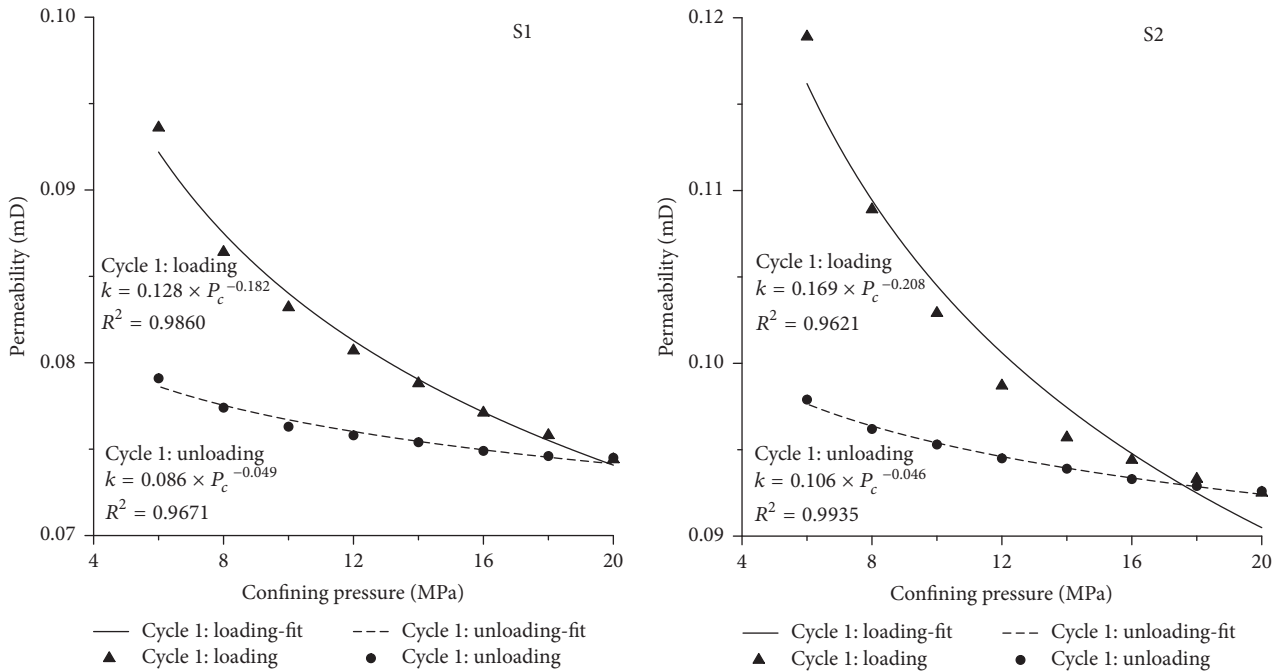


FIGURE 10: Fitting curves and mathematical models of the permeability and the confining pressure for the first cycle experiment.

(3) For the same cycle experiment, the rock permeability curves obtained from the loading stage do not fully overlap with those obtained from the unloading stage, regardless of whether the experiment involves changing the injection pressure or the confining pressure. Thus, even at the same pressure, there are different permeability values. For example, when the injection pressure for sample S2 is varied in the first cycle experiment, the permeability is 0.143 mD at an injection pressure of 6 MPa during the injection pressure loading stage. The permeability changes to 0.168 mD during the unloading stage, representing a difference of approximately 17% (Figure 3). In addition, when the confining pressure for sample S2 is increased to 8 MPa in the first cycle experiment, the difference in the permeability values between the loading stage and the unloading stage is approximately 13% (Figure 7).

(4) Regardless of whether the confining pressure or the injection pressure is changed, the permeability curves obtained from pairs of adjacent cycle experiments do not overlap each other in the three cycle experiments (Figures 3 and 7). When the confining pressure was changed, the permeability values of later cycles were always smaller than that measured in earlier cycles, and there is no overlap in the area between the curves from different cycle experiments. However, when the injection pressure was changed, the permeability curves of different cycle experiments did overlap.

(5) A comparison of the experimental results under the two stress conditions (changing injection pressure and changing confining pressure) shows that the influence of the interval between adjacent cycles on the initial rock permeability is very different. For a constant injection pressure

TABLE 4: Measured pore structure parameters of the rock samples before and after the experiments.

Parameter	S1			S2		
	Initial	Final	Relative change	Initial	Final	Relative change
Surface area (m ² /g)	1.7300	2.5343	46.49%	1.5636	2.3428	49.83%
Total pore volume (mL/g)	0.0083	0.0082	-1.20%	0.0079	0.0076	-3.80%
Micropores volume (mL/g)	0.0006	0.0010	66.67%	0.0006	0.0009	50.00%
Average pore size (nm)	19.19	12.94	-32.57%	20.21	12.98	-35.77%
Most probable pore size (nm)	2.59	2.59	0	2.60	2.60	0

and changing confining pressure, the initial permeability of the sample decreases with increasing cycle number, and the initial permeabilities of Cycle 2 and Cycle 3 are almost equal to the final permeability of the previous cycle (Figure 7). Therefore, the permeability cannot recover to the initial value of the previous cycle over a 24-hour interval, and the rock sample deformation cannot be reversed. For a constant confining pressure and a changing injection pressure, the initial permeabilities of the three cycles are similar (see sample S1 in Figure 3). The permeability curves of the three cycles show little difference (Figure 3), indicating that the permeability of the rock recovers well during the 24-hour intervening interval. In actual engineering projects, interruptions in the CO₂ injection process will cause the injection pressure and confining pressure to increase and decrease many times. Hence, these experimental results have practical significance for actual projects.

4. Effect of Stress Variation on the Pore Structure of Rock

The surface area of the rock samples was calculated via the BET equation, which was derived by Brunauer, Emmett, and Teller, by calculating the saturated adsorption amount of the monomolecular layer at relative pressures of 0.05 to 0.35 [24, 25]. The most probable pore size was calculated via the BJH method proposed by Barret, Joyner, and Halenda using the adsorption branch of the adsorption isotherm. The average pore size was calculated from the amount of nitrogen adsorbed when the relative pressure was close to 1. The pore size distribution, micropore volume, and total pore volume were evaluated via the DFT method [26]. All of the measured parameters are shown in Table 4.

The International Union of Pure and Applied Chemistry (IUPAC) divides pores within materials into three categories: micropores (pores with widths not exceeding approximately 2 nm), mesopores (pores with widths between 2 nm and 50 nm), and macropores (pores with widths exceeding approximately 50 nm) [27]. According to the test results from samples S1 and S2, the pores in both samples before and after the experiments are mesopores. However, the multistage cycle experiments involving increasing and decreasing the injection and confining pressures exerted significant effects on the pore sizes of the rock samples. The average pore diameters for S1 and S2 decreased from initial values of 19.19 nm and 20.21 nm to final values of 12.94 nm and 12.98 nm, respectively. Hence, the relative changes are 32.57% and 35.77%, respectively. Simultaneously, the surface areas of

the rock samples increased significantly, with relative changes of more than 50% for both samples.

Figures 11 and 12 show the curves representing the adsorption isotherms of samples S1 and S2, respectively, before and after the experiments. The desorption branch curves clearly deviate from the adsorption curves in places. When the relative pressure P/P_0 (where P is the current pressure, MPa, and P_0 is the saturated vapor pressure of nitrogen at 77 K, i.e., approximately 0.101 MPa) lies within the range 0 to 0.8, the nitrogen adsorption capacity represented by the isothermal adsorption line increases slowly. When the P/P_0 value lies within the range 0.8~1.0, the nitrogen adsorption capacity increases rapidly. The hysteresis loop transition point appears when P/P_0 is equal to 0.42 (Bertier et al., 2016). This result indicates that the phenomenon of capillary condensation occurs, and hysteresis loops can be observed when $P/P_0 > 0.42$. According to the isotherm classification of the IUPAC [27], the four isotherms are Type I isotherms. Therefore, the pores found in the samples are mainly mesopores. This result is consistent with the previously described results of the average pore size test.

The shape of a hysteresis loop can reflect the pore structure of a rock sample [23]. The IUPAC classifies hysteresis loops into a total of 6 categories of 5 types, specifically H1, H2 (a), H2 (b), H3, H4, and H5 [27]. In this experiment, the adsorption and desorption branches of samples S1 and S2 were almost identical before and after the experiments. The phenomenon of capillary condensation obviously occurs, and the adsorption curve rises sharply only when the relative pressure is close to the saturated vapor pressure. The hysteresis loops belong to Type H3, reflecting the existence of parallel plate-type slit pores in the rock samples. This result indicates that the multistage cycles of increasing and decreasing the injection pressure and confining pressure did not affect the pore type of the rock samples.

Figure 13 shows the pore size redistribution of samples S1 and S2 before and after the experiment. It can be seen that the multistage cycle experiments, which involved changing the injection pressure and the confining pressure, had significant effects on the pore sizes of the samples. The micropore (pore sizes < 2 nm) volumes of S1 and S2 increased by 66.7% and 50% after the experiment, respectively. The number of mesopores in the pore size range between 2 and 10 nm also obviously increased. However, the number of mesopores in the pore size range between 10 and 50 nm did not obviously change. At the same time, the number of macropores (pore sizes > 50 nm) significantly decreased.

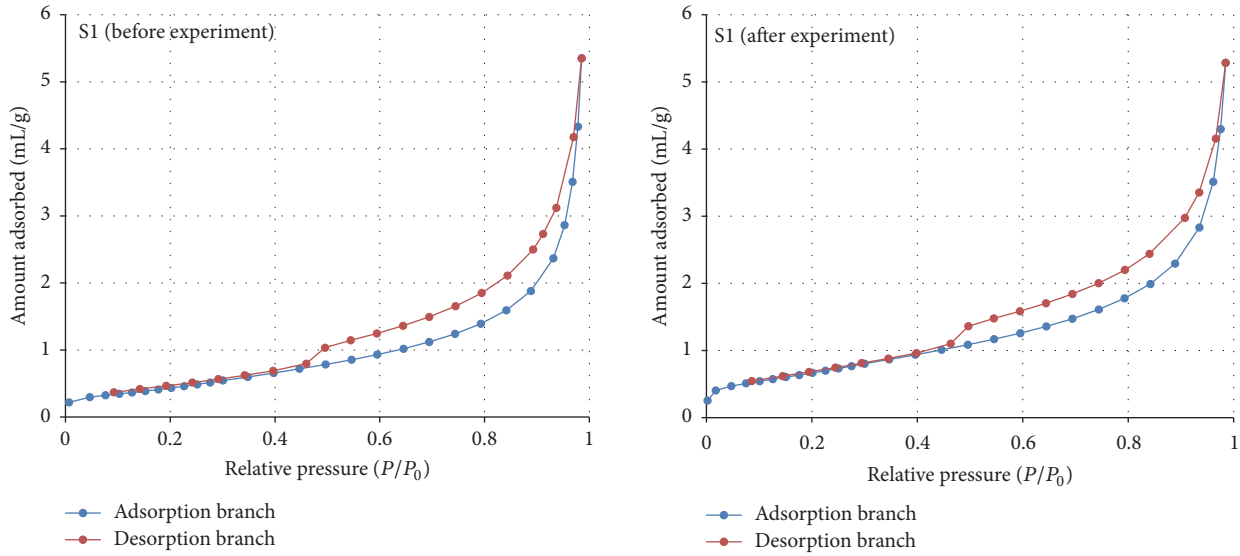
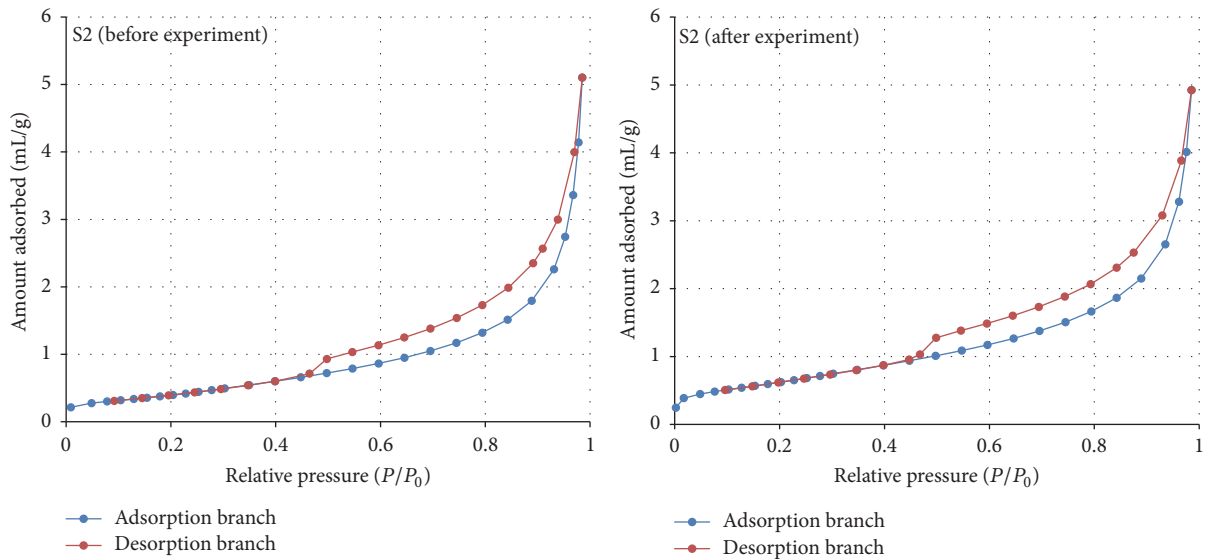
FIGURE 11: N_2 adsorption-desorption isotherms of S1.FIGURE 12: N_2 adsorption-desorption isotherms of S2.

Figure 14 shows the cumulative pore volume curves of the rock samples before and after the experiments. The cumulative pore volumes of samples S1 and S2 after the experiment are greater than those before the experiment. In the pore diameter range of 0–10 nm, the cumulative pore volume curves after the experiments considerably exceed those measured before the experiments. Subsequently, in the pore diameter range of 10–50 nm, the two curves are nearly parallel. This result indicates that little pore size change occurred in the range of 10–50 nm. For pore sizes greater than 50 nm, the gap between the two curves gradually shrinks. In short, the total pore volumes did not change greatly.

Based on the analysis presented above, the multistage cycle experiments involving changes in the injection and

confining pressures had little effect on the pore type of the rock samples. The pores in the rock samples before and after the experiments both belonged to the parallel plate pore type. However, the multistage cycle experiments had significant effects on the pore size distribution. The large increase in surface area indicates that the microstructures of the samples were changed by the multiple cycle stress experiments. As the number and volume of pores smaller than 10 nm increased, macropores with diameters larger than 50 nm decreased. The increase in micropores and mesopores did not greatly affect the seepage capacity of the rock. However, the decrease in macropores caused the permeability of the rock sample to decrease substantially. The permeabilities of samples S1 and S2 diminished from initial values of 0.135 mD and

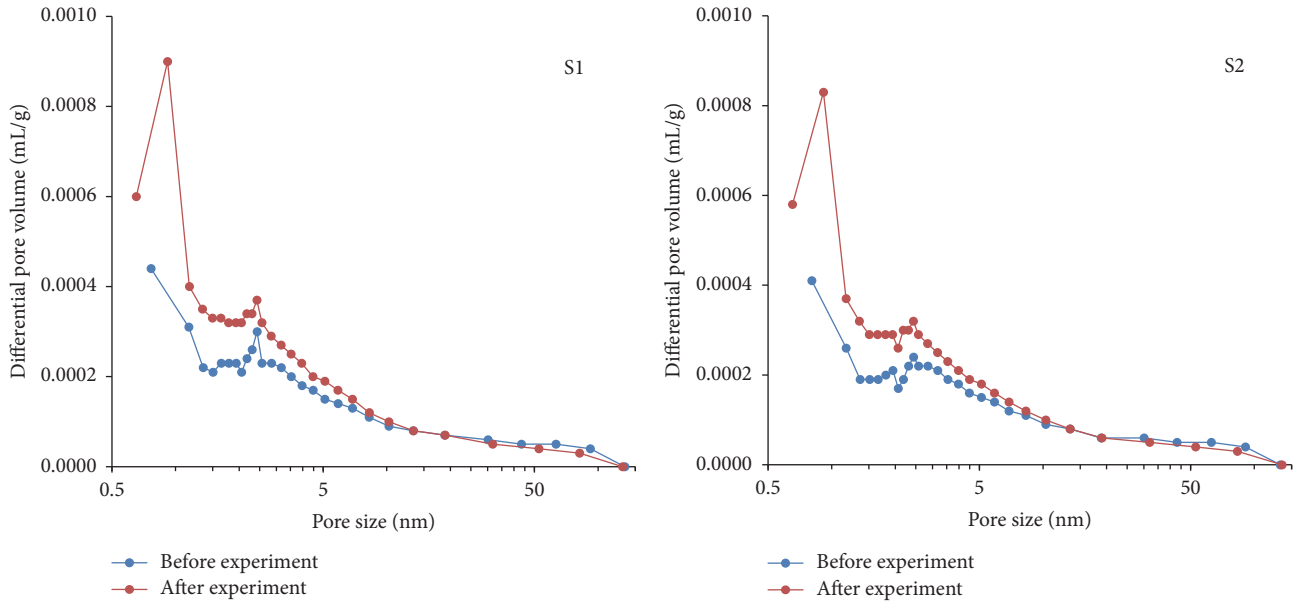


FIGURE 13: Pore size distributions before and after the experiments.

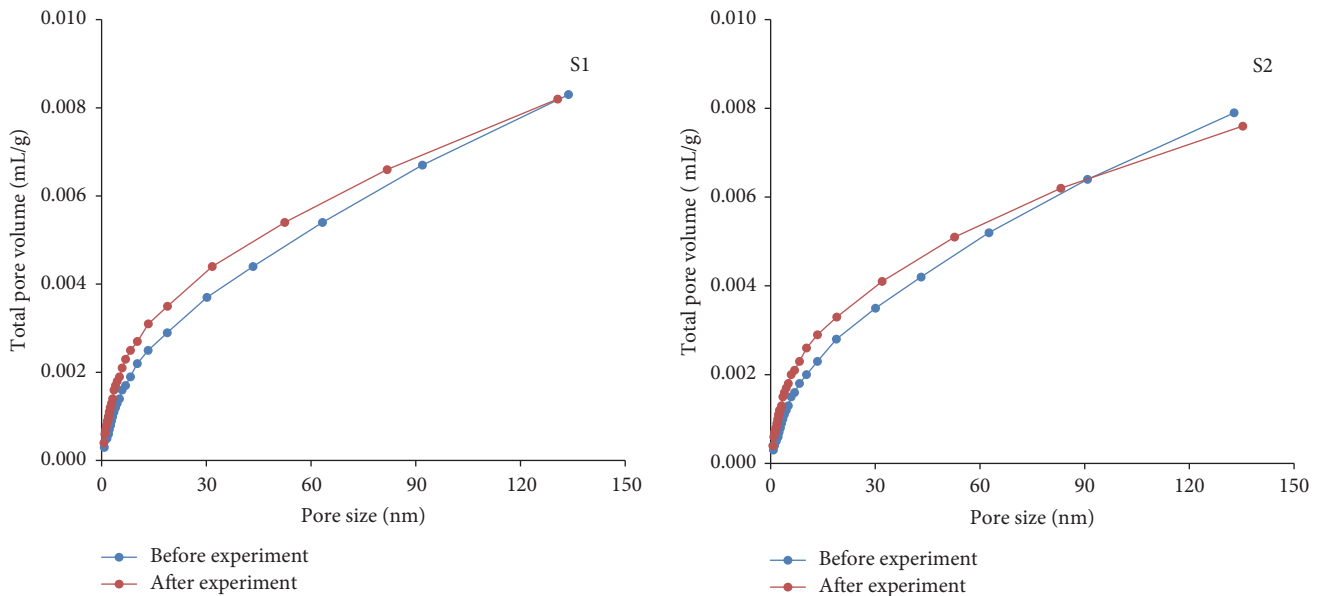


FIGURE 14: Cumulative pore volumes before and after the experiments.

0.133 mD to 0.0747 mD and 0.0915 mD, respectively, after the experiments involving three cycles of increasing and decreasing the injection and confining pressures.

The clay mineral contents of the rock samples influenced the permeability changes. The clay mineral content in S2 is approximately 5 times that in S1. In the first cycle of the injection pressure variation, the average change in permeability was 8.13% for S1 and 11.75% for S2.

There are more intergranular pores in sample S2, which has a greater clay mineral content, and so that sample is more easily affected by increases in injection pressure, which causes its changes in permeability to be greater than those of

sample S1. Under conditions in which the confining pressure changes, the average changes in permeability of S1 and S2 in the first cycle are 7.12% and 6.44%, respectively. The influence of clay mineral content on the permeability change is more obvious under conditions in which the injection pressure changes than when the confining pressure changes.

Related studies have shown that clay minerals have massive intergranular micropores and interlayer cracks. With the increase of clay mineral content, the micropores content increased. However, since the pore sizes of these micropores are small, when the rock sample was saturated with water, the combination water (consists of weak combination water and

strong combination water) on the surface of mineral particles would occupy a lot of void seepage channels.

Under the variable injection pressure, when the injection pressure increases, the proportion of the weak combination water which can participate in seepage in a certain pressure gradient would increase gradually. The higher the clay mineral content in the rock samples, the more significant the change in permeability when the injection pressure increases.

Under the variable confining pressure, the injection pressure keeps constant (4 MPa). Under the constant injection pressure, the macropores and mesopores are the main seepage channels. When the confining pressure increases, the size and the volume of the macropores and mesopores decrease, which makes the permeability of the rock sample reduce. The pores inside the clay minerals are mainly micropores filled with combination water; for this reason, they are not the main seepage channels. Hence, its volume change will not have an obvious effect on permeability.

5. Conclusions and Suggestions

The following conclusions have been reached based on the experimental study of permeability variations in reservoir rock samples from the Liujiagou formation, one of the reservoirs targeted in the CCS demonstration project in the Ordos Basin.

(1) Both the confining pressure and the injection pressure have significant effects on the permeability of this reservoir rock. The relative permeability changes with pressure and between the loading and unloading stages are higher at low pressures than at high pressures. Changing the confining pressure changes the relative permeability by more than 20%. In addition, changing the injection pressure changes the relative permeability by up to 60%.

(2) A positive correlation exists between injection pressure and permeability, but a negative correlation exists between confining pressure and permeability. Based on the experimental data, highly relevant mathematical models that describe the relationship between permeability and injection pressure or confining pressure can be constructed. However, the results show that the constructed models have important differences. Therefore, we cannot use the mathematical model constructed using data from one experiment to predict the permeability changes in another situation. This aspect should receive more attention in the numerical simulations used in practical engineering.

(3) The multistage and discontinuous nature of the injection process in the geological storage of CO₂ means that the effective stress acting on a reservoir will experience repeated loading and unloading. The experimental results show that the initial permeability of the rock is more strongly affected by the changes in the confining pressure compared to changes in the injection pressure. In addition, the effects on rock permeability caused by a changing injection pressure can be diminished by using a sufficiently long injection interval time.

(4) Multistage cycle experiments involving changes in the injection and confining pressures have little effect on the pore types of rock samples, but they have significant effects on the

pore size distribution. The total pore volumes of the samples did not change significantly. However, the proportion of low-permeability micropores and mesopores increased, and the proportion of macropores, representing the main seepage channels, clearly decreased. The above results indicate that the storage capacity of the reservoir will remain stable, but the permeability of the rock will decrease.

(5) The micropore structure of rocks is closely related to the clay minerals in the rocks. For similar rocks with different clay mineral contents, higher clay mineral contents are associated with greater permeability changes during injection pressure variations. The influence of clay mineral contents on permeability changes is more obvious in association with injection pressure changes with confining pressure changes. The injection pressure is a controllable factor in actual CCS projects. Therefore, sufficient attention should be paid to the effects of rock type and clay mineral content on rock permeability in practical CCS projects.

In fact, the permeability of the rock depends on the characters of the material, such as the void space/porous structure, its configuration/volume/geometry, and topology in the medium. These character parameters are stress dependent, but the stress levels are changing in experiment. Therefore, these character parameters are changing, and at the same time, it is difficult to monitor these parameters in real time in an experiment. Due to the heterogeneity of the strata, there is a lot of uncertainty to apply the stress-permeability mathematic model obtained from a rock experiment of a certain strata reservoir to other reservoirs in other sites. That is to say, it is difficult to derive a universal mathematical mode between the permeability and pressure. Thus, the reasonable treatment for a specific stratum reservoir is to take the representative rock sample of the reservoir and obtain the mathematical model between injection pressure and permeability and the permeability change range under the impact of the confining pressure change. And then the mathematical models obtained can be used in the reservoir evaluation.

The focus of this paper is the influence of multiperiod stress changes on rock permeability, so it just considers a single fluid in the experiment. In the actual project of CO₂ geological storage, the underground fluid is mixed phase fluid containing CO₂ [28]. The complexity will greatly increase. The chemical reactions between CO₂ and minerals will also affect the pore structure of the rock, which in turn affects the permeability of the rock. Further studies should explore the effect of mixed fluids, multiphase fluids, and the chemical reactions on rock permeability under different stress conditions. In addition, the influence of pressure on rock deformation should be analyzed according to the stress-strain curve of rock.

Conflicts of Interest

The authors declare that they have no conflicts of interest.

Acknowledgments

This work was supported by the National Natural Science Foundation of China (Grants nos. 41502258 and 41172205), by

a geological survey project (Grant no. 121201012000150010), by China National Science and Technology Major Project (Grant no. 2016ZX05016-005), and by the Graduate Innovation Fund of Jilin University (Grant no. 2016205).

References

- [1] J. Guo, D. Wen, S. Zhang et al., "Potential evaluation and demonstration project of CO₂ geological storage in China," Tech. Rep. 2, Geological Survey of China, 2015.
- [2] Z. Meng, H. Guo, Q. Liu, B. Jiang, and H. Li, "Microscopic pore structure for tight sandstone gas reservoirs in Tarim Basin," *Journal of Central South University*, vol. 46, no. 8, pp. 3032–3039, 2015.
- [3] F. Wang, Z. Sun, H. Liu, T. Xu, and J. Jing, "Experimental study on the variation of permeability of medium-fine feldspar-quartz sandstone low-permeability reservoir under the circulatory increasing or reducing conditions of confining pressure," *Journal of Hydraulic Engineering*, vol. 47, no. 9, pp. 1125–1132, 2016.
- [4] A. Amann-Hildenbrand, J. P. Dietrichs, and B. M. Krooss, "Effective gas permeability of tight gas sandstones as a function of capillary pressure—a non-steady-state approach," *Geofluids*, vol. 16, no. 3, pp. 367–383, 2016.
- [5] Y. Huang and E. Wang, "Experimental study of the laws between the effective confining pressure and rock permeability," *Journal of Tsinghua University*, vol. 47, no. 3, pp. 340–343, 2007.
- [6] I. Fatt and D. Davis, "Reduction in permeability with overburden pressure," *Journal of Petroleum Technology*, vol. 4, article 16, 1952.
- [7] A. McLatchie, R. Hemstock, and J. Young, "The effective compressibility of reservoir rock and its effects on permeability," *Journal of Petroleum Technology*, vol. 10, pp. 49–51, 1958.
- [8] Z. Wu, H. Zhou, J. Ding, L. Ran, and H. Yi, "Research on permeability testing of rock salt under different permeability pressures," *Chinese Journal of Rock Mechanics and Engineering*, vol. 31, no. 2, pp. 3740–3746, 2012.
- [9] J.-X. Wang, L.-S. Hu, C. Ye, Y.-Q. Tang, and P. Yang, "Triaxial permeability test of marble under complex stress path," *Rock and Soil Mechanics*, vol. 31, no. 8, pp. 2389–2398, 2010.
- [10] J. Vairogs, C. L. Hearn, D. W. Dareing, and V. W. Rhoads, "Effect of rock stress on gas production from low-permeability reservoirs," *Journal of Petroleum Technology*, vol. 23, no. 9, pp. 1161–1167, 1971.
- [11] X.-C. Xue, Y.-D. Yan, Z.-Y. Geng, and Y.-P. Zhou, "Study on stress sensitivity of low permeability sandstone reservoir," *Liaoning Chemical Industry*, vol. 44, pp. 1147–1149, 2015.
- [12] S. Peng, Z. Meng, H. Wang, C. Ma, and J. Pan, "Testing study on pore ratio and permeability of sandstone under different confining pressures," *Chinese Journal of Rock Mechanics and Engineering*, vol. 22, no. 5, pp. 742–746, 2003.
- [13] J. B. Jennings, H. B. Carroll, and C. J. Raible, "Relationship of permeability to confining pressure in low permeability rock," in *Proceedings of the SPE/DOE Low Permeability Gas Reservoirs Symposium*, pp. 391–398, Society of Petroleum Engineers, Denver, Colorado, March 1983.
- [14] H. Wang, W. Xu, J. Zuo, J. Shao, and C. Jia, "Evolution law of the permeability and porosity for low-permeability rock based on gas permeability test," *Journal of Hydraulic Engineering*, vol. 46, no. 2, pp. 208–216, 2015.
- [15] L. Lan, Y. Kang, Y. Chen et al., "Discussion on evaluation methods for stress sensitivities of low permeability and tight sandstone reservoirs," *Drilling Fluid and Completion Fluid*, vol. 22, article 79, 2005.
- [16] A. P. Byrnes, K. Sampath, and P. Randolph, "Effect of pressure and water saturation on permeability of western tight sandstones," in *Proceedings of the 5th Annual DOE Symposium on Enhanced Oil and Gas Recovery and Improved Drilling Technology*, pp. 22–24, Elsevier Science, Tulsa, Okla, USA, 1979.
- [17] W. Wang, W. Xu, R. Wang, Y. Cao, H. Wang, and S. Feng, "Permeability of dense rock under triaxial compression," *Chinese Journal of Rock Mechanics and Engineering*, vol. 34, no. 1, pp. 40–47, 2015.
- [18] K. Wang, T. Xu, H. Tian, and F. Wang, "Impacts of mineralogical compositions on different trapping mechanisms during long-term CO₂ storage in deep saline aquifers," *Acta Geotechnica*, vol. 11, no. 5, pp. 1167–1188, 2016.
- [19] W. Kong, B. Bai, X. Li, and N. Wei, "Sealing efficiency of combined caprock for CO₂ storage in saline aquifer," *Chinese Journal of Rock Mechanics and Engineering*, vol. 34, pp. 2671–2678, 2015.
- [20] F. Wang, J. Jing, T. Xu, Y. Yang, and G. Jin, "Impacts of stratum dip angle on CO₂ geological storage amount and security," *Greenhouse Gases: Science and Technology*, vol. 6, no. 5, pp. 682–694, 2016.
- [21] F. Bu, T. Xu, F. Wang, Z. Yang, and H. Tian, "Influence of highly permeable faults within a low-porosity and low-permeability reservoir on migration and storage of injected CO₂," *Geofluids*, vol. 16, no. 4, pp. 769–781, 2016.
- [22] Z. Zhang and Z. Yang, "Theoretical and practical discussion of measurement accuracy for physisorption with micro- and mesoporous materials," *Chinese Journal of Catalysis*, vol. 34, no. 10, pp. 1797–1810, 2013.
- [23] F. Yang, Z. Ning, C. Hu, B. Wang, K. Peng, and H. Liu, "Characterization of microscopic pore structures in shale reservoirs," *Acta petrolei sinica*, vol. 34, pp. 301–311, 2013.
- [24] H. Tian, S. Zhang, S. Liu, and H. Zhang, "Determination of organic-rich shale pore features by mercury injection and gas adsorption methods," *Acta Petrolei Sinica*, vol. 33, no. 3, pp. 419–427, 2012.
- [25] Z. Xiaojun and C. Jingong, "Progress and significance of research on relation between specific surface area and organic matter in argillaceous source rocks," *Oil & Gas Geology*, vol. 3, p. 008, 2012.
- [26] J. Jagiello and M. Thommes, "Comparison of DFT characterization methods based on N₂, Ar, CO₂, and H₂ adsorption applied to carbons with various pore size distributions," *Carbon*, vol. 42, pp. 1227–1232, 2004.
- [27] M. Thommes, K. Kaneko, A. V. Neimark et al., "Physisorption of gases, with special reference to the evaluation of surface area and pore size distribution (IUPAC Technical Report)," *Pure and Applied Chemistry*, vol. 87, no. 9–10, pp. 1051–1069, 2015.
- [28] L. K. Abidoye, K. J. Khudaida, and D. B. Das, "Geological carbon sequestration in the context of two-phase flow in porous media: a review," *Critical Reviews in Environmental Science and Technology*, vol. 45, no. 11, pp. 1105–1147, 2015.

Research Article

Modeling and Analysis of Magnetic Nanoparticles Injection in Water-Oil Two-Phase Flow in Porous Media under Magnetic Field Effect

Mohamed F. El-Amin,^{1,2,3} Ahmed M. Saad,² Amgad Salama,⁴ and Shuyu Sun²

¹College of Engineering, Effat University, Jeddah 21478, Saudi Arabia

²Computational Transport Phenomena Laboratory (CTPL), Division of Physical Sciences and Engineering (PSE), King Abdullah University of Science and Technology (KAUST), Thuwal, Jeddah 23955-6900, Saudi Arabia

³Mathematics Department, Faculty of Science, Aswan University, Aswan 81528, Egypt

⁴Faculty of Engineering, University of Regina, Regina, SK, Canada

Correspondence should be addressed to Mohamed F. El-Amin; mohamed.elamin.kaust@gmail.com

Received 23 February 2017; Revised 20 June 2017; Accepted 26 July 2017; Published 28 August 2017

Academic Editor: Timothy S. Collett

Copyright © 2017 Mohamed F. El-Amin et al. This is an open access article distributed under the Creative Commons Attribution License, which permits unrestricted use, distribution, and reproduction in any medium, provided the original work is properly cited.

In this paper, the magnetic nanoparticles are injected into a water-oil, two-phase system under the influence of an external permanent magnetic field. We lay down the mathematical model and provide a set of numerical exercises of hypothetical cases to show how an external magnetic field can influence the transport of nanoparticles in the proposed two-phase system in porous media. We treat the water-nanoparticles suspension as a miscible mixture, whereas it is immiscible with the oil phase. The magnetization properties, the density, and the viscosity of the ferrofluids are obtained based on mixture theory relationships. In the mathematical model, the phase pressure contains additional term to account for the extra pressures due to fluid magnetization effect and the magnetostrictive effect. As a proof of concept, the proposed model is applied on a countercurrent imbibition flow system in which both the displacing and the displaced fluids move in opposite directions. Physical variables, including water-nanoparticles suspension saturation, nanoparticles concentration, and pore wall/throat concentrations of deposited nanoparticles, are investigated under the influence of the magnetic field. Two different locations of the magnet are studied numerically, and variations in permeability and porosity are considered.

1. Introduction

Industry is now looking seriously into using nanotechnology as a viable tool to solving new challenges in several fields. In particular, there has been interest among oil and gas production companies to explore using nanotechnology in solving challenges related to unconventional oil and gas reservoirs, such as those found in tight and shale formations [1–7]. Nanotechnology has been used in different areas of the oil and gas industry from exploration, drilling, production to reservoir monitoring, and refining. The conventional Enhanced Oil Recovery (EOR) methods have several problems from high cost to low oil recovery in addition to operations problems especially in thermal and chemical methods. The nature of nanoparticles results in some useful characteristics such as

increased surface area, which at the nanoscale size, does matter when it comes to how molecules react to and bond with each other. So, for example, nanoparticles can be used in EOR, because they are small enough to pass through pore throats in typical reservoirs, and they can be retained by the rock. Ju and Fan [8] calibrated a model for nanoparticles transport in two-phase flow in porous media based on the formulation of the colloid model of fine particles transport in two-phase flow in porous media [9]. El-Amin et al. [10–13] have presented modeling and simulations of nanoparticles transport associated with two-phase flow in porous media. On the other hand, experimental studies of using nanoparticles in EOR have been conducted by Suleimanov et al. [14] and Hendranigrat et al. [15].

One of the prospective applications of nanotechnology is nanofluids, as the flow of such fluids can be controlled by the introduction of external magnetic field. This opens the way for various applications from directing flow in reservoir monitoring, diverting flow in acid jobs to control and boost of injection fluid advancement during pressure maintenance to increase oil recovery. The idea of using a strong external magnetic field with large magnetic susceptibility fluid is to mobilize ferrofluid through porous media. Oil recovery can be increased by using nanoparticles with electromagnetic properties (such as iron oxide, Fe_2O_3 , and zinc oxide, ZnO) under waves generated from an electromagnetic source. Both direct and alternating magnetic fields are under investigation; in our case here we will focus on direct magnetic field. The magnetization of the particles and their attraction toward the magnet causes flow of the magnetic particles suspension. The movement of the magnetic nanoparticles under the magnetic field effect is independent of the orientation of the magnet. In the last few years, a number of publications have been considered nanofluids in oil and gas recovery or environmental applications (e.g., [16–23]).

Borglin et al. [24] conducted experiments to measure the magnetic induction, which converted to magnetic field strength, at various distances in a direction aligned with the poles. McCaig and Clegg [25] presented equations which indicate that ferrofluid magnetization is variable at all locations far away from the magnet due to the decreasing magnetic field strength. The gradient of magnetic field strength varies also with distance from the magnet. Moreover, the force on the ferrofluid decreases with distance from a magnet. Therefore, we may conclude that the distance from the magnet is important and should be reconsidered with taking into consideration its location in particular in the core-scale as well as the direction of flow. On the other hand, it is known that, in the presence of an external magnetic field, the nanoparticles in ferrofluid become magnetized and are pulled toward a magnet. In this work, we attempt to discuss the effect of location of the magnet on the transport of the nanoparticles in porous media.

In the current work, we develop a mathematical model to describe the magnetic nanoparticles-water suspension imbibition into an initially oil saturated porous domain under magnetic field effect. The porous medium is considered initially saturated totally with oil except for a residual amount of the other phase. We consider countercurrent imbibition into a small-scale porous core. This countercurrent imbibition refers to the case in which all the porous medium domain boundaries have no flow except one side. Physical variables are investigated under the influences of magnetic field with two different locations of magnet, namely, right and left to the porous core. Numerical experiments for the two cases are performed and results are introduced in graphical representations.

2. Modeling and Mathematical Formulation

Consider suspension of magnetic nanoparticles injected in an isothermal incompressible water-oil two-phase flow under an external magnetic field. In the following, we describe

the mathematical modeling of the problem under consideration.

In the following subsections, we firstly introduce the magnetic force and other magnetic modeling. The magnetic body force, which acts as a body force on the nanoparticles suspension per unit volume, appears in the extended Darcy's law as presented in the second subsection. Other magnetic parameters such as magnetization and magnetic field strength are also presented in the first subsection. Then, the governing flow equations such as momentum (extended Darcy's law) and mass conservation (saturation equation) are provided in the second subsection. The third subsection is devoted to the modeling of nanoparticles transport which is coupled with the flow equations via velocity and saturation. Finally, the initial and boundary conditions are presented in the last subsection.

2.1. Magnetic Force. The magnetization (polarization) of the nanoparticles suspension interacts with the external permanent magnetic field to produce attractive forces on each particle. The external magnetic force acts as a body force on the nanoparticles suspension per unit volume which can be expressed as [16]

$$\mathbf{F}_{\text{mag}} = \mu_0 M \frac{\partial H}{\partial z}, \quad (1)$$

where μ_0 is the magnetic permeability, M is the magnetization, and H is the magnetic field strength. The magnetization M is a function of H , approximated by

$$M = a_1 \tan^{-1}(b_1 H), \quad (2)$$

where the parameters a_1 and b_1 depend on the particular type of the ferromagnetic material. The values of the initial susceptibility and the saturation magnetization are controlled by the parameters a_1 and b_1 , respectively. The larger b_1 leads to a larger initial susceptibility which corresponds to larger particles or agglomeration of particles. The range of a_1 may be of order 10^4 – 10^5 , while the order of b_1 may be of order 10^{-6} – 10^{-5} . The magnetic field strength in 1D may be written as follows [16]:

$$H_z = \frac{B_r}{\pi\mu_0} \left(\tan^{-1} \frac{ab}{z(a^2 + b^2 + z^2)^{1/2}} - \tan^{-1} \frac{ab}{(z+L)(a^2 + b^2 + (z+L)^2)^{1/2}} \right), \quad (3)$$

where B_r is the residual magnetization (in this work, $B_r = 1.19$ [T]) and L is the distance between the poles of the magnet. In Figure 1, F_{mag} , H_z , and $\partial H_z / \partial z$ are plotted against z .

Oldenburg et al. [16] reported that magnetic particles (ferrofluids) could have both miscible and immiscible behaviors with water. For example, an oil-based ferrofluid is immiscible with water while aqueous ferrofluids are miscible in water. The immiscible case should be described by two-phase aqueous/nonaqueous mixtures regardless of external

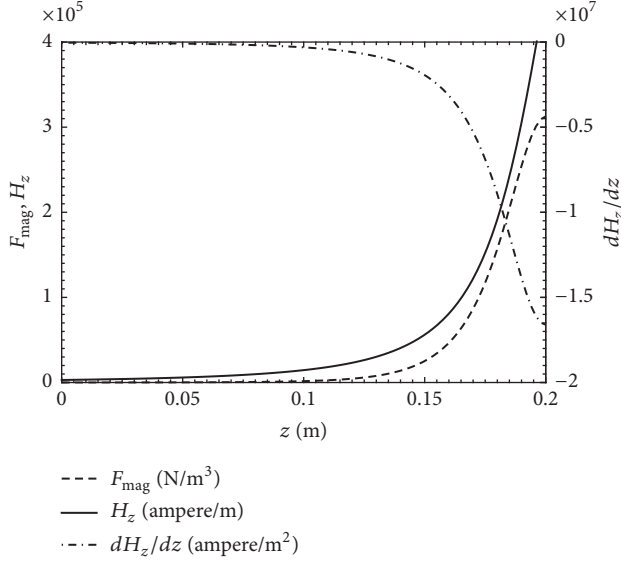


FIGURE 1: F_{mag} , H_z , and $\partial H_z/\partial z$ are plotted against z .

magnetic field strength, while the case of miscible in water should be described as single-phase aqueous mixtures. Under no external magnetic field, the two fluids are miscible. When a magnetic field is applied, it affects the ferrofluid part of the aquatic mixture in such a way that it behaves as immiscible. That is, the ferrofluids motion is dictated by the magnetic field. When the magnetic field is relatively strong, its effect on the ferrofluids may be influential. Therefore, a two-phase flow model is suitable for the flow of ferrofluids under strong external magnetic fields, but when the magnet is at larger distances from the flow (thus segregation effects are unimportant), the fully miscible single-phase liquid model is appropriate. Both of these models assume that the mixture is not so dilute. Pure ferrofluid and dilute colloidal suspension have approximately a thousand particles per cubic meter (see [16, 26]). So, one may conclude that the miscible and immiscible models may be applicable for ferrofluid fractions of 10% in water, and they are probably satisfactory in much more dilute mixtures [16].

In the current model, we treat the water-nanoparticles suspension as a miscible mixture while it is immiscible with the oil phase. Oldenburg et al. [16] assumed that magnetization increases linearly with the ferrofluid mass fraction c ,

$$M(c) = M(c = 1)c. \quad (4)$$

In the case of the immiscible two-phase (water-oil) model, Oldenburg et al. [16] assumed that magnetization increases linearly with the ferrofluid saturation,

$$M(S_w) = M(S_w = 1)S_w. \quad (5)$$

For the immiscible conceptualization, density and viscosity are considered properties of the respective phases, and no mixing relations are required. Therefore, in the current model we consider immiscible two-phase (water-oil) model; however, the water-nanoparticles suspension is a miscible

mixture. So, one may express the the magnetization of this system as,

$$M(S_w, c) = M(S_w = 1, c = 1)S_w c. \quad (6)$$

Following the work of Reeves and Cranwell [27] and Herbert et al. [28] on brine-water mixtures, Oldenburg et al. [16] have assumed that the volumes of pure water and ferrofluid are additive and define for the mixture density as

$$\frac{1}{\rho_w} = \frac{1-c}{\rho_{w,p}} + \frac{c}{\rho_f}, \quad (7)$$

where $\rho_{w,p}$ [kg·m⁻³] is the density of water component and ρ_f [kg·m⁻³] is the density of ferrofluid component.

The viscosity of the nanoparticles-water mixture is calculated by the following linear relationship [16, 28]:

$$\mu_w = \mu_{w,p} (1 + 1.35c), \quad (8)$$

where $\mu_{w,p}$ is the viscosity of pure water.

2.2. Flow Model. Considering the external magnetic force, which acts as a body force as explained in the above subsection, the vertical 1D (i.e., z -direction) velocities of oil phase and nanoparticles-water mixture phase may be written as

$$\begin{aligned} u_o &= -\frac{Kk_{ro}}{\mu_o} \left(\frac{\partial p_o}{\partial z} - \rho_o g \right), \\ u_w &= -\frac{Kk_{rw}}{\mu_w} \left(\frac{\partial p_w}{\partial z} - \rho_w(c)g - \mu_o M(S_w, c) \frac{\partial H}{\partial z} \right). \end{aligned} \quad (9)$$

The mass conservation equation is

$$\phi \frac{\partial S_\alpha}{\partial t} + \frac{\partial u_\alpha}{\partial z} = 0, \quad \alpha = w, o, \quad (10)$$

where ϕ [—] is the porosity, ρ_α [kg·m⁻³] is the density of phase α , S_α [—] is the saturation of phase α , and \mathbf{u}_α [m·s⁻¹] is the velocity of the phase α . w stands for the nanoparticles-water suspension phase, and o stands for the oil phase. K [m²] is the permeability, $k_{r\alpha}$ [—] is the relative permeability of phase α , p_α [Pa] is the pressure of phase α , g [m·s⁻²] is the gravitational acceleration, and μ_α [kg m⁻¹ s⁻¹] is the viscosity of phase α . The fluid saturations for the two-phase flow of water and oil are related by

$$S_w + S_o = 1. \quad (11)$$

In countercurrent imbibition, the sum of the velocities of the wetting and nonwetting phases is zero, that is,

$$u_t = u_w + u_o = 0 \quad (12)$$

The capillary pressure is defined as

$$P_c = P_o - P_w. \quad (13)$$

Since, in this case of study, we have two phases, one magnetized and the other nonmagnetized, the magnetostrictive effect should not be neglected. The magnetized phase pressure will have additional pressure term with the conventional thermodynamic pressure. The resulting pressure is called composite pressure [21], which can be given as

$$p_w^* = p_w + (p_m + p_s + p_n), \quad (14)$$

where p_w is the ferrofluid phase dynamic pressure, p_m is the fluid magnetic pressure, p_s is the magnetostrictive pressure, and p_n is the magnetic normal pressure, which is neglected [21] in this study. Also, one can write

$$p_c^* = p_c - (p_m + p_s),$$

$$p_s = \mu_0 \int_0^H V \left(\frac{\partial M}{\partial V} \right)_{H,T} dH, \quad (15)$$

$$p_m = \mu_0 \int_0^H M dH.$$

The specific volume is given as

$$V = \partial \left(\frac{1}{\rho} \right) = -\frac{1}{\rho^2} \partial \rho, \quad (16)$$

So,

$$p_s = -\mu_0 \int_0^H \rho \left(\frac{\partial M}{\partial \rho} \right)_{H,T} dH, \quad (17)$$

where

$$\frac{\partial M}{\partial \rho} = \left(\frac{\partial M}{\partial a_1} \right)_{b_1,H} \left(\frac{\partial a_1}{\partial \rho} \right) + \left(\frac{\partial M}{\partial b_1} \right)_{a_1,H} \left(\frac{\partial b_1}{\partial \rho} \right) + \left(\frac{\partial M}{\partial H} \right)_{a_1,b_1} \left(\frac{\partial H}{\partial \rho} \right). \quad (18)$$

We may approximate $\partial a_1 / \partial \rho$ and $\partial b_1 / \partial \rho$, when $a_{1,o}$ and $b_{1,o}$ are equal to zero in the nonmagnetized phase, as

$$\frac{\partial a_1}{\partial \rho} \approx \frac{a_1 - a_{1,o}}{\rho_w - \rho_o} = \frac{a_1}{\rho_w - \rho_o},$$

$$\frac{\partial b_1}{\partial \rho} \approx \frac{b_1 - b_{1,o}}{\rho_w - \rho_o} = \frac{a_1}{\rho_w - \rho_o}. \quad (19)$$

Therefore,

$$p_s = \frac{\rho_w a_1}{\rho_w - \rho_o} \mu_0 H \tan^{-1}(b_1 H). \quad (20)$$

Similarly, therefore,

$$p_m = a_1 \left(H \tan^{-1}(b_1 H) - \frac{1}{2b_1} \ln(b_1^2 H^2 + 1) \right). \quad (21)$$

Substituting from (9), (13), (20), and (21) into (12) and eliminating $\partial p_o / \partial z$, we may have

$$\frac{\partial p_w^*}{\partial z} = -f_w \frac{\partial p_c^*}{\partial z} + (\rho_w f_w + \rho_o f_o) g + f_w \mu_0 M(S_w, c) \frac{\partial H}{\partial z}, \quad (22)$$

So, the water velocity becomes

$$u_w = K \lambda_w f_o \left(\frac{\partial p_c^*}{\partial z} - \Delta \rho g + \mu_0 M(S_w, c) \frac{\partial H}{\partial z} \right). \quad (23)$$

Therefore, the saturation equation for the water phase becomes

$$\phi \frac{\partial S_w}{\partial t} + \frac{\partial}{\partial z} \left[K \lambda_w f_o \left(\frac{\partial p_c^*}{\partial z} - \Delta \rho g + \mu_0 M(S_w, c) \frac{\partial H}{\partial z} \right) \right] = 0, \quad (24)$$

where $\lambda_w = k_{rw} / \mu_w$ and $\lambda_o = k_{ro} / \mu_o$ are mobility ratios of water and oil phases, respectively. $\lambda_t = \lambda_w + \lambda_o$ is the total mobility. $f_w = \lambda_w / \lambda_t$ and $f_o = \lambda_o / \lambda_t$ are the flow fraction of water and oil phases, respectively. $\Delta \rho = \rho_w - \rho_o$. The capillary pressure is a function of the normalized saturation which can be given as [29]

$$p_c = p_d \ln S, \quad (25)$$

where p_d is the entry pressure for the imbibition. Moreover, the relative permeabilities are defined as

$$k_{rw} = k_{rw}^0 S^{a_2},$$

$$k_{ro} = k_{ro}^0 (1 - S)^{b_2}, \quad (26)$$

where S is the normalized water phase saturation, which is given as

$$S = \frac{S_w - S_{iw}}{1 - S_{ro} - S_{iw}}, \quad 0 < S < 1, \quad (27)$$

and $k_{rw}^0 = k_{rw}(S = 1)$ and $k_{ro}^0 = k_{ro}(S = 0)$ are the endpoint relative permeability of the water and oil phase, respectively. a_2 and b_2 are positive numbers. S_{iw} is the irreducible water saturation and S_{ro} is the residual oil saturation.

2.3. Nanoparticles Transport Model. Assuming that the nanoparticles exist only in the water phase and have only one size interval. The Brownian diffusion is considered for the nanoparticles and the volumes of pure water and the particles suspension are additive. The transport equation of the nanoparticles-water suspension in the water phase can be written as

$$\phi \frac{\partial (S_w c)}{\partial t} - \frac{\partial c_{s1}}{\partial t} - \frac{\partial c_{s2}}{\partial t} + \frac{\partial}{\partial z} \left(u_w c - \phi S_w (D_{diff} + D_{disp}) \frac{\partial c}{\partial z} \right) = 0, \quad (28)$$

where c [$\text{m}^3 \cdot \text{m}^{-3}$] is the volume concentration of nanoparticles in the water phase. c_{s1} [$\text{m}^3 \cdot \text{m}^{-3}$] is the volume of the nanoparticles in contact with the water phase available on the pore surfaces per unit bulk volume of the porous medium. c_{s2} [$\text{m}^3 \cdot \text{m}^{-3}$] is the volume of the nanoparticles entrapped in

pore throats from the water phase per unit bulk volume of porous medium due to plugging and bridging. D_{diff} [$\text{m}^2 \cdot \text{s}^{-1}$] is the molecular diffusion coefficient which can be calculated using the Stokes-Einstein equation,

$$D_{\text{diff}} = \tau \frac{k_B T}{3\pi\mu_w d}, \quad (29)$$

and τ is the tortuosity of the flow. k_B is the Boltzmann constant; T [K] absolute temperature. The mechanical dispersion coefficient D_{disp} [$\text{m}^2 \cdot \text{s}^{-1}$] is a function of Darcy's velocity and may be given as

$$\phi S_w D_{\text{disp}} = d_{l,w} |u_w|, \quad (30)$$

where $d_{l,w}$ is the longitudinal dispersion coefficient.

The modified Gruesbeck-Collins model [30] for the surface deposition is used in this study [8, 12]. In the presence of a critical velocity of the surface deposition only particle retention occurs while above it retention and entrainment of the nanoparticles take place simultaneously, which can be modeled as

$$\frac{\partial c_{s1}}{\partial t} = \begin{cases} \gamma_d |u_w| c, & u_w \leq u_c \\ \gamma_d |u_w| c - \gamma_e |u_w - u_c| c_{s1}, & u_w > u_c. \end{cases} \quad (31)$$

Also, the rate of entrapment of the nanoparticles in the water phase is given by

$$\frac{\partial c_{s2}}{\partial t} = \gamma_{pt} |u_w| c, \quad (32)$$

where γ_d [m^{-1}] is the rate coefficient for surface retention of the nanoparticles in the water phase. γ_e [m^{-1}] is the rate coefficient for entrainment of the nanoparticles. u_c is the critical velocity for the water phase. γ_{pt} [m^{-1}] is the pore throat blocking constant.

The porosity variation due to nanoparticles deposition is given as [8, 9]

$$\phi = \phi_0 - \delta\phi, \quad \delta\phi = c_{s1} + c_{s2}, \quad (33)$$

where ϕ_0 is the initial porosity. Therefore, permeability can be changed as [8]

$$K = K_0 \left[(1-f) k_f + f \frac{\phi}{\phi_0} \right]^l, \quad (34)$$

where K_0 is the initial permeability and $K = k\mathbf{I}$, $K_0 = k_0\mathbf{I}$, where k [m^2] and k_0 [m^2] are positive constants and \mathbf{I} is a unit matrix. k_f is constant for fluid seepage allowed by the plugged pores. The flow efficiency factor expressing the fraction of unplugged pores available for flow is given by

$$f = 1 - \gamma_f c_{s2}, \quad (35)$$

where γ_f is the coefficient of flow efficiency for the nanoparticles. The exponent l has a value of the range from 2.5 to 3.5.

The variation of relative permeabilities due to the nanoparticles reposition is given by El-Amin et al. [12] as follows:

$$k_{r\alpha,p} = [1 + r_a (\theta_\alpha - 1)] k_{r\alpha}, \quad \alpha = w, o, \quad (36)$$

where θ_α is the ratio of the phase α relative permeability due to nanoparticles adhering; that is,

$$k_{r\alpha,c} = \theta_\alpha k_{r\alpha}, \quad \alpha = w, o, \quad (37)$$

where $k_{r\alpha,c}$ is the relative permeabilities of water/oil phase when the surfaces per unit bulk volume of the porous media is completely occupied by the nanoparticles. $r_a = a_{\text{tot}}/a_{\text{sp}}$ such that

$$a_{\text{sp}} = A\phi \left(\frac{\phi}{K} \right)^{1/2} \quad (38)$$

is a specific area of the sand core and A [m^2] is the cross-sectional area. Also, the total surface area in contact with fluids per unit bulk volume is defined as [8]

$$a_{\text{tot}} = \frac{6\beta}{d} \delta\phi \quad (39)$$

and d is the diameter of the nanoparticles in a given interval size.

2.4. Initial and Boundary Conditions. At the beginning of the flow the following initial conditions are considered:

$$\begin{aligned} S_w &= S_w^0 \quad \text{at } t = 0, \quad 0 \leq z \leq h, \\ c &= c_{s1} = c_{s2} = 0 \quad \text{at } t = 0, \quad 0 \leq z \leq h, \end{aligned} \quad (40)$$

where h is the rock depth and S_w^0 is the initial water saturation. The boundary conditions are

$$\begin{aligned} S_w &= 1 - S_o^0, \\ c &= c_0, \\ c_{s1} &= c_{s2} = 0 \end{aligned} \quad (41)$$

at $t > 0, z = 0,$

$$\frac{dS_w}{dz} = \frac{dc}{dz} = \frac{dc_{s1}}{dz} = \frac{dc_{s2}}{dz} = 0 \quad \text{at } t > 0, z = h,$$

where c_0 is the concentration of nanoparticles-water suspension on the inlet boundary.

3. Results and Discussion

The above highly nonlinear parabolic partial differential equation is solved numerically using an efficient algorithm [31]. The spatial discretization is handled by Galerkin method, while an adaptive time step is used with the time integration. The above governing equations (24), (28), (31), and (32) are solved along with their initial and boundary conditions (40)-(41). The following parameters values are used in the computations; namely [8], $\gamma_d = 16$ [m^{-1}], $\gamma_{pt} = 1.28$ [m^{-1}], $\gamma_e = 30$ [m^{-1}], $u_c = 4.6 \times 10^{-6}$ [$\text{m} \cdot \text{s}^{-1}$], and $D = 5.6 \times 10^{-8}$ [$\text{m}^2 \cdot \text{s}^{-1}$]. The nanoparticles diameter is taken as 40 nm and the inlet concentration $c_0 = 0.0009$. Other different values of c_0 were taken into account in our

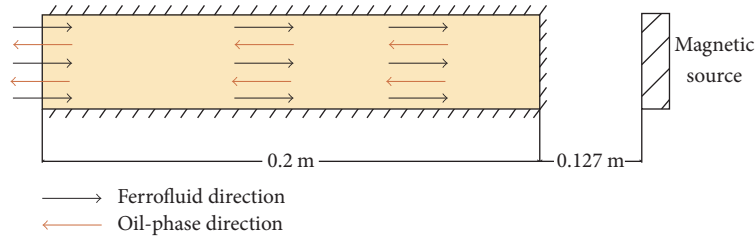


FIGURE 2: Magnet is placed on the right side of the core, with a core length, $h = 0.2$ m, and magnet parameters, $a_1 = 1.5 \times 10^4$, $b_1 = 2.4 \times 10^{-5}$, $Br = 1.19$, $a = b = 0.0254$, $L = 0.127$ m, and $\mu_0 = 4\pi 10^{-7}$, and magnet positioned at $x = 0.2$ m, $y = |x - 0.2|$ m.

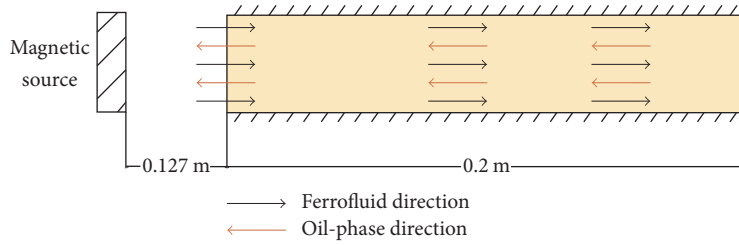


FIGURE 3: Magnet is placed on the left side of the core, with a core length, $h = 0.2$ m, and magnet parameters, $a_1 = 3 \times 10^2$, $b_1 = 3 \times 10^{-5}$, $Br = 1.19$, $a = b = 0.0254$, $L = 0.127$ m, and $\mu_0 = 4\pi 10^{-7}$, and magnet positioned at $x = 0.2$ m, $y = |x - 0.2|$ m.

previous study [12]. The remaining model parameters are [12, 32]; $h = 0.2$ m, $S_{wr} = S_{or} = 0.1$, $a_w = a_o = 0.5$, $\mu_w = \mu_o = 0.001$ [$\text{kg m}^{-1} \text{s}^{-1}$], $\rho_w = 1000$ [$\text{kg} \cdot \text{m}^{-3}$], $\rho_o = 660$ [$\text{kg} \cdot \text{m}^{-3}$], $\phi_0 = 0.3$, $l = 3$, $k_f = 0.6$, $\gamma_f = 0.01$, $k_{rw}^0 = k_{ro}^0 = 1$, $a_2 = b_2 = 4$, $\beta = 0.8$, $k_0 = 20 \times 10^{-15}$ [m^2], $\theta_o = 3$, $\theta_w = 0.6$. Moreover, the magnetic field parameters are $a_1 = 1.5 \times 10^4$, $b_1 = 2.4 \times 10^{-5}$ (when the magnet is on the right side of the core). But when the magnet is on the left side of the core, they are taken as $a_1 = 3 \times 10^2$, $b_1 = 3 \times 10^{-5}$.

In the following we consider two different locations of the magnet, namely, right and left side, with respect to the core and its boundary conditions (see Figures 2 and 3). On other words, the magnet location and flow directions are very important factors in this problem. If the magnet location is on the right side of the no-flow boundary of the core, the magnetic field will be assisting the flow, while the opposite is true when the magnet is placed on the left side of the inflow boundary of the rock (opposing flow).

3.1. Magnet at the Right Side of the Core. Firstly, we present the first case in Figures 4–9. Figure 4 illustrates the nanoparticles-water saturation profiles against the rock length with and without magnetic field effect for various values of the time of imbibition. It is interesting to note from this figure the effect of placing the magnet on the right side of the rock as it increases the saturation of nanoparticles-water suspension on this side while it decreases the saturation on the left side of the rock near to the flow inlet. This can be explained through an important fact that is the magnetic force is proportional to magnetic field strength, so fluid that is closer to the magnet is more strongly magnetized and pulled more strongly toward the magnet. For instance, this is in contrast to gravity driven flow in which gravitational force is

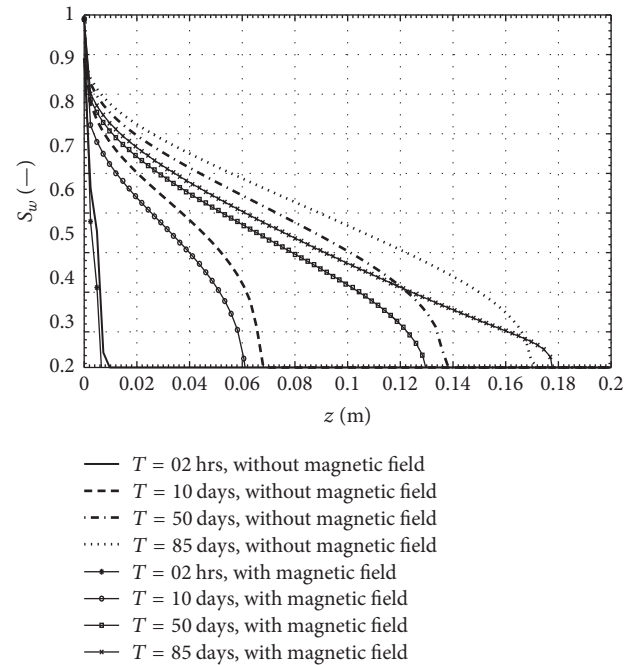


FIGURE 4: Saturations profiles against the core length with and without magnetic field effect for various values of imbibition time: magnet is placed on the right side of the core.

independent of position and fluid is pulled uniformly under gravity.

The nanoparticles concentration is plotted against the rock length in Figure 5, with and without magnetic field effect for various values of the imbibition time. From this figure, it can be seen that after long time of imbibition,

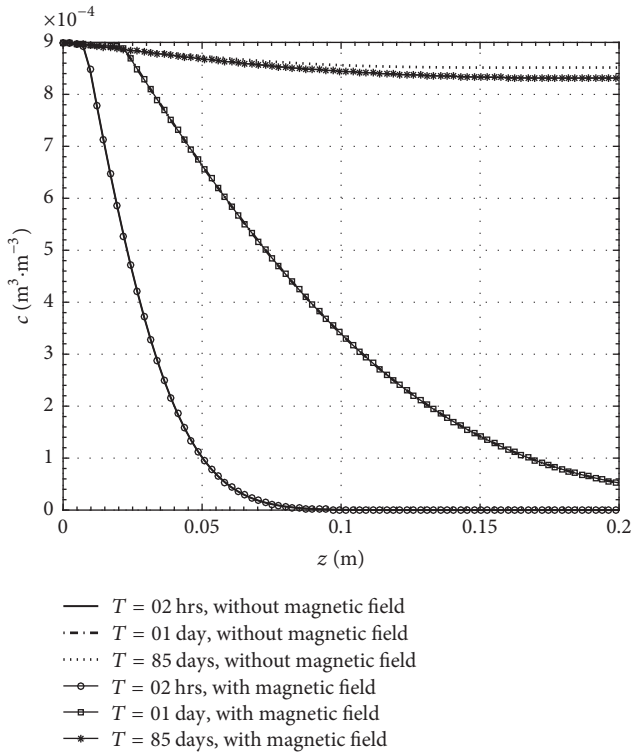


FIGURE 5: Nanoparticles concentration against core length with and without magnetic field effect for various values of imbibition time: magnet is placed on the right side of the core.

the nanoparticles concentration decreases slightly under the effect of the magnetic field. Figure 6 shows the concentration of deposited nanoparticles on the pore wall as plotted against the core length with and without magnetic field effect for various values imbibition times. Also, Figure 7 shows the concentration of deposited nanoparticles on the pore throat which is plotted against the core length with and without magnetic field effect for various values imbibition times. As expected the deposited nanoparticles have an opposite behavior of the nanoparticles in the water; that is, when the nanoparticles concentration in the water decreases, the deposited nanoparticles concentration increases.

In Figure 8, the permeability variation is plotted against the distance, with and without the magnetic field effect for various values of imbibition time when the magnet is located on the right side of the core. It is clear from this figure that the reduction in permeability is related to the quantity of the precipitation of nanoparticles on the wall and the imbibition time. Also, in Figure 9, the porosity variation is plotted against the distance with and without the magnetic field effect for various values of imbibition time when the magnet is located on the right side of the core. It can be seen that the change in porosity is related to the quantity of nanoparticles plugging the throat of the pore and imbibition time.

3.2. Magnet at the Left Side of the Core. Now, we consider the second case, when the magnet is to the left of the rock (which opposes the flow), in Figures 10–13. Saturations

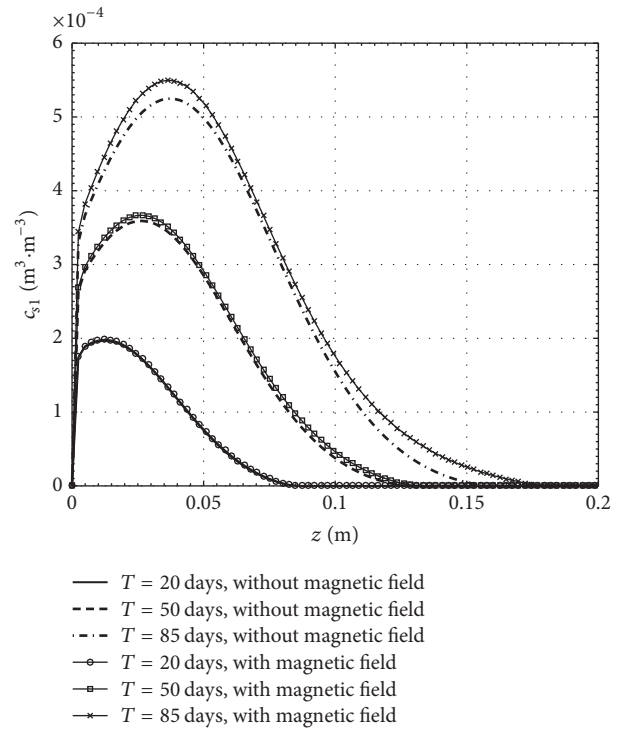


FIGURE 6: Pore wall deposited nanoparticles concentration against core length with and without magnetic field effect for various values of imbibition time: magnet is placed on the right side of the core.

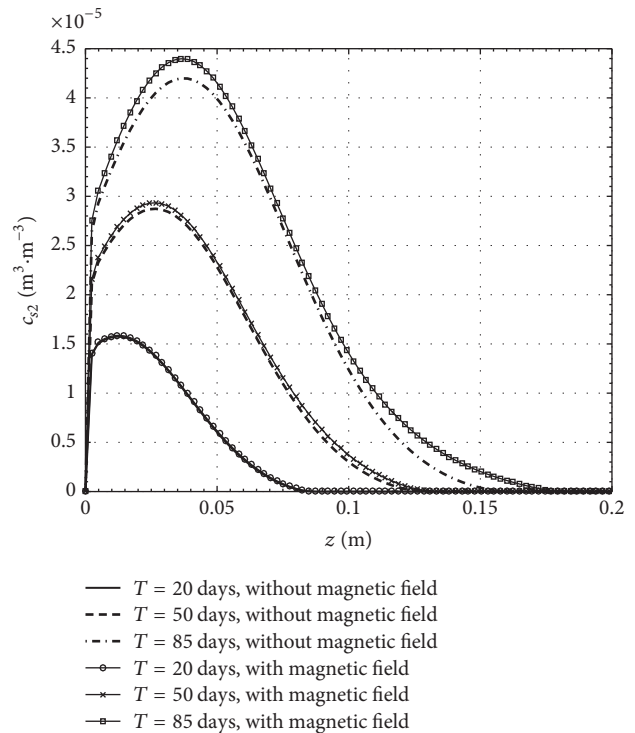


FIGURE 7: Pore throat deposited nanoparticles concentration against core length with and without magnetic field effect for various values of imbibition time: magnet is placed on the right side of the core.

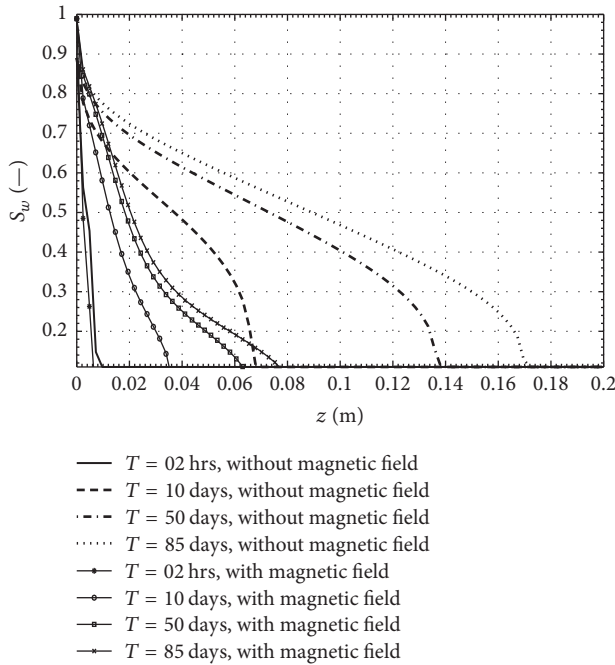


FIGURE 8: Permeability variation against core length with and without magnetic field effect for various values of imbibition time: magnet is placed on the right side of the core.

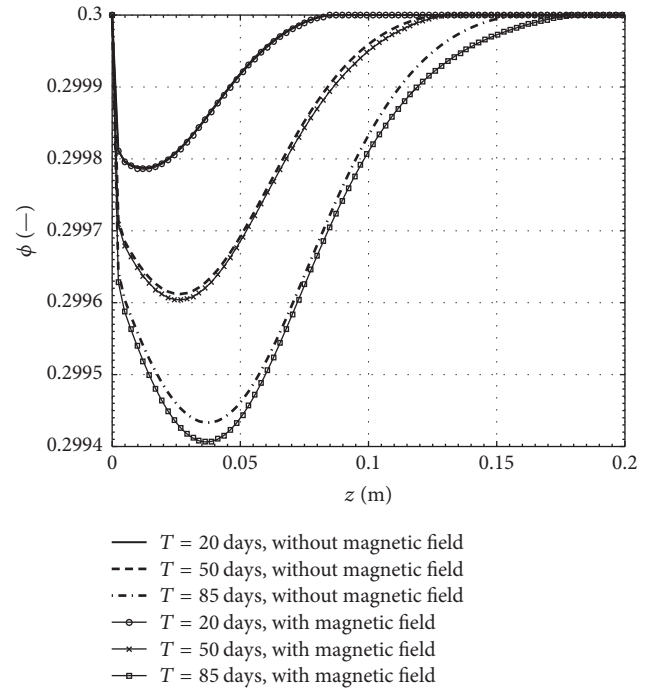


FIGURE 9: Porosity variation against core length with and without magnetic field effect for various values of imbibition time: magnet is placed on the right side of the core.

profiles are plotted in Figure 10, against the core distance with and without magnetic field effect for various values of imbibition time when the magnet is placed on left side of the core. An interesting behavior can be seen in this figure. Unlike the case of the right magnet, the left magnet resists the flow and reduces water invasion. Moreover, Figure 11 shows the profiles of nanoparticles concentration against core length with and without magnetic field effect for various values of imbibition time, in the case of left location of the magnet. It is clear from this figure that the concentration of nanoparticles in water increases especially after long imbibition time. Figure 12 illustrates deposited nanoparticles concentration on the pore wall against the core length, with and without magnetic field effect for various values of imbibition time when the magnet is located on the left side of the core. This figure shows that the magnetic field reduces significantly the deposited nanoparticles on the pore surface. Finally, Figure 13 illustrates the nanoparticles concentration plugging pore throat against core length with and without magnetic field effect for various values of imbibition time when the magnet is located on the left side of the core. One may notice that the magnetic field reduces the nanoparticles plugging pore throat.

Figure 14 illustrates the permeability profiles against the distance with various values of imbibition time, with and without magnetic field effect when the magnet is on the left side. Similarly, the permeability decreases as a consequence of the precipitation of nanoparticles. The permeability has a minor reduction compared to the initial permeability. Figure 15 shows the porosity variation against the distance with various values of imbibition time, with and without

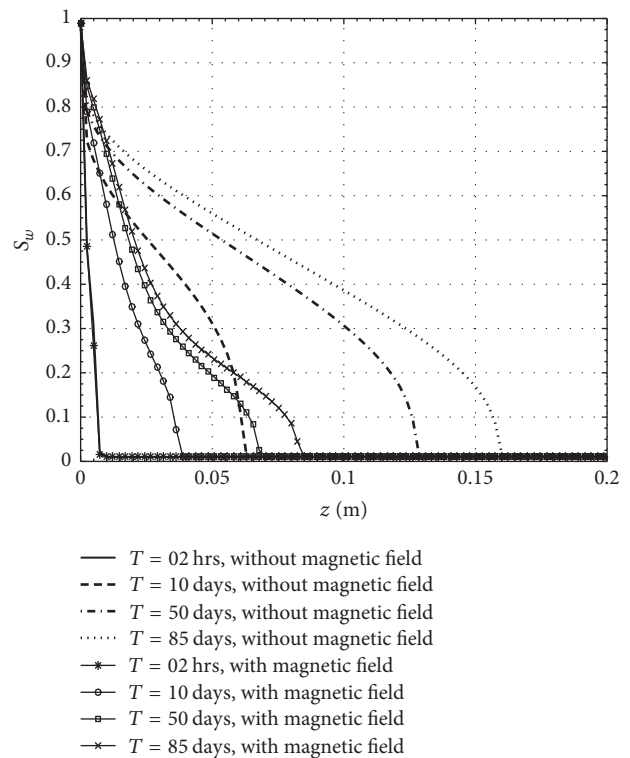


FIGURE 10: Saturations profiles against the core length with and without magnetic field effect for various values of imbibition time: magnet is placed on the left side of the core.

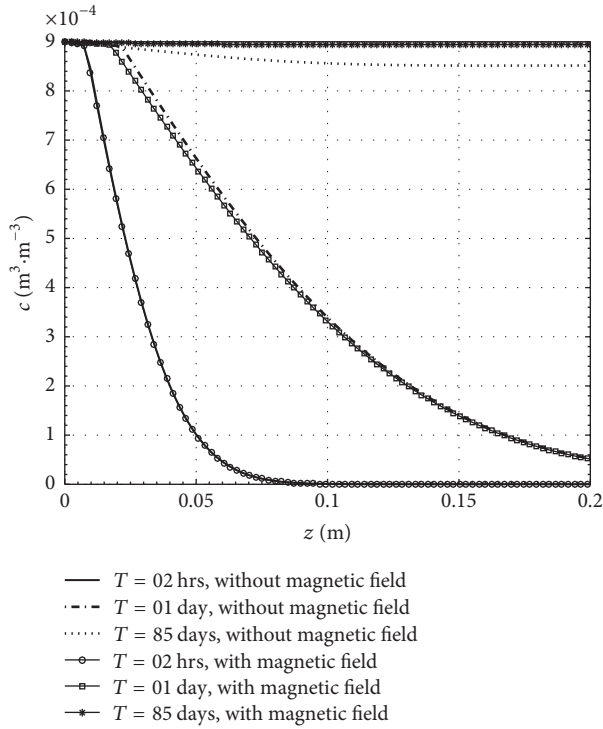


FIGURE 11: Nanoparticles concentration against core length with and without magnetic field effect for various values of imbibition time: magnet is placed on the left side of the core.

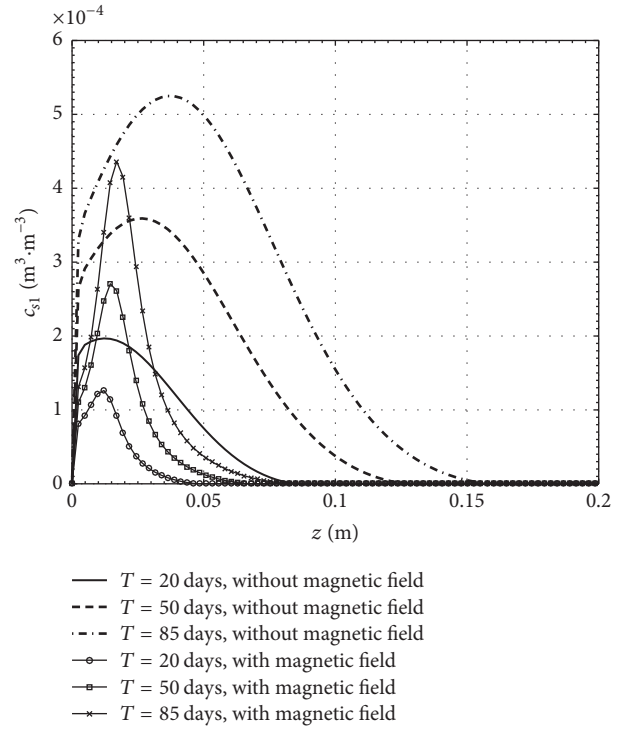


FIGURE 12: Pore wall deposited nanoparticles concentration against core length with and without magnetic field effect for various values of imbibition time: magnet is placed on the left side of the core.

magnetic field effect when the magnet is located on the left side. It is interesting to note reduction in the porosity which is a consequence of the precipitation of nanoparticles on the pore walls. The porosity variation is negligibly small.

4. Conclusions

This paper was devoted to study the magnetic field effects on the the transport of magnetic nanoparticles injected into a two-phase water-oil system in porous media. Firstly, we developed the mathematical model which governs the transport of magnetic nanoparticles in a two-phase, water-oil system in porous media under the effect of an external magnetic field. The countercurrent imbibition in a small-scale porous medium core is considered as an example. Both Brownian diffusion and mechanical dispersion are taken into consideration, with the assumption that only one size interval of the nanoparticles exists. Variation of porosity, permeability, and relative permeabilities due to particles deposition are also considered. Immiscible mixture relationships have been used to determine the magnetization properties, density, and viscosity of this ferrofluid. In such flow field, the pressure includes additional terms, namely, the ferrofluid dynamic pressure, the fluid magnetic pressure, and the magnetostrictive pressure. Two different locations of the magnetic field with respect to the core inflow and no-flow boundaries are considered. Effects of the magnetic field on the physical variables such as saturation, nanoparticles concentrations, porosity, and permeability have been examined.

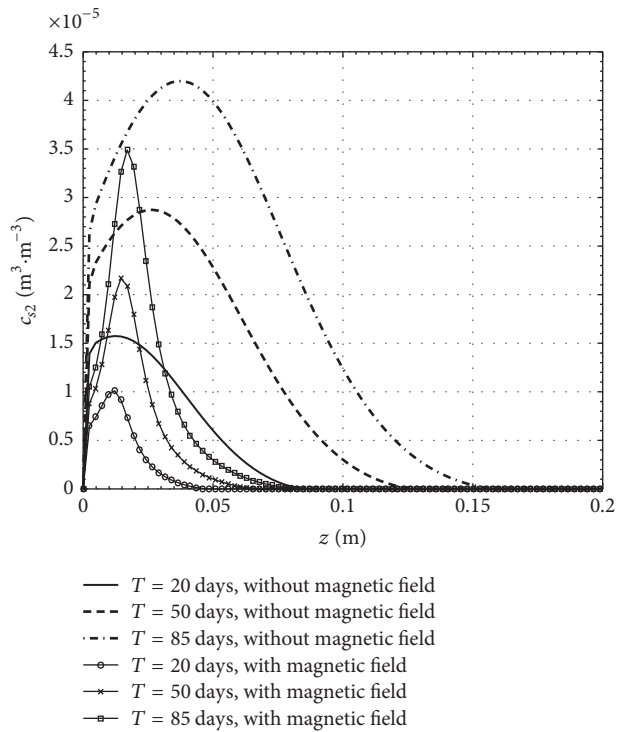


FIGURE 13: Pore throat deposited nanoparticles concentration against core distance with and without magnetic field effect for various values of imbibition time: magnet is placed on the left side of the core.

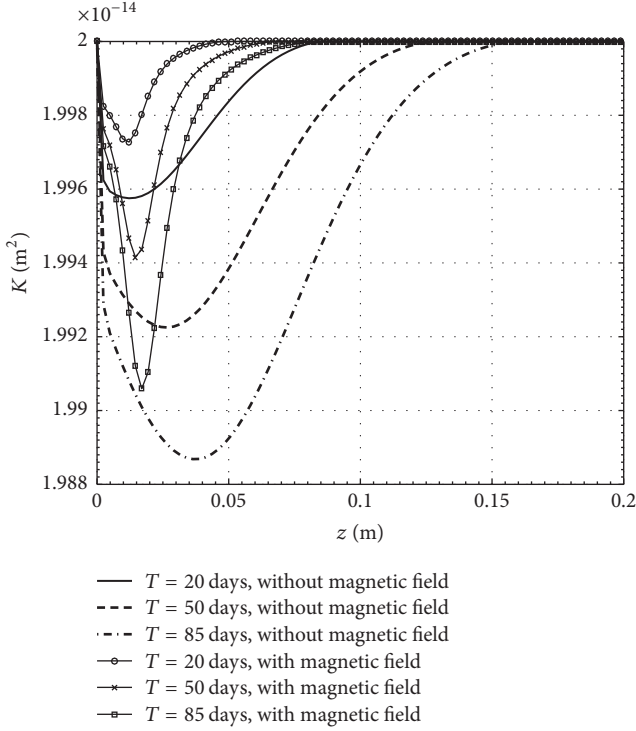


FIGURE 14: Permeability variation against core length with and without magnetic field effect for various values of imbibition time: magnet is placed on the left side of the core.

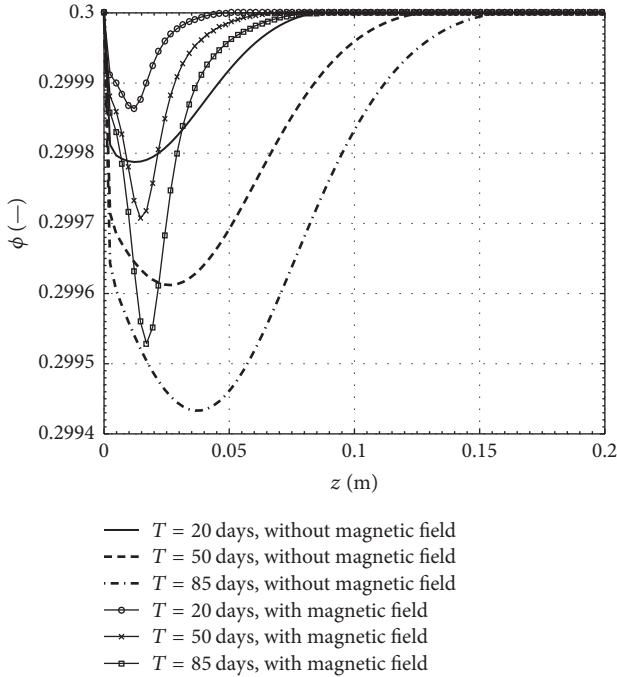


FIGURE 15: Porosity variation against core length with and without magnetic field effect for various values of imbibition time: magnet is placed on the left side of the core.

The important result from this simulation is that the magnetic source location has a significant influence on the physical variables of the model. Based on the flow direction and the location of the magnet, the magnetic field can assist or oppose the flow of this two-phase system. Such observed behavior can be used for different applications depending on whether the goal is to aid or delay the injected fluid advancement. According to this investigation, if the magnet is placed next to the no-flow boundary of the studied countercurrent numerical experiment, the saturation of nanoparticles-water suspension increases. Moreover, the concentration of nanoparticles is observed to decrease slightly, which has been attributed to the slight increase of the deposition of nanoparticles. On the other hand, when the magnet is placed next to the inflow/outflow boundary, the magnet resists the flow of the ferrofluid suspension and decreases water invasion capacity, thereby. Furthermore, the nanoparticles concentration seems to increase under the effect of the magnetic field, and the deposited nanoparticles concentration decreases. Both porosity and permeability are reduced due to the nanoparticles adherence to the walls of the porous media.

Nomenclature

- A : Cross-sectional area [m^2]
- a : Half of width of the magnet [m]
- a_1 : Constant [A m^{-1}]
- a_{tot} : Total surface area in contact with fluids [m^2]
- a_2 : Positive real number [—]
- b : Half of height of the magnet [m]
- b_1 : Constant [m A^{-1}]
- b_2 : Positive real number [—]
- B_r : Residual magnetization [T]
- c : Concentration of nanoparticles in the water phase [$\text{m}^3 \cdot \text{m}^{-3}$]
- c_0 : Concentration of nanoparticles in the water on the inlet boundary [$\text{m}^3 \cdot \text{m}^{-3}$]
- c_{s1} : Concentration of the deposited nanoparticles on the pore surfaces [$\text{m}^3 \cdot \text{m}^{-3}$]
- c_{s2} : Concentration of nanoparticles entrapped in pore throats [$\text{m}^3 \cdot \text{m}^{-3}$]
- d : Diameter of the nanoparticles in a given interval size [m]
- D_{diff} : Molecular diffusion coefficient [$\text{m}^2 \cdot \text{s}^{-1}$]
- D_{disp} : Mechanical dispersion coefficient [$\text{m}^2 \cdot \text{s}^{-1}$]
- $d_{l,w}$: Longitudinal dispersion coefficient [—]
- f : Flow efficiency factor [—]
- F_{mag} : External magnetic force [N]
- f_α : Flow fraction of the phase α [—]
- f_w : Flow fraction of water [—]
- f_o : Flow fraction of oil [—]
- g : Gravitational acceleration [$\text{m} \cdot \text{s}^{-2}$]
- H : Magnetic field strength [A m^{-1}]
- h : Rock depth [m]
- K : Permeability [m^2]
- K_0 : Initial permeability [m^2]
- k_f : Constant for fluid seepage
- $k_{r\alpha}$: Relative permeability of the phase α [—]

$k_{r\alpha,c}$: Relative permeability of the phase α when the surface is completely occupied by the nanoparticles [—]

$k_{r\alpha}^0$: Endpoint relative permeability of the phase α [—]

k_B : Boltzmann constant [—]

l : Constant [—]

L : Distance between the poles of the magnet [m]

M : Magnetization [$A\ m^{-1}$]

p_α : Pressure of the phase α [Pa]

p_w : Ferrofluid phase pressure [Pa]

p_o : Oil phase pressure [Pa]

p_d : Pressure entry [Pa]

p_c : Capillary pressure [Pa]

p_m : Fluid magnetic pressure [Pa]

p_s : Magnetostrictive pressure [Pa]

p_n : Magnetic normal pressure [Pa]

S : Normalized saturation [—]

S_w : Ferrofluid saturation [—]

S_w^0 : Initial ferrofluid saturation [—]

r_a : Specific area of the sand core [—]

S_o : Oil saturation [—]

S_α : Saturation of the phase α [—]

S_{iw} : Irreducible water saturation [—]

S_{ro} : Residual oil saturation [—]

t : Time [s]

T : Absolute temperature [K]

V : Specific volume [$m^3\ Kg^{-1}$]

u_c : Critical velocity [$m\cdot s^{-1}$]

u_α : Velocity of the phase α [$m\cdot s^{-1}$]

u_t : Total velocity [$m\cdot s^{-1}$]

z : Depth [m].

Greek Symbols

γ_d : Rate coefficient for surface retention [m^{-1}]

γ_e : Rate coefficient for surface entrainment [m^{-1}]

γ_{pt} : Constant for pore throat blocking [m^{-1}]

γ_f : Coefficient of flow efficiency

$\rho_{w,p}$: Density of water component [$kg\cdot m^{-3}$]

ρ_f : Density of ferrofluid component [$kg\cdot m^{-3}$]

ρ_α : Density of the phase α [$kg\cdot m^{-3}$]

μ_0 : Magnetic permeability [$T\ m\ A^{-1}$]

$\mu_{w,p}$: Viscosity of pure water [$kg\ m^{-1}\ s^{-1}$]

μ_α : Viscosity of the phase α [$kg\ m^{-1}\ s^{-1}$]

λ_α : Mobility ratio of the phase α [—]

λ_t : Total mobility

ϕ : Porosity [—]

ϕ_0 : Initial porosity [—]

τ : Tortuosity of the flow [—]

θ_α : Ratio of the phase α relative permeability due to nanoparticles adhering [—].

Subscripts and Superscripts

0: Reference value

o: The oil phase

r: Residual

t: Total

w : The nanoparticles-water suspension phase

α : Phase.

Conflicts of Interest

The authors declare that they have no conflicts of interest.

References

- [1] S. Kapusta, L. Balzano, and P. M. Te Riele, "Nanotechnology applications in oil and gas exploration and production," in *Proceedings of the International Petroleum Technology Conference*, Bangkok, Thailand, 2012.
- [2] A. Fletcher and J. Davis, "How EOR can be transformed by nanotechnology," in *Proceedings of the SPE Improved Oil Recovery Symposium*, Tulsa, Okla, USA, 2010.
- [3] M. Sabet, S. N. Hosseini, A. Zamani, Z. Hosseini, and H. Soleimani, "Application of nanotechnology for enhanced oil recovery: A review," *Defect and Diffusion Forum*, vol. 367, pp. 149–156, 2016.
- [4] C. Negin, S. Ali, and Q. Xie, "Application of nanotechnology for enhancing oil recovery: a review," *Petroleum*, vol. 2, no. 4, pp. 324–333, 2016.
- [5] M. Cocuzza, C. Pirri, V. Rocca, and F. Verga, "Current and future nanotech applications in the oil industry," *American Journal of Applied Sciences*, vol. 9, no. 6, pp. 784–793, 2012.
- [6] J. J. Sheng, B. Leonhardt, and N. Azri, "Status of polymer-flooding technology," *Journal of Canadian Petroleum Technology*, vol. 54, no. 2, pp. 116–126, 2015.
- [7] F. Verga, M. Lombardi, G. Maddinelli, and L. Montanaro, "Introducing core-shell technology for conformance control," *Oil & Gas Science and Technology – Revue d'IFP Energies nouvelles*, vol. 72, no. 1, p. 5, 2017.
- [8] B. Ju and T. Fan, "Experimental study and mathematical model of nanoparticle transport in porous media," *Powder Technology*, vol. 192, no. 2, pp. 195–202, 2009.
- [9] X. H. Liu and F. Civian, "A multiphase mud fluid infiltration and filter cake formation model," in *Proceedings of the SPE International Symposium on Oilfield Chemistry*, New Orleans, LA, USA, 1996.
- [10] M. F. El-Amin, A. Salama, and S. Sun, "Modeling and simulation of nanoparticles transport in a two-phase flow in porous media," in *Proceedings of the International Oilfield Nanotechnology Conference and Exhibition*, Society of Petroleum Engineers, Noordwijk, The Netherlands, 2012.
- [11] M. F. El-Amin, S. Sun, and A. Salama, "Modeling and simulation of nanoparticle transport in multiphase flows in porous media: CO₂ sequestration," in *Proceedings of the Mathematical Methods in Fluid Dynamics and Simulation of Giant Oil and Gas Reservoirs*, Society of Petroleum Engineers, Istanbul, Turkey, 2012.
- [12] M. F. El-Amin, A. Salama, and S. Sun, "Numerical and dimensional analysis of nanoparticles transport with two-phase flow in porous media," *Journal of Petroleum Science and Engineering*, vol. 128, pp. 53–64, 2015.
- [13] A. Salama, A. Negara, M. El Amin, and S. Sun, "Numerical investigation of nanoparticles transport in anisotropic porous media," *Journal of contaminant hydrology*, vol. 181, pp. 114–130, 2015.
- [14] B. A. Suleimanov, F. S. Ismailov, and E. F. Veliyev, "Nanofluid for enhanced oil recovery," *Journal of Petroleum Science and Engineering*, vol. 78, no. 2, pp. 431–437, 2011.

- [15] L. Hendraningrat, S. Li, and O. Torsæter, "A coreflood investigation of nanofluid enhanced oil recovery," *Journal of Petroleum Science and Engineering*, vol. 111, pp. 128–138, 2013.
- [16] C. M. Oldenburg, S. E. Borglin, and G. J. Moridis, "Numerical simulation of ferrofluid flow for subsurface environmental engineering applications," *Transport in Porous Media*, vol. 38, no. 3, pp. 319–344, 2000.
- [17] M. Zahn, "Magnetic fluid and nanoparticle applications to nanotechnology," *Journal of Nanoparticle Research*, vol. 3, no. 1, pp. 73–78, 2001.
- [18] N. Yahya, M. Kashif, A. Shafie, H. Solemani, H. M. Zaid, and N. R. A. Latiff, "Improved oil recovery by high magnetic flux density subjected to iron oxide nanofluids," *Journal of Nano Research*, vol. 26, pp. 89–99, 2014.
- [19] N. Kothari, B. Raina, K. B. Chandak, V. Iyer, and H. P. Mahajan, "Application of ferrofluids for enhanced surfactant flooding in IOR," in *Proceedings of the SPE SPE EUROPEC/EAGE Annual Conference and Exhibition*, Barcelona, Spain, 2010.
- [20] S. Ryoo, A. R. Rahmani, K. Y. Yoon et al., "Theoretical and experimental investigation of the motion of multiphase fluids containing paramagnetic nanoparticles in porous media," *Journal of Petroleum Science and Engineering*, vol. 81, pp. 129–144, 2012.
- [21] M. Prodanovic, S. Ryoo, A. R. Rahmani et al., "Effects of magnetic field on the motion of multiphase fluids containing paramagnetic nanoparticles in porous media," in *Proceedings of the SPE Improved Oil Recovery Symposium*, Tulsa, Okla, USA, 2010.
- [22] M. F. El-Amin and T. Brahim, "Numerical modeling of magnetic nanoparticles transport in a two-phase flow in porous media," in *Proceedings of the SPE Reservoir Characterisation and Simulation Conference*, Abu Dhabi, UAE, 2017.
- [23] M. F. El-Amin, A. M. Saad, S. Sun, and A. Salama, "Numerical simulation of magnetic nanoparticles injection into two-phase flow in a porous medium," in *Proceedings of the International Conference on Computational Science, ICCS 2017*, vol. 108, pp. 2260–2264, Procedia Computer Science, Zurich, Switzerland, 2017.
- [24] S. Borglin, G. Moridis, and A. Becker, "Magnetic detection of ferrofluid injection zones," Lawrence Berkeley National Laboratory Report LBL-40127, Berkeley, Calif, USA, 1998.
- [25] M. McCaig and A. G. Clegg, *Permanent Magnets in Theory and Practice*, Pentech Pres, 2 edition, 1987.
- [26] R. E. Rosensweig, *Ferrohydrodynamics*, Cambridge University Press, 1985.
- [27] M. Reeves and R. M. Cranwell, "Theory and implementation of SWIFT II, the Sandia waste-isolation flow and transport model for fractured media," Tech. Rep. SAND83-1159, Sandia National Laboratories, Albuquerque, NM, USA, 1981.
- [28] A. W. Herbert, C. P. Jackson, and D. A. Lever, "Coupled ground-water flow and solute transport with fluid density strongly dependent upon concentration," *Water Resources Research*, vol. 24, no. 10, pp. 1781–1795, 1988.
- [29] M. Pooladi-Darvish and A. Firoozabadi, "Co-current and counter-current imbibition in a water-wet matrix block," *Society of Petroleum Engineers Journal*, vol. 5, no. 1, pp. 3–11, 2000.
- [30] C. Gruesbeck and R. E. Collins, "Entrainment and deposition of fines particles in porous media," *Society of Petroleum Engineers Journal*, vol. 24, pp. 847–856, 1982.
- [31] R. D. Skeel and M. Berzins, "A method for the spatial discretization of parabolic equations in one space variable," *Society for Industrial and Applied Mathematics. Journal on Scientific and Statistical Computing*, vol. 11, no. 1, pp. 1–32, 1990.
- [32] M. F. El-Amin, A. Salama, and S. Sun, "Numerical and dimensional investigation of two-phase countercurrent imbibition in porous media," *Journal of Computational and Applied Mathematics*, vol. 242, pp. 285–296, 2013.

Research Article

Modelling of River-Groundwater Interactions under Rainfall Events Based on a Modified Tank Model

Wen Nie,^{1,2} Yong-chang Liang,³ Lin Chen,⁴ and Wei Shao⁵

¹State Key Laboratory of Geo-Hazard Prevention and Geo-Environment Protection, Chengdu University of Technology, Chengdu 610059, China

²Quanzhou Institute of Equipment Manufacturing, Haixi Institutes, Chinese Academy of Sciences, Quanzhou 362200, China

³State Key Laboratory of Oil and Gas Reservoir Geology and Exploitation, Southwest Petroleum University, Chengdu, Sichuan 610500, China

⁴College of Science, Southwest Petroleum University, Chengdu, Sichuan 610500, China

⁵College of Hydrometeorology, Nanjing University of Information Science and Technology, Nanjing, Jiangsu 210044, China

Correspondence should be addressed to Wen Nie; niewen1026@gmail.com

Received 12 January 2017; Revised 8 May 2017; Accepted 28 May 2017; Published 2 July 2017

Academic Editor: Kundan Kumar

Copyright © 2017 Wen Nie et al. This is an open access article distributed under the Creative Commons Attribution License, which permits unrestricted use, distribution, and reproduction in any medium, provided the original work is properly cited.

A multitank model experiment is employed to simulate the river-groundwater interaction under rainfall events. These experiments involve coarse and fine materials and rainfall events of 45 and 65 mm/hr. We developed a modified tank model for estimation of the groundwater table and river levels in these experiments. Parameter training of our tank model includes two algorithms: (i) the nonincremental learning algorithm-based model can predict the pore water pressure (PWP) in a slope and river under a 65 mm/hr rainfall event (coarse material) with Nash–Sutcliffe efficiency (NSE) = 0.427 and -0.909 and (ii) the incremental learning algorithm-based model can predict the PWP in a slope and river with NSE = 0.994 and 0.995. Then, the river-groundwater interaction was reproduced by a numerical case. The results of the deterministic method of the numerical case and optimized method of the modified tank model matched well.

1. Introduction

River-groundwater interaction of river-slope systems under rainfall events is common in riverbank and basin areas. The general process is described in Figure 1. Estimation of groundwater is usually complicated as a result of groundwater-river interactions, which could relate to the permeability, hydraulic gradients, and hydrogeological properties in the slope-river system [1–5]. The hydrological processes of the river-slope system are strongly linked to stream flow generation, contamination transport, and slope stability [2–10]. The deterministic method commonly uses the Darcy-Richards equation or the Boussinesq equation as hydrological models to simulate the groundwater flow in a slope [9], and the models can be further extended to dual-permeability models for preferential flow simulations [10, 11]. These hydrological models may be integrated with solute transport models to

analyse contamination risks [12] or with soil mechanics models for slope stability analysis [10, 11]. However, solving the deterministic models numerically is usually computationally expensive, and the implementation requires detailed investigation of the geometries and hydraulic properties of the slope material [11]. Compared to the deterministic method, a model based on an optimized method such as the tank model [6] usually does not need material information about permeability and infiltration. It uses historical monitoring data for estimating or training parameters of the assumed model structure [7, 8]. In other words, the method only needs the historical data to carry out parameter estimation for the relation between the input and output of the model. Then the parameters estimated can help decide objectives like groundwater by inputting infiltration. Therefore, these optimized methods can be applied to a wide range of different landslide settings, and we estimate that, for more than 90% of

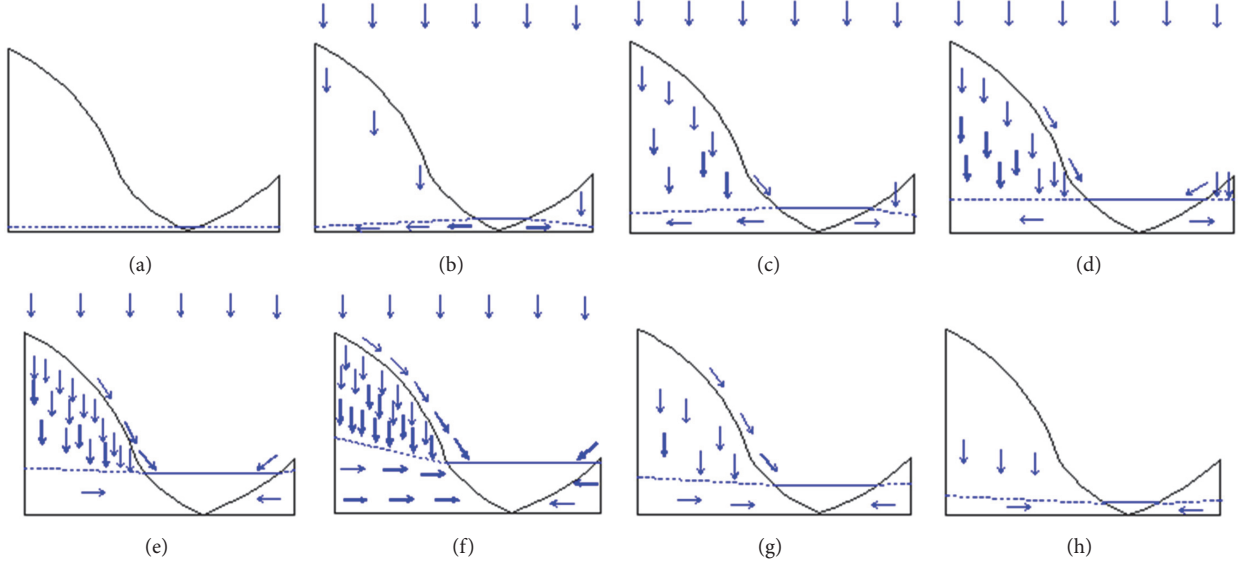


FIGURE 1: River-groundwater interaction under rainfall event: (a) initial state; (b) groundwater level raised by rainfall infiltration and river supply; (c) more rainfall and river supply and overland flow produced; (d) high groundwater table produced by continuous rainfall; (e) groundwater conversely supplies the river level; (f) increased groundwater accelerates the water flow supply to river; (g) overland flow and rainfall infiltration decrease; (h) recovery to the initial state.

all landslides, no explicit parameters for soil suction and so on are available. In our study, a series of physical multitank model experiments are carried out by simulating groundwater table changes in consideration of groundwater-river interactions under rainfall events. A modified conceptual tank model is used to predict the groundwater changes in these experiments. Parameter training in a modified tank model is involved with two algorithms (nonincremental and incremental learning algorithm). Then a numerical case based on the deterministic method is compared to our modified tank model. The remainder of the paper is organized as follows: Section 2 describes the original tank model and our modified tank model. Section 3 introduces the materials, device, and experimental procedure. Section 4 highlights the results of models of experiments and analysis of the original and modified conceptual tank model. The performance of the modified tank model with the nonincremental and incremental learning algorithms is introduced and discussed in Section 5. Section 6 discusses the replicated application of the modified tank models by a numerical riverbank simulation. The conclusions are detailed in Section 7.

2. Original and Modified Tank Models

A tank model is a nonlinear theorized calculation to describe the behaviours of water hydraulic properties [6]. Until now, simple or multitank models have been used for estimation of groundwater in a homogenous slope involving many experimental or real cases [13–18]. The basic mechanism of the multitank model is as shown in Figure 2(a).

Equation (1) indicates the change of groundwater table related to infiltration and drainage in a unit of time in every tank element. Equation (2) shows the infiltration affected by

the perched water table. Equation (3) shows the drainage rate affected by the current groundwater table.

$$\begin{aligned} W_1(t+1) - W_1(t) &= I_1(t), \\ W_2(t+1) - W_2(t) &= I_2(t) - Q_2(t), \\ W_3(t+1) - W_3(t) &= I_3(t), \\ W_4(t+1) - W_4(t) &= I_4(t) - Q_4(t) + Q_2(t), \end{aligned} \quad (1)$$

$$\begin{aligned} I_2(t) &= b_1 W_1(t), \\ I_4(t) &= b_2 W_3(t), \end{aligned} \quad (2)$$

$$\begin{aligned} Q_2(t) &= a_2 W_2(t), \\ Q_4(t) &= a_4 W_4(t), \end{aligned} \quad (3)$$

where t and $t+1$ are the time steps, I_j is the infiltration, W_j is the water table, Q_j is defined as drainage, a_j is a coefficient indicating the relation between drainage and the groundwater table, j is 1, 2, 3, and 4, and b_1 and b_2 are the coefficients indicating the relation between surface infiltration and a perched water table.

Compared to the original tank model, our modified tank model simplifies the structure of the tank model (Figure 2(b)). It considers the maximum infiltration ability and time lag of groundwater induced by the path, material, and moisture content in the previous condition.

$$\begin{aligned} W_1(t+1) - W_1(t) &= a_1 I_1(t + \Delta) - Q_{1-2}(t), \\ W_2(t+1) - W_2(t) &= a_2 I_2(t + \Delta) + Q_{1-2}(t + \Delta_1) \\ &\quad - Q_2(t), \end{aligned} \quad (4)$$

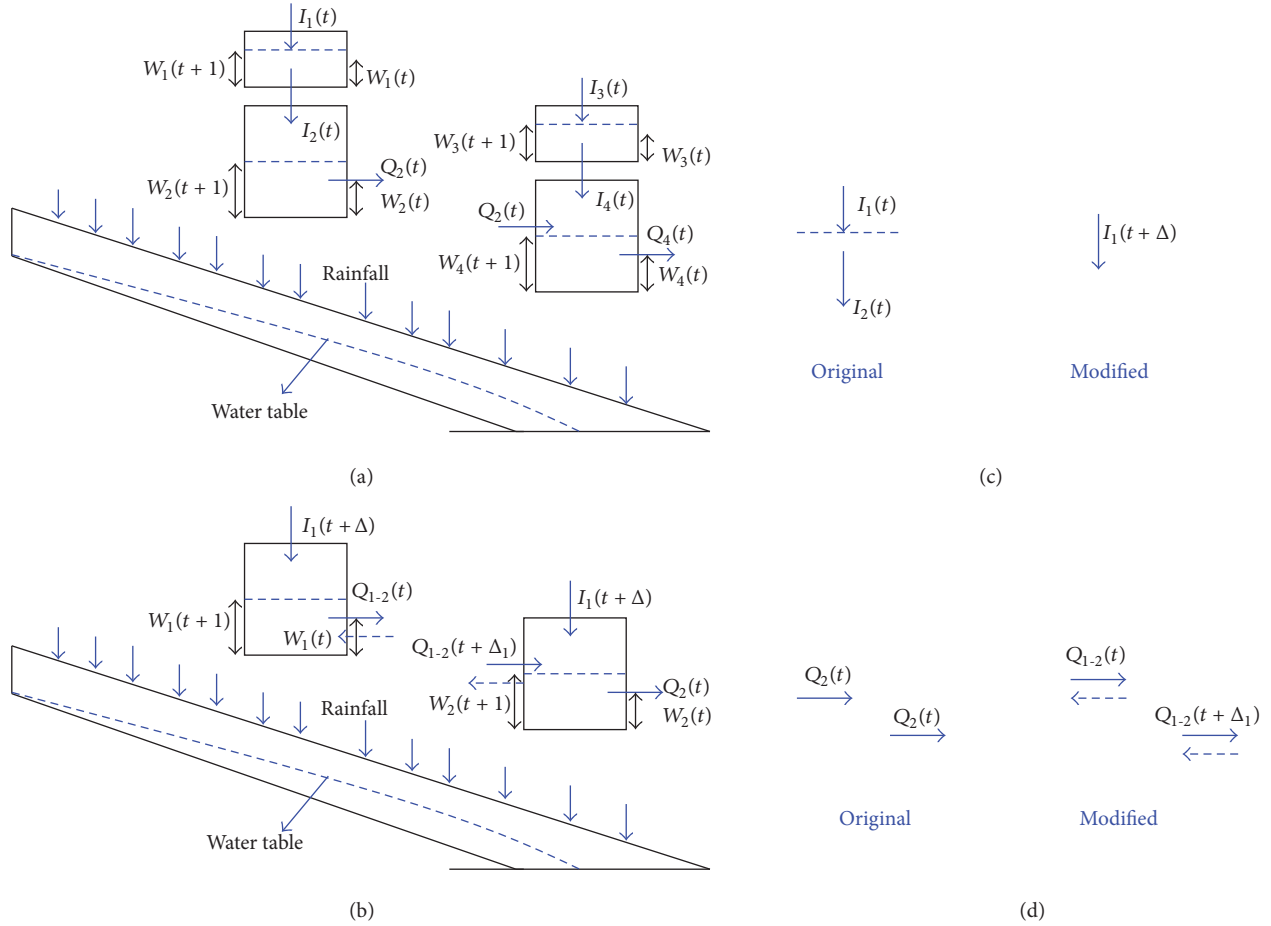


FIGURE 2: Comparison of original and modified multistorage tank models: (a) original multistorage tank model; (b) modified multistorage tank model; (c) optimizing the infiltration time lag; (d) optimizing the lateral water flow time lag.

$$\begin{aligned}
 Q_{1-2}(t) &= b_{1-2}(W_1(t) - W_2(t)), \\
 Q_{1-2}(t + \Delta_1) &= b_{2-1}(W_1(t) - W_2(t)), \\
 Q_2(t) &= b_2 W_2(t).
 \end{aligned}
 \tag{5}$$

Equation (4) indicates the change of the groundwater table in a unit of time in every tank element. These equations consider the time lags resulting from the permeability, infiltration path, and water flow path. Equation (5) shows that the middle water flow supply ($Q_{1-2}(t)$ and $Q_{1-2}(t + \Delta_1)$) depends on the deviation of the water head pressure of two object points, which means that the water flow supply has no fixed direction and in the meantime still has a time lag (the dotted arrow represents a reversible process). The drainage rate ($Q_2(t)$) is affected by the current groundwater table. Specifically, in Figure 2(c), the original tank model calculates the infiltration time lag by increasing the number of tanks in a vertical direction, which introduces more parameters in the model. Meanwhile, the modified tank model innovatively calculates the infiltration time lag before rainfall enters the tank. “ Δ ” is the time lag between the infiltration and the water table induced by it. The time lag can be obtained by analysing the correlation between the water table and infiltration in unit time [19, 20]. In Figure 2(d), the original does not consider the

short time lag of lateral water flow. The modified tank model considers the lateral water flow time lag of “ Δ_1 .” This time lag can be overcome by the different parameter estimations of b_{1-2} and b_{2-1} . Furthermore, in the modified tank model, the direction of lateral water flow depends on the balance of both water tables in the tanks.

3. Experiments and Predictive Model

River-slope system modelling includes a surface tank (surface runoff) and double tanks (slope and river), as shown in Figure 3. Rainfall is simulated by nozzles. Two pore water pressure (PWP) sensors are installed at the bottom of the double tanks for pore water pressure monitoring (model number CYY2, Xi’an Weizheng Technology Corp., Xi’an, China) (diameter: 3 cm; height: 1.6 cm; measuring range: ± 10 kPa; deviation: $\pm 0.2\%$). The drainage of this system is realized by a drain hole. Two types of material from Fengdu Ming Mountain, near Yangtze River Bank, Chongqing, China, are used (shown in Figures 4(a) and 4(b)). The particle-size distribution curves are shown in Figure 4(c). For each group of tank model experiments, we arranged two rainfall events (45 and 65 mm/hr intensity, 36 min duration) and the observation time was 1 hr. Every test in each group was

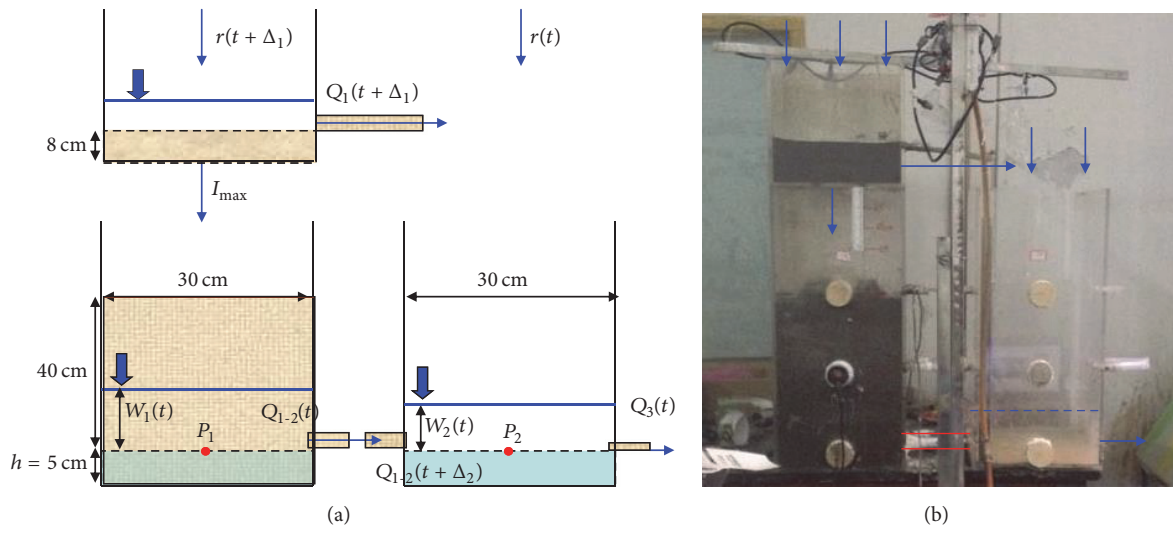
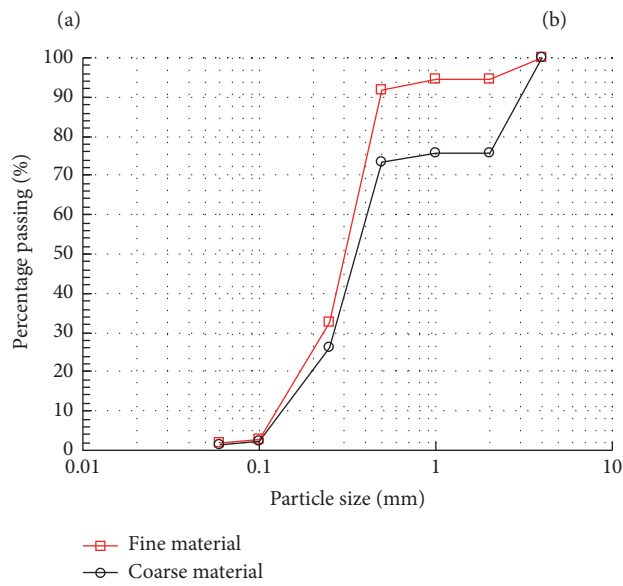


FIGURE 3: River-slope system modelling: (a) schematic diagram and (b) real scene.



(c)

FIGURE 4: Schematic diagram of modified tank model system: (a) fine material; (b) coarse material; (c) particle-size distribution curves.

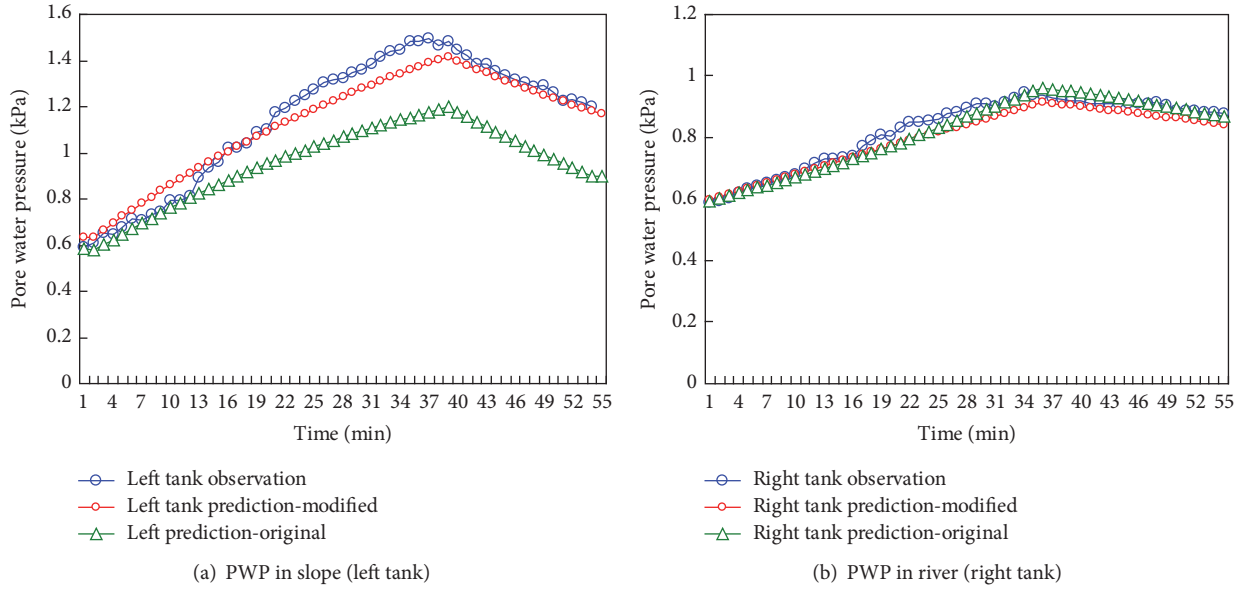


FIGURE 5: Predictions of original and modified tank models (fine material): (a) PWP in slope and (b) PWP in river.

conducted under similar initial conditions, such as geometry, material, and initial moisture content, which was tested by a moisture transducer in the bottom (model number DS200, Beijing Dingtak Technology Corp., Beijing, China) (frequency domain sensors: measuring range: 0–100%; resolution: 0.1%; deviation: $\pm 2\%$; with a soil contact area of less than 20 mm^2 ; deviation: $\pm 3\%$).

Equation (6) indicates the ground water table and river level in the river-slope system in Figure 5.

$$W_1(t+1) - W_1(t) = (r(t+\Delta_1) - Q_1(t+\Delta_1)) - Q_{1-2}(t), \quad (6)$$

$$W_2(t+1) - W_2(t) = r(t) + Q_{1-2}(t+\Delta_2) - Q_3(t),$$

where $W_1(t+1)$ and $W_1(t)$ are the water table in the slope at times $t+1$ and t ; $W_2(t+1)$ and $W_2(t)$ are the water level of the river at times $t+1$ and t ; $r(t+\Delta_1)$ and $Q_1(t+\Delta_1)$ are the rainfall and surface runoff at time $t+\Delta_1$; Δ_1 is the infiltration time lag produced by the path, material permeability, and previous moisture content. $Q_{1-2}(t)$ is the water flow between the slope and river at time t ; $Q_{1-2}(t+\Delta_2)$ is the water flow between slope and river at time $t+\Delta_2$; $Q_3(t)$ is the drainage at time t .

The surface runoff, drainage, and water flow exchanges, which mainly depend on the pressure water head, are expressed by

$$\begin{aligned} Q_3(t) &= b_2 P_2(t), \\ Q_{1-2}(t) &= a_{1-2} (P_1(t) - P_2(t)), \\ Q_{1-2}(t+\Delta_2) &= a_{2-1} (P_1(t) - P_2(t)). \end{aligned} \quad (7)$$

The water table cannot usually be measured directly by sensors and is often proportional to pore water pressure. Thus, the final equation (8) is used to calculate the PWP changes in both slope and river.

$$\begin{aligned} P_1(t+1) - P_1(t) &= a_1 (r(t+\Delta_1) - Q_1(t+\Delta_1)) \\ &\quad - a_{1-2} (P_1(t) - P_2(t)), \\ P_2(t+1) - P_2(t) &= a_2 (r(t) + Q_1(t+\Delta_1)) \\ &\quad + a_{2-1} (P_1(t) - P_2(t)) \\ &\quad - b_2 P_2(t), \end{aligned} \quad (8)$$

where $P_1(t+1)$ and $P_1(t)$ are the PWP in the slope at times $t+1$ and t ; $P_2(t+1)$ and $P_2(t)$ are the PWP of the river bottom at times $t+1$ and t ; a_1 , a_2 , a_{1-2} , a_{2-1} , and b_2 are the relation coefficients. In the high water content layer, the time lag of water flow is relatively low; thus, we use the different coefficients a_{1-2} and a_{2-1} to refine it.

It should be pointed out that the major part of PWP could be static pressure induced by the water table height. Minor components are seepage force and the difference in pressures in the available pore space during drier and wetter periods. Since the tank model is a “grey box model,” we do not know the exact proportions of static pressure, seepage pressure, and pressure dynamics in pore space, but all three are included in our equivalent pore water pressure.

4. A Comparison of the Original and Modified Tank Models

In this section, the performance of the original and modified tank models in physical experiments is shown and we

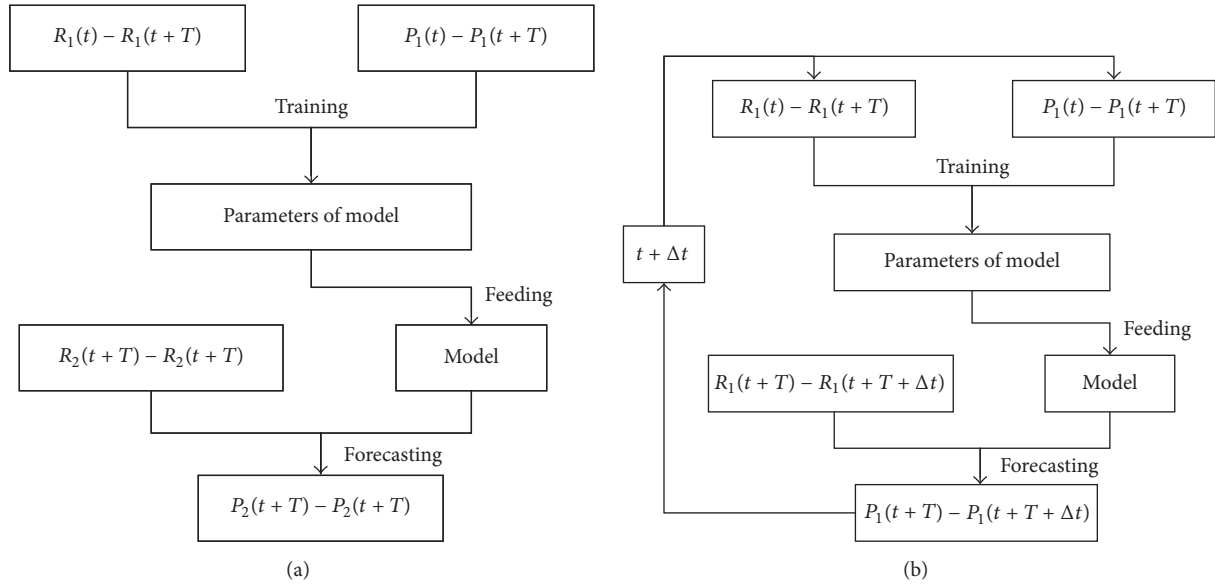


FIGURE 6: Comparison of calculations of parameters as constants and as variables: (a) nonincremental learning algorithm for parameters as constants and (b) incremental learning algorithm for parameters as variables.

introduce the standard Nash–Sutcliffe efficiency (NSE) [21], which is the most widely used criterion for calibration and evaluation of hydrological models with observed data. NSE is dimensionless and is scaled onto the interval [negative infinity to 1.0]. NSE is taken to be the “mean of the observations” [22] and if NSE is smaller than 0, the model is no better than using the observed mean as a predictor. Monitoring data (rainfall and PWP) from physical experiments of an event with a rainfall intensity of 45 mm/hr are employed to estimate the parameters of the original and modified models. The monitoring data (PWP) from the event with a rainfall intensity of 65 mm/hr are used to validate the predictions of the original and modified models. Figure 6 shows the results of the original and modified tank models (fine material).

In Figure 5(a), the left tank means the slope part of the river-slope system. The original tank model does not consider the groundwater-river exchanges. It only considers the water flows from the slope to the river. Thus, in the left tank, the water table is underestimated. In contrast, the modified tank model considers the supply from the river in the beginning. Therefore, the reduction of the PWP is slow, which matches the real situation well. The NSE of the original tank model is 0.438, while the NSE of the modified tank model is 0.973. In Figure 5(b), the right tank represents the river part of the river-slope system. It is found that both the original and modified tank models can describe the process well. This may be because the water level is not so sensitive to amount of rainfall added to the river compared to porosity material-soil mass. In other words, adding the same amount of rainfall can lead to a groundwater table in the soil that is higher than the river level, which also produces more prediction errors because of the porosity. Thus, the error of river level estimation is not obvious for either model. The NSE of the original tank model is 0.972 while that of the modified tank model is 0.955.

5. Nonincremental Constants and Incremental Learning Algorithm Variables in the Modified Tank Model

In this section, the performance of nonincremental constants and incremental learning algorithm variables in a modified tank model are shown and the NSE is still used to evaluate the use of two types of parameters that affect the modified tank model. An incremental learning algorithm is introduced which considers the parameters of the modified tank model as variables instead of constants [23]. The same terminology is used in computer science for machine learning, where model parameters are tuned using an abundance of observations. In other words, we used the previous observed values to train the parameters of the model to predict the object in the next time domain and then repeated the process in the following time domain, which is similar to the dynamically updated method. A comparison of calculations of parameters as constants and as variables is shown in Figure 6. We use the coarse material experiments to show the process.

For the nonincremental learning algorithm, R_1 and P_1 are all the monitoring data from rainfall event 1, which consist of rainfall and PWP under different time domains ($t \cdots T$). All the data are used to train the parameters of the model (constant parameters). Then these parameters are fed into the model. When the new rainfall event R_2 is input into the model, it can make predictions of P_2 under different time domains. For the incremental learning algorithm, parts of R_1 and P_1 , such as data under t to $t + T$, are used to train the parameters of the model. After tuning the parameters, the model can predict the next P_1 under $t + T + \Delta t$ in the same rainfall event by reading the rainfall R_1 under the time domain $t + T + \Delta t$. Then, the new monitoring data under time domain $t + \Delta t + T + \Delta t$ are used to train the parameters again

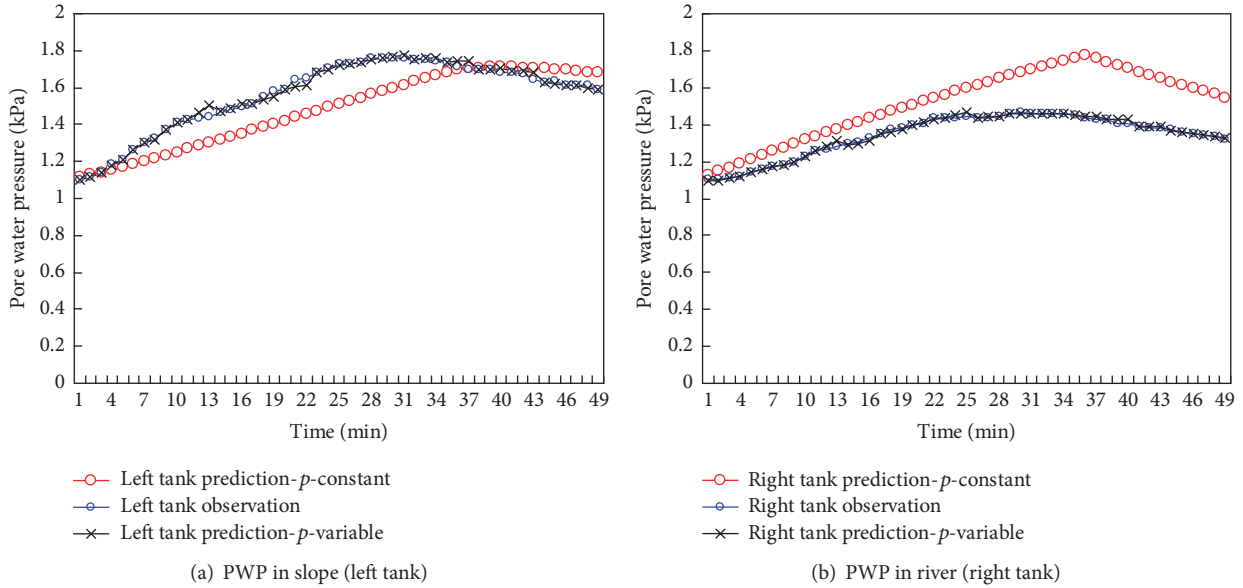


FIGURE 7: A comparison of nonincremental and incremental learning algorithms: (a) PWP in slope and (b) PWP in river.

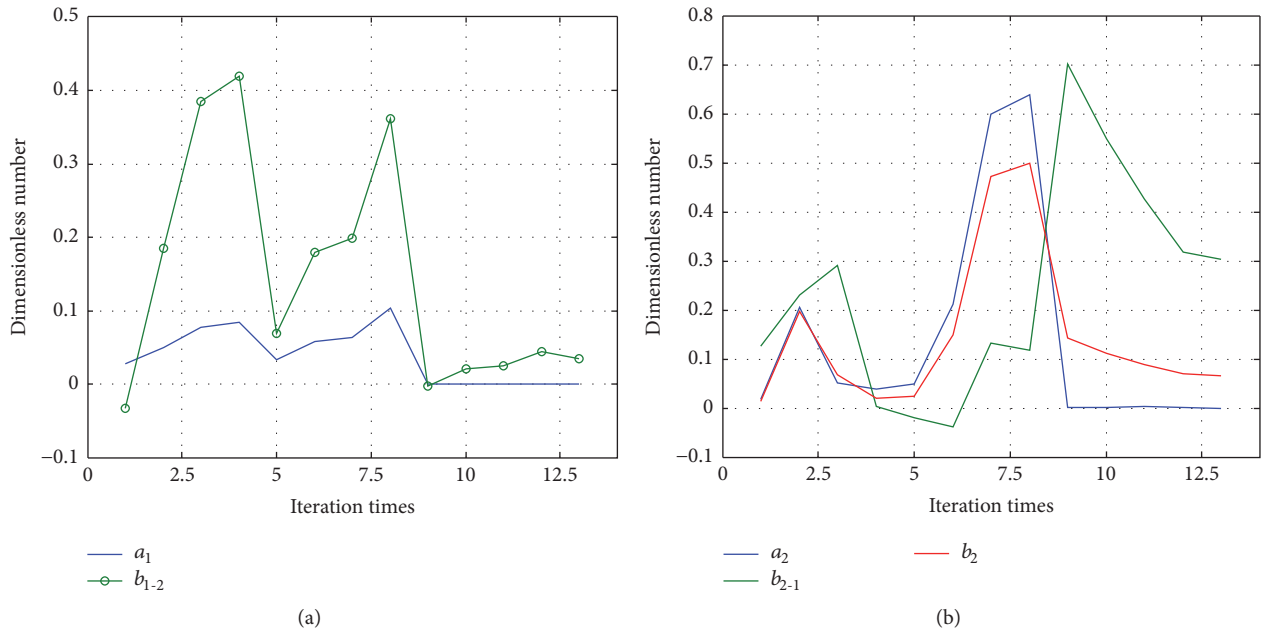


FIGURE 8: Changes of parameters in incremental learning algorithm: (a) parameters in the left tank and (b) parameters in the right tank.

(variable parameters) and then make the new prediction. The cyclic action means that incremental learning takes place.

Figure 7 shows the performances of the models based on the parameter types resulting from the two learning algorithms (nonincremental constants and incremental learning algorithm).

The distribution of pores in coarse material is more uncertain than that in fine materials. Thus, the error of the modified tank model using constant parameters is obvious. The NSEs of the modified tank model with constant parameters are 0.427 and -0.909 . As shown in Figure 7, using

the incremental learning algorithm, the modified tank model with variable parameters has higher NSEs of 0.994 and 0.995 in the slope and river, respectively. The model based on the incremental learning algorithm can more accurately predict the PWP trend but requires continuous parameter estimation. By contrast, the model based on the nonincremental learning algorithm only needs to carry out parameter estimation once based on historical data but sometimes has low accuracy.

Figure 8 indicates the changes of parameters when using the incremental learning algorithm.

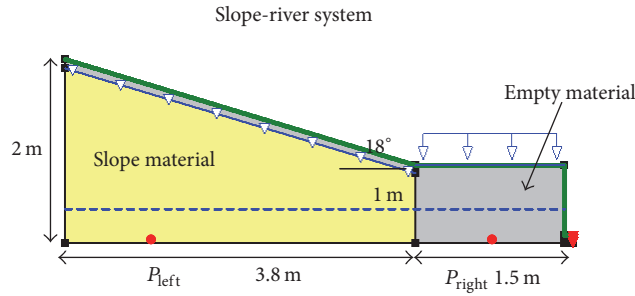


FIGURE 9: Geometry of numerical model.

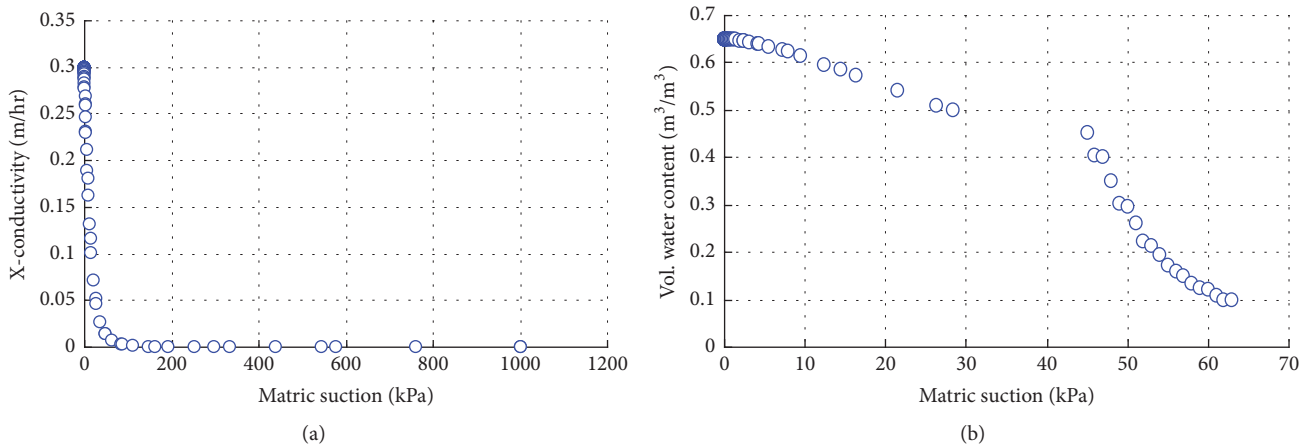


FIGURE 10: Permeability coefficient (fine material): (a) matrix suction versus conductivity and (b) matrix suction versus water content.

It is found that the parameters basically reflect the change of the PWP trend.

- (1) a_1 (PWP sensitivity to rainfall): an increase means the PWP accelerates upward; a decrease means the PWP rate decreases.
- (2) b_{1-2} : an increase means a high water flow output, while a decrease means a low water flow output.
- (3) a_2 (PWP sensitivity to rainfall): an increase means that the PWP accelerates upward; a decrease means that the PWP rate decreases.
- (4) b_{2-1} : an increase means a high water flow input while a decrease means a low water flow input. b_2 : an increase means a high drainage rate while a decrease means a low drainage rate.

6. Replication of Numerical Model

Numerical slopes using the transient groundwater mode of SEEP/W [24] are employed to reproduce the applications of our modified tank model. The estimation of matric suction and conductivity uses Fredlund and Xing's method [25], as shown in Figures 10(a) and 13(a). The link between matric suction and water content uses the model in Kunze et al. [26], as shown in Figures 10(b) and 13(b). In Figure 9, the slope is 2 m deep and 3.8 m long with an angle of 18 degrees and homogeneous materials (main mass). The empty material and

the surface layer have high permeability ($1 - e4$ m/s). The residual (99%) and initial water content (99.99%) in them are very close when simulating the river basin and surface runoff path. The design ensures that the rainfall and potential surface runoff flow into the river swiftly. The toe of the river basin has a drainage point (the pressure head is 0 m). The grid size is $0.1 \text{ m} \times 0.1 \text{ m}$. The observation time of the process is 4 hours and the rainfall input lasts 1 hr. The procedures involving fine and coarse materials are as follows:

- (1) P_{left} (pore water pressure in the slope) and P_{right} (pore water pressure in the river) under rainfall of 45 mm/hr are used as training data for the parameters of the modified tank model.
- (2) P_{left} and P_{right} induced by a rainfall event of 65 mm/hr are predicted using the modified tank model.

The slope part and the river part are treated as a double tank (the left tank is the slope part; the right tank is the river part). Figure 11 indicates the change of the PWP in the left and right tanks under rainfall intensities of 45 and 65 mm/hr. Figure 12 indicates prediction of the modified tank model based on the parameters from the nonincremental learning algorithm.

Figure 14 indicates the change of PWP in the left and right tanks under rainfall intensities of 45 and 65 mm/hr. Figure 15 indicates the prediction of the modified tank model based on the parameters given by the nonincremental learning algorithm.

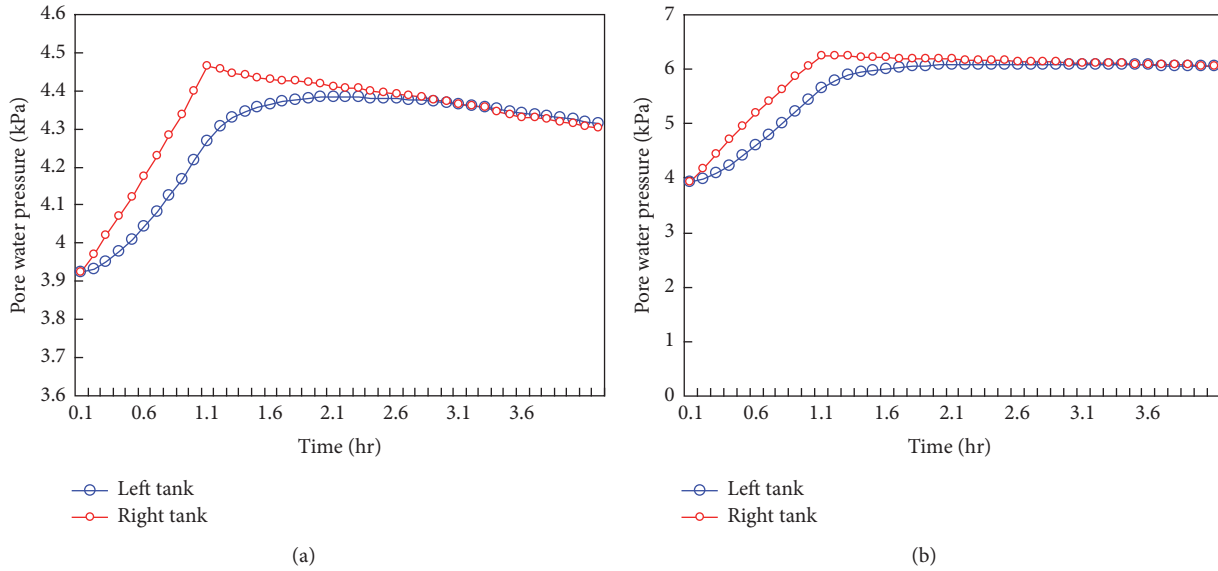


FIGURE 11: Monitoring data of numerical model (fine materials): (a) 45 mm/hr rainfall intensity and (b) 65 mm/hr rainfall intensity.

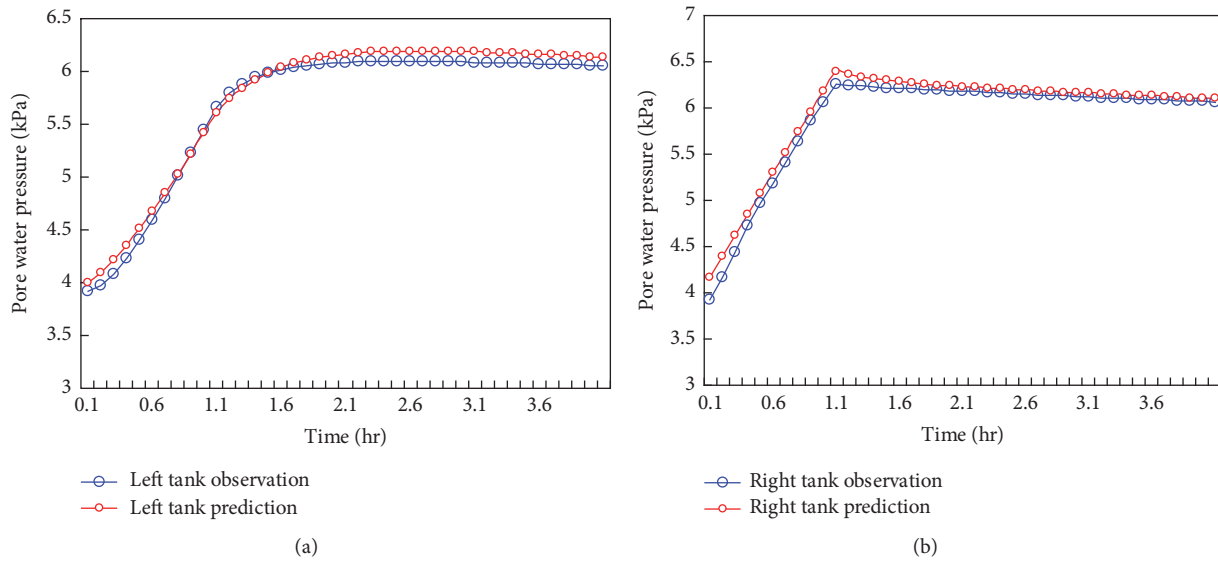


FIGURE 12: Prediction by modified tank model (fine material): (a) left tank and (b) right tank.

7. Concluding Remarks

Modelling of river-groundwater interactions under rainfall events is executed based on tank model experiments. These experiments involve fine (coarse) materials and rainfall intensities of 45 and 65 mm/hr. We developed modified tank models with nonincremental and incremental learning algorithms to describe the process. A numerical case reproduces the river-groundwater interactions and validates the prediction by our modified model. Future work will take the direction of obtaining field measurements in order to compare model predictions against field observations.

Currently, the valuable conclusions include the following:

- (1) The modified tank model not only describes the changes of PWP in the slope and river more accurately than the original model but also has a simpler structure.
- (2) The model based on the incremental learning algorithm can more accurately predict the PWP trend but needs continuous parameter estimation. The model based on the nonincremental learning algorithm only needs to perform parameter estimation once, based on historical data, but has low accuracy.
- (3) The modified tank model can match the deterministic method well based on the numerical model case.

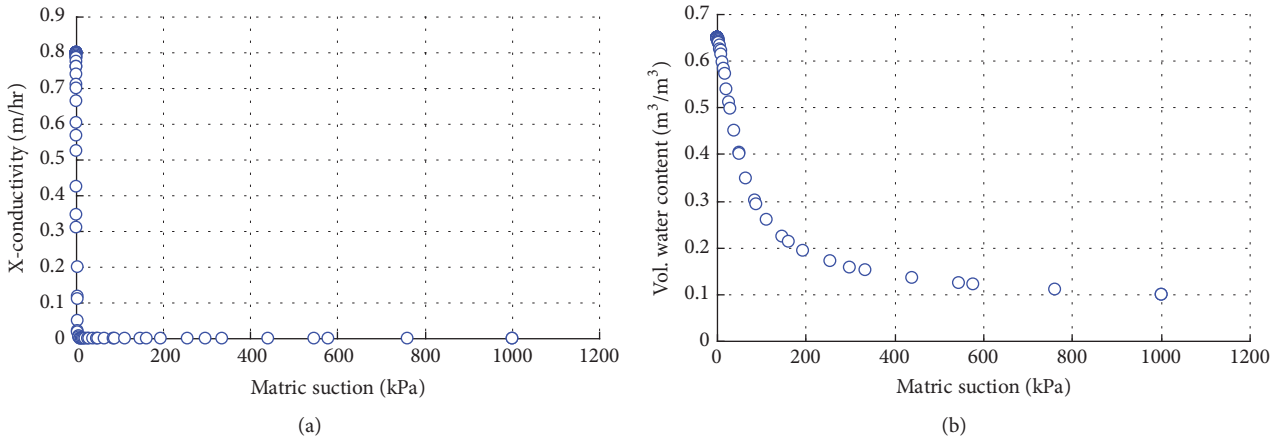


FIGURE 13: Permeability coefficient (coarse material): (a) matrix suction versus conductivity and (b) matrix suction versus water content.

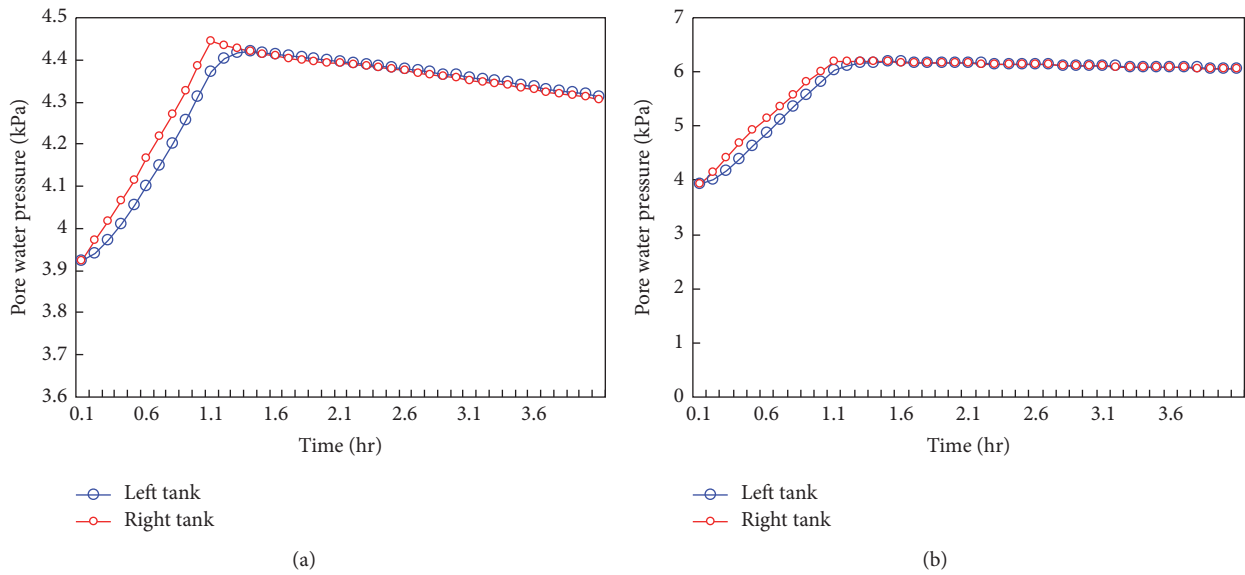


FIGURE 14: Monitoring data of numerical model (coarse materials): (a) 45 mm/hr rainfall intensity and (b) 65 mm/hr rainfall intensity.

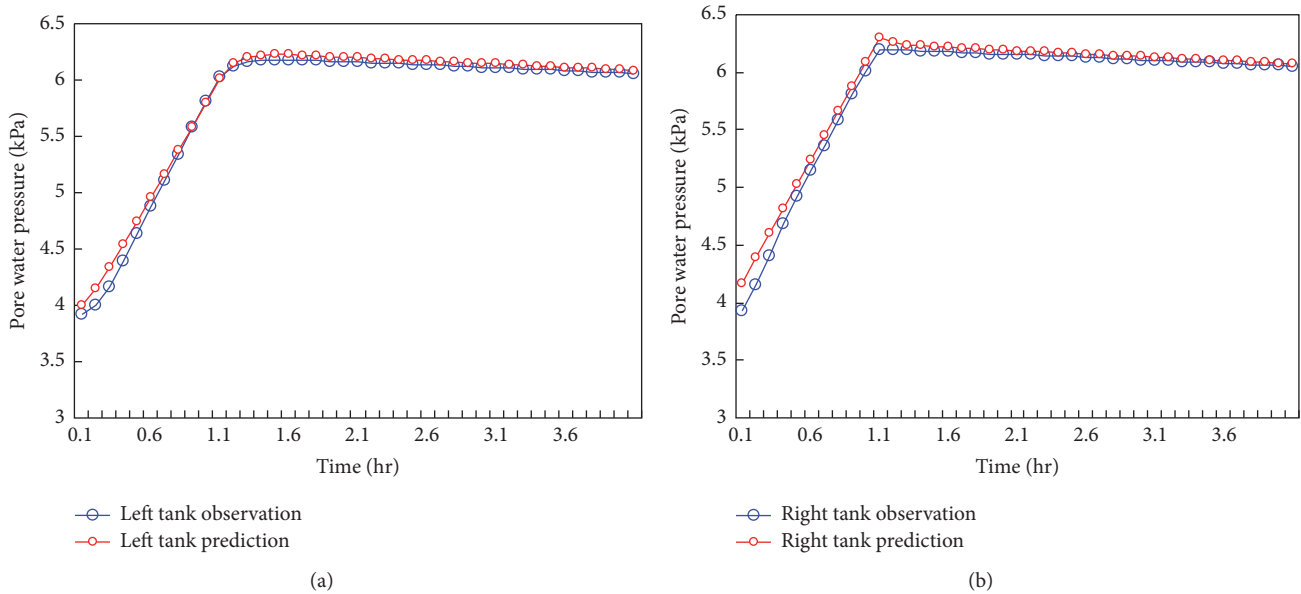


FIGURE 15: Prediction by modified tank model (coarse material): (a) left tank and (b) right tank.

Conflicts of Interest

The authors declare that they have no conflicts of interest.

Acknowledgments

The research is supported by the Opening Fund of the State Key Laboratory of Geo-Hazard Prevention and Geo-Environment Protection (Chengdu University of Technology), SKLGP2017K006.

References

- [1] M. Trémoières, I. Eglin, U. Roeck, and R. Carbiener, "The exchange process between river and groundwater on the Central Alsace floodplain (Eastern France)—I. The case of the canalised river Rhine," *Hydrobiologia*, vol. 254, no. 3, pp. 133–148, 1993.
- [2] C. Doussan, E. Ledoux, and M. Detay, "River-groundwater exchanges, bank filtration, and groundwater quality: Ammonium behavior," *Journal of Environmental Quality*, vol. 27, no. 6, pp. 1418–1427, 1998.
- [3] W. D. Gollnitz, "Infiltration rate variability and research needs," in *Riverbank Filtration*, pp. 281–290, Springer, Amsterdam, The Netherlands, 2003.
- [4] D. O. Rosenberry and R. W. Healy, "Influence of a thin veneer of low-hydraulic-conductivity sediment on modelled exchange between river water and groundwater in response to induced infiltration," *Hydrological Processes*, vol. 26, no. 4, pp. 544–557, 2012.
- [5] S. Mutiti and J. Levy, "Using temperature modeling to investigate the temporal variability of riverbed hydraulic conductivity during storm events," *Journal of Hydrology*, vol. 388, no. 3–4, pp. 321–334, 2010.
- [6] Y. Ishihara and S. Kobatake, "Runoff Model for Flood Forecasting," *Bulletin of the Disaster Prevention Research Institute*, vol. 29, no. 1, pp. 27–43, 1979.
- [7] F. Faris and F. Fathani, "A coupled hydrology/slope kinematics model for developing early warning criteria in the Kalitlaga Landslide, Banjarnegara, Indonesia," in *Progress of Geo-Disaster Mitigation Technology in Asia*, pp. 453–467, Springer, Berlin, Germany, 2013.
- [8] N. A. Abebe, F. L. Ogden, and N. R. Pradhan, "Sensitivity and uncertainty analysis of the conceptual HBV rainfall-runoff model: Implications for parameter estimation," *Journal of Hydrology*, vol. 389, no. 3–4, pp. 301–310, 2010.
- [9] S. K. Kampf and S. J. Burges, "A framework for classifying and comparing distributed hillslope and catchment hydrologic models," *Water Resources Research*, vol. 43, no. 5, Article ID W05423, 2007.
- [10] W. Shao, T. A. Bogaard, M. Bakker, and R. Greco, "Quantification of the influence of preferential flow on slope stability using a numerical modelling approach," *Hydrology and Earth System Sciences*, vol. 19, no. 5, pp. 2197–2212, 2015.
- [11] W. Shao, T. Bogaard, M. Bakker, and M. Berti, "The influence of preferential flow on pressure propagation and landslide triggering of the Rocca Pitigliana landslide," *Journal of Hydrology*, vol. 543, pp. 360–372, 2016.
- [12] J. M. Köhne, S. Köhne, and J. Šimůnek, "A review of model applications for structured soils: a water flow and tracer transport," *Journal of Contaminant Hydrology*, vol. 104, no. 1–4, pp. 4–35, 2009.
- [13] M. Nishihgaki, *Research on behavior of groundwater and its application to foundation engineering [M.S. thesis]*, Kyoto University, Kyoto, Japan, 1979.
- [14] M. Michiue, "A method for predicting slope failures on cliff and mountain due to heavy rain," *Natural Disaster Science*, vol. 7, no. 1, pp. 1–12, 1985.
- [15] K. Takahashi, Y. Ohnishi, J. Xiong, and T. Koyama, "Tank model and its application to groundwater table prediction of slope," *Chinese Journal of Rock Mechanics and Engineering*, vol. 27, no. 12, pp. 2501–2508, 2008.
- [16] K. Takahashi, *Research of underground water numerical analysis method that considering water circulation system [Ph.D. thesis]*, Department of Urban and Environmental Engineering, Kyoto University, Kyoto, Japan, 2004.
- [17] J. Xiong, Y. Ohnishi, K. Takahashi, and T. Koyama, "Parameter determination of multi-tank model with dynamically dimensioned search," in *Proceedings of the Symposium Rock Mechanics*, vol. 38, pp. 19–24, Japan, 2009.
- [18] T. Ichimura, T. Ryohei, and S. Daiken, "Evaluation of hydraulic properties of slope ground based on monitoring data of moisture contents," in *Proceedings of the 4th Japan-Taiwan Joint Workshop on Geotechnical Hazards from Large Earthquakes and Heavy Rainfalls*, Sendai, Japan.
- [19] S. Matsuura, S. Asano, and T. Okamoto, "Relationship between rain and/or meltwater, pore-water pressure and displacement of a reactivated landslide," *Engineering Geology*, vol. 101, no. 1–2, pp. 49–59, 2008.
- [20] W. Nie, M. Krautblatter, and K. Thuro, "Porenwasserdruckänderungen aufgrund von Regen und Schneeschmelze in einer tiefgreifenden Massenbewegung," 2013.
- [21] J. E. Nash and J. V. Sutcliffe, "River flow forecasting through conceptual models part I—a discussion of principles," *Journal of Hydrology*, vol. 10, no. 3, pp. 282–290, 1970.
- [22] A. H. Murphy, "Skill scores based on the mean square error and their relationships to the correlation coefficient," *Monthly Weather Review*, vol. 116, no. 12, pp. 2417–2424, 1988.
- [23] W. Nie, R. Q. Huang, Q. G. Zhang, W. Xian, F. L. Xu, and L. Chen, "Prediction of experimental rainfall-eroded soil area based on S-shaped growth curve model framework," *Applied Sciences*, vol. 5, no. 3, pp. 157–173, 2015.
- [24] Geo-slope International Ltd., "Seep/W User's Guide for Finite Element Seepage Analysis," Calgary, Alberta, Canada, 2007.
- [25] D. G. Fredlund and A. Xing, "Equations for the soil-water characteristic curve," *Canadian Geotechnical Journal*, vol. 31, no. 4, pp. 521–532, 1994.
- [26] R. J. Kunze, G. Uehara, and K. Graham, "Factors important in the calculation of hydraulic conductivity," *Soil Science Society of America Journal*, vol. 32, no. 6, pp. 760–765, 1968.

Research Article

Logging Characteristics and Identification Methods of Low Resistivity Oil Layer: Upper Cretaceous of the Third Member of Qingshankou Formation, Daqingzijing Area, Songliao Basin, China

Congjun Feng,^{1,2} Murray Gingras,³ Mengsi Sun,^{1,2} and Bing Wang⁴

¹State Key Laboratory of Continental Dynamics, Northwest University, Xi'an 710069, China

²Department of Geology, Northwest University, Xi'an 710069, China

³Earth & Atmospheric Sciences, Faculty of Science, University of Alberta, Edmonton, AB, Canada T6G 2E3

⁴College of Geophysics and Information Engineering, China University of Petroleum, Beijing 102249, China

Correspondence should be addressed to Congjun Feng; fengcj@nwu.edu.cn

Received 13 February 2017; Accepted 27 April 2017; Published 29 May 2017

Academic Editor: Amgad Salama

Copyright © 2017 Congjun Feng et al. This is an open access article distributed under the Creative Commons Attribution License, which permits unrestricted use, distribution, and reproduction in any medium, provided the original work is properly cited.

This study focuses on low resistivity thick layer sandstone in the X~XII groups of the third member of Qingshankou Formation at Daqingzijing oilfield, along with comprehensive data of logging, core, oil test, and production test. Based on the current data, we characterized the logs of low resistivity thick-layer sandstone, quantitatively identified calcareous sandstone and low resistivity reservoir, predicted the reservoir thickness, and further explored the causes of low resistivity reservoir of the region. The resistivity of thick layer sandstone in the X~XII groups of Qingshankou Formation can be classified into low amplitude logfacies, middle amplitude logfacies, and sharp high amplitude logfacies. Sharp high amplitude logfacies sandstone is the tight sandstone of the calcareous cementation. Low amplitude logfacies sandstone is water layer. For the middle amplitude logfacies sandstone, water layer or oil-water layer can be identified with the identification standard. Low amplitude structure, high clay content, high irreducible water saturation, and high formation water salinity are attributed to the origin of low resistivity oil layer.

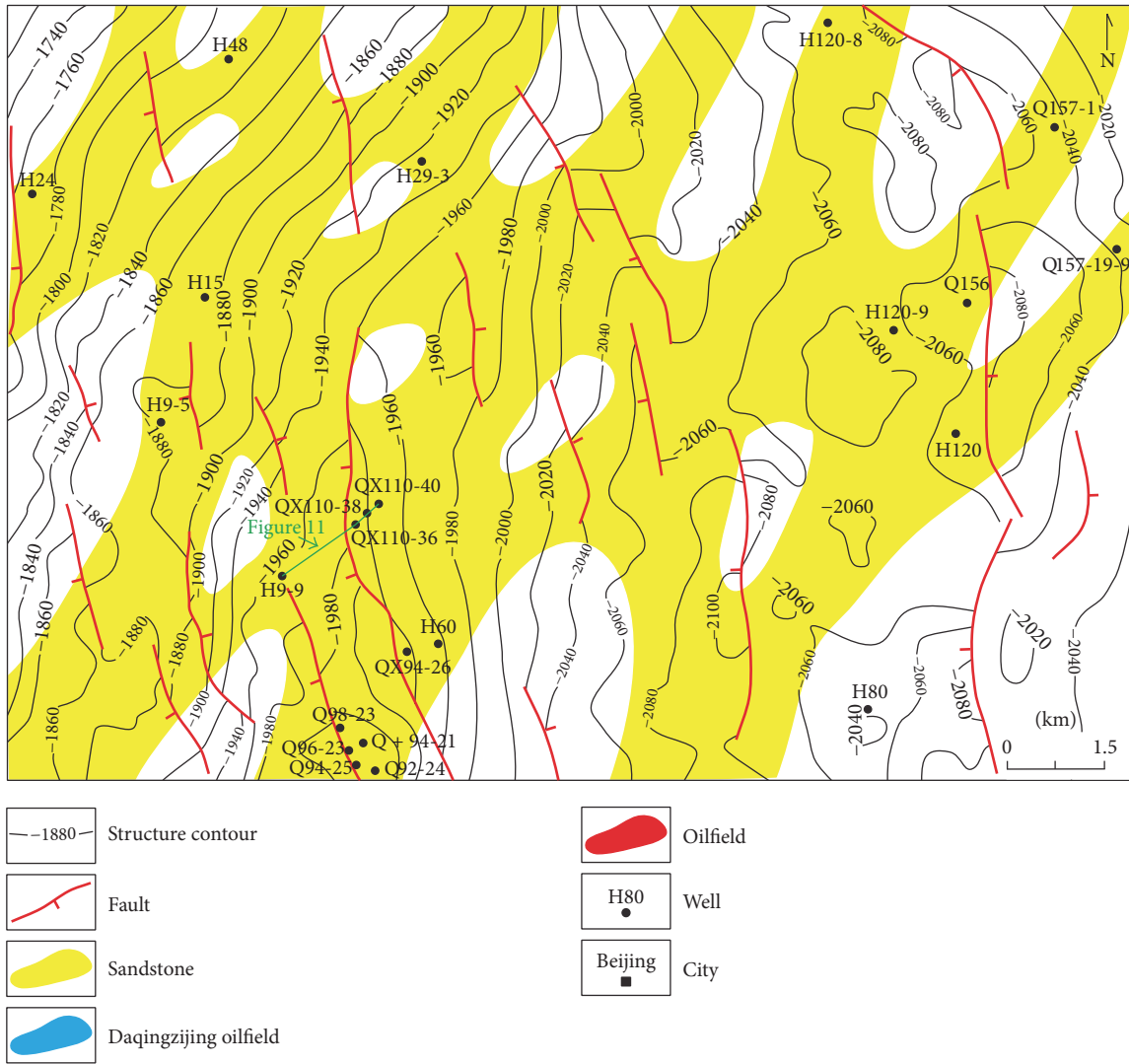
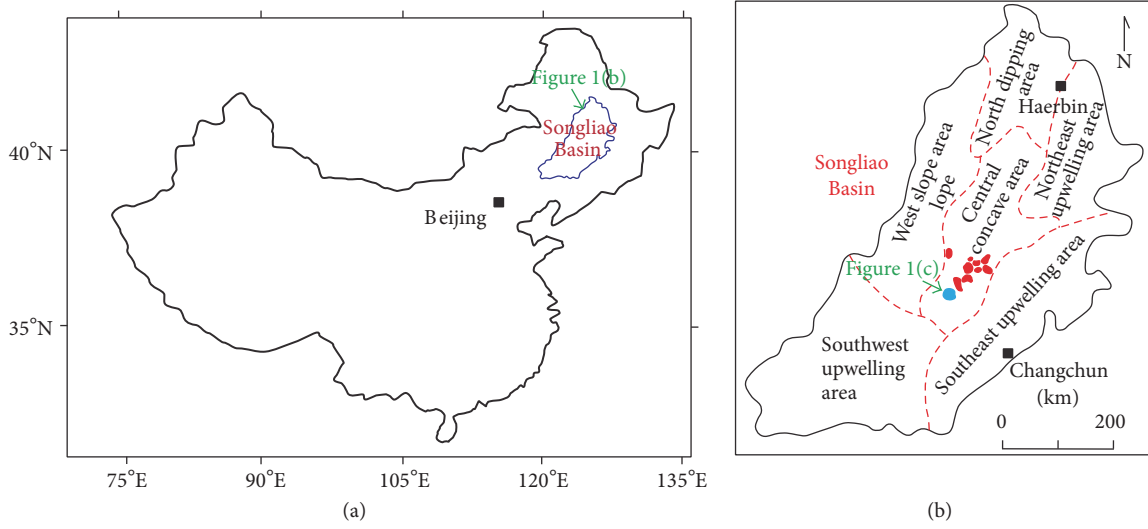
1. Introduction

Songliao Basin is a large Mesozoic to Cenozoic hydrocarbon-bearing sedimentary basin in Northeast China (Figure 1(a)), with a total area of about 260,000 km². The basin is diamond shaped with its long axis oriented NNE. Six secondary structural units are present in the basin, including the central concave, the southwest uplift, the southeast uplift, the northeast uplift, the western slope, and the northern dip areas [1, 2]. Previous studies showed that this basin is filled with continentally associated clastic strata, with multiple oil-bearing layers, of which Cretaceous and Tertiary lacustrine units are the most important [3–6].

The Daqingzijing oilfield is located in the south central concave of Songliao Basin (Figure 1(b)). The overall structure is an asymmetric syncline with axial NNE direction that has

a steeply dipping west limb and nearly horizontal east limb. It has a practical exploration area of 1500 km² that possesses reserves of approximately 700 million barrels of crude oil. The main reservoir unit is the Cretaceous Qingshankou Formation wherein the depth of oil formation ranges from 1600 m to 2500 m. The Qingshankou Formation is characterized by low porosity, low permeability, and low resistivity sandstone reservoirs [7]. Reservoir microfacies, resource distribution, and identification of low resistivity resource accumulations are urgent areas of research for this oilfield [7–10].

The identification and evaluation of low resistivity reservoirs are technically challenging [11–16]. This study focuses on the low resistivity thick sandstone in the X~XII groups of the K₂qn³ (the third member of Qingshankou Formation) at Daqingzijing oilfield and summarizes petrophysical well-log response characteristics and its logfacies of low resistivity



(c)

FIGURE 1: Location map of the study area. (a) Location map of Songliao Basin. (b) Songliao Basin structural zones. (c) Structural characteristics and sandstone distribution map within the study area.

thick layer sandstone based on comprehensive well-log, core, oil, and production test data. The petrophysical interpretations of the different types of logging curve are discussed. A secondary aim of this paper is to establish quantitative parameters for identification of the calcareous sandstone, low resistivity reservoir, and reservoir thickness and further understand the causes of low resistivity reservoir in the area. The results will provide guidance for the identification of the calcareous sandstone and low resistivity oil reservoirs elsewhere.

2. Geological Setting

2.1. Stratigraphic Characteristics. From bottom to top, the formations of Songliao Basin are the Huoshiling Formation (J_3h), Shahezi Formation (K_1h), Yingcheng Formation (K_1y), Dengloulou Formation (K_1d), Quantou Formation (K_1q), Qingshankou Formation (K_2qn), Yaojia Formation (K_2y), Nenjiang Formation (K_2n), Sifangtai Formation (K_2s), Mingshui Formation (K_2m), Yi'an Formation (E_2y), Da'an Formation (Nd), and Taikang Formation (Qt) [17–19]. The Daqingzijing oilfield has four oil-bearing horizons: the Fuyu, Gaotaizi, Putaohua, and Heidimiao Formations. The main oil-bearing level is Gaotaizi reservoir of the Qingshankou Formation (K_2qn) (Figure 2(a)) [20]. There are three members that comprise the Qingshankou Formation: these are referred to as K_2qn^1 , K_2qn^2 , and K_2qn^3 . Regarded as a deeply buried lacustrine unit, the lithology of K_2qn^1 is dominated by gray-dark shale, gray mudstone, argillaceous siltstone, and siltstone; it includes four sand-dominated levels, which range in thickness between 70 and 100 meters. The lithology of K_2qn^2 is mainly dominated by gray mudstone, argillaceous siltstone, and siltstone representing delta front sedimentary environment; it includes five sand-dominated levels, which range in thickness between 160 and 200 meters. The lithology of K_2qn^3 is mainly dominated by gray mudstone, argillaceous siltstone, siltstone, and sandstone representing distal lacustrine and delta front sedimentary environments (Figure 2(b)) [21].

2.2. Lithology and Physical Property. Based on the identification and analysis of thin sections, lithologies of the X–XII sandstones of K_2qn^3 Formation are identified as lithic arkose and feldspathic lithic sandstone, of which the average content of quartz is 38.5%, feldspar is 51.6%, and lithic fragments are 36.9% (Figure 3(a)). Core logging shows that the X–XII sand groups of K_2qn^3 Formation consist of calcareous siltstone, calcisiltite, argillaceous siltstone, and siltstone (Figure 3(b)).

Statistical analysis of 336-core sample from 8 cores in the area shows that the porosity of the sandstone of the X–XII sand groups of K_2qn^3 Formation ranges within 8%–17% with an arithmetic mean of 11.7% (Figure 3(c)). The permeability is distributed within $0.02\text{--}160 \times 10^{-3} \mu\text{m}^2$ with average value of $4.5 \times 10^{-3} \mu\text{m}^2$ (Figure 3(d)), all of which indicates that K_2qn^3 is a typical low porosity and low permeability reservoir.

3. Well Logging Response Characteristics of Thick Layer Sand Bodies

3.1. Well Logging Curve Types of Thick Layer Sand Bodies. Distributary channel sand bodies have been interpreted to

reside in the delta front sedimentary environment of the study area [7] (Figure 2). Channels are locally amalgamated into sandstone bodies that are >15 m thick. The GR curves of the thick sandstones are box type with abrupt changes at top and bottom (Figure 4). In this area a reasonable cut-off for sandstone versus mudstone is 90API.

The RILD (deep induction logging resistivity) and RILM (medium induction logging resistivity) curves of the thick sand bodies are mainly manifested as one of the following 3 profiles. (1) Low amplitude logfacies proffer a low amplitude, nearly flat curve, indicating that the resistivity of the sandstone is similar to the resistivity of overlaying mudstone section (Figure 4(a)), with the average value of RILD between 4.4 and $10 \Omega\cdot\text{m}$ (Table 1). (2) Middle amplitude logfacies near the middle of the logarithmic induction scale again produce a flat curve, indicating that the resistivity of the thick sand bodies is higher than the resistivity of overlaying mudstone section and the low amplitude sandstone (Figures 4(b) and 4(c)), with the average value of RILD between 7.5 and $13.7 \Omega\cdot\text{m}$ (Table 1). (3) Sharp-high amplitude logfacies refer to the resistivity of the thick sand bodies that is apparently sharp higher than the resistivity of low and middle amplitude kind (Figures 4(a) and 4(b)), with the average value of RILD between 7.4 and $23.9 \Omega\cdot\text{m}$ (Table 1). The sharp-high amplitude induction response is mainly positioned at the top or bottom of thick sandstones (Figures 4(b) and 4(c)). The above 3 kinds of curves of the thick layer sand bodies can be merged together, which are presented as follows: (1) sharp-high, low, and sharp-high amplitude combination (Figure 4(a)); (2) middle, sharp-high amplitude combination (Figure 4(b)); (3) sharp-high, middle, low, and sharp-high amplitude combination (Figure 4(c)); (4) sharp-high, middle, and low amplitude combination (Figure 4(d)).

3.2. Electrical Characteristics of Thick Layer Sand Bodies. Resistivity of thick layer sand bodies of eleven oil test and production wells is shown in Figure 5. The results showed that the RILD and RILM curves present the characteristics of double peak feature. The first peak of RILD is $12 \Omega\cdot\text{m}$; the second peak of RILD is $28 \Omega\cdot\text{m}$ (Figure 5(a)). The first peak of RILM is $10 \Omega\cdot\text{m}$; the second peak of RILM is $28 \Omega\cdot\text{m}$ (Figure 5(b)). Overall, the resistivity of the thick sand bodies is low; as such we characterize it as low resistivity reservoir. Identification of quantitative relationship between the double peaks feature of the three types of logfacies and the variable well-log response makes interpretation of the reservoir fluid content problematic.

4. Identification of Low Resistivity Oil Layers

4.1. Identification of Calcareous Interlayers. The RILD and RILM curves are characterized by sharp-high amplitude at the top and bottom of the thick layer sand bodies (Figure 4). There are two likely explanations of the increase of reservoir resistivity: (1) there is oil or natural gas in the sandstone or other nonconducting fluid or gas [22, 23]; (2) the reservoir is relatively tight (tight reservoir), therefore leading to the increase of resistivity and decrease of acoustic time simultaneously [24]. The AC value of the sharp-high amplitude of

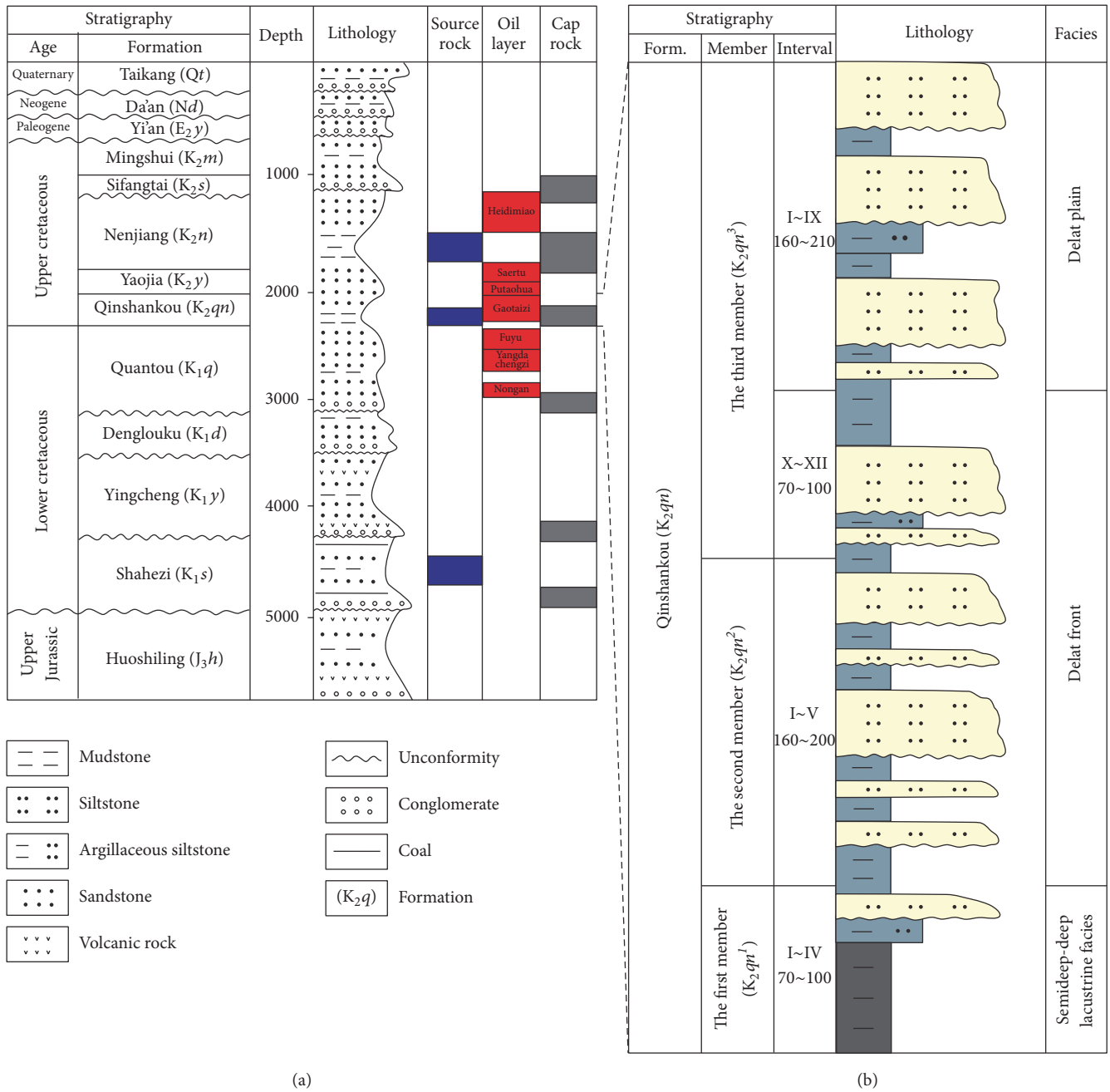


FIGURE 2: Stratigraphic column in Daqingzijing area. (a) Stratigraphy of the Songliao Basin. (b) Detailed stratigraphic characteristics of the Qingshankou Formation in the Daqingzijing area of the Songliao Basin.

thick layer sand bodies decreases compared to the middle and low amplitude section (Figure 4 and Table 1). Therefore, the section of sharp-high amplitude (resistivity increases and the acoustic time decreases) likely indicates a tight sandstone section.

Based on the identification of the core samples through the scanning electron microscope, calcite cements are common in the study area (Figure 6). The carbonate content of thick sand bodies in five cored wells ranges from 0.8% to 58.3%, with the average value of 13.1%; the carbonate cement content of most samples is distributed within 0.8%~20%

(Figure 7(a)). Normally, the impact of calcite cements on the porosity of sandstone is relatively small when calcite < 25%. However, above 25%, carbonate crystals fill the void space and pore throats with poikilitic cement. The porosity of sandstone reservoir decreases with increasing carbonate content (Figure 7(b)), leading to increased resistivity and decreased acoustic time. In short, carbonate cementation is the main factor that leads to sharp-high amplitude at the top and bottom of the thick sand bodies in the study area.

As the increase of the resistivity value is mainly caused by carbonate cementation rather than oil or gas in sandstone

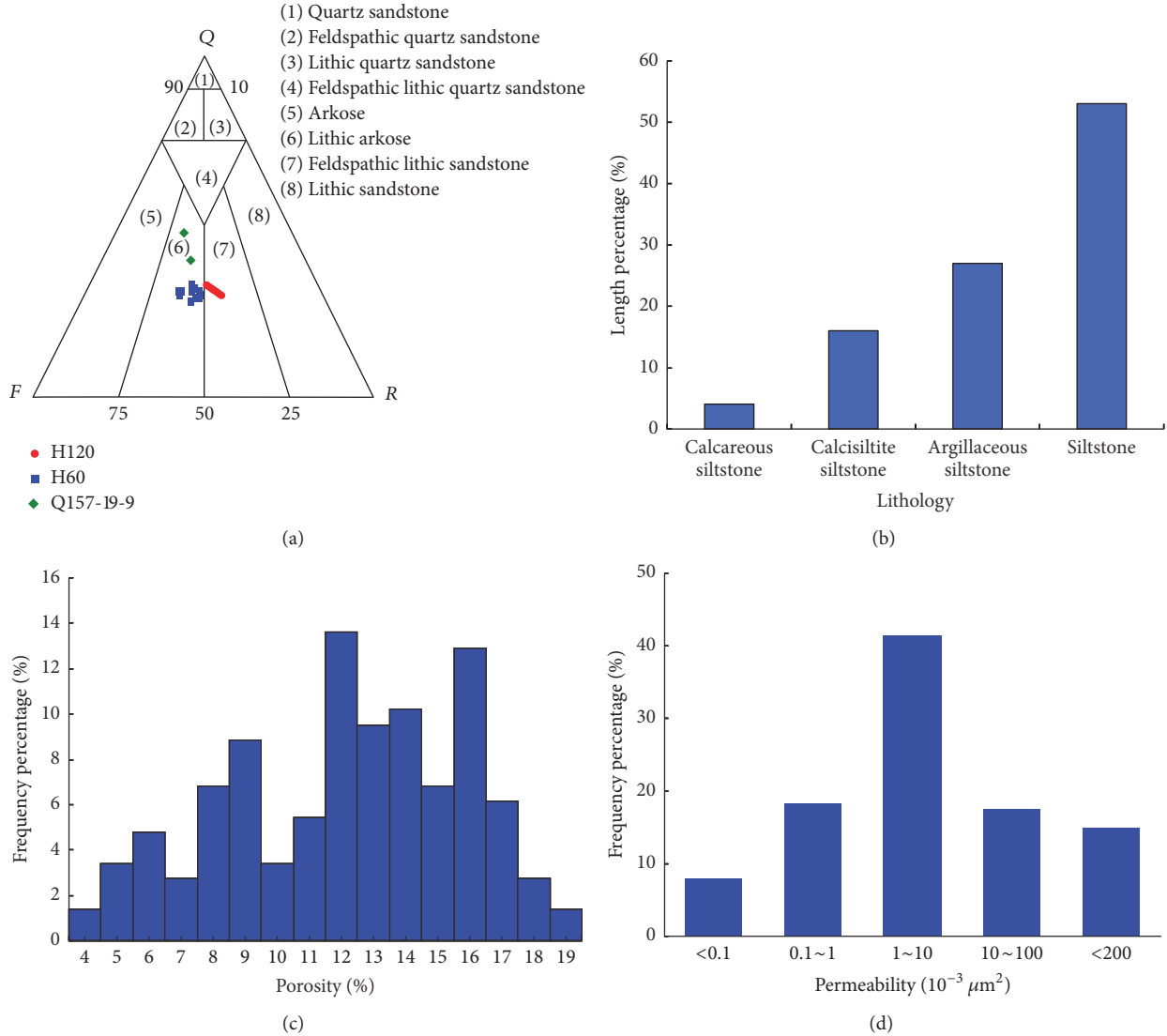


FIGURE 3: Diagram of lithology and physical property of the core well at Daqingzijing area. (a) Rock type. (b) Lithologic distribution histogram. (c) Porosity distribution histogram. (d) Permeability distribution histogram.

reservoirs, the sharp-high amplitude of calcareous sandstone section should be identified separately during the process of identifying the oil layer and the water layer based on the resistivity value. Based on the statistics of RILD of sharp-high, middle, and low amplitude of thick layer sand bodies from ten oil tests and production wells, the average RILD of sharp-high amplitude ranges within $7.4 \Omega\cdot\text{m} \sim 26.4 \Omega\cdot\text{m}$ with maximum distributed within $9.1 \Omega\cdot\text{m} \sim 30.3 \Omega\cdot\text{m}$. The average RILD of middle amplitude ranges within $7.5 \Omega\cdot\text{m} \sim 14.1 \Omega\cdot\text{m}$, while the average RILD of low amplitude ranges within $4.4 \Omega\cdot\text{m} \sim 10 \Omega\cdot\text{m}$ (Table 1). As shown in the cross plot of RILD and AC of the three above types, there is a significant RILD overlap within $7 \Omega\cdot\text{m} \sim 15 \Omega\cdot\text{m}$ for the sharp-high and middle amplitude, as well as AC overlap within $230 \mu\text{s}/\text{m} \sim 245 \mu\text{s}/\text{m}$ (Figure 8(a)); therefore, it is not practical to identify the calcareous interlayers by using RILD and AC cross plot.

Because the sharp-high, middle, and low amplitude curve types are all based on the comparison of the RILD to that of

the adjacent sandstone section, two new parameters, JRT and JAC, were constructed to characterize the relative variability. The specific formula is as follows:

$$\begin{aligned} \text{JRT} &= \frac{\text{RILD}_{\max}}{\text{RILD}_{\text{ave}}} \\ \text{JAC} &= \frac{\text{AC}_{\min}}{\text{AC}_{\text{ave}}} \end{aligned} \quad (1)$$

JRT is relative resistivity, dimensionless; RILD_{\max} is maximum RILD of sandstone section in the adjacent sharp-high amplitude, $\Omega\cdot\text{m}$; RILD_{ave} is average RILD of sandstone section in the sharp-high, middle, and low amplitude, $\Omega\cdot\text{m}$; JAC is relative acoustic, dimensionless; AC_{\min} is minimum AC of sandstone section in the adjacent sharp-high amplitude, $\mu\text{s}/\text{m}$; AC_{ave} is average AC of sandstone section in the sharp-high, middle, and low amplitude, $\mu\text{s}/\text{m}$; JRT and JAC were calculated according to (1) for sharp-high, middle, and low

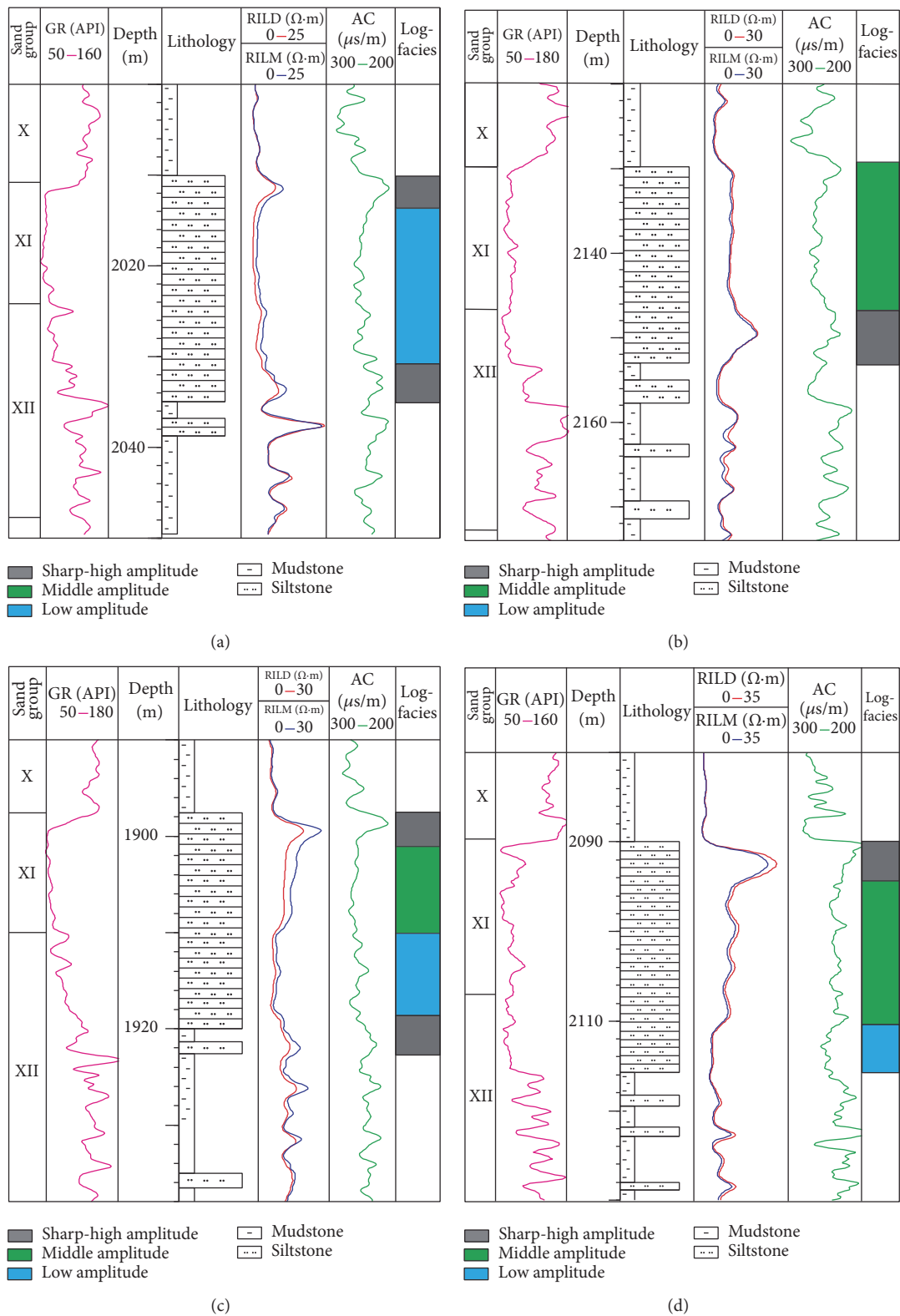


FIGURE 4: Petrophysical log response characteristics and logfacies of thick sand bodies in the Daqingzijing. (a) Integrated petrophysical and geological dataset of H15 well. (b) Integrated petrophysical and geological dataset of Qx 94-26 well. (c) Integrated petrophysical and geological dataset of H24 well. (d) Integrated petrophysical and geological dataset of Qx 110-36 well. GR means natural gamma ray logging, RILD means deep induction logging resistivity, RILM means medium induction logging resistivity, and AC means acoustic logging.

TABLE 1: Response value of different curve types of thick layer sand bodies.

Well	Interval depth (m)		Logfacies	RILD _{ave} (Ω·m)	RILD _{max} (Ω·m)	JRT	AC _{ave} (μs/m)	AC _{min} (μs/m)	JAC
H120-8	2188	2192	Sharp-high	11	13.2	1.2	219.2	215.2	0.98
	2192	2212	Middle	8.4		1.6	242.7		0.89
H24	1898	1901	Sharp-high	9.4	12.8	1.4	235.2	210.7	0.90
	1901	1910	Middle	7.5		1.7	261.4		0.81
	1910	1918	Low	4.4		2.1	256.4		0.82
	1918	1922	Sharp-high	7.4	9.1	1.2	241.2	228.6	0.95
H15	2010	2013	Sharp-high	7.4	10	1.4	223.1	209.7	0.94
	2013	2031	Low	4.4		2.3	250.4		0.84
	2031	2035	Sharp-high	8.9	11	1.2	231.9	218.7	0.94
H120-9	2215	2229	Middle	10		1.4	238.2		0.87
	2229	2235	Sharp-high	11.8	14.2	1.2	215.1	208.3	0.97
Qx94-26	2130	2147	Middle	10.4		2.0	252.2		0.88
	2147	2153	Sharp-high	14.9	20.4	1.4	237.4	222	0.94
Q98-23	2130	2138	Sharp-high	18.5	22	1.2	220.7	211.1	0.96
	2138	2147	Middle	14.1		1.6	238.5		0.89
	2147	2152	Low	10		2.2	242.6		0.87
Q+94-21	2130	2156	Middle	10.7		2.8	231.9		0.86
	2156	2162	Sharp high	26.4	30.1	1.1	224.4	198.8	0.89
Q94-25	2122	2139	Middle	10.7		2.8	233.4		0.88
	2139	2146	Sharp-high	22.9	30.3	1.3	216	206.5	0.96
Q96-23	2130	2157	Middle	12.6		2.3	244.7		0.88
	2157	2162	Sharp-high	22	28.9	1.3	228.4	215.9	0.95
Qx110-36	2090	2094	Sharp-high	23.9	27.7	1.2	217.2	193.6	0.89
	2094	2110	Middle	13.7		2.0	234.3		0.83
	2110	2115	Low	7.2		3.8	247.4		0.78

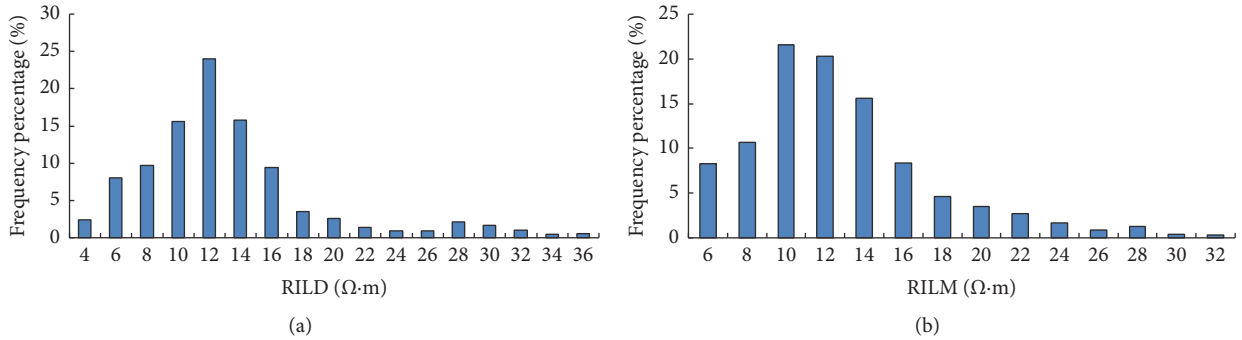


FIGURE 5: Histogram of the resistivity of the thick layer sand bodies in Daqingzijing. (a) RILD resistivity distribution histogram. (b) RILM resistivity distribution histogram.

amplitude of sandstone section (Table 1). As indicated from the JRT and JAC cross plot, JRT value of the sharp-high amplitude sandstone is less than 1.4, and the JAC value is greater than 0.88, while the JRT value of middle and low amplitude sandstone is greater than 1.4, and the JAC value is less than 0.88 (Figure 8(b)). The cross plot of JRT and JAC can clearly distinguish the sharp-high, middle, and low amplitude sandstone and identify the sharp-high amplitude calcareous sandstone.

4.2. Identification of Low Resistivity Oil Layers. Based on the statistics of the RILD of middle and low amplitude of thick sandstone in ten oil test and production well, the average RILD in the middle amplitude sandstone section is between 7.5 Ω·m and 14.1 Ω·m, while in the low amplitude sandstone section it is between 4.4 Ω·m and 10 Ω·m (Table 1), leading to a significant overlap for the RILD of middle and low amplitude sandstone in the range of 7.5 Ω·m~10 Ω·m; this makes it hard to identify the oil and water layer with only

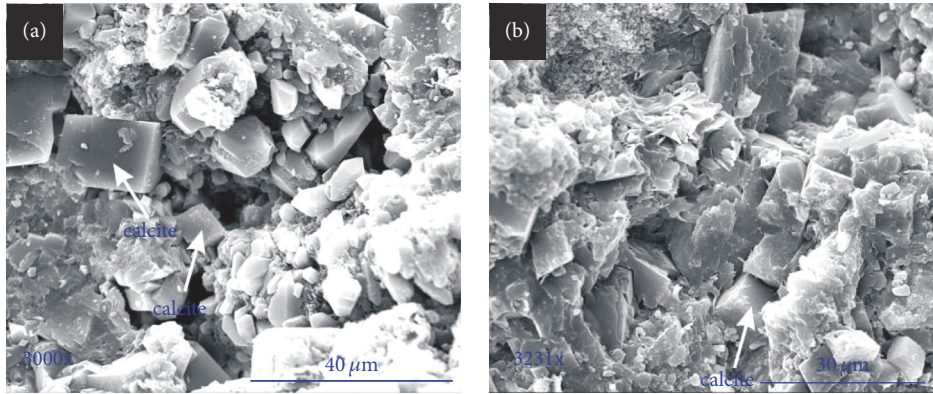


FIGURE 6: Scanning electron microscope of sandstone samples from the thick sand bodies in the Daqingzijing area. (a) Calcite cementation in H47 well 2171.1 m. (b) Calcite cement in Q156 well 2191.8 m.

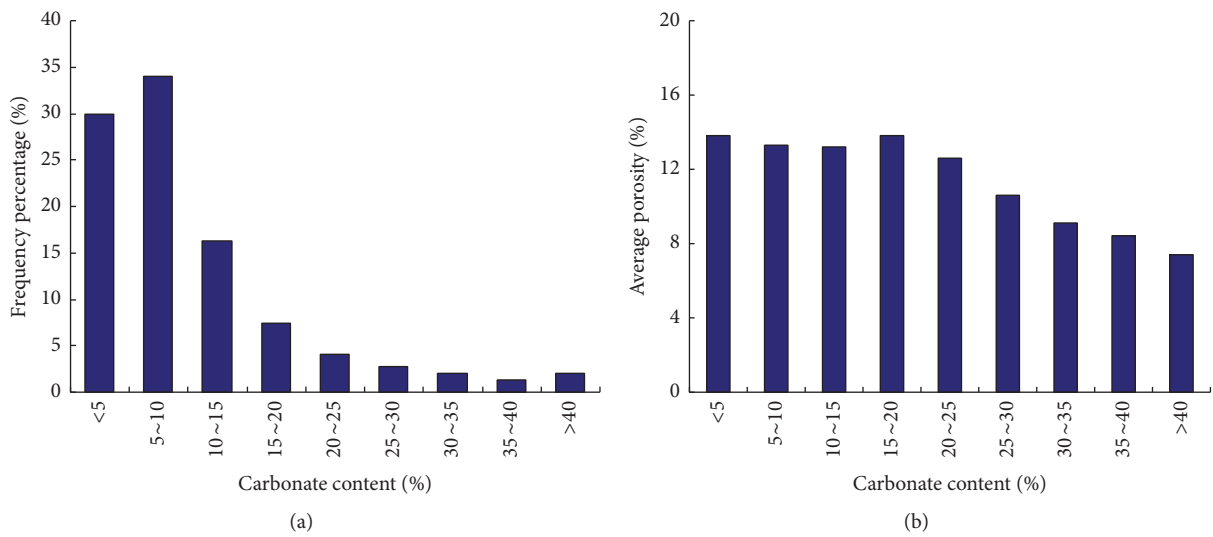


FIGURE 7: The distribution of carbonate content and its relationship with average porosity. (a) Carbonate content distribution histogram. (b) Carbonate content and average porosity.

RILD. For example, in the H24 well, the average RILD in the middle amplitude sandstone section is $8.2 \Omega \cdot m$, and the test data proves it as water layer, while in the Qx110-36 well, the average RILD in the middle amplitude sandstone section is $13.7 \Omega \cdot m$, but the test data proves it as oil-water layer (Table 2).

The data from eleven test and production wells in the study area show that the average RILM is greater than the average RILD in water layer sandstone (Table 2), such as in H15 (Figure 4(a)) and H24 (Figure 4(c)). The average RILD is greater than the average RILM in oil layer sandstone (Table 2), such as in Qx94-26 (Figure 4(b)) and Qx110-36 (Figure 4(d)). This is due to a fact that the formation of water resistivity is less than that of mud filtrate, and the mud filtrate resistivity is less than that of oil layer. When the mud filtrate invades into the water layer, the resistivity of the mixed formation water in the intrusive zone is certainly greater than that of the water layer, which explains why RILM value is greater than RILD. Moreover, if the mud filtrate invades into oil layer, the resistivity of the mixed liquid in the invasion zone is expected

to be less than that of the oil layer, and consequently RILD is greater than RILM.

A new parameter ΔRT is constructed based on the characteristics of RILD and RILM, which is the average RILD minus the average RILM. Based on the analysis between productivity and cross plot of ΔRT and RILD, we can found that the water layer's ΔRT is less than 0, such as H120-8, H24, H15, and H120-9 (Table 2, Figure 9). However, the oil-water layer's ΔRT is greater than 0, such as H160, Qx94-26, Qx92-24, Q98-23, Q+94-21, Q94-25, Q96-23, and Qx110-36 (Table 2, Figure 9).

Based on the statistical results of resistivity of the test and the production data (Table 2), the RILD and RILM cross plot is regarded as a standard resistivity identification method to distinguish oil-water layer from water layer, whereas the average value of RILM is difficult to distinguish the oil-water layer from water layer (Figure 10). The average RILD is greater than $10.4 \Omega \cdot m$ in oil-water layer and less than $10.4 \Omega \cdot m$ in water layer (Figure 10, Table 2), because the average RILD of

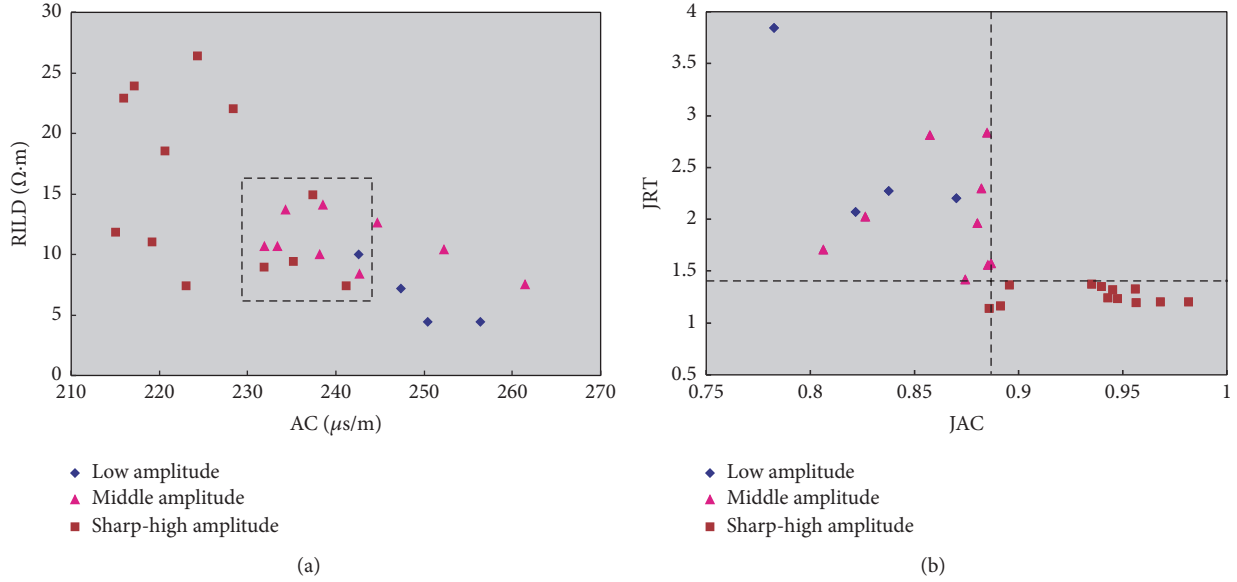


FIGURE 8: Standard identification of calcareous interlayers (sharp-high amplitude logfacies). (a) Cross plot of the parameters RILD and AC is invalid to identify low amplitude, middle amplitude, and sharp-high amplitude logfacies. (b) Cross plot of the parameters JRT and JAC is effective to identify sharp-high amplitude type from those three logfacies.

TABLE 2: Production distribution of part of wells in the area of the Daqingzijing.

Well	Logfacies	Test interval (m)		ΔRT	$RILD_{ave}$ ($\Omega \cdot m$)	$RILM_{ave}$ ($\Omega \cdot m$)	Oil t/day	Water t/day	Test/production
H120-8	Middle	2192	2196	-4.7	10	14.7		7.73	Water layer
H24	Middle	1901	1905	-2.8	8.2	11		24.6	Water layer
H15	Sharp-high	2031	2035	-1.3	9.4	10.7		55.4	Water layer
H120-9	Middle	2220.4	2228.4	-2.1	10.2	12.3		5.6	Water layer
Qx94-26	Middle	2130	2147	0.7	10.4	9.7	8.3	21.2	Oil-water layer
Qx92-24	Middle	2134	2158	1	13	12	7.4	15.5	Oil-water layer
Q98-23	Middle	2138	2147	1.4	15.6	14.2	5.4	9.2	Oil-water layer
Q+94-21	Middle	2130	2156	0.9	11.1	10.2	2.2	5.2	Oil-water layer
Q94-25	Middle	2125	2135	1.7	10.7	9	11	15.4	Oil-water layer
Q96-23	Middle	2130	2140	1.7	13.4	11.7	10	13.4	Oil-water layer
Qx110-36	Middle	2094	2110	1	13.7	12.7	8.9	23.6	Oil-water layer

low amplitude sandstone is less than $10 \Omega \cdot m$ (Table 2), so low amplitude type sandstones are all water layer; if the average RILD of middle amplitude sandstone is greater than $10.4 \Omega \cdot m$, it is oil-water layer, or else, it is water layer (Table 1).

Based on the deduction of the sharp-high amplitude calcareous interlayers, the fluid identification standard of thick layer sand bodies is as follows: (1) if the sandstone is low amplitude type and ΔRT ($RILD - RILM$) < 0 , it is water layer; (2) if the sandstone is middle amplitude type, the average $RILD < 10.4 \Omega \cdot m$, and ΔRT ($RILD - RILM$) < 0 , it is water layer; (3) if the sandstone is middle amplitude type, the average $RILD > 10.4 \Omega \cdot m$, and ΔRT ($RILD - RILM$) > 0 , it is oil-water layer.

5. Discussion

Sandstone in the X~XII sand groups of K_2qn^3 at Daqingzijing oilfield is regarded as a typical low resistivity oil layer. Genetic factors of low resistivity oil layer are very diverse, with low amplitude structure [25], sedimentary facies [26], interstitial materials [27], irreducible water [28], formation water salinity [29], drilling mud invasion, and other factors. This paper will discuss four aspects: low amplitude structure, interstitial material, irreducible water, and formation water salinity.

5.1. Low Amplitude Structure. The sandstone thickness of oil-water layers which is characterized by middle amplitude

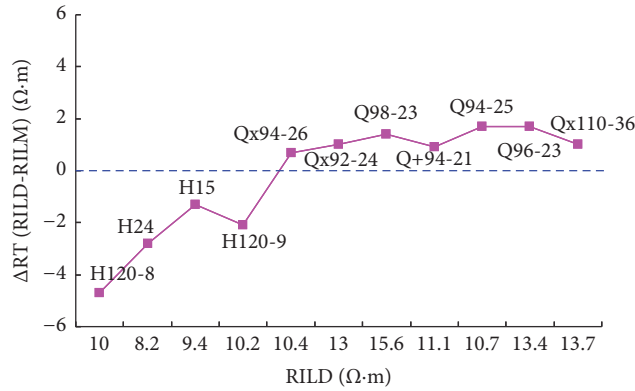


FIGURE 9: Δ ART and RILD cross plot of thick layer sand bodies at Daqingzijing area.

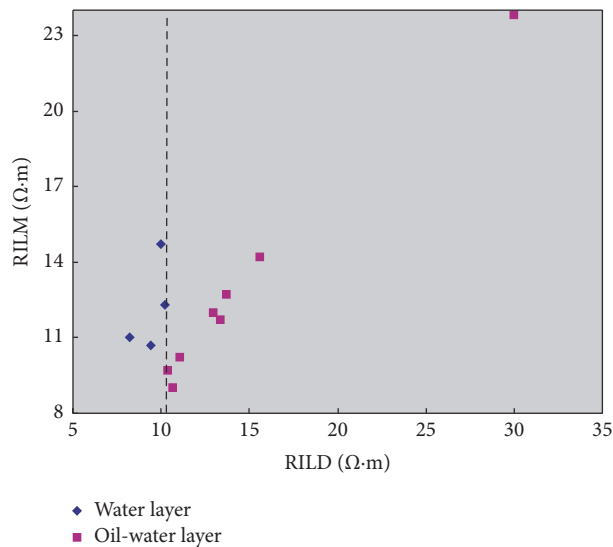


FIGURE 10: RILD and RILM cross plot at Daqingzijing area.

curve type has various values (Table 2); because the reservoir of the study area is low structure reservoir, the oil column height is less than 20 m. Different area of drilling wells in the oil reservoir is considered as oil-water layer if the sand body was on top of the oil-water interface and characterized by middle amplitude curve type; the thickness of the middle amplitude curve segment is the oil layer thickness (Figures 1(c) and 11, Qx110-36). However, it is considered as water layer if the sand body was under the oil-water interface and characterized by low amplitude curve type (Figures 1(c) and 11, Qx110-38, Qx110-40). Moreover, the sharp-high type sandstone because of calcareous interlayer is distributed at the top of the thick layer sand body and is effective cap rock.

5.2. Characteristics of Interstitial Materials. Through a quantitative analysis of X diffraction data, the total amount of clay minerals of the low resistivity oil layer of K_2qn^3 varies within 1.8%~5.8%, with an average of amounts to 4%. The clay mineral compositions are mainly dominated by illite-montmorillonite mixed-layer and illite, with high cation exchange adsorption capacity and strong conductivity. In

addition, most of the cementing materials were subject to argillization due to the epigenesis, which may provide a desirable condition for the existence of a large number of irreducible water [30], therefore forming a good conductive system that reduces reservoir resistivity.

5.3. Characteristics of Formation Irreducible Water. Based on the NMR data in well Q157-19-9, T2 cut-off method showed that the irreducible water saturation is around 30%~65%. High irreducible water saturation makes the formation serve as an effective molecular conductive network. This leads to a relatively low resistivity of the oil formation in a fresh water environment (Figure 12).

5.4. Salinity Characteristics of Formation Water. The formation water salinity in the Daqingzijing area of K_2qn^3 differs largely, ranging from 23662.4 mg/L to 28317.1 mg/L, with a mean value of 26257.6 mg/L. Statistical results of formation water salinity showed that the regional salinity is relatively high; this indicates that the low resistivity reservoir is related to the high formation water salinity of K_2qn^3 Formation (Table 3).

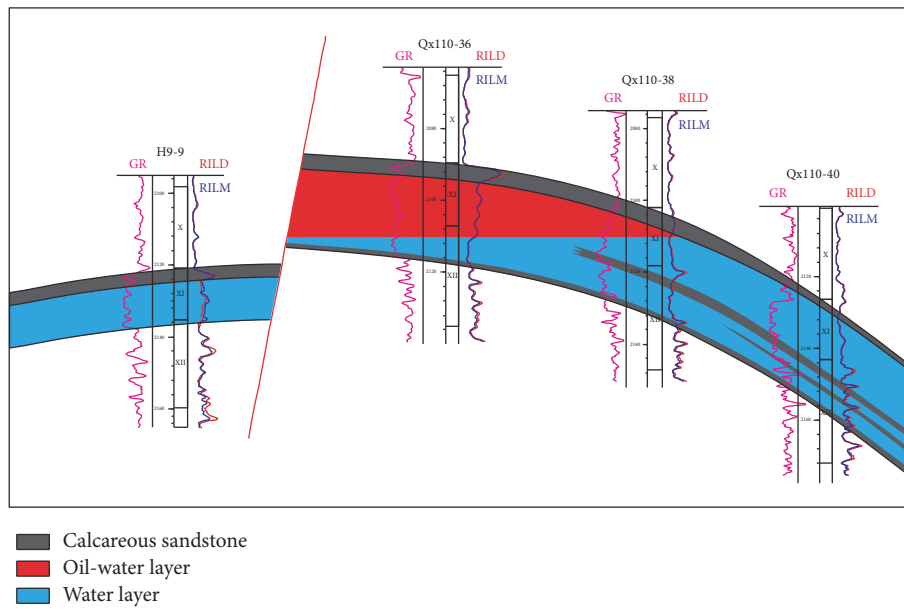


FIGURE 11: Reservoir profile of H9-9~Qx110-40 at Daqingzijing area. The thickness of the middle amplitude curve segment is the oil layer thickness.

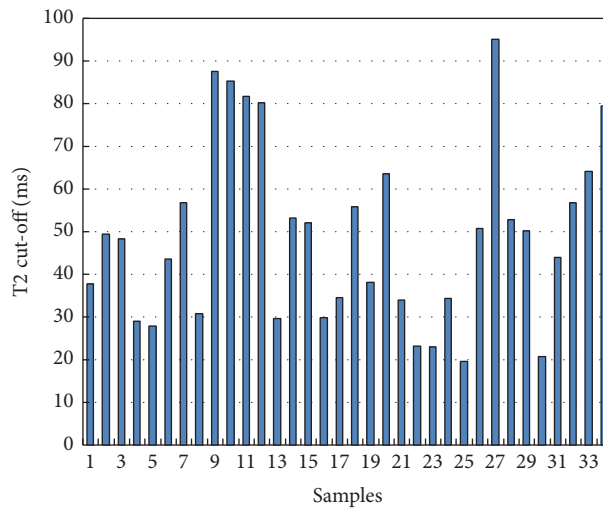


FIGURE 12: T2 cut-off value and irreducible water saturation distribution in the area of Daqingzijing.

TABLE 3: Salinity statistics of Daqingzijing area.

Well	K ⁺ -Na ⁺ (mg/L)	Mg ²⁺ (mg/L)	Ca ²⁺ (mg/L)	Cl ⁻ (mg/L)	SO ₄ ²⁻ (mg/L)	CO ₃ ²⁻ (mg/L)	Water type	Total (mg/L)
Q157-17-9	9820.9	23.1	178.4	10528.6	5589.7	1501.1	NaHCO3	27641.8
Q157-1	10038.1	15.6	171.9	10324.8	6308.3	1458.4	NaHCO3	28317.1
H80	9108.9	19	291.8	11229.9	3958.6	801.2	NaHCO3	25409.4
H120	8420.5	67.6	227.3	10335.1	3621.5	990.4	NaHCO3	23662.4

6. Conclusion

(1) The resistivity of the thick layer sand body of the study area is mainly distributed within $6\ \Omega\cdot\text{m}\sim 32\ \Omega\cdot\text{m}$ and is featured as double peak; this indicates that the thick layer is a typical low resistivity reservoir. The resistivity curves of the thick layer sand bodies include three logfacies: low, middle, and sharp-high amplitude, and each of them can be merged together, which are presented as the following 4 types: sharp-high, low, sharp-high amplitude combination; middle, sharp-high combination; sharp-high, middle, low, sharp-high amplitude combination; and sharp-high, middle, low amplitude combination.

(2) Thick sandstone of sharp-high amplitude (resistivity increases and the acoustic time decreases) represents the tight sandstone with calcareous cementation. Low amplitude sandstone is water layer while ΔRT (RILD-RILM) < 0 . For middle amplitude sandstone, if the average RILD $< 10.4\ \Omega\cdot\text{m}$ and ΔRT (RILD-RILM) < 0 , it is water layer; while if the average RILD $> 10.4\ \Omega\cdot\text{m}$ and ΔRT (RILD-RILM) > 0 , it should be oil-water layer.

(3) The features of low amplitude structure, high clay mineral content, high irreducible water saturation, and high formation water salinity in this study area all make the formation as an effective molecular conductive network. This greatly enhances the conductivity and leads to the low resistivity of the reservoir.

Conflicts of Interest

The authors declare that they have no conflicts of interest.

Acknowledgments

This study was supported by National Natural Science Foundation of China (nos. 41502127, 41390451, and 41204094), Opening Foundation of State Key Laboratory of Continental Dynamics, Northwest University (no. BJ14267), and Postdoctoral Fund of China (no. 2015M572594).

References

- [1] J. Ren, K. Tamaki, S. Li, and Z. Junxia, "Late Mesozoic and Cenozoic rifting and its dynamic setting in Eastern China and adjacent areas," *Tectonophysics*, vol. 344, no. 3-4, pp. 175-205, 2002.
- [2] L. S. Shu, Y. F. Mu, and B. C. Wang, "The oil-gas-bearing strata and the structural features in the Songliao Basin, NE China," *Journal of Stratigraphy*, vol. 27, no. 4, pp. 340-347, 2003.
- [3] C. N. Zou, S. H. Xue, W. Z. Zhao et al., "Depositional sequences and forming conditions of the Cretaceous stratigraphic lithologic reservoirs in the Quantou-Nengjiang Formations, South Songliao Basin," *Petroleum Exploration and Development*, vol. 31, no. 2, pp. 16-19, 2004.
- [4] Y. Wang, Y.-M. Wang, Z.-K. Zhao et al., "Origin and evolution of the west slope belt in Member 4 of Quantou Formation to Yaojia Formation, South Songliao Basin," *Petroleum Exploration and Development*, vol. 32, no. 3, pp. 33-90, 2005.
- [5] H. W. Deng, H. B. Wu, N. Wang, and A. C. Timothy, "Division of fluvial sequence stratigraphy: an example from the lower cretaceous Fuyu oil-bearing layer, the Songliao Basin," *Oil & Gas Geology*, vol. 28, no. 5, pp. 621-627, 2007.
- [6] C. L. Li, J. Xie, P. P. Chen, Z. L. Fan, and Z. Q. Sun, "High-resolution sequence stratigraphy model of the delta system in Daqingzijing area, JiLin Province," *Journal of Stratigraphy*, vol. 38, no. 3, pp. 355-362, 2014.
- [7] Z.-S. Wei, X.-M. Song, Z.-X. Tang, X. Chu, and G. Yang, "Sedimentary facies and lithologic oil pools of the Upper Cretaceous Qingshankou Formation in Daqingzijing area, Changling Sag, southern Songliao Basin," *Petroleum Exploration and Development*, vol. 43, no. 1, pp. 28-33, 2007.
- [8] M. D. Yang, M. H. Yang, Z. X. Tang, Y. H. Wang, X. Chu, and J. F. Wang, "Analysis of hydrocarbon distribution in Daqingzijing area of the Southen Songliao Basin," *Petroleum Geology and Experiment*, vol. 25, no. 3, pp. 252-256, 2003.
- [9] J. G. Wang, T. Q. Wang, P. S. Wei et al., "Identification of unconformity plane at the bottom of Qingsan Member in the Songliao Basin and its implication for petroleum geology," *Acta Geologica Sinica*, vol. 83, no. 1, pp. 79-88, 2009.
- [10] Y. J. Zhao, Z. D. Bao, J. Fu, Z. Q. Wang, Z. M. Liu, and H. Zhao, "Control of hydrocarbon migration and accumulation processes in the low-contrast reservoir," *Geological Science and Technology Information*, vol. 29, no. 2, pp. 71-76, 2010.
- [11] G. M. Hamada, M. S. Al-Blehed, M. N. Al-Awad, and M. A. Al-Saddique, "Petrophysical evaluation of low-resistivity sandstone reservoirs with nuclear magnetic resonance log," *Journal of Petroleum Science and Engineering*, vol. 29, no. 2, pp. 129-138, 2001.
- [12] A. Cerepi, C. Durand, and E. Brosse, "Pore microgeometry analysis in low-resistivity sandstone reservoirs," *Journal of Petroleum Science and Engineering*, vol. 35, no. 3-4, pp. 205-232, 2002.
- [13] C.-M. Yang, C.-C. Zhou, and X.-Z. Cheng, "Origin of low resistivity pays and forecasting of favorable prospecting areas," *Petroleum Exploration and Development*, vol. 35, no. 5, pp. 600-605, 2008.
- [14] L. Yan, S.-Q. Tan, B.-Z. Pan, P. Zhang, and Y.-M. Liu, "Genetic mechanism and logging evaluation method for low resistivity reservoirs: Taking Guantao Formation of Gangbei area for instance," *Journal of Jilin University (Earth Science Edition)*, vol. 40, no. 6, pp. 1456-1462, 2010.
- [15] V. I. Isaev, G. A. Lobova, and E. N. Osipova, "The oil and gas contents of the Lower Jurassic and Achimovka reservoirs of the Nyuro'l'ka megadepression," *Russian Geology and Geophysics*, vol. 55, no. 12, pp. 1418-1428, 2014.
- [16] V. Mashaba and W. Altermann, "Calculation of water saturation in low resistivity gas reservoirs and pay-zones of the Cretaceous Grudja Formation, onshore Mozambique basin," *Marine and Petroleum Geology*, vol. 67, pp. 249-261, 2015.
- [17] P. J. Wang, X. D. Du, J. Wang, and D. P. Wang, "The chronostratigraphy and stratigraphic classification of the Cretaceous of the Songliao Basin," *Acta Geologica Sinica*, vol. 69, no. 4, pp. 372-381, 1995.
- [18] F.-X. Gong, Y.-H. Shan, G. Lin, Z.-A. Li, and S.-L. Liu, "Mechanism of early post-rift normal faults in the central Songliao basin, northeastern China," *Earth Science Journal of China University of Geosciences*, vol. 33, no. 4, pp. 547-554, 2008.
- [19] R. F. Ge, Q. L. Zhang, L. S. Wang, and G. A. Xie, "Tectonic Evolution of Songliao basin and the prominent tectonic regime transition in eastern China," *Geological Review*, vol. 56, no. 2, pp. 181-195, 2010.

- [20] J.-Z. Li, T. Yang, L.-W. Wang, and T. Jiang, "Fault structure and its controlling role to hydrocarbon accumulation in Daqingzijing area, Southern Songliao Basin," *Petroleum Exploration and Development*, vol. 31, no. 1, pp. 18–20, 2004.
- [21] Z. J. Liu, P. C. Sun, R. Liu, Q. T. Meng, Y. Y. Bai, and Y. B. Xu, "Research on geological conditions of shale coexistent energy mineralization (accumulation): take the Qingshankou Formation in Upper Cretaceous, Songliao Basin for example," *Acta Sedimentologica Sinica*, vol. 32, no. 3, pp. 593–600, 2014.
- [22] W. W. Givens, "A conductive rock matrix model (CRMM) for the analysis of low-contrast resistivity formations," *The Log Analyst*, vol. 28, no. 2, pp. 138–151, 1987.
- [23] T. Han, M. B. Clennell, and M. Pervukhina, "Modelling the low-frequency electrical properties of pyrite-bearing reservoir sandstones," *Marine and Petroleum Geology*, vol. 68, pp. 341–351, 2015.
- [24] X. Y. Zhao, L. B. Zeng, Z. Q. Liu et al., "Characteristics of calcareous interbeds and their impact on distribution of natural fractures in tight sandstone reservoirs," *Geological Review*, vol. 61, no. 1, pp. 163–171, 2015.
- [25] Y. J. Wang, X. M. Song, L. P. He, N. X. Chen, and H. W. Yu, "Geologic origin of low-resistivity layers in deep reservoir of Gaoshangpu Oilfield," *Acta Petrolei Sinica*, vol. 31, no. 3, pp. 426–431, 2010.
- [26] J.-L. Wu, J.-M. Sun, J.-J. Zhu, S.-C. Geng, Z.-C. Li, and Y.-C. Zhang, "Study on macro-geologic control genesis of micro-geological causes in low-resistivity oil layer of Jiyang depression," *Journal of China University of Petroleum: Edition of Natural Science*, vol. 30, no. 3, pp. 22–25, 2006.
- [27] Z. L. Huang, X. G. Pu, C. N. Liang, and Z. P. Wei, "Characteristics and formation mechanism of low-resistivity reservoirs in the Southern Songliao Basin," *Natural Gas Industry*, vol. 26, no. 8, pp. 27–30, 2006.
- [28] H. H. Yu, H. Q. Li, B. Guo, H. T. Sun, and H. X. Zhang, "Low-resistivity oil layers fine evaluation approaches based on mechanism," *Journal of Jilin University (Earth Science Edition)*, vol. 42, no. 2, pp. 335–343, 2012.
- [29] Q.-H. Chen, S.-P. Sun, and Q. Li, "Genetic analysis on low-resistive formation of Dongying Formation in Gudong Oilfield," *Journal of China University of Petroleum: Edition of Natural Science*, vol. 28, no. 3, pp. 9–12, 2004.
- [30] J. M. Sun, K. W. Wang, and J. J. Zhu, "Microcosmic influence factor for electrical properties of low-resistivity reservoir in Jiyang Depression," *Acta Petrolei Sinica*, vol. 27, no. 5, pp. 61–65, 2006.

Research Article

Determining the REV for Fracture Rock Mass Based on Seepage Theory

Lili Zhang,^{1,2} Lu Xia,² and Qingchun Yu²

¹Department of Earthquake Science, Institute of Disaster Prevention, Sanhe 065201, China

²School of Water Resources and Environment, China University of Geosciences, Beijing 100083, China

Correspondence should be addressed to Lili Zhang; zhanglilil68@126.com

Received 9 January 2017; Revised 8 March 2017; Accepted 20 April 2017; Published 14 May 2017

Academic Editor: Shuyu Sun

Copyright © 2017 Lili Zhang et al. This is an open access article distributed under the Creative Commons Attribution License, which permits unrestricted use, distribution, and reproduction in any medium, provided the original work is properly cited.

Seepage problems of the fractured rock mass have always been a heated topic within hydrogeology and engineering geology. The equivalent porous medium model method is the main method in the study of the seepage of the fractured rock mass and its engineering application. The key to the method is to determine a representative elementary volume (REV). The FractureToKarst software, that is, discrete element software, is a main analysis tool in this paper and developed by a number of authors. According to the standard of rock classification established by ISRM, this paper aims to discuss the existence and the size of REV of fractured rock masses with medium tractility and provide a general method to determine the existence of REV. It can be gleaned from the study that the existence condition of fractured rock mass with medium tractility features average fracture spacing smaller than 0.6 m. If average fracture spacing is larger than 0.6 m, there is no existence of REV. The rationality of the model is verified by a case study. The present research provides a method for the simulation of seepage field in fissured rocks.

1. Introduction

Seepage problems of the fractured rock mass have always been a heated topic within hydrogeology and engineering geology. Many problems that are closely related to the research of fracture seepages, including the stability of dam foundation and seepage, the stability of bedrock side slopes under the influence of groundwater, fissure deposit, the prevention of mine water inrush, and the leakage and diffusion of nuclear waste. However, the study of the seepage problems of the fractured rock mass is still in its preliminary stage at present. The general method regards fractured media as porous media and uses the permeability tensor of porous media to describe the seepage characteristics of the fractured media. There are different types of structural plane in fractured rock mass, which lead to the complexity of rock mass characteristics. Therefore, the study on rock mass model is always one of the important problems in rock mechanics. The representative elementary volume (REV) is the basis to determine a rock mass mechanics model, and it is necessary to research the REV of fractured rock mass effectively, so that the REV size of the fractured rock mass can be determined.

The concept of the REV was the first introduced in continuum mechanics by Bear [1], and it is to be used to describe the flow in the porous media. The parameter of interest is both homogeneous and statistically stationary, which will ensure consistency in flow simulation studies. The REV is defined in two situations on (1) unit cell in a periodic microstructure and (2) volume containing a very large set of microscale elements, possessing statistically homogeneous properties. The REV has been discussed by many authors [2–17]. The REV of a fractured rock mass is the smallest volume in during the study of parameter when the hydraulic conductivity is a constant value. One special concern is the evaluation of the REV of the fractured rock masses, due to the fact that fluid flow in fractured rock masses is of high scale effect [2, 18–23]. Previous studies assumed that the anisotropy was achieved by making use of different correlation lengths in the horizontal and vertical directions, and flow barriers were modeled stochastically [24–36].

Snow [37] concluded the math expressions of single and infinite fracture permeability tensors, assuming that the fracture seepages did not interfere with each other, while the overall permeability tensor of fracture network was the

linear superposition of all fractures. As the fracture network was the same as the porous media, the permeability can be expressed by a permeability tensor. A fractured network can be approximately viewed as a porous medium, which was if the equivalent porous media of fractures are existent, then the permeability coefficients can be expressed by a symmetric second-order tensor. Li and Zhang [38] also conducted research on the REV of fractures. Bear [1] proved that if $r = K_q^{1/2}$ or $r = K_j^{-1/2}$ in the polar coordinate system, mapping can form an ellipse (under the condition of three-dimensional ellipsoid), where r represents radius vector, K_q represents permeability coefficient in the direction of the flow line, and K_j represents permeability coefficient in the direction of the hydraulic gradient. Long and Witherspoon [39] proposed that if the representative elementary volume of the fractured rock mass (REV) existed, the following two conditions must be met:

- (1) The media must be uniform in the area of study; that is, the average permeability coefficient of the area of study changes along with the scope of the study with big change; then it can be determined that this area of study is uniform.
- (2) In the polar coordinate system, the equivalent permeability coefficient k in each direction within the area of study can be described using an ellipse approximately at this time $r = \sqrt{K}$.

2. Introduction to FractureToKarst Software

This paper uses discrete fracture network (DFN) software, according to the standard of rock classification established by ISRM, and discusses the existence of REV of fractured rock masses with medium tractility. The discrete fracture network (DFN) software FractureToKarst for seepage in fracture rock mass is a kind of software using the Monte Carlo method. It can generate a two-dimensional fracture network of arbitrary shapes, set the common statistical parameters of fracture, filter the fractures within the area of study, and proceed with automatic discrete can be set. The head value and equivalent permeability coefficient of each node can be calculated by using the water balance principle. In the study, set an aspect ratio for the area of study 2:1 [40], calculate an equivalent permeability coefficient every 10° rotation of the area of study, every area of study can get 36 equivalent permeability coefficients, and discuss whether the direction of the equivalent permeability coefficient in polar coordinates can be described as a permeability coefficient ellipse or not, thus determining the existence of REV.

2.1. Mathematical Model. Mathematical model is the water dynamic model of the system. Fracture network is composed of a single, flat, smooth fracture, in a state of the laminar flow in a single fracture and can be described by the cubic law:

$$Q = \frac{\rho g}{12\mu} B^3 \frac{\Delta H}{L}. \quad (1)$$

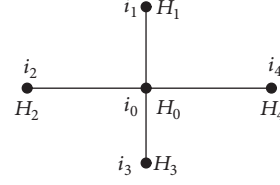


FIGURE 1: A unit in discrete fracture networks.

Type. Q is the boundary flux; ρ is the density of water; g is the gravitational acceleration; μ is flow dynamic viscosity coefficient; B is fracture width; ΔH is two-head difference of the fracture; L is the length of the fracture section.

In the fracture network, each node can establish a hydraulic link equation by the water balance principle:

$$\sum_{j=1}^n Q_{ij} + Q_b = 0 \quad (n = 1, 2, 3, \dots). \quad (2)$$

Type. Q_{ij} is the node flux; Q_b is the boundary flux. The hydrodynamic equations can be constructed by combining formula (1) and formula (2), and the head distribution of the fracture node within the system can be derived by the equations.

2.2. Model Algorithm. Model algorithm is a numerical method. The detailed steps are as follows.

(1) Grid discretization: all the fractures can be divided into the smallest fracture section by the nodes. Each node and connected fractures make a unit balance zone, as shown in Figure 1.

(2) For the hydraulic head, assign an initial value and boundary treatment: the node head is constant in the boundary of fixed water level. The initial water head of the rest of the nodes is 0.99 times the maximum elevation value. The node head of the impermeable boundary is equal to the adjacent nodes water head.

(3) For the hydraulic head, do iteration calculation: calculate the hydraulic head values of all nodes using the iterative methods based on formulas (1) and (2).

(4) Calculate the permeability coefficient: completing the hydraulic head calculation follows evaluating the equivalent permeability coefficient K in the flow direction using Darcy's law.

(5) Calculate the permeability coefficient in any direction: keep the shape of the area of study unchanged, make it rotate around its center, and calculate an equivalent permeability coefficient every 10° rotation; then we can get 36 equivalent permeability coefficients K .

(6) Draw: in the polar coordinate system, it is appropriate to use the equivalent permeability coefficients of 36 directions in Step (5) to draw the diagram, to see whether it can form an ellipse, so we know whether the REV is existent or not.

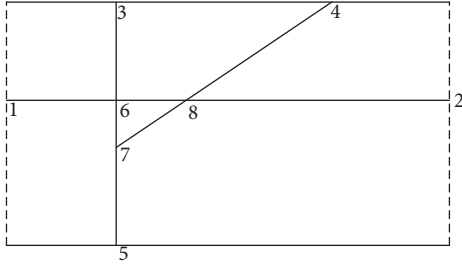


FIGURE 2: Sketch of fracture network.

3. Analytical Solution for Validation of the Software FractureToKarst

Assume that there is a fracture network as shown in Figure 2, the right and left boundaries being the given head border and the upper and lower two boundaries being the impermeable boundary; the start-point and end-point coordinates of the fractures are $[(1, 0), (1, 2)], [(0.5, 1.5), (3, 0)], [(0, 0.8), (4, 0.8)]$.

Assume the hydraulic head of two kinds of in and out of boundary values $H_1 = 20.5$, $H_2 = 0.5$, respectively. Using the principle of water balance and the cubic flow law, there is

$$\frac{\rho g B^3}{12\mu} \sum_{j=1}^n \frac{H_i - H_j}{L_{ij}} = 0 \quad (n = 1, 2, 3, \dots). \quad (3)$$

If $A = \rho g B^3 / 12\mu$, there are

$$H_1 = 20.5$$

$$H_2 = 0.5$$

$$A \frac{H_6 - H_3}{L_{6,3}} = 0$$

$$A \frac{H_8 - H_4}{L_{8,4}} = 0$$

$$A \frac{H_7 - H_5}{L_{7,5}} = 0$$

$$A \left(\frac{H_1 - H_6}{L_{1,6}} + \frac{H_3 - H_6}{L_{3,6}} + \frac{H_8 - H_6}{L_{8,6}} + \frac{H_7 - H_6}{L_{7,6}} \right) = 0$$

$$A \left(\frac{H_6 - H_7}{L_{6,7}} + \frac{H_8 - H_7}{L_{8,7}} + \frac{H_5 - H_7}{L_{5,7}} \right) = 0$$

$$A \left(\frac{H_6 - H_8}{L_{6,8}} + \frac{H_4 - H_8}{L_{4,8}} + \frac{H_2 - H_8}{L_{2,8}} + \frac{H_7 - H_8}{L_{7,8}} \right) = 0.$$

Type. $H_1 \sim H_8$ is the water head; $L_{i,j}$ is the length of fracture section between the two nodes; ρ is the density of water; g is the gravitational acceleration; μ is flow dynamic viscosity coefficient.

Through (4), we can obtain that the values of $L_{i,j}$ and the hydraulic head values for each node are

$$L_{1,6} = L_{6,1} = 1.0000$$

$$H_1 = 20.5000$$

$$L_{2,8} = L_{8,2} = 2.3333$$

$$H_2 = 0.5000$$

$$L_{3,6} = L_{6,3} = 0.8000$$

$$H_3 = 15.1794$$

$$L_{4,8} = L_{8,4} = 1.5549$$

$$H_4 = 12.9146$$

$$L_{5,7} = L_{7,5} = 0.8000$$

$$H_5 = 14.4100$$

$$L_{6,7} = L_{7,6} = 0.4000$$

$$H_6 = 15.1794$$

$$L_{6,8} = L_{8,6} = 0.6667$$

$$H_7 = 14.4100$$

$$L_{7,8} = L_{8,7} = 0.7775$$

$$H_8 = 12.9146.$$

The equivalent permeability coefficient of the flow direction k is obtained through Darcy's law:

$$k = 0.1173 \text{ m/s}. \quad (6)$$

Use FractureToKarst to build fracture network, and input parameters, the value of the water head, and the equivalent permeability coefficient are shown in Figure 3.

The calculation result in that the program equals the manual computation result, proving that the program is correct.

4. Simulation of the Fracture Network

According to the standard of rock classification established by ISRM, fractured rock mass with medium tractility refers to rock mass whose trace length is more than 3 m and less than 10 m. Because the permeability of two sets of orthogonal fracture rock masses is closest to being isotropic, the described ellipse is closest to being a circle.

According to the fracture spacing classification of ISRM, the spacing within 20~60 mm is very dense spacing. Within 10 m \times 10 m, two sets of orthogonal fractures were generated, the average spacing is 0.06 m, and the aperture is 0.0001 m. The two sets of fracture parameters are shown in Table 1 (two sets of fracture identification for I and II in Table 1). Here, put some fractures in the same direction as a set of fractures. The distribution types of the trace length and the direction are the normal distribution, and the gap width is the logarithmic normal distribution. The right and left boundaries are the

TABLE 1: Input data of the simulation fractures.

	Geometric parameters	Average	Standard deviation	Minimum	Maximum
I	Trace length (m)	6	0.1	3	10
	Gap width (m)	0.01	0.0002	0.0099999	0.01
	Direction (°)	90	0.0002	89.99999	90.1
II	Trace length (m)	8	0.1	3	10
	Gap width (m)	0.01	0.0002	0.0099999	0.01
	Direction (°)	1	0.0002	0.00009	0.11

```

Water Head:
1 20.5000
2 0.5000
3 15.1794
4 12.9146
5 14.4100
6 15.1794
7 14.4100
8 12.9146
water budget:
1.1732
Balance error , total discharge & Kp(m/s)
0.0008 1.1732 0.117319227455739

```

FIGURE 3: Calculation results of the FractureToKarst.

given head border and the upper and lower two boundaries are the impermeable boundary.

From Table 1, two sets of orthogonal fractures can be built. The first set has 276 fractures, and the second set has 208 fractures, with a total of 484 generating fractures. The diagram of generated fractures is shown in Figure 4(a). The equivalent permeability coefficient of the study area changes with the scope of the study without changes, so the study area is uniform. Within 10 m × 10 m, select five study areas of 1.0 m × 0.5 m, 2.0 m × 1.0 m, 3.0 m × 1.5 m, 4.0 m × 2.0 m, and 6.0 m × 3.0 m, and the diagram of generated fractures of FractureToKarst is shown in Figures 4(b)–4(f).

Acquire the permeability coefficients of all the directions in the five regions and make a comprehensive comparison chart of permeability coefficients (shown in Figure 5). Analyzing Figure 5, it can be concluded that every equivalent permeability coefficient is basically stable when the area of study is larger than 1.0 m × 0.5 m. There is no dramatical change for the permeability coefficients in the four regions 2.0 m × 1.0 m, 3.0 m × 1.5 m, 4.0 m × 2.0 m, and 6.0 m × 3.0 m, so more than 1.0 m × 0.5 m in the area of study can be approximately viewed as a homogeneous medium region.

In Figure 5, the meaning of all the symbols as follows.

“△” is the area of study of 1.0 m × 0.5 m; “●” is the area of study of 2.0 m × 1.0 m; “▽” is the area of study of 3.0 m × 1.5 m; “○” is the area of study of 6.0 m × 3.0 m; “◇” is the area of study of 7.0 m × 3.5 m.

5. The Fitting Calculation of the Uniform Basin

5.1. Calculation of Regional Rotation. As the uniform basin 1.0 m × 0.5 m was determined above, taking the initial angle as

the angle between the horizontal direction and the flow direction, rotate the whole area of study clockwise to calculate an equivalent permeability coefficient every 10°; then each area of study has 36 equivalent permeability coefficients, as shown in Table 2.

Table 2 shows that the maximum value of the permeability coefficient is 0.127 m/s when the angle is 0° and 180° between the flow direction and the horizontal orientation (because the angle between the two direction is 180°, so they are the same one flow field); the minimum value of the permeability coefficient is 0.076 m/s when the angle is 40° and 220° between the flow direction and the horizontal orientation. The reason for this phenomenon is that the calculation in Table 2 is derived from the data of the fracture network in Table 1, where 0° (180°) and 90° (270°) are two groups of orthogonal fractures. In Table 1, at four points at angles 0° (180°) and 90° (270°), there will be a local maximum value. The permeability coefficient at 0° (180°) is the local maximum value of fractures in the 0° (180°) direction, and the permeability coefficient at 40° (220°) is the minimum value between the two local maximum values.

5.2. The Polar Coordinate Fitting of the Permeability Coefficient. Assuming that point P is any one point on the ellipse in the polar coordinate system, A, B are, respectively, the two endpoints, and C is the focus of the ellipse. The semi-major axis and the semi-minor axis of the ellipse are assumed as a and b , respectively. This results in

$$\frac{x^2}{a^2} + \frac{y^2}{b^2} = 1$$

$$x = \rho \cos \theta$$

$$y = \rho \sin \theta.$$

Assuming that $\theta = T + \theta$, T is a parameter, that is, the angle between the principal axis of the ellipse and the polar coordinate 0° axis.

Solve (7), where the ellipse equation of the permeability coefficient in the polar coordinate system is

$$\rho = \frac{ab}{\sqrt{a^2 - (a^2 - b^2) \cos^2(\theta + T)}}. \quad (8)$$

Draw the ellipse according to Table 2 and (8) in the polar coordinate system and fit it, as shown in Figure 6. Fitting parameters and fitting values are shown in Table 3.

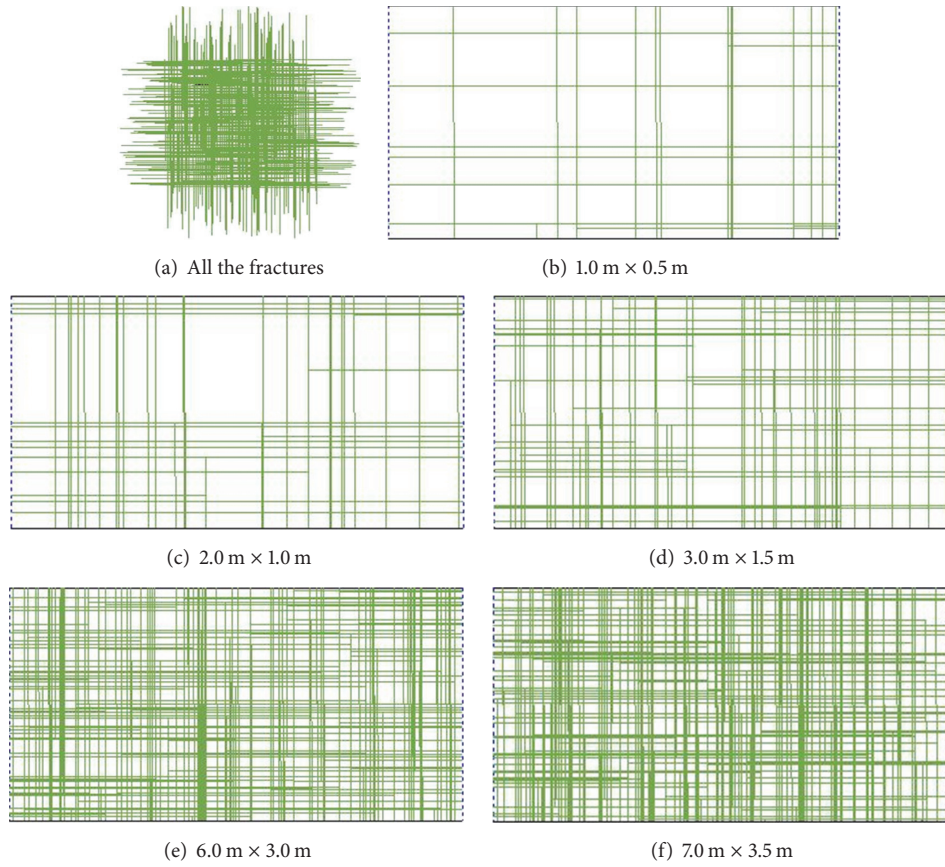


FIGURE 4: Sketch of fracture of research area.

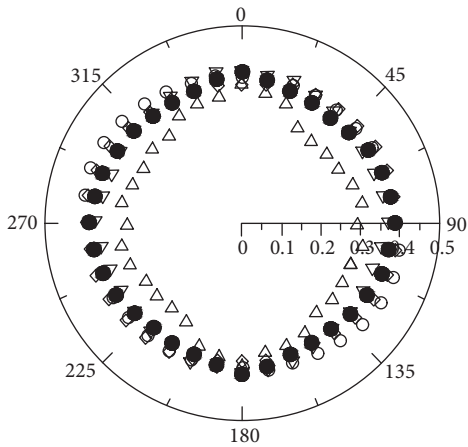


FIGURE 5: Comprehensive comparison chart of permeability coefficients of the five research areas.

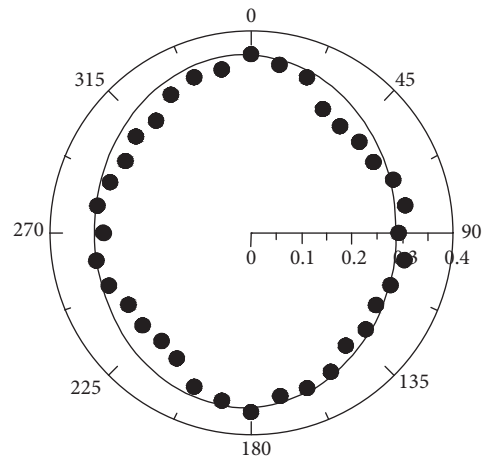


FIGURE 6: Curve fitting.

The semi-major axis and the semi-minor axis of the fitting ellipse are $a = 0.3121083582$, $b = 0.298487332$, respectively, where $T = 2.359065441$ radians, and the fitting equation is

$$\rho = \frac{0.093160391}{\sqrt{0.097411627 - 0.00831694 \cos^2(\theta + 2.359065441)}} \quad (9)$$

6. Determination of the REV

Öhman et al. have conducted a considerable amount of useful research [41–43] on the equivalent medium in the fractured rocks to compare the similarity between the equivalent permeability coefficient of numerical simulation and the ellipse in different area of studies. These two scholars have obtained

TABLE 2: Geometry parameters of the simulation fractures.

Angle (°)	Permeability coefficient K (m/s)	\sqrt{K}	Angle (°)	Permeability coefficient K (m/s)	\sqrt{K}
0	0.126663410	0.355898033	180	0.126663410	0.355898033
10	0.114747073	0.338743374	190	0.114747073	0.338743374
20	0.106263067	0.325980163	200	0.106263067	0.325980163
30	0.080940329	0.284500139	210	0.080940339	0.284500156
40	0.076023022	0.275722728	220	0.076023022	0.275722728
50	0.078325363	0.279866689	230	0.078325363	0.279866689
60	0.079387274	0.281757474	240	0.079387279	0.281757483
70	0.089760691	0.299600886	250	0.089760691	0.299600886
80	0.096157073	0.310092040	260	0.096157068	0.310092031
90	0.085050877	0.291634835	270	0.085050877	0.291634835
100	0.095708250	0.309367501	280	0.095708256	0.309367510
110	0.087766937	0.296254851	290	0.087766937	0.296254851
120	0.082587428	0.287380285	300	0.082587424	0.287380277
130	0.088829021	0.298041978	310	0.088829026	0.298041987
140	0.084262835	0.290280615	320	0.084262835	0.290280615
150	0.101059987	0.317899334	330	0.101059987	0.317899334
160	0.107171601	0.327370739	340	0.107171601	0.327370739
170	0.108014187	0.328655118	350	0.108014187	0.328655118

TABLE 3: Geometry parameters of the simulation fractures.

Angle (°)	\sqrt{K} fitted values	Angle (°)	\sqrt{K} fitted values	Angle (°)	\sqrt{K} fitted values
0	0.305109085	120	0.299326230	240	0.31116251
10	0.307460936	130	0.298577917	250	0.309507266
20	0.309569772	140	0.298590634	260	0.298487333
30	0.311157685	150	0.299363128	270	0.305030972
40	0.312004897	160	0.300818305	280	0.302734029
50	0.311990387	170	0.302805783	290	0.300760951
60	0.31116251	180	0.305109085	300	0.299326230
70	0.309507266	190	0.307460936	310	0.298577917
80	0.298487333	200	0.309569772	320	0.298590634
90	0.305030972	210	0.311157685	330	0.299363128
100	0.302734029	220	0.312004897	340	0.300818305
110	0.300760951	230	0.311990387	350	0.302805783

the minimum values of the square of the simulation value and fitting value, with the following formula:

$$\text{RMS} = \frac{2}{K_{\text{major}} + K_{\text{minor}}} \times \sqrt{\frac{\sum_1^n (K_s(\theta) - K_f(\theta))^2}{n}} \quad (10)$$

RMS is the fitting correlation coefficient of the ellipse, $K_s(\theta)$ is the simulation value, and $K_f(\theta)$ is the fitting value.

Depending on its similarity to the elliptic curve, RMS can be divided into three categories:

- (1) When $\text{RMS} \leq 0.2$, the size of the area of study can be used as the REV of the fractured rock mass.

- (2) When $0.4 > \text{RMS} > 0.2$, the size of the area of study can be used as the REV of the fractured rock mass under certain conditions.

- (3) When $\text{RMS} \geq 0.4$, the size of the area of study cannot be used as the REV of the fractured rock mass.

Therefore, after comparing Tables 2 and 3, it can be gleaned that the fitting result is quite ideal, with the correlation coefficient $\text{RMS} = 0.132064722$. The REV of the fractured rock mass of this kind exists, whose size is $1.0 \text{ m} \times 0.5 \text{ m}$.

Further research shows that the REV of very dense spacing ($< 0.02 \text{ m}$) of the fractured rock mass exists, and it is less than $1.0 \text{ m} \times 0.5 \text{ m}$. The REV of the dense spacing ($0.06 \sim 0.2 \text{ m}$) of the fractured rock mass is $2.0 \text{ m} \times 1.0 \text{ m}$. The REV of medium spacing ($0.2 \sim 0.6 \text{ m}$) of the fractured rock

mass is $10.0\text{ m} \times 5.0\text{ m}$. The REV is not the existence of the fractured rock mass of wide spacing ($0.6\sim 2.0\text{ m}$), with very wide spacing ($2.0\sim 6.0\text{ m}$) and utmost spacing ($>0.6\text{ m}$) because their fractures have no connection and have no hydraulic conductivity, and thus the REV does not exist.

7. Conclusions and Suggestions

In conclusion, the existence of REV is closely related to the fracture conditions. Not all types of fractured rock mass have REV. The more intensive the fractures are, the better the penetration is, the better the permeability of the rocks is, which means the easier it is to become equivalent to porous media. Thus, the following conclusions can be made:

- (1) The existence condition of the REV for fractured rock mass with medium tractility is that the average spacing of the fractures should be less than or equal to 0.6 m ; that is to say, the size of the REV of extremely dense spacing of the fractured rock mass is less than $1.0\text{ m} \times 0.5\text{ m}$; the size of the REV of very dense spacing of the fractured rock mass is $1.0\text{ m} \times 0.5\text{ m}$; the size of the REV of dense spacing of the fractured rock mass is $2.0\text{ m} \times 1.0\text{ m}$; the size of the REV of medium spacing of the fractured rock mass is $10.0\text{ m} \times 5.0\text{ m}$.
- (2) When the average spacing of the fractures is more than 0.6 m , the REV of wide spacing and very wide spacing and extremely wide spacing of the fractured rock mass does not exist.
- (3) Although this study has obtained certain achievement in the scale effects of the REV of the discrete fracture medium, there are still some shortcomings, including the influence of the different distribution of the geometric elements and the influence of the distribution of the different gap lengths, which all require further discussion.

Conflicts of Interest

The authors declare that they have no conflicts of interest.

Acknowledgments

This work was financially supported by the Foundation for Teachers from China Earthquake Administration (Grant no. 20150102), by the Foundation for Hebei Province Science and Technology Planning Project (Grant no. 162776436), and by the National Natural Science Foundation of China (Grant no. 41272387).

References

- [1] J. Bear, *Dynamics of Fluids in Porous Media*, Elsevier, New York, USA, 1972.
- [2] J. C. S. Long and P. A. Witherspoon, "Porous media equivalents for networks of discontinuous fractures," *Water Resources Research*, vol. 18, no. 3, pp. 645–658, 1982.
- [3] M. Hassanizadeh and W. G. Gray, "General conservation equations for multi-phase systems, I: averaging procedure," in *Flow through porous media, recent developments: a computational mechanics publications*, G. F. Pinder, Ed., pp. 1–16, 1983.
- [4] H. H. Haldorsen, "Simulator parameter assignment and the problem of scale in reservoir engineering," in *Reservoir characterization*, L. W. Lake and H. B. Carroll, Eds., pp. 293–340, Academic Press, Orlando, USA, 1986.
- [5] G. H. Shi, "Manifold method of material analysis," in *Transaction of the 9th Army Conference on Applied Mathematics and Computing*, pp. 57–76, USA, 1991.
- [6] G. H. Shi, "Manifold method," in *Manifold method. Proceeding of first International Forum on Discontinuous Deformation Analysis (DDA) and Simulations of Discontinuous Media*. TSI Press, pp. 52–204, Albuquerque, NM, Mexico, USA, 1996.
- [7] G. Shi, "Producing joint polygons, cutting joint blocks and finding key blocks for general free surfaces," *Chinese Journal of Rock Mechanics and Engineering*, vol. 25, no. 11, pp. 2161–2170, 2006.
- [8] A. Hurst, "Sedimentary flow units in hydrocarbon reservoirs: some shortcomings and a case for high-resolution permeability data," in *The geological modelling of hydrocarbon reservoirs and outcrop analogues*, S. Flint and I. D. Bryant, Eds., pp. 191–204, 1993, Special publication No. 15 of the international association of sedimentologists.
- [9] B. Noetinger, "The effective permeability of a heterogeneous porous medium," *Transport in Porous Media*, vol. 15, no. 2, pp. 99–127, 1994.
- [10] P. S. Ringrose, Pickup G E, J. Jensen L, and M. Forrester, "The Ardross reservoir gridblock analogue: sedimentology, statistical representative and flow upscaling," in *Reservoir characterization recent advances. Am assoc petrol geol memoir*, R. Schatzinger and J. Jordan, Eds., vol. 71, pp. 265–276, The Ardross reservoir gridblock analogue, sedimentology, 1999.
- [11] P. S. Ringrose, E. Skjetne, and C. Elfvenbein, "Permeability Estimation Functions Based on Forward Modeling of Sedimentary Heterogeneity," in *Proceedings of the SPE Annual Technical Conference and Exhibition*, Denver, Colo, USA, October 2003.
- [12] P. Ringrose, K. Nordahl, and R. Wen, "Vertical permeability estimation in heterolithic tidal deltaic sandstones," *Petroleum Geoscience*, vol. 11, no. 1, pp. 29–36, 2005.
- [13] K. Nordahl and P. Ringrose, *Identifying the representative elementary volume for permeability in heterolithic deposits using numerical rock models*. *Math Geosci*, vol. 40, 2008.
- [14] R. Al-Raoush and A. Papadopoulos, "Representative elementary volume analysis of porous media using X-ray computed tomography," *Powder Technology*, vol. 200, no. 1-2, pp. 69–77, 2010.
- [15] L. Xia, M. Li, Y. Chen, Y. Zheng, and Q. Yu, "Blockiness level of rock mass around underground powerhouse of Three Gorges Project," *Tunnelling and Underground Space Technology*, vol. 48, pp. 67–76, 2015.
- [16] L. Xia, Y. Zheng, and Q. Yu, "Estimation of the REV size for blockiness of fractured rock masses," *Computers and Geotechnics*, vol. 76, pp. 83–92, 2016.
- [17] K. Esmaeili, J. Hadjigeorgiou, and M. Grenon, "Estimating geometrical and mechanical REV based on synthetic rock mass models at Brunswick Mine," *International Journal of Rock Mechanics and Mining Sciences*, vol. 47, no. 6, pp. 915–926, 2010.
- [18] A. M. Shapiro and J. Andersson, "Steady state fluid response in fractured rock: A boundary element solution for a coupled, discrete fracture continuum model," *Water Resources Research*, vol. 19, no. 4, pp. 959–969, 1983.

- [19] C.-H. Lee, B.-W. Deng, and J.-L. Chang, "A continuum approach for estimating permeability in naturally fractured rocks," *Engineering Geology*, vol. 39, no. 1-2, pp. 71-85, 1995.
- [20] K.-B. Min, L. Jing, and O. Stephansson, "Determining the equivalent permeability tensor for fractured rock masses using a stochastic REV approach: Method and application to the field data from Sellafield, UK," *Hydrogeology Journal*, vol. 12, no. 5, pp. 497-510, 2004.
- [21] P. Blum, R. Mackay, M. S. Riley, and J. L. Knight, "Performance assessment of a nuclear waste repository: upscaling coupled hydro-mechanical properties for far-field transport analysis," *International Journal of Rock Mechanics and Mining Sciences*, vol. 42, no. 5-6, pp. 781-792, 2005.
- [22] P. Blum, R. Mackay, M. Riley, and J. Knight, "Hydraulische Modellierung und die Ermittlung des repräsentativen Elementarvolumens (REV) im Kluftegestein," *Grundwasser*, vol. 12, no. 1, pp. 48-65, 2007.
- [23] A. Baghbanan and L. Jing, "Hydraulic properties of fractured rock masses with correlated fracture length and aperture," *International Journal of Rock Mechanics and Mining Sciences*, vol. 44, no. 5, pp. 704-719, 2007.
- [24] A. Desbarats, "Support effects and the spatial averaging of transport properties," *Mathematical Geology*, vol. 21, no. 3, pp. 383-389, 1989.
- [25] S. H. Begg, R. R. Carter, and P. Dranfield, "Assigning effective values to simulator gridblock parameters for heterogeneous reservoirs," *SPE Reservoir Engineering (Society of Petroleum Engineers)*, pp. 455-463, 1989.
- [26] C. Deutsch, "Calculating Effective Absolute Permeability in Sandstone/Shale Sequences," *SPE Formation Evaluation*, vol. 4, no. 3, pp. 343-348, 1989.
- [27] A. Henriette, C. G. Jacquin, and P. M. Adler, "The effective permeability of heterogeneous porous media," *Phys Chem Hydrodyn*, vol. 11, no. 1, pp. 63-80, 1989.
- [28] R. Norris and J. Lewis, "The Geological Modeling of Effective Permeability in Complex Heterolithic Facies," in *Proceedings of the 66th annual technical conference and exhibition*, Dallas, TX, USA, 1991.
- [29] B. Noetinger and C. Jacquin, "Experimental Tests of a Simple Permeability Composition Formula," *Society of petroleum engineers preprint SPE 22841*, 1991.
- [30] P. Corbett, S. Anggraeni, and D. Bowen, "The use of the probe permeameter in carbonates addressing the problems of permeability support and stationarity," *Log Analyst*, vol. 40, no. 5, pp. 316-326, 1999.
- [31] V. C. Tidwell and J. L. Wilson, "Permeability upscaling measured on a block of Berea Sandstone: Results and interpretation," *Mathematical Geology*, vol. 31, no. 7, pp. 749-769, 1999.
- [32] V. C. Tidwell and J. L. Wilson, "Heterogeneity, permeability patterns, and permeability upscaling: Physical characterization of a block of Massillon sandstone exhibiting nested scales of heterogeneity," *SPE Reservoir Evaluation and Engineering*, vol. 3, no. 4, pp. 283-291, 2000.
- [33] Y. Bernabé, U. Mok, B. Evans, and F. J. Herrmann, "Permeability and storativity of binary mixtures of high- And low-permeability materials," *Journal of Geophysical Research B: Solid Earth*, vol. 109, no. 12, pp. 1-12, 2004.
- [34] J. M. McKinley, C. D. Lloyd, and A. H. Ruffell, "Use of variography in permeability characterization of visually homogeneous sandstone reservoirs with examples from outcrop studies," *Mathematical Geology*, vol. 36, no. 7, pp. 761-779, 2004.
- [35] M. D. Jackson, A. H. Muggeridge, S. Yoshida, and H. D. Johnson, "Upscaling permeability measurements within complex heterolithic tidal sandstones," *Math Geol*, vol. 35, no. 5, pp. 446-454, 2003.
- [36] M. D. Jackson, S. Yoshida, A. H. Muggeridge, and H. D. Johnson, "Three-dimensional reservoir characterization and flow simulation of heterolithic tidal sandstones," *AAPG Bulletin*, vol. 89, no. 4, pp. 507-528, 2005.
- [37] D. T. Snow, *A parallel plate model of fractured permeable media: [dissertation] [dissertation, thesis]*, Berkeley, Univ. of Calif, [dissertation], 1965.
- [38] J. H. Li and L. M. Zhang, "Geometric parameters and REV of a crack network in soil," *Computers and Geotechnics*, vol. 37, no. 4, pp. 466-475, 2010.
- [39] J. C. Long and P. A. Witherspoon, "The relationship of the degree of interconnection to permeability in fracture networks," *Journal of Geophysical Research*, vol. 90, no. B4, pp. 3087-3097, 1985.
- [40] Q. Yu, D. Chen, and G. Xue, "Hydrodynamics of discontinuous fracture network," *Earth Science-journal of China University of Geosciences*, vol. 20, no. 4, pp. 474-478, 1995.
- [41] J. Öhman and A. Niemi, "Upscaling of fracture hydraulics by means of an oriented correlated stochastic continuum model," *Water Resources Research*, vol. 39, no. 10, pp. 1277-1289, 2003.
- [42] J. Öhman, A. Niemi, and C.-F. Tsang, "A regional-scale particle-tracking method for nonstationary fractured media," *Water Resources Research*, vol. 41, no. 3, pp. 1-16, 2005.
- [43] J. Öhman, A. Niemi, and C.-F. Tsang, "Probabilistic estimation of fracture transmissivity from Wellbore hydraulic data accounting for depth-dependent anisotropic rock stress," *International Journal of Rock Mechanics and Mining Sciences*, vol. 42, no. 5-6, pp. 793-804, 2005.

Research Article

A Pore-Scale Simulation on Thermal-Hydrromechanical Coupling Mechanism of Rock

Rui Song,¹ Mengmeng Cui,² Jianjun Liu,^{1,3} P. G. Ranjith,⁴ and Yun Lei^{1,5}

¹School of Geoscience and Technology, Southwest Petroleum University, Chengdu 610500, China

²School of Petroleum and Natural Gas Engineering, Southwest Petroleum University, Chengdu 610500, China

³State Key Laboratory of Oil and Gas Reservoir Geology and Exploitation, Southwest Petroleum University, Chengdu 610500, China

⁴Deep Earth Energy Research Laboratory, Department of Civil Engineering, Monash University, Melbourne, VIC 3800, Australia

⁵Shenyang Research Institute, China Coal Technology & Engineering Group Corp., Shenyang 110016, China

Correspondence should be addressed to Rui Song; songrui0506@126.com and Jianjun Liu; liujj0906@sina.com

Received 24 February 2017; Accepted 28 March 2017; Published 18 April 2017

Academic Editor: Yi Wang

Copyright © 2017 Rui Song et al. This is an open access article distributed under the Creative Commons Attribution License, which permits unrestricted use, distribution, and reproduction in any medium, provided the original work is properly cited.

Thermal-hydrromechanical (THM) coupling process is a key issue in geotechnical engineering emphasized by many scholars. Most existing studies are conducted at macroscale or mesoscale. This paper presents a pore-scale THM coupling study of the immiscible two-phase flow in the perfect-plastic rock. Assembled rock matrix and pore space models are reconstructed using micro-CT image. The rock deformation and fluid flow are simulated using ANSYS and CFX software, respectively, in which process the coupled physical parameters will be exchanged by ANSYS multiphysics platform at the end of each iteration. Effects of stress and temperature on the rock porosity, permeability, microstructure, and the displacing mechanism of water flooding process are analyzed and revealed.

1. Introduction

Thermal-hydrromechanical (THM) coupling processes in geotechnical media play an important role in a wide range of engineering applications. Many significant issues, such as resources mining (e.g., coal, geothermal energy, natural gas, and oil) [1, 2], traffic engineering (e.g., tunnel and metro) [3], and underground repository (e.g., chemotoxic and nuclear waste and CO₂ as well as natural gas sequestration) [4, 5], attracted the scholars' attentions greatly.

Many scientific efforts have been exerted to reveal the THM interaction mechanism in the geotechnical systems. Since most geotechnical applications are characterized by long-term operating (several tens or hundreds of years) and large scales in size (several hundreds or thousands of meters in length, width, and depth), it is impossible to conduct in situ physical experiments. Therefore, mathematical models and simulation codes are emphasized by scholars. The THM coupling model originates from the isothermal hydrromechanical (HM) coupling mechanism (also named fluid-solid interaction). The first HM coupled theory is the 1D consolidation theory of soil proposed by Terzaghi, followed

by Biot's 3D consolidation theory with isothermal and elastic consolidation [6]. By introducing the nonisothermal terms to the extended Biot's equation [7] or using the averaging approach of the mixture theory, the basic THM coupling models are established [8]. In this interacting process, the rock is regarded as continuous mass points with characteristic parameters of both fluid and solid, which are governed by momentum, mass, and energy conservation laws. In this case, the porosity and fluid saturation are adopted to represent the storage capacity and mobility of fluid. Meanwhile, the elastic modulus, Poisson's ratio, cohesive strength, internal frictional angle, and other parameters of rock are used to reflect the deformability of rock. As discussed in the international DECOVALEX (DEvelopment of COupled models and their VALidation against EXperiments), coupled conservation equations can be solved by the finite element method (FEM) or discrete finite element method, and sometimes both are used to handle the problem of fluid flow in fractures [9, 10]. On this basis, extensive improvements have been achieved, mainly concerning the fluid flow equation or solid constitutive model.

Theoretically, multiphase models based on Navier-Stokes equations in porous media are applied for THM coupling analysis in geotechnical materials, which covers the immiscible or miscible multiphase flow of Newtonian fluid or non-Newtonian fluid [11]. In the same way, verities of plastic rock models, such as the ideal elastic-plastic model [12], the viscoelastoplastic model [13], Mohr-Coulomb [14], Drucker-Prager [15], and the damage model [16], have been proposed with the purpose of acquiring the rock constitutive model which better reflect the features of natural rock. Many codes have also been employed to model and calculate these coupling equations, such as COMSOL, ABAQUS, RPPA, FLAC, UDEC, ROCMAS, THAMES, FRACTION, COMPASS, FROCK and CODE_BRIGHT, FRT-THM, FLAC-TOUGH, and FRACTure [17–19]. However, as tremendous grids of the models are required to construct the complex and disordered pore structure of rock, the above studies have significant shortcomings that are neglecting the fluid flow in the micropore space of rock.

Experiments on rock at micro- or mesoscale are more feasible in consideration of the size of the test sample. The mesoscopic THM coupled study refers to the fluid flow test on rock core under the condition of pressure and temperature obtained from experiments or numerical simulation. Nowadays, the uniaxial/triaxial test of rock at HTHP (High Temperature, High Pressure) is widely used in the laboratory to acquire mechanical properties [20]. A multiphase flow displacement device has been added to the triaxial system to test the variation of fluid transport properties [21]. Acoustic emission device is employed to monitor the cracking development during the loading process [22]. NMR can be adopted to investigate the movable fluid in this process [23]. However, these devices cannot be used at the same time. Micro-CT is another approach for investigating the status of fluid flow or solid deformation and crack [24], but the resolution is limited by the core holder (for pressure or temperature loading) [25]. In addition, it is difficult to conduct real-time monitoring according to the time requirements for a full scan [26]. Equipment with smaller size and better measuring accuracy is essential to satisfy the requirements of microscopic experiments. Thus, it is difficult to conduct the 3D real-time investigation and research on micromesoscopic THM coupled process at HTHP, in which case most existing studies of this kind are monitored by surface imaging technology, for example, SEM [27]. The 3D printing rock-like specimen has been adopted to print the rock matrix and investigate the inner fluid flow or crack development [28], but the microstructure and mechanical properties of substitutions are different from the natural rock. Numerical simulation based on micromesoscopic modelling of rock has been regarded as a platform to study the THM coupled process of rock.

The developments of the imaging technologies, such as nano- or micro-CT technology and SEM, make it possible to investigate the rock structure and minerals distribution at the resolution of micron or nanometer [29]. On this basis, pore-scale modelling has been emphasized as an effective means to conduct fluid flow or deformation simulation [30]. In literature, the pore-scale modelling methods can be classified into two categories: pore network model and grids model [31]. The

former one is characterized by topologically representative network with idealized assumptions, which is efficient for the prediction of multiphase flow but is confined to fluid simulation only [32]. The second one is reconstructing the grids or mesh models from a binarized three-dimensional image, and then simulations are conducted using LBM or Navier-Stokes (NS) equations [33–35]. The volume tracking method including volume of fraction (VOF), Level Set (LS), or Level Set Method Progressive Quasistatic (LSMPQS) method is usually adopted along with the NS equations [36, 37]. Models of this kind can reproduce the image of rock but contain large amounts of elements because of the complex microrock structure, which in consequence are computationally demanding. Another advantage of this approach is that it is able to establish rock matrix models [38], which can be assembled with the corresponding pore model and used for the multiphysics coupled simulation. However, there are still some challenges in mesh quality controlling, modelling of the mineral distribution, and the remesh algorithm of fluid-solid interface since the shape of the rock structure varies in the THM coupled process. In mesoscopic aspects, the crack of the rock is the main concern. This allows the matrix in micropore models and crack to be established and simulated using the same methods as the microscopic simulation. However, most studies relevant to crack development and THM coupled process are limited to 2D [39].

This paper presents a fully THM coupled process in the rock using the reconstructed and assembled pore-scale models of rock matrix and pore space. Then the effects of stress and temperature on the pore structure, petrophysical properties, and water flooding efficiency are analyzed.

2. Pore-Scale Modelling and Boundary Conditions

The pore-scale models of both pore space and rock matrix are generated using the algorithm proposed in our previous paper [40]. The rock samples used in this paper are drilled from the original rock sample and scanned by Zeiss Xradia MICROXCT-400 of the State Key Laboratory of Oil and Gas Reservoir Geology and Exploitation in Southwest Petroleum University. A cube of voxels is extracted from the original micro-CT images and used as an input to the reconstructing process. The detailed information of the rock images used in this paper is listed in Table 1. The distribution of pore radius of the samples used in this study is shown in Figure 1.

As is shown in Figure 2(a), the reconstructed rock matrix and pore space models are assembled. In the simulation, the deformation of rock matrix is analyzed using ANSYS, while the fluid flow in the micropore of rock is simulated by CFX. The initial boundary conditions are applied in the Workbench platform. Taking the sample MS1 as an example, its boundary conditions of pore space and rock matrix are presented in Figures 2(b) and 2(c), respectively. The front and back surface of matrix along z direction are fixed. The other surfaces are imposed on confining pressure. The pressure gradient is applied between the front and back surface of pore space along z direction. The interface between rock matrix and pore is defined as FSI boundary. Other surfaces of pore space

TABLE 1: Rock sample image information.

Number	Rock type	Image resolution $\mu\text{m}/\text{pixel}$	Size/pixel	Porosity	Number of computational elements	
					Matrix	Pore
B1	Berea sandstone	5.345	400^3	19.65%	6428360	1571640
C1	Carbonate	3.314	400^3	17.12%	6630176	1369824
MS1	Synthetic sandstone	2.055	300^3	34.86%	2198473	1176527
S5	Sandstone from Shengli Oilfield, China	2.51	400^3	12.11%	7031198	968802
S6	Sandstone from Shengli Oilfield, China	5.01	200^3	40.34%	4772656	3227344

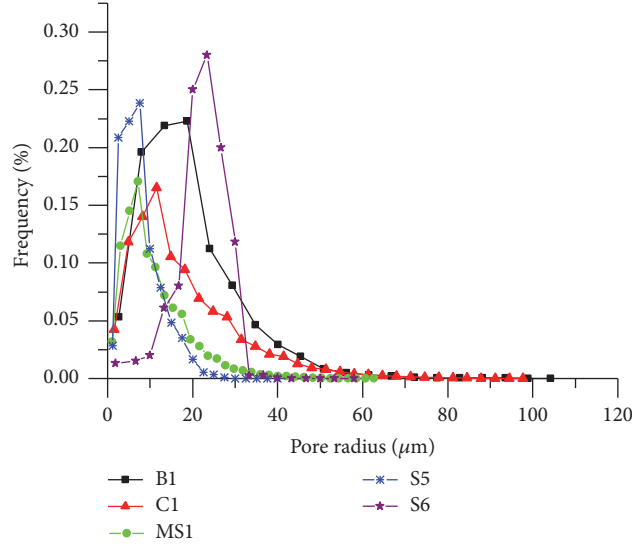


FIGURE 1: Pore radius distribution of images used in this paper.

are defined as impermeable boundary. Constant temperature boundaries are defined for both solid and fluid parts.

Rock matrix is assumed as isotropic, homogenous, and ideal elastic-plastic, thus only a limited range of stress and temperature values are simulated in this study. The rock properties used in the simulation are presented in Table 2, in which the mechanical parameters of rock are tested by microindentation test of rock sample. And the fluid properties at 273 K are listed in Table 3.

3. Mathematical Model of THM Coupling in Rock

The mathematical model of multiphase flow in deformable rock contains two parts: governing equations of fluid flow and solid deformation.

3.1. Governing Equations of Fluid Flow. VOF (volume of fraction) model in CFX software is used to simulate the immiscible water and oil in the reservoir. The continuity equation for the i th phase is [41]

$$\frac{1}{\rho_i} \left[\frac{\partial}{\partial t} (\alpha_i \rho_i) + \nabla \cdot (\alpha_i \rho_i \vec{v}_i) \right] = 0, \quad (1)$$

$$\sum_{i=1}^n \alpha_i = 1,$$

where α_i is volume fraction of i_{th} fluid in the cell and ρ_i is i_{th} fluid's density. When $n = 1$, the equation is just the continuity equation for the single flow.

The properties in the transport equations are determined by the volume fraction of the component phases in each cell:

$$\rho = \sum_{i=1}^n \alpha_i \rho_i, \quad (2)$$

$$\mu = \sum_{i=1}^n \alpha_i \mu_i.$$

All other properties (e.g., viscosity) are computed in this manner.

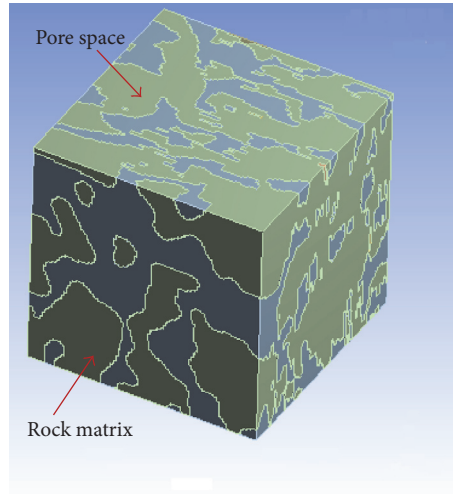
Navier-Stokes equation is used as the conservation of momentum for the fluid flow [41]:

$$\frac{\partial}{\partial t} (\rho \vec{v}) + \nabla \cdot (\rho \vec{v} \vec{v}) = -\nabla p + \nabla \cdot [\mu (\nabla \vec{v} + \nabla \vec{v}^T)] + \rho \vec{g} + \vec{F}. \quad (3)$$

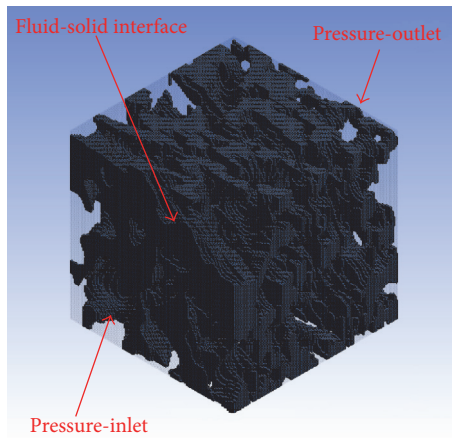
The energy equation is shared by all the phases in the control volume and can be described as [41]

$$\frac{\partial}{\partial t} (\rho E) + \nabla \cdot (\vec{v} (\rho E + p)) = \nabla \cdot (k_{\text{eff}} \nabla T), \quad (4)$$

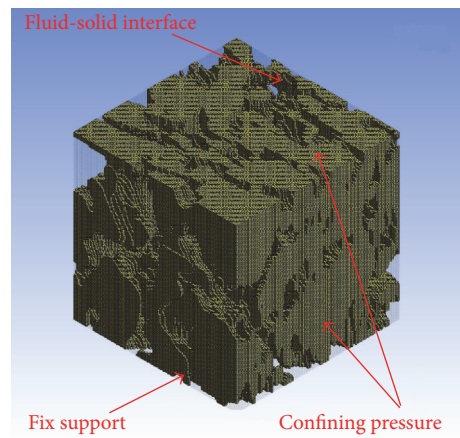
$$k_{\text{eff}} = \sum_{i=1}^n k_{i,\text{eff}},$$



(a) Assembled rock matrix and pore space model



(b) Boundary condition of pore space



(c) Boundary condition of rock matrix

FIGURE 2: Reconstructed model and boundary conditions of sample MS1.

TABLE 2: Rock properties of different sample.

Sample number	Density /kg·m ⁻³	Elastic modulus /GPa	Property		
			Poisson's Ratio	Yielding strength /MPa	Thermal expansion/ $\times 10^{-5} \text{ } ^\circ\text{C}^{-1}$
B1	2100	18.43	0.225	92.9	3.5
C1	2700	76.26	0.24	250	6
MS1	2300	14.19	0.31	81	5
S5	2675	20.13	0.28	73	6
S6	2500	9.35	0.29	67	6

TABLE 3: Fluid properties used in the simulation at the temperature of 273 K.

Fluid	Density (kg/m ³)	Viscosity (cP)	Interfacial tension (mN/m)	Contact angle θ_w ($^\circ$)	
				Drainage	Water flooding
Water	890	48	1	[10, 40]	[30, 60]
Oil	1200	1	1	[10, 40]	[30, 60]

where $k_{i,\text{eff}}$ is the effective thermal conductivity of i_{th} phase and the energy E and temperature T are calculated by the mass-weighted average value of all phases:

$$E = \frac{\sum_{i=1}^n \alpha_i \rho_i E_i}{\sum_{i=1}^n \alpha_i \rho_i}, \quad (5)$$

$$T = \frac{\sum_{i=1}^n \alpha_i \rho_i T_i}{\sum_{i=1}^n \alpha_i \rho_i},$$

where T_i and E_i represent the energy and temperature of i_{th} phase, respectively.

The interfacial tension between two immiscible phases is unneglectable in the micropores of rock, which would lead to high capillary force. Here, the continuum surface force (CSF) model proposed by Brackbill et al. in 1992 [42] is used as follows:

$$\nabla p = \sigma \left(\frac{1}{R_1} + \frac{1}{R_2} \right). \quad (6)$$

In the CSF model, the phase interface curvature can be calculated by the local gradients of phase interface normal, which is determined by the volume fraction gradient of i_{th} phase:

$$n = \nabla \alpha_i. \quad (7)$$

By the divergence theorem, the force on the interface can be transferred into the volume force. It has the following form:

$$F_{\text{vol}} = \sigma_{ij} \frac{\rho \kappa_i \nabla \alpha_i}{(1/2)(\rho_i + \rho_j)}, \quad (8)$$

$$\kappa = \nabla \cdot \hat{n},$$

where σ_{ij} is the surface tension coefficient and κ is defined in terms of the divergence of the unit normal (\hat{n}) of phase interface.

Considering the wall adhesion effect, the contact angle between the solid surface and the fluid is adopted to modify the unit normal (\hat{n}) of phase interface nearby the surface

$$\hat{n} = \hat{n}_w \cos \theta_w + \hat{t}_w \sin \theta_w, \quad (9)$$

where \hat{n}_w is the unit vectors normal to the wall and \hat{t}_w is tangential to the wall, respectively, and θ_w is the contact angle. In the simulation process, the structured mesh model is divided into different parts. The contact angle, which follows a uniform distribution with a range of given interval, is assigned randomly to each part to obtain uniformly wet system. The wettability of the model is determined by the mathematical expectation of the given interval of the contact angle.

Using CFX software, the outlet flow rate can be acquired. Then the absolute permeability is calculated in the following term [43]:

$$K = \frac{\mu_i Q_i L}{A \Delta p}. \quad (10)$$

Then the relative permeability is given by [43]

$$k_{rp} = \frac{Q_{si}}{Q_i}, \quad (11)$$

where Q_i is the total single-phase flow rate through the model and Q_{si} is the total flow rate of phase i in multiphase conditions with the same imposed pressure drop. And both Q_i and Q_{si} can be acquired by the *Fluent* software.

3.2. Governing Equations of Rock Matrix Deformation. The three-dimensional equilibrium differential equation is

$$\sum_j \frac{\partial \sigma_{ij}}{\partial x_j} + f_i = 0. \quad (12)$$

Here σ_{ij} is the stress tensor and f_i is the body force.

The three-dimensional geometric equations of the rock matrix are

$$\varepsilon_{i,j} = \frac{1}{2} \left(\frac{\partial u_i}{\partial x_j} + \frac{\partial u_j}{\partial x_i} \right). \quad (13)$$

Here ε is strain and u is the displacement component.

The elastic physical equations are

$$\varepsilon_x = \frac{1}{E} [\sigma_x - \mu (\sigma_y + \sigma_z)],$$

$$\gamma_{xy} = \frac{2(1+\mu)}{E} \tau_{xy},$$

$$\varepsilon_y = \frac{1}{E} [\sigma_y - \mu (\sigma_x + \sigma_z)],$$

$$\gamma_{yz} = \frac{2(1+\mu)}{E} \tau_{yz},$$

$$\varepsilon_z = \frac{1}{E} [\sigma_z - \mu (\sigma_x + \sigma_y)],$$

$$\gamma_{zx} = \frac{2(1+\mu)}{E} \tau_{zx}, \quad (14)$$

and here E is elastic modulus and μ is Poisson's ratio.

4. THM Coupling Simulation

Based on the rock mesh model, the THM coupling mechanism in rock and its influence on water flooding process in the petroleum industry are analyzed using both ANSYS and CFX software. The fluid used in the single-phase flow simulation is water, and both oil and water are used for two-phase flow. In the CFX solver, a laminar flow is assumed. A transient model is used with the second-order backward Euler scheme. Automatic timestep and a convergence criterion of 10^{-6} are used. In the ANSYS solver, a transient structural solver is used to apply the boundary conditions of solid part and the default solver control is used. The mechanical input file will be generated and used as input to the ANSYS multifield solver.

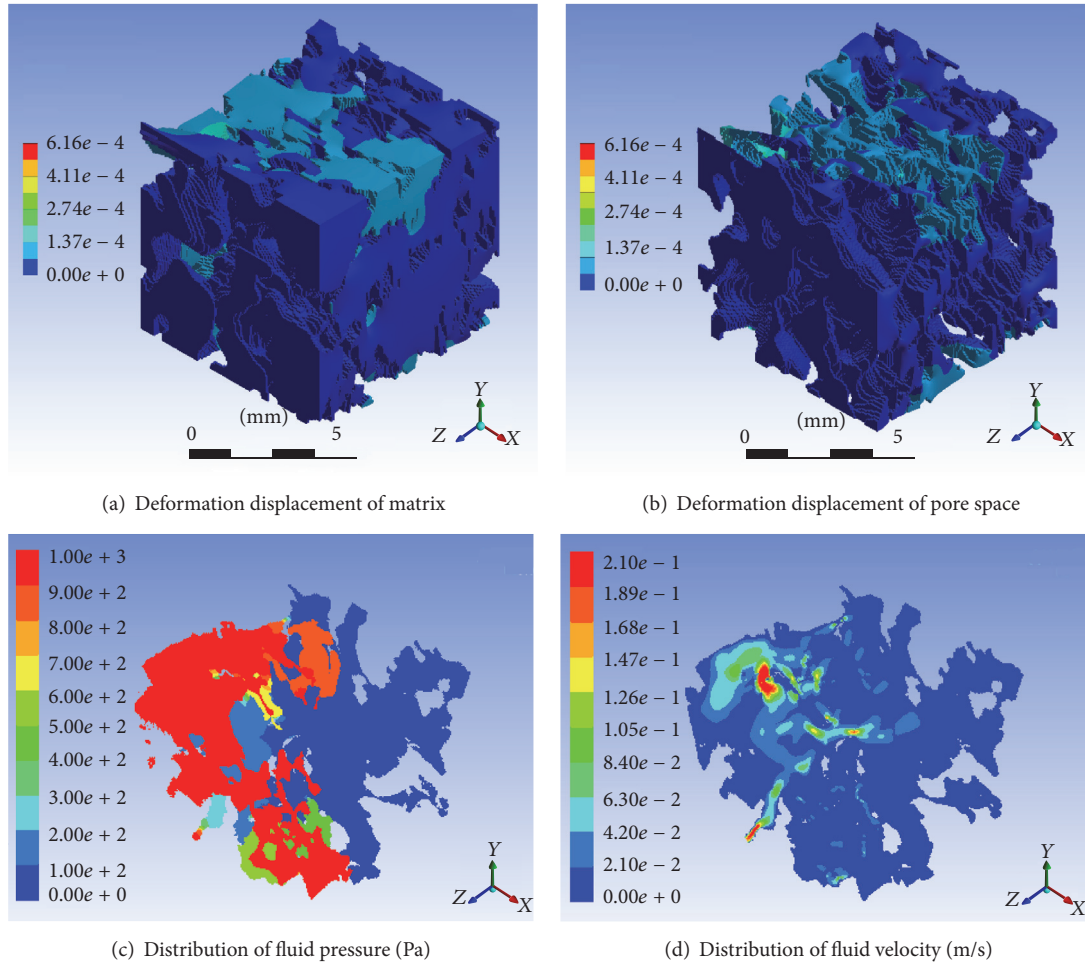


FIGURE 3: THM simulation of model MS1 under the condition that the confining pressure is 20 MPa and the pore pressure is 1000 Pa.

5. Single-Phase Flow

5.1. Influences of Effective Pressure on Porosity and Permeability. Based on the structured mesh models of samples B1, CL, MS1, and S6, the evolution mechanism of effective pressure is analyzed. Taking sample MS1 as an example, under the condition of $p_{\text{inlet}} = 1000 \text{ Pa}$, $p_{\text{co}} = 20 \text{ MPa}$, and the constant temperature of 273 K , the deformation displacement of both matrix model and interface of pore model is presented in Figures 3(a) and 3(b). Due to the complexity and inhomogeneity of microstructure of rock, the strain distribution is also characterized by inhomogeneity. Meanwhile, the fluid pressure and velocity distribution are shown in Figures 3(c) and 3(d). It indicates that water flows mainly along the channels with larger size and better connectivity to reduce the flowing resistance.

As is shown in Figure 4, the porosity and permeability decrease along with the rising of the confining pressure under the condition of constant pore pressure (i.e., the rising of the effective pressure). The rate of porosity drop becomes slower when the confining pressure is beyond 30 MPa, which means the plastic deformation occurs inside the rock matrix.

The reason lies in that rock is assumed as isotropic, homogeneous, and ideal elastic-plastic, and thus the strain would not change when the load is beyond its yield strength. Meanwhile, it shows a negative correlation between the drop rate of porosity and the elastic modulus of rock.

In addition, comparative analysis on the variation of permeability with the porosity under the same load is shown in Figure 5. It is found that the decline of the permeability is larger than the porosity. Taking model S6 as an example, when the porosity declines by 10%, the permeability drop ratio reaches almost 20%. This indicates that the permeability of rock is more sensitive to the confining pressure than the porosity.

5.2. Effects of Temperature on Porosity and Permeability. In this section, the effects of temperature on the porosity and permeability under the condition of constant confining pressure (20 MPa) and pore pressure (5 MPa) are analyzed. The rock is assumed to be elastic under the temperature, and only the thermal expansion of rock in the temperature range of $[20^\circ\text{C}, 100^\circ\text{C}]$ is analyzed. The plastic deformation and the crack development under the temperature in the simulation

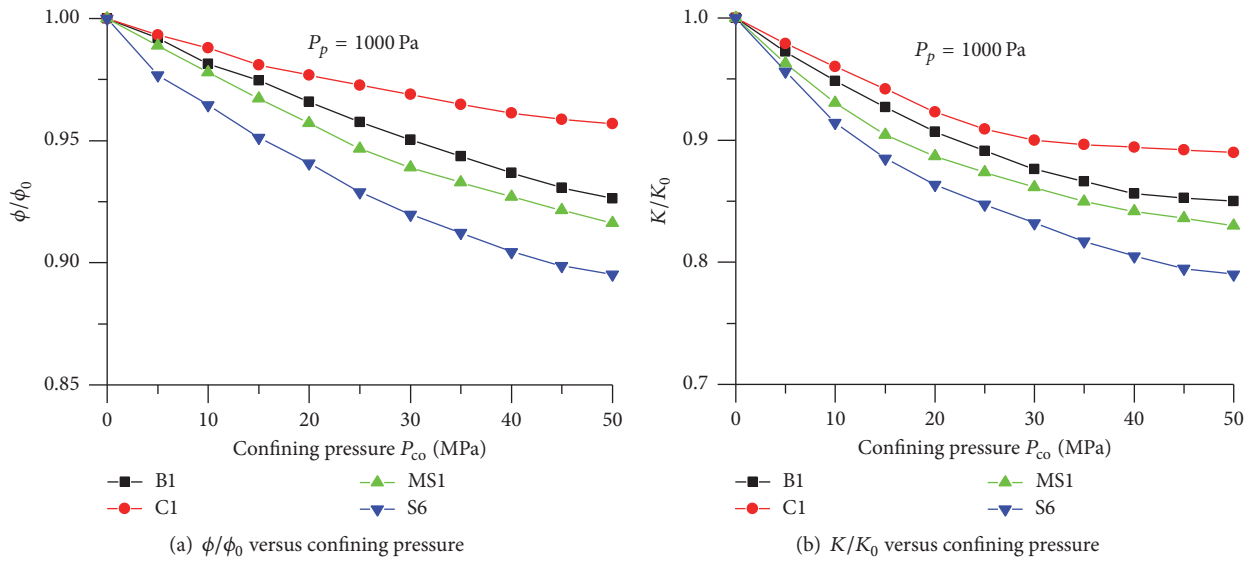


FIGURE 4: Variation of porosity and permeability with the rising of confining pressure and constant pore pressure. ϕ/ϕ_0 refers to the ratio of the porosity under the simulation condition to the origin sample, so it is with K/K_0 referring the permeability.

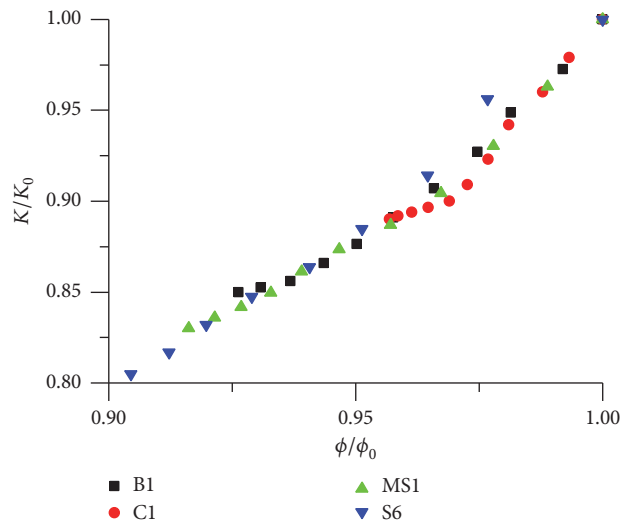


FIGURE 5: Permeability variation versus porosity variation.

are not considered. The thermal strain of model MS1 is presented in Figure 6, characterized by nonhomogeneous distribution.

As is shown in Figure 7, the porosity and permeability of rock decrease with the rising of the temperature under the condition of constant confining and pore pressure, which is in contrast with the traditional experimental benchmark data, especially in a high temperature. This is because the rock matrix expands with the rising of the temperature, but the expansion would also lead to microcrack, which will enlarge the porosity and permeability of rock, too. When the temperature is varied from 20 °C to 100 °C, the porosity drop is less than 2%, but the maximum permeability drop is about 5%, which means the permeability is also more sensitive to the temperature than the porosity.

Based on the simulation, the permeability variation of model MS1 with the effective pressure and temperature along x , y , and z direction is presented in Figure 8. In the simulation, the confining pressure is variable and the pore pressure is constant to be 5 MPa. It can be found that the permeability and its drop rate vary for different direction with the rising of effective pressure and temperature. Considering the isotropic assumption of rock, the complex and disorder structure of rock is the main reason to this phenomenon.

6. Two-Phase Flow

Considering that the oil solubility in water is small enough to neglect, the VOF (volume of fraction) model is used to simulate the immiscible displacement process between water

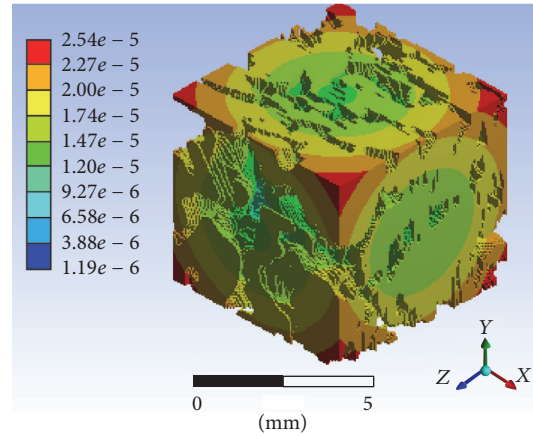


FIGURE 6: Thermal strain distribution of model MS1 under the temperature of 100°C.

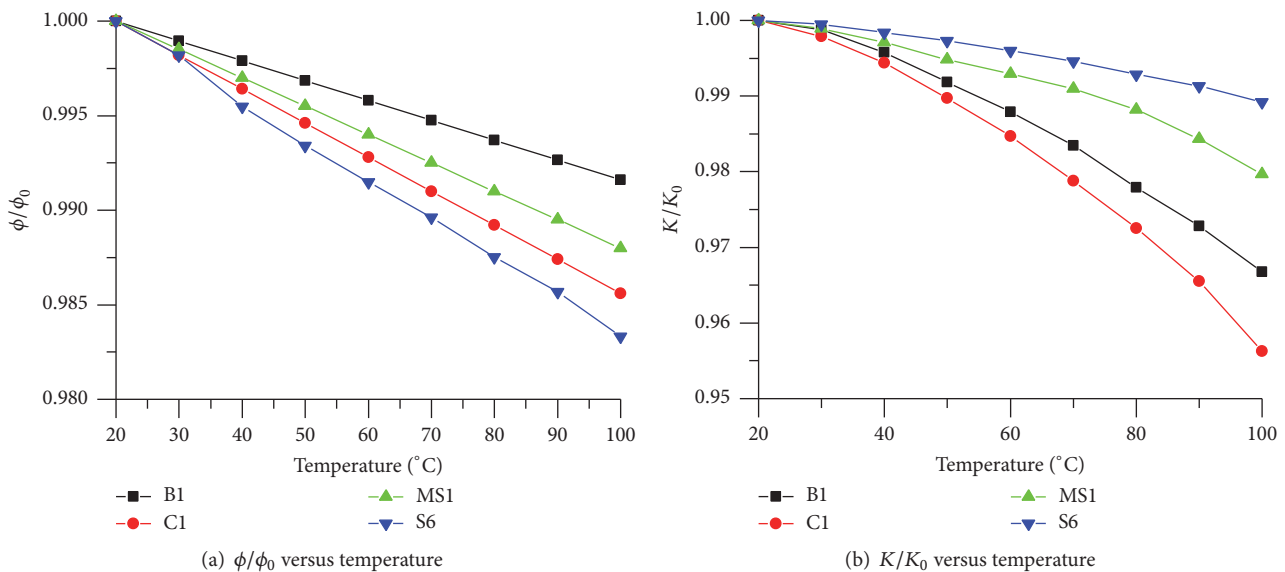


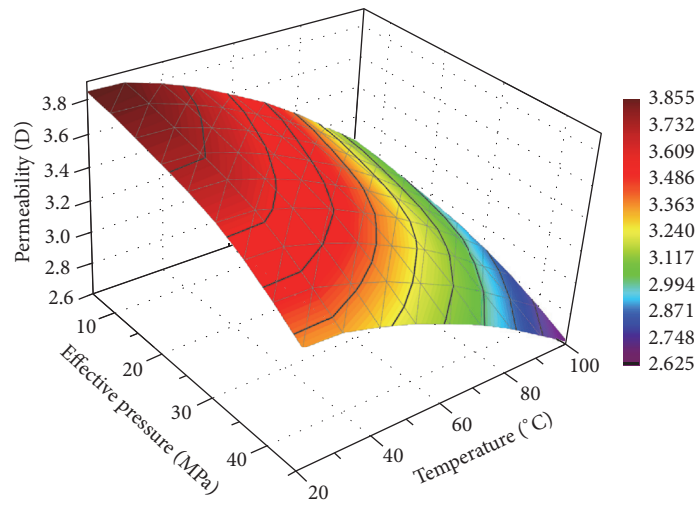
FIGURE 7: Variation of porosity and permeability with temperature.

and oil in the reservoir. The core sample is initially saturated with water to represent the original stratum without oil. Then the first-cycle oil flooding is proceeded to represent the formation of oil, in which process the core sample becomes more oil-wet. After that, water injection is simulated to represent the water flooding development of the reservoir. The oil distribution of MS1 after the first cycle of oil flooding process and the second cycle of water flooding process is shown in Figure 9.

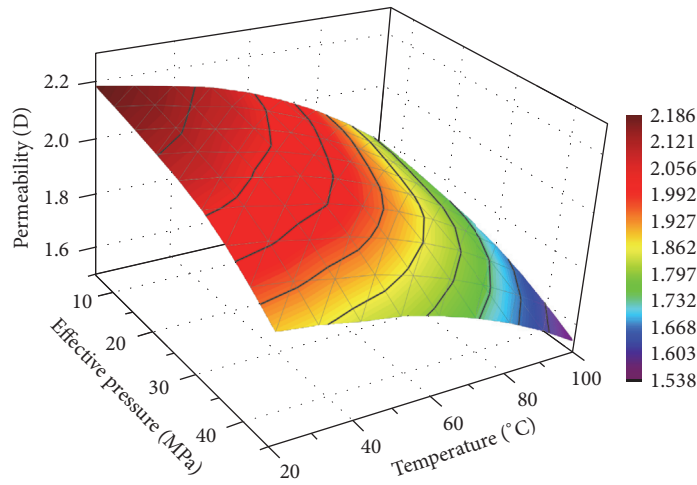
6.1. Influences of Effective Pressure on Water Flooding Efficiency. The effects of confining pressure on water flooding efficiency under the condition of constant pore pressure (1000 Pa) and temperature (20°C) are analyzed. The variations of relative permeability curves of model S5 and MS1 are presented in Figure 10. It is found that, with the rising of the confining pressure (i.e., the rising of the effective pressure),

the relative permeability of both water and oil decreases, which means the decline of the fluid mobility. In this case, the residual oil saturation increases. The reason lies in that the size of pore space (especially the throat) decreases with the rising of the effective pressure, which leads to a higher capillary pressure and a lower oil recovery. Thus, higher pressure of induced water contributes to EOR in the water flooding process.

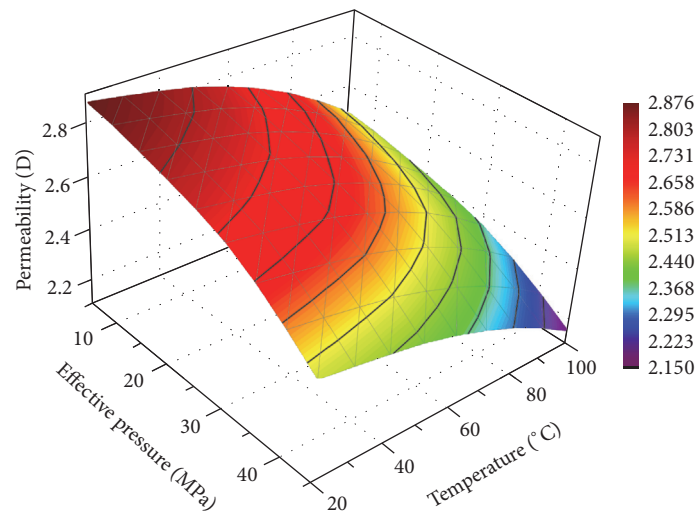
6.2. Effects of Temperature on Water Flooding Efficiency. As is shown in Figure 11, with the rising of temperature, the relative permeability of both water and oil increases. Though the pore size reduces caused by the expansion of the rock matrix with the rising of temperature, the decrease of water and oil viscosity improves the fluid mobility. Meanwhile, the decline of oil-water mobility ratio reduces the fingering effect in the displacing process, which promotes the sweep efficiency and



(a) Permeability versus effective pressure and temperature along x direction



(b) Permeability versus effective pressure and temperature along y direction



(c) Permeability versus effective pressure and temperature along z direction

FIGURE 8: Permeability variation of model MS1 with effective pressure and temperature along x, y, and z direction.

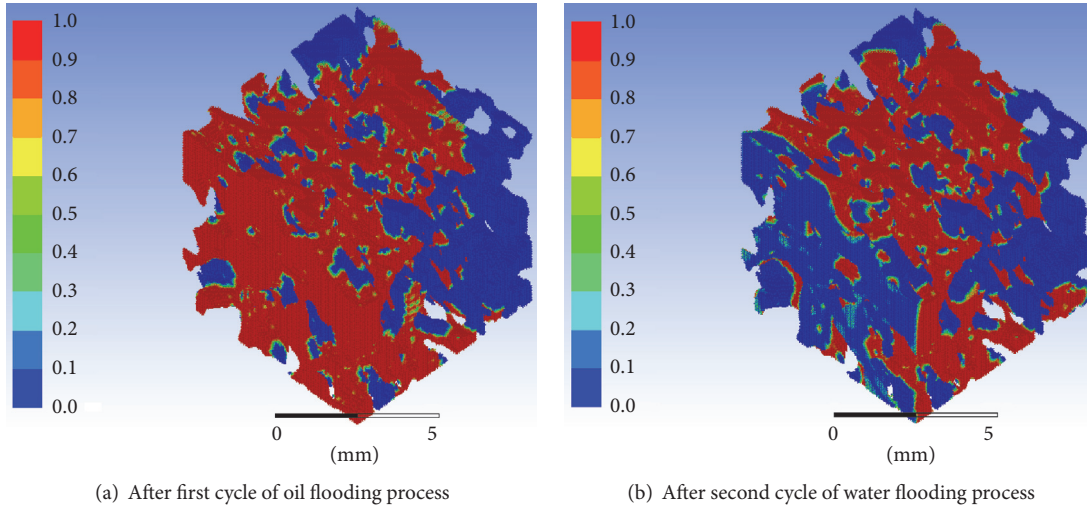


FIGURE 9: Oil volume fraction of MS1 after oil flooding and water flooding process; the red parts represent the oil phase.

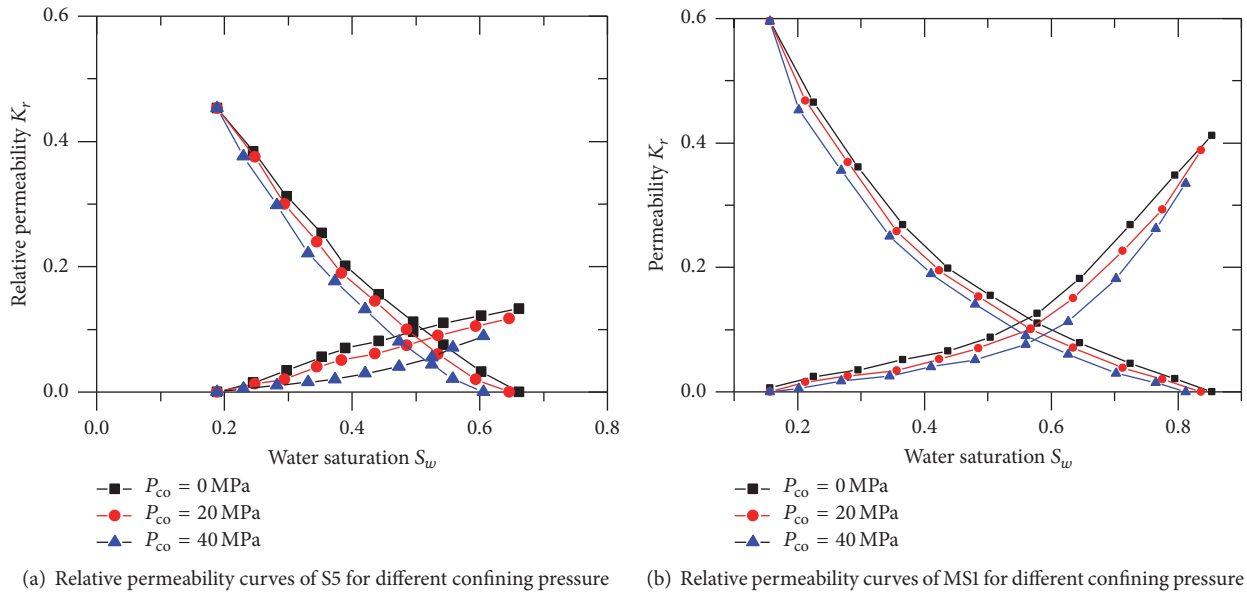


FIGURE 10: Effects of stress on the relative permeability.

oil recovery as well. Thus, high temperature of induced water is beneficial to enhance oil recovery, especially for heavy oil with high viscosity.

7. Conclusion

In this paper, a pore-scale study on the thermal-hydrumechanical coupling simulation of porous rock is conducted. Based on the structured mesh models of rock matrix and pore space, the effects of stress and temperature on the microstructure, porosity, permeability, and relative permeability in the linear elastic and linear thermal-expanding process are analyzed. The results indicate that the rising of effective pressure or temperature would lead to the decline of the porosity and permeability, and the drop ratio of permeability is larger than

that of porosity. The relative permeability of oil and water decreases with the increasing of the effective pressure, so it is with the oil recovery. However, the relative permeability of the two phases and oil recovery increase as a result of the fluid mobility improvement by the rising of temperature. Thus, high temperature and high pressure of induced water are beneficial to enhance oil recovery, especially for heavy oil with high viscosity. Though the petroleum industry is the main concern in this paper, the outcomes can be applied to other kinds of THM coupling process of porous media.

Conflicts of Interest

The authors declare that they have no conflicts of interest.

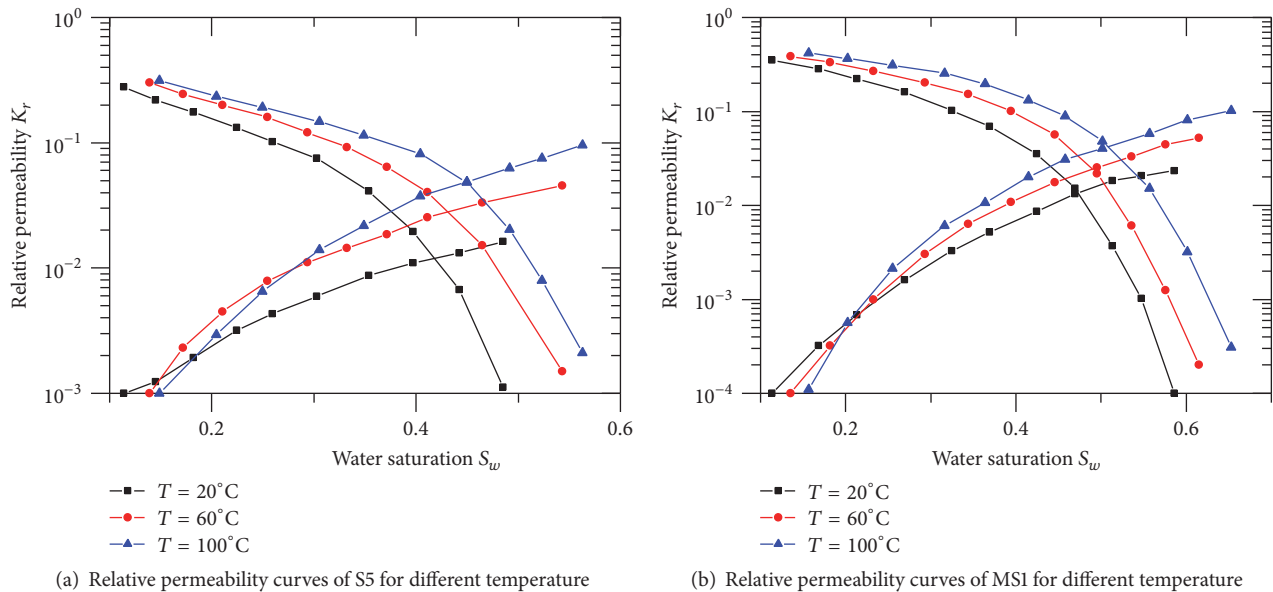


FIGURE 11: Effects of temperature on the relative permeability.

Acknowledgments

This paper is financially supported by National Science and Technology Major Project of China under Grant no. 2017ZX05013001-002.

References

- [1] J. Rutqvist, "Fractured rock stress-permeability relationships from in situ data and effects of temperature and chemical-mechanical couplings," *Geofluids*, vol. 15, no. 1-2, pp. 48–66, 2015.
- [2] S. A. Bea, U. K. Mayer, and K. T. B. Macquarrie, "Reactive transport and thermo-hydro-mechanical coupling in deep sedimentary basins affected by glaciation cycles: model development, verification, and illustrative example," *Geofluids*, vol. 16, no. 2, pp. 279–300, 2016.
- [3] Z. X. Sun, X. Zhang, Y. Xu et al., "Numerical simulation of the heat extraction in EGS with thermal-hydraulic-mechanical coupling method based on discrete fractures model," *Energy*, vol. 120, pp. 20–33, 2017.
- [4] D. Wu, Y. Zhang, R. Zhao, T. Deng, and Z. Zheng, "A coupled thermal-hydraulic-mechanical application for subway tunnel," *Computers & Geotechnics*, vol. 84, pp. 174–182, 2017.
- [5] O. Kolditz, S. Bauer, C. Beyer et al., "A systematic benchmarking approach for geologic CO₂ injection and storage," *Environmental Earth Sciences*, vol. 67, no. 2, pp. 613–632, 2012.
- [6] F. Dupray, C. Li, and L. Laloui, "THM coupling sensitivity analysis in geological nuclear waste storage," *Engineering Geology*, vol. 163, pp. 113–121, 2013.
- [7] M. F. Kanfar, Z. Chen, and S. S. Rahman, "Fully coupled 3D anisotropic conductive-convective porothermoelasticity modeling for inclined boreholes," *Geothermics*, vol. 61, pp. 135–148, 2016.
- [8] L. Jing, "A review of techniques, advances and outstanding issues in numerical modelling for rock mechanics and rock engineering," *International Journal of Rock Mechanics and Mining Sciences*, vol. 40, no. 3, pp. 283–353, 2003.
- [9] M. Hassanizadeh and W. G. Gray, "General conservation equations for multi-phase systems: 1. Averaging procedure," *Advances in Water Resources*, vol. 2, pp. 131–144, 1979.
- [10] L. Jing, O. Stephansson, C. F. Tsang, L. J. Knight, and F. Kautsky, *DECOVALEX II Project Executive Summary*, No. SKI-R-99-24, Swedish Nuclear Power Inspectorate, 1999.
- [11] M. Sahimi, *Flow and Transport in Porous Media and Fractured Rock: From Classical Methods to Modern Approaches*, John Wiley & Sons, New York, NY, USA, 2011.
- [12] K. R. Rajagopal, A. Z. Szeri, and W. Troy, "An existence theorem for the flow of a non-newtonian fluid past an infinite porous plate," *International Journal of Non-Linear Mechanics*, vol. 21, no. 4, pp. 279–289, 1986.
- [13] J. Rutqvist, D. Barr, R. Datta et al., "Coupled thermal-hydrological-mechanical analyses of the Yucca Mountain Drift Scale Test—comparison of field measurements to predictions of four different numerical models," *International Journal of Rock Mechanics and Mining Sciences*, vol. 42, no. 5-6, pp. 680–697, 2005.
- [14] T. V. Gerya and D. A. Yuen, "Robust characteristics method for modelling multiphase visco-elasto-plastic thermo-mechanical problems," *Physics of the Earth and Planetary Interiors*, vol. 163, no. 1–4, pp. 83–105, 2007.
- [15] P.-Z. Pan, X.-T. Feng, X.-H. Huang, Q. Cui, and H. Zhou, "Coupled THM processes in EDZ of crystalline rocks using an elasto-plastic cellular automaton," *Environmental Geology*, vol. 57, no. 6, pp. 1299–1311, 2009.
- [16] L. Laloui, M. Nuth, and L. Vulliet, "Experimental and numerical investigations of the behaviour of a heat exchanger pile," *International Journal for Numerical and Analytical Methods in Geomechanics*, vol. 30, no. 8, pp. 763–781, 2006.
- [17] L. C. Li, C. A. Tang, S. Y. Wang, and J. Yu, "A coupled thermo-hydrologic-mechanical damage model and associated application in a stability analysis on a rock pillar," *Tunnelling and Underground Space Technology*, vol. 34, pp. 38–53, 2013.

- [18] O. Stephanson, L. Jing, and C. F. Tsang, *Coupled Thermo-hydro-mechanical Processes of Fractured Media: Mathematical and Experimental Studies*, vol. 79, Elsevier, Amsterdam, The Netherlands, 1997.
- [19] J. Taron, D. Elsworth, and K.-B. Min, "Numerical simulation of thermal-hydrologic-mechanical-chemical processes in deformable, fractured porous media," *International Journal of Rock Mechanics & Mining Sciences*, vol. 46, no. 5, pp. 842–854, 2009.
- [20] B. Vásárhelyi and A. Bobet, "Modeling of crack initiation, propagation and coalescence in uniaxial compression," *Rock Mechanics and Rock Engineering*, vol. 33, no. 2, pp. 119–139, 2000.
- [21] H. T. Hall, "Some high-pressure, high-temperature apparatus design considerations: equipment for use at 100 000 atmospheres and 3000°C," *Review of Scientific Instruments*, vol. 29, no. 4, pp. 267–275, 1958.
- [22] G. J. Fischer and M. S. Paterson, "Measurement of permeability and storage capacity in rocks during deformation at high temperature and pressure," *International Geophysics*, vol. 51, pp. 213–252, 1992.
- [23] T.-F. Wong, C. David, and W. Zhu, "The transition from brittle faulting to cataclastic flow in porous sandstones: mechanical deformation," *Journal of Geophysical Research B: Solid Earth*, vol. 102, no. 2, pp. 3009–3025, 1997.
- [24] H. Li, H. Guo, S. Zhou, Z. Meng, and X. Wang, "NMR analysis of movable remaining oil of low permeability reservoir," *Journal of Southwest Petroleum University (Science & Technology Edition)*, vol. 38, no. 1, pp. 119–127, 2016 (Chinese).
- [25] S. Iglauer, A. Paluszny, C. H. Pentland, and M. J. Blunt, "Residual CO₂ imaged with X-ray micro-tomography," *Geophysical Research Letters*, vol. 38, no. 21, pp. 1440–1441, 2011.
- [26] T. Bultreys, M. A. Boone, M. N. Boone et al., "Fast laboratory-based micro-computed tomography for pore-scale research: illustrative experiments and perspectives on the future," *Advances in Water Resources*, vol. 95, pp. 341–351, 2015.
- [27] P. Liu, Y. Ju, P. G. Ranjith, Z. Zheng, and J. Chen, "Experimental investigation of the effects of heterogeneity and geostress difference on the 3D growth and distribution of hydrofracturing cracks in unconventional reservoir rocks," *Journal of Natural Gas Science and Engineering*, vol. 35, pp. 541–554, 2016.
- [28] K. Hadley, "Comparison of calculated and observed crack densities and seismic velocities in westerly granite," *Journal of Geophysical Research*, vol. 81, no. 20, pp. 3484–3494, 1976.
- [29] F. M. Ezzein and R. J. Bathurst, "A transparent sand for geotechnical laboratory modeling," *Geotechnical Testing Journal*, vol. 34, no. 6, pp. 590–601, 2011.
- [30] T. Bultreys, W. De Boever, and V. Cnudde, "Imaging and image-based fluid transport modeling at the pore scale in geological materials: a practical introduction to the current state-of-the-art," *Earth-Science Reviews*, vol. 155, pp. 93–128, 2016.
- [31] R. Hilfer and T. Zauner, "High-precision synthetic computed tomography of reconstructed porous media," *Physical Review E*, vol. 84, no. 6, Article ID 062301, 2011.
- [32] M. J. Blunt, B. Bijeljic, H. Dong et al., "Pore-scale imaging and modelling," *Advances in Water Resources*, vol. 51, pp. 197–216, 2013.
- [33] P. V. Marcke, B. Verleye, J. Carmeliet, D. Roose, and R. Swennen, "An improved pore network model for the computation of the saturated permeability of porous rock," *Transport in Porous Media*, vol. 85, no. 2, pp. 451–476, 2010.
- [34] P. Mohammadmoradi and A. Kantzas, "Pore-scale permeability calculation using CFD and DSMC techniques," *Journal of Petroleum Science and Engineering*, vol. 146, pp. 515–525, 2016.
- [35] Z. Liu and H. Wu, "Pore-scale study on flow and heat transfer in 3D reconstructed porous media using micro-tomography images," *Applied Thermal Engineering*, vol. 100, pp. 602–610, 2016.
- [36] A. Ferrari and I. Lunati, "Direct numerical simulations of interface dynamics to link capillary pressure and total surface energy," *Advances in Water Resources*, vol. 57, no. 9, pp. 19–31, 2013.
- [37] P. Mohammadmoradi and A. Kantzas, "Petrophysical characterization of porous media starting from micro-tomographic images," *Advances in Water Resources*, vol. 94, pp. 200–216, 2016.
- [38] J. Liu, R. Song, and M. Cui, "Numerical simulation on hydromechanical coupling in porous media adopting three-dimensional pore-scale model," *The Scientific World Journal*, vol. 2014, Article ID 140206, 8 pages, 2014.
- [39] S. Q. Yang, *Strength Failure and Crack Evolution Behavior of Rock Materials Containing Pre-Existing Fissures*, Science Press, Beijing, China, 2015.
- [40] R. Song, J. Liu, and M. Cui, "A new method to reconstruct structured mesh model from micro-computed tomography images of porous media and its application," *International Journal of Heat and Mass Transfer*, vol. 109, pp. 705–715, 2017.
- [41] *ANSYS User's Guide*, ANSYS, 2012.
- [42] J. U. Brackbill, D. B. Kothe, and C. Zemach, "A continuum method for modeling surface tension," *Journal of Computational Physics*, vol. 100, no. 2, pp. 335–354, 1992.
- [43] H. A. Sheldon and A. Ord, "Evolution of porosity, permeability and fluid pressure in dilatant faults post-failure: implications for fluid flow and mineralization," *Geofluids*, vol. 5, no. 4, pp. 272–288, 2005.

Research Article

Computing and Comparing Effective Properties for Flow and Transport in Computer-Generated Porous Media

Rebecca Allen and Shuyu Sun

King Abdullah University of Science and Technology, Thuwal 23955-6900, Saudi Arabia

Correspondence should be addressed to Shuyu Sun; shuyu.sun@kaust.edu.sa

Received 18 October 2016; Accepted 7 December 2016; Published 13 February 2017

Academic Editor: Micol Todesco

Copyright © 2017 Rebecca Allen and Shuyu Sun. This is an open access article distributed under the Creative Commons Attribution License, which permits unrestricted use, distribution, and reproduction in any medium, provided the original work is properly cited.

We compute effective properties (i.e., permeability, hydraulic tortuosity, and diffusive tortuosity) of three different digital porous media samples, including in-line array of uniform shapes, staggered-array of squares, and randomly distributed squares. The permeability and hydraulic tortuosity are computed by solving a set of rescaled Stokes equations obtained by homogenization, and the diffusive tortuosity is computed by solving a homogenization problem given for the effective diffusion coefficient that is inversely related to diffusive tortuosity. We find that hydraulic and diffusive tortuosity can be quantitatively different by up to a factor of ten in the same pore geometry, which indicates that these tortuosity terms cannot be used interchangeably. We also find that when a pore geometry is characterized by an anisotropic permeability, the diffusive tortuosity (and correspondingly the effective diffusion coefficient) can also be anisotropic. This finding has important implications for reservoir-scale modeling of flow and transport, as it is more realistic to account for the anisotropy of *both* the permeability and the effective diffusion coefficient.

1. Introduction

When modeling subsurface flow and transport in a reservoir, it is common practice to represent the geological formation with effective properties instead of resolving the precise location of fluid and solid phase. Effective properties such as permeability, diffusivity, and tortuosity can be computed from pore-scale modeling of fluid flow and transport through a porous media sample (i.e., a core sample) taken from a geological formation. Permeability and effective diffusivity are the well-known and important properties used in Darcy- and reservoir-scale flow and transport equations, while tortuosity is given less importance and subject to multiple definitions. Tortuosity is generally defined as a ratio between the effective path traveled by a species and the unit length of the domain. As noted in [1], different types of tortuosity (geometric, hydraulic, diffusive, dispersive, and electrical) are distinguished by the type of species transport under consideration. Hydraulic tortuosity refers to the effective path traveled by a fluid particle driven by a force, while diffusive tortuosity refers to the effective path traveled by a species driven by molecular diffusion [1].

Pore-scale modeling is performed on digital samples of porous media, which can be obtained using imaging and conversion techniques as those described in [2, 3], or by using an algorithm that generates samples which possess the same statistical characteristics of a real porous media sample [4–6]. Table 1 presents a summary of studies which used either *real* or *computer-generated* porous media samples; real refers to a digital sample obtained by imaging and conversion to binary form, and computer-generated refers to a digital sample obtained by an algorithm or random reconstruction. We note that Table 1 is only a short list of *recent* works on the topic, and that pore-scale simulation to obtain effective properties dates back to Cancelliere et al. [7] and possibly earlier.

In regard to obtaining effective properties at the pore-scale, we are motivated to distinguish between two different types of tortuosity (namely, hydraulic and diffusive) that have been identified. While a few studies have compared tortuosity definitions and have shown they are indeed quantitatively different within the same pore structure [8, 9], other studies continue to use these definitions interchangeably or do not distinguish the type of tortuosity they are computing.

TABLE 1: Recent work using real or computer-generated porous media samples: comparison of sample types, porosities, and computed properties.

Study	Real sample	Computer-generated sample	Porosity range	Effective properties computed
[16]		3D fibrous material (membrane)	0.45–0.9	permeability, hydraulic tortuosity
[15]	3D samples: Fontainbleau (F), Berea (B), Carbonate (C)	Sphere pack	F: 0.147, B: 0.184, C: 0.247, Spheres: 0.343	Permeability, electrical resistivity, among others
[14]		2D staggered cylinders, 3D body-centered-cubic spheres	0.25–0.98	Permeability, hydraulic tortuosity
[53]	3D vuggy limestone		0.16–0.81	Permeability
[21]	3D samples of volcanic tuff, glass bead column, sandpack, sandstones, carbonates	3D samples generated by level-set percolation	Real: 0.43, 0.6 Generated: 0.35, 0.6	Permeability, hydraulic tortuosity
[12]	3D carbonate, sandpacks, sandstone		0.17–0.38	Permeability
[22]		3D samples generated by spherical/nonspherical grain models	0.05–0.55	Permeability, hydraulic tortuosity
[13]		2D randomly distributed freely overlapping squares	0.367–0.99	Hydraulic tortuosity

The usefulness of hydraulic tortuosity becomes apparent when formulating a prediction for permeability, such as the Kozeny-Carman equation. Also, tortuosity can be seen as a more intuitive quantity for fluid flow and transport through a pore geometry than permeability or the effective diffusion coefficient.

The outline of this work is as follows: first we will conduct a literature review on the methods commonly used to compute the effective properties of digital porous media; then we will present the details of these methods we employed herein, followed by three example geometries (in-line array of uniform shapes, staggered-array of squares, and randomly distributed squares) and our obtained trends between porosity and the effective properties. We will conclude with the main findings of this work.

2. Literature Review on Effective Properties

2.1. Permeability. From the list given in Table 1, an important and commonly computed effective property is permeability. The notion of a porous media's permeability can be understood in terms of Darcy's equation, which computes a macroscale fluid velocity \mathbf{u} by

$$\mathbf{u} = -\frac{\mathbf{k}}{\mu} \cdot (\nabla P + \rho \mathbf{g}), \quad (1)$$

where \mathbf{k} is the permeability tensor. The other quantities are fluid viscosity and density μ and ρ , macroscale pressure P , and gravitational acceleration \mathbf{g} . Eqn. (1) can be obtained

mathematically by the method of homogenization [10, 11], which is a multiscale expansion of the fluid flow equations at the pore-scale (i.e., Stokes equations); see Section 3.

Out of the papers listed in Table 1, the general approach to compute the permeability field of the porous media sample is as follows:

- (1) *Obtain pore-scale geometries:* converted from real media sample images or generated by an algorithm that may or may not use media parameters such as grain size distribution and so on.
- (2) *Solve Stokes flow in pore space of media:* different solvers have been used (finite difference [12], finite element, lattice Boltzmann [13–16], explicit jump method [15], etc.), from academically developed codes, commercial software, and open-source software.
- (3) *Compute permeability:* assuming Darcy's equation is valid for the pore structure and flow field results, permeability is computed based on volume averages of velocity and pressure field.

A further step is to fit the permeability data to a formula which proposes a relationship between permeability and other porous media properties, known as the Kozeny-Carman (KC) equation [17, 18].

2.2. Kozeny-Carman Equation. An idealized pore geometry of parallel cylindrical channels was used to formulate the

Kozeny-Carman (KC) equation [17]. This equation proposes a relationship between porosity ϕ and permeability k , as well as other parameters such as hydraulic tortuosity τ_h and specific surface area S , and is

$$k = \frac{\phi^3}{\beta_k \tau_h^2 S^2}, \quad (2)$$

where β_k is a fitting parameter (sometimes referred to as the shape factor or the KC constant, though inconsistently) which is used to account for different channel configurations. A range of shape factors have been presented in literature [17, 18] which correspond to cylindrical, elliptical, rectangular, and triangular cross-sectional channel shapes. The parameter τ_h in (2) is the ratio between effective path traveled by the fluid particle and the length of the sample: $\tau_h = L_e/L_s$. In order to be consistent with the literature we are referencing and comparing our results against, we call this the hydraulic tortuosity, although we recognize that other work refers to τ_h^2 as the hydraulic tortuosity as similarly pointed out in [19]. The specific surface area is the ratio of fluid-solid interface area A^{f-s} to the total volume in the domain:

$$S = \frac{A^{f-s}_{\text{pores}}}{V_{\text{tot}}}. \quad (3)$$

Notice that (2) is not written as direction-specific. In fact, Carrier III [20] mentions that a limitation of the KC equation is that it does not explicitly account for anisotropy (a direction-specific property) even though the permeability of a real geological formation is typically greater in the horizontal than in the vertical direction. Despite this limitation, the Kozeny-Carman equation could still apply to direction-specific flows, where $k = k_{ii}$ and $\tau_h = \tau_{h,ii}$ are the permeability and hydraulic tortuosity in the principal directions, respectively.

Various studies [14, 21, 22] include attempts at establishing a modification to the KC equation, or propose a shape factor β_k for a specific class of porous media. Xu and Yu [23] compiled a list of 11 studies that proposed a modification to the KC equation, and each work corresponded to a different media type (textile, glass and fiber, square particles, sandstone, etc.). These proposed KC modifications included different parameters like effective porosity, percolation threshold, grain radius, fractal dimension, interconnectivity parameter, and others.

2.3. Tortuosity

2.3.1. Different Types of Tortuosity. As stated in the introduction, different types of tortuosities have been defined according to the type of species transport under consideration. Previous works have recognized this and some provided a comparison between specific tortuosity types [1, 8, 13]. What is important is that these forms of tortuosity should not be expected to be the same in the same porous structure [24], unless the pore size distribution is very narrow as pointed out in Ghanbarian et al. [8]. Perhaps unintentionally, a few previous studies have failed to distinguish the difference between tortuosity types. For example, Ohkubo [25] measured *diffusive* tortuosity through porous media that was

represented by plate-like obstacles and used the diffusive tortuosity results to compute fitting coefficients present in Koponen et al.'s [26] tortuosity-porosity trend equation. However, Koponen et al.'s [26] trend was empirically derived from simulation results that computed *hydraulic* tortuosity. Also, Sun et al. [27] applied the method of homogenization to the diffusive transport equation in order to compute the effective diffusion coefficient of periodic unit cells and the corresponding tortuosity. What they did not point out was that their approach gave them the diffusive tortuosity, while some of the trends they compared their results to were with respect to hydraulic tortuosity. Unless tortuosity types are quantitatively identical in the same class of porous media, use of a trend that is specific to one type of tortuosity should not immediately be used to describe the trend of another type of tortuosity.

A few studies [8, 9, 28] have focused on quantifying the difference between two specific tortuosities in the same structure. For example, hydraulic and electrical tortuosity were compared in both David [28] and Zhang and Knackstedt [9]. David [28] used a network as an analog for the media pore space, and the study focused on quantifying the tortuosity of the critical or preferential pathway, not the tortuosity of the entire flow field. Zhang and Knackstedt [9] computed tortuosity using the entire flow field which they obtained by numerical simulations for fluid flow (via lattice Gas Automata) and electrical current (via finite difference). Both of these works found that the hydraulic tortuosity was higher than electrical tortuosity in the same structure (up to an order of magnitude in low porosity configurations [9]). Once again, it was emphasized in Ghanbarian et al.'s [8] review that due to the difference between tortuosity types their models are not interchangeable.

Regarding diffusive tortuosity, both Quintard et al. [29] and Valdés-Parada et al. [1] stated that its quantification becomes more complex when more than just passive diffusion is occurring in the system. Valdés-Parada et al. [1] showed how the quantification of diffusive tortuosity can be different depending on the consideration of different mass transport terms (i.e., passive diffusion only, or diffusion with convection, reaction, or hydrodynamic dispersion). They concluded that the consideration of passive diffusion leads to the only appropriate definition of tortuosity. Their work focused on mass transport of species through fluid and did not measure hydraulic tortuosity.

2.3.2. Various Tortuosity-Porosity Trends. Many authors have theoretically or empirically derived tortuosity as a function of porosity (see Tables 2 and 3, where the tortuosity corresponds to fluid flow (hydraulic) and diffusive transport, resp.). Similar tables that summarize the theoretically and empirically derived trends proposed in literature appear in Shen and Chen [30], Boudreau [31], and Ahmadi et al. [32]. The most recent and complete comparison of tortuosity trends (or models) that we have seen to date was made by Ghanbarian et al. [8], which includes an explicit comparison between many different tortuosity types, namely, geometric, hydraulic, electrical, diffusive, and even tortuosity models, for unsaturated porous media.

TABLE 2: Past work on hydraulic tortuosity.

Study	Samples considered	Tortuosity–porosity fit	Notes
[54]	Packed beds	$\tau = 1 + p \ln\left(\frac{1}{\phi}\right)$	p is function of particle shape
[19]	2D random overlapping monosized squares, $0.5 < \phi < 1$	$\tau = 1 + 0.8(1 - \phi)$	
[26]	2D random overlapping monosized squares, $0.4 < \phi < 1$	$\tau = 1 + 0.65 \frac{1 - \phi}{(\phi - \phi_c)^{0.19}}$	ϕ_c is critical porosity
[24]	2D random overlapping monosized squares	$\tau \propto 1 + R \frac{S}{\phi}$	R is hydraulic radius, S is specific surface area
[13]	2D freely overlapping squares	$\tau \propto 1 + (1 - \phi)^{1/2}$	

TABLE 3: Past work on diffusive tortuosity.

Study	Samples considered	Tortuosity–porosity fit	Notes
[48]*	Array of cylinders (2D)	$\tau = 2 - \phi$	
[50]**	Diffusion of electrolytes in membrane	$\tau = \left(\frac{2 - \phi}{\phi}\right)^2$	
[52]	Bed of uniform spheres (applicable to overlapping, nonuniform spheres)	$\tau = 1 - \frac{1}{2} \ln \phi$	
[43]	Isotropic system, $0 < \phi < 0.5$	$\tau = \phi^{-0.4}$	
[31]	Fine-grained uncemented sediments	$\tau = (1 - \ln(\phi^2))^{1/2}$	
[55]	Isotropic representative unit cell	$\tau = \frac{\phi}{1 - (1 - \phi)^m}$	2D: $m = \frac{1}{2}$, 3D: $m = \frac{2}{3}$
[56]	Random, partial overlapping shapes	$\tau = \frac{1}{1 - \alpha(1 - \phi)}$	α = shape factor
[46]	Voronoi channel geometries, $0.2 < \phi < 0.6$	$\tau = (0.75\phi^{-1.0819})^{1/2}$	

* As referenced in [57].

** As referenced in [30, 31].

In the same way that the KC equation is specific to a given class of porous media, any porosity-tortuosity trend that is empirically derived depends on the porous media considered. Some authors rely on synthetic porous media, such as 2D randomly distributed squares [13, 19, 24, 26, 33, 34], 3D high porosity plate-like obstacles [25], or unit cells of centered uniform shapes, while others rely on real samples of media taken by imaging (via scanning electron microscopy (SEM) or X-ray microtomography) and digitization.

Additionally, it is important to note that empirically derived trends are applicable to a limited range of porosity only, as the trend was developed given simulated data of a certain porosity range. The porosity limit could be a result of the idealized geometry under consideration. Ghanbarian et al. [8] noticed that most tortuosity models were derived by focusing on the higher porosity structures and recommended that research moves more to focus on the lower porosity structure where the porosity approaches the percolation threshold (i.e., the minimum porosity for which flow is still possible through structure).

While many trends (or models) have been proposed to compute tortuosity as a function of porosity and other fitting parameters, Valdés-Parada et al. [1] stated that *any* definition of tortuosity should not be considered as a function of porosity but rather a function of the pore geometry only. The idea behind this statement seems to rest in the

fact that there is no universally agreed upon trend between tortuosity and porosity as pointed out by Matyka et al. [24] and that the geometrical features of a pore structure should have more influence on the overall tortuosity of flow or transport through the geometry than the value of porosity. However, since it is possible that a unique relationship between tortuosity and porosity can indeed exist for special classes of porous media [24], the development of tortuosity-porosity trends remains to be an insightful topic of research.

Also, Liu and Kitanidis [35] stated that tortuosity is a tensorial property. Despite this statement, the majority of work does not report directional-specific quantities which may leave the reader with the impression that tortuosity is a scalar quantity. A scalar quantity could be appropriate in pore geometries that exhibit an anisotropic microstructure while still exhibiting an isotropic macrostructure. For example, pore geometry composed of randomly distributed squares is geometrically anisotropic at the microscale; however the effective properties computed for the REV can be isotropic in nature. In this work, we demonstrate this point by example.

3. Methods to Compute Effective Properties

3.1. Permeability. The method of homogenization has been used to mathematically derive Darcy's equation from the Stokes equations. Through this derivation, the macroscopic

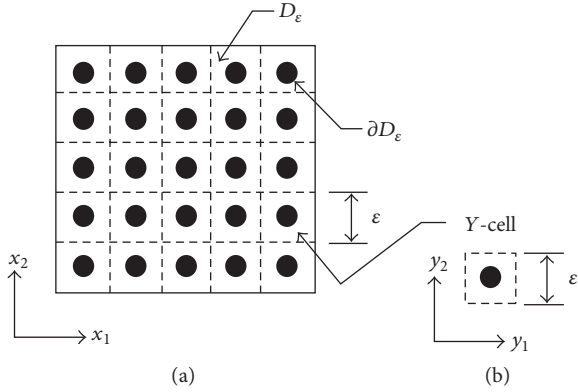


FIGURE 1: Macroscale (a) and microscale (b) domains used in the homogenization problem. The solid structure in the Y-cell illustrates the geometry of our first example: in-line array of solid shapes (i.e., circles or squares).

property known as permeability k_{ij} is defined as the spatial average of a *rescaled* pore space velocity $N_{ij}(y)$. In the following, we present the basic steps that lead to such a definition, and the reader is referred to [11] for more derivation details.

The problem is first defined by the macroscale (a) and microscale (b) systems shown in Figure 1, where the macroscale domain is comprised of repeating unit cells of size ϵ , which is comprised of both fluid and solid space. Due to periodicity, the macroscale domain of porosity ϕ can be represented by the unit cell with periodic boundaries. Assuming slow and steady flow of incompressible fluid through the pore space of the media, the governing equations are given by the Stokes equations as follows:

$$-\frac{\partial}{\partial x_i} p_\epsilon + \mu \frac{\partial}{\partial x_j} \frac{\partial}{\partial x_j} v_{\epsilon,i} = -\rho g_j, \quad (4)$$

$$\frac{\partial}{\partial x_i} v_{\epsilon,i} = 0, \quad (5)$$

where $i = 1, 2, 3$ and $j = 1, 2, 3$ and repeated indices imply summation, p is pressure, μ is fluid viscosity, v_i is the pore space fluid velocity, ρ is fluid density, and g_j is gravitational acceleration. The boundary condition at the fluid-solid interface is given by

$$v_i = 0, \quad (6)$$

which comes from the no-flow and no-slip boundary conditions. Although the slip boundary condition is necessary in certain contexts (such as gas flow and non-Newtonian fluid), the no-slip boundary condition is a valid assumption for viscous flow in porous media and is widely used in modeling studies of pore-scale flow [12, 15, 24].

In the Stokes equations, p_ϵ and $v_{\epsilon,i}$ can vary within the pore space and thus are functions of the macroscale (x) and microscale (ϵ); however μ , g , and ρ are treated as constants and are thus functions of the macroscale (x) only. By defining a fast variable $y = x/\epsilon$, the cell of unit length ϵ is scaled into the Y-cell (shown in Figure 1(b)), where $0 \leq y \leq 1$. A

multiscale expansion is used to write p_ϵ and $v_{\epsilon,i}$ in terms of their leading and higher order terms as follows:

$$p_\epsilon = p\left(x, \frac{x}{\epsilon}\right) = p^{(0)}(x, y) + \epsilon p^{(1)}(x, y) + \dots, \quad (7)$$

$$\begin{aligned} v_{\epsilon,i} &= v_i\left(x, \frac{x}{\epsilon}\right) \\ &= v_i^{(0)}(x, y) + \epsilon v_i^{(1)}(x, y) + \epsilon^2 v_i^{(2)}(x, y) + \dots \end{aligned} \quad (8)$$

Upon substitution of the expanded variables into (4)–(6) and then the collection of like order terms, the second-order pressure term and the third-order velocity term are

$$\begin{aligned} p^{(1)}(x, y) &= Q_j(y) \left(-\rho g_j + \frac{\partial}{\partial x_j} p^{(0)}(x) \right), \\ v^{(2)}(x, y) &= \frac{N_{ij}(y)}{\mu} \left(-\rho g_j + \frac{\partial}{\partial x_j} p^{(0)}(x) \right), \end{aligned} \quad (9)$$

such that $Q_j(y)$ and $N_{ij}(y)$ satisfy

$$-\frac{\partial}{\partial y_i} Q_j(y) + \frac{\partial}{\partial y_k} \frac{\partial}{\partial y_k} N_{ij}(y) = \delta_{ij}, \quad (10)$$

$$\frac{\partial}{\partial y_i} N_{ij}(y) = 0, \quad (11)$$

with the fluid-solid boundary condition given by

$$N_{ij}(y) = 0. \quad (12)$$

In the above formulation, $Q_j(y)$ and $N_{ij}(y)$ are functions of the microscale only and are independent of macroscale quantities μ , ρ , and g_j . They can be thought of as rescaled pressure and pore space velocity, respectively, and (10)–(11) can be thought of as rescaled Stokes equations to be solved within the Y-cell. In (10), δ_{ij} is the Kronecker delta function ($\delta_{ij} = 1$ for $i = j$, and $\delta_{ij} = 0$ for $i \neq j$).

Upon further mathematical steps (collecting of like order terms, taking the spatial average over the cell, and applying the divergence theorem and the periodicity of the cell), the spatial average of $v^{(2)}(x, y)$ in the cell is found to be divergence free; $\nabla \cdot \langle v^{(2)}(x, y) \rangle_y = 0$. This implies that the macroscopic flow equation is satisfied by Darcy's equation (1), that is,

$$\begin{aligned} \frac{\partial}{\partial x_i} \left(\frac{k_{ij}}{\mu} \left(\frac{\partial}{\partial x_j} p(x) - \rho g_j \right) \right) &= 0 \rightarrow \\ \frac{\partial}{\partial x_i} u_i(x) &= 0, \end{aligned} \quad (13)$$

where $p(x)$ is the macroscale pressure and $u_i(x)$ is the macroscale velocity, when the full permeability tensor for an n -dimensional problem is defined as

$$k_{ij} := \langle N_{ij}(y) \rangle_y = \frac{1}{Y} \int_Y N_{ij}(y) dY, \quad (14)$$

where Y is the volume of the Y -cell (solid and fluid space combined).

In this work, we use the staggered grid finite difference method (i.e., the marker and cell or MAC scheme [36]) for the numerical solution of the rescaled Stokes problem defined by (10)–(12) in the Y -cell. Our numerical implementation using a matrix-oriented approach is explained in [37]. To illustrate the numerical scheme, let us consider the following Stokes problem (in its original form before being rescaled by homogenization) in two-dimensional space: find the pore space velocity $v = (v^x, v^y)^T$ and the pressure p such that

$$-\mu\Delta v + \nabla p = f, \quad \text{in } \Omega := (0, L_x) \times (0, L_y), \quad (15)$$

$$\nabla \cdot v = 0, \quad \text{in } \Omega, \quad (16)$$

$$v = \mathbf{0}, \quad \text{on } \partial\Omega, \quad (17)$$

where the velocity has a unique solution while the pressure is unique up to an additive constant. Here L_x and L_y denote the length of the rectangular domain Ω in the x - and y -directions, respectively.

To construct a staggered grid finite difference scheme for the Stokes problem, we introduce a possibly nonuniform grid of Ω as follows:

$$0 = x_0 < x_1 < \dots < x_M = L_x, \quad (18)$$

$$0 = y_0 < y_1 < \dots < y_N = L_y.$$

The grid is comprised of fluid and solid cells (each cell being fully occupied by one phase), and the computational scheme acts uniquely on the computational cells belonging to the fluid. The pressure at the (fluid) cell center $(x_{i+1/2}, y_{j+1/2})$ is $p(x_{i+1/2}, y_{j+1/2})$ approximated by $p_{i+1/2, j+1/2}$. Similarly, we approximate the x -velocity v^x at each x -edge (fluid) center $v^x(x_i, y_{j+1/2})$ by $v_{i, j+1/2}^x$, and the y -velocity v^y at each y -edge (fluid) center $v^y(x_{i-1/2}, y_j)$ by $v_{i-1/2, j}^y$.

By integrating the x -component of (15) over cell $\Omega_{i, j+1/2} = (x_{i-1/2}, x_{i+1/2}) \times (y_j, y_{j+1})$, we have

$$\begin{aligned} & - \left[\int_{y_j}^{y_{j+1}} \left(\frac{\partial v^x}{\partial x}(x_{i+1/2}, y) - \frac{\partial v^x}{\partial x}(x_{i-1/2}, y) \right) dy \right. \\ & \left. + \int_{x_{i-1/2}}^{x_{i+1/2}} \left(\frac{\partial v^x}{\partial y}(x, y_{j+1}) - \frac{\partial v^x}{\partial y}(x, y_j) \right) dx \right] \\ & + \int_{y_j}^{y_{j+1}} (p(x_{i+1/2}, y) - p(x_{i-1/2}, y)) dy \\ & = \int_{\Omega_{i, j+1/2}} f^x(x, y) dx dy. \end{aligned} \quad (19)$$

We then approximate those edge integrals by midpoint values and the volume integral by its center value and divide both sides by $|\Omega_{i, j+1/2}| = (x_{i+1/2} - x_{i-1/2})(y_{j+1} - y_j)$.

By introducing the following forward and backward difference operators:

$$\Delta_x^+ v_{i, j+1/2}^x = \frac{v_{i+1, j+1/2}^x - v_{i, j+1/2}^x}{x_{i+1} - x_i}, \quad (20)$$

$$\Delta_x^- p_{i+1/2, j+1/2} = \frac{p_{i+1/2, j+1/2} - p_{i-1/2, j+1/2}}{x_{i+1/2} - x_{i-1/2}}$$

and similar notations for operations in the y -direction, we can express the results as

$$\begin{aligned} & - \frac{\Delta_x^+ v_{i, j+1/2}^x - \Delta_x^- v_{i, j+1/2}^x}{x_{i+1/2} - x_{i-1/2}} - \frac{\Delta_y^+ v_{i, j+1/2}^x - \Delta_y^- v_{i, j+1/2}^x}{y_{j+1} - y_j} \\ & + \Delta_x^- p_{i+1/2, j+1/2} = f_{i, j+1/2}^x. \end{aligned} \quad (21)$$

Similarly, by integrating the y -component of (15) over cell $\Omega_{i-1/2, j} = (x_{i-1}, x_i) \times (y_{j-1/2}, y_{j+1/2})$ and then applying midpoint quadrature rule, we can obtain

$$\begin{aligned} & - \frac{\Delta_x^+ v_{i-1/2, j}^y - \Delta_x^- v_{i-1/2, j}^y}{x_i - x_{i-1}} - \frac{\Delta_y^+ v_{i-1/2, j}^y - \Delta_y^- v_{i-1/2, j}^y}{y_{j+1/2} - y_{j-1/2}} \\ & + \Delta_y^- p_{i-1/2, j+1/2} = f_{i-1/2, j}^y. \end{aligned} \quad (22)$$

By integrating (16) over cell $\Omega_{i-1/2, j+1/2} = (x_i - x_{i-1}) \times (y_j, y_{j+1})$, we obtain its discrete form

$$\Delta_x^- v_{i, j+1/2}^x + \Delta_y^+ v_{i-1/2, j}^y = 0. \quad (23)$$

Eqns. (21)–(23) form a linear equation system for the pressure and velocity, and the equation system defines the MAC scheme for the Stokes problem of (15)–(17). Note that the no-flow boundary condition supplies the zero velocity component that acts normal to any fluid-solid interface, and periodic conditions are applied along the domain's external boundaries.

We apply this numerical scheme to solve the set of rescaled Stokes equations in Eqns. (10)–(12). Our computer-generated media samples are 2-dimensional (2D); thus the set is solved with different forcings δ_{ij} where $i = 1, 2$ and $j = 1, 2$. Upon obtaining the rescaled pore space velocity $N_{ij}(y)$ in the Y -cell, we then compute the full permeability tensor by (14). If our computer-generated media are characterized by a nondiagonal tensor, we determine the principal components of the permeability tensor by diagonalization [11, 38]. The notation used in our results section is \mathbf{k} and \mathbf{k}^* for the permeability tensors in coordinate systems $\{\mathbf{x}\}$ and $\{\mathbf{x}^*\}$, respectively, that is,

$$\begin{aligned} \mathbf{k} &= \begin{bmatrix} k_{11} & k_{12} \\ k_{21} & k_{22} \end{bmatrix}, \quad \text{in } \{\mathbf{x}\} \implies \\ \mathbf{k}^* &= \begin{bmatrix} k_{\max} & 0 \\ 0 & k_t \end{bmatrix}, \quad \text{in } \{\mathbf{x}^*\}. \end{aligned} \quad (24)$$

3.2. Hydraulic Tortuosity. The approach commonly used in literature to compute hydraulic tortuosity is presented in Koponen et al. [19, 26], and further validation of this approach is given in Duda et al. [13]. In this approach, the

hydraulic tortuosity τ_h or a particular direction is computed based on the pore space fluid velocities driven by a force. For example, the hydraulic tortuosity of flow that is driven in the x direction is

$$\tau_{h,x} = \frac{\langle v_{\text{mag}} \rangle_{\Omega}}{\langle v_x \rangle_{\Omega}}, \quad (25)$$

where $\langle \cdot \rangle_{\Omega}$ is the spatial average in the unit cell domain Ω , v_{mag} is the magnitude of the fluid velocities (i.e., the fluid speed), and v_x is the velocity component in the x direction. The spatial average of v_x in Ω is

$$\langle v_x \rangle_{\Omega} = \frac{1}{|V|} \int_{V_f} v_x^f dV_f = \frac{1}{|V|} \sum_{i,j} v_x^f(i,j) \Delta V_f, \quad (26)$$

where V is the volume of Ω (pore and solid space combined), V_f is the fluid space, and the integral is taken over the fluid space only. The spatial average for v_{mag} is taken in the same way. The tortuosity in the y direction is computed in a similar manner as follows:

$$\tau_{h,y} = \frac{\langle v_{\text{mag}} \rangle_{\Omega}}{\langle v_y \rangle_{\Omega}}, \quad (27)$$

where the velocity is the solution for flow driven in the y direction. We note that (25) and (27) correspond to the hydraulic tortuosity as we have defined it in Section 2.2; that is $\tau_h = L_e/L_s$. If the term τ_h^2 which appears in the Kozeny-Carmen equation is labelled as the hydraulic tortuosity, then (25) and (27) should be squared.

While this method has been used in many works (i.e., [26, 33, 39, 40]), other approaches to compute hydraulic tortuosity have been proposed. For example, Matyka et al. [24] took measurements of streamlines that passed through a given cross-sectional area in the domain with a constant flux (i.e., not all streamlines in the domain would be measured). The aim of this approach is to capture the hydraulic tortuosity of the main conducting channels in a pore geometry. Also, Ahmadi et al. [32] formulated analytical functions for hydraulic tortuosity based on volume averaging of mass balance equations.

In our work we follow Koponen et al.'s [19, 26] approach as given by (25)–(27); however we do not compute the pore space velocity fields v_x and v_y explicitly. Instead, during the permeability computation for our 2D pore geometries, we obtain the rescaled pore space velocity fields N_{ij} in the Y -cell, where $i = 1, 2$ and $j = 1, 2$. It can be seen that N_{11} and N_{21} are related to v_x and v_y , respectively, for flow that is driven by $\mathbf{g} = (\hat{g}, 0)$ and that N_{12} and N_{22} are related to v_x and v_y , respectively, for flow that is driven by $\mathbf{g} = (0, \hat{g})$. Thus, it is mathematically equivalent to compute the hydraulic tortuosities by

$$\begin{aligned} \tau_{h,x} &= \frac{\langle \sqrt{N_{11} + N_{21}} \rangle_{\Omega}}{\langle N_{11} \rangle_{\Omega}}, \\ \tau_{h,y} &= \frac{\langle \sqrt{N_{12} + N_{22}} \rangle_{\Omega}}{\langle N_{22} \rangle_{\Omega}}, \end{aligned} \quad (28)$$

where Ω refers to the domain of the Y -cell, and the spatial averages of N_{ij} are computed in the same way as shown by (26). Since the numerical scheme computes N_{ij} on the fluid edge-centers, we compute the fluid cell-center quantities by averaging across the grid cells, where $N_{ij} = 0$ on the fluid-solid interfaces as per the boundary condition in (12).

As mentioned, we diagonalize the permeability tensor to obtain the principal permeability components and the principal directions θ and $\theta + \pi/2 := \hat{\theta}$. Thus, in order to make an appropriate comparison between direction-specific permeability and hydraulic tortuosity, we compute the hydraulic tortuosity in these principal directions. For example, τ_h in the principal direction θ is

$$\tau_{h,\theta} = \frac{\langle |N_i^{\theta}| \rangle_{\Omega}}{\langle N_{\theta} \rangle_{\Omega}}, \quad (29)$$

where $|N_i^{\theta}| = \sqrt{(N_1^{\theta})^2 + (N_2^{\theta})^2}$ and where N_1^{θ} , N_2^{θ} , and N_{θ} are obtained by vector transformations from N_{ij} . τ_h in the other principal direction $\hat{\theta}$ is similarly obtained. The notation we use in our results section is $\tau_{h,\text{max}} = \tau_{h,\theta}$ and $\tau_{h,t} = \tau_{h,\hat{\theta}}$.

3.3. Effective Diffusion Coefficient and Diffusive Tortuosity. The problem is similarly defined by the two scales illustrated in Figure 1. Within the pore space, the diffusive and convective transport of a species of concentration c is given by

$$\begin{aligned} \frac{\partial}{\partial t} c_{\varepsilon} + \frac{1}{\varepsilon} v_{\varepsilon,i} \frac{\partial}{\partial x_i} c_{\varepsilon} &= \frac{\partial}{\partial x_i} D_{ij} \frac{\partial}{\partial x_j} c_{\varepsilon}, \\ n_i D_{ij} \frac{\partial}{\partial x_j} c_{\varepsilon} &= 0, \\ v_{\varepsilon,i} &= 0, \end{aligned} \quad (30)$$

where $v_{\varepsilon,i}$ is divergence free (5), ε implies the variables are functions of the microscale, and D_{ij} is the molecular diffusion coefficient. The last two equations give the boundary conditions on the fluid-solid interface. Using similar homogenization steps as presented in Section 3.1, the multiscale expansion

$$\begin{aligned} c_{\varepsilon} &= c \left(x, \frac{x}{\varepsilon} \right) \\ &= c^{(0)}(x, y) + \varepsilon c^{(1)}(x, y) + \varepsilon^2 c^{(2)}(x, y) + \dots \end{aligned} \quad (31)$$

and (8) are substituted into the governing transport equations (30). Upon collecting like order terms, the second-order term of c is

$$c^{(1)}(x, y) = P_k(x, y) \frac{\partial}{\partial x_k} c^{(0)}(x), \quad (32)$$

where $c^{(0)}(x)$ is the macroscale concentration and $P_k(x, y)$ satisfies

$$\frac{\partial}{\partial y_i} \frac{\partial}{\partial y_i} P_k(x, y) = 0, \quad (33)$$

$$n_i \frac{\partial}{\partial y_i} P_k(x, y) = -n_k, \quad (34)$$

where (34) gives the boundary condition and n_i is a unit vector normal to the fluid-solid interface (positive in the direction away from the fluid space). Eqns. (33) and (34) correspond to the assumption of an isotropic molecular diffusion coefficient, that is, $D_{ij} = D\delta_{ij}$. Upon further algebra and averaging over the Y -cell, the macroscale transport equation is obtained as follows:

$$\phi \frac{\partial}{\partial t} c(x) = \frac{\partial}{\partial x_i} D_{ik}^{\text{eff}*} \frac{\partial}{\partial x_k} c(x), \quad (35)$$

where the effective diffusion coefficient $D_{ik}^{\text{eff}*}$ is given by

$$\frac{D_{ik}^{\text{eff}*}}{D} = \frac{1}{Y} \int_Y \left(\delta_{ik} + \frac{\partial}{\partial y_i} P_k(x, y) \right) dY. \quad (36)$$

Intuitively, the more tortuous the porous media, the slower the rate of effective diffusion; thus a commonly used relationship between effective and molecular diffusivity is

$$D_{ik}^{\text{eff}*} = \frac{D\phi}{\tau_{d,ik}}, \quad (37)$$

where $\tau_{d,ik}$ is the diffusive tortuosity [41].

The above approach to compute the effective diffusion coefficient and the diffusive tortuosity has been used in several previous studies, which formulate (33)–(36) using the method of volume averaging [1, 42–45] or by the method of homogenization [27]. Other approaches to compute diffusive tortuosity include simulation of the diffusion process using a random walk [25] or numerically solving the microscale diffusion equation using lattice Boltzmann modeling [46]. Typically, the effective diffusivity is computed and then used to calculate diffusive tortuosity by the inverse relationship shown in (37).

By (36) and (37), diffusive tortuosity is computed by

$$\tau_{d,ik} = \left(I_{ik} + \frac{1}{|Y_f|} \int_{Y_f} \left(\frac{\partial}{\partial y_i} P_k(x, y) \right) dy_f \right)^{-1}, \quad (38)$$

where $Y_f = \phi Y$ and where $P_k(x, y)$ is the solution to (33) with the boundary condition in (34). This is the same formulation that was used in Sun et al. [27] by the method of homogenization and in Kim et al. [43] and Valdés-Parada et al. [1] by the method of volume averaging.

The full diffusive tortuosity can also be diagonalized using the same procedure outlined in Section 3.1 to obtain the components $\tau_{d,\text{max}}$ and $\tau_{d,t}$ corresponding to the principal directions. The rotation required to obtain the principal components of \mathbf{k}^* is not necessarily identical to the rotation required to obtain the principal components of τ_d^* , as will be shown by one of the following pore geometry examples (randomly distributed squares).

4. Results

While real geological formations are typically of low porosity ($\phi < 0.3$), we have generated several idealized geometries within the porosity range of $0.33 < \phi < 1$. These idealized

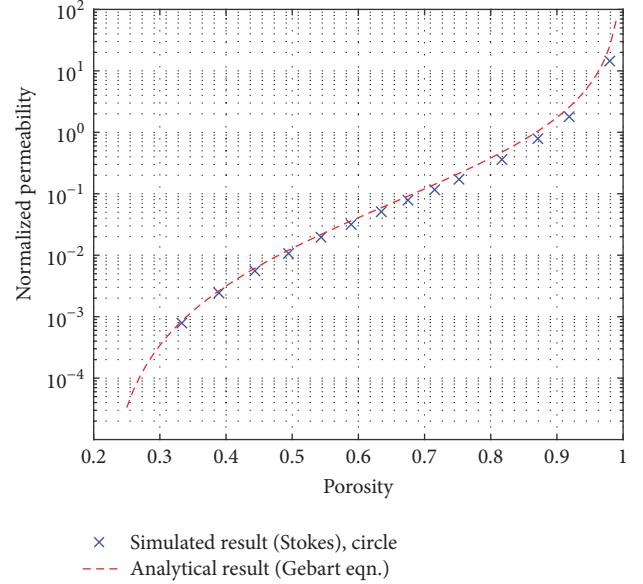


FIGURE 2: Permeability-positivity trend for in-line array of circles (i.e., infinitely long cylinders). Permeability units are nondimensional (i.e., unit length \times unit length). The permeability is isotropic and is normalized by r^2 , where r is the solid circle radius [47] analytical solution was given in (A.2).

geometries and porosities have been used in literature (see Table 1) and thus provide ground for comparison and opportunity to make useful comparisons of the effective properties in high porosity representations of porous media.

Permeability, hydraulic tortuosity, and diffusive tortuosity are computed for each pore geometry using the methods outlined in Sections 3.1, 3.2, and 3.3, respectively. Each pore geometry is generated by defining certain input parameters (i.e., radius of solid circle, side length of square, and density of randomly distributed squares), and these inputs are summarized in Table 4. By using a range of values for the input parameters, we obtain unit cells which we treat as representative elementary volumes over a range of porosities. After computing the permeability and tortuosity, we plot the data to observe permeability-positivity and tortuosity-positivity trends.

4.1. In-Line Array of Uniform Shapes. The unit cell, or Y -cell, in Figure 1(b) illustrates our first type of generated pore geometry, and the shape in the center of the cell is either a circle or square. A range of porosities of the unit cell are obtained by changing the radius of the solid circle or the length of the solid square centered in the cell.

4.1.1. Permeability and Hydraulic Tortuosity. The full permeability tensor was computed for $0.33 < \phi < 1$, and results are plotted in Figure 2. Following [14], we computed and plotted the analytical solution from Gebart [47] which is explained in Appendix A. Permeability is isotropic (i.e., $k_{xx} = k_{yy}$) for this pore geometry. The range of our simulated data fits well against the analytical solution. We computed

TABLE 4: Input parameters used to generate different pore-geometries (or different Y-cells) and their corresponding porosity ranges. In this table, cell refers to a cell in the mesh used to discretize the Y-cell.

Geometry	Initial mesh dimensions	Inputs	Porosity range
In-line array of shapes (see Figure 1)	50×50 cells (Y-cell length: 1 unit)	(a) Circle diameter: 44 to 8 cells (b) Square length: 48 to 2 cells	$0.33 < \phi < 1$ $0.07 < \phi < 1$
Staggered array of squares (see Figure 7)	100×50 cells (Y-cell length: $L_b = 0.5$ units, $a/b = 1$, $L_a/L_b = 1$ as per Figure 8)	Square length: 40 to 8 cells	$0.36 \leq \phi < 1$
Randomly distributed squares (see Figure 14)	100×100 cells (Y-cell length: 1 unit)	Increasing density of squares (with constant square length: 0.01 unit = 1 cell)	$0.45 \leq \phi < 1$

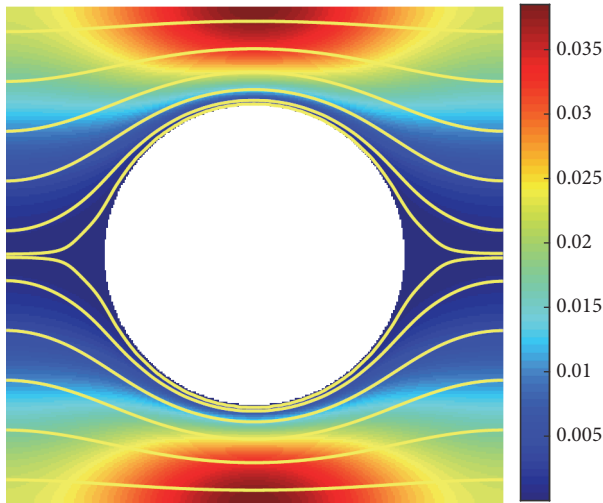


FIGURE 3: Fluid flow past a solid circle, $\phi = 0.71$, driven by g_x . Non-dimensional fluid speed (i.e., magnitude of velocities) is indicated by color, and flow path is indicated by flow lines (direction is left to right). Speed profile and flow path driven by g_y are same as shown but rotated 90 degrees.

our permeability data on increasingly finer meshes until the permeability converged within a 1% relative error. To reach this convergence criteria after starting with a mesh size of 50×50 , the lowest porosity cell required a refined mesh of 500×500 , and the highest porosity cell required 300×300 . The shape of the circular edge was refined at each mesh refinement in order to represent the circle as realistically as possible and to minimize artifacts caused by discretization.

We obtained the hydraulic tortuosity in the x and y directions, for porosities within the range $0.33 < \phi < 1$, with the same convergence criteria used to obtain permeability. Figure 3 illustrates the fluid speed and direction for a unit cell of $\phi = 0.71$, and the hydraulic tortuosity in both x and y directions were computed to be $\tau_{h,x} = \tau_{h,y} = 1.0185$. The fluid speed is highest in the pore space that is uninterrupted by the solid, and the flow lines indicate the direction is parallel to the macroscopic flow. The flow lines diverge in the region that is interrupted by the solid; however the fluid speed is essentially zero in that pore space. So, while these flow lines

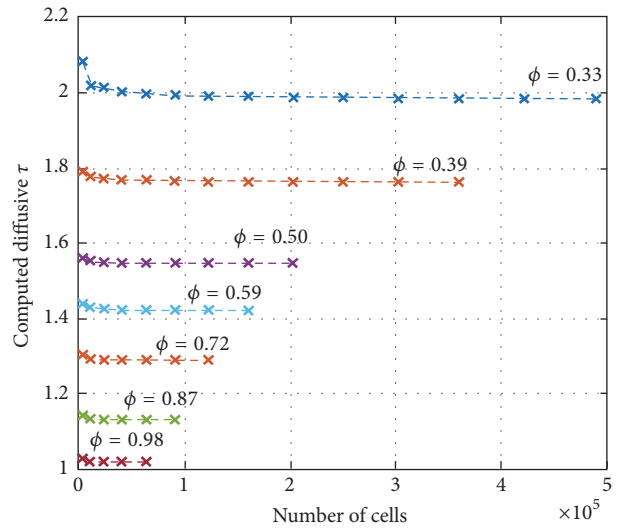


FIGURE 4: Number of grid cells required to reach converged τ_d (using a convergence criteria of 0.1% relative error) for select porosities of in-line array of circles.

appear to illustrate a tortuous pathway through this geometry, the tortuosity in either direction is in fact calculated to be ≈ 1 because the highest speeds are acting along a nontortuous pathway. In the pore space that is not restricted or interrupted in the direction parallel to the driving force, the fluid velocity is able to develop into the parabolic profile that characterizes channel flow.

4.1.2. Diffusive Tortuosity. We obtained the full diffusive tortuosity tensor on increasingly refined meshes until the tortuosity converged within a 0.1% relative error. Starting with a mesh of 50×50 , the lowest porosity required a refined mesh of 700×700 , while the highest porosity required 250×250 to meet the convergence criteria. Solid edges were also refined with mesh refinement, as mentioned previously. In Figure 4, we plot the convergence behavior of τ_d for a select number of porosity cases in order to illustrate that each porosity case convergences with similar behavior. Figure 5(a) illustrates the fields of P_k ($k = 1, 2$ or x, y) for a unit cell of $\phi = 0.71$, which were obtained by solving the homogenized problem

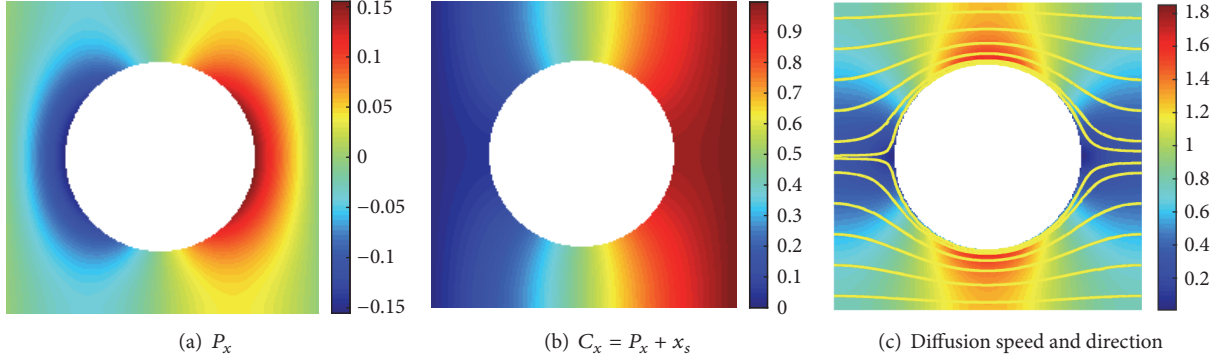


FIGURE 5: Fields for a unit cell of $\phi = 0.71$, comprised of a solid circle: (a) solution to the homogenized problem, (b) concentration field transformed from P_k , and (c) magnitude of concentration gradient $\sqrt{(\nabla_x C_x)^2 + (\nabla_y C_x)^2}$ (diffusion speed) and direction. The fields with respect to y are the same as shown above but rotated by 90 degrees.

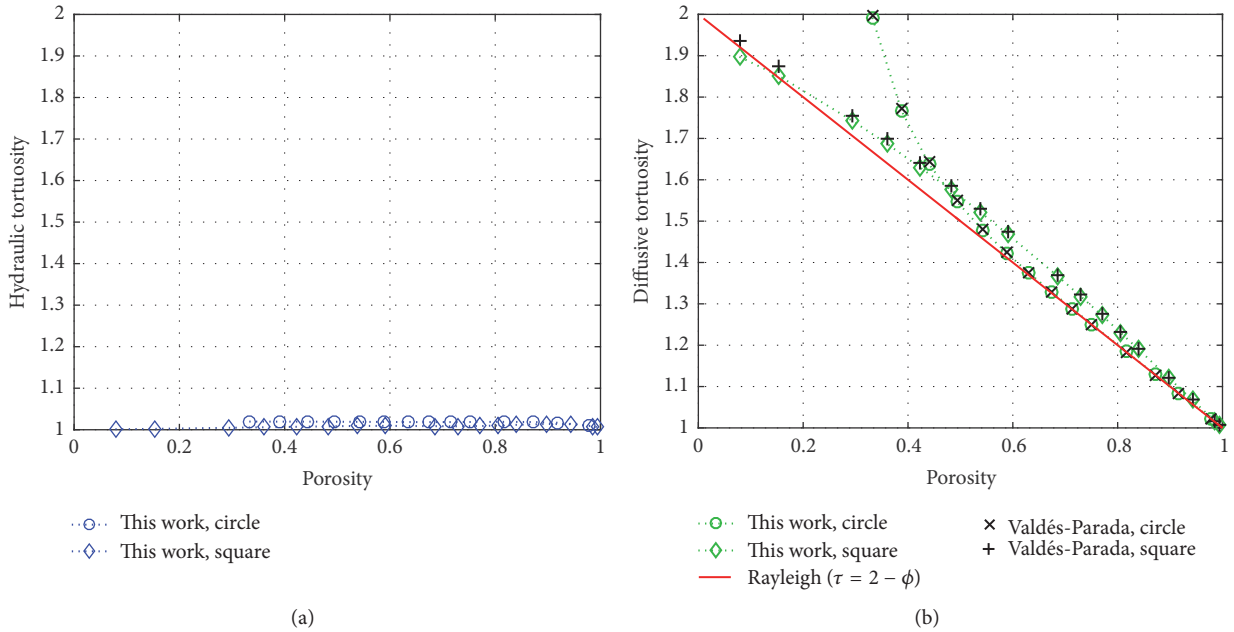


FIGURE 6: Tortuosity-positivity trends for in-line array of uniform shapes (circle or square). (a) Hydraulic tortuosity is a very weak function of porosity. (b) Diffusive tortuosity for in-line array of squares follows the analytical solution ($\tau = 2 - \phi$) from [48] closely, and both in-line array of squares and in-line array of circles match closely results by F. J. Valdés-Parada (provided via personal communication, December 3, 2016).

described in Section 3.3. The resulting diffusive tortuosity tensor is

$$\tau_d = \begin{bmatrix} \tau_{d,xx} & \tau_{d,xy} \\ \tau_{d,yx} & \tau_{d,yy} \end{bmatrix} = \begin{bmatrix} 1.2887 & -1 \times 10^{-16} \\ -1 \times 10^{-16} & 1.2887 \end{bmatrix}, \quad (39)$$

where $\tau_d = (\tau_d^t)^{-1}$. Notice the tensor is symmetric and diagonal (i.e., $\tau_{d,xy} = \tau_{d,yx} = 0$ to machine precision) and isotropic (i.e., $\tau_{d,xx} = \tau_{d,yy}$). To illustrate the passive diffusive transport through this geometry, we have illustrated the diffusion speed and direction in Figure 5(c), which was computed from the concentration field illustrated in Figure 5(b). This concentration field satisfies $\nabla^2 C = 0$ with Dirichlet boundary

conditions on the right and left boundaries such that the concentration gradient across the unit cell is one.

4.1.3. Comparison of Tortuosities for In-Line Array Unit Cells.

The comparison between our isotropic results for τ_h and τ_d illustrated in Figure 6 allows us to emphasize that these tortuosity types are quantitatively different. This may be surprising at first, since the streamlines in Figures 3 and 5(c) appear to indicate that the flow fields are relatively analogous. However, the fluid speeds shown in Figure 3 are such that the fastest moving flow exists along the nontortuous pathway, while the fastest passive diffusive transport (or highest concentration gradient) shown in Figure 5(c) exists along

TABLE 5: Hydraulic and diffusive streamline comparison: in-line array of circles, $\phi = 0.71$. Flow is from left to right. $(0, y_{s,j})$ indicate the starting location of the j th streamline.

	Hydraulic streamlines	Diffusive streamlines
$(0, y_{s,j})$	$\lambda(y_j)$ in Figure 3	$\lambda(y_j)$ in Figure 5(c)
0.05	1.0011	1.0010
0.15	1.0107	1.0103
0.25	1.0348	1.0348
0.35	1.0827	1.0852
0.45	1.1665	1.1814
0.495	1.2444	1.2732
0.505	1.2444	1.2732
0.55	1.1665	1.1814
0.65	1.0827	1.0852
0.75	1.0348	1.0348
0.85	1.0107	1.0103
0.95	1.0011	1.0010

the circle's rounded fluid-solid boundary. This difference in speeds (or streamline weights) leads to a quantitative difference between these two tortuosity types.

To further make our point, we quantitatively compare the hydraulic and diffusive streamlines in Figures 3 and 5(c). The length $\lambda(y)$ of 12 streamlines with starting positions given by $(0, y_{s,j})$ is tabulated in Table 5. These lengths are computed by $\lambda_j = l_j/L$, where l_j is the length of the j th streamline and $L = 1$ for the length of the pore geometry. This table reveals that the length (or tortuosity) of a hydraulic streamline is relatively similar to the diffusive streamline with the same starting location. However, the hydraulic speeds are such that the fastest moving flow exists along the nontortuous pathway, while the fastest diffusive flow (or highest concentration gradient) exists along the circle's rounded fluid-solid boundary. These speeds mean that individual streamlines contribute to the effective tortuosity with different weights; since the weight of an individual hydraulic streamline is different from the diffusive streamline, the overall hydraulic and diffusive tortuosity of the unit cell are expected to be quantitatively different.

In Figure 6, we plot the approximate analytical solution from Rayleigh [48], which is $\tau = 2 - \phi$ (see Table 3). Given a system comprised of a periodic array of cylinders, one can imagine that there is a limit as to how small the porosity can become before the pore space is no longer conducting. We find that the diffusive tortuosity data for in-line array of squares fits to this solution with an expected convex shape (comparison between Rayleigh's [48] analytical solution and simulated data for in-line array of squares was shown in Figure 4 of Valdés-Parada et al. [1]), but the data for in-line array of circles deviates as its critical porosity ($\phi_c = 1 - \pi/4 \approx 0.21$) is approached. At first glance, one might think the reason for this discrepancy is due to an inadequate mesh refinement: as the solid circle becomes larger, the fluid space between adjacent solids becomes smaller, and a finer mesh may be required to obtain an accurate solution. However,

the convergence of our in-line array of circles results was demonstrated in Figure 4. Furthermore, our results match quite closely those obtained by F. J. Valdés-Parada (provided via personal communication, December 3, 2016) using the finite element method. As such, our diffusive tortuosity rather is exhibiting validated convex and concave trends.

In terms of the hydraulic tortuosity, we observe that it is independent of porosity (or a very weak function of ϕ) for this isotropic (symmetrical) geometry. Regardless of the solid circle's radius, the fluid speeds are highest in the pore space that lies parallel to the driving force direction, as noted in Figure 3. Since the fluid speeds are highest along a nontortuous pathway, the tortuosity of the macroscopic flow through the unit cell is computed to be close to one. We can expect the scenario to be different for a geometry that contains solids which interrupt the main flow path, as seen in the next example of staggered solids.

4.2. Staggered-Array of Uniform Shapes. Figure 7 illustrates our second type of pore geometry. Unlike the previous pore geometry, staggered-array of uniform shapes is an anisotropic geometry. Input parameters to define this geometry are illustrated in Appendix B (Figure 8), and for the following staggered-array examples, $a/b = 1$ and $L_a/L_b = 1$. By varying the solid square length, a range of porosities are obtained.

4.2.1. Permeability and Hydraulic Tortuosity. The permeability for our second pore geometry was computed for a range of porosities. Starting with an initial mesh resolution of 100×50 , the meshes required refinement up to a maximum of 700×350 in order to meet the convergence criteria of $k_{rel\ error} < 1\%$.

This pore geometry configuration is anisotropic (i.e., $k_{xx} \neq k_{yy}$), and the trend of the principal permeabilities over the porosity range tested is shown in Figure 9. The analytical solution for an in-line array of cylinders (i.e., Gebart [47]) is plotted against our staggered-array permeability for comparison, while a fit is not expected. The permeability is characterized by an anisotropic ratio as follows:

$$\gamma = \frac{k_{yy}}{k_{xx}}, \quad (40)$$

where $k_{yy} > k_{xx}$ for all porosities studied, as shown in Figure 10.

The hydraulic tortuosity in the x and y directions was computed using the same convergence criteria used to obtain permeability. Our results for a staggered-array unit cell of $\phi = 0.73$ are shown in Figure 11 and the resulting hydraulic tortuosities were $\tau_{h,x} = 1.3539$ and $\tau_{h,y} = 1.0567$. In this example, the pore geometry is such that there is not a straight (or uninterrupted) flow path when the flow is driven in the x direction. However, there is a straight flow path when the flow is driven in the y direction. Due to this characteristic, we observe that the hydraulic flow is more tortuous in the x direction than in the y direction, which is confirmed by the anisotropic ratio for hydraulic tortuosity plotted in Figure 10. By observing Figure 11, we notice that the fluid speeds are highest in the pore regions located between two square corners. We also notice in Figure 11(a) that the

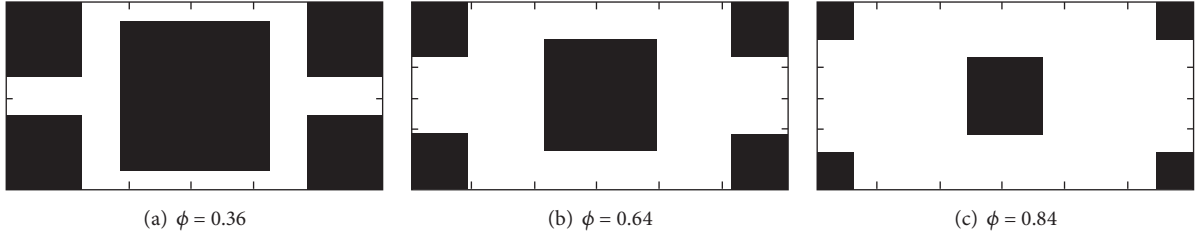


FIGURE 7: Unit cell for staggered-array of uniform shapes (i.e., squares), represented by cells with periodic boundaries and porosity ϕ . For all staggered-array examples: $a/b = 1$ and $L_a/L_b = 1$ (refer to Figure 8 for dimension details).

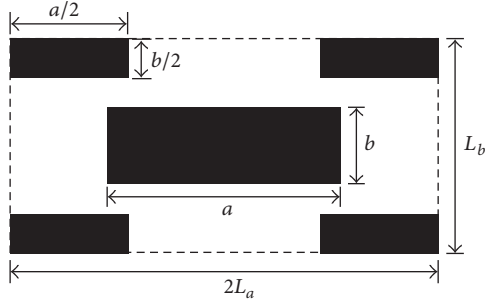


FIGURE 8: A staggered (anisotropic) unit cell with dimensions $\phi = 0.6$, $a/b = 3$, and $L_a/L_b = 1$.

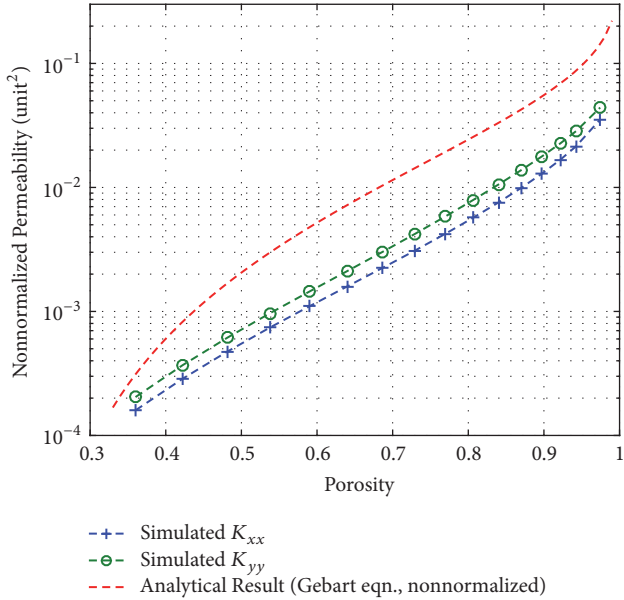


FIGURE 9: Permeability-porosity trend for staggered-array of squares.

fluid speed is close to being constant along a sinusoidal flow path which appears to occupy most of the pore space, except towards the fluid-solid boundaries. The horizontally driven flow is interrupted by the center square and causes the flow path to diverge. However, in Figure 11(b), the vertically driven

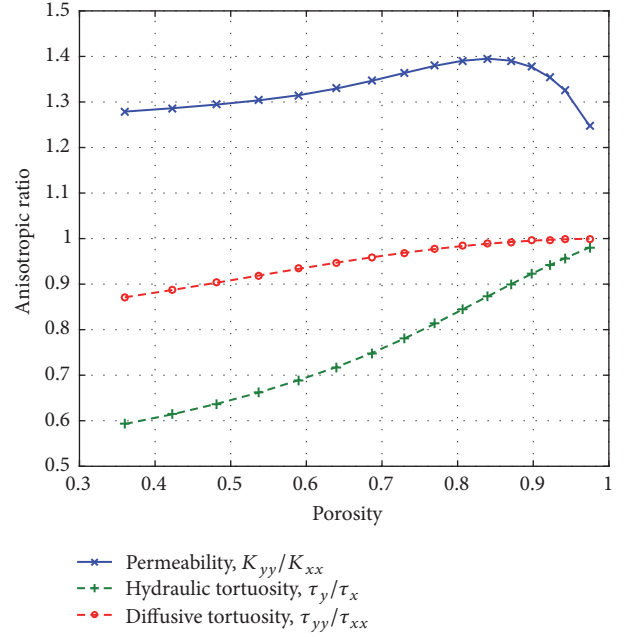


FIGURE 10: Anisotropic ratios in staggered-array of squares. For all porosities, the anisotropic ratios for hydraulic and diffusive tortuosity are less than one, indicating that the hydraulic flow and passive diffusive transport are more tortuous in the x direction than in the y direction. The hydraulic flow is more permeable in the y direction.

flow is not interrupted to the extent that would cause the flow path to become sinusoidal. Instead, the geometry of the pore space allows for a straight flow path to develop. We do not notice this sinusoidal flow path of constant speed, rather we notice that the speed is more localized (i.e., speed is highest between adjacent solid corners and lowest along solid square sides).

4.2.2. Diffusive Tortuosity. We obtained the full diffusive tortuosity tensor for this staggered geometry using a convergence criteria of $\tau_{d,rel\ error} < 0.1\%$. Starting with a uniform mesh of 100×50 , the lowest porosity required a refined mesh of 1000×500 while the highest porosity required 200×100 in order to meet the convergence criteria. Results for a

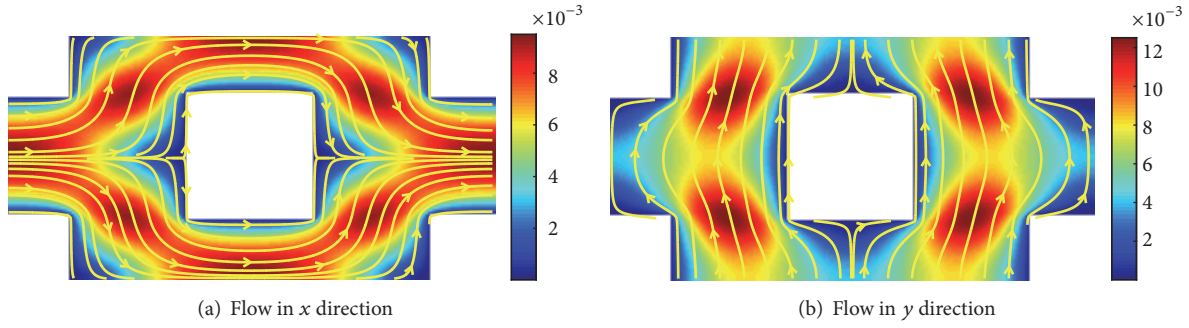


FIGURE 11: Fluid flow through a staggered-array of squares, $\phi = 0.73$. Fluid speed (i.e., magnitude of velocities) is indicated by color, and direction is indicated by flow lines. Fluid speed is nondimensional.

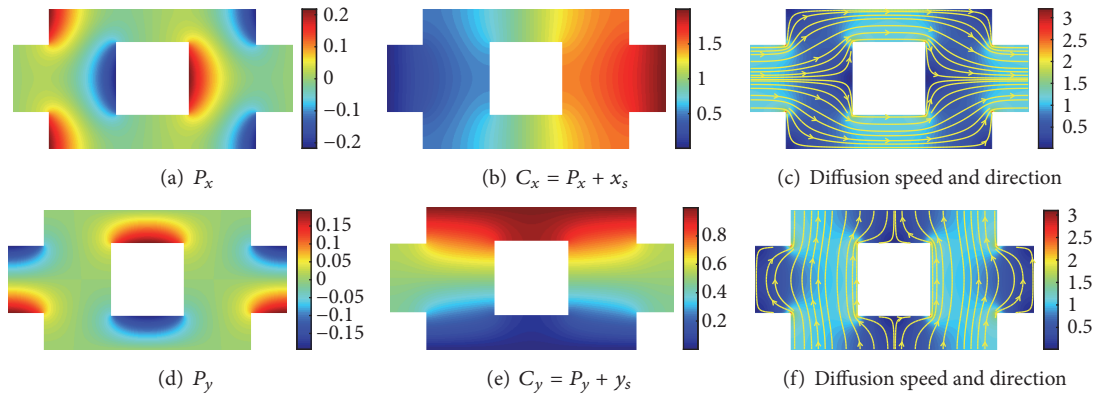


FIGURE 12: Fields for a staggered-array unit cell of $\phi = 0.73$: (a, d) solution to the homogenization problem, (b, e) concentration field transformed from P_k (assuming concentration gradient across unit cell is one), and (c, f) magnitude of concentration gradient (diffusion speed) and direction.

staggered-array unit cell of $\phi = 0.73$ are shown in Figure 12, and the diffusive tortuosity tensor is

$$\tau_d = \begin{bmatrix} \tau_{d,xx} & \tau_{d,xy} \\ \tau_{d,yx} & \tau_{d,yy} \end{bmatrix} = \begin{bmatrix} 1.3514 & -1 \times 10^{-15} \\ 1 \times 10^{-17} & 1.3092 \end{bmatrix}, \quad (41)$$

where the tensor is symmetric and diagonal (i.e., $\tau_{d,xy} = \tau_{d,yx} = 0$ to machine precision) and anisotropic (i.e., $\tau_{d,xx} \neq \tau_{d,yy}$). In this geometry of staggered squares, $\tau_{d,xx} > \tau_{d,yy}$, and thus passive diffusive transport is more tortuous in the x direction due to an interrupted flow path.

4.2.3. Comparison of Tortuosities for Staggered-Array Unit Cells. Our results for hydraulic and diffusive tortuosity over the range of porosities are plotted in Figure 13. Diffusive tortuosity data from Ryan et al. [49] and Kim et al. [43] (both obtained from Kim et al. [43]) are also plotted for comparison. While the works of Ryan et al. [49] and Kim et al. [43] were based on using the method of volume averaging to obtain the boundary-value problem for diffusivity presented in Section 3.3, we are able to compare our results to theirs since both homogenization and volume averaging

approaches lead to the same boundary-value problem. To solve the boundary-value problem presented in Section 3.3, Ryan et al. [49] employed the finite difference method while Kim et al. [43] employed the boundary element method. We note that one of Kim et al.'s [43] data points shown in Figure 13(b) unexpectedly corresponds to a diffusive tortuosity of less than 1. After confirming this value from Table 6 of their work (where $a/b = 1$, $L_a/L_b = 1$), we do not have an explanation as to how τ_d could be smaller than 1, other than a possible typographical error. Since they reported values for the parameter $\phi \mathbf{D}^{\text{eff}}/D$ rather than τ_d explicitly, it may not have been easily apparent to them that one of their values corresponded to $\tau_d < 1$. (Refer to Appendix B where we explain more about the notation as well as compare our numerical results against more of their results.) Regarding the diffusive tortuosity, our simulated data fits closely to these two literature data; however, in Figure 13(a) we observe our $\tau_{d,xx}$ data diverges at lower porosities ($\phi < 0.6$). While the exact reason for this discrepancy is not clear, possible causes may be attributed to the difference in numerical methods employed or the geometry of the staggered-array (especially at lower porosities that contain very narrow flow channels).

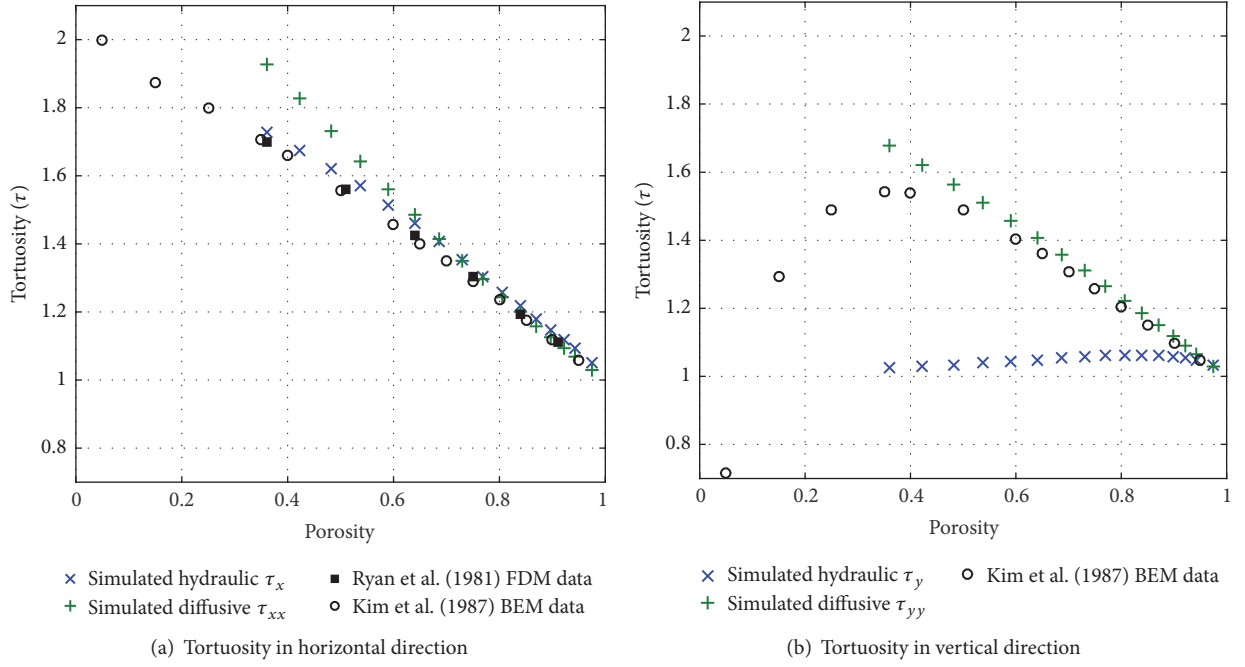


FIGURE 13: Tortuosity-porosity trends for staggered-array of squares. Simulated data is plotted against (diffusive) data from literature that employed finite difference (FD) and boundary element (BE) methods. In this geometry, hydraulic tortuosity in the y direction is a weak function of porosity.

TABLE 6: Data comparison for diffusive tortuosity.

ϕ	Unit cell specs.		Kim et al.'s [43] results		Our results	
	a/b	L_a/L_b	$\phi D_{xx}^{\text{eff}}/D$	$\phi D_{yy}^{\text{eff}}/D$	$\phi \tau'_{d,xx}$	$\phi \tau'_{d,yy}$
0.74	15	1	0.741	0.028	0.7396	0.0234
0.80	15	1	0.787	0.116	0.7959	0.1107
0.88	15	1	0.870	0.225	0.8675	0.2197
0.91	15	1	0.902	0.301	0.9112	0.3022
0.6	1	1	0.427	0.412	0.3863	0.4125
0.65	1	1	0.478	0.464	0.4397	0.4630
0.7	1	1	0.535	0.519	0.4940	0.5140
0.75	1	1	0.596	0.581	0.5625	0.5782
0.8	1	1	0.664	0.648	0.6439	0.6547
0.85	1	1	0.738	0.722	0.7221	0.7289
0.9	1	1	0.819	0.805	0.8064	0.8097
0.95	1	1	0.907	0.897	0.8976	0.8985
0.6	3	1	0.494	0.161	0.4814	0.1620
0.65	3	1	0.562	0.209	0.5465	0.2085
0.7	3	1	0.627	0.270	0.6187	0.2693
0.75	3	1	0.689	0.345	0.6747	0.3453
0.8	3	1	0.748	0.434	0.7350	0.4341
0.85	3	1	0.807	0.541	0.8012	0.5405
0.9	3	1	0.868	0.667	0.8627	0.6637
0.95	3	1	0.933	0.817	0.9282	0.8201

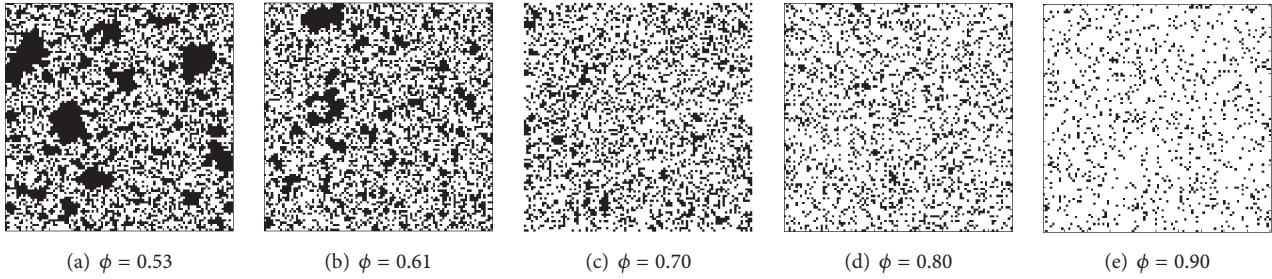


FIGURE 14: Various pore structures for randomly distributed squares geometry. Any fluid area isolated from flow path is converted to solid; thus ϕ is effective porosity of geometry.

Figure 13(b) shows a closer fit between our $\tau_{d,yy}$ data to the literature data, in comparison with the fit shown in Figure 13(a). Since the narrowest channels exist at the lowest porosity and are oriented in the x direction, this observation implies our diffusive tortuosity data may be sensitive to the mesh resolution between adjacent solid boundaries. Despite the difference between our data to that reported in literature, the anisotropic nature of this geometry is evident from our results. Over the range of porosities, we observe that the hydraulic flow is predominantly parallel to the driving force, unless an obstacle prevents a straight flow path. Thus, $\tau_{h,x} > \tau_{h,y}$ for all porosities as shown in Figure 13, and $\tau_{h,y}$ is a very weak function of porosity. The anisotropic ratios of the tortuosities are

$$\frac{\tau_{h,y}}{\tau_{h,x}}, \quad \frac{\tau_{d,yy}}{\tau_{d,xx}} \quad (42)$$

and are plotted in Figure 10, along with the permeability ratio previously defined. Over the whole porosity range, both anisotropic ratios of the tortuosities are less than one, indicating the hydraulic flow and passive diffusive transport are more tortuous in the x direction than in the y direction. The hydraulic tortuosity shows a greater degree of anisotropy than diffusive tortuosity because $\tau_{h,x} \approx 1$ for all porosities while $\tau_{h,y}$ increases towards the lower porosities.

4.3. Randomly Distributed Squares. Our third pore geometry generated comprised of randomly distributed squares, which is a type commonly used in literature (e.g., [13, 19, 26]). In those works, squares are freely overlapping; however, in our work, our square size is equivalent to the cell size of the initial mesh resolution, and thus no squares overlap. In this geometry, periodic boundary conditions were implemented by checking for the existence of any solid-fluid interfaces along the external boundaries of the domain, and, if detected, no-flow boundary conditions were applied at the interface (i.e., the velocity component acting normal to the fluid-solid interface was assigned a value of zero in the system of equations). We imposed the constraint given by Koza et al. [34] (i.e., the ratio of obstacle length to domain length < 0.01) which was recommended to avoid anisotropic-related statistical errors. This same constraint was also respected

in Duda et al. [13]. Our geometries ranged from (effective) porosities of $0.45 < \phi < 0.99$. Example pore geometries are shown in Figure 14. Our algorithm to generate these pore geometries included a step to check for any fluid sites that may be isolated from the flow path, which if found were changed to be solid sites. By filling in the isolated fluid sites, we were able to represent the effective porosity of the geometry, as noted in Koponen et al. [26]. Since lower porosity geometries contained more solid sites than higher porosities, they were especially susceptible to isolated fluid sites. Filling in the isolated sites created large solids within the pore geometry (especially noted in Figure 14(a)), and the impact of these solids on results will be discussed. Due to the nature of this randomly generated geometry, we used between 8 and 11 realizations of a given porosity between 0.46 and 0.95 and 5 realizations for the porosity of 0.97. Thus the following results are presented as averaged quantities with error bars to indicate the spread between the maximum and minimum quantities computed.

4.3.1. Permeability and Hydraulic Tortuosity. We computed permeability using a convergence criteria of $k_{rel\ error} < 1\%$. Starting with an initial mesh of 100×100 , the lowest porosity required a refined mesh of 400×400 and the highest porosity required 200×200 to meet the convergence criteria.

The full permeability tensors (in coordinate system $\{\mathbf{x}\}$) for these pore geometries were symmetric and nondiagonal; thus a transformation was done to obtain the diagonal tensor in the principal coordinate system $\{\mathbf{x}^*\}$. The full permeability components and diagonal permeability components are plotted in Figure 15. The nature of the anisotropic ratio of the diagonal permeability tensor will be discussed and shown later in Figure 16(b).

We computed hydraulic tortuosity from the flow field results which were obtained using the convergence criteria for permeability previously mentioned. For a configuration case of $\phi = 0.7$, results for hydraulic flow are shown in Figure 17 and the computed hydraulic tortuosities are $\tau_{h,x} = 1.3727$ and $\tau_{h,y} = 1.3393$. From Figure 17, the tortuous nature of the fluid pathways is evident. We note that a few ‘‘hot spots’’ of fastest moving fluid (with speeds $v_{mag} > 5 \times 10^{-5}$) exist in the geometry, while the rest of the pore space is characterized by moderate ($1 \times 10^{-5} < v_{mag} < 5 \times 10^{-5}$) to slow ($v_{mag} < 1 \times 10^{-5}$) moving fluid. The high speeds

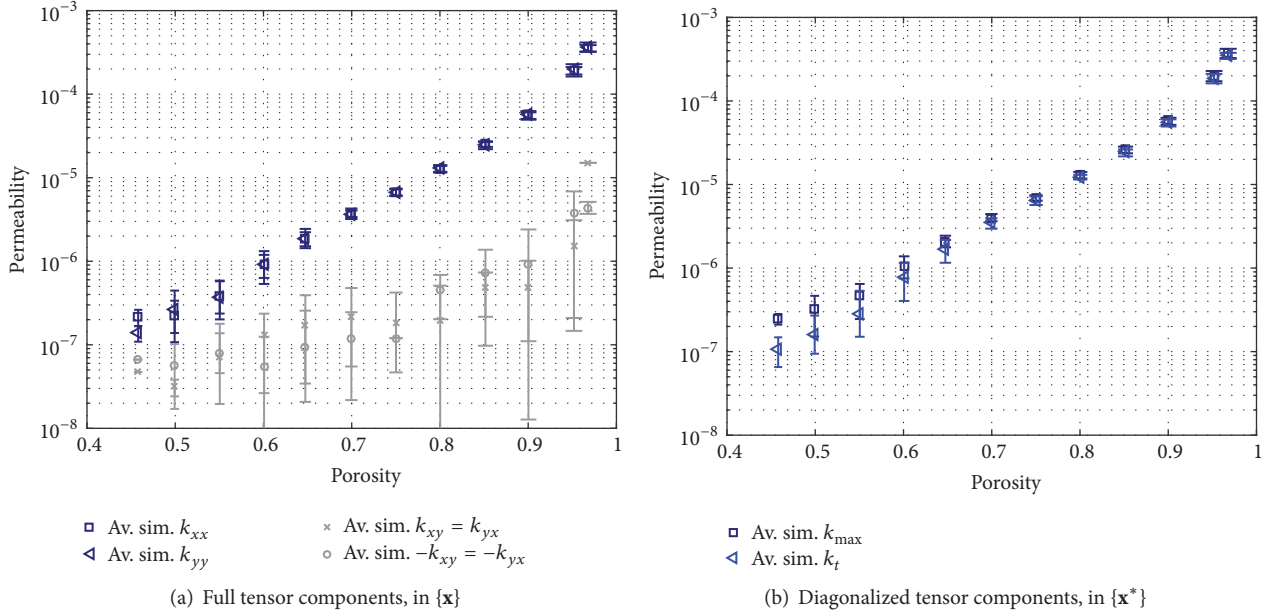


FIGURE 15: Permeability-porosity trend for randomly distributed squares. The full permeability tensor contains nonzero off-diagonal components (absolute values are plotted; however negative and positive quantities are indicated by different symbols) and is diagonalized to obtain the principal permeability components, k_{\max} and k_t . $\{\mathbf{x}\}$ and $\{\mathbf{x}^*\}$ are related by rotation angle θ_k , which is plotted in Figure 16(a). The anisotropic ratio of the principal components is plotted in Figure 16(b).

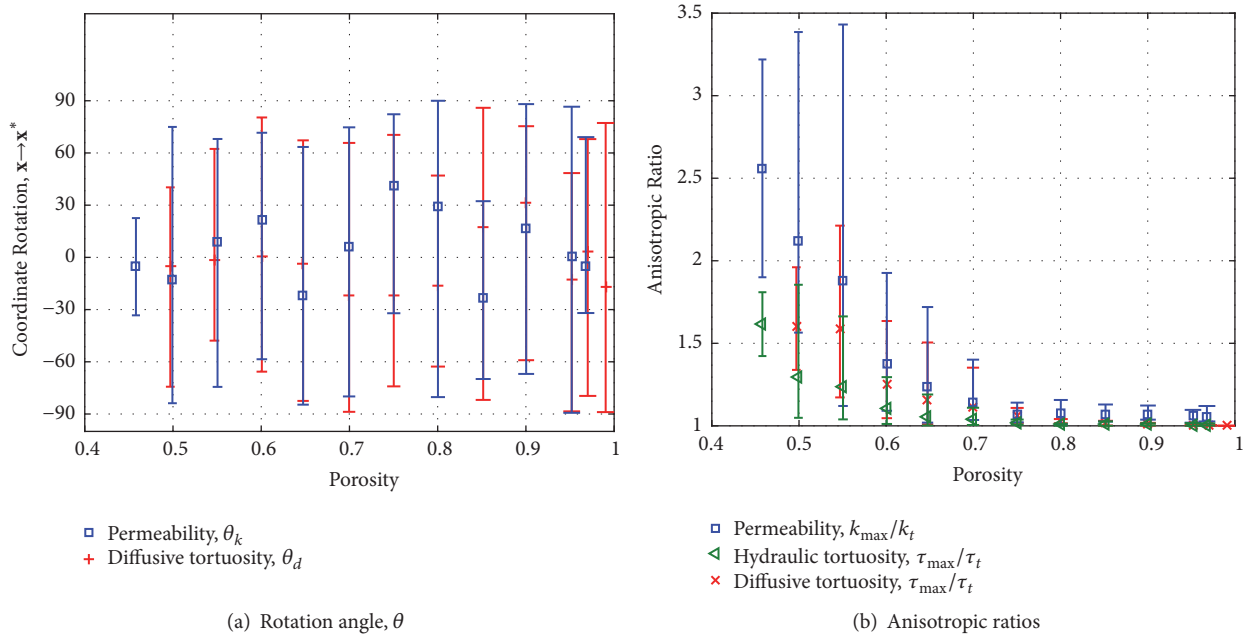


FIGURE 16: Anisotropic ratios in geometries comprised of randomly distributed squares: (a) rotation to obtain diagonal tensors (\mathbf{k}^* and τ_d^*) is independent of porosity; (b) anisotropic ratios of diagonal tensors and anisotropic ratio of hydraulic tortuosity. At lower porosities ($\phi < 0.6$), anisotropic properties have been induced.

exist within the pore geometry's narrow channels, and, upon magnifying these regions, we observed a parabolic velocity profile indicative of channel flow. While Figure 17 illustrates fluid flow in the y direction only, similar characteristics were found for flow in the x direction; thus we have omitted

those illustrations. The computed hydraulic tortuosity at this porosity is essentially isotropic; that is, $\tau_{h,x} \approx \tau_{h,y}$. So while the geometry is comprised of randomly distributed squares, the overall geometry exhibits an isotropic hydraulic tortuosity. (However, this is not the case at lower porosity

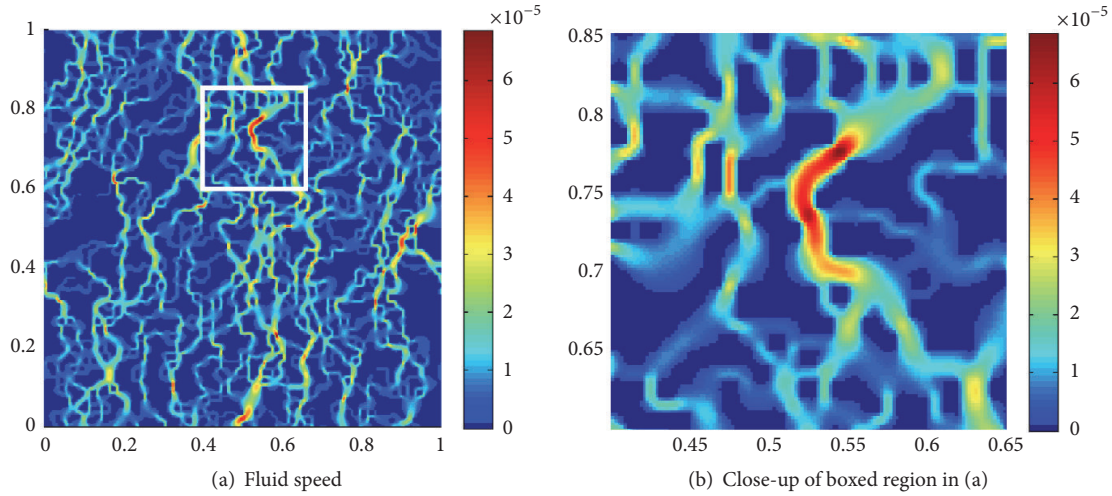


FIGURE 17: Flow (driven by g_y) through randomly distributed squares, $\phi = 0.70$. Nondimensional fluid speed is indicated by color. Zero speed at solid sites is kept as dark blue for clarity of illustration (while these fluid speeds do not actually exist).

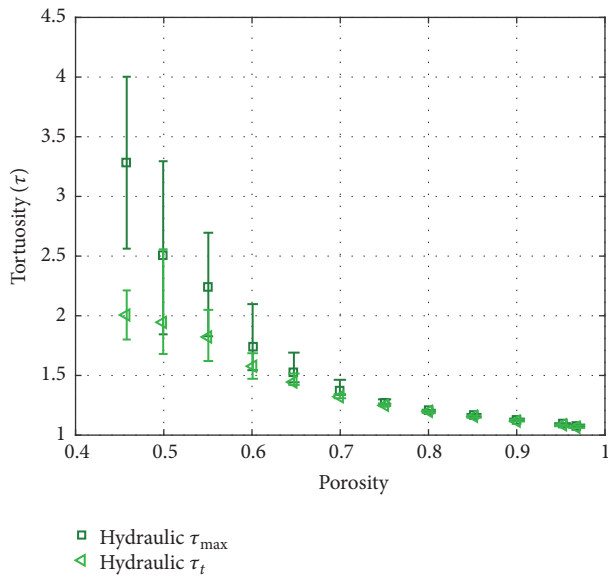


FIGURE 18: Hydraulic tortuosity-positivity trend for randomly distributed squares. The flow pathways are more tortuous as geometry is comprised of more solid squares (i.e., lower porosity).

configurations, as the anisotropic ratios which we will discuss later using Figure 16(b) will indicate.) In agreement with results presented in [13], the trend shown in Figure 18 indicates that the flow pathways are more tortuous as the geometry is comprised of more solid squares.

4.3.2. *Fit to Kozeny-Carman Equation.* As presented in Section 2.2, the Kozeny-Carman equation relates permeability k to porosity ϕ , hydraulic tortuosity τ_h , specific surface area S , and a fitting coefficient β_k (which we refer to as the shape factor). Specific surface area for the range of porosities was computed by (3) and is shown in Figure 19. The specific

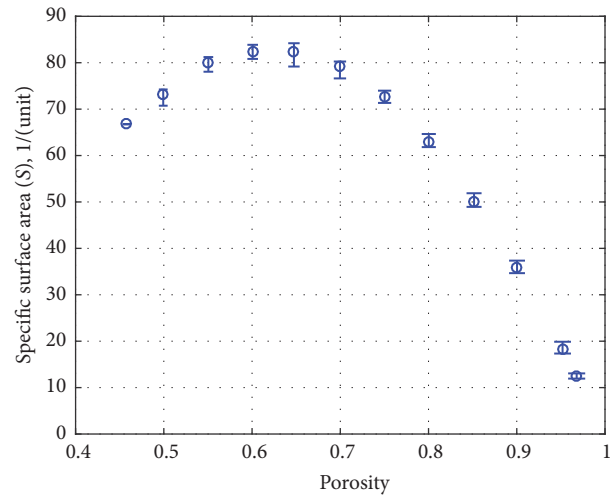


FIGURE 19: Specific surface area for randomly distributed squares, over the range of porosities studied. Specific surface area increases linearly as porosity decreases; however this trend deviates at lower porosities due to the large nonuniform shapes introduced into the lower porosity geometries.

surface area increases as the porosity decreases because the geometry is comprised of more solid squares. However, once the porosity is lowered to the point where isolated fluid sites must be converted to large solid areas, the fluid-solid interfacial area is reduced along with the specific surface area. We computed the shape factor β_k by (2) for this particular pore geometry, using our permeability, hydraulic tortuosity, and specific surface area data presented in Figures 15(a), 18, and 19, respectively. The trend for β_k over the porosities is plotted in Figure 20, and we observe that the shape factor does not change significantly within a porosity interval of $0.7 < \phi < 0.90$, which was similarly reported in Duda et al. [13].

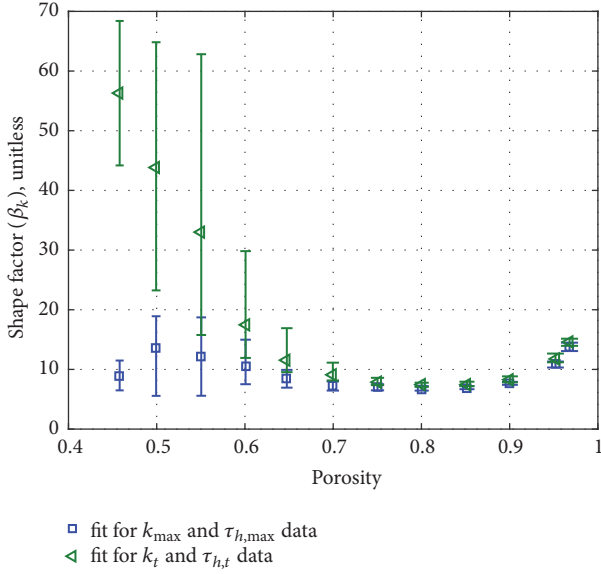


FIGURE 20: Shape factor, β_k , used to fit simulated permeability and hydraulic tortuosity data to Kozeny-Carman equation for geometries comprised of randomly distributed squares. β_k appears to be constant between $0.7 < \phi < 0.9$.

4.3.3. Diffusive Tortuosity. We obtained diffusive tortuosity for this geometry using different convergence criteria for three ranges of porosities due to high mesh refinement requirements. Convergence criteria of $\tau_{\text{rel error}} < 3\%$, 2% , and 1% were used for porosity ranges of $0.45 < \phi < 0.58$, $0.58 < \phi < 0.7$, and $0.7 < \phi < 0.99$, respectively. The geometries were generated using a mesh of 100×100 , and the convergence criteria required a refinement of 2000×2000 for the lowest porosity and 200×200 for the highest porosity. Results for a geometry of $\phi = 0.7$ are shown in Figure 21, and the resulting diffusive tortuosity tensor is

$$\tau_d = \begin{bmatrix} \tau_{d,xx} & \tau_{d,xy} \\ \tau_{d,yx} & \tau_{d,yy} \end{bmatrix} = \begin{bmatrix} 2.7584 & -0.2914 \\ -0.2914 & 2.6175 \end{bmatrix}. \quad (43)$$

Notice the tensor is symmetric (i.e., $\tau_{d,xy} = \tau_{d,yx}$) but *not* diagonal (i.e., the off-diagonal components are nonzero). As such, we diagonalized the full diffusive tortuosity tensor and results for the whole porosity range studied are presented in Figure 22.

4.3.4. Comparison of Tortuosities for Randomly Distributed Squares. Our hydraulic and diffusive tortuosity data are plotted in Figure 23 for a range of porosity values, along with some of the trends from literature that we reported in Tables 2 and 3. The trend from Koponen et al. [26] was obtained for hydraulic tortuosity for randomly distributed squares. The trend from Mackie and Meares [50] was for diffusive transport of electrolytes through a membrane, and their expression for the tortuosity-porosity trend was credited in the past as one of the most successfully employed correlations for membrane systems [51]. The trend from Weissberg [52] was also for diffusive transport, through a geometry comprised of uniform spheres. It was given as an upper bound

for effective diffusion and thus could be considered as the lower bound for diffusive tortuosity since they are inversely related. Our hydraulic data fits moderately close with the Koponen et al.'s [26] trend. Our diffusion data follows a similar trend to Mackie and Meares [50] until $\phi < 0.6$ and remains above Weissberg's [52] lower bound. In general, our data demonstrates that diffusive tortuosity is not equivalent to hydraulic tortuosity and can be up to ten times greater, especially at low porosities.

4.3.5. Induced Anisotropic Properties at Lower Porosity Geometries. Due to the method we used to generate the randomly distributed squares geometry, anisotropic properties were introduced into the pore structure, especially at lower porosities. This is evident in Figure 24, where low and medium porosities are compared. The lower porosity has large, nonuniform solid shapes within the geometry. To represent the connected pore space or effective pore space [26], we filled in the isolated fluid sites, which resulted from the random distribution of squares in the domain. The result is a nonuniform distribution of solids in the geometry and an induced degree of anisotropy that is shown in Figure 16(b). (Note that Figure 16(a) shows that the rotation required to obtain the diagonal tensors, \mathbf{k}^* and τ_d^* , is independent of porosity.) At the higher porosities, the degree of anisotropy of all three properties is moderately close to one, and thus we could consider those geometries as exhibiting isotropic behavior. As the porosity is lowered, the permeability and diffusive tortuosity become anisotropic and the degree of anisotropy of the permeability is higher than that of the diffusive tortuosity. The degree of anisotropy of hydraulic tortuosity is less than diffusive tortuosity and is close to being isotropic for most of the porosity range. A possible reason for this finding is that hydraulic flow develops preferential pathways where the fluid speed is highest along a pathway that is unhindered by solids, as shown in Figure 25(b). If vertical and horizontal preferential pathways are geometrically similar, an isotropic hydraulic tortuosity is exhibited. On the other hand, the diffusive speeds are highest adjacent to the fluid-solid boundaries, as seen in Figure 25(d); thus the geometry of the pore structure appears to impact the diffusive tortuosity more than it impacts the hydraulic tortuosity. (This point is also illustrated by comparing the flows in a higher porosity, in Figures 17(b) and 21(d).)

5. Conclusion

In this study, we computed the effective properties known as permeability, hydraulic tortuosity, and diffusive tortuosity, using well-known and commonly employed formulations based on the method of homogenization. While we noted that past work has recognized the difference between tortuosity types, we emphasized that a few studies have failed to distinguish the difference and have mistakenly used them interchangeably. In this work, hydraulic tortuosity was computed based on the approach given in Koponen et al. [19, 26]. Their approach uses pore space velocity fields \mathbf{v} ; however we used the rescaled velocity fields N_{ij} which we obtained by solving a set of rescaled Stokes equations formulated

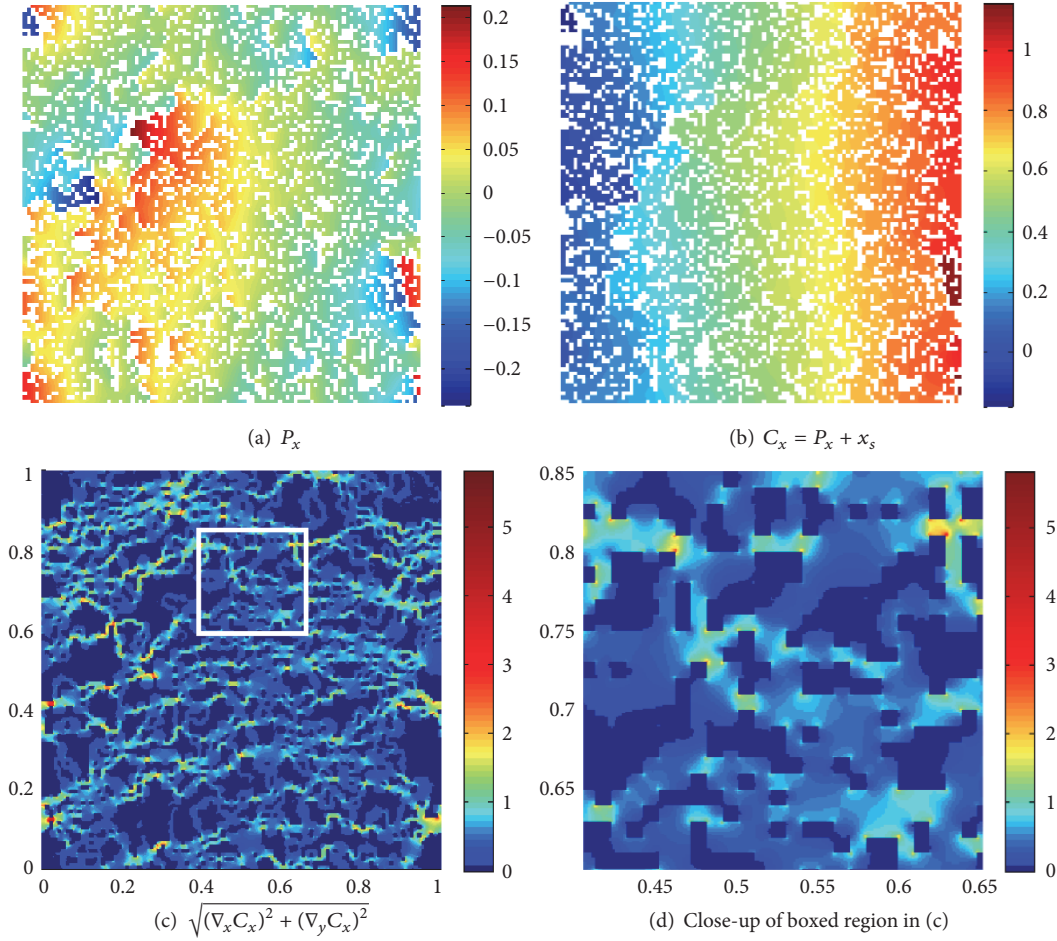


FIGURE 21: Fields for geometry of randomly distributed squares, $\phi = 0.7$: (a) solution to the homogenization problem, (b) concentration field transformed from P_k (assuming concentration gradient across unit cell is one), and (c, d) magnitude of concentration gradient (diffusion speed).

by homogenization ((10)–(12)). Using N_{ij} in (28) is mathematically equivalent to using \mathbf{v} in (25) and (27). Diffusive tortuosity was computed by solving the homogenized or boundary-value problem given for the effective diffusion coefficient, as employed in Kim et al. [43], Valdés-Parada et al. [1], and Sun et al. [27].

We generated several different pore geometries, including both in-line array and staggered-array of uniform shapes, and randomly distributed squares. For the in-line array of circles geometry, our simulated permeability data was validated against the analytical solution from Gebart [47], and our simulated diffusive tortuosity data was validated against Rayleigh’s [48] trend. We studied the anisotropy of the computed properties and fit data from one of the pore geometries to the Kozeny-Carman equation to obtain the shape factor β_k .

The main findings from the geometries studied are as follows:

- (1) Hydraulic tortuosity is *not* equal to diffusive tortuosity in the same pore geometry. In the in-line array of uniform shapes (either circle or square),

hydraulic tortuosity was weakly dependent on porosity, while diffusive tortuosity was almost linearly related to porosity (recall Figure 6). In the randomly distributed squares geometry, the diffusive tortuosity was greater (up to a factor of ten) than hydraulic tortuosity as porosity decreased (recall Figure 23). In all examples, hydraulic speeds were highest along the mid-channel space between adjacent solids and formed a parabolic velocity profile, while diffusive speeds were highest along the fluid-solid boundary which could be extremely irregular or complex (as seen in the randomly distributed squares geometry); we suspected this boundary impact on flow to be the main reason why these two tortuosity types were quantitatively different in the same pore geometry.

- (2) Results from the three different pore geometry configurations used in this work indicate that $\tau_d > \tau_h$ for the majority of the porosity range tested. However, we do not claim that this relationship is necessarily true for all types of porous media. For example, a pore

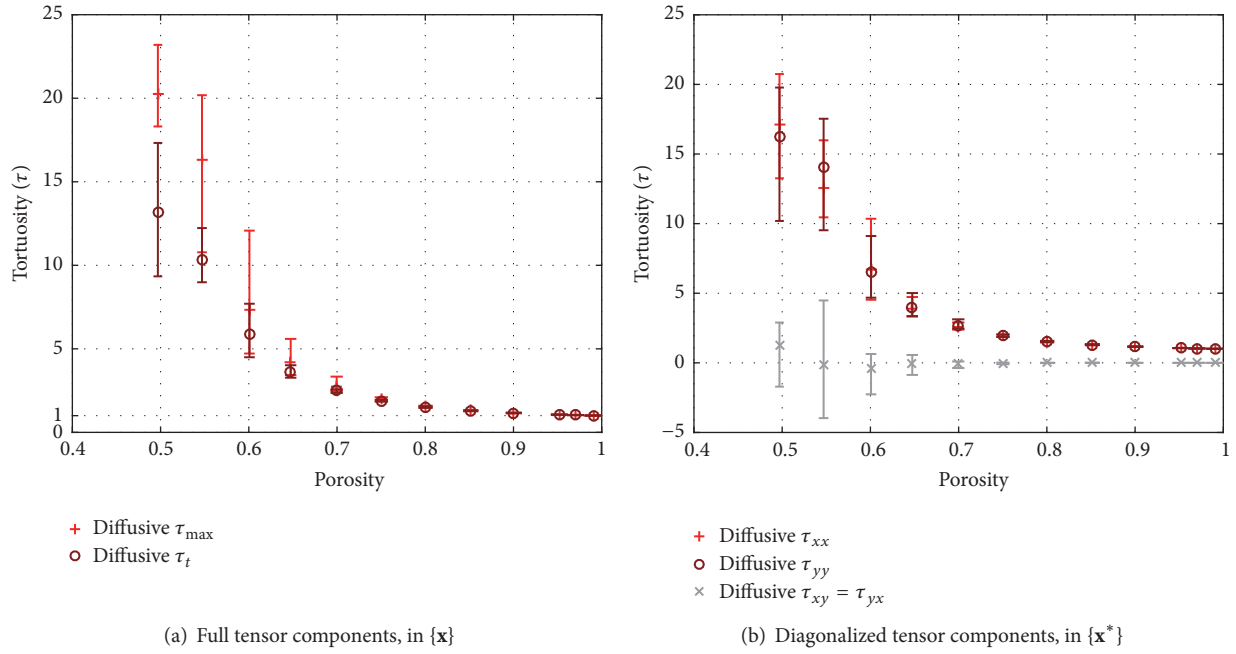


FIGURE 22: Diffusive tortuosity-positivity trend for randomly distributed squares. The full diffusive tortuosity tensor contains nonzero off-diagonal components and is diagonalized to obtain the principal diffusive tortuosity components, $\tau_{d,\max}$ and $\tau_{d,t}$. $\{x\}$ and $\{x^*\}$ are related by rotation angle θ_d , which is plotted in Figure 16(a). The anisotropic ratio of the principal components is plotted in Figure 16(b).

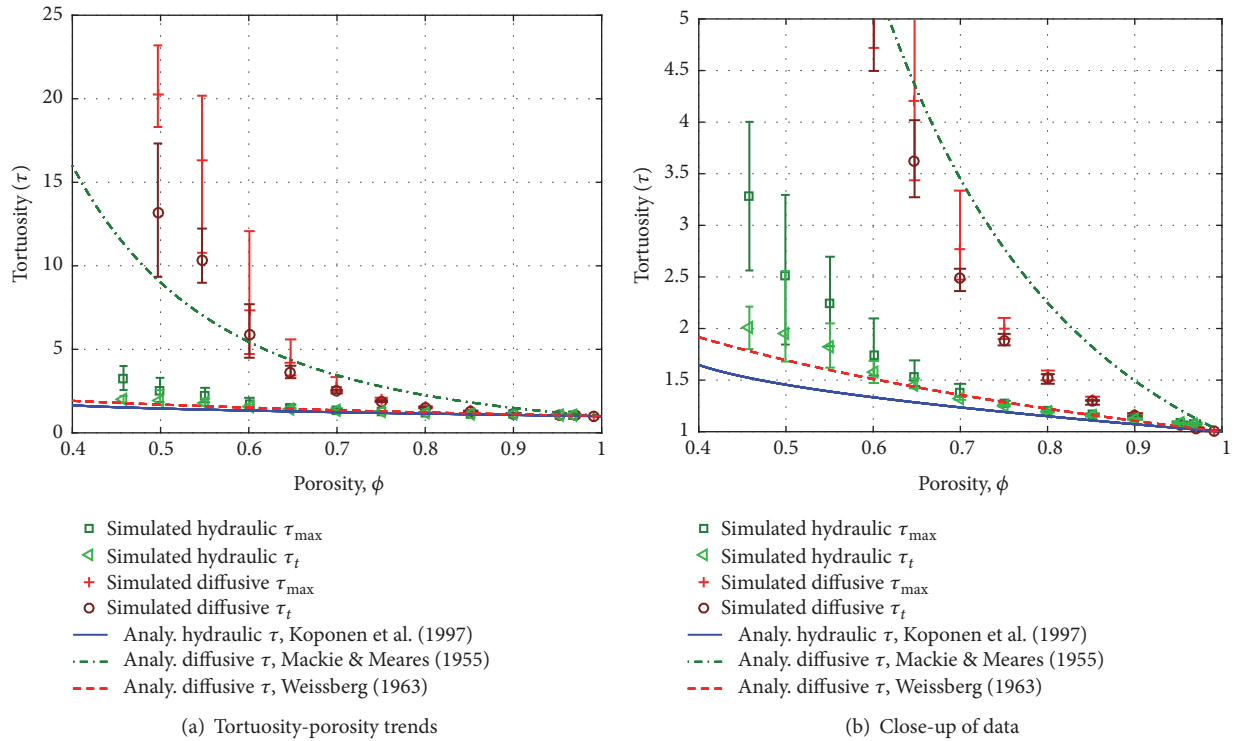


FIGURE 23: Comparison of hydraulic ($\tau_{h,x}$ and $\tau_{h,y}$) and diffusive ($\tau_{d,xx}$ and $\tau_{d,yy}$) tortuosity trends for pore structures of randomly distributed squares, against trends reported in literature.

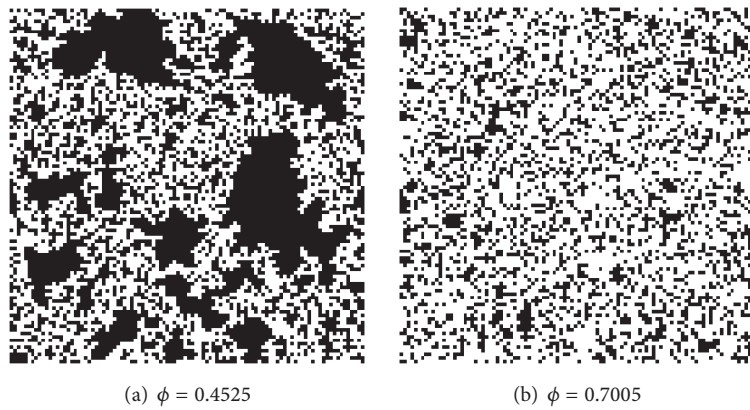


FIGURE 24: Induced anisotropy in lower porosity geometries comprised of randomly distributed squares.

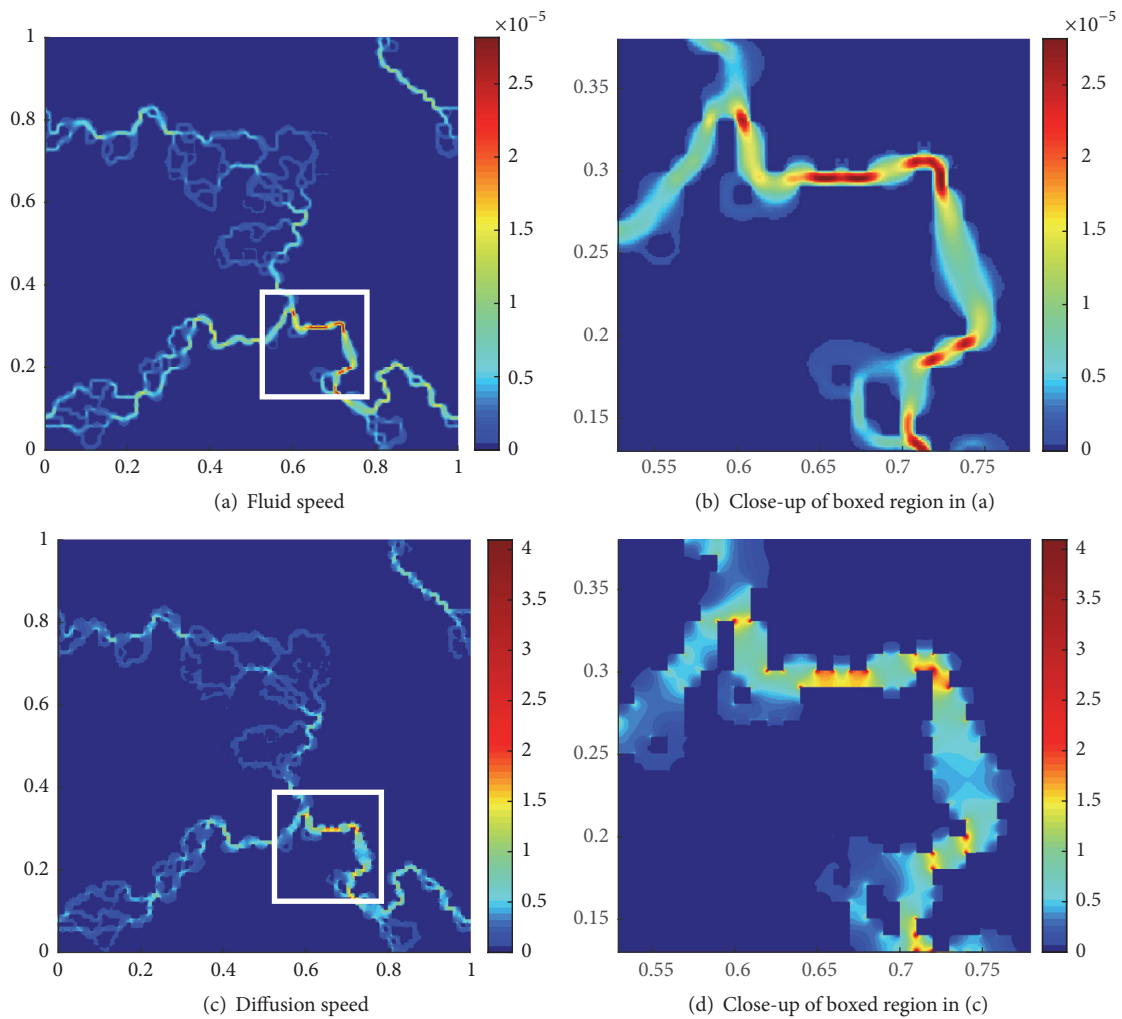


FIGURE 25: Comparison of hydraulic and diffusive flows through a low porosity geometry comprised of randomly distributed squares: $\phi = 0.45$. (a, b) Fluid flow driven by g_x . (c, d) Diffusive flow driven by $\nabla C = 1$ from west to east. “Hot spots” of fastest moving hydraulic flow are evident in channel centers, while diffusive speeds are fastest along fluid-solid boundaries.

network model that was considered in Ghanbarian et al. [8] led to the conclusion that $\tau_d \leq \tau_h$. Thus we simply note an equality held true for the three types of synthetic porous media tested in our work.

- (3) Related to the first point, hydraulic and diffusive tortuosity (as well as permeability) can exhibit different anisotropic behavior in the same pore geometry. In the staggered-array of uniform shapes (square), we observed that the hydraulic tortuosity had a greater degree of anisotropy compared to diffusive tortuosity's anisotropy (recall Figure 10). This behavior was due to the nature of the geometry, which allowed for a nontortuous hydraulic flow in one of the principal directions. In the randomly distributed squares, the large nonuniform shapes that were introduced into the geometry as a result of isolated fluid sites led to an induced anisotropic behavior; at higher porosities, all properties exhibited essentially isotropic behavior, but at lower porosities, \mathbf{k} and τ_d became anisotropic by varying degrees. It is interesting to note that τ_h displays the least degree of anisotropic behavior; this finding may be related to the existence of preferential pathways or regions of high-speed flow through minimally tortuous pathways within the pore geometry.
- (4) Two geometries (i.e., staggered-array of squares, randomly distributed squares) demonstrated that when the permeability is anisotropic, the effective diffusion coefficient (which is inversely proportional to diffusive tortuosity) can also be anisotropic however not necessarily by the same degree. In general, the degree of anisotropic permeability was greater than the degree of anisotropic diffusion in the same pore geometry (recall Figures 10 and 16(b)). This finding has important implications for flow and transport modeling at reservoir-scale because the use of Darcy's equation and a transport equation (with a diffusive flux term) requires permeability and the effective diffusion coefficient as input parameters, respectively.
- (5) A few qualitative statements can be made regarding the flow behavior demonstrated in some of the examples (i.e., staggered-array of squares and randomly distributed squares). Hydraulic tortuosity and permeability are generally related; the more tortuous the flow pathway is in a direction, the slower the fluid speed is and the less permeable it is in that direction. Lower porosity geometries are characterized by slower fluid speeds and more tortuous hydraulic pathways, in addition to more tortuous diffusive pathways. By (37), which shows the effective diffusion coefficient is inversely proportional to diffusive tortuosity, we can deduce that the more tortuous the diffusing flow in a direction, the slower the rate of (effective) diffusive transport.

Appendix

A. Validation of Permeability Calculation

To validate our numerical implementation and computation of permeability, we compared our results with the analytical solution given by Gebart [47]. This analytical solution of permeability corresponds to an in-line array of infinitely long cylinders. The porosity is computed as a function of the cylindrical radius r as follows:

$$\phi = \frac{V_f}{V_t} = \frac{V_t - V_s}{V_t} = 1 - \frac{V_s}{V_t} = 1 - \frac{\pi r^2}{L^2}, \quad (\text{A.1})$$

where V_f, V_s are the fluid and solid volumes, respectively, $V_t = V_f + V_s$ is the total volume, and the unit cell is $L \times L$. Thus by varying r , the porosity is also varied. Gebart's [47] analytical solution for permeability (normalized by r) as a function of porosity is

$$\frac{K}{r^2} = c_g \left(\sqrt{\frac{1 - \phi_c}{1 - \phi}} - 1 \right)^{5/2}, \quad (\text{A.2})$$

where c_g is the geometric factor which depends on the fiber arrangement, and ϕ_c is the critical porosity (percolation threshold). For a quadratic fiber arrangement, the geometric factor is $16/9\pi\sqrt{2}$, and the percolation threshold is $\phi_c = 1 - \pi/4$ for an array of cylinders.

B. Validation of Diffusive Tortuosity Calculation

For benchmarking purposes, we computed the diffusive tortuosity for staggered unit cells and compared our results to those reported by Kim et al. [43], who used the boundary element method (BEM). In our work, we used finite difference. The method to compute the diffusive tortuosity tensor was presented Section 3.3, and for a 2D problem the tensor components are computed by

$$\begin{bmatrix} \tau_{d,xx} & \tau_{d,xy} \\ \tau_{d,yx} & \tau_{d,yy} \end{bmatrix} = \begin{bmatrix} 1 + \frac{1}{V_f} \int_{V_f} \frac{\partial P_x}{\partial x} dV_f & \frac{1}{V_f} \int_{V_f} \frac{\partial P_y}{\partial x} dV_f \\ \frac{1}{V_f} \int_{V_f} \frac{\partial P_x}{\partial y} dV_f & 1 + \frac{1}{V_f} \int_{V_f} \frac{\partial P_y}{\partial y} dV_f \end{bmatrix}^{-1}, \quad (\text{B.1})$$

where $V_f = Y_f$. Note that diffusive tortuosity is the inverse of the diffusive tortuosity factor, that is, $\tau_d = (\tau'_d)^{-1}$. Recalling (37), the diffusive tortuosity factor is related to the effective diffusion coefficient by

$$\phi \tau'_d = \frac{\phi \mathbf{D}^{\text{eff}}}{D}, \quad (\text{B.2})$$

where $\phi \mathbf{D}^{\text{eff}} = \mathbf{D}^{\text{eff}*}$. The form of (B.2) helps to make appropriate comparisons in Table 6. The input parameters required

to construct the staggered unit cell are porosity ϕ , a/b ratio, and L_a/L_b ratio, and it is constructed to meet the configuration presented in Figure 8. Kim et al. [43] performed measurements on many staggered unit cell cases, and Table 6 presents a comprehensive comparison of our results against their data.

Disclosure

Rebecca Allen is now at SINTEF Digital, Mathematics and Cybernetics, Forskningsveien 1, 0314 Oslo, Norway.

Competing Interests

The authors declare that there is no conflict of interests regarding the publication of this paper.

Acknowledgments

The authors gratefully acknowledge that the research reported in this publication was supported by funding from King Abdullah University of Science and Technology (KAUST). The authors gratefully acknowledge and thank Dr. Francisco J. Valdés-Parada for providing the diffusive tortuosity results for in-line array of circle and square geometries, which were used for comparison in Figure 6 with permission.

References

- [1] F. J. Valdés-Parada, M. L. Porter, and B. D. Wood, "The role of tortuosity in upscaling," *Transport in Porous Media*, vol. 88, no. 1, pp. 1–30, 2011.
- [2] M. A. Knackstedt, S. Latham, M. Madadi, A. Sheppard, T. Varslot, and C. Arns, "Digital rock physics: 3D imaging of core material and correlations to acoustic and flow properties," *Leading Edge*, vol. 28, no. 1, pp. 28–33, 2009.
- [3] H. Andrä, N. Combaret, J. Dvorkin et al., "Digital rock physics benchmarks—part I: imaging and segmentation," *Computers & Geosciences*, vol. 50, pp. 25–32, 2013.
- [4] S. Torquato and Y. Jiao, "Robust algorithm to generate a diverse class of dense disordered and ordered sphere packings via linear programming," *Physical Review E. Statistical, Nonlinear, and Soft Matter Physics*, vol. 82, no. 6, article 061302, 2010.
- [5] C. L. Y. Yeong and S. Torquato, "Reconstructing random media," *Physical Review E. Statistical, Nonlinear, and Soft Matter Physics*, vol. 57, no. 1, pp. 495–506, 1998.
- [6] A. Yang, C. T. Miller, and L. D. Turcoliver, "Simulation of correlated and uncorrelated packing of random size spheres," *Physical Review E - Statistical Physics, Plasmas, Fluids, and Related Interdisciplinary Topics*, vol. 53, no. 2, article 1516, 1996.
- [7] A. Cancelliere, C. Chang, E. Foti, D. H. Rothman, and S. Succi, "The permeability of a random medium: comparison of simulation with theory," *Physics of Fluids A: Fluid Dynamics*, vol. 2, no. 12, pp. 2085–2088, 1990.
- [8] B. Ghanbarian, A. G. Hunt, R. P. Ewing, and M. Sahimi, "Tortuosity in porous media: a critical review," *Soil Science Society of America Journal*, vol. 77, no. 5, pp. 1461–1477, 2013.
- [9] X. Zhang and M. A. Knackstedt, "Direct simulation of electrical and hydraulic tortuosity in porous solids," *Geophysical Research Letters*, vol. 22, no. 17, pp. 2333–2336, 1995.
- [10] E. Sanchez-Palencia, "Homogenization method for the study of composite media," in *Asymptotic Analysis II*, pp. 192–214, Springer, 1983.
- [11] J. Bear and A. H. Cheng, *Modeling Groundwater Flow and Contaminant Transport*, vol. 23 of *Theory and Applications of Transport in Porous Media*, Springer, 2010.
- [12] P. Mostaghimi, M. J. Blunt, and B. Bijeljic, "Computations of absolute permeability on micro-CT image," *Mathematical Geosciences*, vol. 45, no. 1, pp. 103–125, 2013.
- [13] A. Duda, Z. Koza, and M. Matyka, "Hydraulic tortuosity in arbitrary porous media flow," *Physical Review E*, vol. 84, no. 3, Article ID 036319, pp. 1–8, 2011.
- [14] A. Ebrahimi Khabbazi, J. S. Ellis, and A. Bazylak, "Developing a new form of the Kozeny-Carman parameter for structured porous media through lattice-Boltzmann modeling," *Computers & Fluids*, vol. 75, pp. 35–41, 2013.
- [15] H. Andrä, N. Combaret, J. Dvorkin et al., "Digital rock physics benchmarks—part II: computing effective properties," *Computers & Geosciences*, vol. 50, pp. 33–43, 2013.
- [16] A. Nabovati, J. Hinebaugh, A. Bazylak, and C. H. Amon, "Effect of porosity heterogeneity on the permeability and tortuosity of gas diffusion layers in polymer electrolyte membrane fuel cells," *Journal of Power Sources*, vol. 248, pp. 83–90, 2014.
- [17] P. Carman, "Fluid flow through granular beds," *Transactions-Institution of Chemical Engineers*, vol. 15, 1937.
- [18] P. C. Carman, "Permeability of saturated sands, soils and clays," *The Journal of Agricultural Science*, vol. 29, no. 2, pp. 262–273, 1939.
- [19] A. Koponen, M. Kataja, and J. Timonen, "Tortuous flow in porous media," *Physical Review E*, vol. 54, no. 1, pp. 406–410, 1996.
- [20] W. D. Carrier III, "Goodbye, Hazen; hello, Kozeny-Carman," *Journal of Geotechnical and Geoenvironmental Engineering*, vol. 129, no. 11, pp. 1054–1056, 2003.
- [21] J. D. Hyman, P. K. Smolarkiewicz, and C. Larrabee Winter, "Pedotransfer functions for permeability: a computational study at pore scales," *Water Resources Research*, vol. 49, no. 4, pp. 2080–2092, 2013.
- [22] F. D. E. Latief and U. Fauzi, "Kozeny-Carman and empirical formula for the permeability of computer rock models," *International Journal of Rock Mechanics and Mining Sciences*, vol. 50, pp. 117–123, 2012.
- [23] P. Xu and B. Yu, "Developing a new form of permeability and Kozeny-Carman constant for homogeneous porous media by means of fractal geometry," *Advances in Water Resources*, vol. 31, no. 1, pp. 74–81, 2008.
- [24] M. Matyka, A. Khalili, and Z. Koza, "Tortuosity-porosity relation in porous media flow," *Physical Review E*, vol. 78, no. 2, Article ID 026306, 2008.
- [25] T. Ohkubo, "Tortuosity based on anisotropic diffusion process in structured plate-like obstacles by Monte Carlo simulation," *Transport in Porous Media*, vol. 72, no. 3, pp. 339–350, 2008.
- [26] A. Koponen, M. Kataja, and J. Timonen, "Permeability and effective porosity of porous media," *Physical Review E*, vol. 56, no. 3, pp. 3319–3325, 1997.
- [27] Z. Sun, X. Tang, and G. Cheng, "Numerical simulation for tortuosity of porous media," *Microporous and Mesoporous Materials*, vol. 173, pp. 37–42, 2013.
- [28] C. David, "Geometry of flow paths for fluid transport in rocks," *Journal of Geophysical Research*, vol. 98, no. 7, pp. 12–278, 1993.

- [29] M. Quintard, L. Bletzacker, D. Chenu, and S. Whitaker, "Non-linear, multicomponent, mass transport in porous media," *Chemical Engineering Science*, vol. 61, no. 8, pp. 2643–2669, 2006.
- [30] L. Shen and Z. Chen, "Critical review of the impact of tortuosity on diffusion," *Chemical Engineering Science*, vol. 62, no. 14, pp. 3748–3755, 2007.
- [31] B. P. Boudreau, "The diffusive tortuosity of fine-grained unlithified sediments," *Geochimica et Cosmochimica Acta*, vol. 60, no. 16, pp. 3139–3142, 1996.
- [32] M. M. Ahmadi, S. Mohammadi, and A. N. Hayati, "Analytical derivation of tortuosity and permeability of monosized spheres: a volume averaging approach," *Physical Review E - Statistical, Nonlinear, and Soft Matter Physics*, vol. 83, no. 2, article 026312, 2011.
- [33] A. Nabovati and A. C. M. Sousa, "Fluid flow simulation in random porous media at pore level using the lattice Boltzmann method," *Journal of Engineering Science and Technology*, vol. 2, no. 3, pp. 226–237, 2007.
- [34] Z. Koza, M. Matyka, and A. Khalili, "Finite-size anisotropy in statistically uniform porous media," *Physical Review E*, vol. 79, no. 6, Article ID 066306, pp. 1–7, 2009.
- [35] Y. Liu and P. K. Kitanidis, "Tortuosity and Archie's law," in *Advances in Hydrogeology*, P. K. Mishra and K. L. Kuhlman, Eds., chapter 6, pp. 115–126, Springer, New York, NY, USA, 2013.
- [36] F. H. Harlow and J. E. Welch, "Numerical calculation of time-dependent viscous incompressible flow of fluid with free surface," *The Physics of Fluids*, vol. 8, no. 12, pp. 2182–2189, 1965.
- [37] S. Sun, A. Salama, and M. F. El Amin, "Matrix-oriented implementation for the numerical solution of the partial differential equations governing flows and transport in porous media," *Computers and Fluids*, vol. 68, pp. 38–46, 2012.
- [38] J. R. Fanchi, "Mathematics of fluid flow," in *Petroleum Engineering Handbook*, L. W. Lake, Ed., chapter 2, pp. 45–76, Society of Petroleum Engineers, 2007, [http://petrowiki.org/PEH%3AMathematics of Fluid Flow](http://petrowiki.org/PEH%3AMathematics%20of%20Fluid%20Flow).
- [39] A. Ghassemi and A. Pak, "Pore scale study of permeability and tortuosity for flow through particulate media using Lattice Boltzmann method," *International Journal for Numerical and Analytical Methods in Geomechanics*, vol. 35, no. 8, pp. 886–901, 2011.
- [40] M. Icardi, G. Boccardo, D. L. Marchisio, T. Tosco, and R. Sethi, "Pore-scale simulation of fluid flow and solute dispersion in three-dimensional porous media," *Physical Review E—Statistical, Nonlinear, and Soft Matter Physics*, vol. 90, no. 1, Article ID 013032, 2014.
- [41] M. M. Clark, *Transport Modeling for Environmental Engineers and Scientists*, John Wiley & Sons, 2nd edition, 2009.
- [42] J. A. Ochoa, S. Whitaker, and P. Stroeve, "Determination of cell membrane permeability in concentrated cell ensembles," *Biophysical Journal*, vol. 52, no. 5, pp. 763–774, 1987.
- [43] J. Kim, J. Ochoa, and S. Whitaker, "Diffusion in anisotropic porous media," *Transport in Porous Media*, vol. 2, no. 4, pp. 327–356, 1987.
- [44] A. E. Sáez, J. C. Perfetti, and I. Rusinek, "Prediction of effective diffusivities in porous media using spatially periodic models," *Transport in Porous Media*, vol. 6, no. 2, pp. 143–157, 1991.
- [45] S. Beyhaghi and K. M. Pillai, "Estimation of tortuosity and effective diffusivity tensors using closure formulation in a sintered polymer wick during transport of a nondilute, multicomponent liquid mixture," *Special Topics and Reviews in Porous Media*, vol. 2, no. 4, pp. 267–282, 2011.
- [46] Y. Yong, X. Lou, S. Li, C. Yang, and X. Yin, "Direct simulation of the influence of the pore structure on the diffusion process in porous media," *Computers & Mathematics with Applications*, vol. 67, no. 2, pp. 412–423, 2014.
- [47] B. R. Gebart, "Permeability of unidirectional reinforcements for RTM," *Journal of Composite Materials*, vol. 26, no. 8, pp. 1100–1133, 1992.
- [48] L. Rayleigh, "LVI. On the influence of obstacles arranged in rectangular order upon the properties of a medium," *Philosophical Magazine Series 5*, vol. 34, no. 211, Article ID 481502, pp. 481–502, 1892.
- [49] D. Ryan, R. Carbonell, and S. Whitaker, "A theory of diffusion and reaction in porous media," in *Proceedings of the American Institute of Chemical Engineers*, vol. 71 of *AICHE Symposium Series 202*, pp. 46–62, January 1981.
- [50] J. S. Mackie and P. Meares, "The diffusion of electrolytes in a cation-exchange resin membrane. I. Theoretical," *Proceedings of the Royal Society A: Mathematical, Physical and Engineering Sciences*, vol. 232, no. 1191, pp. 498–509, 1955.
- [51] S. B. Iversen, V. K. Bhatia, K. Dam-Johansen, and G. Jonsson, "Characterization of microporous membranes for use in membrane contactors," *Journal of Membrane Science*, vol. 130, no. 1–2, pp. 205–217, 1997.
- [52] H. L. Weissberg, "Effective diffusion coefficient in porous media," *Journal of Applied Physics*, vol. 34, no. 9, pp. 2636–2639, 1963.
- [53] M. C. Sukop, H. Huang, P. F. Alvarez, E. A. Variano, and K. J. Cunningham, "Evaluation of permeability and non-Darcy flow in vuggy macroporous limestone aquifer samples with lattice Boltzmann methods," *Water Resources Research*, vol. 49, no. 1, pp. 216–230, 2013.
- [54] J. Comiti and M. Renaud, "A new model for determining mean structure parameters of fixed beds from pressure drop measurements: application to beds packed with parallelepipedal particles," *Chemical Engineering Science*, vol. 44, no. 7, pp. 1539–1545, 1989.
- [55] E. du Plessis, S. Woudberg, and J. Prieur du Plessis, "Pore-scale modelling of diffusion in unconsolidated porous structures," *Chemical Engineering Science*, vol. 65, no. 8, pp. 2541–2551, 2010.
- [56] L. Pisani, "Simple expression for the tortuosity of porous media," *Transport in Porous Media*, vol. 88, no. 2, pp. 193–203, 2011.
- [57] J. A. Ochoa-Tapia, P. Stroeve, and S. Whitaker, "Diffusive transport in two-phase media: spatially periodic models and Maxwell's theory for isotropic and anisotropic systems," *Chemical Engineering Science*, vol. 49, no. 5, pp. 709–726, 1994.